Electrophilic Fluorination of Organometallic Fragments

Lewis Marshall Hall

Doctor of Philosophy

University of York

Chemistry

September 2018

Abstract

The electrophilic fluorination of protio-substituted ruthenium alkynyl complexes, $[Ru(\eta^5\text{-}C_5Me_5)(PPh_3)_2(C{\equiv}C\text{-}H)]$, $[Ru(\eta^5\text{-}C_5Me_5)(dppe)(C{\equiv}C\text{-}H)]$, and *trans*-$[ClRu(dppe)_2(C{\equiv}C\text{-}H)]$ is reported, along with a discussion on the influence of fluorine on the spectroscopic parameters of fluorovinylidene complexes. The synthesis of the first mononuclear organometallic fluoroalkynyl complexes ($[Ru(\eta^5\text{-}C_5Me_5)(PPh_3)_2(C{\equiv}C\text{-}F)]$, $[Ru(\eta^5\text{-}C_5Me_5)(dppe)(C{\equiv}C\text{-}F)]$, and $[ClRu(dppe)_2(C{\equiv}C\text{-}F)]$) is also reported. Their stability towards dimerisation and the nature of the alkynyl ligand were probed by computational and spectroscopic methods. The reactivity of the ruthenium fluoroalkynyl complexes with an electrophilic source of fluorine afforded difluorovinylidene complexes, $[Ru(\eta^5\text{-}C_5Me_5)(dppe)(=C=CF_2)]^+$ and *trans*-$[ClRu(dppe)_2(=C=CF_2)]^+$.

The reactivity of ruthenium fluorovinylidene complexes, $[Ru(\eta^5\text{-}C_5Me_5)(PPh_3)_2(=C=CFH)]^+$, $[Ru(\eta^5\text{-}C_5Me_5)(dppe)(=C=CFH)]^+$, *trans*-$[ClRu(dppe)_2(=C=CFH)]^+$, $[Ru(\eta^5\text{-}C_5H_5)(PPh_3)_2(=C=CFPh)]^+$, and $[Ru(\eta^5\text{-}C_5H_5)(dppe)(=C=CFPh)]^+$, have been explored. Attempts to liberate a fluoroalkyne were unsuccessful on addition of: carbon monoxide, dihydrogen, acetonitrile, and triphenylphosphine. Facile methods for accessing fluorinated carbene complexes (e.g. $([Ru(\eta^5\text{-}C_5H_5)(dppe)(=CFCPhHF)]^+$) by addition of nucleophiles and acids are discussed, along with the liberation of fluorinated alkenes (e.g. FHC=CFPh) in the presence of a chloride source.

The reactivity of complexes *trans*-$[ClRu(dppe)_2(C{\equiv}CR)]$ (R= electron-donating and electron-withdrawing groups) towards electrophilic fluorinating agents, NFSI, $[FTMP]BF_4$, and Selectfluor, have been explored. Fluorination of *trans*-$[ClRu(dppe)_2(C{\equiv}CR)]$ complexes to give the corresponding *trans*-$[ClRu(dppe)_2(=C=CFR)]^+$ complexes was only observed with Selectfluor. One-electron oxidation of *trans*-$[ClRu(dppe)_2(C{\equiv}CR)]$ complexes was observed for all fluorinating agents. The mechanism of fluorination was probed by experimental and computational approaches, including radical-trap and combined UV-Vis-NMR experiments. The study revealed that oxidation and fluorination are competing pathways.

The fluorination of *trans*-$[ClRu(dppe)_2(C{\equiv}CPh)]$, by NFSI, $[FTMP]BF_4$, and Selectfluor, was probed through relaxed potential energy surface (PES) scans with Density Functional Theory (DFT) studies. The PES scans for both a closed-shell 'S_N2' and open-shell single electron transfer (SET) mechanism were explored. The scans suggest that fluorination using Selectfluor occurs by a rapid 'SET' mechanism.

List of Contents

List of Tables

List of Figures

List of Schemes

List of Accompanying Material

A compact disk is attached at the back of this thesis which contains:

- CIF files for X-ray crystallography.
- Computational information, tables of energies, coord.xyz files, vibrational frequencies, and SCF energies.
- Additional UV-Vis spectra for Chapter 4.
- NMR Data.
- An electronic copy of this thesis.

Acknowledgements

Writing this acknowledgements section has been one of the hardest parts of my thesis to write. How personal do I make it? Where do I start? Have I thanked everyone? I have met so many amazing people that have had a massive impact on me, it is impossible to go through them all. There have been many ups and many more downs, but without the support of these people, the work here would never have been possible.

Where would I be without my two fantastic supervisors Jason Lynam and John Slattery. A massive thank you to you both for all the support and advice you have given to me over the years, without it I would not be where I stand today. Not to mention thank you for providing me this opportunity to work with you both.

I would also like to thank Heather Fish for all the time you have spent training me to use, and maintain, the NMR spectrometers, as well as taking an interest in my progress and wellbeing. Thank you, Adrian, Natalie, Sam, and Rachel for spending countless hours solving terrible crystallographic data with lots of disorder; Karl and Rosaria for running all of my mass spectrometry experiments (I'm sorry for all the time you have spent running samples which did not contain what I wanted); Abby for your hard work repairing the many broken NMR and Schlenk tubes over the years; Steve and Mike for the all the chats we have had in stores and the free stuff you have given me. I would like to say a big thank you to Naser and Charlotte for all your hard work in E114, you are not thanked enough.

I would like to thank all the lunch group, which has constantly changed throughout the years, for providing such funny, interesting, and downright weird lunchtime conversions. So thank you Lucy, Lizzie, Luisa, Lucia, Ellis, Tom, Dan, Peter, the other Peter, Ben, Natalie, Danni, Lucy B, Frances, Charlotte, Joe, Dennis, Dilli, Ximeng, Claire, Nina, Rachel, Chris, the other Chris, the other, other, Chris, Mauricio, Alessio, Martin, Ale, Will, and the others I have shamefully forgot to mention.

I would like to especially thank all the SLUG members I have come to know. In particularly I would like to thank Lizzie for teaching me everything she knew about using Schlenk lines and gloveboxes. Lucia, thank you for all your help running the lab together and keeping me company when everyone else had left. I hope you are happy that the one time you jokingly called me lazy in front of Steve has stuck for good and now I am forever nicknamed 'lazy' in stores. Here you go Frances and Lucy, I want to thank you profusely, for all of the fun,

limericks and puns, I wish you all the best, truly. Joe and Charlotte, Ying and Yang, thank you both for providing such fun company along with Dilli and Ximeng, I wish you all the best in your research. Rachel, thank you for taking up the mantle of running the lab with Chris, and I hope you enjoy your time in Australia.

Chris, a big shout out goes to you. I have had so much fun working with you in the lab, all the songs and all the quotes, not to mention all the laughs we have had outside the lab. Best of luck with the rest of your PhD.

Luisa, I want to say a special thank you to you for all the times you have listened to my problems and been a source of great help. I will always remember the summer project I did with you in my second year of undergraduate and the natural gift I had with preparing cell cultures. I wish you all the best with your future, you will make an excellent academic.

Lucy, I cannot thank you enough for all your help and support, not to mention all the fun we've had. I will always remember the late-night drives with you and Luisa with fondness. I hope you continue to enjoy your work and keep in touch. I am looking at what you wrote to me in your acknowledgements right now, 'may all your NMRs be clean and your reactions catalytic.' I can't help but laugh at how much the opposite has been true. I can only pass this same wish onto Chris and Rachel and hope they have a more successful outcome. May history never repeat itself.

Nina don't go changing! Continue to change the lives and views of all those you meet for the better. You are an amazing person and care so much about your work and other people. You have been a massive, positive, influence on my life and I count myself exceedingly privileged to be your friend. Also, thanks for your help I guess. I hope you finish your PhD in three years, I know you can do it. Best of luck.

Martin, I couldn't ask for a better housemate, even if I tried. You have been an amazing friend and I want to thank you for putting up with me this past year. It has been a blast living with you and I wish I still could. I wish you all the best for your PhD, and hang on in there, it will be worth it.

Finally, I cannot begin to thank my parents enough for all the support and encouragement they have provided me throughout my life, but particularly during my PhD. Thank you for believing in me, I hope I make you proud.

Author's Declaration

I declare that the research presented in this thesis is, to the best of my knowledge, original and was carried out under the supervision of Dr Jason Lynam and Dr John Slattery in the Chemistry Department of the University of York between October 2014 and September 2018. This work has not been previously presented for an award at this, or any other, university. Contributions from other authors and co-workers are listed below and referenced in the appropriate chapters throughout this thesis.

- Mass spectrometry experiments were performed by Mr Karl Heaton or Miss Rosaria Cercola.
- X-ray crystallography data was collected by, or with the assistance of, Dr Adrian Whitwood, Dr Natalie Pridmore, Mr Sam Hart, or Mrs Rachel Parker.
- Elemental analyses were performed by Dr Graeme McAllister.
- DFT calculations for alkyne dimerisation reported in Chapter 2 were performed by Dr John Slattery.
- DFT calculations for bond dissociation energies (with the exception of the entries for *trans*-[ClRu(dppe)$_2$(C≡CR)] and [Ru(η^5-C_5Me_5)(PPh_3)$_2$(C≡CR)]) reported in Chapter 2 were performed by Dr Jason Lynam.
- The Brueckner coupled-cluster calculations reported in Chapter 2 were performed by Dr David Tew, University of Bristol.

The computational and experimental results presented in Chapter 2 were published in:

A Structurally Characterized Fluoroalkyne; Mr. Lewis M. Hall, Dr. David P. Tew, Dr. Natalie E. Pridmore, Dr. Adrian C. Whitwood, Dr. Jason M. Lynam, and Dr. John M. Slattery, *Angew. Chem. Int. Ed.*, 2016, **56**, 7551-74556.

Thesis Numbering System

(1) All compounds in Chapter 1 are labelled with **[1-#]** or **1-#** prefix.

(2) All compounds, known or novel, outside of Chapter 1 are given a unique number with not prefix

(3) All metal compounds are denoted within square brackets, i.e. **[#]**, with cationic or anionic complexes denoted by the counterion or charge next to the brackets, e.g. **[#]**$^{+}$ or **[#]**BF_4.

(4) Organic compounds are denoted by bold numbers, e.g. **#**.

(5) If more than one derivative of a complex or compound have been referred to in this thesis, the different substituents are denoted by a letter following the compound number, e.g. **[#a]** or **#a**.

Chapter 1. Introduction

1.1 Fluorine and its Application

"Fluorine leaves nobody indifferent; it inflames emotions, be that affections or aversions. As a substituent it is rarely boring, always good for a surprise, but often completely unpredictable."

-Prof. Dr. M. Schlosser[1]

Despite decades of progress in fluorination chemistry, this quote by Professor Schlosser is still as applicable today as it was decades ago. It will, likely as not, still be applicable in years to come as our current understanding of fluorination chemistry is still faced with many challenges.

The difficulty of selective C-F bond formation is mirrored in nature as fluorine, despite being the 13th most abundant element in the Earth's crust, is almost absent in the natural world. The strength of C-F bonds and the large energy of dehydration of fluoride contribute to its absence in biological systems.[2] More importantly, most sources of fluoride are found in minerals, such as fluorite (CaF_2),[3] and are not easily accessible to biological systems. In contrast to the large number of organo-chlorine and organo-bromine compounds known,[4] only six fluorine-containing natural products have been identified in a small number of plant species and only two strains of bacteria (Figure 1).[2]

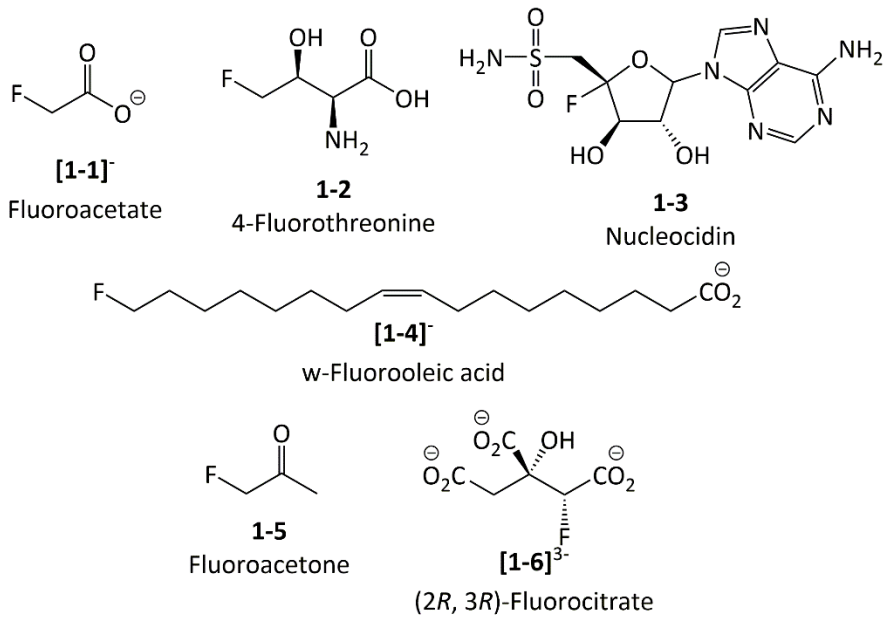

Figure 1: Fluorinated natural products; [1-1]$^-$ to 1-3 identified in two strains of bacteria while [1-4]$^-$ to [1-6]$^{3-}$ were identified in a small number of plants.

To date only one fluorinating enzyme, 5'-fluoro-5'-deoxyadenosine synthase, has been identified from the bacteria, *Streptomyces cattleya*.[5, 6] The enzyme binds and desolvates fluoride anions, generating a potent nucleophile and catalysing the formation of a fluorine transfer agent (5'-fluoro-5'-deoxyadenosine, **1-8**). From this metabolite, fluoroaldehyde and subsequently fluoroacetate and 4-fluorothreonine have been isolated (Scheme 1).[7, 8]

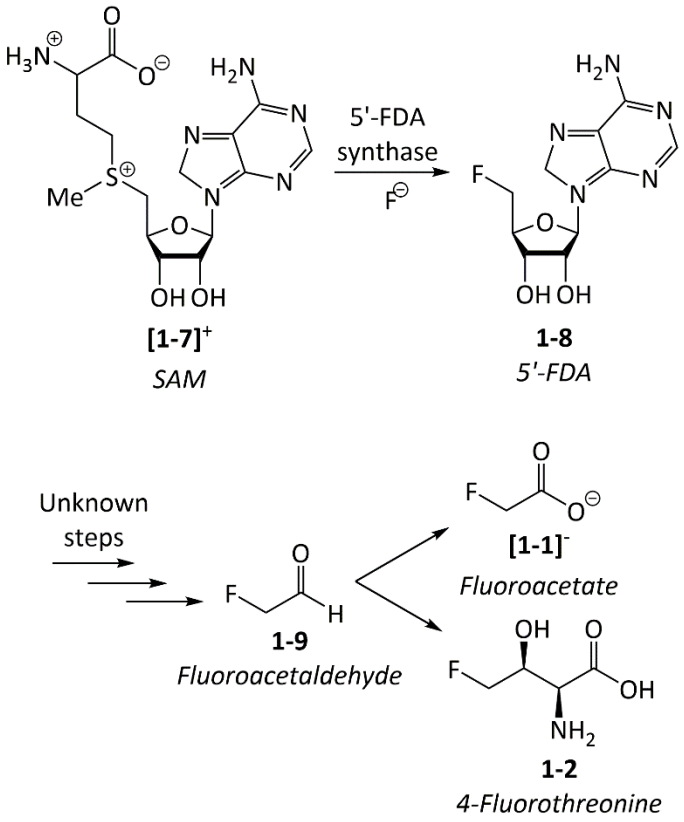

Scheme 1: Biological incorporation of inorganic fluoride into fluorinated metabolites.

Unlike biological fluorine, examples of anthropogenic fluorine are numerous and can be found in a range of applications such as: agrochemicals, pharmaceuticals, plastics, membranes, coatings, lubricants, liquid crystals, dyes, surfactants, radiotracers, propellants, and coolants. The large number of different applications fluorinated compounds are used for stems from the unique properties fluorine exhibits as substituent of a molecule or polymer.

With 25% of pharmaceuticals and 30% of agrochemicals containing fluorine, the biological significance is inherent. Fluorine is found in active compounds that act as: herbicides/safeners, fungicides, insecticides/acaricides,[9] antibacterial, antifungal, antiviral, antidepressant, antipsychotic, anti-inflammatory, and antilipemic molecule. In addition, it is also found in anaesthetics and used in the treatment of cancer, as well as metabolic, cardiovascular, and central nervous system related diseases (Figure 2).[10-14] The introduction of fluorine is desirable to enhance the pharmacokinetic (metabolic stability, bioavailability, and tissue distribution) and physiochemical properties (pK_a, solubility/lipophilicity, conformation, electrostatic potential) of a bioactive molecule.

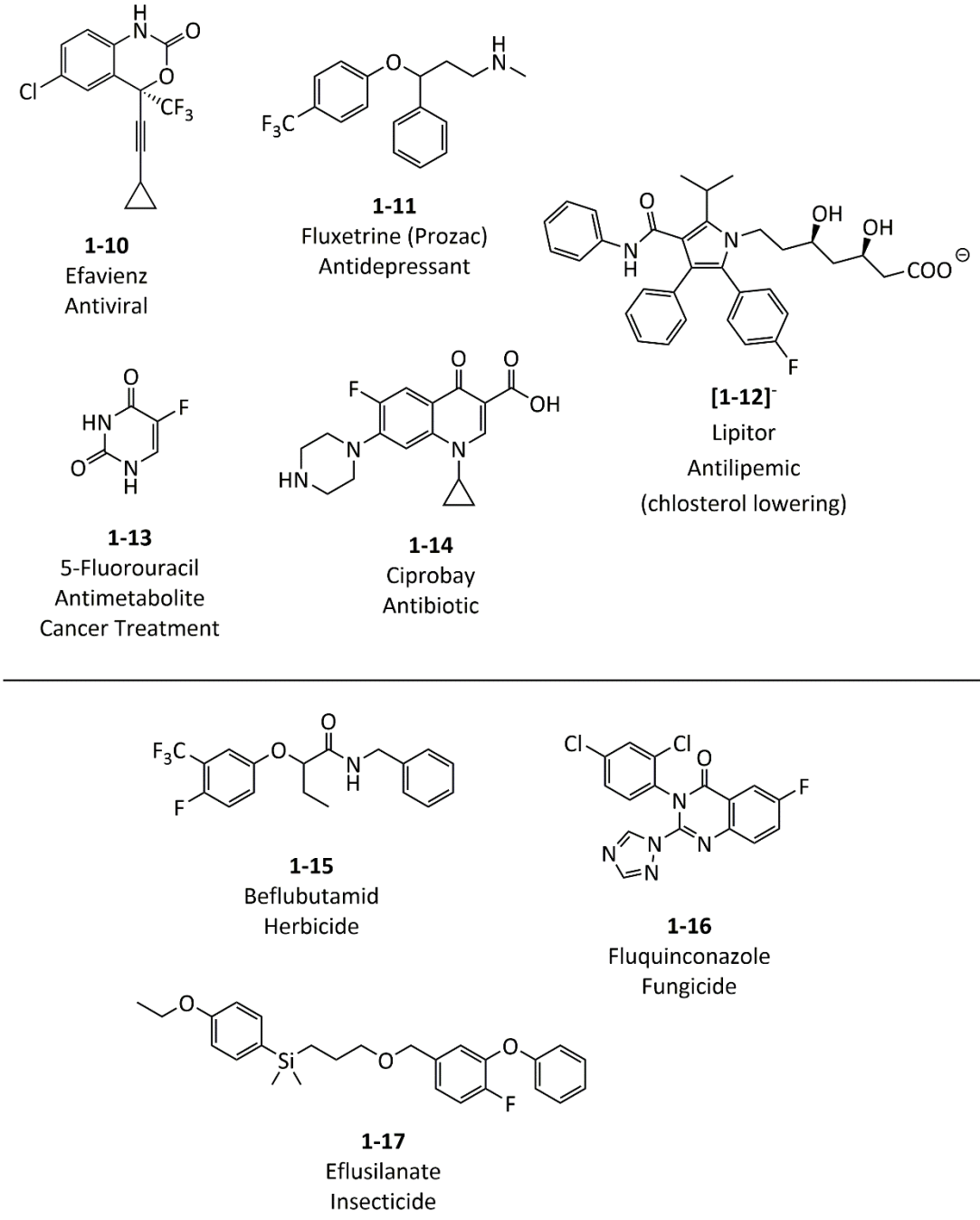

Figure 2: Examples of fluorinated pharmaceuticals, 1-10 to 1-14, and fluorinated agrochemicals, 1-15 to 1-17.

Incorporating fluorine can help tune the lipophilicity in order to increase membrane penetration, improving bioavailability and molecule localisation. Due to fluorine being resistant to metabolic oxidation, replacing susceptible alcohol groups and protons with fluorine can improve the duration of activity and prevent metabolic degradation to particular metabolites, while maintaining electronic or steric properties. Fluorine can perturb the electronic distribution within the molecule increasing non-covalent interactions and altering the acidity/basicity of neighbouring groups, thus increasing the strength of binding or

activity. Fluorine can also contribute directly to activity by acting as a sacrificial inhibitor of the target protein/enzyme, e.g. 5-fluorouracil (**1-1**), whose mode of action is through irreversible attack of fluorine by thymidylate synthase.[10-15]

Perfluorinated solvents have been used as a reaction medium to; simplify synthetic workup where two-phase separation is difficult, increase solubility of reagents/ decrease solubility of products, allow easy extraction of catalysts, or where reagents and intermediates are incompatible with aqueous phases. These solvents are immiscible in aqueous media as well as most common organic solvents and are also used for their non-polar properties and low intermolecular forces.[16-19]

Fluorinated polymers such as, Nafion®, polytetrafluoroethylene (PTFE or Teflon®), polyfluoroalkoxy alkanes (PFA), and fluorinated ethylene propylenes (FEP), have found use in a wide range of applications. These include applications such as insulators, coatings/films, alternatives to glass, membranes, elastomers, and sealants. Fluorinated polymers are also used for applications where corrosion resistance, electrical resistance, chemical inertness, and hydrophobicity are important (Figure 3).[20] Fluorinated polymers are also being applied in the field of genetics as promising gene carriers due to their low cytotoxicity and efficient gene transfection.[21]

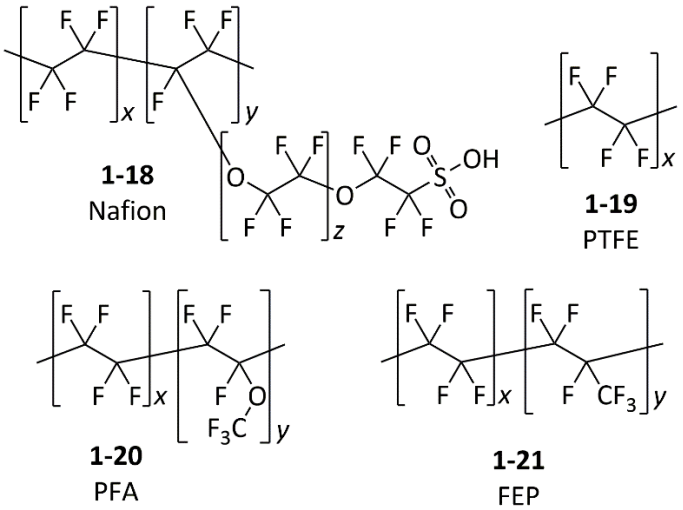

Figure 3: Examples of fluorinated polymers 1-18 to 1-21.

^{19}F NMR spectroscopy has become a powerful tool owing to the isotope's 100 % natural abundance, nuclear spin of ½, high gyromagnetic ratio (40.1 MHz T^{-1}), and high sensitivity to changes in the local environment. The high sensitivity makes ^{19}F-NMR spectroscopy particularly applicable for studying conformational changes and binding in structural biology

and drug-discovery.[22, 23] In addition, the quantitative nature of the technique allows it to be used to monitor reaction kinetics without the disadvantage of having overlapping signals associated with proton NMR spectroscopy.[22, 24-26] This spectroscopic technique can also help elucidate reaction mechanisms and help identify possible intermediates.[27] As such, strategies to incorporate fluorine in molecules close to sites of interest are highly desirable. ^{19}F is also being studied for use in MRI techniques as a 'secondary colour' alongside ^{1}H MRI to overcome some of the limitations with ^{1}H MRI and in ^{19}F MRI for *in vivo* monitoring of distribution and metabolism of fluorine-containing molecules. [28-33]

The non-natural fluorine-18 isotope is a radioactive isotope which decays, with high radio purity (97%), by positron emission. The half-life of 107 minutes makes fluorine-18 a suitable candidate as a radiotracer for positron emission tomography (PET), a non-invasive imaging technique increasingly being used in medical imaging of cancer.[34, 35] This requires rapid late-stage fluorination methodologies to be developed which are capable of delivering high purity radiotraces utilising available sources of fluorine-18.

The emphasis on developing new fluorination protocols is heavily influenced by the lack of biological systems, limiting access to fluorinated molecules and materials through synthetic means only. Current work is underway to utilise and genetically engineer fluorinase enzymes with the aim of selective, mild, and tolerant late stage fluorination transformations in aqueous media.[36] However, such an approach is still in very early development and requires significant advances to be made in the field of genetic engineering to be achieved.

Over the past two decades fluorination chemistry has made significant progress with the development of commercially available, mild, easy-to-handle fluorinating agents, such as N-fluorobenzenesulfonimide **1-24**, that are synthesised from elemental fluorine (Figure 4).[37]

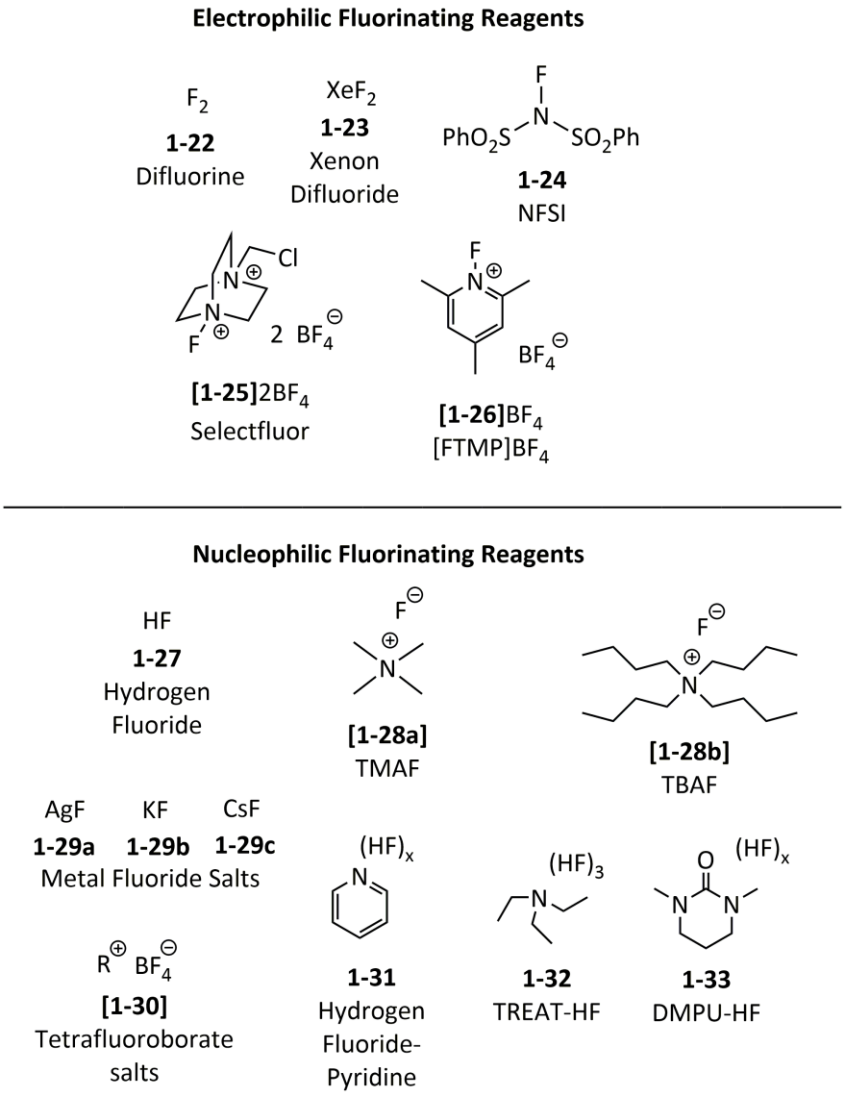

Figure 4: Examples of common electrophilic and nucleophilic fluorinating reagents.

Alternative methods for accessing fluorinated products through selective defluorination, mono-, di-, and trifluoromethylation, in addition to trifluoromethylthiolation, are beyond the scope of this introduction but are covered extensively in reviews by: Kiplinger *et al.*,[38] Ahrens *et al.*[39] (hydrodefluorination); Yang *et al.*[40] (mono-, di-, trifluoromethylation, and trifluoromethylthiolation) and the references therein. This introduction covers a selection of metal-mediated and catalysed mono- and di-fluorination strategies, while organic fluorination methodologies are beyond the scope of this introduction but covered in other fluorination reviews.[40-47]

1.2 Nucleophilic Fluorination

For similar reasons to fluorine's absence from nature, nucleophilic fluorination is challenging due to strong solvation effects which increases the kinetic barrier associated with C-F bond formation. Consequently, the presence of hydrogen bond donors attenuates the nucleophilicity of fluoride, while rigorous exclusion of donors results in fluoride exhibiting basic behaviour which often leads to unwanted side-products.[48] Metal-free nucleophilic fluorination is often limited to electron deficient substrates or activated substrates.

Nevertheless, aromatic nucleophilic fluorination procedures using aryl halogens and triflates are typically more atom efficient than electrophilic fluorination procedures using organoboron and organostannane reagents which are often synthesised from aryl halogens and triflates. While nucleophilic fluorination was typically regarded as more cost effective than electrophilic fluorination, this is less so the case with most modern nucleophilic approaches using more expensive fluoride salts, additives or catalysts.

Hydrogen fluoride is the most inexpensive nucleophilic fluorinating agent available. However, in anhydrous form it is highly corrosive and volatile, limiting its practicality and use. Nevertheless, the development of milder sources in the form of amine solutions, such as pyridinium poly(hydrogen fluoride), **1-31**, and triethylamine trihydrofluoride (TREAT-HF), **1-32**, have made use of hydrogen fluoride more accessible and practical. Most commonly used fluoride sources are alkali/metal fluorides, such as KF, which although cheap, are weakly nucleophilic and poorly soluble due to high lattice energy. However, this can be offset through the use of cation chelating agents such as crown ethers and cryptands. [49] More soluble fluoride sources include tetramethylammonium fluoride (TMAF), [**1-28a]**, and tetrabutylammonium fluoride (TBAF), [**1-28b]**, as well as neutral sulfur trifluoride reagents.

1.2.1 The Balz-Schiemann and Halex Reactions

Two of the most well-known and important fluorination reactions, the Balz-Schiemann[50] reaction and the Halex (halogen exchange)[51] reaction, transformed fluorination chemistry by granting access to fluorinated arenes (Scheme 2). Nevertheless, the substrate scope was limited to electron deficient arenes and anilines with long reaction times and low yield, in addition to using potentially explosive reagents. These reactions have been modified and improved over the years to overcome some of the original limitations and are still being widely used in industry today in the manufacturing of fluorinated reagents and building blocks.[52-54]

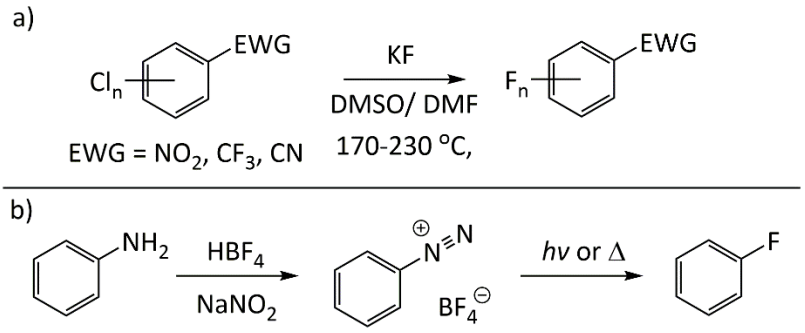

Scheme 2: a) Halex reaction and b) Balz-Schiemann reaction.

While the development of soluble fluoride sources, such as anhydrous tetrabutylammonium fluoride (TBAF), has improved the efficiency of nucleophilic fluorination, these reagents still contain traces of water when dried under vacuum.[48, 55] Rigorously anhydrous TBAF has been prepared by S_NAr (Scheme 3a) which led to mild fluorination of chloro- and nitro-arenes in good to excellent yields.[52] While the reaction times varied significantly from under five minutes to over 5 days, rate enhancement was observed compared to use of vacuum-dried TBAF.[48] However strong basic behaviour was observed and the S_NAr method to access rigorously anhydrous TBAF and other ammonium fluorides require use of ammonium cyanide salts and hexafluorobenzene.[55]

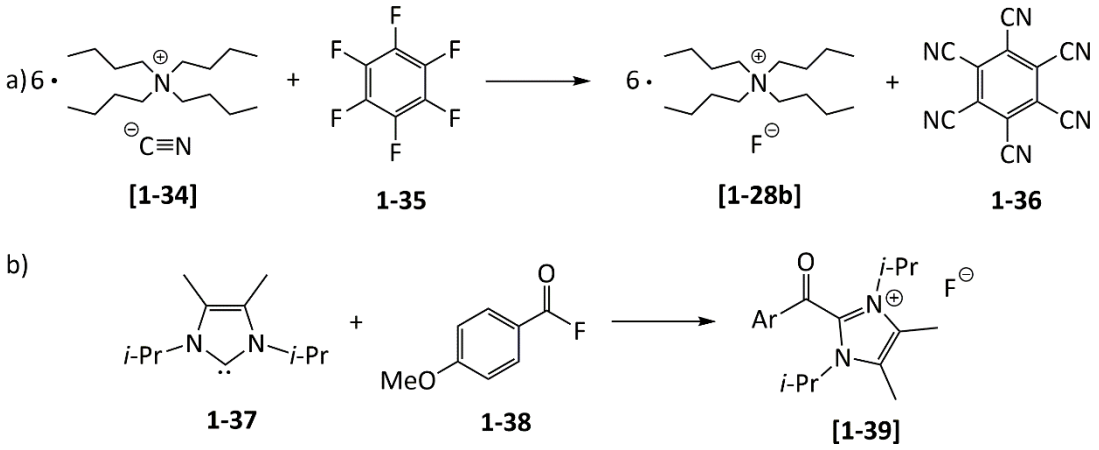

Scheme 3: a) Synthesis of rigorously dry tetrabutylammonium fluoride, b) synthesis of acyl azolium fluoride.

Ryan *et al.*[56] recognised that acyl azolium fluoride salts (Scheme 3b), prepared from their corresponding acyl fluorides and *N*-heterocyclic carbenes (NHCs), could be used as alternative sources of soluble anhydrous fluoride for the mild nucleophilic fluorination of chloro- and nitro-arenes. The structure of the NHC was crucial for obtaining the maximum yield; replacing the backbone hydrogens of the imidazolium ring with methyl groups was

found to increase yield through the elimination of detrimental hydrogen bonding interactions with fluoride. The nitrogen substituents were also important to modulate the stability and solubility, with *iso*-propyl groups being optimal substituents.

S_NAr fluorination proceeded at room temperature in DMF, and was tolerant of methoxy, nitrile, and trifluoromethyl substituents. However, selectivity towards monofluorinated products was diminished using substrates with additional halide substituents (Scheme 4). In addition, while synthesis of [^{18}F]-radiolabelled acyl fluorides is possible, the current protocol utilised is unsuitable for PET radiotracer synthesis due to reaction times being beyond that of the isotope's half-life.

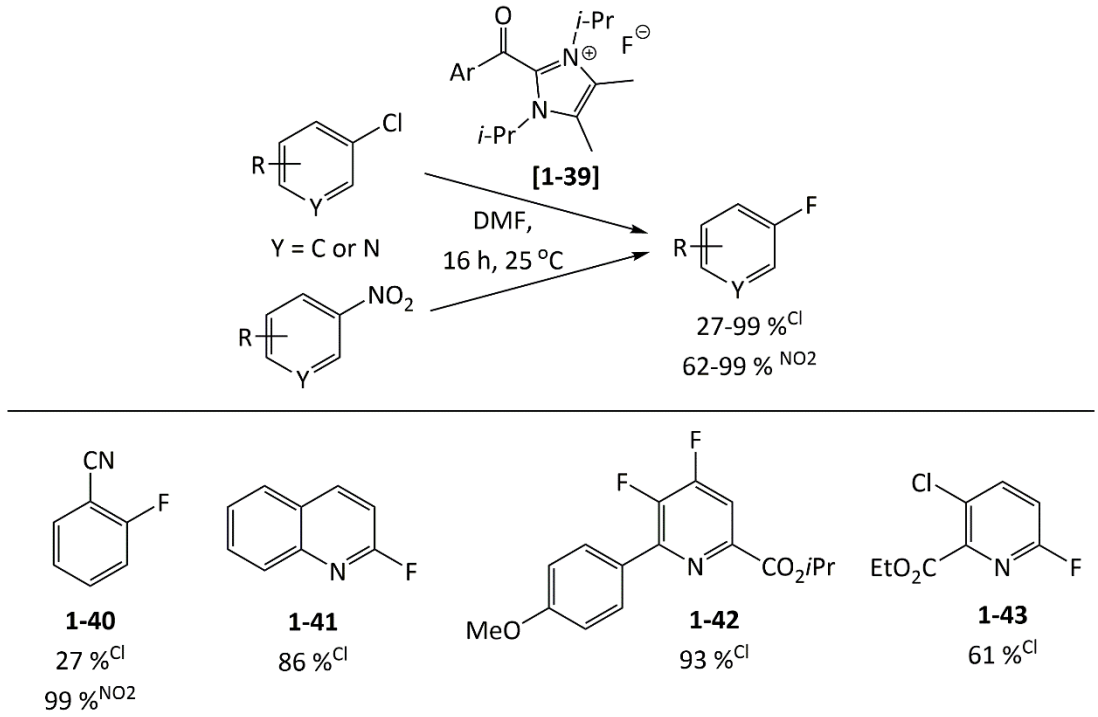

Scheme 4: Fluorination of chloro- and nitro-arenes by halide exchange using acyl azolium fluoride.

Although great progress has been made in this field of chemistry to improve the conditions and yields, metal-free nucleophilic fluorination reactions are still limited compared to modern metal-mediated strategies in this respect.

1.2.2 Metal-Mediated and Metal-Catalysed Aromatic C-F Bond Formation

The limited substrate scope of the Balz-Schiemann and Halex reactions, including modified versions and other direct procedures, is well documented, with a clear need for mild nucleophilic fluorination of electron-rich and electron-neutral substrates.[50, 51, 53, 54, 57] The use

of metals has been crucial in overcoming some of the challenges associated with nucleophilic fluorination.

The Buchwald group developed a palladium-catalysed strategy using **1-44** and **[1-45]** to access aryl fluorides from aryl triflates in high yield (57-85 %) using CsF (Scheme 5).[58] A variety of functional groups could be tolerated including; amines, ethers, esters, and nitro substituents, as well as heteroaromatic groups such as quinine. However, substrates bearing Lewis basic groups *ortho* to triflate did not undergo fluorination presumably due the group coordinating to the metal centre inhibiting transmetalation. Other limitations included the need for high temperatures (up to 130 ˚C) and formation of regioisomers. Although the addition of cyclohexane suppressed the formation of regioisomers, these side products were still produced in up to 8 % yield.

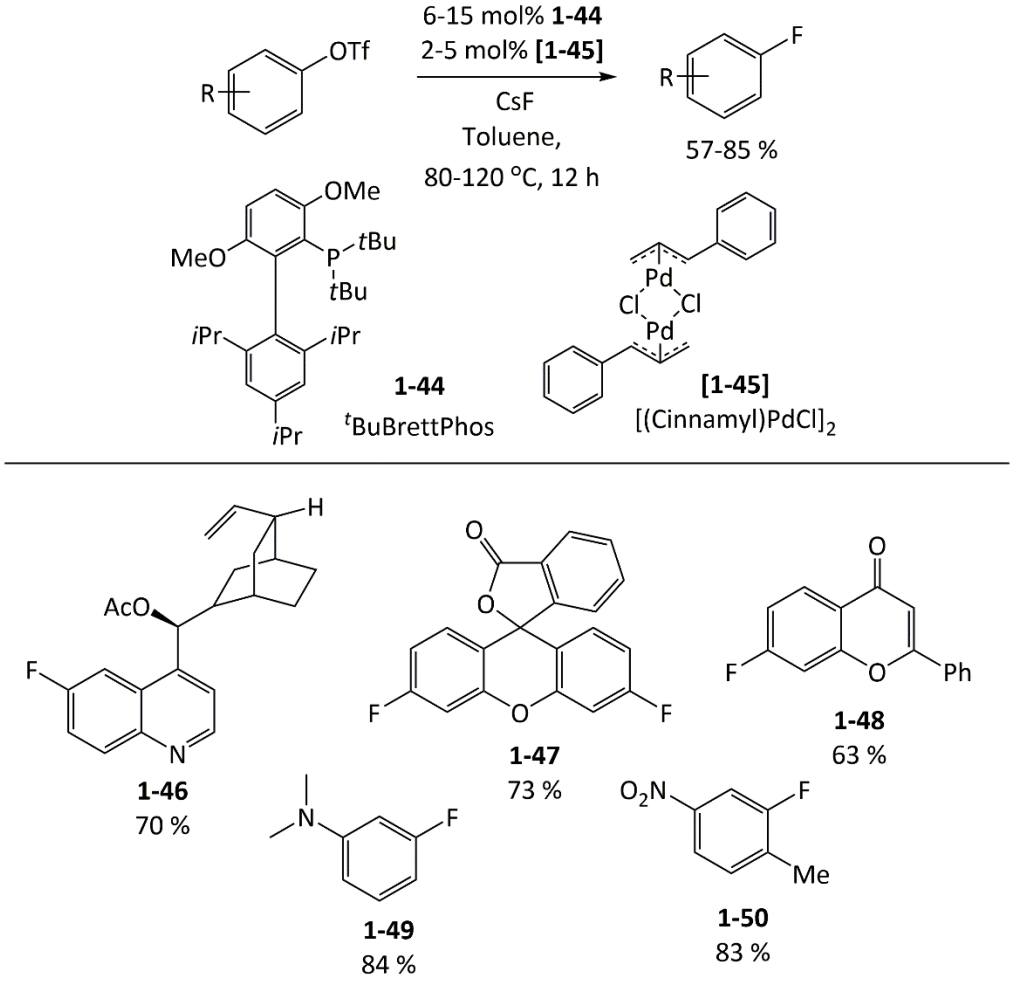

Scheme 5: Palladium-catalysed fluorination of aromatic triflates.

While nucleophilic fluorination using aryl triflates has been described, the Hartwig group developed a copper-mediated method using aryl iodides (Scheme 6).[59] The main benefit of

halide exchange is the circumvention of additional synthetic steps required to access commonly used reagents such as stannanes and triflates, making aryl halides a greener and more efficient choice of substrates. Aryl fluorides were synthesised in modest to near quantitative yield (40-96 %) from aryl iodides using excess (^{t}BuCN)$_2$CuOTf, **[1-51]**, and AgF. However harsh conditions were required (22 hours at 140 ˚C) limiting the scope to substrates bearing robust functional groups and moieties. In addition, rigorous exclusion of water was needed to obtain high yield and minimise protodehalogenation.

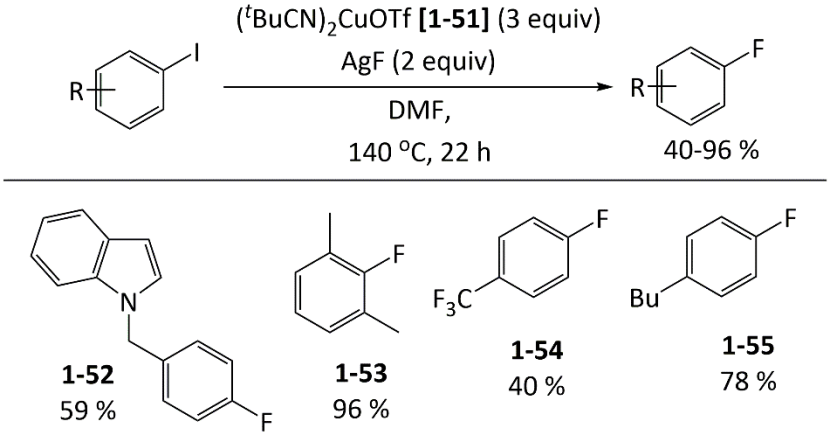

Scheme 6: Copper-mediated fluorination of aryl iodides.

The proposed mechanism (Scheme 7) is believed to proceed through reversible oxidative addition of an aryl iodide to a Cu(III)-I species, **[1-56]**, which undergoes halide exchange with AgF to form **[1-57]** as an intermediate. Reductive elimination from **[1-57]** affords the desired aryl fluoride. A one electron transfer mechanism was ruled out on the basis of selectivity and altered reaction kinetics using aryl bromides.

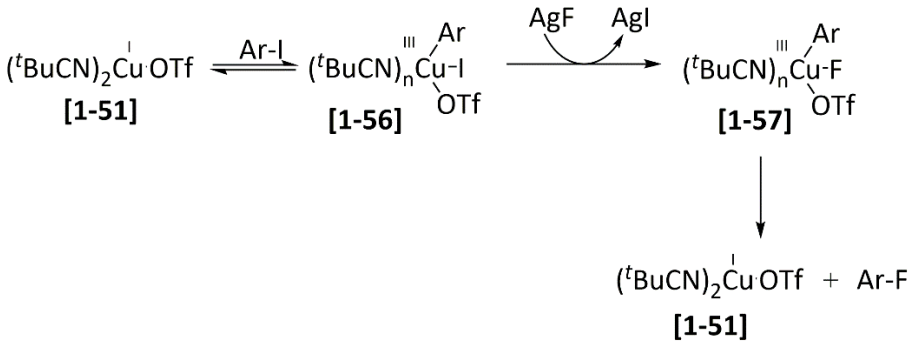

Scheme 7: Proposed mechanism for copper mediated fluorination of aryl iodides through oxidative addition of the substrate to form [1-56], halide exchange and subsequent reductive elimination from [1-57].

1.2.3 Metal-Mediated and Metal-Catalysed C(sp^2)-F Bond Formation

Gold has been extensively studied for its ability to mediate the formation of C-C, C-O, C-N, and C-S bonds in alkyne cyclisation and addition reactions.[60-65] Only recently has gold been demonstrated to mediate the formation of C-F bonds in hydrofluorination reactions with alkynes.[66-68] Akana *et al*.[66] demonstrated selective *trans*-hydrofluorination of internal alkynes bearing electron-rich and electron-deficient aromatic groups and alkyl chains upon reaction with triethylamine stabilised HF (Scheme 8). In the case of asymmetric alkynes, fluorine was preferentially delivered to the least hindered position, i.e. the alkyl bearing carbons. The mechanism is believed to proceed by reversible addition of (NHC)Au(I)-F across the alkyne C≡C, followed by protodemetalation yielding the hydrofluorinated product without geminal-dihydrofluorination being observed.

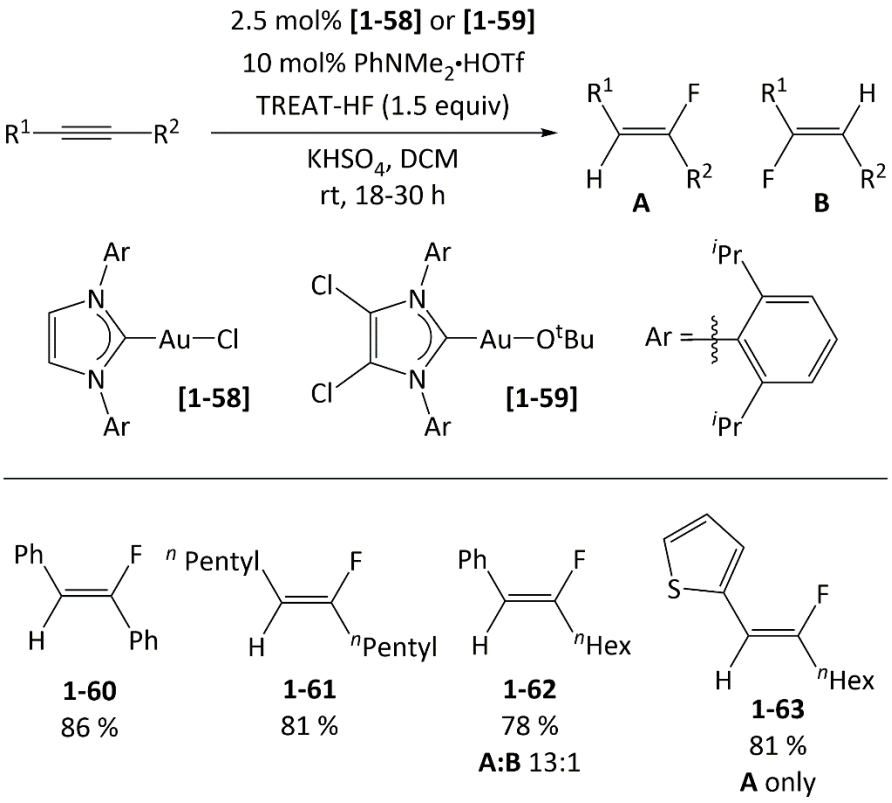

Scheme 8: Gold-catalysed hydrofluorination of alkynes.

Gorske *et al*.[67] attempted to improve regio-selectivity through use of carbonyl- and nitrogen-based directing groups (Scheme 9). Esters, while demonstrating a directing group effect, had varying selectivity dependent on the distance between the alkyne C≡C bond and the directing group, as too did the choice of substituent. Although increased regio-selectivity was achieved, these substrates suffered from lower conversion (16 % yield with a ratio of

regioisomers of 95:5). Carbamate directing groups displayed high regio-selectivity with good conversion to fluoroalkenes. However, methyl bearing alkynes lost stereo-specificity producing a mixture of stereoisomers with preference for the *Z*-isomer (lowest *Z*-/*E*-ratio 84:16). Dicarbonyl substrates failed to react or produced a mixture of stereo-isomers in low yield (16 % with 71:29 *Z*-/*E*-ratio).

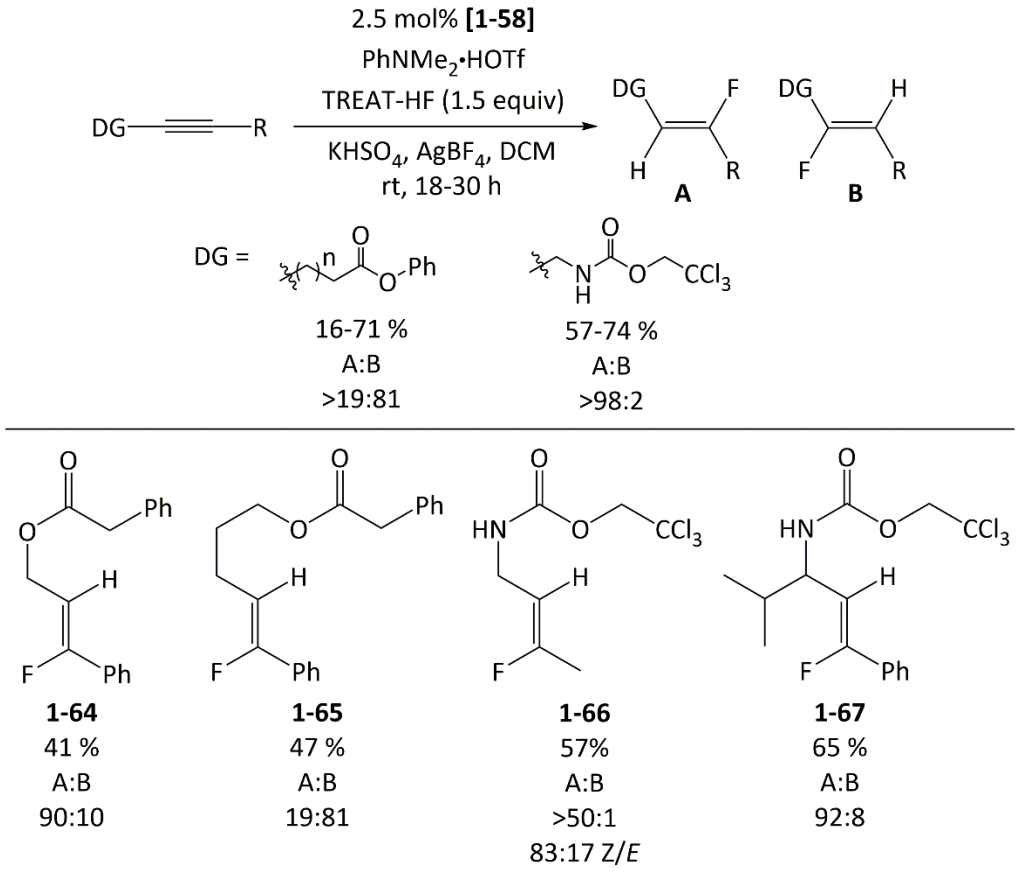

Scheme 9: Gold-catalysed stereoselective hydrofluorination of alkynes bearing ester and carbamate directing groups.

Regioselectivity is speculated to arise from templated complexation of gold to the alkyne by the carbonyl directing group **[1-68]**, activating the alkyne such that fluoride preferentially attacks the alkyne to form the most energetically favourable metallacycle **[1-69]** (Scheme 10). Subsequent protonation of the gold metallacycle **[1-70]**$^+$ and reductive elimination affords the fluoroalkene with regio- and stereo-selectivity.

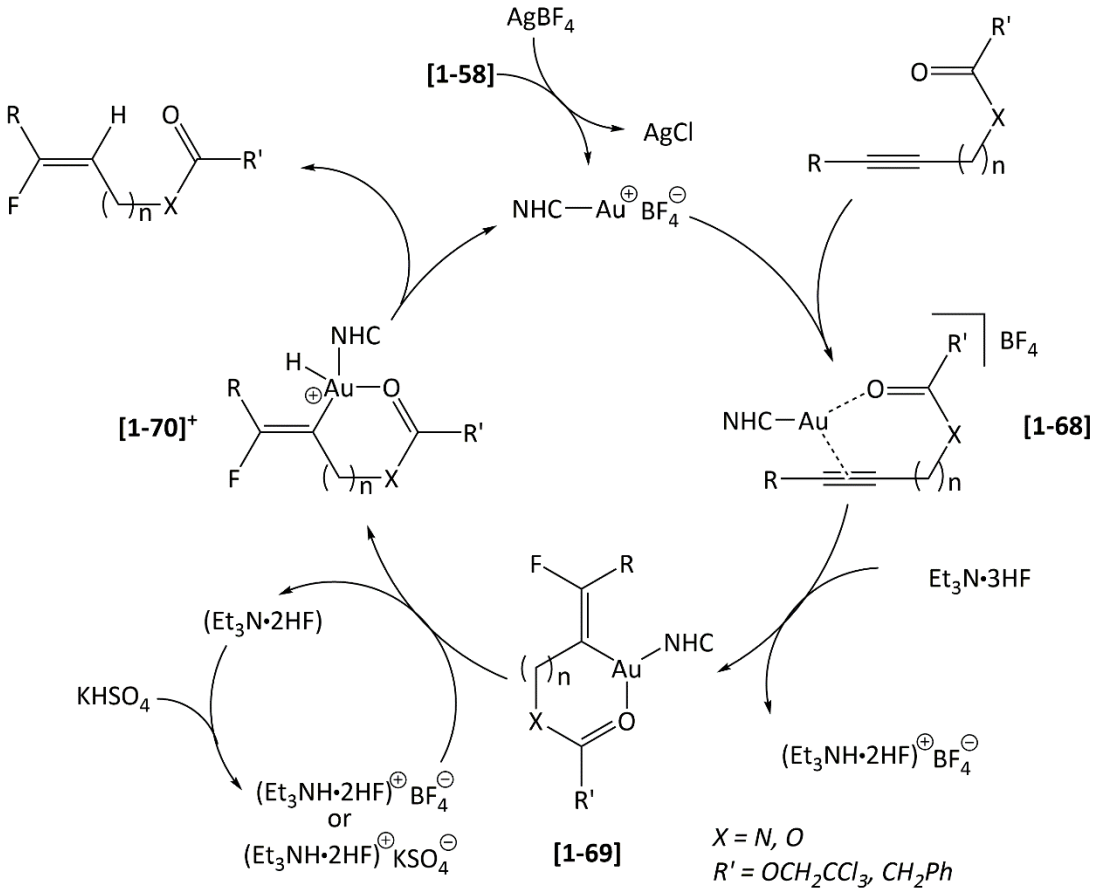

Scheme 10: Proposed mechanism for fluorination of carbonyl bearing alkynes. The carbonyl group templates coordination to the catalyst allowing regioselective fluorination of [1-68]. Protonation of [1-69] and reductive elimination from [1-70] yields the fluoroalkene with regioselectivity.

Okoromoba *et al.*[68] have recently demonstrated gold catalysed hydrofluorination of alkynes using 1,3-dimethyl-3,4,5,6-tetrahydro-2(1H)-pyrimidinone (DMPU)·HF (Scheme 11), an alternative source of hydrogen fluoride which is reportedly less basic and a more weakly coordinating ligand of metals than pyridine and triethylamine stabilised HF reagents. Regioselective fluorination of terminal alkynes to afford the Markovnikov addition product was achieved with good to excellent yields (67-96%). Internal alkynes could also be hydrofluorinated in excellent yields (84-85%) with higher catalyst loading. Under optimised conditions alkene substituents were unreactive towards DMPU·HF, **1-33**, allowing clean conversion to the monohydrofluorinated product. The reaction was also tolerant of esters, electron-rich and deficient aromatic substituents, and acidic C-H groups. The mechanism of hydrofluorination or the role of the gold catalyst was not discussed.

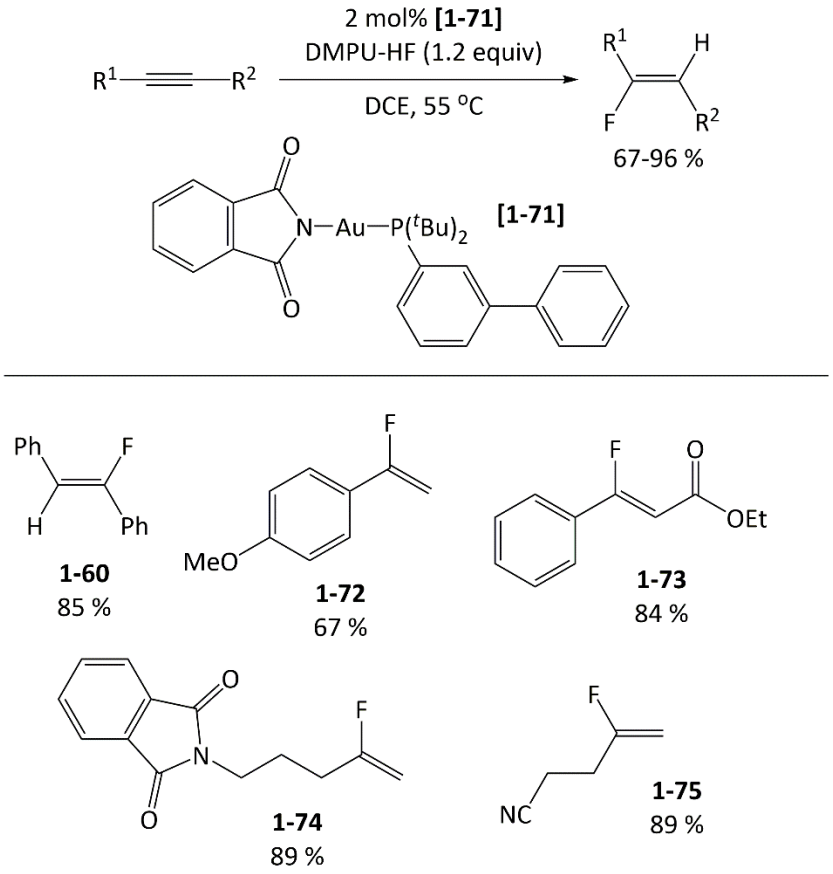

Scheme 11: Gold-catalysed Markovnikov hydrofluorination of alkynes.

1.2.4 Metal-Mediated and Metal-Catalysed C(sp^3)-F Bond Formation

The use of allylic fluorides as synthetically useful fluorine-containing building blocks has led to their extensive study to develop new high regio- and stereo-selective strategies to access them. However, traditional strategies using sulfur trifluoride (SF_3) and allylic alcohols suffered from poor regio- and enantio-selectivity.[69]

While early strategies to access branched allylic fluorides by deoxyfluorination[41, 70] had poor selectivity for the desired product, Katcher *et al.*[71] have more recently demonstrated a highly regio-selective palladium-catalysed strategy to access branched allylic fluorides from primary allylic chlorides (Scheme 12).

The high regio-selectivity is believed to arise from strong hydrogen-bonding between fluoride and the Trost ligand, **1-77**, directing fluorination. The reaction was tolerant of alkyl bromides, aldehydes, ethers and protected amines, as well as α-branching and heterocyclic substrates. However, fluorination of linear allylic chlorides, while giving high branched product selectivity, resulted in moderate to poor enantioselectivity (21-71 %) due to the lack

of steric hindrance or electronic bias to induce asymmetric attack of fluoride. In addition fluorination of cinnamyl chloride to **1-81** under these conditions favoured the linear fluorinated product (1:4) with no enantioselectivity. Selectivity for the linear product has also been reported for the fluorination of various cinnamyl substrates.[72] Poor selectivity using Trost ligands (**1-77**) were observed for several substrates, but the use of triphenylphosphine was found to circumvent this problem. While fluorination of an alcohol-containing allylic chloride is possible, competitive intramolecular esterification lowered the yield of the desired product. In addition, an exocyclic methylene-containing allylic chloride and tertiary allylic chloride suffered from competitive diene formation (20-30%) reducing the efficiency.

Nevertheless, further functionalisation to various fluorinated motifs was demonstrated in good to excellent yield with high retention of stereochemistry (Scheme 13). The diversity of the reaction coupled with additional transformations shows great potential for the development of a general reaction. Only cross metathesis suffered a loss in enantioselectivity due to the harsh conditions required.

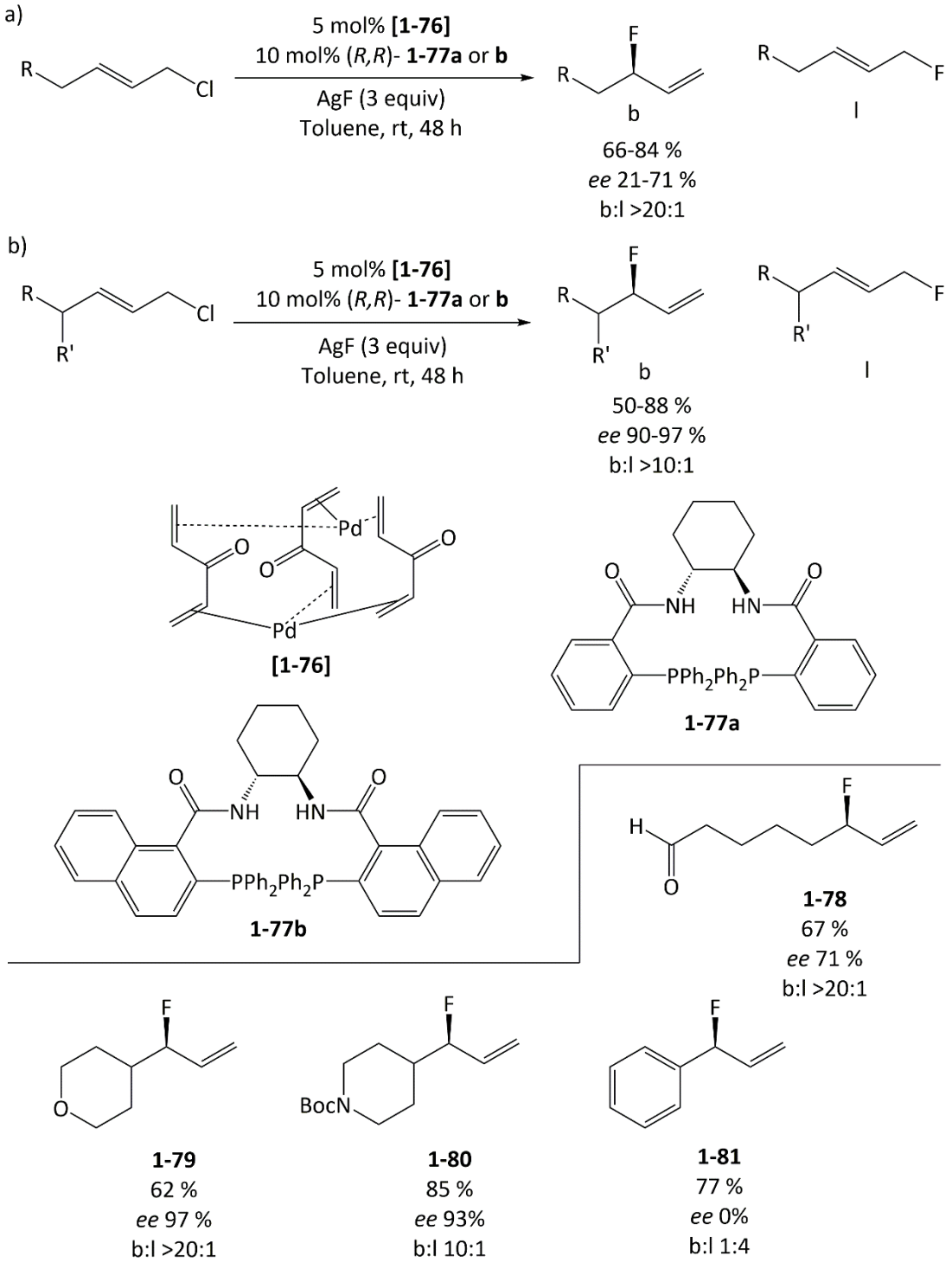

Scheme 12: Palladium-catalysed nucleophilic fluorination of allylic chlorides favouring branched allylic fluorides.

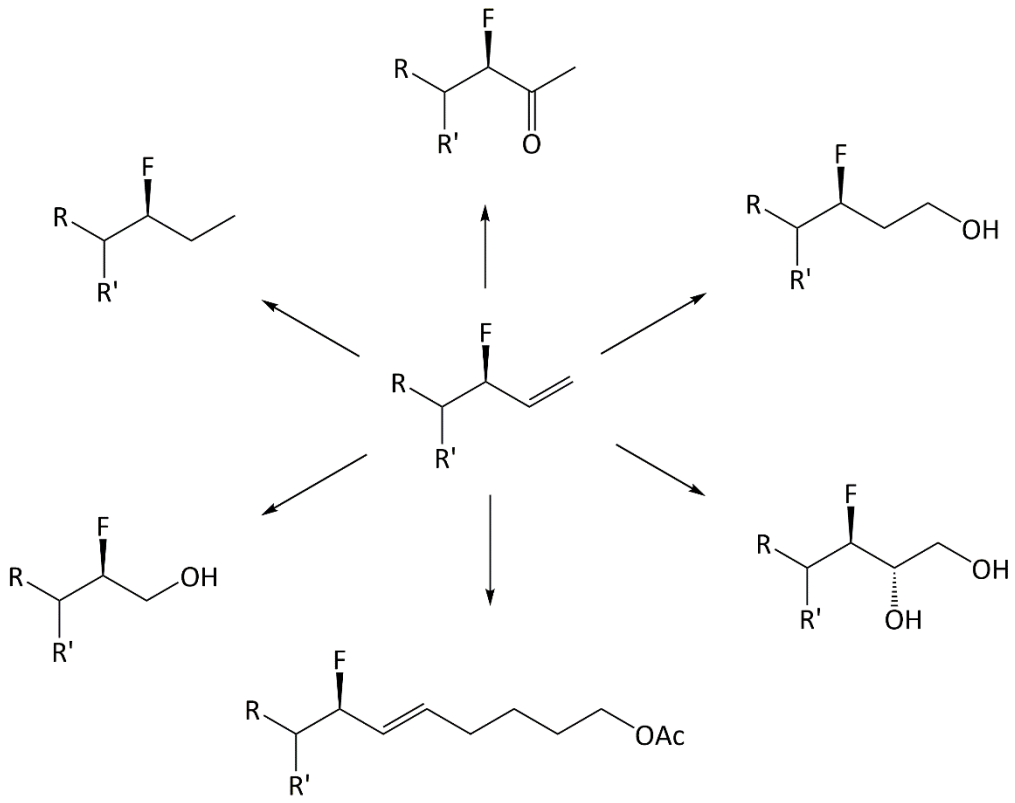

Scheme 13: Derivatisation of allylic fluorides.

Prior to acyclic systems, a palladium-catalysed strategy for fluorinating six-membered cyclic allylic chlorides through halide displacement was developed (Scheme 14).[73] Heterocyclic substrates bearing ether, protected amine, amide, alcohol and ester functional groups were tolerated. However, diene side products were observed under optimised conditions lowering the efficiency. This being said, other background reactions with AgF were circumvented by the use of non-polar solvents. While the yield of cyclic allylic fluorides varied between substrates, the reported enantioselectivity of the reaction was found to be greater than 85 % ee for all studied substrates and is a considerable improvement on deoxyfluorination strategies.[41, 70]

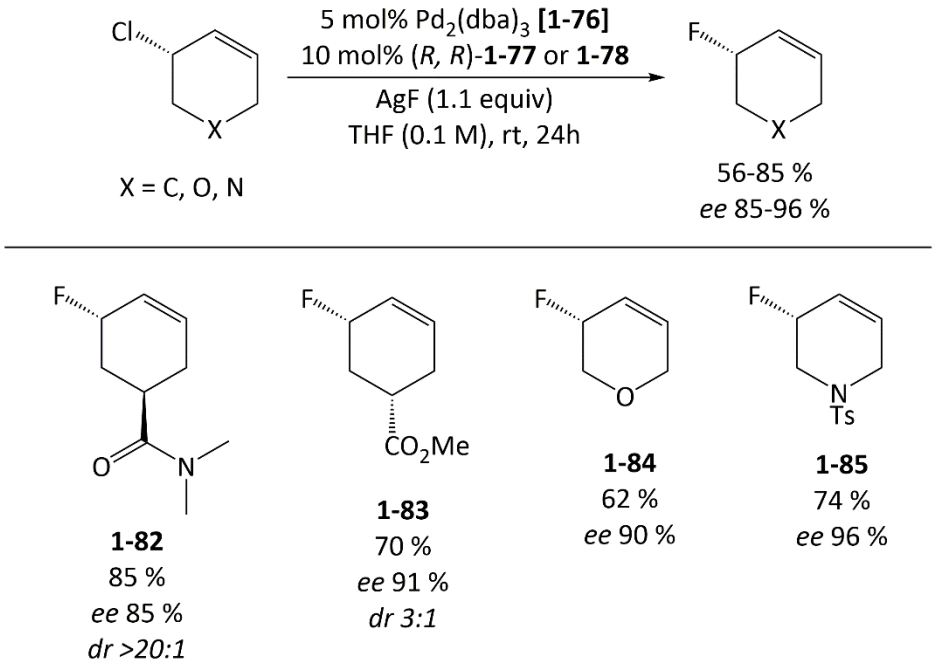

Scheme 14: Palladium-catalysed fluorination of cyclic allylic chlorides.

The high degree of stereo-retention observed suggested a double inversion mechanism was in effect, i.e. attack by palladium then attack by fluoride. A subsequent detailed mechanistic study was in agreement with fluorination proceeding through an outer sphere bimetallic transition state rather than through reductive elimination of C-F from a single centre.[74] The elucidated pathway (Scheme 15) initially involves coordination and subsequent oxidative addition of the allyl halide to the Pd(0) centre, **[1-87]**, followed by halide exchange to produce **[1-88]**. This intermediate is in equilibrium with **[1-89]**F and the two species react in a bimetallic transitions state **[1-90]**F‡, with fluorine being transferred in an S_N2 manner. This generates the coordinated allyl fluoride, alongside a coordinately unsaturated Pd species which re-enters the catalytic cycle. Dissociation from the metal centre provides the allylic fluoride with retention of stereochemistry.

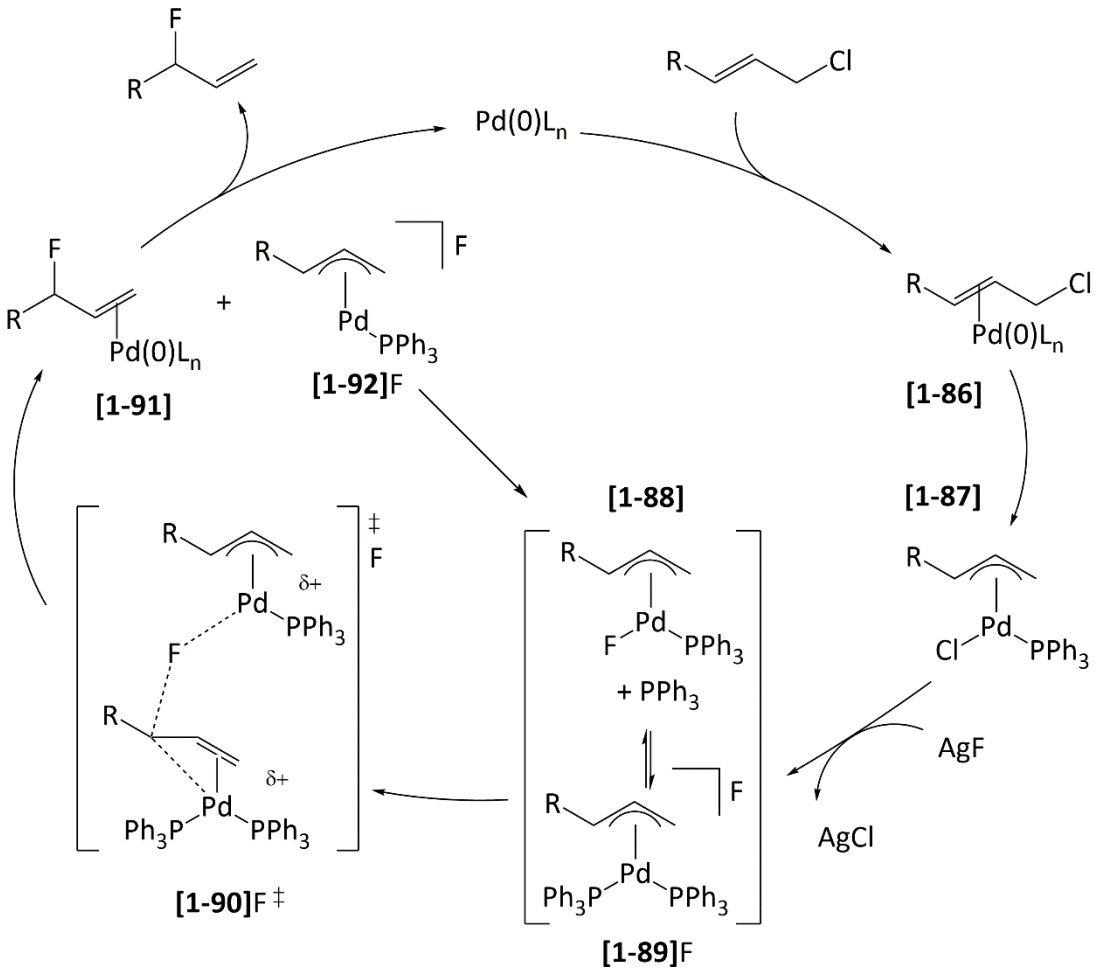

Scheme 15: Proposed mechanism of fluorination leading to stereoselective formation of allylic fluorides through a bimetallic transition state [1-90]F‡.

Complementary to work by the Doyle group, the Gouverneur group demonstrated a palladium-catalysed strategy to access primary allylic fluorides using allylic *p*-nitrobenzoates (Scheme 16).[72] Carbonates were highlighted as suitable leaving groups due to their greater reactivity, enabling fluoride to displace the carbonate groups. Under mild conditions, branched and linear allylic *p*-nitrobenzoates were fluorinated to the corresponding allylic fluorides. Branched substrates were generally converted in higher yield than the linear substrates, with electron rich linear allylic fluorides being isolated in lowest yield due to their sensitivity to workup. Conversely, the fluorination procedure is sufficiently mild to tolerate sensitive functional groups or compounds such as a benzyl chloride and 1-fluoro-2-phenylethylene. Reducing the reaction time to 5 and 30 minutes enabled incorporation of [^{18}F] using [^{18}F]TBAF, however, the decay-controlled radiochemical yield varied from 9-42% and 10-52% respectively.

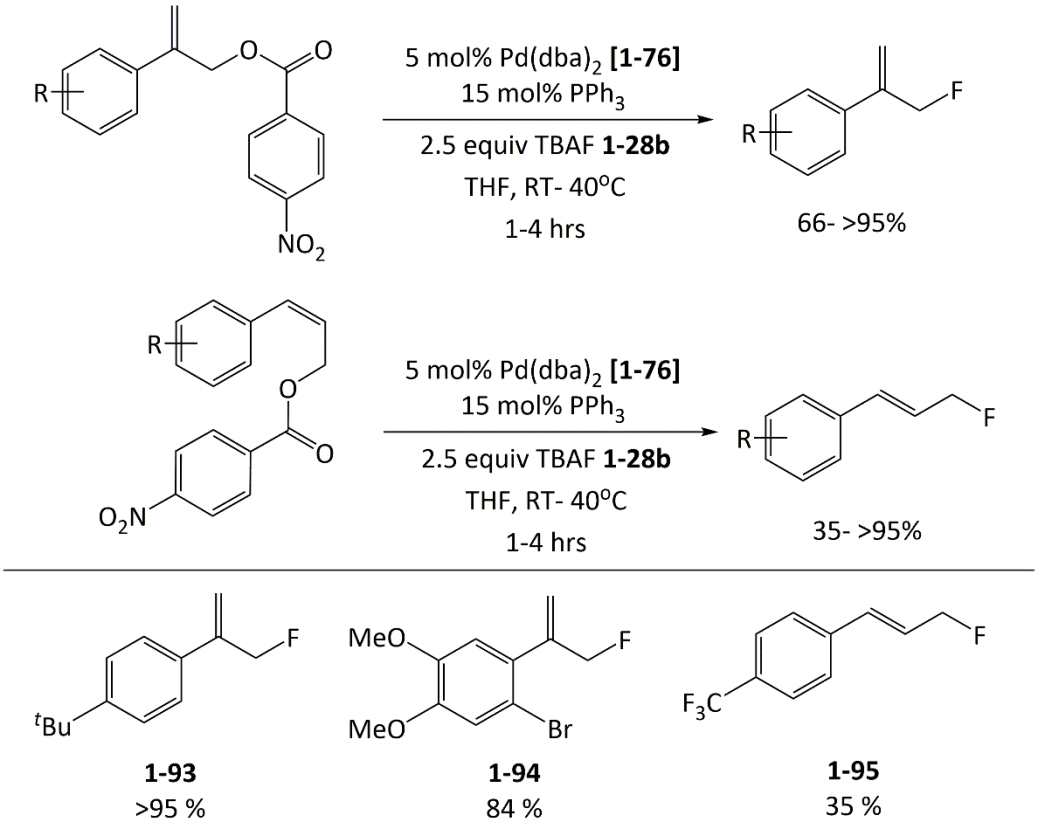

Scheme 16: Palladium-catalysed synthesis of primary allylic fluorides using allylic p-nitrobenzoates.

The reaction is limited to substrates bearing a *p*-nitrobenzoate leaving group or substituents capable of being functionalised to an allylic *p*-nitrobenzoate. In addition, the competing elimination pathway to diene formation is a significant problem for the fluorination of non-primary *p*-nitrobenzoates.

In subsequent work, allylic methylcarbonates were also fluorinated to their corresponding linear and branched allylic fluorides with high regioselectivity in the presence of an iridium catalyst (Scheme 17). Complementary to the previous fluorination procedures, stereoselective synthesis of *Z*-allylic fluorides was also reported, enabling allylic fluorides to be synthesised asymmetrically to the stereoisomer of choice.[75]

Imides, carbamates, ethers and esters were tolerated under the optimised reaction conditions. While allylic fluorides were reported in only moderate to good yield (32-68%), the catalytic protocol displayed high levels of stereo- and regio-selectivity. Formation of allylic alcohol as a side product may contribute to the moderate yields observed.

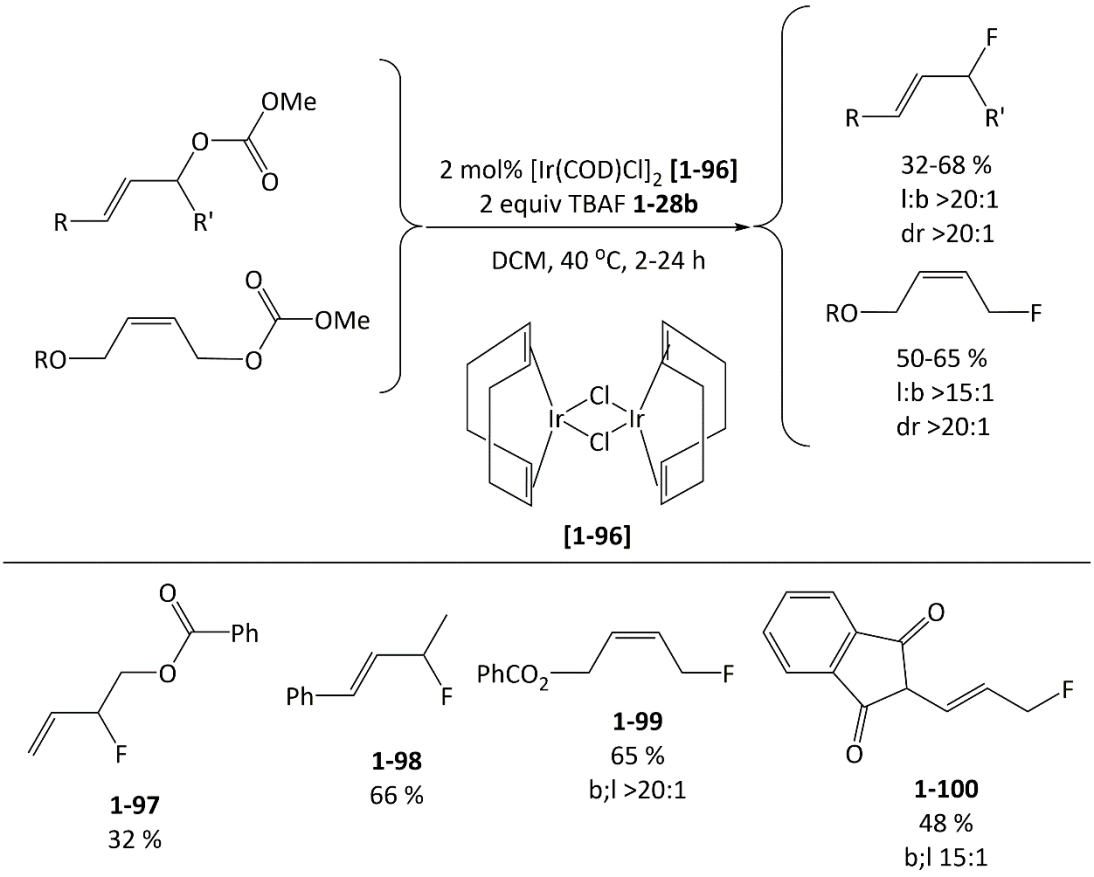

Scheme 17: Iridium-catalysed fluorination of carbonate bearing alkenes affording *E*- and *Z*- allylic fluorides.

Use of an enantiopure allylic carbonate resulted in overall stereoretentative fluorination being observed (Scheme 18). However, loss of *R*-/*S*-stereoselectivity was consistent with the formation of an allyl intermediate capable of undergoing C-C bond rotation prior to attack of fluoride.

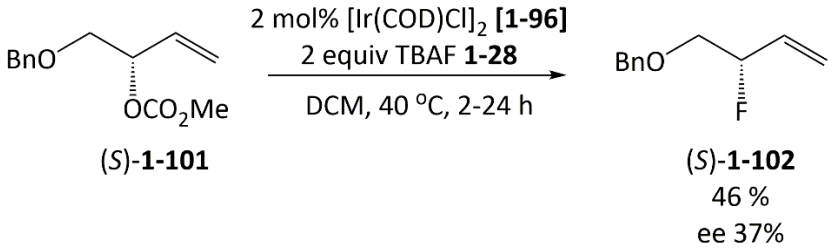

Scheme 18: Iridium-catalysed stereoretentative fluorination of enantiopure allylic carbonate (s)-1-102.

Radiolabelled branched and linear, *E*- and *Z*-allylic fluorides were accessible using [^{18}F]Et_4NF with improved radiochemical yields over fluorination of allylic *p*-nitrobenzoates. However,

the main drawback being the longer reaction time (30 minutes), reducing the imaging time for PET.

Gem-difluorination of alkynes (Scheme 19) was initially a side product observed from monohydrofluorination reported by Okoromoba *et al.*[68] Addition of a Lewis acid, such as $KHSO_4$ or $Ga(OTf)_3$, was found to increase conversion to the dihydrofluorinated product and optimisation of the conditions allowed for the isolation of *gem*-difluoroalkanes and benzyl *gem*-difluorides in excellent yield (79-94%).

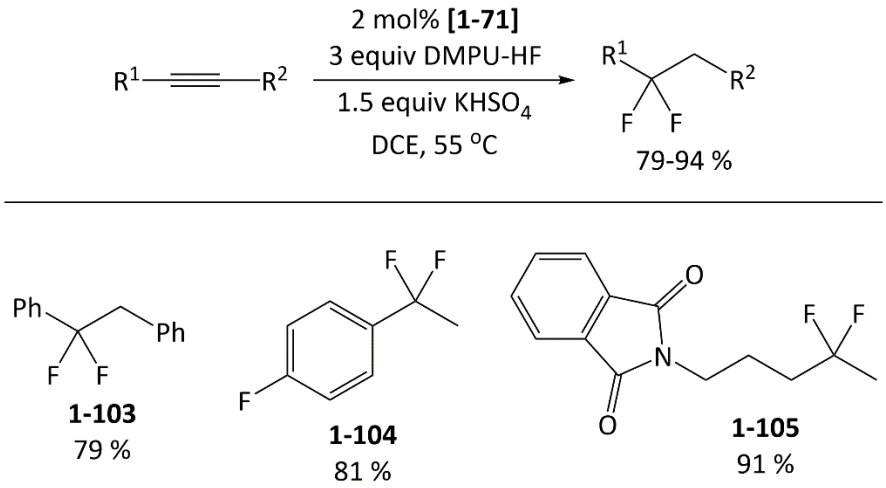

Scheme 19: Gem-dihydrofluorination of alkynes catalysed by Au(NHC) [1-71].

The Sanford group further developed their direct C-H activation/fluorination strategy of 8-methyl-quinoline derivatives[76] to use a nucleophilic source of fluorine rather than an electrophilic source (Scheme 20).[77] As demonstrated by Wu *et al.*[78] the electrophilic fluorinating agent plays a twofold role of fluorine source and oxidant, which could be replicated through using a fluoride source and an external oxidant. Fluorination of 8-methyl-quinoline derivatives proceeded with similar yields (39-70 %) as the strategy using an electrophilic fluorinating agent. [76] However, only traces of fluorinated product was observed for the methoxy- substituted substrate. Heating the reaction in dichloromethane at reflux and the use of large excesses (5 equivalents) of AgF increases the safety risks and reduces sustainability. In addition, the need for a directing group, as before, currently limits the substrate scope of these reactions significantly.

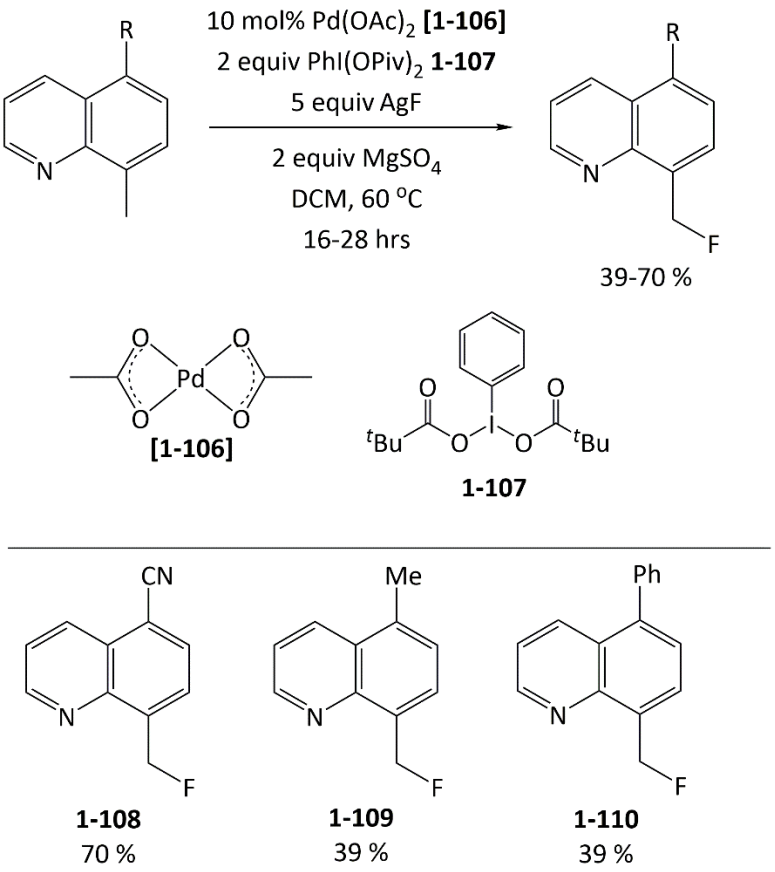

Scheme 20: Palladium-catalysed fluorination of 8-methyl-quinoline derivatives.

There are two postulated mechanisms for fluorination (Scheme 21), both involve the formation of the high valent Pd(IV)-F intermediate and reductive elimination of the product. The mechanisms differ on the pathway to the Pd(IV) intermediate, whether through oxidative addition of pivalate to palladium followed by fluoride substitution (pathway A) or by initial substitution of pivalate with fluoride to form a ArI(III)F_2 (pathway B). It is not clear which pathway is followed.

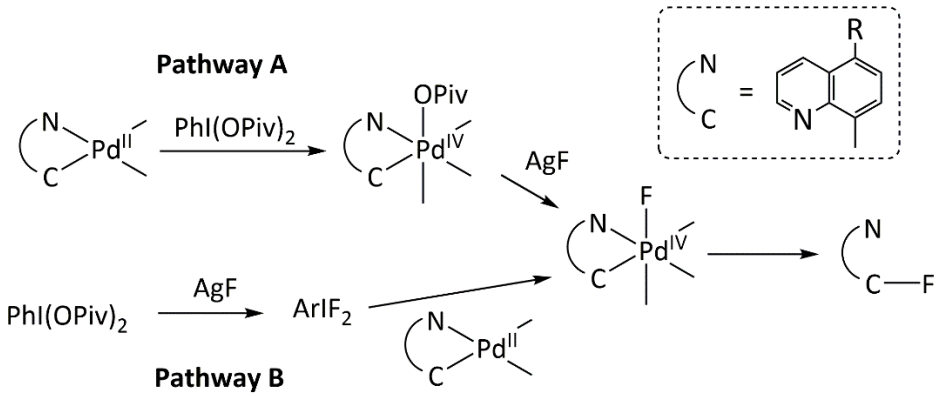

Scheme 21: Two proposed pathways for the nucleophilic fluorination of 8-methylquinoline derivatives. Pathway A proceeds through oxidation of Pd(II) to Pd(IV) followed by transmetallation to a Pd(IV)-F intermediate, wheras pathway B proceeds through fluorination of the oxidant and then oxidative addition to palladium to form the Pd(IV)-F intermediate. Reductive elimination affords the fluorinated product in both pathways.

1.3 Electrophilic Fluorination

Early electrophilic fluorination procedures were limited to the use of elemental fluorine, F_2, restricting research in this field to the small number of research groups and facilities capable of storing and manipulating the gas. The extreme reactivity of elemental fluorine makes it difficult to control the selectivity, as well as the degree of fluorination in a reaction. In addition, such methods are also intolerant of many functional groups. Nevertheless, fluorination using diluted elemental fluorine can be achieved through application of continuous flow and batch processes, but selective fluorination remains challenging.[57, 79-84]

The development of commercially available stable and easy-to-handle electrophilic fluorinating agents has opened up the field to any synthetic laboratory. Rapid development of new fluorination methods followed, significantly expanding the scope and capability of fluorination chemistry.[42-46]

1.3.1 Metal-Mediated and Metal-Catalysed Aromatic C-F Bond Formation

Traditional organometallic approaches to access aryl fluorides, such as the use of aryl lithium and aryl Grignard reagents, suffered from protodemetalation side-products, limited substrate scope, and functional group tolerance. This highlighted the need for more robust and tolerant fluorination strategies to be developed.[85, 86]

More general and tolerant fluorination procedures have been developed with aryl Grignard reagents (Scheme 22), as a consequence of alternative magnesium insertion reactions and optimised reaction conditions. This allowed aryl fluorides to be synthesised from both electron rich and deficient aryl bromides.[87, 88]

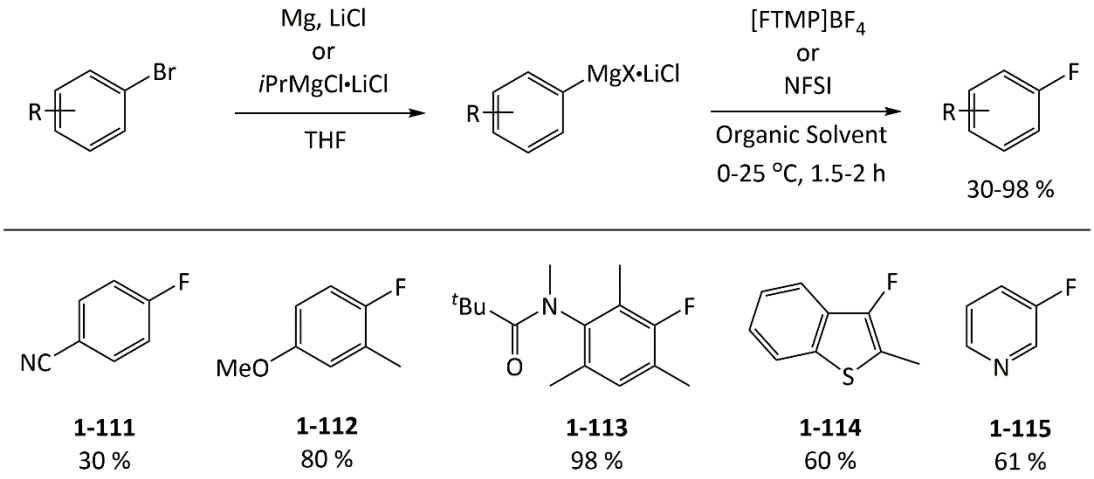

Scheme 22: Electrophilic fluorination of Grignard reagents.

1.3.1.1 Palladium-Mediated and Palladium-Catalysed Aromatic Fluorination

The Sanford[76] group was the first to demonstrate transition-metal catalysed fluorination of arenes through the use of *ortho*- directing groups (Scheme 23). Previous attempts at catalytic fluorination were unable to reductively eliminate the fluorinated products in the final stages of catalysis due to the strength of the metal-fluoride bond.[89]

Hull *et al.*[76] overcame the challenge of reductively eliminating from the palladium centre through the application of an electrophilic fluorinating agent instead of a nucleophilic one. Rather than attempting reductive elimination from Pd(II) to Pd(0), as with fluoride, the oxidising nature of electrophilic fluorinating agents allowed access to a high valent Pd(IV) fluoride intermediate capable of undergoing reductive elimination to yield the fluorinated product.

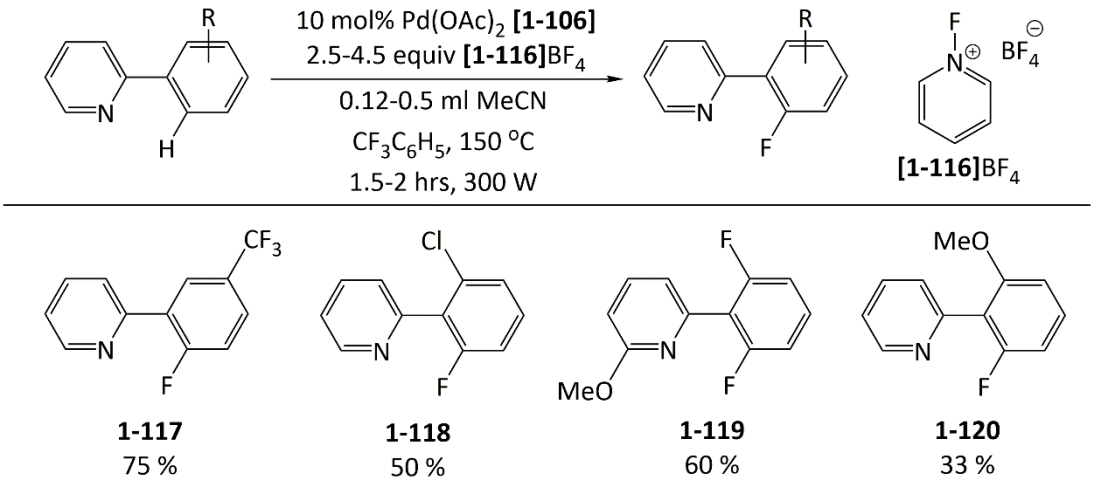

Scheme 23: Palladium-catalysed fluorination of 2-phenyl pyridine derivatives.

At the time of publishing the proposed mechanism was thought to proceed through either direct attack of the Pd-C bond by 'F^{+}' or through oxidative addition of fluorine to form a Pd(IV) intermediate, **[1-122]**. Further investigations by both the Sanford and Ritter groups confirmed the existence of Pd(IV) complexes and concluded the mechanism proceeded through the formation of these high valent intermediates (Scheme 24).[90-93]

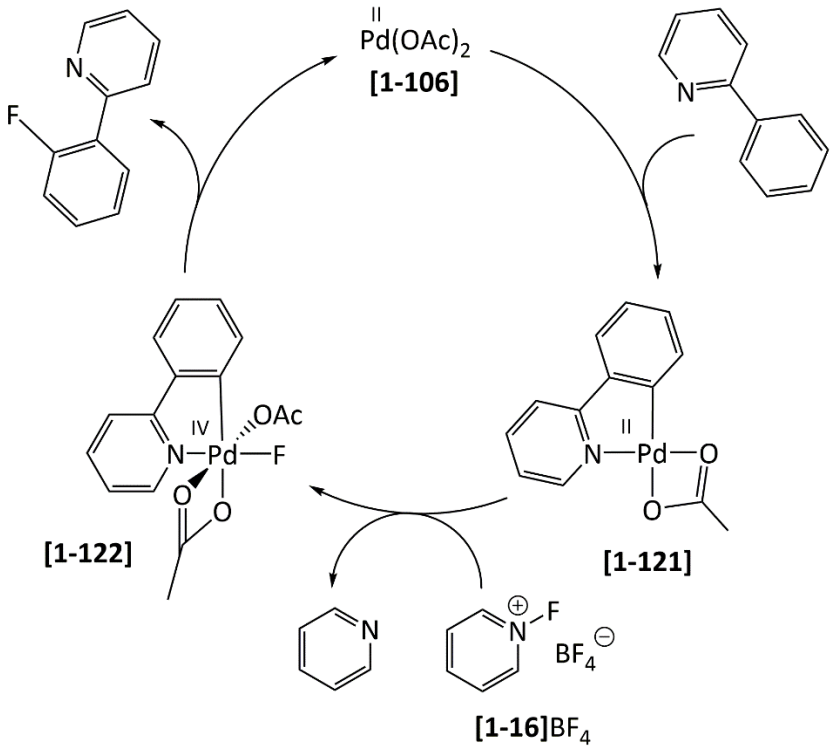

Scheme 24: The proposed mechanism proceed through oxidative addition of fluorine to [1-121] to form a Pd(IV) fluoride intermediate, [1-122]. Reductive elimination affords the fluorination product.

The Yu[94] group reported *ortho*-fluorination of triflamide protected benzylamines using NMP (*N*-methyl-2-pyrrolidone) as a promoter (Scheme 25). As with the reaction developed by Hull *et al.* the nitrogen moiety templates substrate coordination to the Pd catalyst, directing activation of the *ortho*- C-H bond, resulting in regioselective C-F bond formation. The role of *N*-methyl-2-pyrrolidone as a promoter remains to be elucidated. However, it was found to be crucial for obtaining the best yields. The method was tolerant of halide, trifluoromethyl, and methyl substituents, producing fluorinated products in moderate to good yield. The removal of the protecting triflamide group could be achieved through a number of routes to access a range of functional groups, providing a more general method to *ortho*-fluorinated benzyl derivatives (Scheme 26).

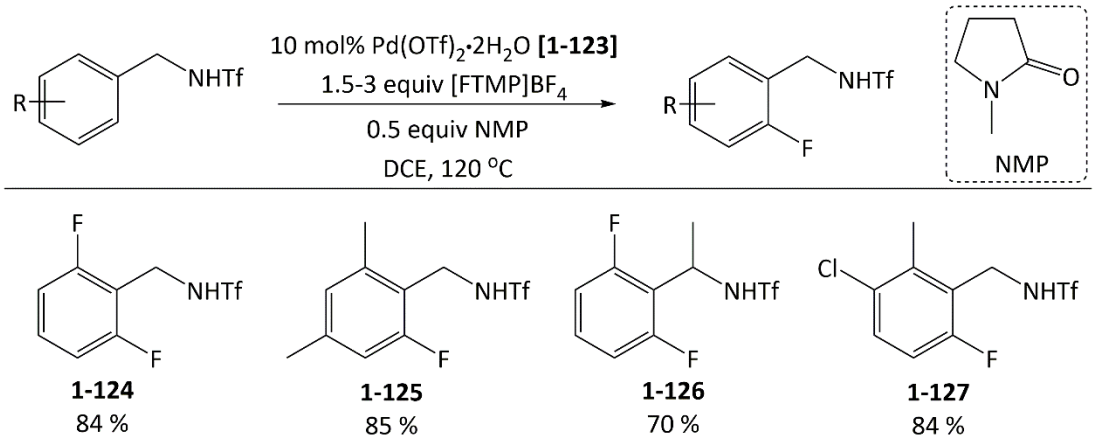

Scheme 25: Palladium-catalysed ortho fluorination of triflamide protected benzylamines.

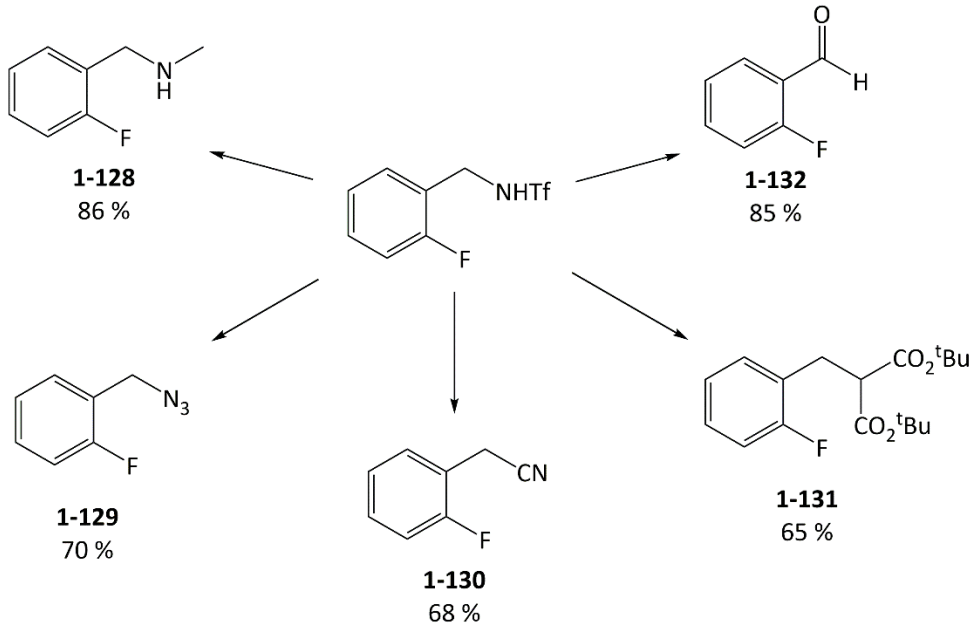

Scheme 26: Derivatisation of fluorinated benzylamines.

The main drawback to this method was the poor selectivity for the monofluorinated product, which Chan *et al.*[95] improved on using a weakly coordinating perfluorinated aryl amide auxiliary which allowed rapid dissociation of the monofluorinated product from the catalyst (Scheme 27). The procedure worked for a range of alkyl- and halide- substituted benzoic acids with moderate to good yields, with only trace quantities of the difluorinated product observed. Removal of the auxiliary ligand gave the fluoro-benzoic acid.

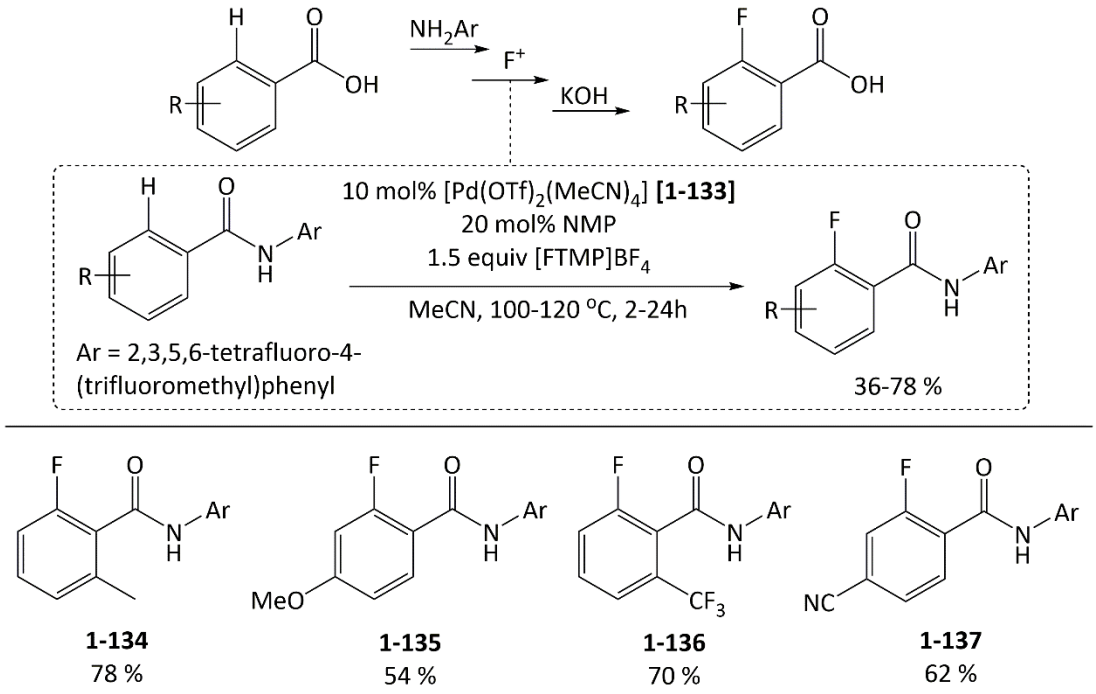

1-134 78 %

1-135 54 %

1-136 70 %

1-137 62 %

Scheme 27: Palladium-catalysed fluorination of weakly coordinating perfluorinated aryl amide auxiliary. The auxiliary can be removed by treatment of the product with KOH.

More recently Gutierrez *et al*.[96] demonstrated pallidum-catalysed C-H fluorination of arenes directed by a removeable oxazoline group. Treatment of aryloxazolines with NFSI and $[Pd(NO_3)_2]$ as a catalyst, afforded *ortho*-fluorinated arenes in 12-92 % yield (Scheme 28). Electron-rich substrates afforded fluorinated products in greater yield, while electron-deficient substrates proceeded with poor yield or, in the case of the *ortho*-nitrobenzene substituted aryloxazoline, no reactivity at all. It was proposed the more electron-rich substrates enhanced the Lewis basicity of the nitrogen on the oxazoline group, presumably facilitating fluorination through binding ability to palladium.

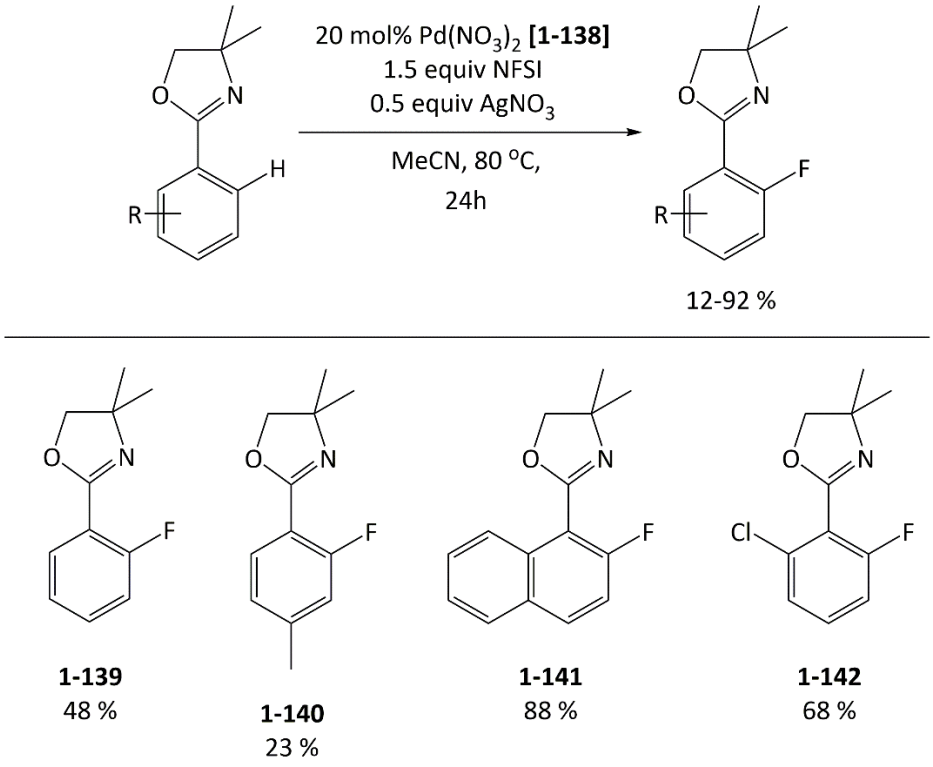

Scheme 28: C-H fluorination of aryloxazolines catalysed by palladium nitrate.

Addition of silver nitrate as a promoter was found to increase conversion. However, the exact role the promoter plays in the mechanism is not yet understood. The mechanism is proposed to proceed by the palladium II/IV cycle based on the other literature for Pd-catalysed fluorination (Scheme 29). Coordination of the oxazoline group to palladium directs C-H bond activation at the *ortho*-position of the ring. Fluorination of the palladium affords a Pd(IV)-fluoride intermediate which reductively eliminates the fluorinated aryloxazoline. Hydrolysis of fluorinated aryloxazolines was demonstrated under basic conditions to afford the corresponding carboxylic acid.

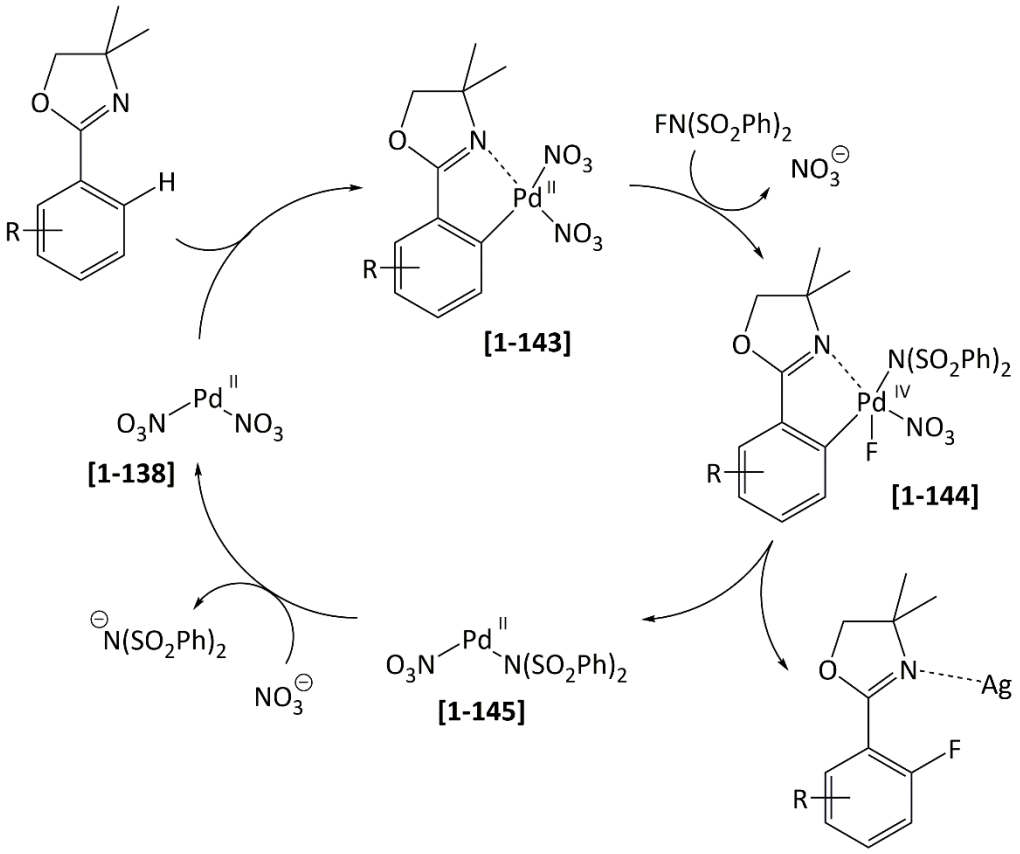

Scheme 29: Fluorination of aryloxazolines is proposed to proceed by templated C-H bond activation and formation of a palladium(IV)-fluoride intermediated. Reductive elimination affords the fluorinated aryloxazoline.

Testa *et al*.[97] recently reported a greener direct C-H halogenation of aryltetrazines for use in biochemical, material, and energy applications, which were previously accessed in poor yield through multi-step synthesis. The group detailed mono-, di-, and tetra-fluorination of *ortho*-C-H bonds of **[1-146]** using NFSI and 10 mol% $[Pd(dba)_2]$ as catalyst.

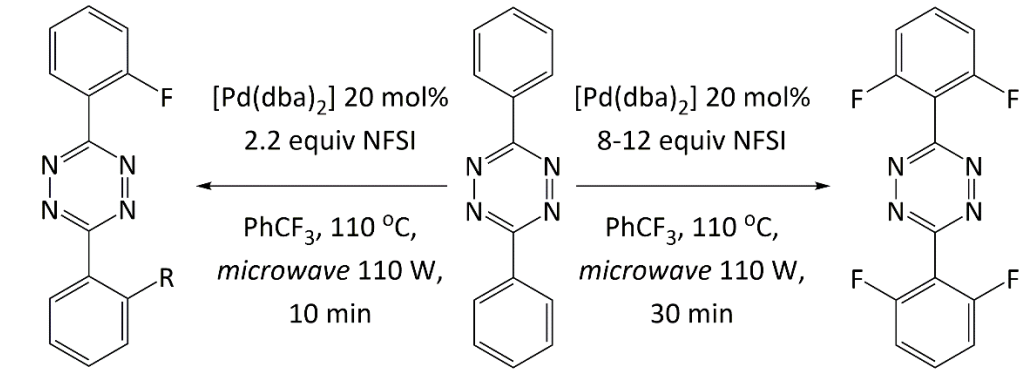

1-147
a, R = H; **b**, R = F
a:b, 77:23
90 %

1-146

1-147c
74 %

Scheme 30: Mono-, di-, tetra-fluorination of 1-146 was achieved under microwave conditions.

While C-H bond activation and subsequent fluorination is desirable, the necessity of directing groups limits the substrate scope at present. Nevertheless, fluorination has been demonstrated as proof of concept that such an approach is possible.

Furuya *et al*.[90] described a palladium-mediated strategy to access aryl fluorides from the corresponding aryl boronic acids (Scheme 31), which significantly expanded the substrate scope previously established by the Sanford[76] and Yu[94] groups. The versatility of the reaction stems from the accessibility and availability of boronic acids. Initial transmetalation from boron to palladium, forms an aryl Pd(II) complex, which is subsequently reacted with Selectfluor to afford the aryl fluoride in modest to high yield (31-82 %). It is proposed that the most likely pathway for fluorination is through formation of a high valent Pd(IV)-F intermediate, followed by subsequent reductive elimination of the fluorinated product. Electron-rich and electron-deficient aryl boronic acids were tolerated including alcohol groups which are susceptible to deprotonation under anhydrous fluoride conditions.

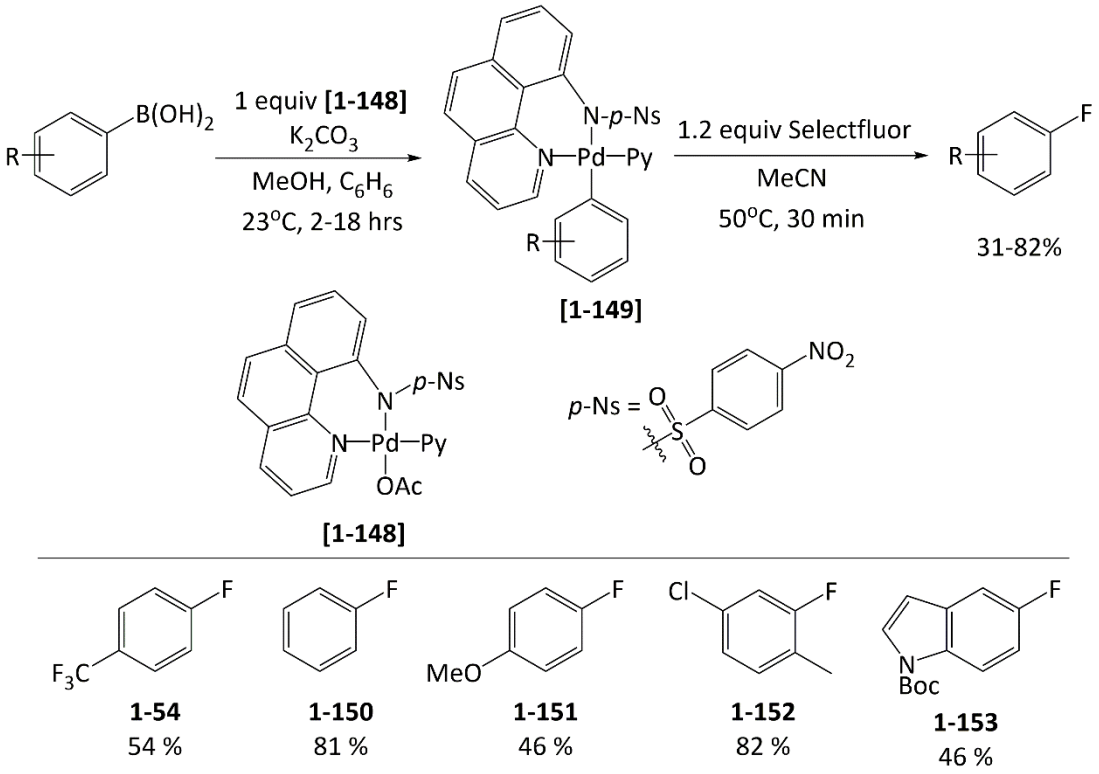

Scheme 31: Fluorination of aryl-palladium complexes synthesised from the corresponding aryl boronic acids.

Owing to slow transmetalation, catalytic turnover using boron reagents has been challenging. However, Mazzotti *et al.*[98] have developed an unusual palladium-catalysed system which is believed to circumvent transmetalation entirely, allowing catalytic fluorination of aryl trifluoroborates to be achieved in good to near quantitative yield (63-99 %) (Scheme 32). Although tolerant of air and moisture, as well as protic functional groups, such as alcohols and carboxylic acids, this method is not tolerant of methoxy substituted arenes or electron-deficient substrates. These often formed mixtures of constitutional isomers and/or difluorinated products. Nevertheless, the method was also applicable to other organoboron reagents including boronic acids, with good to excellent yield.

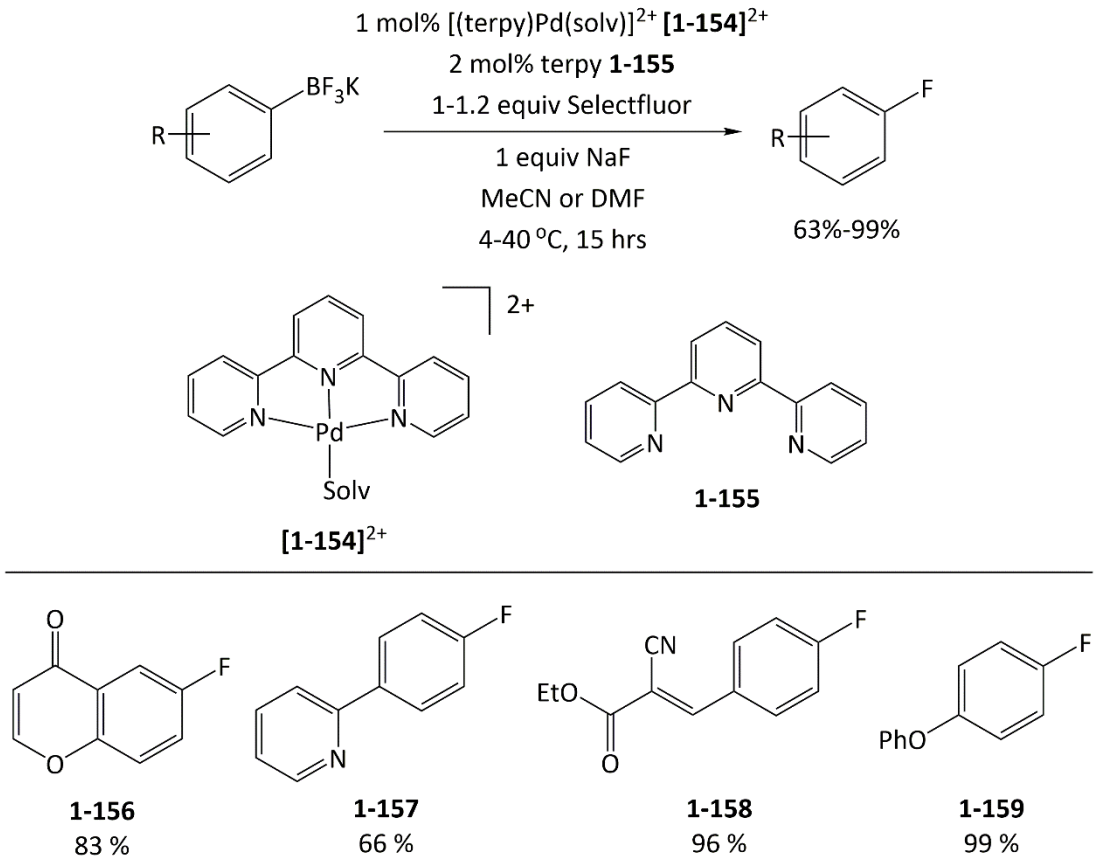

Scheme 32: Palladium-catalysed fluorination of potassium trifluoroborates.

Unlike previous palladium-mediated strategies, the proposed mechanism does not proceed through an organopalladium-fluoride complex (Scheme 33). Palladium is believed to act solely as a redox centre for single electron transfer (SET). An active Pd(II) species undergoes one electron oxidation by Selectfluor, generating a bis-terpyridyl Pd(III) intermediate and a cationic Selectfluor radical, **1-161**. Radical fluorine transfer to the aryl trifluoroborate forms the C-F bond, which is followed by SET from the Pd(III) species to form the aryl fluoride, BF_3, and the regenerated Pd(II) species.

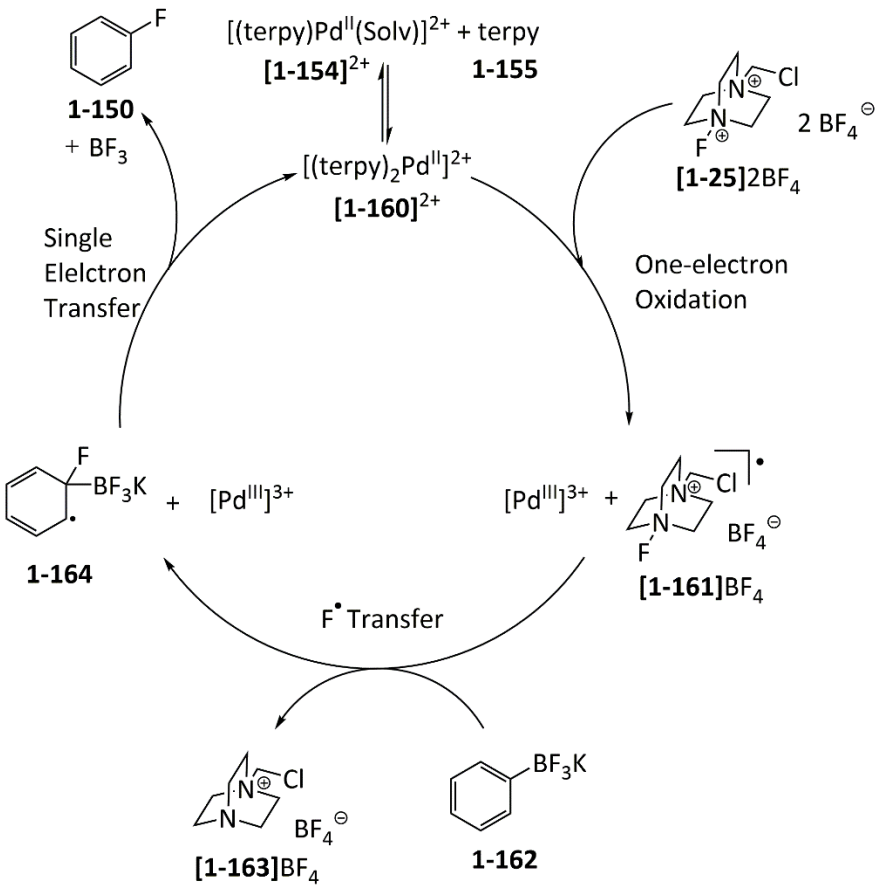

Scheme 33: Fluorination is proposed to proceed through SET mediated by palladium, generating 1-161. Fluorine transfer to 1-164 is followed by SET to afford the aryl fluoride.

With the aim of developing a facile late-stage fluorination procedure suitable for radiotracer synthesis, the strategy was adapted to use a fluoride source and external oxidant in place of an electrophilic fluorinating agent, to replicate the two-fold role an electrophilic fluorinating agent plays.[93, 99] The use of fluoride sources over fluorenium sources is desirable as synthesis of [^{18}F] electrophilic fluorinating agents require use [^{18}F] F_2 limiting its preparation to specially equipped facilities capable of handling elemental fluorine.

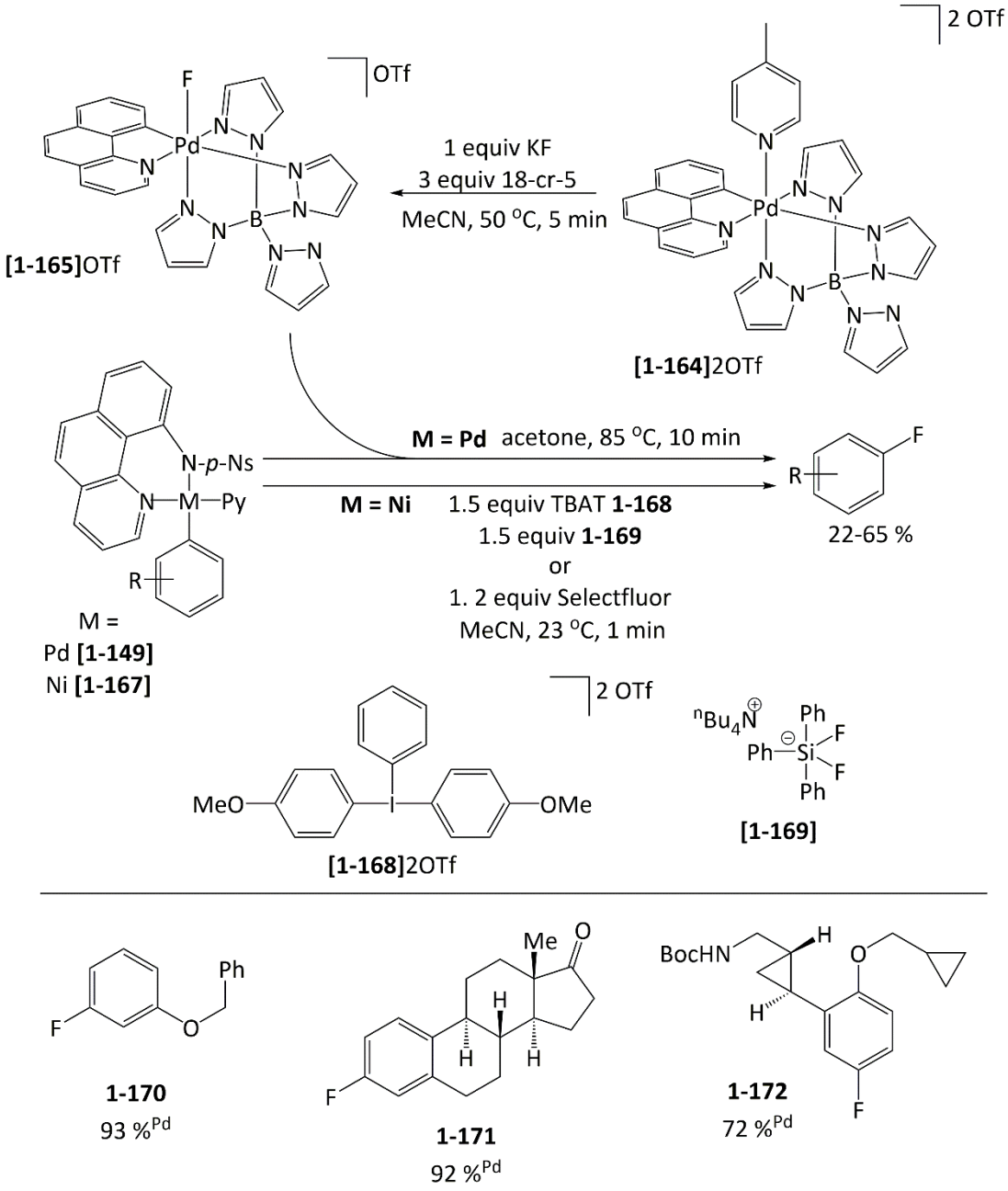

Scheme 34: Rapid fluorination of palladium and nickel aryl complexes, [1-149] and [1-167], for late stage fluorination. Palladium aryl complexes [1-149] undergo fluorination by [1-165]OTf over ten minutes, while nickel aryl complexes [1-167] undergo nucleophilic fluorination over one minute.

Prior to fluorination, complex **[1-149]** was prepared by transmetalation using aryl boronic acids as reported in earlier work.[90] While the active fluorinating agent, **[1-165]**OTf, which was designed to act as an oxidative fluorine transfer agent based upon the work by Stahl *et al.*,[100] was prepared within 5 minutes by reacting the parent complex **[1-164]**2OTf with KF (Scheme 34).[93] The parent complex **[1-166]** was chosen with tetrapyrazolylborate and terpyridyl ligands to minimise the risk of the complex undergoing reductive elimination of undesired C-F products prior to fluorine transfer.

Combining **[1-149]** and **[1-165]**OTf afforded aryl fluorides in 67-93 % yield over 10 minutes. The strategy was applied to radiolabelled fluoride yielding the desired aryl fluorides in under 60 minutes with relatively low radiochemical yield (RCY= 10-30 %).

In a further development, the strategy was applied to analogous nickel complexes,[99] which readily underwent fluorination yielding the radiolabelled aryl fluoride in under a minute at room temperature using aqueous [$^{18}F^-$] and an oxidant (Scheme 34). This alternative approach was more time and cost effective compared to the use of palladium, as only one nickel complex requires synthesis and the cost of nickel is lower than palladium. Overall the radiochemical yield was in line with current methods being developed (RCY= 13-58 %).

The Ritter group[101] more recently designed a palladium catalyst which favoured oxidative addition of fluorine prior to interaction with the substrate to form a tricationic high-valent palladium-fluoride intermediate, **[1-178]**$^{3+}$, capable of oxidative fluorine transfers to arenes, circumventing the need for C-H metalation of the substrate. Such an approach has not been observed or reported for other catalytic fluorination reactions, which typically proceed by initial metalation of the substrate followed by oxidative addition of fluorine. Oxidation of dicationic **[1-173]**$^{2+}$ to form the palladium(IV)-fluoride intermediate was proposed to be promoted by a destabilising interaction between the lone-pair of the un-coordinated nitrogen atom and the filled d_z^2 orbital of palladium according to DFT calculations. The high reactivity afforded to **[1-178]**$^{3+}$ enabled fluorination of unactivated arenes bearing both electron-rich and electron-poor substrates in yields of 30 to 85 % (Scheme 35). As with other non-directed C-H fluorination strategies, a mixture of *ortho*- and *para*- fluorinated products was obtained. The procedure was tolerant of nitriles, bromides, chlorides, heterocycles, and carbonyl containing groups (e.g. esters and amides). However, functional groups such as amines and thiols were not tolerated due to their incompatibility with electrophilic fluorinating agents. Additionally, electron-deficient arenes such as methyl-benzoates were not reactive enough for fluorination with **[1-178]**$^{3+}$ to proceed.

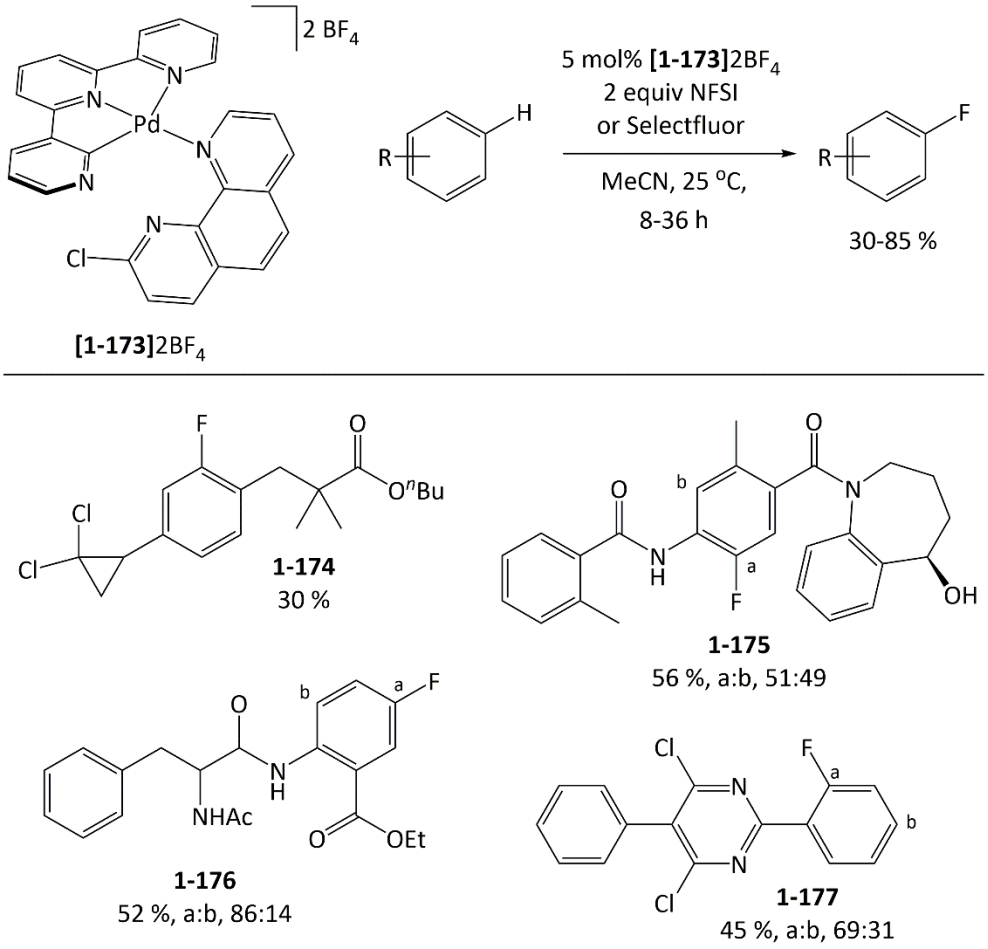

Scheme 35: Fluorination of unactivated arenes catalysed by [1-173]2BF$_4$ *via* an 'oxidation first' mechanism.

On the basis of the DFT calculations, fluorination is proposed to proceed by a fluoride-coupled electron transfer in which both electron-transfer and fluorine transfer occur in the transition state. The transition state is calculated to exhibit singlet diradical character with spin density residing on both the palladium and aryl carbon atoms (Scheme 36). The reaction is proposed to proceed by two fluoride-coupled electron transfers in the same transition state with a barrier of 21.8 kcal mol^{-1}. Subsequent deprotonation affords the fluorinated arene. Although **[1-178]**$^{3+}$ could not be isolated due to rapid reduction, the analogous palladium(IV)-fluoride **[1-181]**$^{3+}$ was isolated. Complex **[1-181]**$^{3+}$ was found to react with **1-180** to afford **1-182** supporting the 'oxidation first' mechanism.

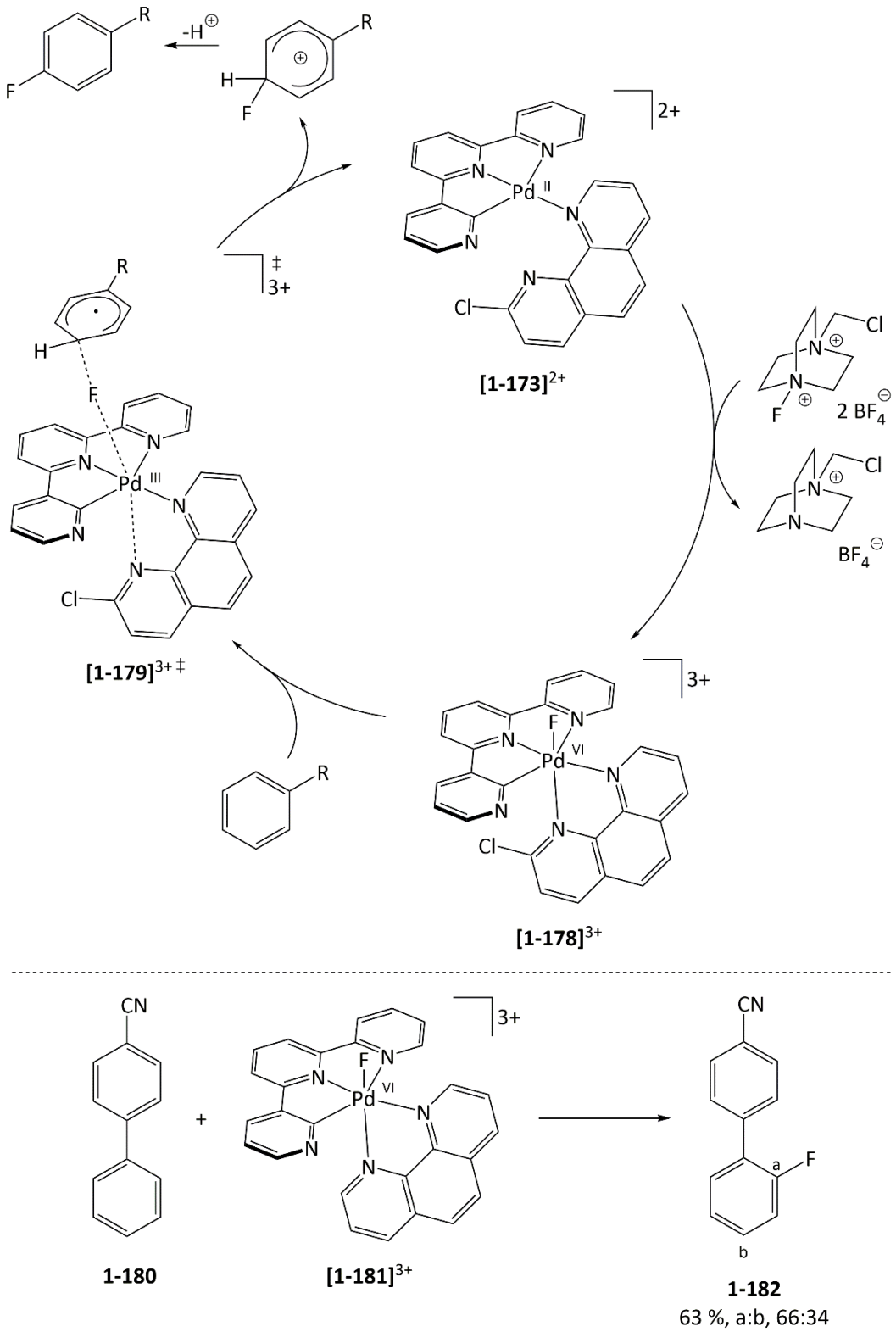

Scheme 36: Fluorination of unactivated arenes reported by Ritter *et al*. is proposed to proceed by oxidative fluorination of [1-173]$^{2+}$ to afford palladium(IV)-fluoride [1-178]$^{3+}$. Fluorination of the arene is believed to proceed *via* transition state [1-179]$^{3+}$, with deprotonation affording the fluorinated product. The palladium(IV)-fluoride [1-178]$^{3+}$ was isolated and when combined with 1-80 affords the fluorinated product 1-82.

1.3.1.2 Silver-Mediated and Silver-Catalysed Aromatic Fluorination

Silver was identified by the Ritter group as a metal capable of redox participation, like palladium, and was postulated its potential use in the synthesis of aryl fluorides.[90, 92] Unlike palladium, silver is not known to undergo two electron processes but one electron processes, giving rise to unusual postulated mechanisms.[102-104] Through the use of commercially available aryl stannanes, aryl fluorides were afforded in good to excellent yields (63-83 %) using super-stoichiometric AgOTf (Scheme 37).[103] Electron-rich and electron-deficient arenes were tolerated including biologically active molecules, such as quinine and estrone, which were fluorinated in good yield through three-step, triflation, stannylation and fluorination.

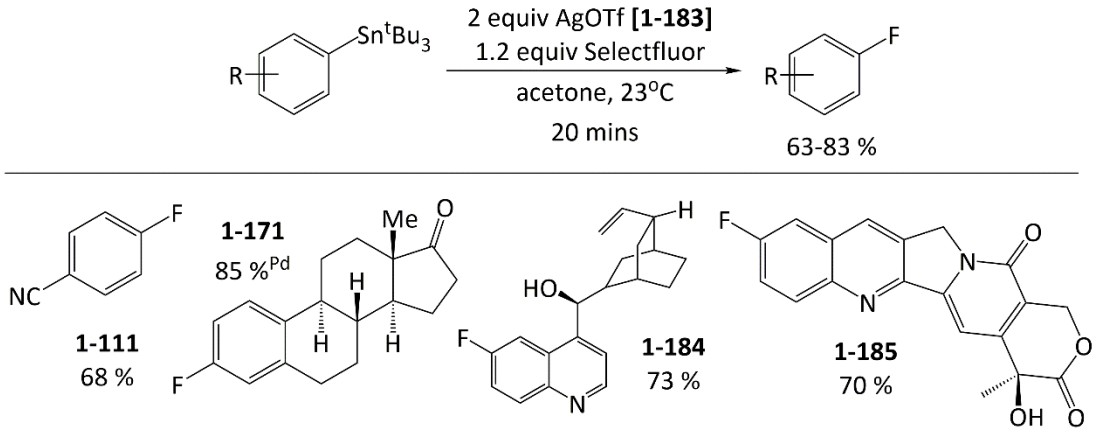

Scheme 37: Silver-mediated fluorination of aryl stannanes.

Despite the high functional group tolerance and the wide range of commercially available or accessible arylstannanes, organostannane reagents are notoriously toxic making them impractical to handle and costly to dispose of. In addition, a significant quantity of the hydrodestannylated by-products (10-20%) were observed, making workup challenging.

The isolation of bimetallic complexes coupled with unaltered yields in the presence of a radical scavenger, suggested the mechanism (Scheme 38) involves initial transmetalation from tin to silver to form an (ArAg^I)·(Ag^{I}OTf) intermediate **[1-186]** (supported by spectroscopic data), followed by oxidative fluorination to form a bimetallic Ag(II)-Ag(II) species **[1-187]**. Reductive elimination of the aryl fluoride is believed to proceed through metal-metal participation whereby more than one metal centre is involved in the redox process.

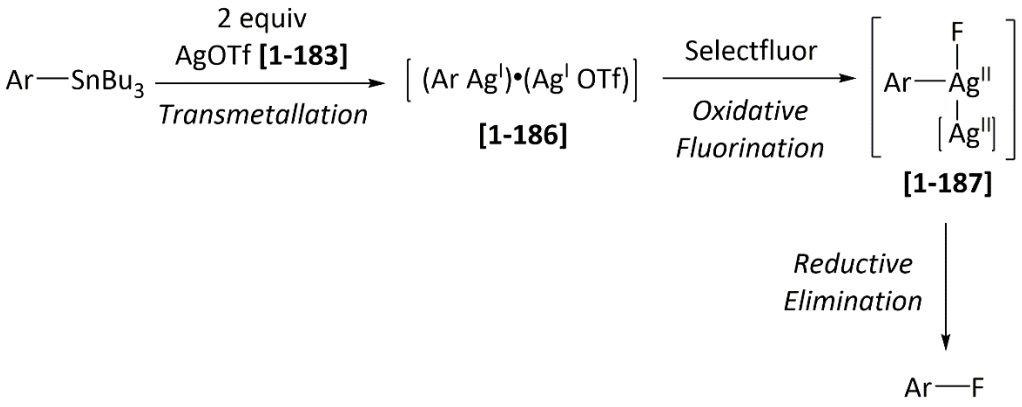

Scheme 38: Fluorination is believed to proceed through transmetallation to a bimetallic silver intermediate [1-186], followed by fluorination and subsequent reductive elimination of the aryl fluoride.

Tang *et al*.[104] optimised the conditions used, enabling a catalytic method to be developed using 5 mol% Ag_2O rather than 2 equivalents of AgOTf. The yield of previously studied substrates was improved overall (65-92 %) and the formation of the protodestannylated product reduced to less than 5 %. The substrate scope was also expanded to include tolerance of alcohols, sulfones and bridgehead amines. However, carboxylic acids were not well tolerated and are believed to form silver carboxylate species, while sulfide and amine bearing substrates failed to react. Amines formed *N*-fluoro species which ultimately eliminated HF, while sulfides are believed to act as nucleophiles with Selectfluor in unproductive pathways. Despite the Buchwald group having described a fluorination procedure directly from triflates,[58] a precursor to aryl stannanes, the silver catalysed fluorination described by the Ritter group displayed greater tolerance towards protic functional groups and proceeded under milder conditions.

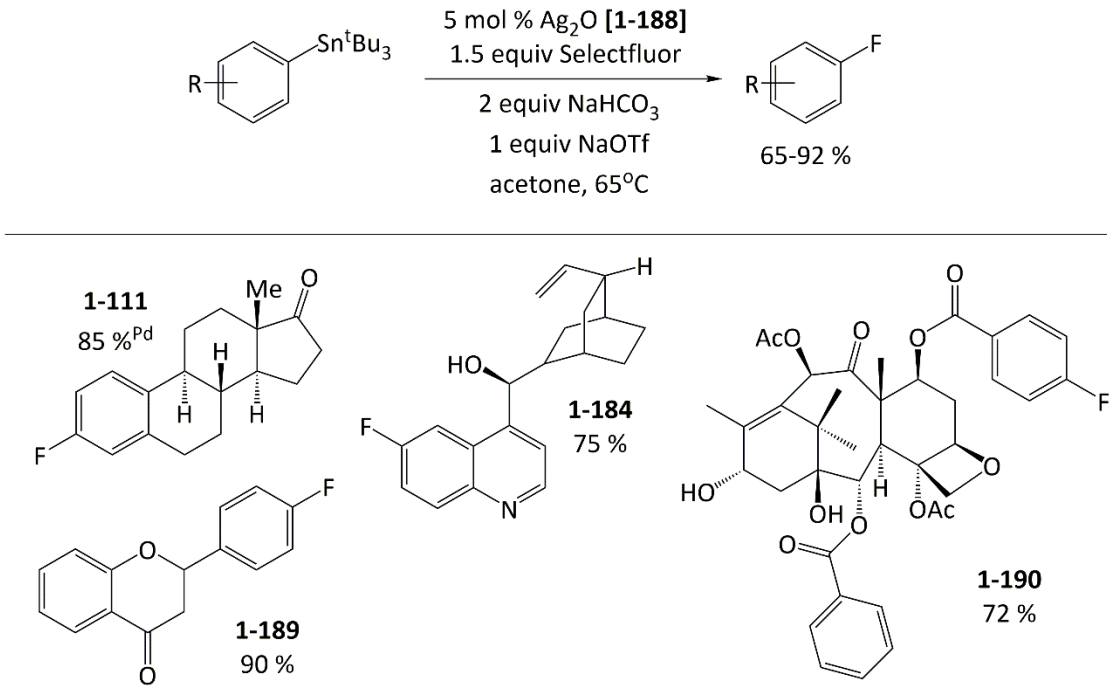

Scheme 39: Silver-catalysed fluorination of aryl stannanes.

The mechanism for fluorination is believed to proceed through initial transmetalation of the aryl stannanes to **[1-188]**, which undergoes fluorination to a bimetallic silver fluoride-aryl complex, **[1-166]**. Subsequent reductive elimination affords the aryl fluoride (Scheme 40).

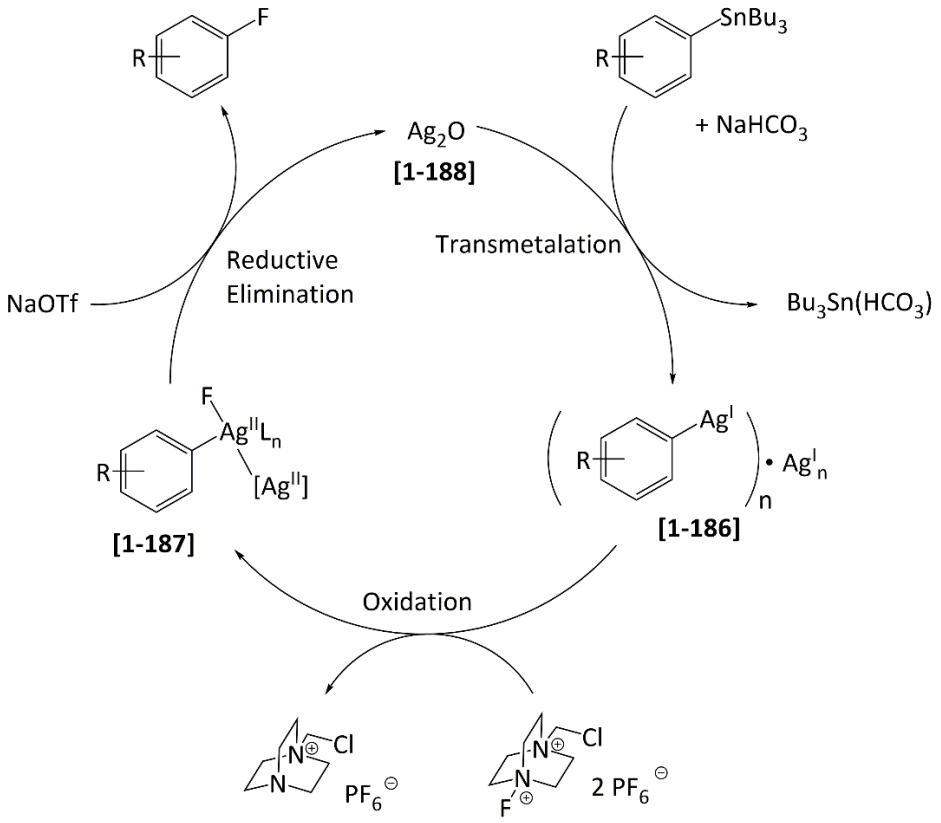

Scheme 40: Catalytic cycle proposed for silver-catalysed fluorination proceeding through transmetalation, fluorination and reductive elimination.

Furuya *et al*. also demonstrated that silver could be used in place of palladium to mediate the fluorination of arylboronic acids and esters.[102] The commercial availability and synthetic accessibility of boronic acids, coupled with their low toxicity and high stability make them preferable alternatives to stannanes. Fluorination was achieved in high yield (70-86%) by a two-step process; initial transmetalation to form an aryl silver(I) intermediate, followed by subsequent electrophilic fluorination by Selectfluor (Scheme 41). The method was also applicable to pinacolate and neopentyglycolate esters in lower yield (70 % and 87 % respectively, versus 95 % for the analogous boronic acid). The need for super-stoichiometric AgOTf under optimum conditions suggests fluorination proceeds by the same mechanism proposed for the fluorination of arylstannanes.[103] The reaction tolerated the same functional groups as the reaction utilising aryl stannanes but with no analogous hydrodestannylated by-products. The generality of this method is greater with the development of various catalytic methods for incorporation of boronic acids, allowing C-F bond formation from unactivated arenes.[105] While the move from aryl stannanes to aryl boronic acids improved the environmental impact and safety aspects of their previous work, a catalytic method was not described.

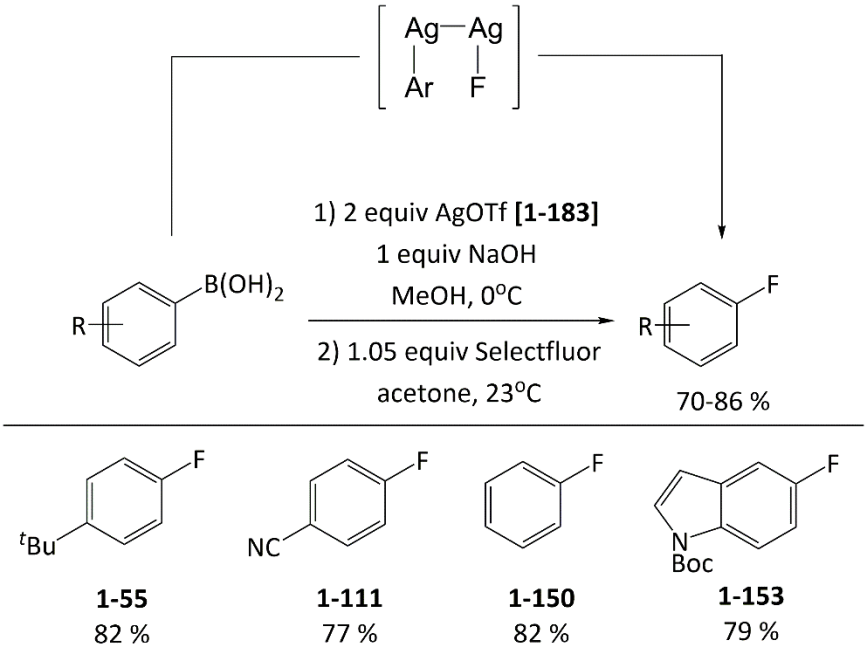

Scheme 41: Silver-mediated fluorination of aryl boronic acids.

Dubbaka *et al.*[106] extended the scope to include one-pot silver-mediated fluorination of potassium trifluoroborates in moderate to excellent yield (35-91 %). A range of aryltrifluoroborate salts containing both weak and strong electron withdrawing and electron donating groups in *ortho*-, *meta*-, and *para*-positions were well tolerated (Scheme 42). However, 2-5 % protodemetalation was observed in all cases of isolated product making purification challenging. Other boronic acid derivatives, including pinacol esters, under the same conditions resulted in poor conversion. Super-stoichiometric equivalents of AgOTf were required under optimal conditions as reported previously[102] which again could be indicative of a bimetallic mechanism in play.[103] The method is tolerant of a range of functional groups and proceeds under mild conditions. However, the need for super-stoichiometric silver reduces the practicality of industrial scale up and its sustainability. In addition, the long reaction times (5-15 h) render it unsuitable for PET radiotracer synthesis.

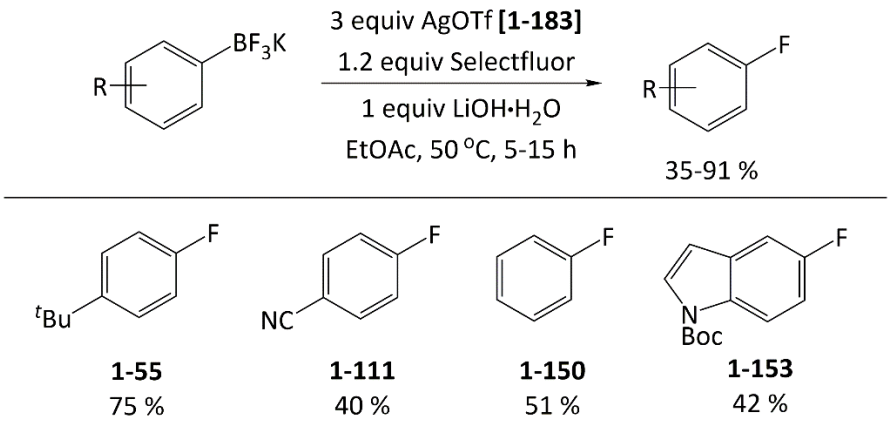

Scheme 42: Silver-mediated fluorination of potassium trifluoroborates.

Attempts to use a cheaper and more sustainable iron mediator[107] in place of silver resulted in poor regioselectivity for substrates with strong electron donating substituents and non-*para*- substituents, and inconsistent yields for the desired product (2-60%) similar to metal free reactions (Scheme 43).[108, 109]

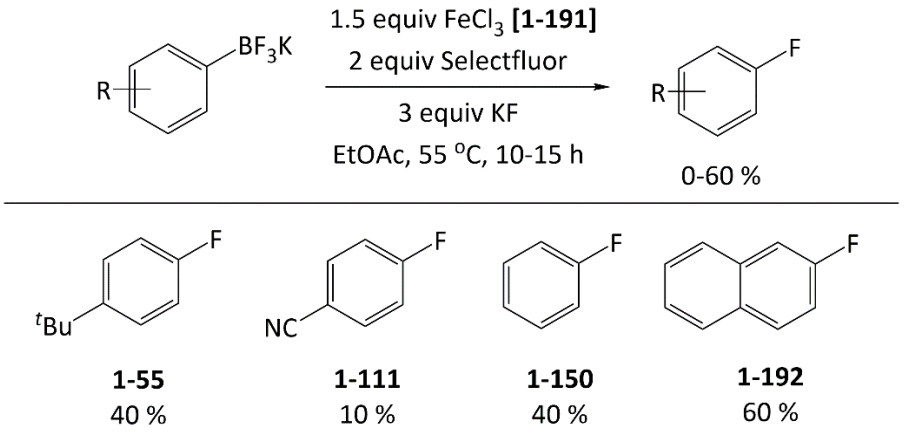

Scheme 43: Iron-mediated fluorination of potassium trifluoroborates.

1.3.1.3 Copper-Mediated and Copper-Catalysed Aromatic Fluorination

Based on the work by Fier *et al.*[59] using a Cu(III)-F species and aryl iodides (see section 1.2.2), Ye and Sanford were able to demonstrate a milder copper-mediated fluorination procedure reverting back to the use an electrophilic fluorinating agent and aryl stannanes or trifluoroborates (Scheme 44).[110] Both aryl stannanes and aryl trifluoroborates were fluorinated in a two-step procedure involving initial formation of a copper (III) fluoride intermediate, **[1-193]**, followed by transmetalation and subsequent reductive elimination of the aryl fluoride. Aryl fluorides were afforded in 60-93 % and 40-82 % yield for stannanes and trifluoroborates respectively. Electron-rich and electron-deficient substrates were well

tolerated. However, protic functional groups such as alcohols, amines, and carboxylic acids were again not tolerated. The yields were not improved upon compared to the nucleophilic strategy,[59] or to the palladium- and silver-mediated/ catalysed strategies.[98, 102-104, 106]

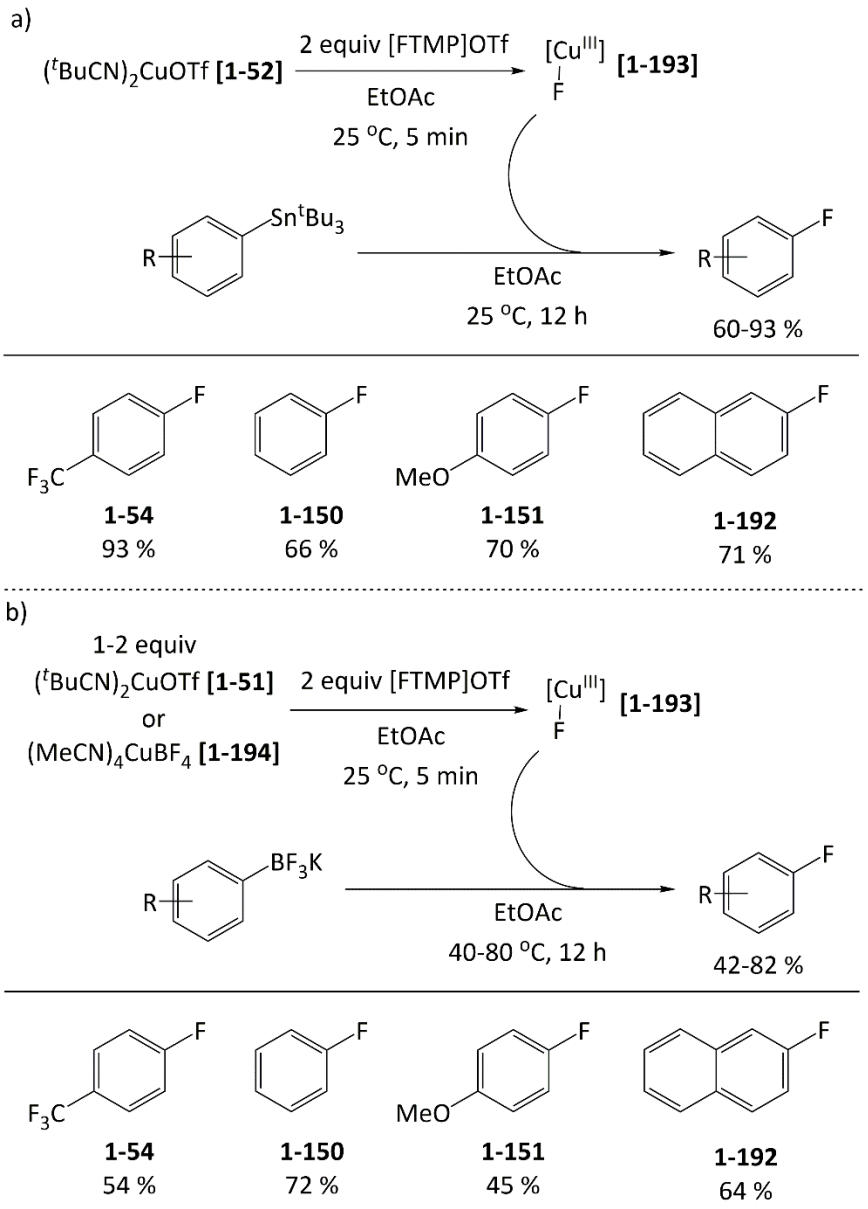

Scheme 44: a) Fluorination of aryl stannanes and b) aryl potassium trifluoroborates by a copper fluoride species [1-172].

1.3.2 Metal-Mediated and Metal-Catalysed C(sp^2)-F Bond Formation

Fuyura *et al.* were able to fluorinate alkenyl boronic acids, under the same conditions as aryl boronic acids (Scheme 45), in good yield (65-74 %).[102] Unlike previous methods, the fluorination of the alkenyl boronic acids proceeded with retention of stereochemistry, suggesting stereospecific boron-silver transmetalation and stereospecific reductive

elimination of the fluoroalkene. The feasibility of one-pot hydrofluorination was demonstrated through hydroboration and subsequent silver-mediated fluorination of phenylacetylene to afford *E*-β-fluorostyrene in 76 % yield (Scheme 45). The need for super-stoichiometric silver suggests a bimetallic silver intermediate as proposed for other silver catalysed/mediated strategies (e.g. Scheme 40).

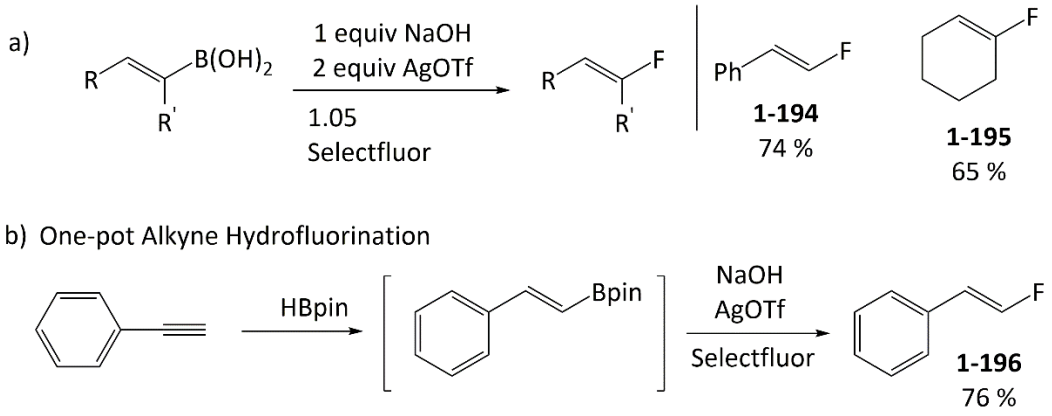

Scheme 45: Silver-mediated fluorination of alkenyl boronic acids and one-pot hydrofluorination of phenylacetylene.

1.3.3 Metal-Mediated and Metal-Catalysed C(sp^3)-F Bond Formation

Alongside catalytic fluorination of phenylpyridines, Hull *et al*.[76] also demonstrated fluorination of 8-methyl quinolone derivatives in modest to good yield (49-57%) with functional group tolerance similar to phenylpyridine derivatives. Isolated Pd(IV) fluoride intermediates supported the hypothesis that pallidum catalysed alkyl C-F bond formation also proceeded through high valent palladium intermediates followed by reductive elimination of the coupled product.[111]

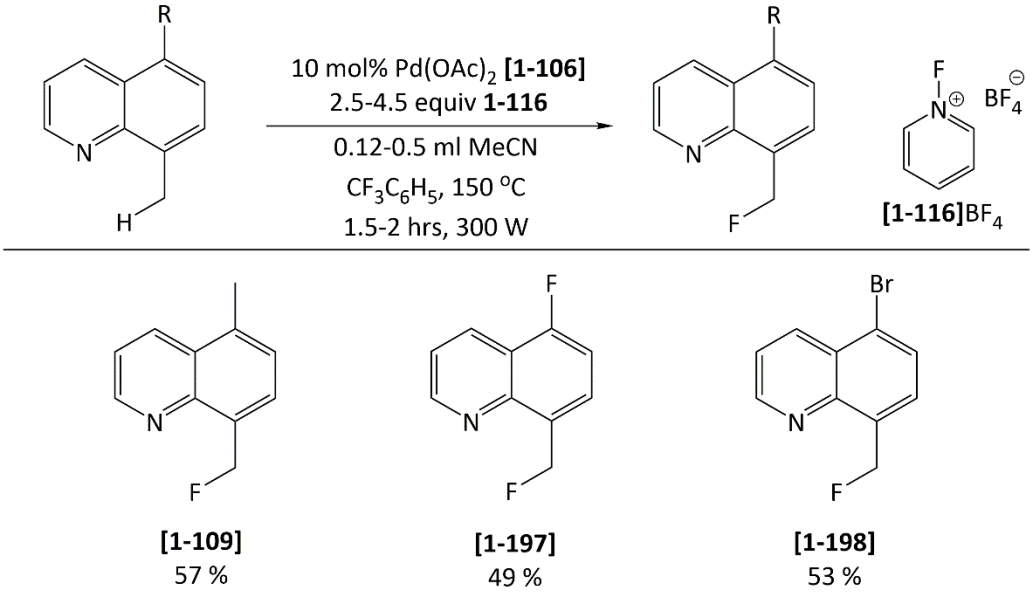

Scheme 46: Hull *et al.* demonstrated catalytic fluorination of 8-methyl quinolone derivatives.

The Gouverneur group developed a mild hydrofluorination strategy which employs the sequential addition of hydride and fluorenium (F^+) with high diastereoselectivity (Scheme 47) rather than sequential addition of fluoride and acid.[112]

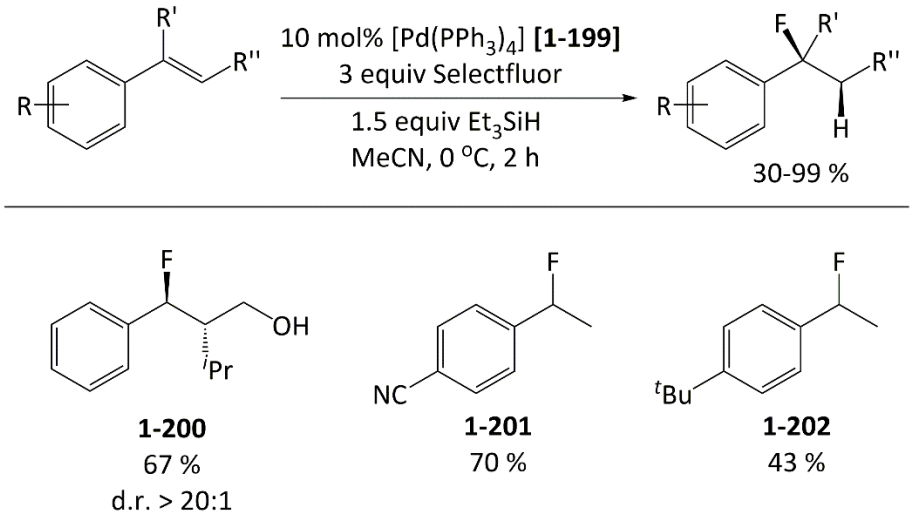

Scheme 47: Palladium-catalysed regioselective *cis*-hydrofluorination of allylic arenes.

This palladium-catalysed method enabled regioselective *cis*-hydrofluorination of allylic arenes to afford benzylic fluorides in modest to near quantitative conversion (30-99 %), with electron-neutral and electron-deficient allylic arenes displaying the highest conversion. Hydrofluorination of *Z*- and *E*- styrenes gave the corresponding *syn*- and *anti*- benzylic fluoride respectively with greater than 20:1 diastereoisomeric ratio, which is consistent with

a *cis*- specific hydrofluorination mechanism. A wide range of functional groups, such as ether, amine, halide, sulfonimide, nitrile, nitro, esters, and alcohol groups, are well tolerated.

Excess Selectfluor was required under optimised conditions which is believed to play the twofold role of fluorenium source and oxidant to oxidise the Pd(0) precatalyst to an active Pd(II) species (Scheme 48). Subsequent activation of the silane generates the Pd(II) hydride species **[1-203]** which reversibly forms η^3-benzylic intermediate **[1-204]** through *syn*-hydropalladation. Fluorination of **[1-204]** by Selectfluor to **[1-205]** is followed by reductive elimination to generate the benzylic fluoride. Diastereoselectivity is consistent with the formation of Pd(IV)-F species **[1-205]** rather than displacement of palladium by fluorine in an S_N2 like mechanism.

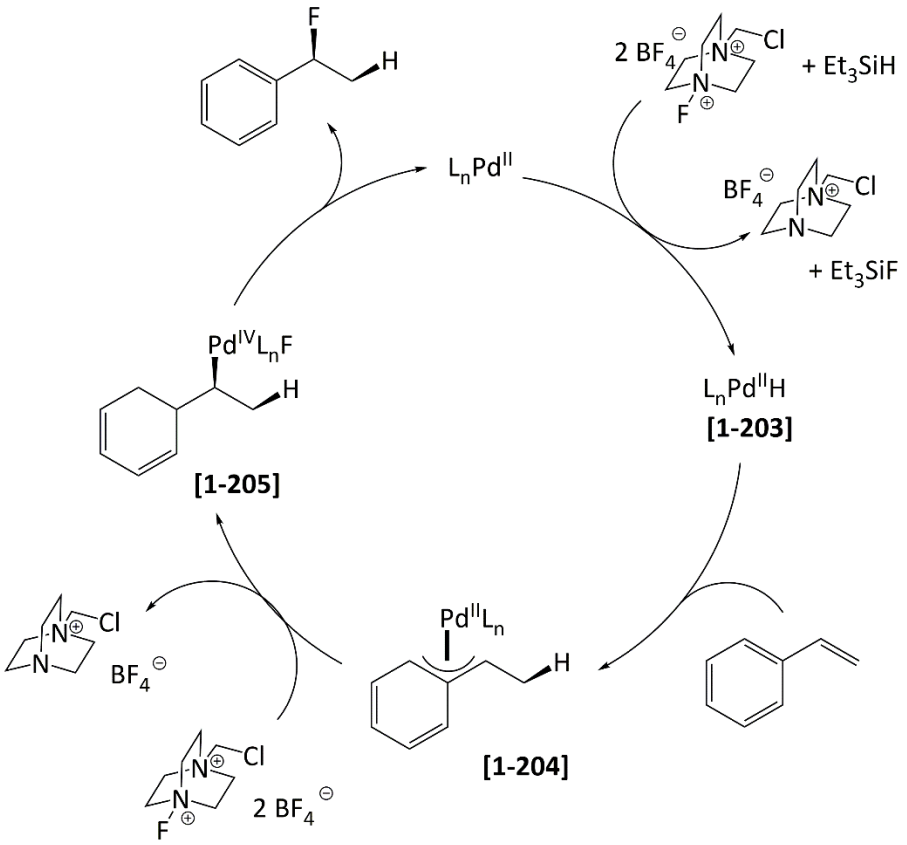

Scheme 48: Proposed mechanism for *cis*-hydrofluorination of alkenes through *syn*-hydropalladation of allylic arene [1-204] and reductive elimination from [1-205].

Alkyl fluorides can also be accessed through atom efficient aminofluorination of styrene using NFSI as both the fluorine and amine source (Scheme 49).[113] A mixture of electron-rich and electron-deficient styrenes were tolerated producing regioselective aminofluorinated products in modest to excellent yield (37-88%). The mechanism remains unclear but is believed to proceed *via* a Pd(II/IV) cycle rather than a Pd(0/II) cycle. Formation of

difluorinated by-products is believed to occur by β-hydride elimination and hydrofluorination of the fluoroalkene.

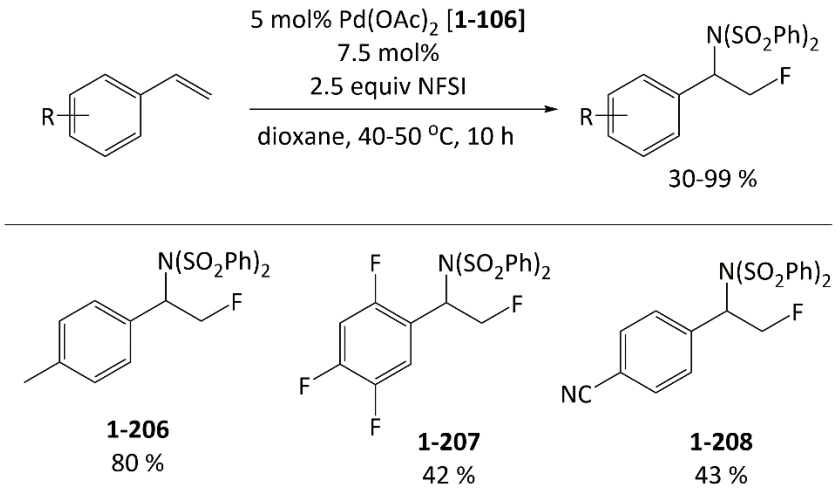

Scheme 49: Palladium catalysed fluoroamination of allylic arene affording alkyl fluorides.

1.3.3.1 Platinum-Mediated Fluorination

High valent Pt(IV) intermediates have also been studied for C-F coupling reactions, although successful coupling *via* a reductive elimination pathway has only recently been reported (Scheme 50).[114] Prior attempts resulted in the formation of stable difluoride complexes[115] which failed to reductively eliminate the alkyl fluoride. Zhao *et al*. achieved stereoretentive fluorination through steric crowding of the Pt centre using a bulky phosphine ligand, Triphos (Scheme 50). The steric requirement of the phosphine ligand helps to favour C-F reductive elimination, while simultaneously disfavouring β-hydride elimination. Nevertheless, β-hydride elimination still proceeded as a non-productive pathway. The scope of the reaction has yet to be explored, yet the method has demonstrated the concept of platinum-mediated fluorination.

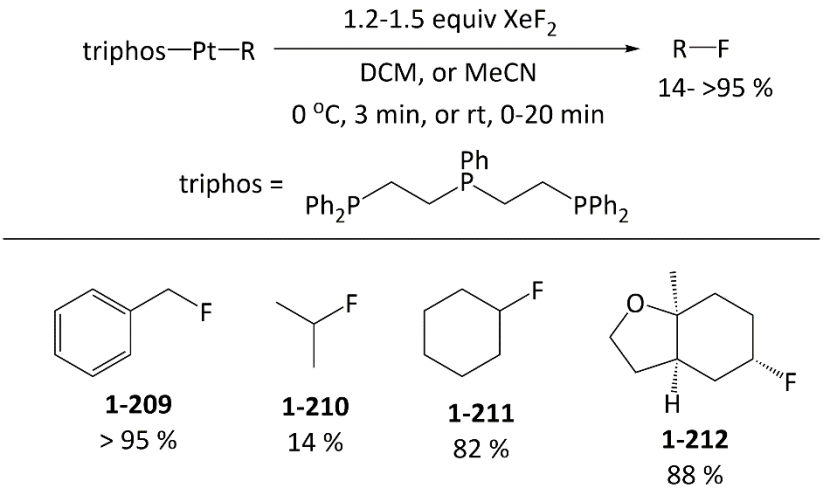

Scheme 50: Fluorination of alkyl platinum complexes and subsequent reductive elimination of alkyl fluorides from sterically crowded high valent Pt(IV)-F intermediates.

1.3.3.2 Gold-Mediated and Gold-Catalysed Fluorination

Au(III) alkyl complexes are known to undergo facile reductive elimination of alkyl halides (Cl, Br, and I).[116] However Au(III) fluoride complexes are an exception. These complexes are surprisingly stable toward reductive elimination due to the strength of the Au(III)-F bond.[117, 118] Nevertheless, as seen with platinum-mediated fluorination, increasing the steric bulk around the metal centre allowed for alkyl fluorides to be observed upon consumption of all other coupling partners (Scheme 51).[119] Initially, yields of alkyl fluoride were lower than 17% with β-hydride elimination effectively outcompeting C-F coupling. The use of cyclic substrates promoted C-F reductive elimination over β-hydride elimination, but not sufficiently to completely inhibit it. In some cases, a mixture of fluorinated products was obtained, suggesting the alkyl ligands are able to undergo rearrangement. Substrates lacking β-hydrogens were either unable to undergo regio-selective fluorination or underwent γ-hydride elimination, the only exception being benzylic ligands.

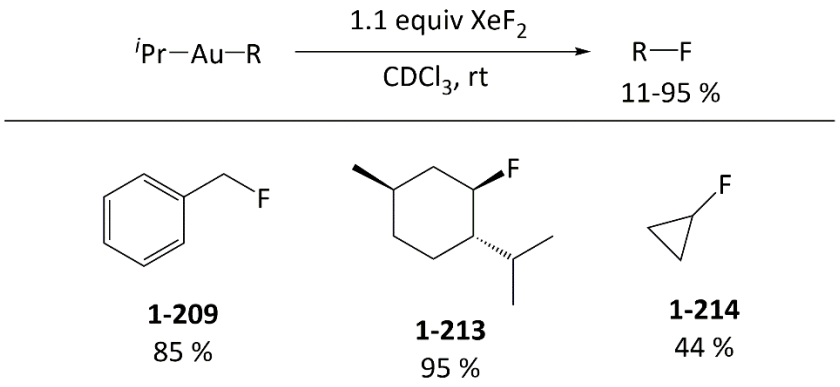

Scheme 51: Fluorination of alkyl gold complexes and sequent reductive elimination of alkyl fluorides from sterically crowded Au(III)-F intermediates.

The proposed mechanism describes dissociation of fluoride from the difluoride complex to give a coordinatively unsaturated cationic Au(III) intermediate, **[1-215]**$^{+}$, from which C-F bond formation or β-hydride elimination/abstraction by fluoride can occur. From this intermediate the alkyl ligand may undergo rearrangement, giving rise to mixtures of products.

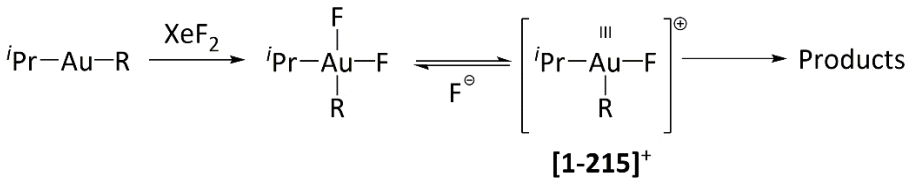

Scheme 52: The mechanism is proposed to proceed by the formation of [1-215]$^{+}$**.**

While gold-mediated fluorination has been demonstrated, the limited substrate scope and competing β-hydride elimination pathway have great implications for future development of gold catalysis and direct C-H bond activation-fluorination of alkanes in general. The challenge of C_{sp^3}-H bond activation/fluorination extends to copper as well, with the same side products having been observed with similar substrates using a copper catalyst in a proposed radical mechanism.[120]

As seen with Au(III), selective fluorination of benzylic substrates is less challenging compared to other alkyl substrates and has been studied with other metals including, manganese,[121] iron,[122] and silver.[123]

Due to the poor selectivity of deoxyfluorination of allylic alcohols, Thibaudeau and Gouverneur described an alternative regio-selective method to allylic fluorides through the use of allylic trimethylsilanes accessed by traditional cross-metathesis (Scheme 53).[124] The

regio-selectivity of fluorodesilylation was believed to arise from the presence of the trimethylsilyl leaving group which stabilised charge localised on the carbon β to silicon. Protected alcohols, carboxylic acids, aldehydes and amines, along with esters were tolerated under reaction conditions. However, an α,β-unsaturated carbonyl did not undergo fluorodesilylation due to the strong electron withdrawing effect of the carbonyl. While regioselectivity was achieved, enantioselectivity was not studied or reported.

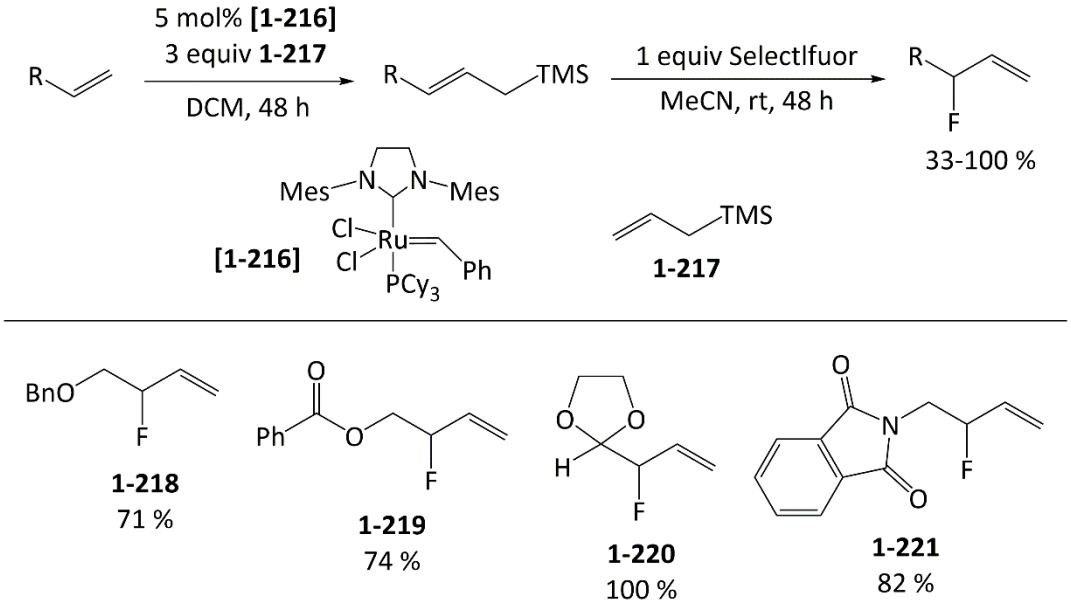

Scheme 53: Regioselective formation of allyic fluorides through fluorodesilylation of allylic trimethylsilanes.

1.3.3.3 Rhodium-Catalysed Fluorination

A recent example described by Yuan *et al*,[125] demonstrated oxyfluorination of diazocarbonyls using **1-222** and an alcohol in the presence of a rhodium catalyst (Scheme 54). Additionally, the procedure could also be applied to the oxytrifluoromethylation of diazocarbonyls as well. Electron-poor diazocarbonyls afforded the fluorinated compound in higher yields than electron-rich diazocarbonyls. Aliphatic and heterocyclic diazocarbonyls could also be tolerated. Although isolation of the desired fluorinated product was possible, the oxyfluorination of an ester substituted substrate gave a complex mixture of products due to higher reactivity. The oxygen nucleophile could also be changed to include a variety of electron-rich and electron-poor substrates, including unsaturated alcohols bearing alkene and alkyne groups. During optimisation, Selectfluor was found to be unsuitable, with no desired product being observed. However, no comment was made on the outcome of the reaction or a possible explanation given for the lack of product. The procedure could also be

applied to the synthesis of bioactive alcohols, for example, cholesterol was successfully oxyfluorinated to afford a 1:1 diasteromeric mixture in 68 % yield.

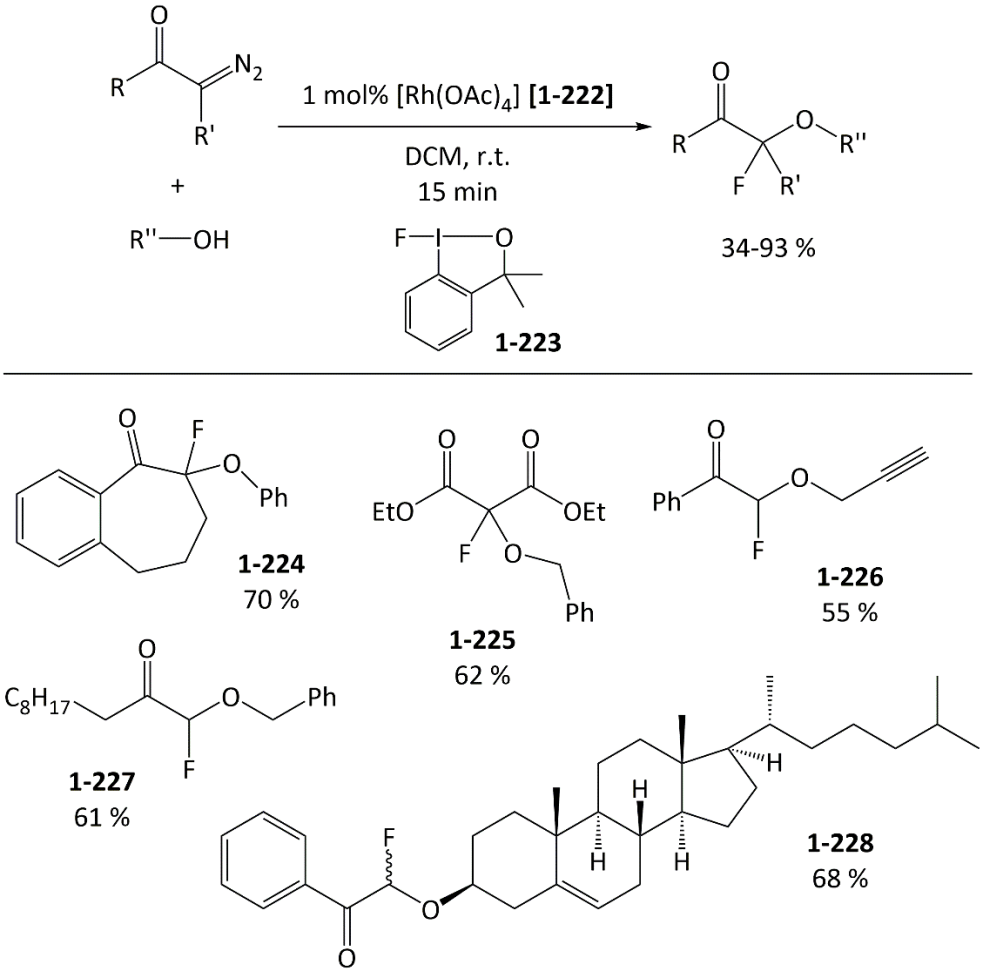

Scheme 54: Rhodium-catalysed oxyfluorination of diazocarbonyl with 1-223 and respective alcohol

The reaction conducted in the absence of the fluorinating agent afforded nucleophilic addition of the alcohol which suggested C-O bond formation occurs prior to fluorination. Based on this and literature data,[126, 127] the mechanism for oxyfluorination (Scheme 55) was proposed to proceed by the formation of a rhodium carbene complex, **[1-229]**. Insertion of the alcohol into the rhodium carbene bond affords an onium ylide, **[1-229]**. Electrophilic fluorination and subsequent proton transfer affords the oxyfluorinated product. The fluorination step is proposed to proceed by either oxidative addition of the fluorinating agent to rhodium, followed by reductive elimination, or *via* σ-bond metathesis.

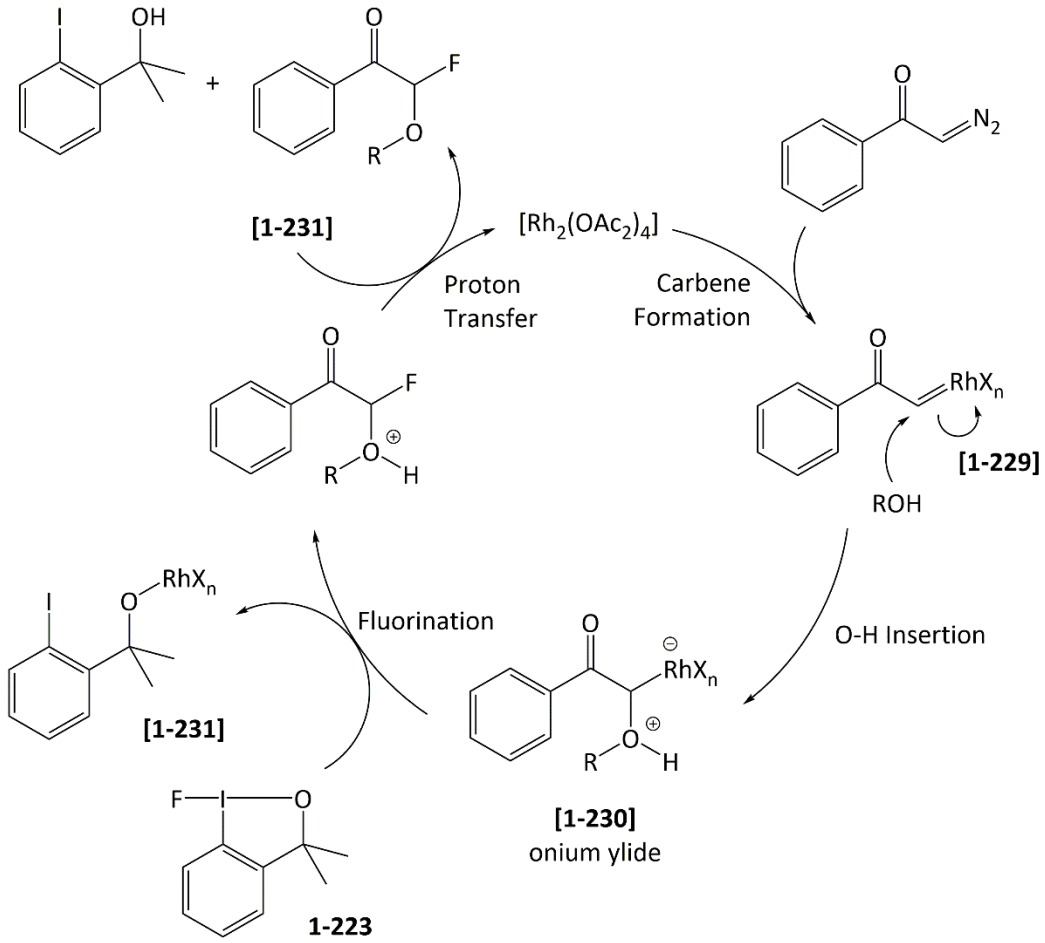

Scheme 55: Oxyfluorination of diazocarbonyls is proposed to proceed by initial formation of a rhodium carbene complex. Insertion of the alcohol into the rhodium carbene bond affords onium ylide, [1-230]. Fluorination of the onium ylide and subsequent proton transfer affords the oxyfluorinated product and regenerates the rhodium catalysed.

1.4 Radical Fluorination

In addition to fluorination methodologies that are proposed to proceed by a two-electron process, fluorination has also been proposed to proceed by radical mechanisms.

As with hydrofluorination of alkynes (section 1.2.3), the same approach has been employed with alkenes in the synthesis of alkyl fluorides. While use of HF reagents typically results in harsh conditions limiting the substrate scope to robust substrates, milder metal mediated strategies have been developed such as an iron(III)/$NaBH_4$ mediated[128] and cobalt catalysed[129] strategies (Scheme 56). Both reactions are proposed to proceed by the formation of an alkyl radical which abstracts fluorine from the fluorinating agent to afford alkyl fluorides.

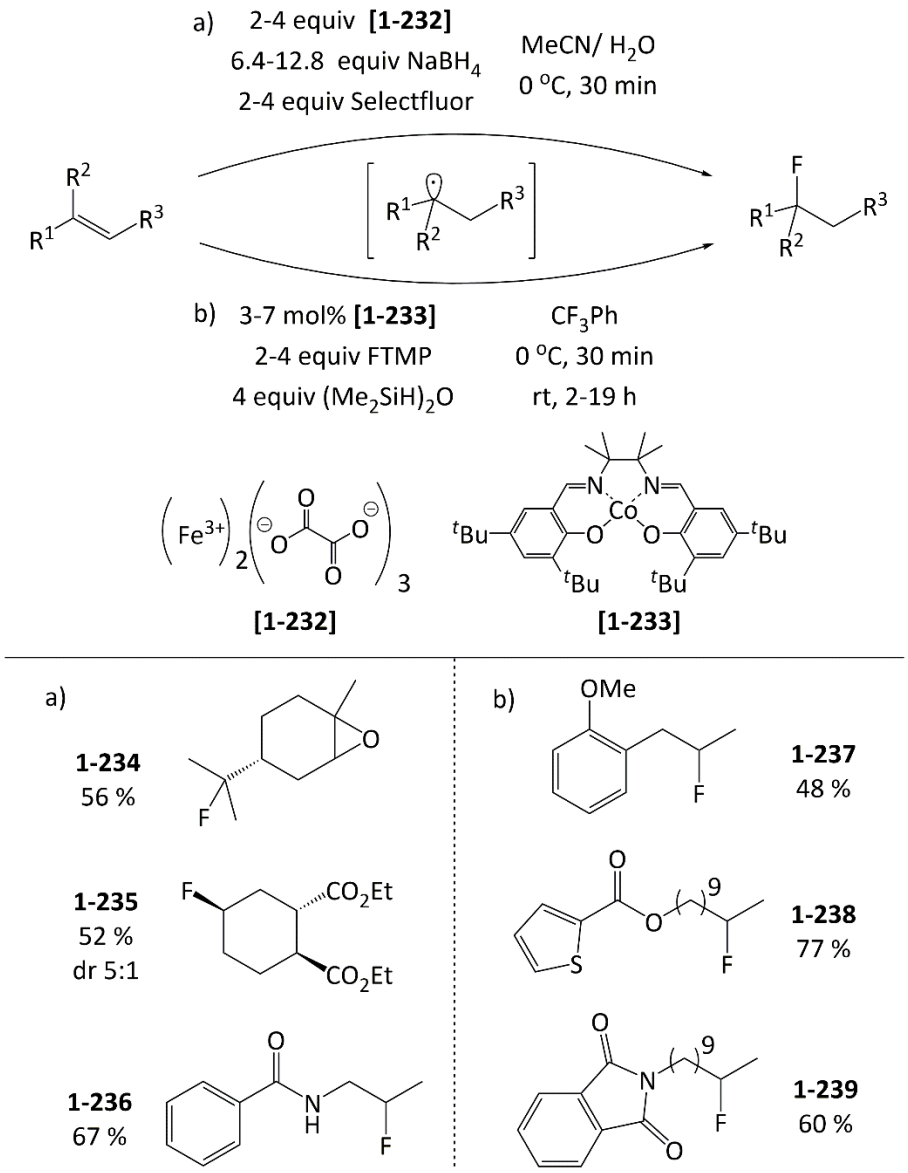

Scheme 56: a) Iron-mediated and b) copper-catalysed hydrofluorination of unactivated alkenes by a radical mechanism.

Li *et al*.[130] demonstrated silver-catalysed fluorination of alkyl borates. Primary, secondary, and tertiary alkyl boronic acids and pinacolate esters were fluorinated in moderate to excellent yield (55-93 %) in a two-phase solvent mixture (Scheme 57). The reaction was tolerant of amines, amides, esters, acids, nitriles, carbonyls, and alkenes, while being unreactive toward aryl boronic acids under the same conditions. Increased conversion was observed through the addition of TFA as a co-solvent, which is thought to increase the solubility of boron reagents in the aqueous phase.

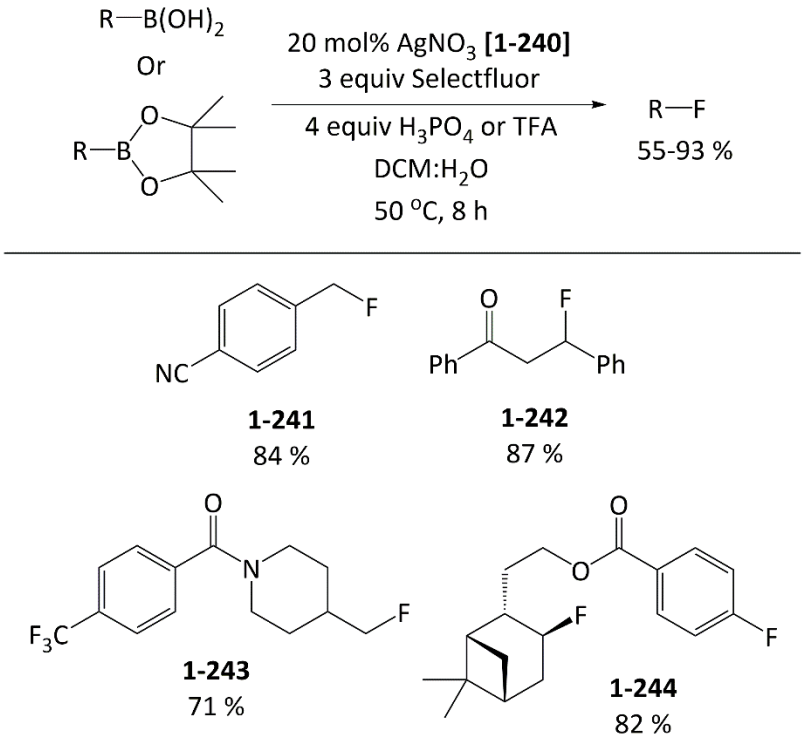

Scheme 57: Silver-catalysed radical fluorination of alkyl boronic acids and pinacolate esters.

The practicality of the reaction was demonstrated through one-pot Ru-catalysed hydroborylation of **1-232** and subsequent Ag-catalysed fluorination to yield **1-233**, as well as one-pot anti-Markovnikov hydrofluorination of unactivated alkenes, through Rh- and Co-catalysed hydroborylation and subsequent Ag-catalysed fluorination (Scheme 58).

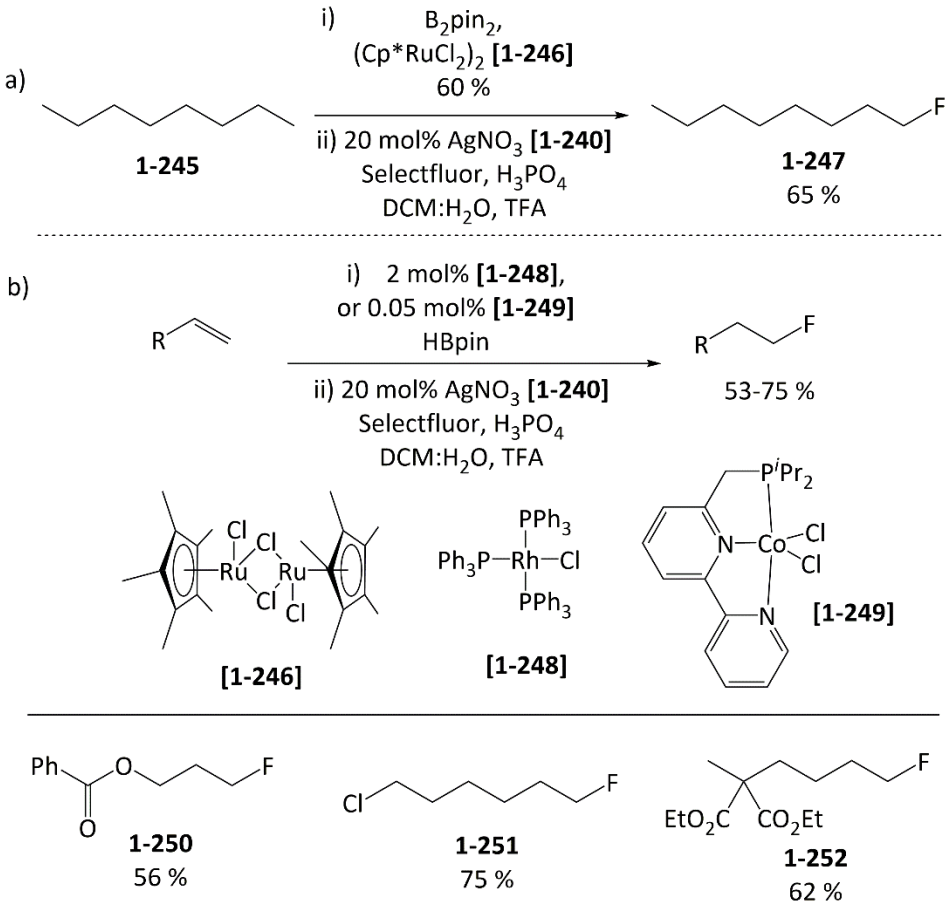

Scheme 58: a) One-pot Ru-catalysed hydroborylation and Ag-catalysed fluorination of alkanes. b) one-pot anti-Markovnikov hydrofluorination of unactivated alkenes, through Rh- and Co-catalysed hydroborylation and subsequent Ag-catalysed fluorination.

The proposed mechanism (Scheme 59) is believed to proceed by formation of an Ag(III) fluoride intermediate from Ag(I) and Selectfluor, rather than forming a divalent Ag(II) species, as detailed in previous work.[131, 132] Deborylation is triggered by single electron transfer from the metal to the boron reagent, forming an alkyl radical and an Ag(II) fluoride species. The abstraction of fluorine by the alkyl radical regenerates Ag(I) and affords the observed alkyl fluoride. This radical mechanism has been proposed in previous work by the Li group for silver catalysed decarboxylative fluorination of aliphatic carboxylic acids[131] and silver catalysed phosphonofluorination of unactivated alkenes.[132]

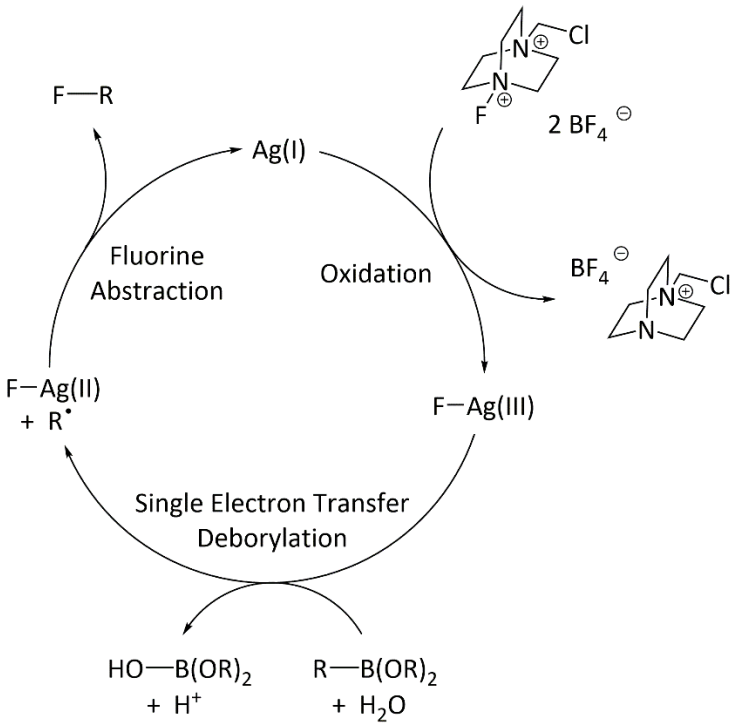

Scheme 59: Silver-catalysed fluorination of alkyl boronic acids is believed to proceed through oxidative fluorination of a Ag(I) species, followed by SET induced deborylation generating an alkyl radical which abstracts fluorine from a Ag(II)-F.

Phosphonofluorination of alkenes was also proposed to proceed *via* a radical mechanism. It was found that both terminal and internal alkenes could be phosphonofluorinated in modest to excellent yield (44-93%). However, electron deficient substrates and easily oxidisable functional groups were not tolerated (Scheme 60). The proposed mechanism only differs to that in Scheme 59 in so much as SET generates a phosphonium radical which subsequently attacks the alkene to afford the alkyl radical. The alkyl radical undergoes fluorination as proposed above by fluorine abstraction. The phosphonofluorinated products could potentially be used in Horner-Wadsworth-Emmons olefinations or other transformations. Silver-mediated fluorotrifluoromethylation of unactivated alkenes is also believed to proceed *via* a similar radical mechanism.[133]

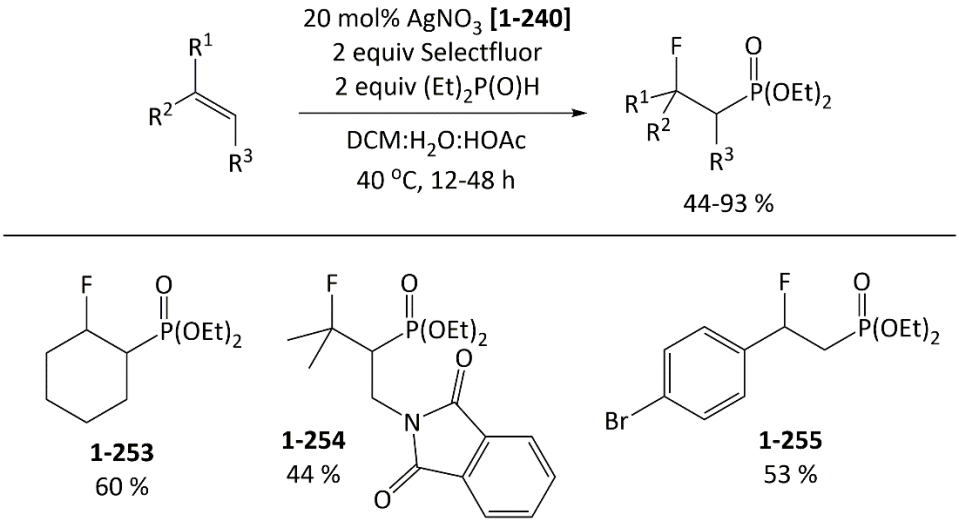

Scheme 60: Silver-catalysed phosphonofluorination of unactivated alkenes.

Decarboxylative fluorination of aliphatic carboxylic acids could also be used to access alkyl fluorides in moderate to excellent yield (47-95 %, Scheme 61)[131] by a radical mechanism catalysed by silver nitrate. Fluorination of ester and benzoic derivatives was not observed with fluorination occurring chemioselectively towards aliphatic carboxylic acids exclusively, with tertiary acids reacting preferentially over secondary acids and so forth. The availability of carboxylic acids, and the selectivity of the reaction, makes decarboxylative fluorination a powerful synthetic tool. Unlike deoxyfluorination, this method does not suffer from competing side reactions such as hydrogenation, hydroxylation, and rearrangement. The mechanism is proposed to proceed in a mechanism similar to that described in Scheme 59 with single electron oxidation of the carboxylic acid forming an alkyl radical and carbon dioxide.

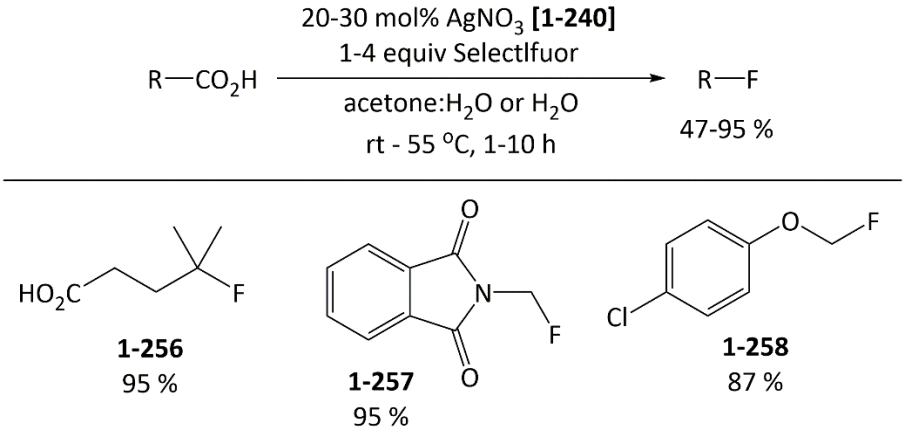

Scheme 61: Silver-catalysed decarboxylative fluorination of aliphatic carboxylic acids.

Use of $[Ru(bpy)_3]2Cl$, **[1-259]**2Cl, as a photocatalyst enabled decarboxylative fluorination to be achieved with visible light rather than near-UV (Scheme 62).[134] Again, the substrate scope was limited and the reaction required the use of 500 W lamps.

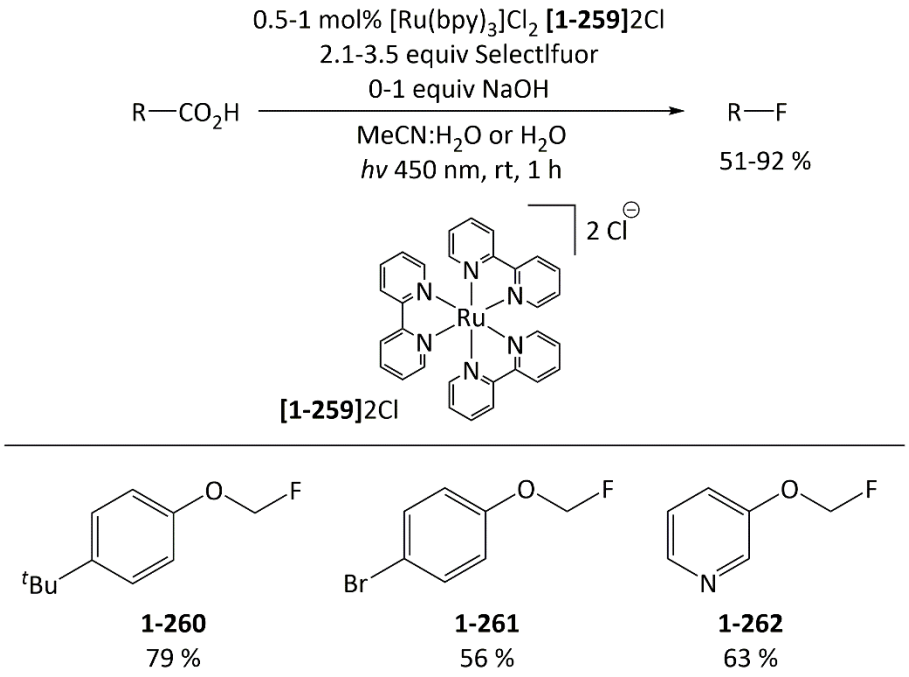

Scheme 62: Ruthenium-photocatalysed decarboxylative fluorination.

Ventre *et al*.[135] extended photo-catalysed decarboxylative fluorination to aliphatic carboxylic acids using **[1-262]**$[PF_6]_2$ or **[1-263]**$[PF_6]_2$ (Scheme 63). Fluoroalkanes were obtained from phenyl-, carbonyl-, protected amine-, ether-, and alcohol-containing aliphatic carboxylic acids in good to excellent yield (70-99%), using lower power 25 W lamps.

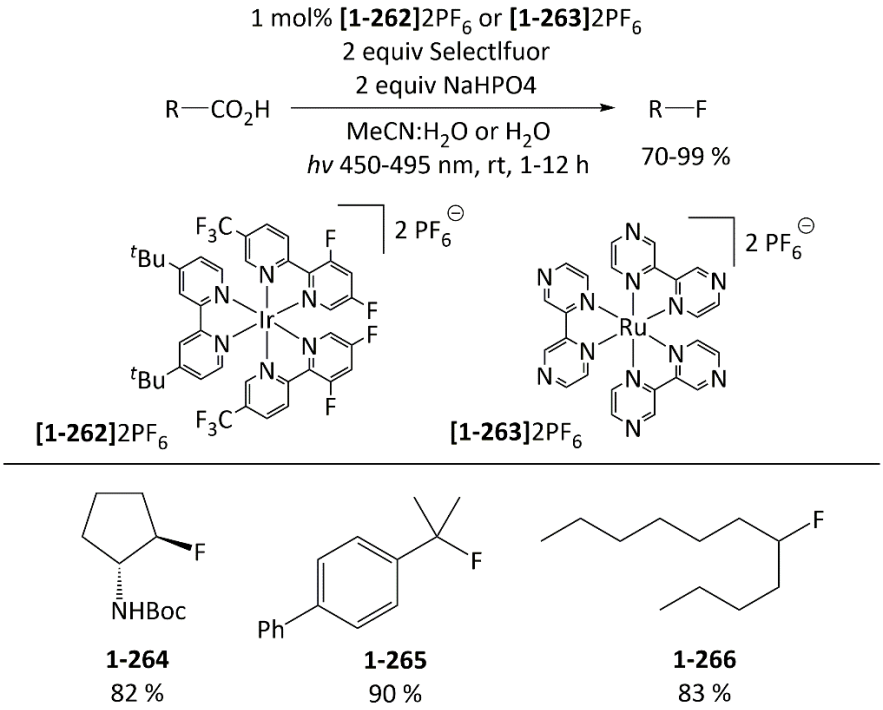

Scheme 63: Iridium- or ruthenium-photocatalysed decarboxylative fluorination of aliphatic carboxylic acids.

The mechanism is also believed to proceed through single electron transfer induced decarboxylation, followed by radical attack of the fluorinating agent to afford the alkyl fluoride (Scheme 64).

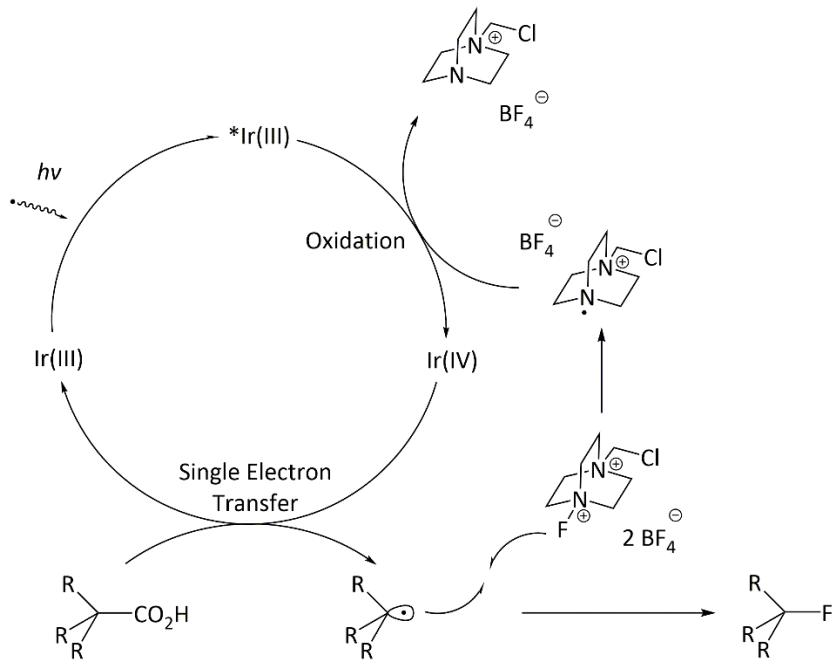

Scheme 64: SET induced decarboxylation by high valent photocatalyst and subsequent fluorination of the alkyl radical afforded alkyl fluorides from their respective carboxylic acid.

More recently, thermal- and photo-initiated fluorination of benzylic C-H bonds was demonstrated using a decatungstenate catalyst. However, the yields of benzyl fluoride varied significantly, being as low as 7 and 9 % and no higher than 75% (Scheme 65). Thermal radical initiation using AIBN gave lower yields than photocatylsed methods and failed to react with several of the substrates.

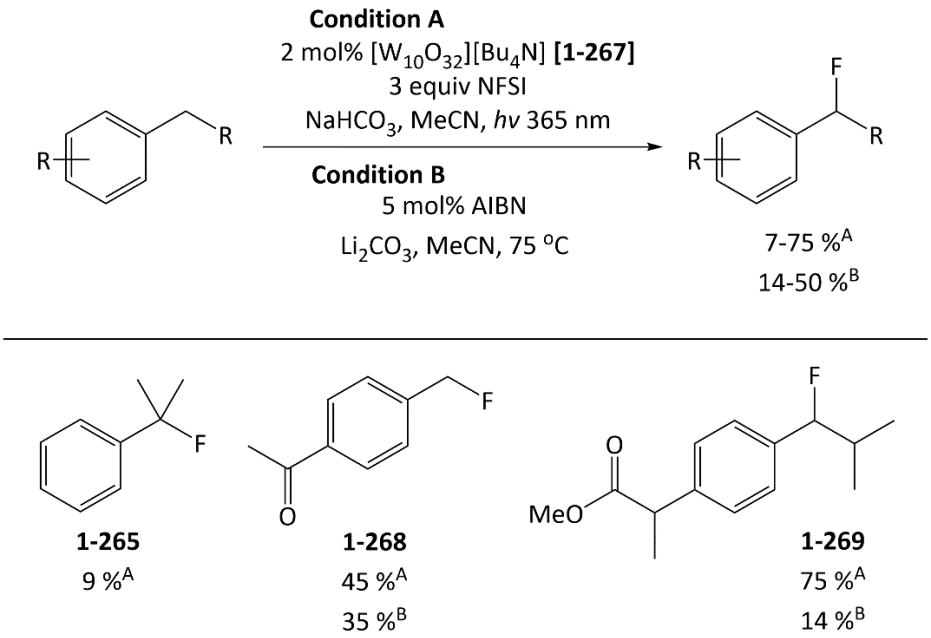

Scheme 65: Photocatalysed (condition A) and thermally initiated (condition B) benzylic fluorination.

An alternative radical strategy for accessing benzyl fluorides catalysed by copper (Scheme 66), afforded benzyl fluorides in modest yield (28 and 47 %). Fluorination was applicable to aliphatic and allylic substrates with modest to good yield (Scheme 66).[120] A detailed mechanistic study (Scheme 67)[136] proposed the most likely pathway involves single electron oxidation of Cu(I) by Selectfluor to Cu(II) through abstraction of fluorine, generating a radical dication. The radical dication is believed to abstract hydrogen from the substrate affording an alkyl radical which undergoes fluorination by Selectfluor. In place of copper, triethylborane in the presence of oxygen could be used as a radical initiator, leading to slightly lower yields under milder conditions.[137]

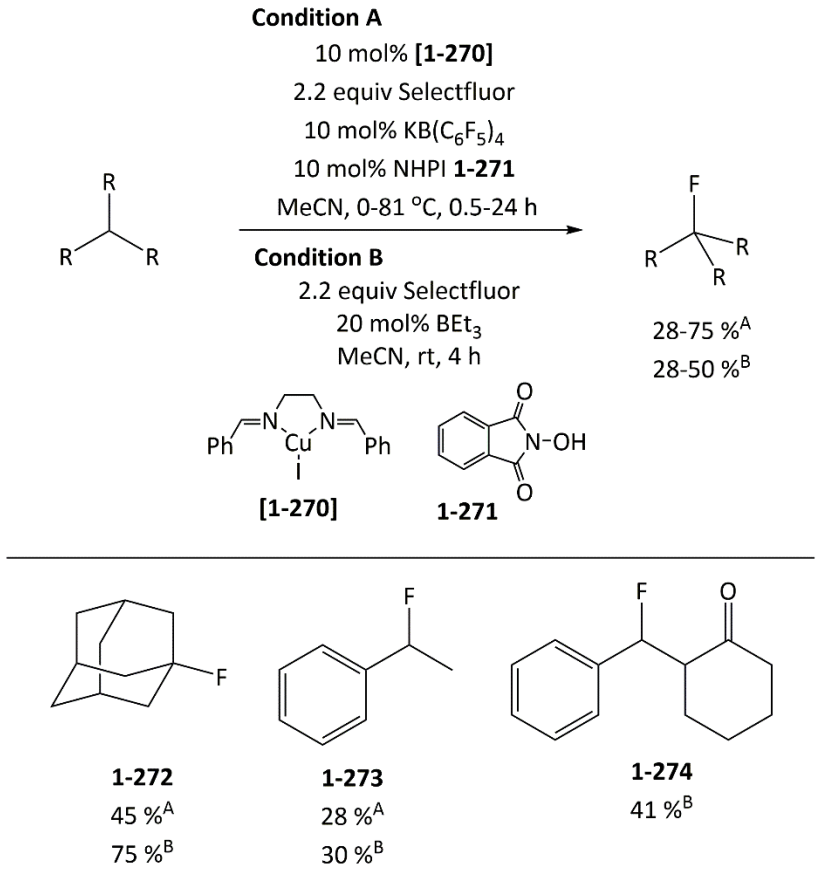

Scheme 66: Copper-catalysed (condition A) or triethylboron catalysed (condition B) fluorination of alkanes.

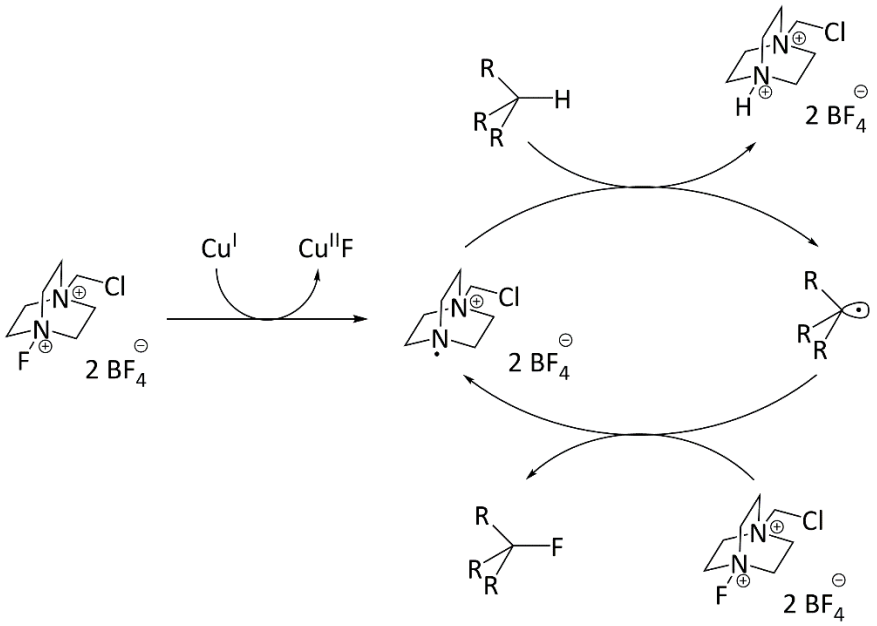

Scheme 67: Proposed mechanism for radical fluorination of alkanes *via* SET hydrogen abstraction and subsequent radical fluorination.

In contrast to the undirected examples of C-H fluorination, Groendyke *et al*.[138] have recently demonstrated a directed approach using *N*-fluoro-2-methylbenzamides which selectively undergo fluorine transfer in the presence of an iron catalyst (Scheme 68). The reaction proceeds with benzylic, allylic, and alkyl C-H bonds and is tolerant toward a range of functional groups, including alkenes and alkynes, without the need for noble metal additives. The group also demonstrated that difluorination was possible with a bis-*N*-fluoroamide bearing substrate to afford **1-277**. Both electron-rich and electron-deficient substrates were tolerated although electron-deficient substrates required longer reaction times. However, 2,6-disubstituted substrates were found to afford the fluorinated product in only trace quantities and high decomposition of the N-F bond was observed. It is believed the presence of *ortho*-substituents prevents or slows proton abstraction, enabling side reactions to compete effectively with fluorination.

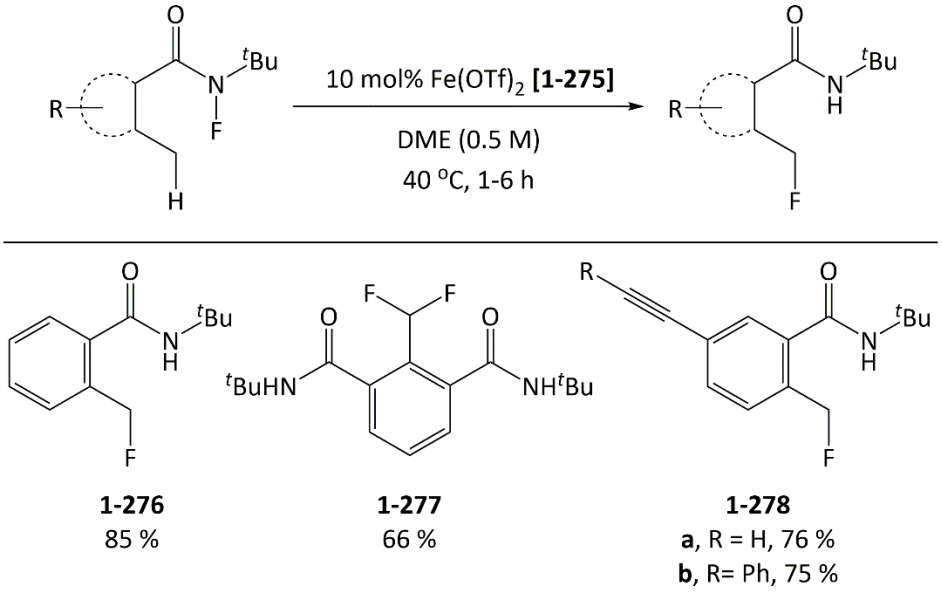

Scheme 68: Iron-catalysed fluoroimide-directed C-H fluorination.

Although the exact mechanism is not known, the involvement of radicals was proposed based on the formation of ring-opened fluorinated products, **1-280b** and **1-281b**, when the cyclopropyl substituted substrate was treated with the iron catalyst. The addition of radical traps did not conclusively prove a radical mechanism due to reduction of the radical trap by iron(II). An organometallic mechanism was proposed on the basis of DFT calculations, in which fluorination of iron triflate affords an iron(III)-fluoride intermediate and substrate radical. 1,5-Proton migration affords a carbon-centred radical which abstracts fluorine from the iron(III)-fluoride intermediate (Scheme 69).

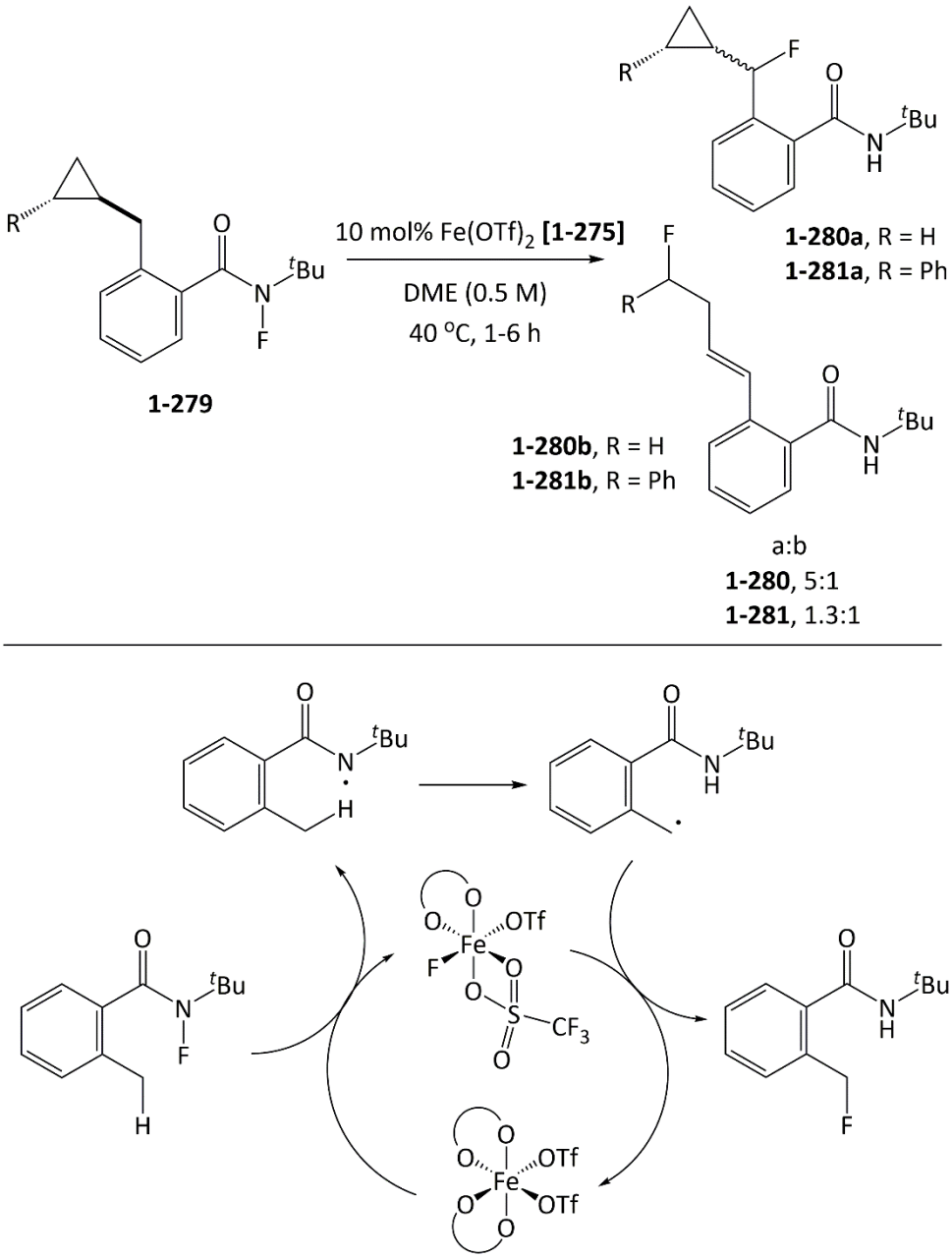

Scheme 69: Reaction of 1-279 in the presence of $Fe(OTf)_2$ accords a mixture of ring-opened and closed products suggesting the involvement of radical intermediates. The reaction is proposed to proceed by fluorine abstraction by iron(II) to afford an organic radical which undergoes rapid 1,5-proton migration and subsequent fluorine abstraction from an iron(III)-fluoride intermediate.

Copper-catalysed aminofluorination of styrene with NFSI regioselectively generated benzyl fluorides in modest to excellent yield (32-85 %, Scheme 70).[139] Electron donating substituents were generally less well tolerated giving poorer yields than electron deficient styrene. The regioselectivity is complementary to metal free conditions and the palladium catalysed aminofluorination reaction demonstrated by Qiu *et al.*[113, 139] Based on a radical clock experiment and DFT calculations, Zhang *et al*. proposed a radical mechanism involving direct fluorination of the benzyl radical by NFSI.

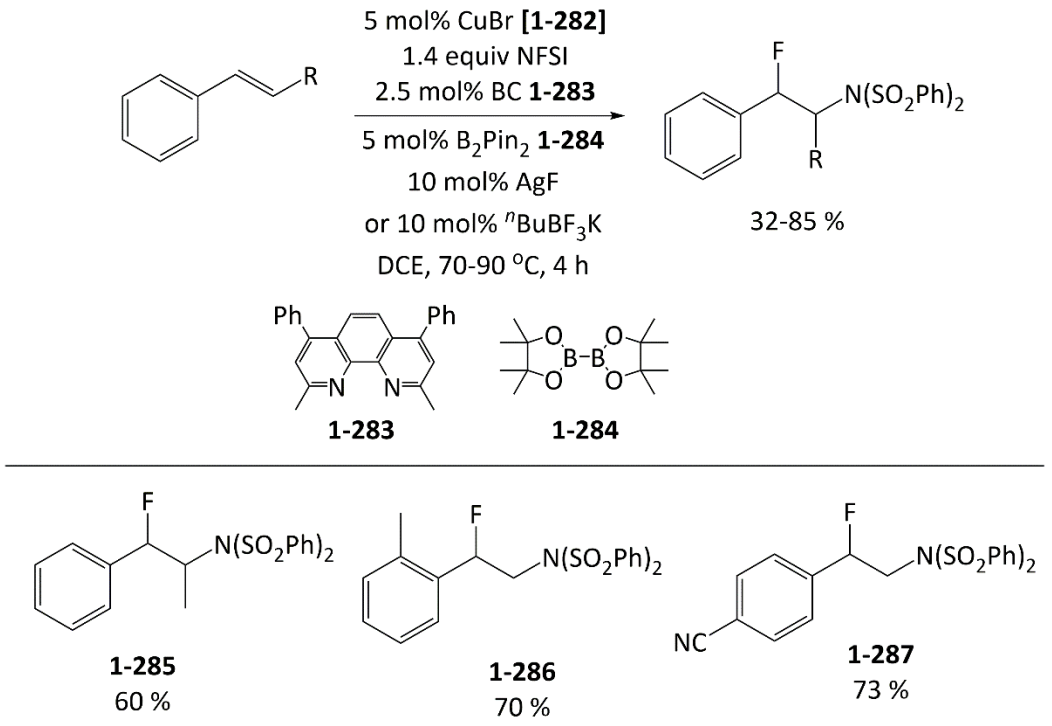

Scheme 70: Copper-catalysed radical fluoroamination of styrene derivatives.

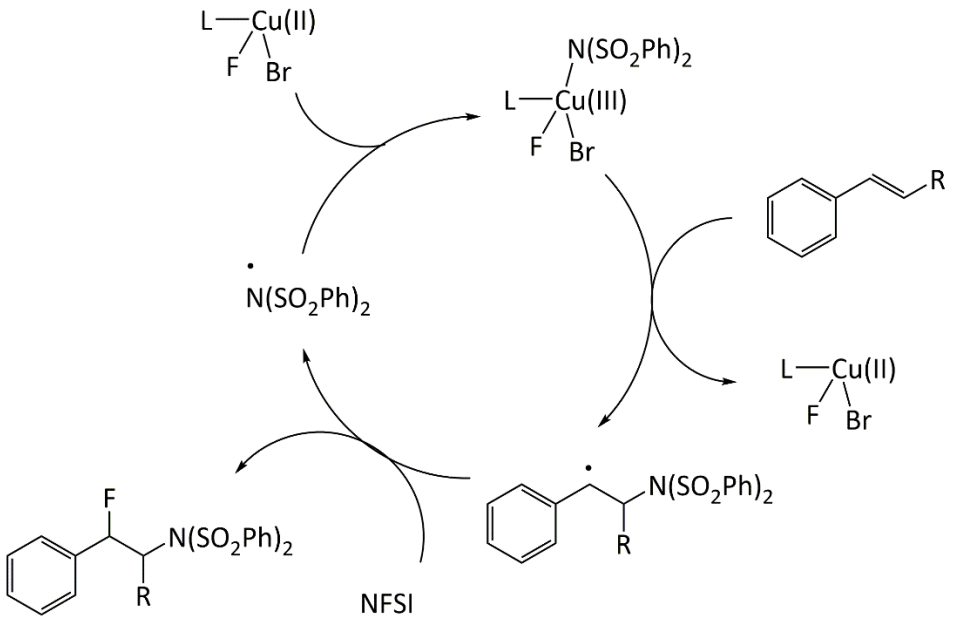

Scheme 71: Fluorination is proposed to proceed through fluoroamination of a CuBr complex to generate a Cu(III)-F intermediated. Radical amination of styrene generates a benzyl radical which undergoes fluorination to afford the benzyl fluoride.

1.5 Summary of Fluorination Strategies

Our understanding of fluorination chemistry has rapidly progressed over the years and continues to show no sign of plateauing out. Aromatic fluorination has most widely been studied due to the high demand for aromatic transformations in drug discovery and is the area of fluorine chemistry where substrate scope has been expanded the most.

Industrial scale up of modern approaches is not currently feasible or practical on the most part due to the cost of the reagents and catalysts required. Most electrophilic and nucleophilic fluorination reactions are unable to match the cost effectiveness of the Halex reactions or other methods utilising cheap, but harsh, fluorine sources such as F_2 and HF. Nevertheless, future developments could enable more selective and tolerant methods to be employed using cheaper fluorine sources, or the development of cost-effective fluorinating agents exhibiting controlled reactivity and functional group tolerance without being susceptible to side reactions. Modern approaches are, however, applicable to nano-scale manufacturing and applications requiring only small quantities of a fluorinated molecule with high regio- and stereo-selectivity, such as the synthesis of [^{18}F] radiolabelled PET tracers and drug discovery.

The emphasis on developing new biocatalytic methodologies is heavily influenced by the lack of fluorination in biological systems, limiting access to fluorinated molecules and materials through synthetic means only. In the future, it could be possible that biological fields will have progressed sufficiently to allow for the development of artificial enzymes to become a reality and enable access to tolerant and regio- and stereo-specific fluorination reactions using complex substrates.

Although a tolerant, facile, and selective fluorination strategy using sustainable and inexpensive reagents remains elusive, our current understanding has significantly expanded the repertoire of fluorination procedures available. Novel fluorination procedures for accessing sp^2- and sp^3- hybridised C-F bonds in a regio- and stereo-selective manner are still highly sought after, especially from non-activated substrates. There is a distinct lack of procedures or methodology that enables access to, or utilisation of, sp-hybridised C-F substrates. Access to fluoroalkynes or their synthons would be highly beneficial both in terms of providing new building blocks but also novel and highly substituted frameworks. The work presented in this thesis aims to investigate the possibility of stabilised fluoroalkynes and using fluorinated vinylidene complexes as possible synthons.

1.6 Introduction to Vinylidenes

1.6.1 Organic Vinylidenes

Vinylidenes are high energy unsaturated carbenes formed through the tautomerisation of alkynes. The simplest alkyne-vinylidene pair is ethyne and vinylidene which tautomerises *via* a 1,2-hydrogen shift and has an energy difference of *ca.* 185 kJ mol^{-1} (Scheme 72).[140-142]

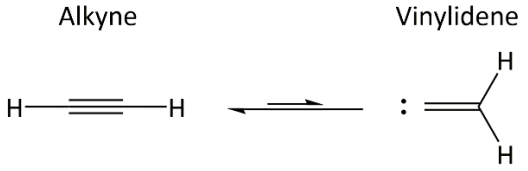

1-288 **1-289**

Scheme 72: Tautomerisation of ethyne to vinylidene.

The presence of only six valent electrons on the terminal carbon of the vinylidene makes these species exceptionally reactive, with the lifetime of vinylidene being reported in the region of 10^{-10} s^{-1}.[143] As such, the equilibrium heavily favours the alkyne tautomer, particularly for terminal alkynes which have little to no barrier for the 1,2-hydrogen shift back. Even the lowest vinylidene-alkyne energy difference, between difluorovinylidene and 1,2-difluoroethyne, is significantly high at *ca.* 130 kJ mol^{-1}.[140] Due to the substantial activation barrier to isomerisation (*ca.* 136 kJ mol^{-1}) the difluorovinylidene is sufficiently stable kinetically to enable its observation in low temperature matrices. The high barrier to isomerisation compared to terminal alkynes is attributed to the high strength of the C-F bonds and the anti-aromatic transition state for fluorine migration.[144-146]

Accessing organic vinylidenes often requires harsh conditions to overcome the high energy barrier making their synthetic application limited. One of the few examples includes the synthesis of (±)-isoptychanolide, which is proposed to proceed *via* a transient vinylidene intermediate formed by heating the alkyne at 620 K (Scheme 73a).[147] Another example is the conversion of 1-phenyl-1-buten-3-yne to naphthalene through thermal activation at 923 K, which again is believed to proceed through a vinylidene intermediate (Scheme 73b).[148]

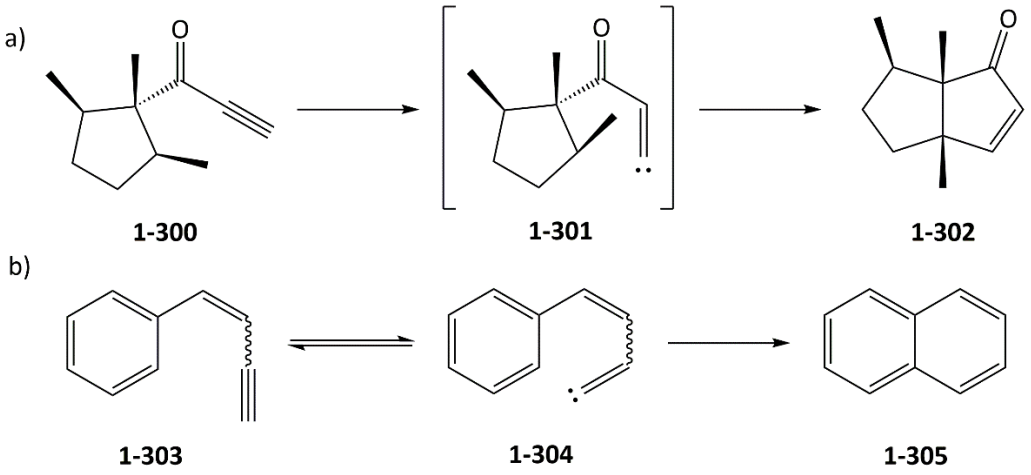

Scheme 73: Synthesis of a) (±)-isoptychanolide, 1-302, and b) naphthalene, 1-305, were proposed to proceed by organic vinylidene intermediates.

1.6.2 Metal Vinylidene Complexes

However, it is only through coordination to a metal centre that the vinylidene can be stabilised and the alkyne-vinylidene energy difference reversed. A wide variety of transition-metal centres are found to stabilise vinylidenes, typically Group 4-9 metals, including iron, manganese, cobalt, ruthenium, iridium, tungsten, titanium, rhenium, molybdenum, and osmium. Typically, the vinylidene tautomer is favoured and the stability increased with increasing electron density on the metal. The stability of metal vinylidene complexes is such that many examples have been isolated, characterised, and their reactivity explored. The ease of which metal vinylidene complexes can be accessed has been widely utilised in many metal-mediated and -catalysed reactions over the years.[149-154]

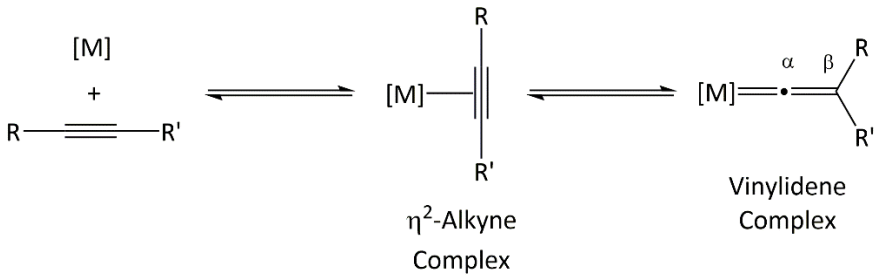

Scheme 74: Coordination of alkynes to a metal centre can favour tautomerisation to the vinylidene form.

Coordination to the metal lowers the energy difference between the metal-vinylidene and metal-alkyne pair through synergic bonding, with calculated energy differences reported in the range of 67.8 to 103.5 kJ mol^{-1} for rhodium, ruthenium, and gold.[144] For most of the rhodium and ruthenium complexes calculated the vinylidene tautomer is thermodynamically

favoured over the alkyne tautomer. Conversely, the gold alkyne-vinylidene energy difference is only lowered to the point of favouring the vinylidene tautomer with difluorovinylidene, otherwise the gold-alkyne tautomer is preferential. It is therefore unsurprising that a stable gold vinylidene complex remains elusive.

Electron rich metal centres generally favour isomerisation to the vinylidene as a result of metal-*d* alkyne-π orbital repulsion. Electron deficient metal centres generally favour 2-electron donation from η^2-alkyne coordination. Modification of the ancillary ligands, such as phosphine ligands, can further increase the stability of the metal-vinylidene or enable fine-tuning of the electronic and steric properties of the metal-centre to alter reactivity.[155]

1.6.3 Electronic Structure of Fischer Vinylidenes

As with carbenes, metal-vinylidene complexes are categorised as either Fischer- or Schrock-type complexes depending on the distribution of the electron density in the ligand. Schrock-type vinylidenes are defined as having an electrophilic metal-centre and beta-carbon and a nucleophilic alpha-carbon. This type of metal-vinylidene complex is usually observed for early transition-metals (Group 4 and 5) and are often highly reactive due to the high oxidation states of the metal. Fischer-type metal-vinylidene complexes are defined as having a nucleophilic metal-centre and beta-carbon and an electrophilic alpha-carbon. This type of metal-vinylidene complex is the most commonly isolated and usually formed with the late transition-metals (Group 6-9, with Group 10 vinylidenes being proposed as transient intermediates) in low oxidation states.[142]

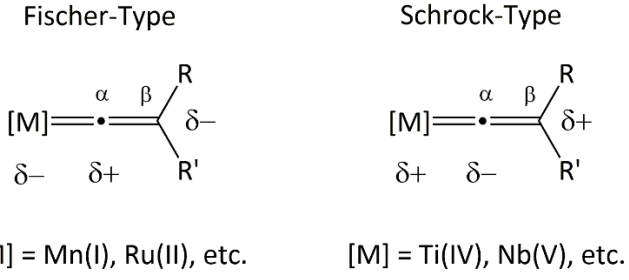

Scheme 75: Fischer- and Schrock-type vinylidene complexes.

Due to the different electronic nature, the reactivity displayed by the two types of metal-vinylidene complexes is significantly different. Fischer-type vinylidenes undergo nucleophilic attack at the alpha-carbon and are capable of reacting with electrophiles through either the metal-centre or vinylidene beta-carbon. The reverse is true for Schrock-type vinylidene

complexes which are capable of reacting with electrophiles through the vinylidene alpha-carbon and nucleophiles through the vinylidene beta-carbon.[142]

The differences in polarisability across the vinylidene ligand, and consequently reactivity, can be rationalised by consideration of orbital interactions. Below is the MO diagram for a Fischer-type metal-vinylidene fragment which are typically observed with d^6 metal centres (Scheme 76).[142]

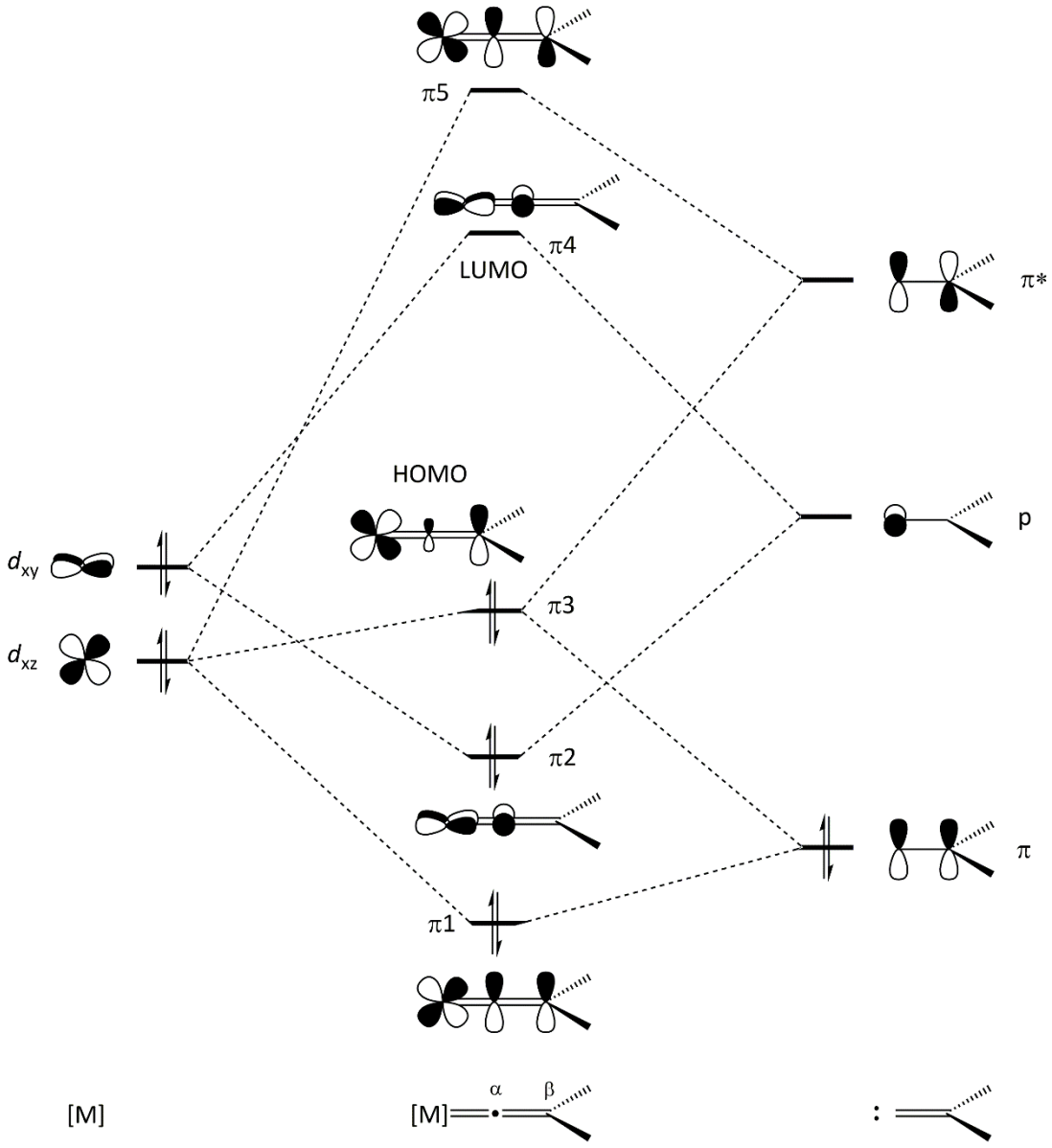

Scheme 76: Simplified molecular orbital diagram of a Fischer-type vinylidene fragment, [M] = Ru(II), and Mn(I) etc.[142]

Mixing of two symmetry-allowed t_{2g} d-orbitals of the metal with the two vinylidene π-MOs and non-bonding p-orbital of the terminal carbon gives rise to the five frontier MOs of a Fischer-type metal-vinylidene fragment. The highest occupied molecular orbital (HOMO, π_3) consists of a π-antibonding interaction between the metal d_π-orbital and the π-system of the vinylidene which is itself π-bonding. The beta-carbon provides the highest orbital contribution to the MO along with the metal. Therefore, electron density is predominately located around the beta-carbon and the metal-centre, giving rising to their nucleophilic behaviour. The lowest unoccupied molecular orbital (LUMO, π_4) consists of a π-antibonding interaction between the metal d_π-orbital and the vacant p-orbital of the vinylidene alpha carbon, where the p-orbital of the alpha carbon provides the highest orbital contribution to the MO. This accounts for the electrophilic nature of the alpha-carbon and preferential site of nucleophilic attack.[142]

1.6.4 Preparation and Pathways to Metal-Vinylidene Formation

There are numerous different synthetic strategies for accessing metal-vinylidene complexes, the most common being the tautomerisation of 1-alkynes at the metal centre. Tautomerisation can proceed *via* four main pathways; (A) 1,2-hydrogen shift,[156-158] (B) oxidative addition to an alkynyl-hydrido species and subsequent 1,3-hydrogen shift or M-H deprotonation-C_β protonation,[159-162] (C) 1,2-hydride shift and subsequent α-hydride-elimination,[159] (D) ligand assisted proton shuttle (LAPS)[163, 164] (Scheme 77).

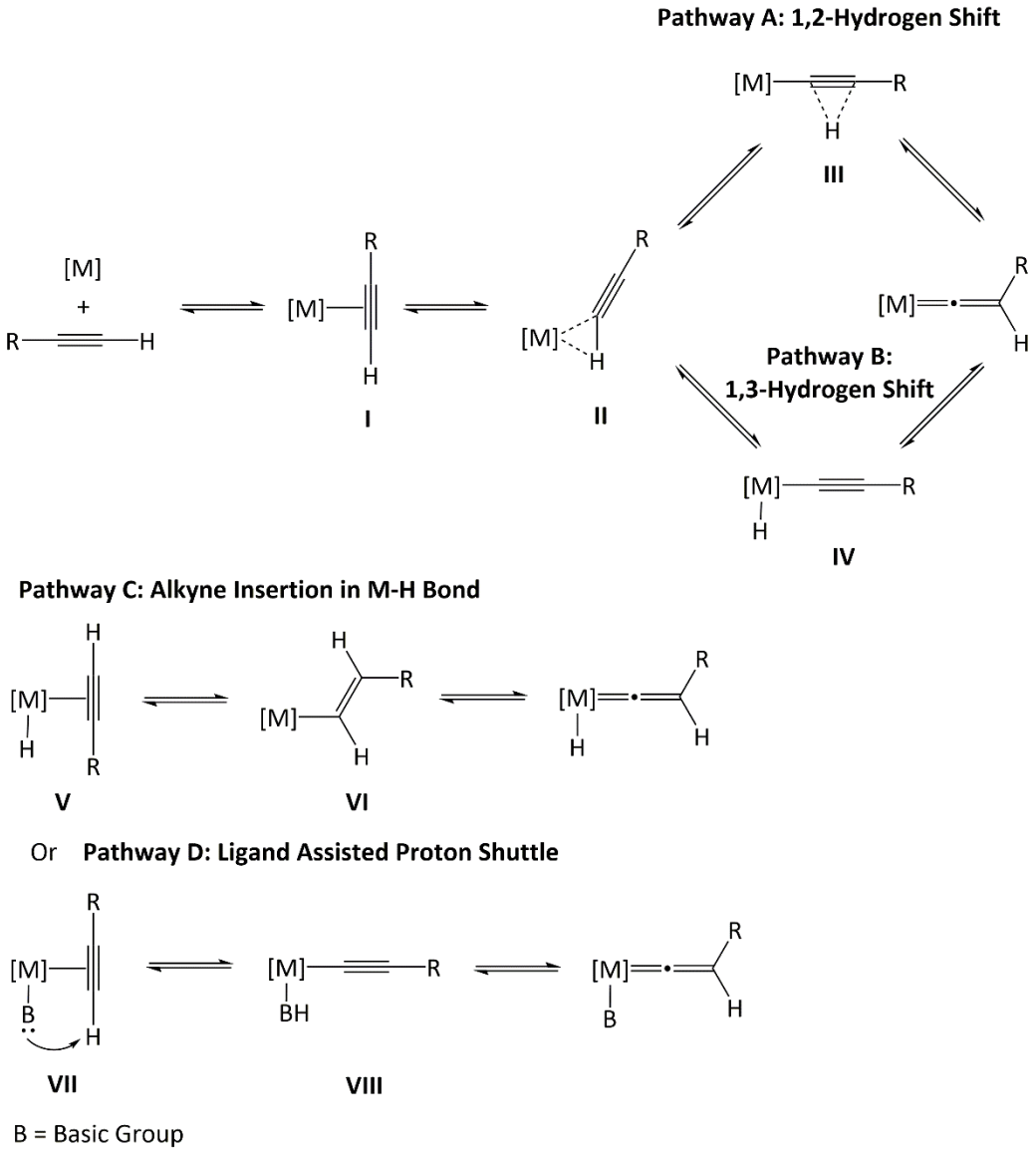

Scheme 77: Proposed mechanisms for metal-vinylidene formation.

Pathways A and B are the most commonly proposed mechanisms for tautomerisation, while pathways C and D are less common due to the need of a co-ordinately unsaturated hydride complex or LAPS capable ligand respectively.

All the above mechanisms proceed by initial formation of an η^2-alkyne complex, requiring a coordinatively unsaturated metal centre and consequently a precursor with a sufficiently labile or displaceable ligand. Pathway A proceeds through metal slippage to the terminal C-H bond (**II**), facilitating the 1,2-hydrogen shift through **III** to afford the vinylidene complex. Invoking formation of **II** and **III** as intermediates was found to lower the transition state from 230 kJ mol^{-1} for direct 1,2-hydrogen shift to 121 kJ mol^{-1} in the computational investigation by Silvestre and Hoffmann.[165]

Pathway B is interchangeable with A, in which slippage of the metal facilitates C-H bond activation resulting in oxidative insertion of the metal to afford an alkynyl-hydrido intermediate **IV**. The vinylidene complex forms through a unimolecular 1,3-hydrogen shift, as shown by crossover experiments rather than a concerted bimolecular 1,3-hydrogen shift proposed previously.[161, 166, 167] Pathway B is disfavoured for most d^6 metals, such as ruthenium(II), due to the formation of a high energy d^4-species,[152, 159, 160, 168] but has been proposed and demonstrated for more electron-rich metal complexes such as those of rhodium(I) or iridium(I).[157, 165, 169-171]

The preference of pathway A or B is dependent on the steric and electronic properties of the metal-centre in question, with pathway A dominant for electron-poor complexes and pathway B becoming more interchangeable with pathway A with increasing electron density on the metal.[161]

Pathway C is an alternative mechanism proposed for the tautomerisation of alkynes at metal-hydride complexes. Tautomerisation proceeds from the η^2-alkyne complex **V** by alkyne insertion into the metal-hydride bond to afford a vinyl intermediate **VI.** Subsequent α-hydride elimination from **VI** affords the vinylidene complex.[172-174]

Alkyne tautomerisation assisted by non-innocent ligands capable of acting as intramolecular bases (e.g. acetate or pyridyl-functionalised phosphine ligands) is described by pathway D. The deprotonation of η^2-alkyne complex by an intramolecular base **VII** affords the alkynyl intermediate **VII**, which is subsequently protonated at the beta-carbon to afford the vinylidene complex.[163, 164, 175]

In addition to the tautomerisation of terminal alkynes, alkynes bearing heavy Group 14 substituents, e.g. trialkylsilyl[176-180] or triphenylstannane,[181] have also been demonstrated to undergo isomerisation to afford the disubstituted vinylidenes through migration. The presence of a heavy Group 14 substituent lowers the alkyne-vinylidene activation barrier allowing more facile rearrangement. More uncommon examples of other migratory groups are the alkylselenium, alkylthiol,[182] and iodide bearing alkynes.[183-185] More recently ruthenium, iron, and iridium disubstituted vinylidene complexes have been synthesised from internal alkynes, such as PhC≡CPh, through 1,2-migration of carbon substituents under more forcing conditions.[186-189] For example, Mutoh *et al*.[187] demonstrated that heating [Ru(η^5-C_5H_5)(dppe)Cl], **[1-306]** with PhC≡CPh and $NaBAr^F_4$ in $C_2H_4Cl_2$ at 70 °C for one hour afforded

the disubstituted vinylidene complex [Ru(η^5-C_5H_5)(dppe)(=C=CPh_2)]BAr^F_4, **[1-307]**BAr^F_4 (Scheme 78).

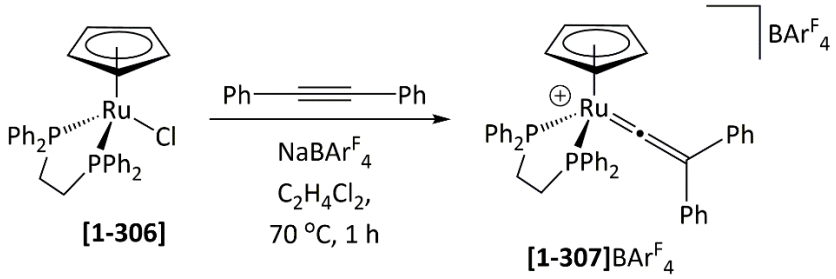

Scheme 78: Under more forcing conditions disubstituted vinylidene complexes have been synthesised directly from the corresponding disubstituted alkyne.

Aside from the tautomerisation of 1-alkynes, another convenient route to accessing vinylidene complexes involves the addition of electrophiles to metal-alkynyl complexes (Scheme 79). This approach has been widely exploited to form many complex and unusual disubstituted vinylidene complexes.[142]

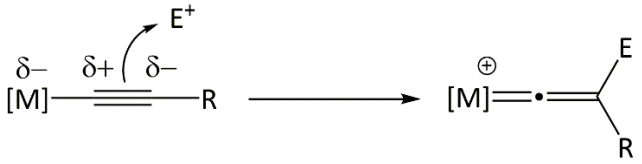

Scheme 79: Addition of electrophiles to alkynyl complexes afford disubstituted vinylidene complexes.

The coordination of alkynyl ligands to a metal centre results in the formation of a polarised alkynyl ligand with an electron-rich metal and beta-carbon, which is capable of reacting with electrophiles. Exploiting the polarizability of the Ru-C≡C moiety and the steric bulk around the metal allows attack of the electrophile to occur at the beta-carbon affording the vinylidene complex. Addition of a proton source to an alkynyl complex affords the monosubstituted vinylidene complexes. Alkylated vinylidenes can be accessed through addition of haloalkanes, triflates and alkyoxoniums (R_3O^+). Reactions with halogens, acylium, azoarenes, arylthiol, arylseleno, tropylium, and trityl cations have also been used to afford the corresponding disubstituted vinylidene complexes.[142, 149] This method of vinylidene synthesis forms the basis of the outer-sphere electrophilic fluorination strategy utilised in Chapters 2 and 4. The formation of halogenated vinylidene complexes is discussed at the start of Chapter 2.

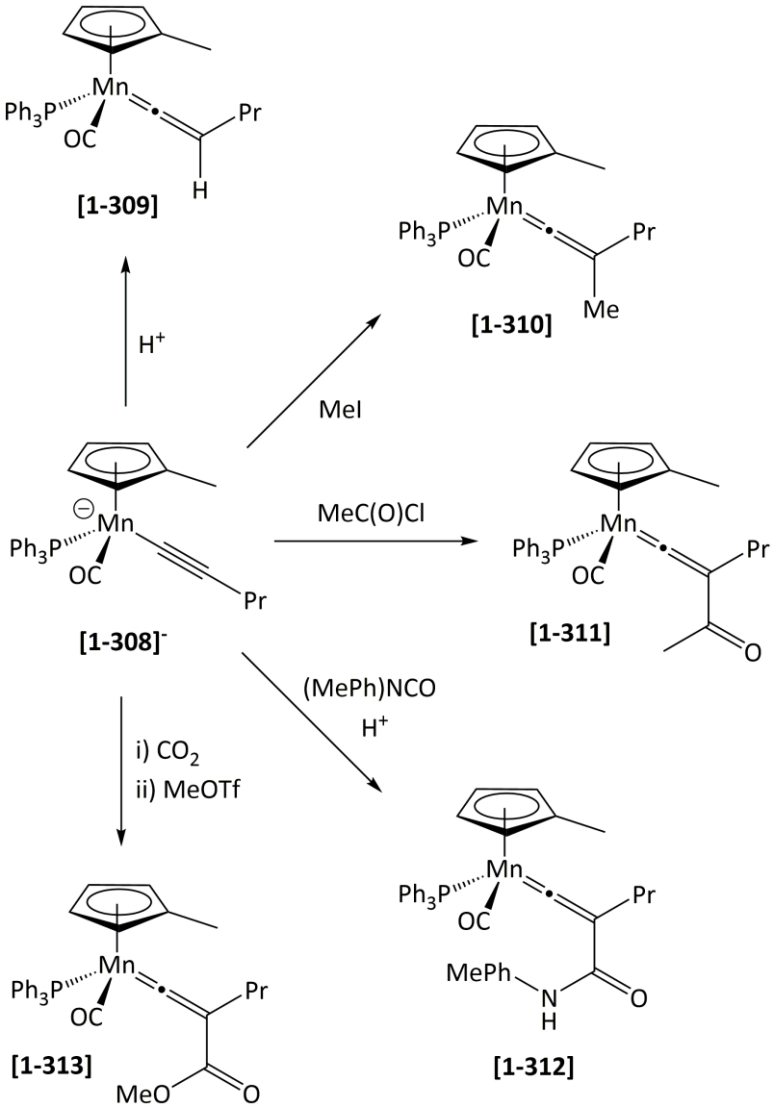

Scheme 80: Examples of vinylidene formation through reaction of [1-308] with various electrophiles.

Other, less common routes to vinylidene complexes include sequential nucleophilic addition and protonation to allenylidenes complexes, as well as deprotonation of carbyne complexes bearing a β-proton (Scheme 81).[142]

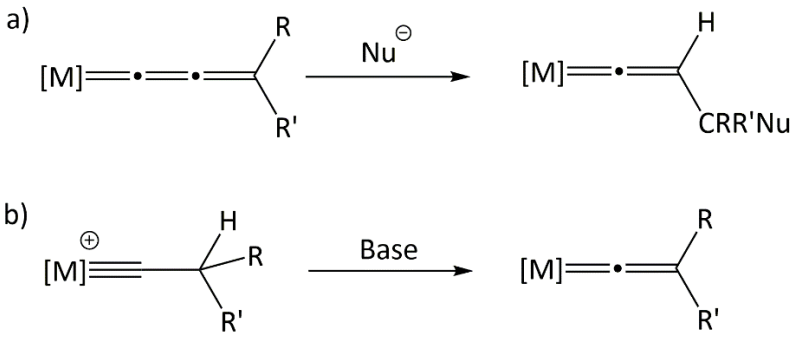

Scheme 81: Formation of vinylidene complexes can also occur by a) addition of a nucleophile to a cumulene complex or b) addition of base to a carbyne complex.

1.6.5 Characterisation of Vinylidene Complexes

Metal vinylidene complexes are typically characterised by NMR and IR spectroscopy due to their diagnostic signals, as well as X-ray crystallography. Characterisation can also be supported by other techniques such as mass spectrometry and UV-Vis spectroscopy.[149, 153, 190-192] Vinylidene complexes exhibit characteristic carbon resonances in the $^{13}C\{^{1}H\}$ NMR spectrum due to the polarisation of the M=C=C fragment. The metal-bound carbon undergoes significant deshielding and is observed between δ 258-396. The β-carbon is observed at resonances either more shielded or more typical of sp^2-carbons (between δ 87-143).[149] Changes in the chemical shifts are dependent on the electronic nature of the metal and substituents due to energy differences between the filled and vacant orbitals on the vinylidene fragment.[193, 194] Metal-vinylidene complexes exhibit characteristic C=C stretching frequencies around 1600 cm^{-1} in the IR spectrum. [149]

A review of metal vinylidene complex bond metrics, obtained by X-ray crystallography, revealed that mononuclear vinylidene complexes display short M=C bond lengths between 1.689 and 2.046 Å and C=C bond lengths between 1.25 and 1.41 Å. The M=C bond lengths are consistent with a bond order of two, while the C=C bond lengths are consistent with a bond order between two and three. The M=C=C bond angle tends towards linearity and are observed between 161° and 180°.[149]

1.6.6 Reactivity of Vinylidene Complexes

As discussed in section 1.6.3, the polarisation of Fischer-type vinylidene ligands results in an electron-poor alpha-carbon and an electron-rich beta-carbon capable of reacting with nucleophiles and electrophiles respectively (Scheme 82). However, the presence of a positively charged metal-centre restricts the reaction of electrophiles to predominantly

neutral vinylidene complexes. The presence of both electrophilic and nucleophilic sites enables vinylidene complexes to participate in cyclisation reactions. The electronic nature of the vinylidene ligand, coupled with their facile synthesis, has allowed this ligand class to be exploited in many stoichiometric and catalytic reactions as shown in the numerous reviews which explore their reactivity. [142, 154, 195, 196] Typical reaction patterns of vinylidene complexes and examples of their reactivity are detailed below.

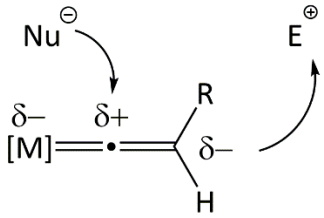

Scheme 82: Polarisation of the vinylidene ligand enables reactivity toward both nucleophiles and electrophiles.

1.6.6.1 Nucleophilic Reactions

Metal-vinylidene complexes exhibit stark differences in reactivity compared with their parent alkyne or η^2-alkynyl complex, allowing these complexes to be exploited in the formation of new organic or organometallic species. For example, metal η^2-alkyne complexes react with nucleophiles to afford the Markovnikov addition product, whereas vinylidene complexes react to form the formal anti-Markovnikov addition product (Scheme 83). The reactivity is rationalised by consideration of the LUMO in both cases. The LUMO of the η^2-alkyne complex consists of a π-antibonding interaction between the metal centred orbital and the π* system of the alkyne. Attack by a nucleophile may occur at either position with slippage of the metal to give a vinyl complex with the nucleophile bonded to the beta-carbon. The LUMO of the vinylidene is based predominantly on the metal alpha-carbon, activating this position to nucleophilic attack to afford a vinyl complex with the nucleophile bonded to the alpha-carbon.[142, 174]

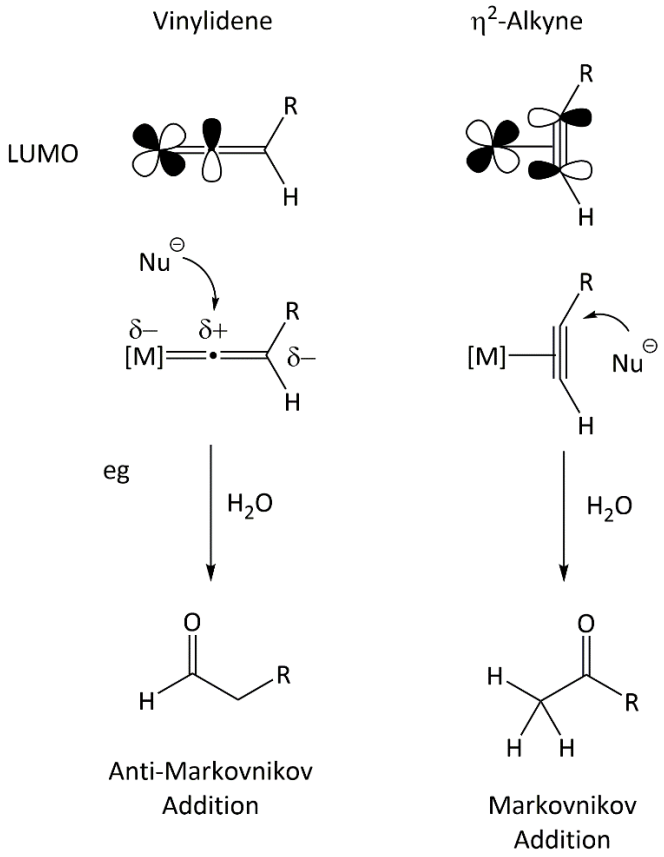

Scheme 83: Nucleophilic attack of the vinylidene complex, e.g. hydrolysis, occurs at the α-carbon due to the LUMO residing predominantly on this carbon and affords the anti-Markovnikov addition product. Markovnikov addition is observed through the addition of nucleophiles to the η²-alkyne complex as the LUMO residues on both carbons of the alkyne ligand.

Metal vinylidene complexes react with nucleophiles to afford the corresponding vinyl complex or, in the presence of a source of protons, the carbene complex. For example, metal vinylidene complexes react with water to form a hydroxy carbene complex which can subsequently undergo keto-enol tautomerisation and elimination of an aldehyde.[174] Similarly, the reaction with alcohols afford the corresponding alkoxy carbene complexes but are unable to undergo elimination (Scheme 84). The formation of amino-, thio-, and halo-carbene complexes can also be accessed through addition of ammonia, primary and secondary amines, primary thiols, and hydrogen halides respectively to vinylidene complexes (Scheme 84). Addition of heterocyclic amine bases, phosphines, halogen nucleophiles, hydride, and carbon nucleophiles afford the corresponding metal vinyl complexes (Scheme 84).[142, 154, 195]

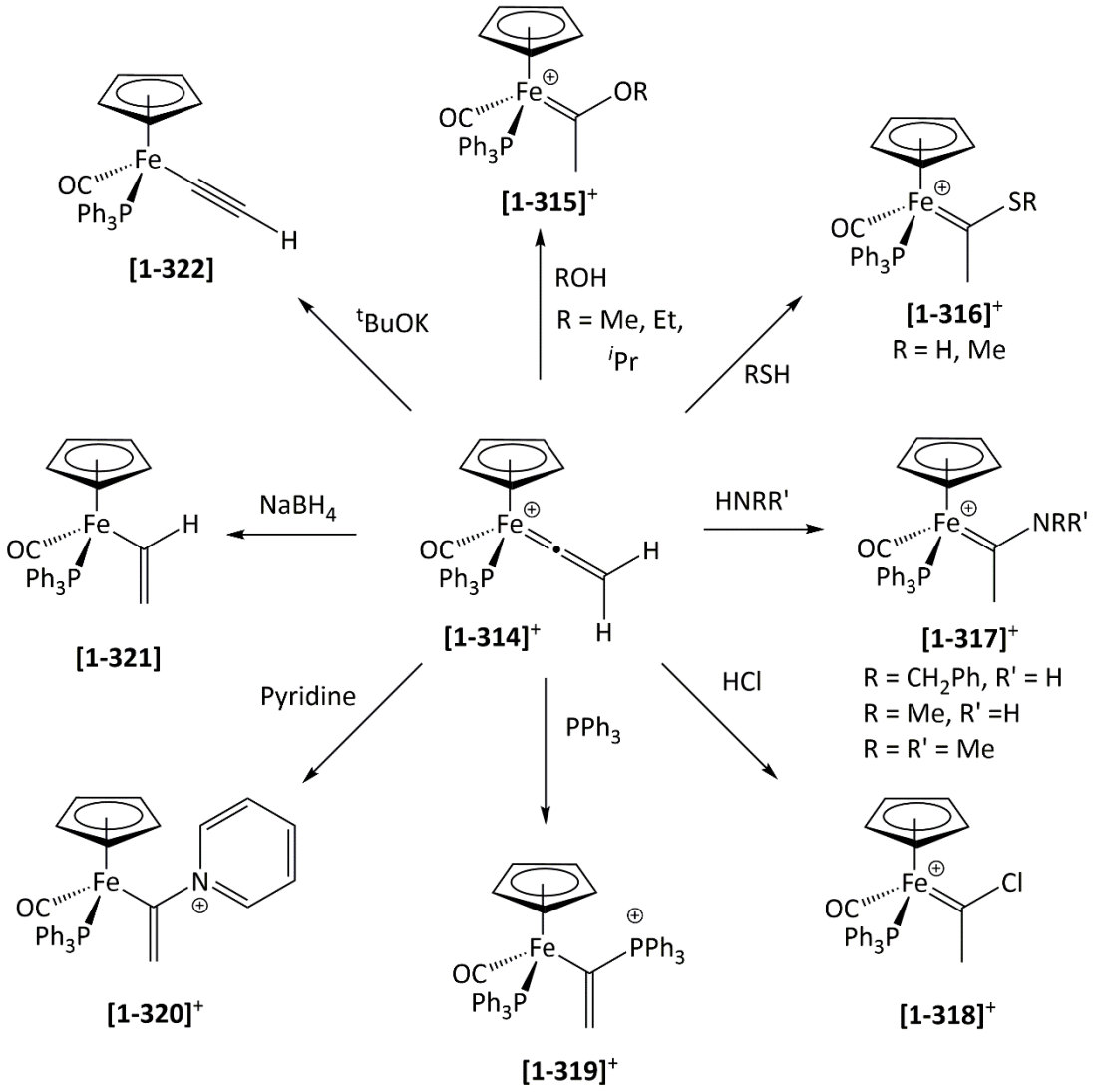

Scheme 84: Example reactions of [1-314]$^+$ with various nucleophiles.[197, 198]

Protio-substituted, or terminal, vinylidene complexes undergo deprotonation by a suitably bulky or non-nucleophilic base to afford alkynyl complexes. This approach is commonly used in conjunction with further functionalisation to generate disubstituted vinylidene complexes. Deprotonation of complexes of the type [Ru(=C=CPhCH$_2$R)], e.g. **[1-323]**$^+$, undergo intramolecular attack at the α-carbon to afford cyclopropenes, e.g. **[1-324]**. Addition of electrophiles to these cyclopropene complexes afford vinylidene complexes with additional functionalisation at the γ-position.[199]

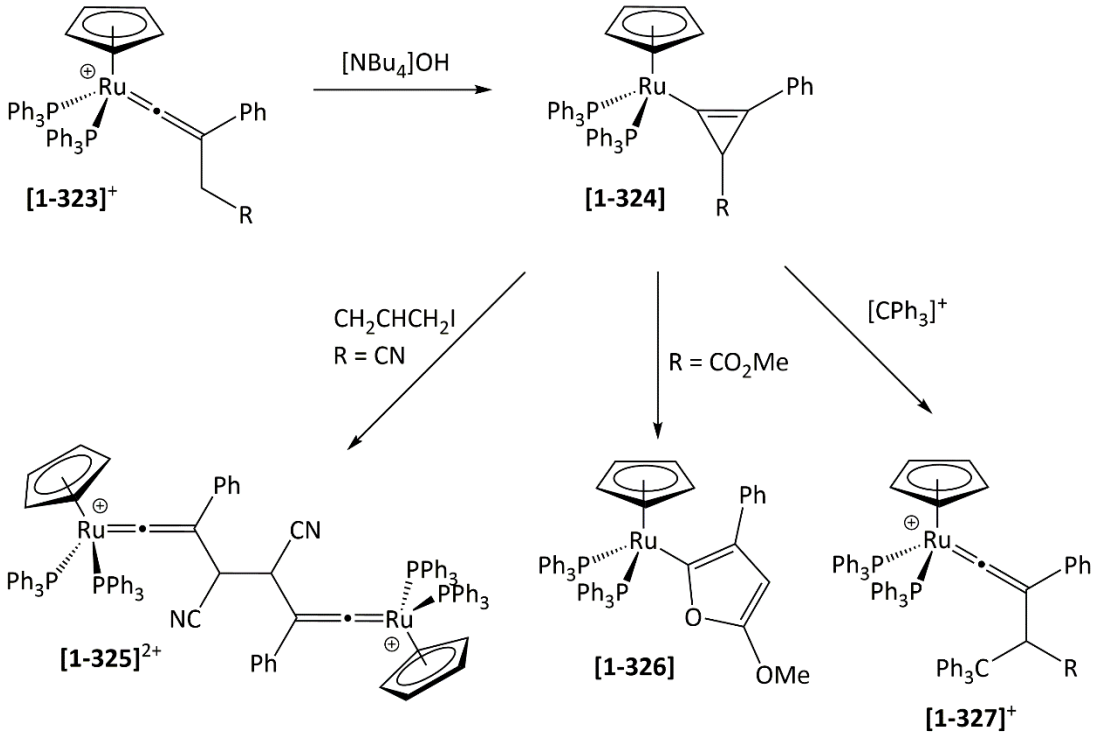

Scheme 85: Deprotonation of [1-323]$^+$ at the γ-position of the vinylidene ligand affords the cyclopropene complex, [1-324], which can undergo further reactions with electrophiles.

1.6.6.2 Electrophilic Reactions

Reaction with electrophiles are typically limited to neutral vinylidene complexes. For example, protonation of neutral vinylidene complexes with strong non-coordinating acids, e.g. HBF_4, affords the corresponding carbyne complexes.[200-205] Alkylation has been demonstrated through the reaction of methyltriflate with **[1-331]** to afford the vinylcarbyne complex **[1-332]**OTf.[206] Similarly, **[1-328]** reacts with $Sn(CH{=}CH_2)_4$ to form an allyl complex, **[1-330]**.[207] Terminal vinylidene complexes may undergo a reaction with $[CPh_3]^+$ to afford a vinylidene with CPh_3 in place of hydrogen.[208]

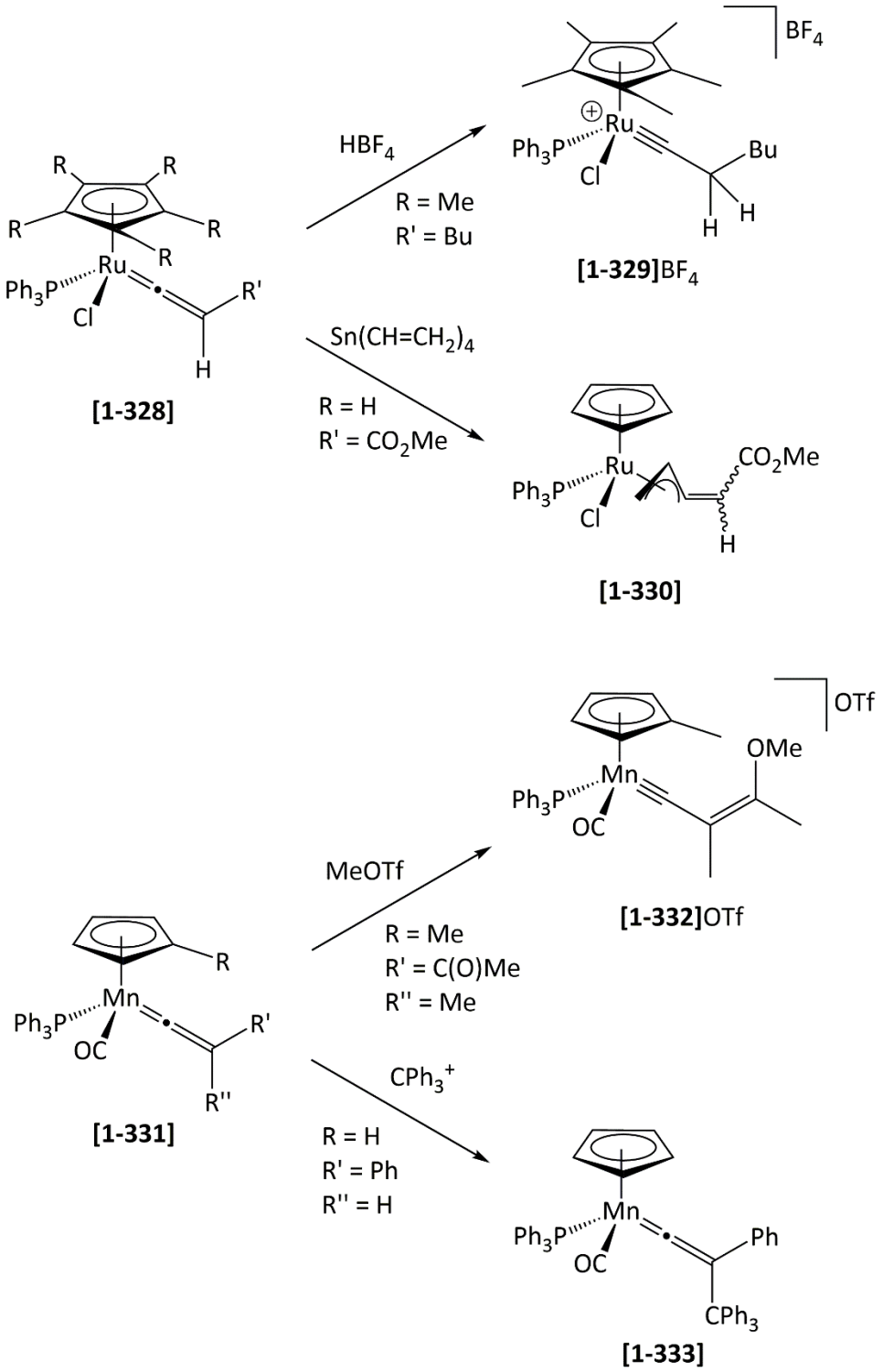

Scheme 86: Example reactions of neutral vinylidene complexes with electrophiles.

1.6.6.3 Cyclisation and Dimerisation Reactions

Vinylidene complexes have been proposed for a multitude of cyclisation, cycloaddition, and dimerisation reactions as covered in several comprehensive reviews.[142, 154, 195, 196] Coordination of alkynes bearing tethered nucleophiles, such as hydroxyl groups, are believed

to form metal vinylidene intermediates which undergo intramolecular nucleophilic attack at the α-carbon to afford cyclised carbene complexes (Scheme 87).[209]

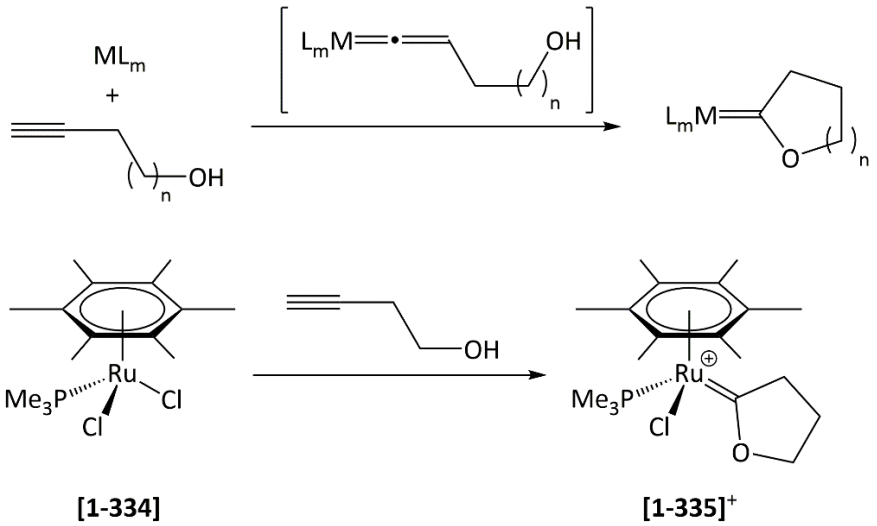

[1-334] **[1-335]$^+$**

Scheme 87: The coordination of alkynes bearing tethered nucleophiles afford cyclised carbene complexes which are proposed to proceed *via* a vinylidene intermediate.[209]

Addition of unsaturated reagents, e.g. alkenes, to vinylidene complexes can result in [2+2] cycloaddition to afford cyclic carbene intermediates or products. For example, Murakami *et al*. reported alkyne-alkene coupling in which they proposed the vinylidene complex undergoes [2+2] cycloaddition with the alkene to afford **[1-338]$^+$** as an intermediate (Scheme 88). β-elimination and subsequent reductive elimination affords a 1,3-diene product as a mixture of isomers.[210]

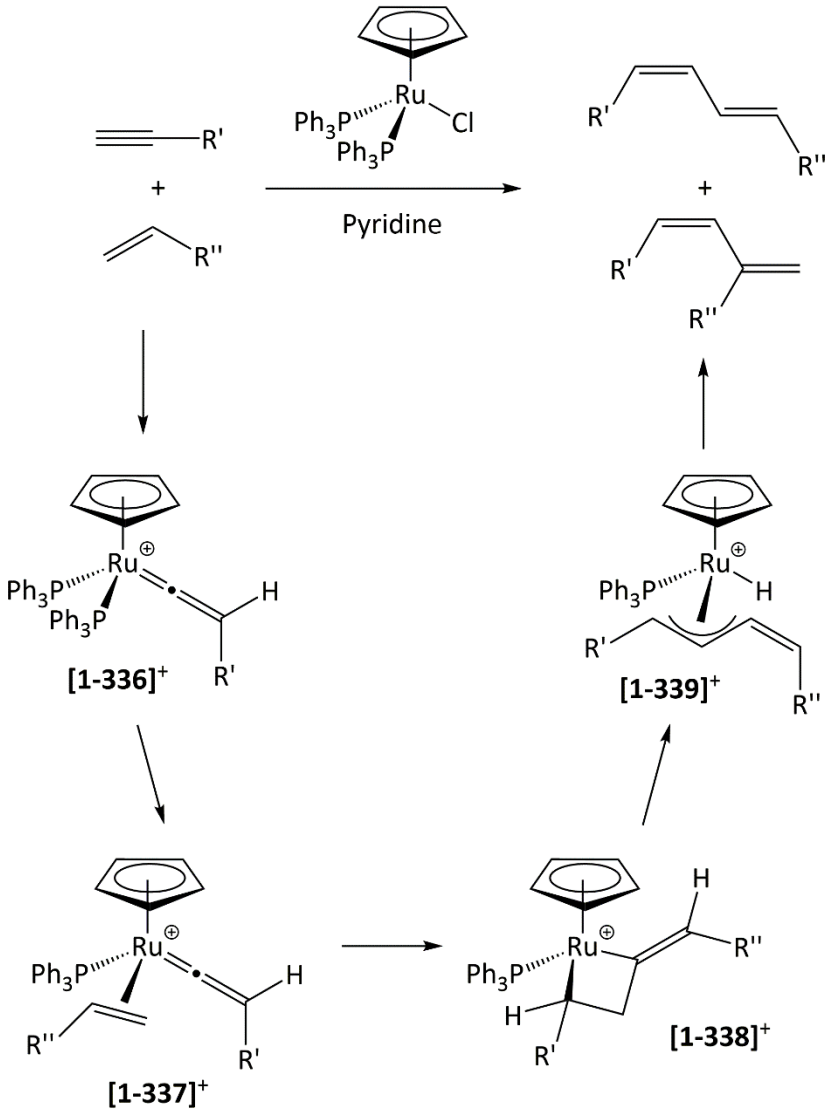

Scheme 88: Alkyne-alkene coupling proceeds by the formation of a vinylidene-alkene intermediate which undergoes formal [2+2] cycloaddition to form [1-338]$^{+}$.[210]

Vinylidene complexes have also been demonstrated to react with imines in [2+2] cycloaddition reactions to afford the corresponding cyclic carbene complexes. For example, the neutral rhenium and manganese vinylidene complexes, **[1-340]**, undergo [2+2] cycloaddition with *N*-benzylideneaniline to afford carbene complexes **[1-341]** (Scheme 89). Excess imine resulted in further reaction of **[1-341a]** to afford **[1-342]**.[211]

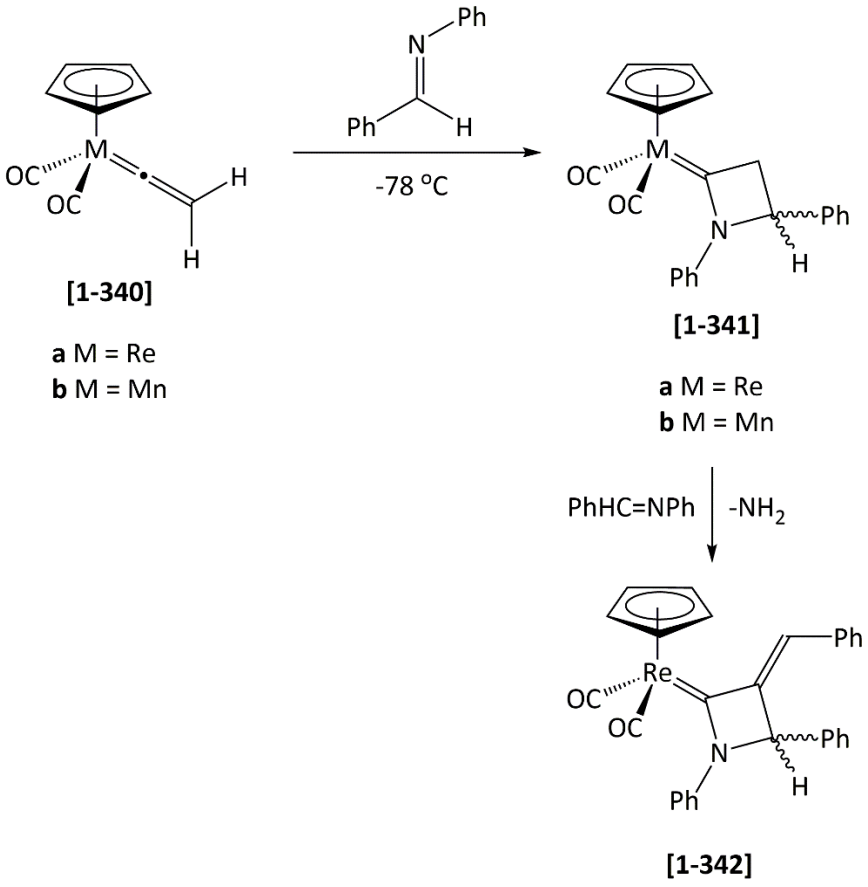

Scheme 89: Cycloaddition of *N*-benzylideneaniline to [1-340] affords carbene complex [1-341], excess *N*-benzylideneaniline reacts with [1-341] to afford [1-342].[211]

Similarly, vinylidene complexes are proposed to undergo [4+2] cycloaddition with alkynes as suggested by Elakkari *et al*.[212] in the cyclisation of arylethynes using a rhodium or ruthenium porphyrin catalyst (Scheme 90). The authors proposed the coordination of a terminal alkyne to the porphyrin catalyst forms a reactive vinylidene complex which undergoes a formal Diels-Alder reaction with an arylethyne to afford 1-arylnaphthalenes.[212]

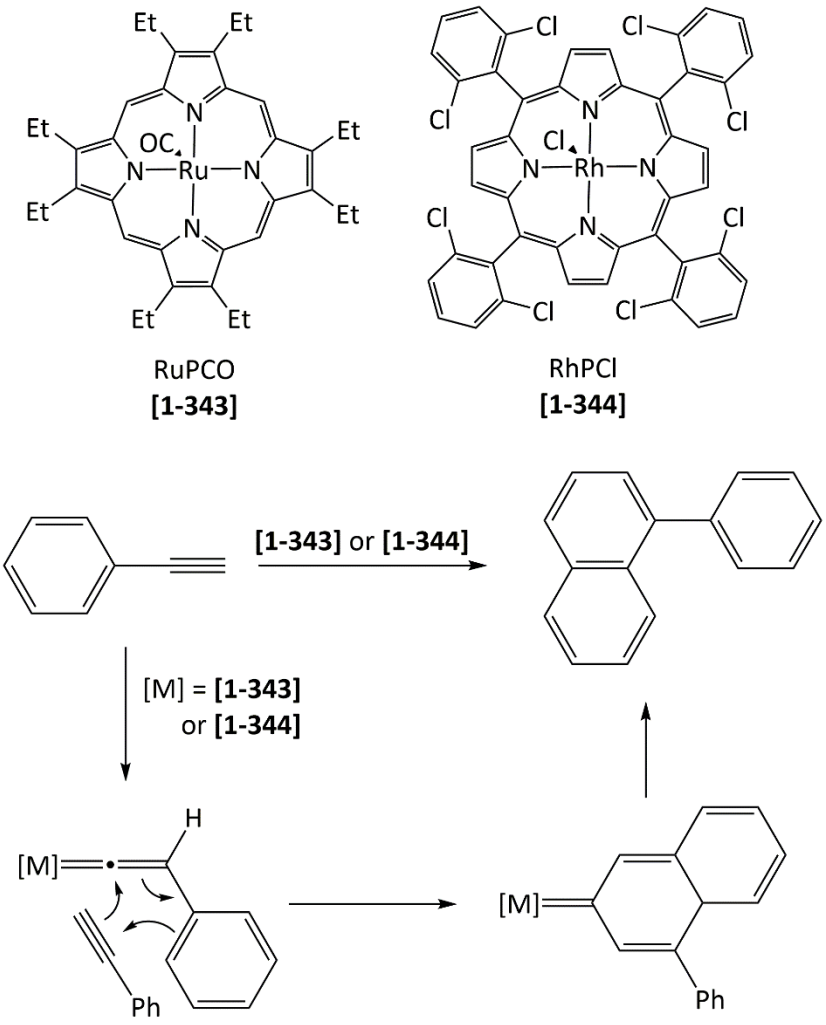

Scheme 90: Metal porphyrin catalysed arylethyne dimerisation *via* [4+2] cycloaddition.[212]

Alkyne dimerisation has become a facile method for accessing highly unsaturated building blocks. Dimerisation can afford a mixture of head-to-head and head-to-tail enynes, along with butatriene compounds (Scheme 91).[142, 195, 213] Mechanistic investigations[196, 213] revealed that head-to-head alkyne dimerisation proceeds *via* migration of the alkynyl ligand onto the α-carbon of the vinylidene ligand from an alkynyl-vinylidene intermediate, **II**. Protonation of the vinyl species **IV** releases the head-to-head enyne **1-346** from the metal centre. However, if protonation is slow, typically due to the presence of bulky alkyne substituents, rearrangement of the vinyl ligand to a cumulenyl ligand (**V**) can occur. Protonation of the metal-bound carbon affords a butatriene product **1-347**.[214, 215] The formation of head-to-tail enynes, **1-344**, can only be explained by direct insertion of the η^2-alkyne into the σ Ru-C bond of the alkynyl ligand from **I** to afford **II**.

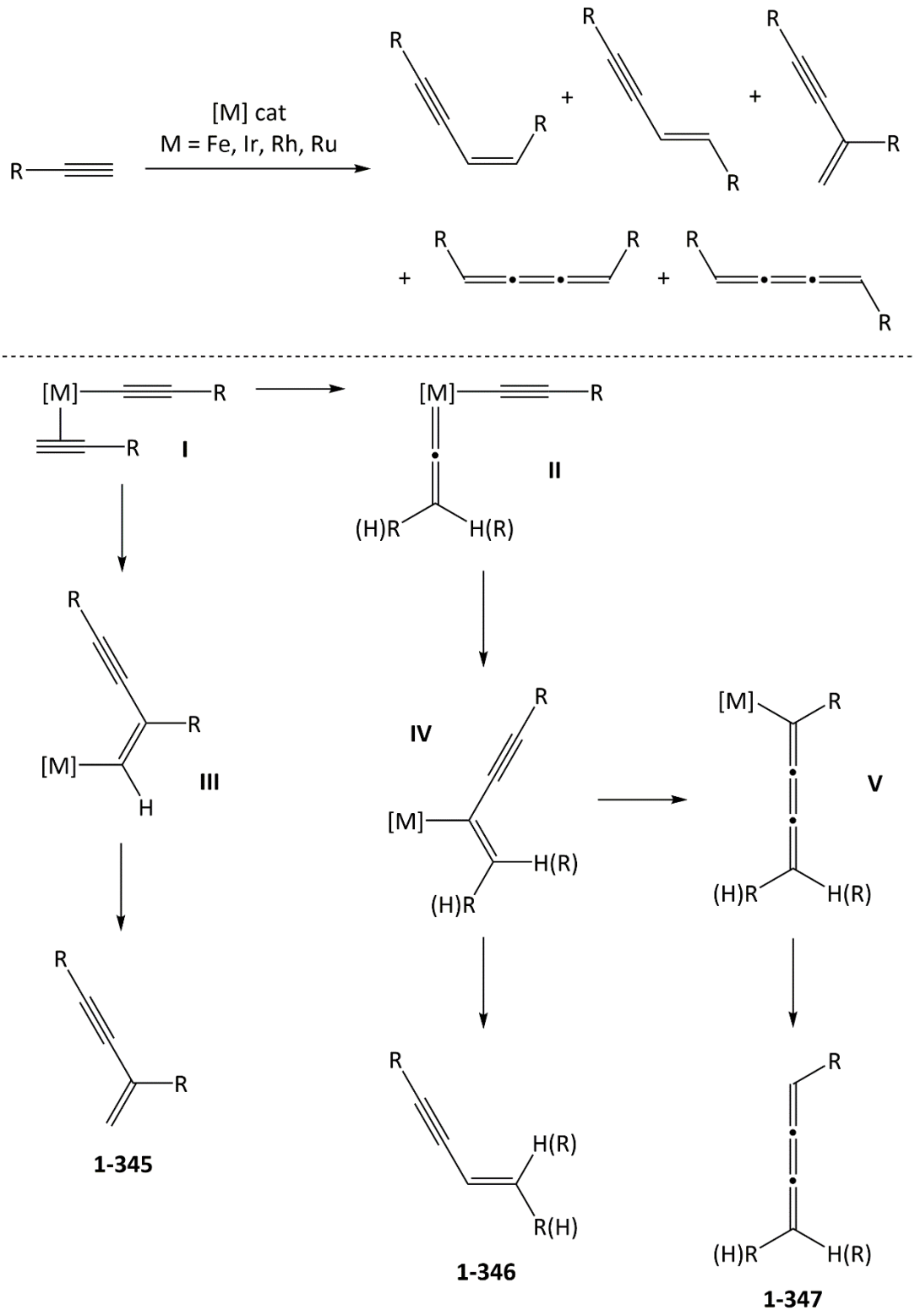

Scheme 91: Dimerisation of alkynes affords enyne and butatriene products. Formation of head-to-tail enynes is proposed to proceed by direct insertion of the η^2-alkyne into the σ Ru-C bond of the alkynyl ligand from I. Head-to-head enynes are proposed to form through migration of the alkynyl ligand onto the α-carbon of the vinylidene ligand from an alkynyl-vinylidene intermediate, II. Butatriene products occur through rearrangement of IV to V.

The ratio of products and the stereoselectivity is heavily influenced by the steric bulk of the alkyne substituent and that of the ancillary ligands around the metal centre. For example, bulky alkynes such as *tert*-butylethyne favour the formation of butatrienes over enynes. The choice of catalyst and ligand set can influence the stereochemical outcome of dimerisation by favouring or disfavouring rotational conformers of the intermediates. Yi and Liu[216] demonstrated that high stereoselectivity could be achieved for dimerisation of phenylethyne catalysed by $[RuH_3(\eta^5\text{-}C_5Me_5)(PR_3)]$. Using the sterically bulk tricyclohexylphosphine favours the formation of the *Z*-enyne (*Z*:*E* = 9:1) *via* **[1-348a]** due to steric repulsion between the phosphine and the phenyl group of the vinylidene (Scheme 92). The use of trimethylphosphine favours the *E*-enyne (*Z*:*E* = 1:9) *via* **[1-348b]** due to the steric repulsion between the phenyl groups of the alkynyl and vinylidene ligands being more significant the interactions with the phosphine.

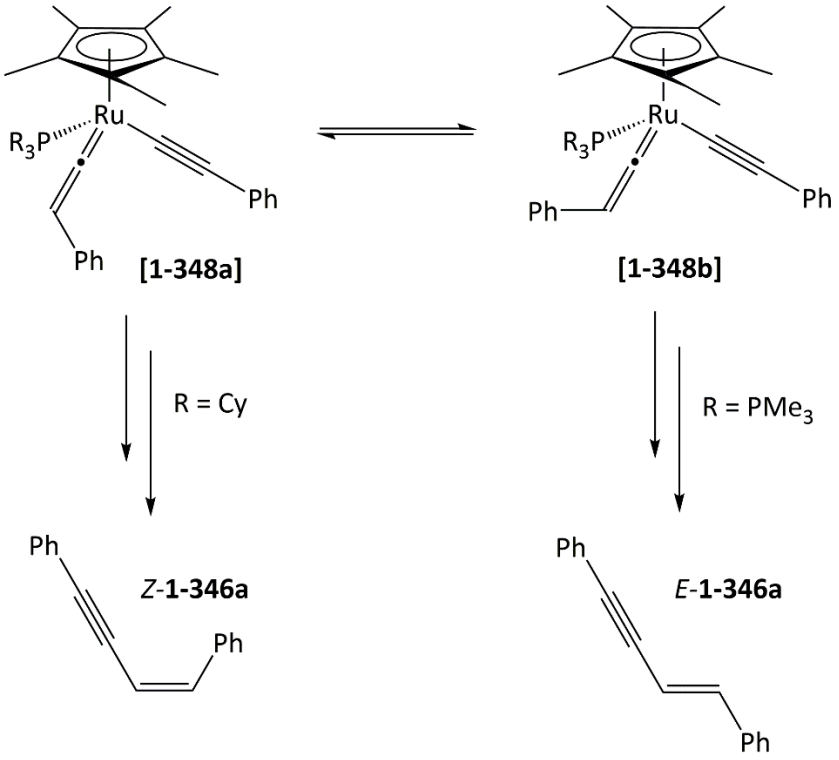

Scheme 92: Stereoselective dimerisation of phenylethyne.

The diverse reactivity of metal vinylidene complexes and the numerous catalytic reactions which are proposed to proceed *via* these as intermediates provide a great opportunity for fluorinated vinylidene complexes to be utilised. The incorporation of fluorinated vinylidene complexes into catalytic reactions has the potential to enable novel fluorinated compounds to be accessed. In order to identify possible applications for fluorinated vinylidene

complexes, their fundamental organometallic chemistry has to be investigated and their reactivity understood. This forms the basis of the work presented in this thesis.

Chapter 2. Exploration of Electrophilic Fluorination of Unsubstituted Ruthenium Alkynyl Complexes and Synthesis of Fluoroalkynyl Complexes

2.1 Halogenated-Vinylidene Complexes

As discussed in Chapter 1, addition of an electrophile to a metal alkynyl complex offers a facile route to disubstituted vinylidene complexes. Bruce *et al*.[217] employed this strategy to access halogenated half-sandwich vinylidene complexes of ruthenium and osmium by addition of the respective dihalogen reagent to the readily-accessible alkynyl complexes (Scheme 93). These reactions were improved upon and expanded by the Lynam and Slattery groups, e.g. using *N*-chlorosuccinimide as a replacement for chlorine gas.[218]

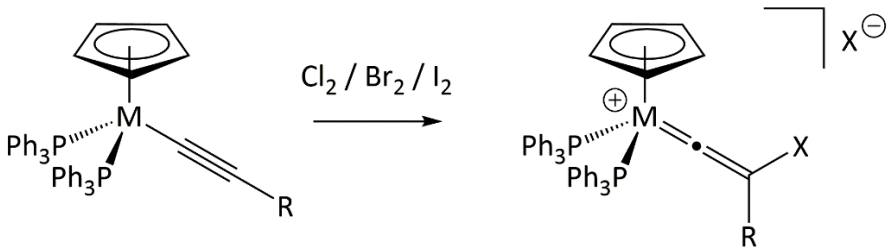

[1] **[2]$^+$**

	X	R	M
a	Cl	Ph	Ru
b	Br	C_6H_4-4-Br	Ru
c[a]	Br	Ph	Ru
d	I	Ph	Ru
e	I	Ph	Os
f	I	C_6F_5	Ru
g	I	Me	Ru

Scheme 93: Synthesis of halogenated vinylidene complexes, [2]$^+$, from respective alkynyl complexes [1] reported by Bruce *et al*.[217] a – reported by Milner *et al*.[218]

2.1.1 Dimeric Fluorinated-Vinylidene Complexes

Access to fluorinated vinylidene ligands was, until recently, limited to a few examples of dimeric iron and iridium complexes.[219-221] The first example was described by Schulze and Seppelt[219] through the reaction of difluoromalonyl dichloride with $[Fe_3(CO)_{11}]^{2-}$ to afford the bridged difluorovinylidene vinylidene complex, **[5]**, which was characterised by X-ray crystallography. Although no intermediates were observed, the reaction was assumed to proceed through nucleophilic attack of difluoromalonyl dichloride by an iron fragment and the oxygen of a bridging carbonyl group to form **[4]**. Loss of an iron carbonyl fragment and CO_2 afforded **[5]** (Scheme 94).

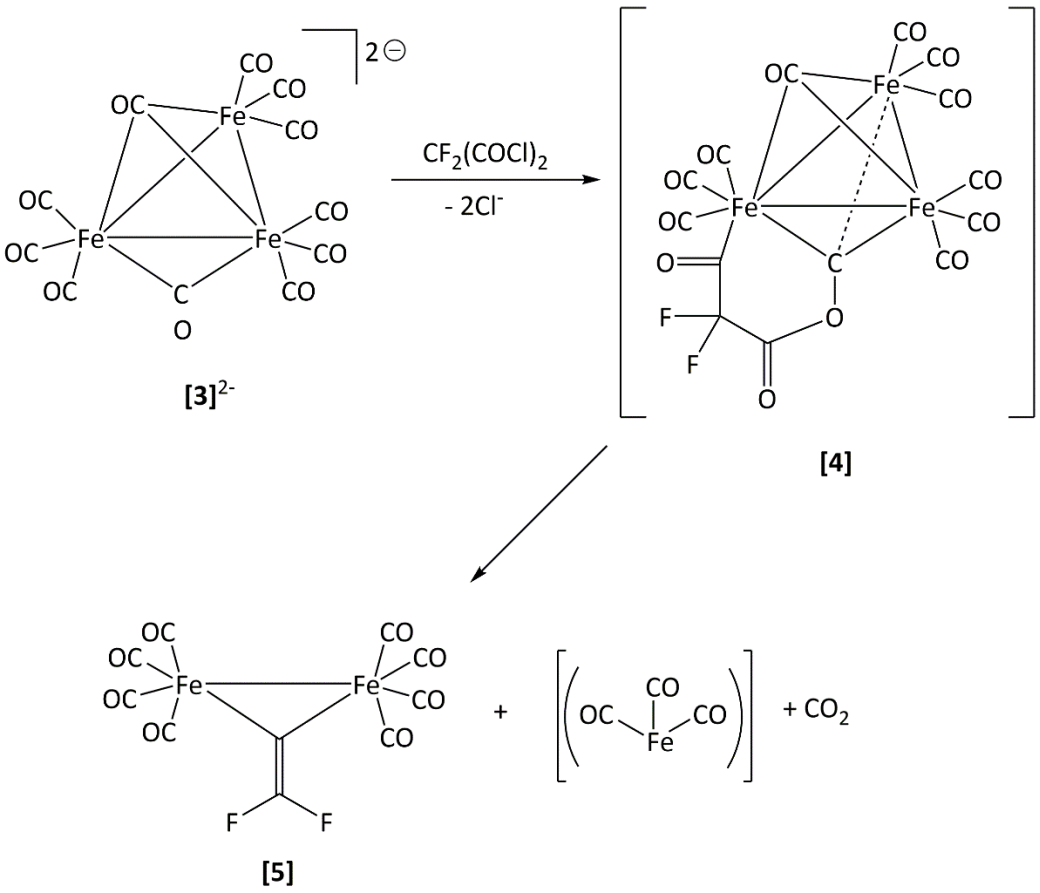

Scheme 94: Proposed synthetic route to formation of difluorovinylidene complex [5] from difluoromalonyl dichloride and $[3]^{2-}$.

More recently dimeric iridium fluorovinylidene complexes have been reported by Cowie *et al.* through the coordination of perfluoroethylene or trifluoroethylene to $[6]^+$ followed by double fluorine abstraction with a strong Lewis acid (Scheme 95).[220, 222]

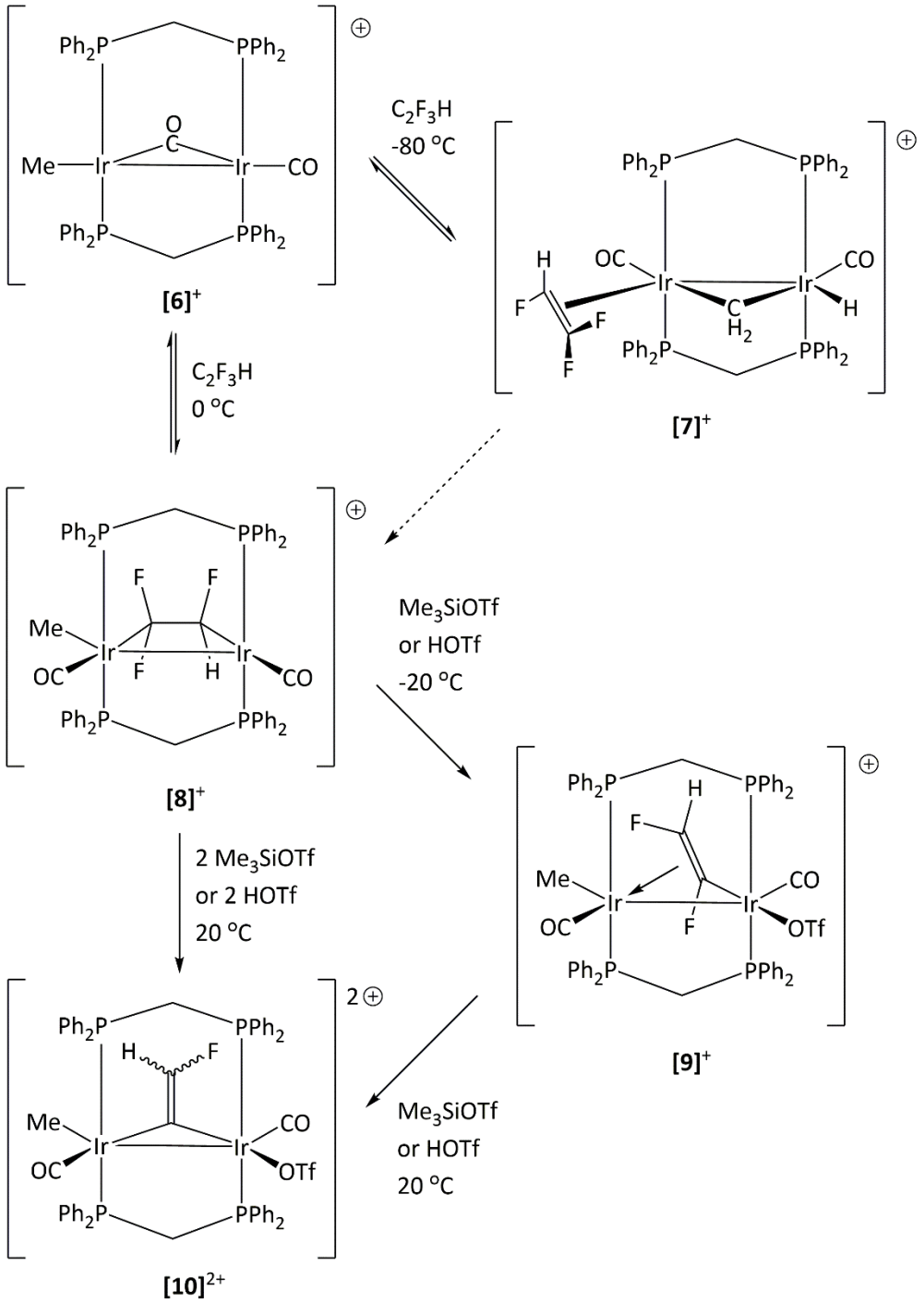

Scheme 95: Coordination of trifluoroethylene to $[6]^+$ and subsequent fluorine abstraction afforded intermediate $[9]^+$ or double fluorine abstraction to afford difluorovinylidene complex $[10]^{2+}$.

Reversible coordination of trifluoroethylene to **[6]**$^{+}$ affords the kinetic product **[7]**$^{+}$ at -80°C, which, upon warming, converts to the thermodynamic product **[8]**$^{+}$ and **[6]**$^{+}$. Addition of one equivalent of trimethylsilyl triflate or triflic acid to **[8]**$^{+}$ at -20 °C afforded the *cis*-difluorovinyl-bridge complex **[9]**$^{+}$ stereo-selectively and in quantitative yield. The absence of the *trans*-**[9]**$^{+}$ was rationalised on the basis of hyperconjugation making the *cis*-isomer thermodynamically favoured. Addition of a second equivalent of trimethylsilyl triflate or triflic acid to **[9]**$^{+}$ resulted in fluorine abstraction from the α-carbon of **[9]**$^{+}$ to afford the bridged difluorovinylidene complex, **[10]**$^{2+}$. Alternatively **[10]**$^{2+}$ could be accessed directly through addition of two equivalents of trimethylsilyl triflate or triflic acid to **[8]**$^{+}$ at 20 °C. Unfortunately, the preliminary reactivity study revealed that **[10]**$^{2+}$ was unreactive toward a hydrogen atmosphere.[220, 222]

Bridged coordination of the fluorinated alkene by the two iridium centres (**[8]**$^{+}$) was quintessential for lowering C-F bond activation. Fluorine abstraction could not be observed without the interaction of the fluorovinyl ligand with second metal centre. The bridging mode effectively changes hybridisation of the alkene carbons from sp^2 to sp^3 through 'pyramidalisation' to form what is essentially a dimetallated fluoroalkane from which fluorine abstraction is feasible.[220, 222]

In addition to accessing a fluorinated vinylidene complex through C-F bond activation, Cowie *et al*. also described the formation of an analogous dimeric iridium fluorovinylidene complex **[12]**$^{+}$ as a minor product through double C-H bond activation of fluoroethylene at 20 °C in dichloromethane (Scheme 96). A difluorovinylidene complex, **[13]**$^{+}$, was also reported through C-H and C-F bond activation.[221]

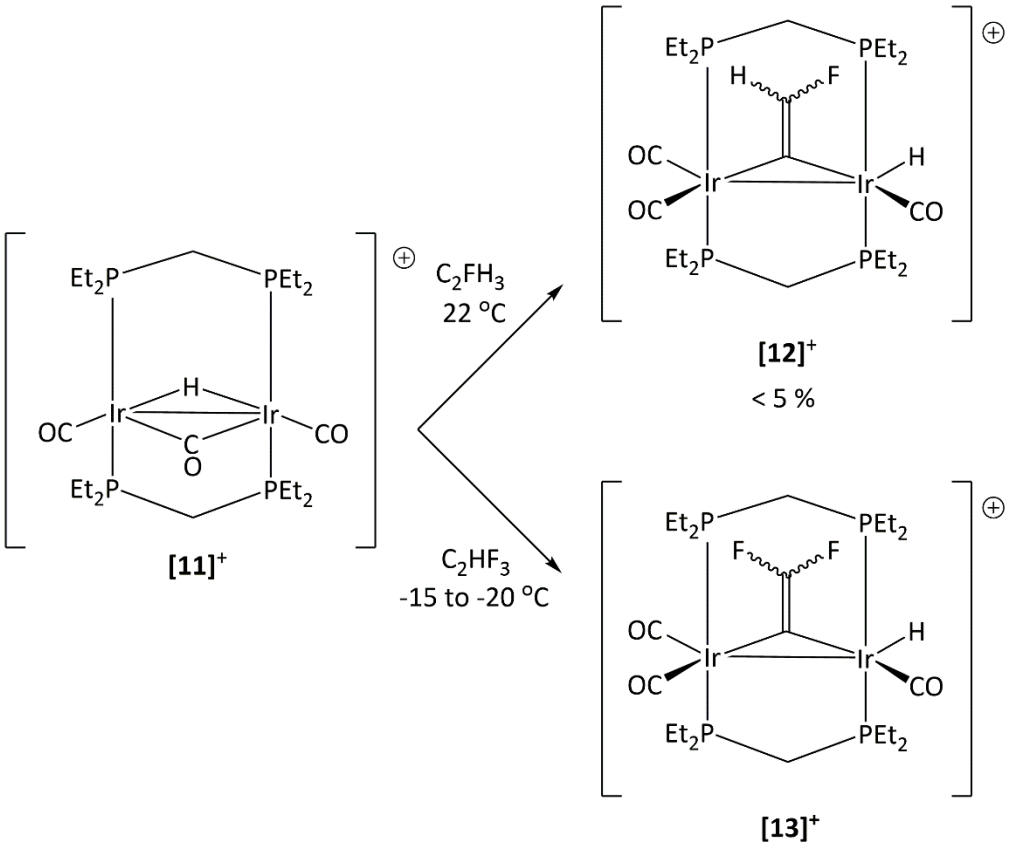

Scheme 96: The fluorovinylidene complex [13]$^+$ was synthesised as a by-product from [11]$^+$ and fluoroethylene through double C-H bond activation.

2.1.2 Monomeric Fluoro-Vinylidene Complexes

Examples of monomeric fluorovinylidene complexes have only been recently been described by the Lynam and Slattery groups.[218, 223, 224] It was demonstrated that ruthenium half-sandwich alkynyl complexes, **[14]**, bearing both electron-rich and -poor aryl or *tert*-butyl substituents, underwent facile and selective fluorination in the presence of a latent source of electrophilic fluorine, 'F^+', to afford monomeric ruthenium fluorovinylidene complexes, **[15]**$^+$ (Scheme 97).[225]

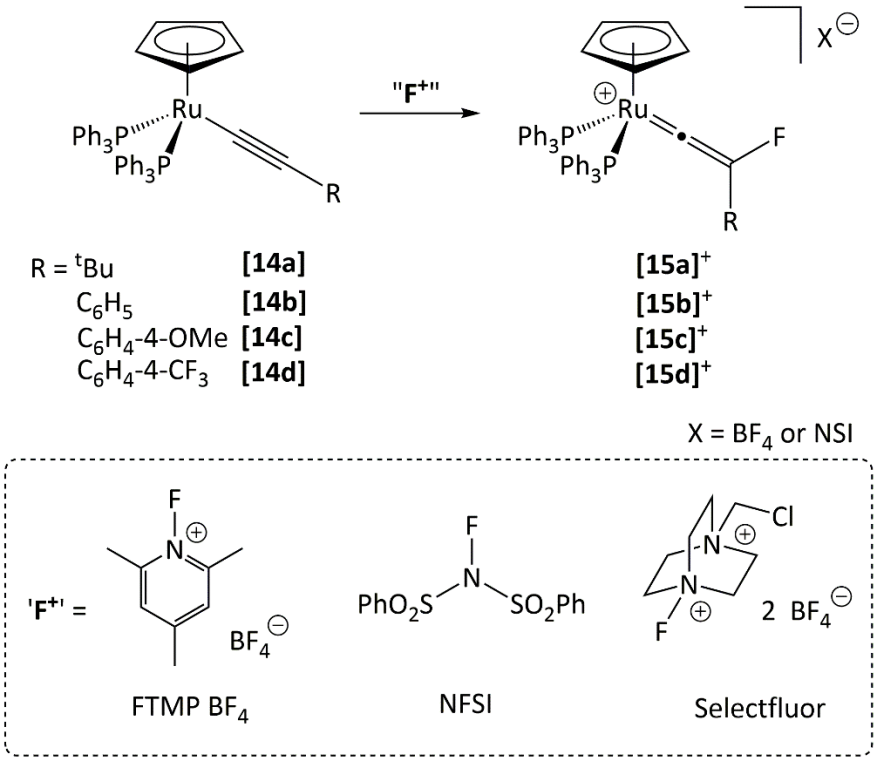

Scheme 97: Reaction of half sandwich ruthenium alkynyl complexes [14] with a latent source of 'F$^+$' afforded the first examples of fluorovinylidene complexes, [15]$^+$.

In conjunction with previous work describing a novel mechanism for C-F bond formation within the coordination sphere of a metal,[225] the mechanism for fluorination was proposed to proceed by direct fluorination of the alkynyl ligand rather than through the formation of a high oxidation state ruthenium-fluoride intermediate. This mechanism, termed outer sphere electrophilic fluorination (OSEF), affords β-fluorinated products, complementary in selectivity to those metal-mediated fluorination strategies which proceed *via* metal-fluoride intermediates (see Chapter 1).[225]

The previous work[225] described regio- and stereo-selective fluorination of ruthenium pyridylidene complex **[16]** to afford **[17a]**$^+$, which, in the presence of an additional equivalent of latent 'F+' and base, undergoes further fluorination to generate the difluorinated pyridylidene complex **[17b]**$^+$ (Scheme 98). Low temperature NMR spectroscopy did not reveal any evidence for the formation of a ruthenium-fluoride intermediate which was supported by the DFT investigation which predicted the formation of the fluorovinylidene complex from possible ruthenium-fluoride intermediates to be unfavourable. Similarly, no intermediates were observed between 195 K and 295 K in the low temperature NMR spectroscopic study for fluorination of **[16]** by [FTMP]BF_4.

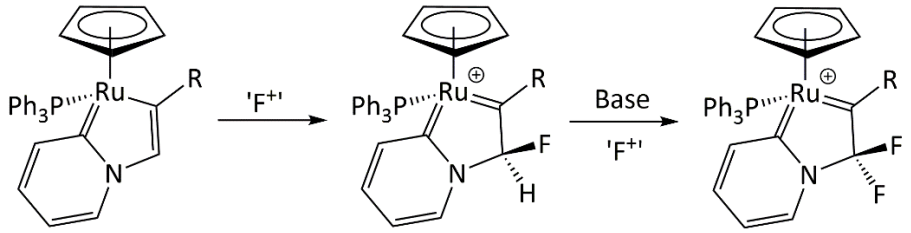

[16]
R = C_6H_4-4-CF_3

[17a]BF_4

[17b]BF_4

Scheme 98: Addition of a latent source of 'F$^+$' to [16] afforded [17a]$^+$ stereo- and regio-selectively; addition of a second equivalent of 'F$^+$' and base afforded [17b]$^+$.

Incorporation of fluorine into the vinylidene ligand of **[15]**$^+$ was accompanied by large downfield shifts in the carbon NMR spectrum for the vinylidene α- and β-carbon chemical shifts which were observed at around δ 390 and 200 respectively.[218, 223] Fluorination was also accompanied by a large bathochromic shift in the lowest energy absorption bands in the UV-Vis absorption spectra as a consequence of the π-donor reducing the HOMO-LUMO transition energy.[218]

In an attempt to liberate the fluoroalkyne from the coordination sphere of the metal, **[15b]**$^+$ was heated in acetonitrile at 50 °C for two weeks. There was no evidence for the liberation of the fluoroalkyne or the presence of the cyclisation products, instead phosphine addition to the vinylidene was observed, generating the *ortho*-metallated phosphonium fluorovinyl complex, **[18]**$^+$ (Scheme 99).[223]

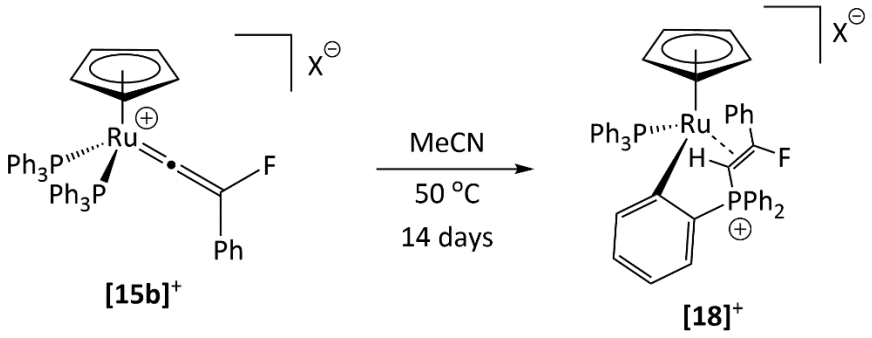

Scheme 99: Heating [15b]$^+$ in acetonitrile at 50 °C over two weeks afforded [18]$^+$.

Incorporation of fluorine did not inhibit nucleophilic attack at the vinylidene α-carbon as shown by the successful nucleophilic addition of pyridine and fluoride to **[15b]**$^+$ to form the corresponding vinyl complexes, **[20]** and **[23]** respectively (Scheme 100, steps i and iii). The pyridine-substituted vinyl complex **[20]** underwent further reaction upon standing in pyridine to afford metallocycle **[21]**$^+$ through formal loss of HF and one triphenylphosphine ligand (Scheme 100, step ii). Although no intermediates could be detected spectroscopically, DFT calculations suggest the reaction proceeds by loss of phosphine and *ortho*-metalation of the vinyl-pyridine, followed by C-F bond cleavage assisted by free pyridine. The corresponding alkynyl species undergoes pyridine addition to form the observed product, **[21]**$^+$.[218, 223]

Fluorovinylidene complexes, **[15b]**BF_4 and **[19]**BF_4, underwent hydrolysis to afford the anti-Markovnikov addition product **25** in the presence of tetrabutylammonium chloride (Scheme 100, steps iv and v/vi respectively). In the case of **[19]**$^+$ hydrolysis proceeded at a faster rate and afforded the aldehyde product (**26**) initially, with slow conversion to **25** over six days. Hydrolysis of the isotopically labelled alkynyl complex **[15b]**BF_4 revealed that formal migration of fluorine occurs rather than phenyl migration in the conversion of **26** to **25**.[218]

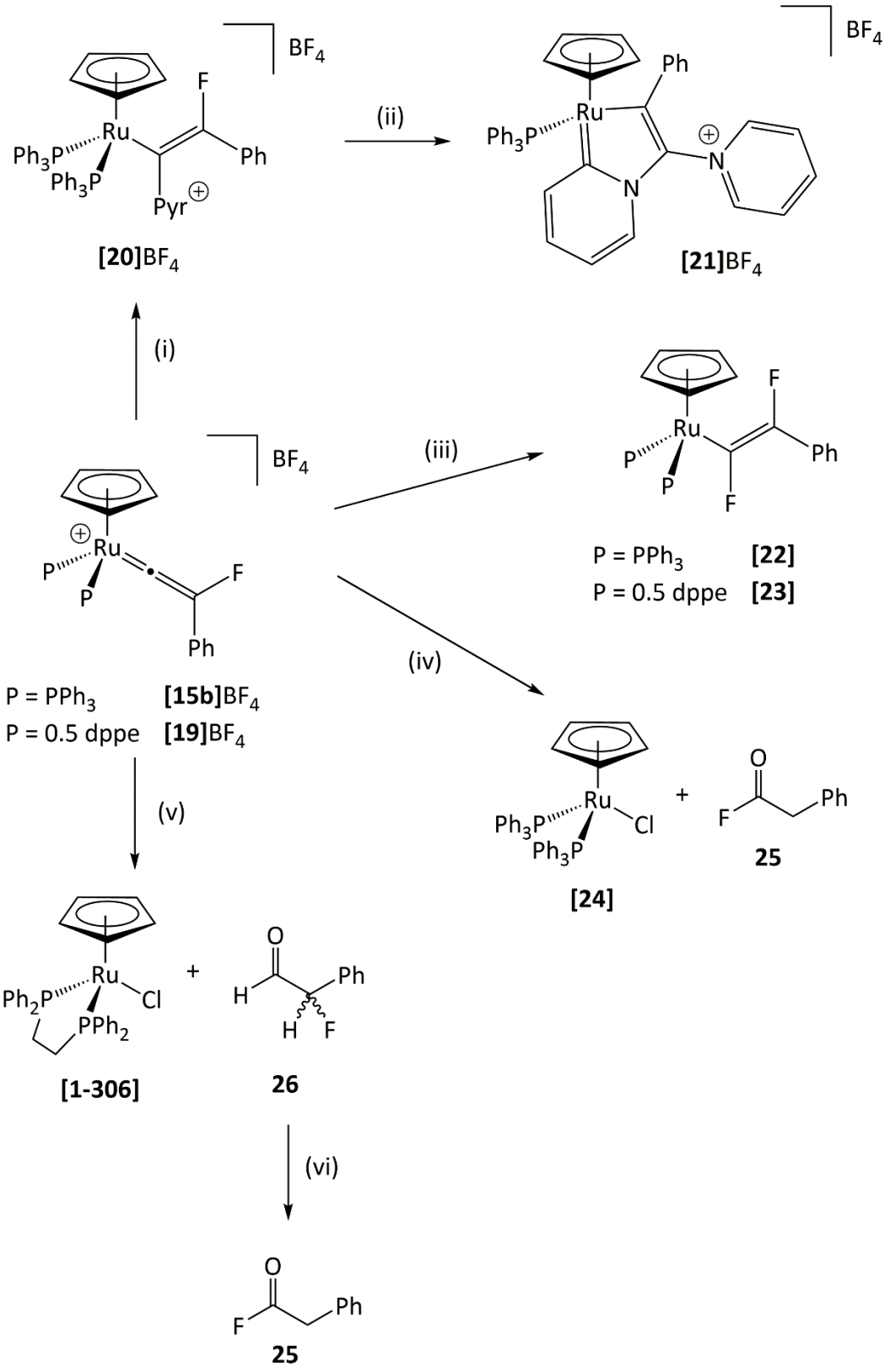

Scheme 100: Reactivity of fluorovinylidene complexes [15b] and/or [19] with; (i) pyridine, 20 °C, < 5 min; (ii) pyridine, -HF, 20 °C, 10 days; (iii) TREAT-HF, d^8-THF, 25 °C, 10 min; (iv) N^nBu_4Cl, CD_2Cl_2, 25 °C, 14 days; (v) N^nBu_4Cl, CD_2Cl_2, 25 °C; (vi) CD_2Cl_2, 25 °C, 6 days.[218, 223]

2.1.3 Fluorination of Unsubstituted Alkynyl Complexes

In contrast to the fluorination of **[14]** with a latent source of 'F^{+}' to afford fluorovinylidene complexes **[15]**$^{+}$ in a facile and selective manner *via* OSEF (Scheme 97), addition of [FTMP]BF_4 to a dichloromethane solution of **[14e]** did not afford the corresponding fluorovinylidene complex but rather the fluorinated cyclobutenylidinium complex **[27]**BF_4.[226]

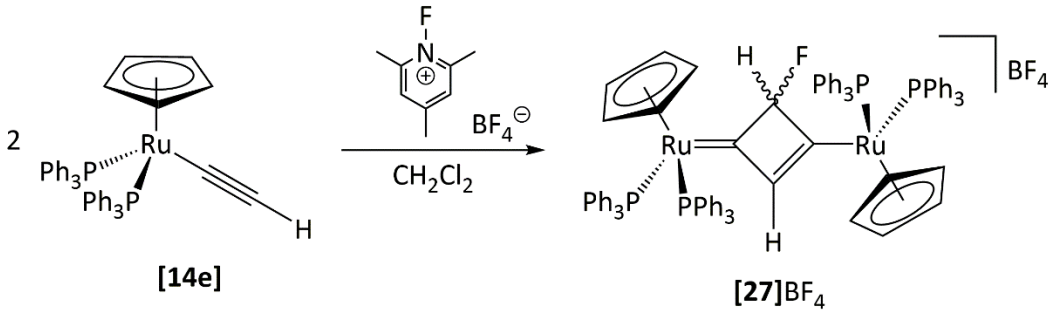

Scheme 101: Addition of [FTMP]BF_4 to [14e] resulted in the formation of [27]BF_4.

The use of half an equivalent of [FTMP]BF_4 or *N*-fluorobenzenesulfonimide as the latent source of 'F^{+}' was found to cleanly afford **[27]**BF_4 while addition of Selectfluor afforded **[27]**BF_4 with additional by-products. Conducting the reaction of **[14e]** with [FTMP]BF_4, NFSI, or Selectfluor at 176 K did not suppress the formation of **[27]**$^{+}$.[226]

Replacing the cyclopentadienyl capping ligand in **[14e]** for the bulkier 1,2,3,4,5-pentamethylpentacyclopentadienyl (Cp*) ligand was found to inhibit the formation of the cyclobutenylidinium complex. Addition of a latent source of 'F^{+}' to **[28a]** at room temperature afforded the desired fluoro-vinylidene complex **[30a]**$^{+}$ as a minor product (Scheme 102). However, due to the increased basicity of the Cp* analogues, protonation effectively out competed fluorination under these conditions forming **[29]**$^{+}$ as the major product. The presence of excess electrophilic fluorinating agent and trace quantities of fluoride also resulted in the sequential incorporation of two additional fluorine atoms to form **[31]**$^{+}$ as a minor product. Additionally, excess fluorinating agent generated a significant quantity of fluorotriphenylphosphonium ($FPPh_3^{+}$) and difluorotriphenylphosphorane (F_2PPh_3) which were identified by the large P-F couplings in the ^{19}F and $^{31}P\{^{1}H\}$ NMR spectra and signals in the mass spectrum.[226]

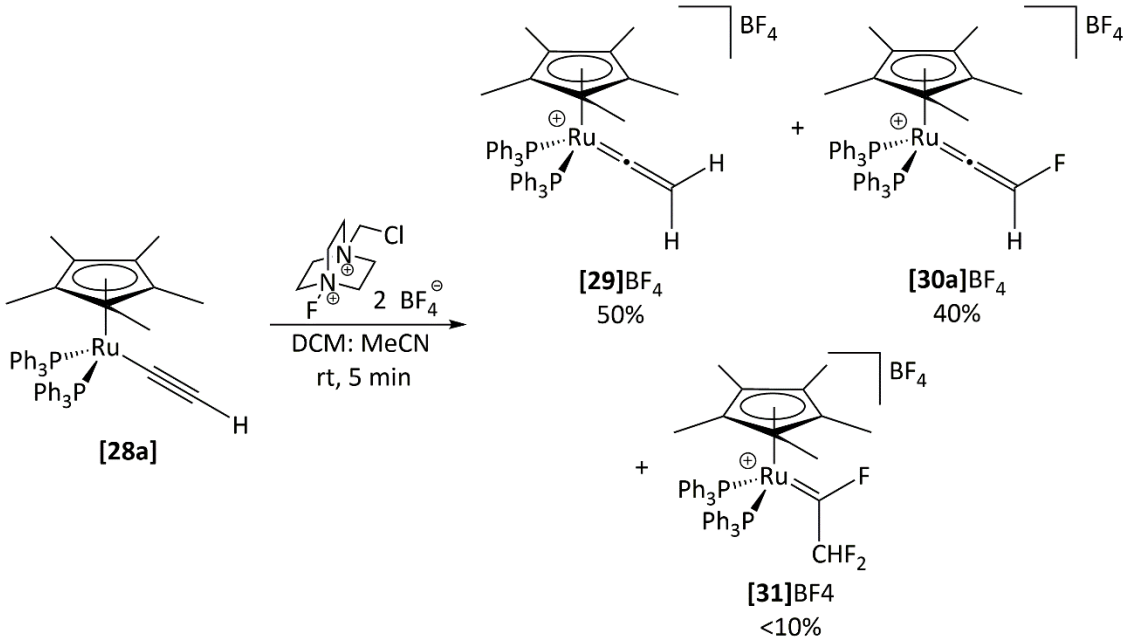

Scheme 102: Reaction of [28a] with Selectfluor afforded a mixture of products including [30a]BF_4 as a minor product.

Characteristic doublet resonances were observed in the ^{1}H and ^{19}F NMR spectra of **[30a]**BF_4 in CD_2Cl_2 at δ 8.63 and δ -234.8 respectively with geminal coupling of 81 Hz, corresponding to the vinylidene substituents. However, the carbon chemical shifts for the vinylidene ligand were not observable due to the other impurities. High-resolution ESI-MS detected a molecular ion peak at 805.2068 m/z which corresponds to **[30a]**$^{+}$. The structure was confirmed by single-crystal X-ray diffraction of suitable crystals of the hexafluorophosphate salt, grown by slow diffusion from a DCM: pentane solvent system (Figure 5).[226]

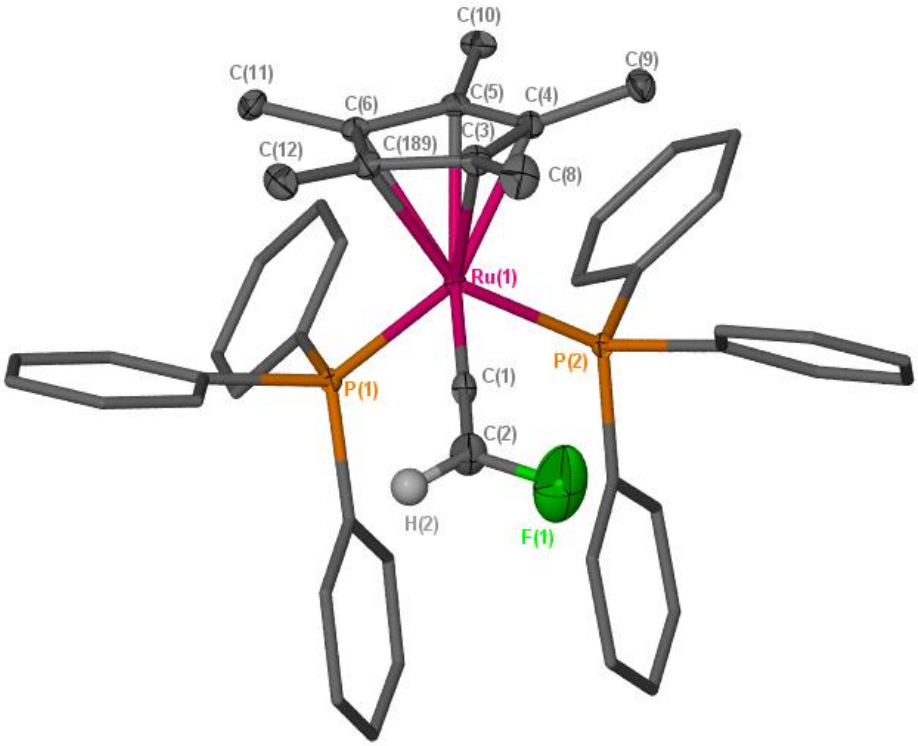

Figure 5: Crystal structure of [30a]PF_6. Hexafluorophosphate counter-ion, residual solvent, and hydrogens (with the exception of the vinylidene proton), have been omitted for clarity. Selected bond lengths (Å): Ru(1)-C(1), 1.839(2); C(1)-C(2), 1.304(4); C(2)-F(1), 1.355(3); C(2)-H(2), 0.97(3); Ru(1)-C(Cp ring), 2.30 average; Ru(1)-P(1), 2.3650(6); Ru(1)-P(2), 2.3523(6). Selected bond angles (°): Ru(1)-C(1)-C(2), 171.9(2); C(1)-C(2)-F(1), 122.2(3); C(1)-C(2)-H(2), 126.2(17); F(1)-C(2)-H(2), 111.6(17); P(1)-Ru(1)-P(2), 96.57(2).

2.2 Fluoroalkynes

The synthesis of 1-fluoroalkynes is limited to a few examples of often highly unstable compounds which readily oligomerise even under low temperature conditions. Fluoroethyne (**33a**) can be generated by pyrolysis of fluoromaleic anhydride (**32**) at 650 °C (Scheme 103). Above -80 °C fluoroethyne explosively cyclotrimerises to 1,2,4-trifluorobenzene (**34**) but can be handled in gaseous form at atmospheric pressure.[227]

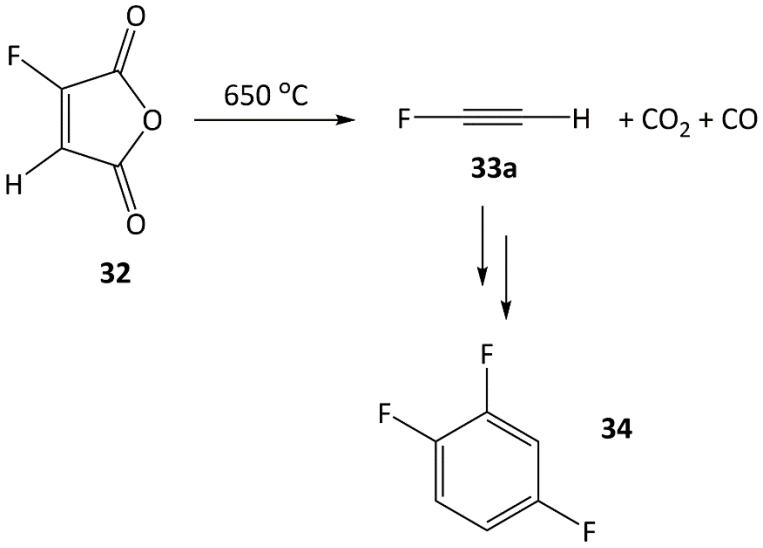

Scheme 103: Pyrolysis of 33c affords fluoroethyne which explosively reacts in the condensed phase or more slowly in the gas phase to afford 34.

Similarly, 1,2-difluoroethyne (**33b** was generated by high temperature decomposition of a fluorinated precursor. Vacuum pyrolysis of perfluoro-1,2,3-trirazine (**35**) at 700 °C afforded 1,2-difluoroethyne (**33b**) relatively cleanly (Scheme 104). Decomposition occurs above -196 °C with a half-life of *ca.* 15 minutes at 27 °C and 2.5 mbar. Decomposition affords an unidentified polymer and fluorine-containing species including, :CF_2, C_2F_4, C_3F_4, and perfluoropropyne (**33c**).[228]

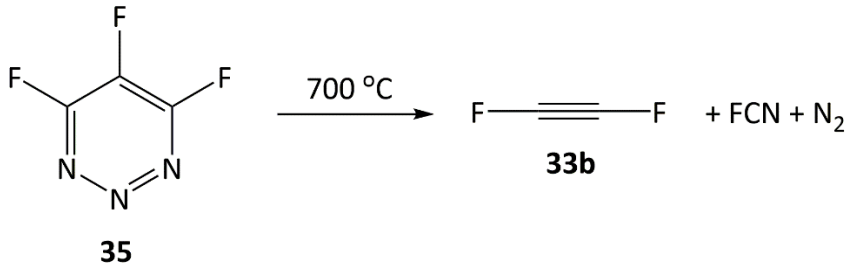

Scheme 104: Pyrolysis of 42 at 700 °C affords 1,2-difluoroethyne, 33e.

Perfluoropropyne (**33c**) was isolated by two routes independently, from either **36** and **37**, or **38** (Scheme 105). In contrast to the poor stability of the other fluoroalkynes discussed here, perfluoropropyne displayed significantly higher stability, being stable in the gas phase for one month at 25 °C at 10 cmHg or four days at 20 °C at 1.25 atm. Polymerisation of perfluoropropyne was observed in the liquid phase at higher pressures.[229]

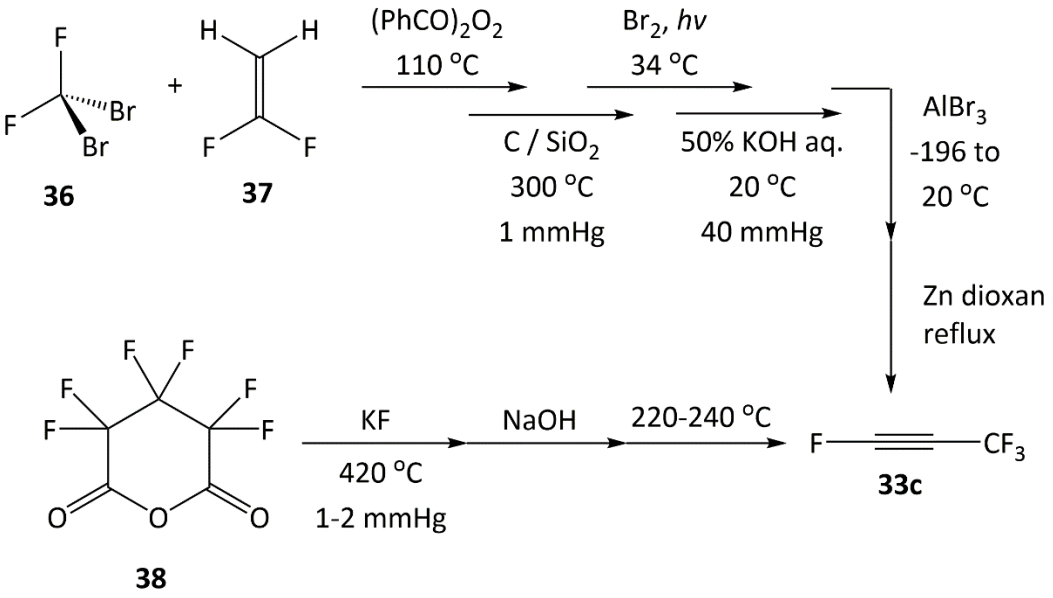

Scheme 105: Synthesis of perfluoropropyne, 33c, *via* 36 and 37, or 38.

1-Chloro-2-fluoroethyne, **33d**, was synthesised by deprotonation of **39** and elimination of lithium chloride from **40** (Scheme 106). Like fluoroethyne, **33d** displayed explosive reactivity when condensed and also exhibited reactivity with the ether solvent at low temperature.[230]

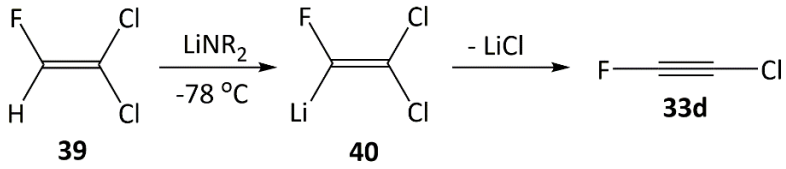

Scheme 106: Synthesis of 1-chloro-2-fluoroethyne, 33d, by dehalogenation of 39 with a lithium amide base.

The *tert*-butyl substituted fluoroalkyne, **33e**, generated by dehalogenation of **41** or **42** at 120 °C, undergoes cyclotrimerisation below 0 °C to form a mixture of **43** (Scheme 107).[231] A DFT and intermediate trapping investigation[232] proposes cyclotrimerisation of fluoroalkynes (Scheme 108) proceeds by initial stereoselective [2+2] cycloaddition to afford **c** *via* diradical **b**. Addition of a haloalkyne to **c** generates a 1,4-diradical trimer, **d**. The nature of the

cyclotrimer observed (**g** or **h**) is determined by the Dewar benzene formed (**e** or **f**) by ring closing of the diradical **d**.[233]

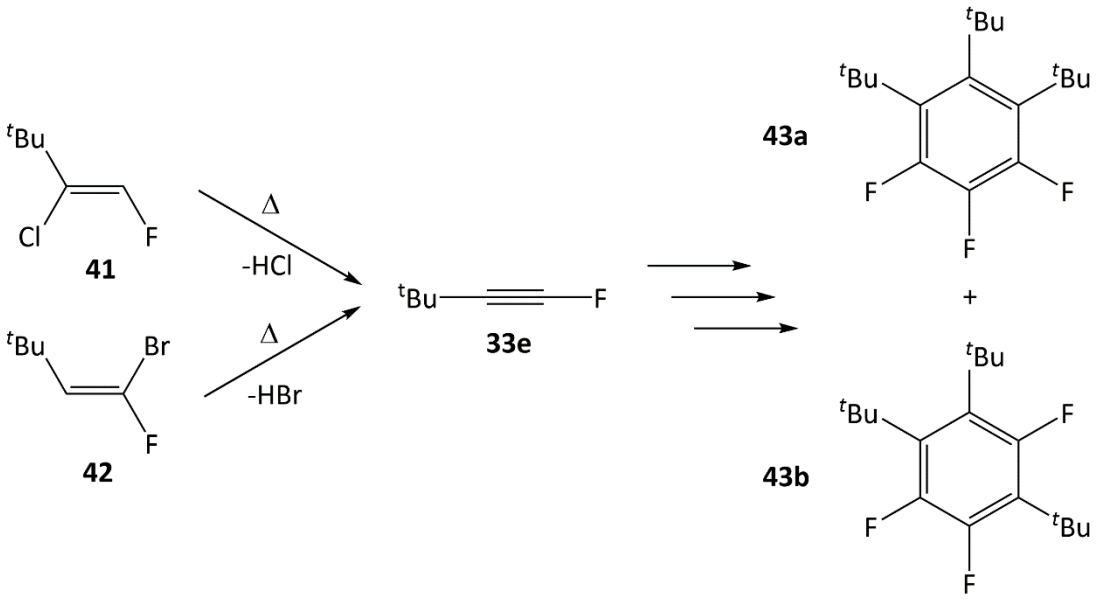

Scheme 107: Dehalogenation of 41 or 42 affords fluoroalkyne 33e which cyclotrimerises to a mixture of 43a and 43b.

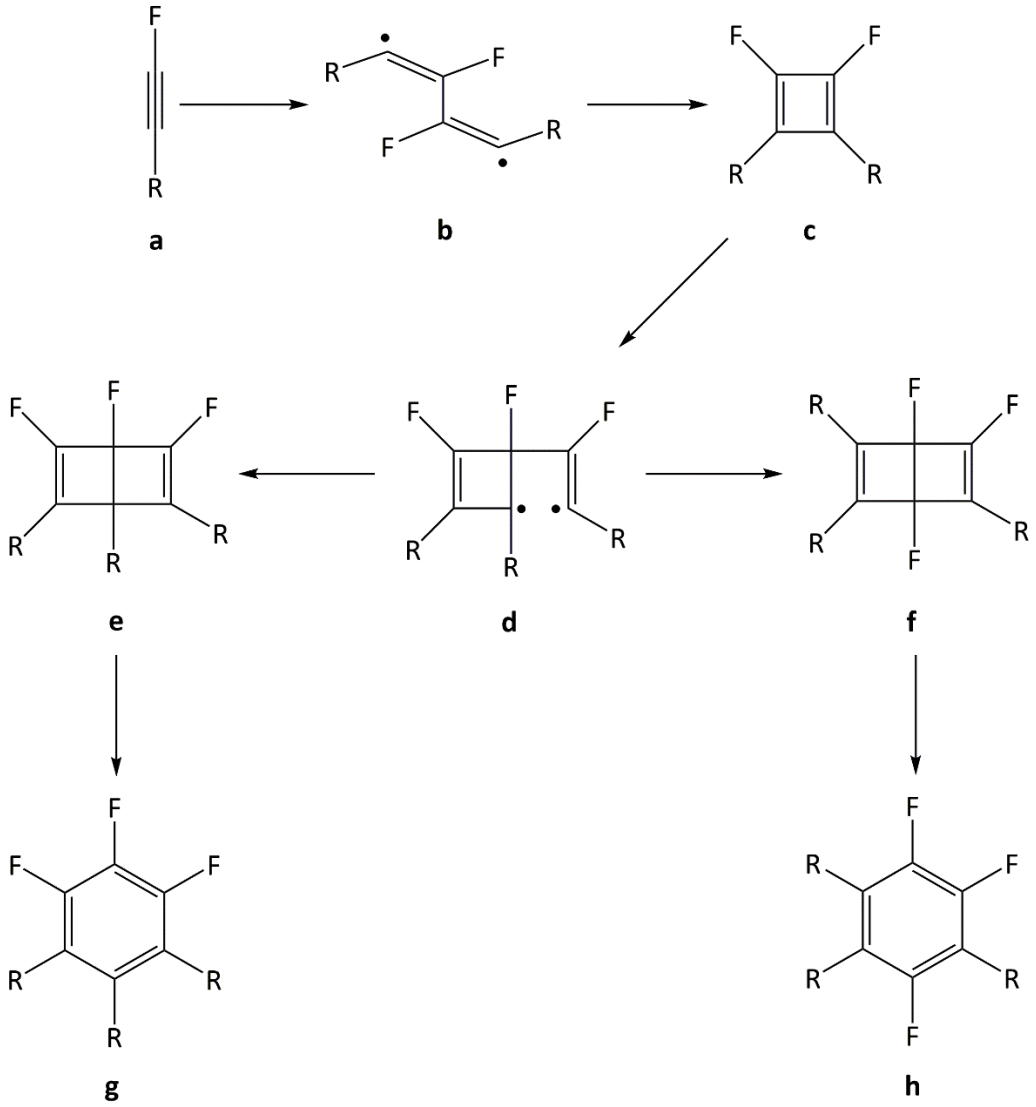

Scheme 108: Proposed mechanism for cyclotrimerisation of fluoroalkynes *via* low lying diradical b which cyclises to c. Addition of a third fluoroalkyne affords d from which the pathway diverges to either e or f through recombination.

In contrast to most fluoroalkynes, other haloalkynes display significantly greater stability and have been utilised in numerous synthetic applications. The ready thermal cyclotrimerisation of fluoroalkynes compared to chloroalkynes has been attributed to the low energy barrier for initial dimerisation (**c** *via* **b**) due to a smaller singlet-triplet energy gap for fluoroalkynes.[232, 234]

Due to the harsh conditions required for synthesis, difficulty in handling, and often high reactivity, the application of fluoroalkynes in synthetic chemistry has so far been unviable. Access to stable synthetic synthons would enable the reactivity and application of fluoroalkynes to be explored. Characterisation of fluoroalkynes has been primarily limited to melting points and gas-phase IR spectroscopy, with some instances of low temperature

fluorine NMR spectroscopy being employed. One of the main aims of this chapter was to develop methodology to access stable metal fluoroalkynyl complexes to better understand the reactivity and structure of this reactive class of compounds.

2.3 Fluorination of [Ru(η^5-C$_5$H$_5$)(PPh$_3$)$_2$(-C≡C-H], [14e]

Metal vinylidene complexes are widely encountered, or postulated, as intermediates in a range of important metal-mediated transformations of alkynes.[142, 154, 195] By making use of the novel outer-sphere electrophilic fluorination (OSEF) strategy developed within the Lynam and Slattery groups,[218, 225] this chapter describes efforts to apply this methodology to the fluorination of unsubstituted alkynyl complexes and discuss the formation of stable metal fluoroalkynyl complexes.

As discussed in section 2.1.3, electrophilic fluorination of **[14e]** did not afford **[44a]**BF_4 but rather **[27]**BF_4.[226] The incorporation of fluorine into the product is believed to proceed by initial OSEF to form the fluoro-vinylidene **[44a]**$^+$ as an intermediate which then rapidly undergoes cyclisation with an equivalent of the alkynyl starting material to afford **[27]**$^+$ (Scheme 109). The formation of fluorovinylidene complexes **[15]**$^+$ is accompanied by a colour change from yellow to green. In the synthesis of **[27]**$^+$ a green solution was observed immediately after addition of the fluorinating agent, as observed with the formation of the other fluoro-vinylidene complexes reported previously. After less than one minute the solution turned dark orange which presumably corresponded to the formation of **[27]**$^+$. The initial observation of a green solution could be indicative of the formation of **[44a]**$^+$.

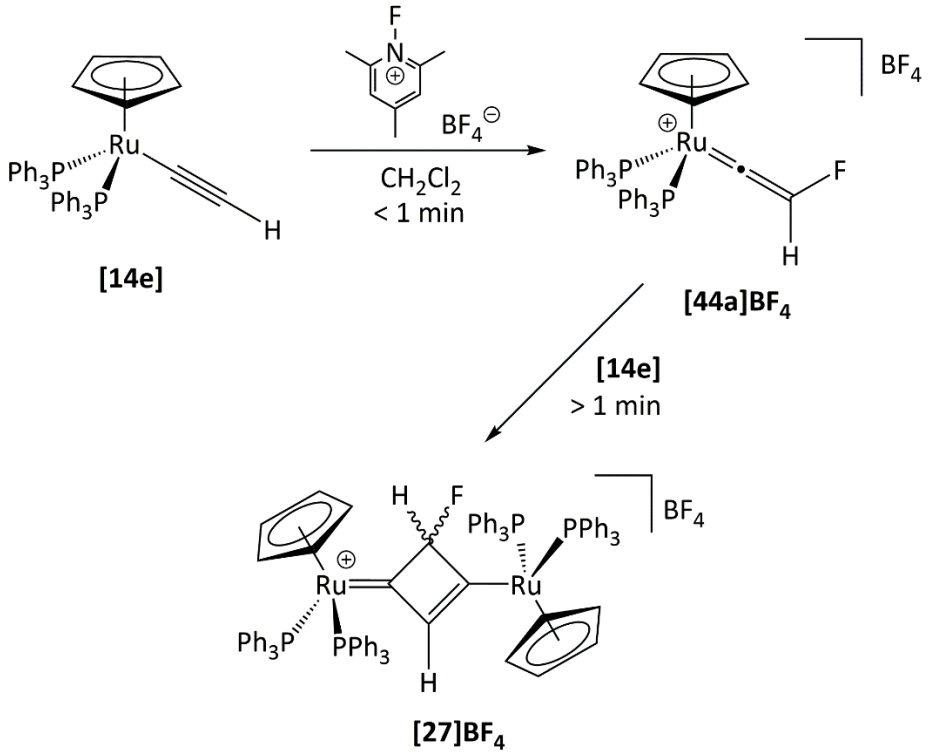

Scheme 109: Addition of [FTMP]BF_4 to [14e] is proposed to afford [44a]BF_4 as a transient intermediate which reacts with [14e] over one minute to afford [27]BF_4 as the final product.

It was envisaged that inhibition of the cyclisation pathway would enable the isolation of **[44a]**$^+$, which could then be deprotonated with a suitable base to afford the fluoroalkynyl complex **[14f]** (Scheme 110).

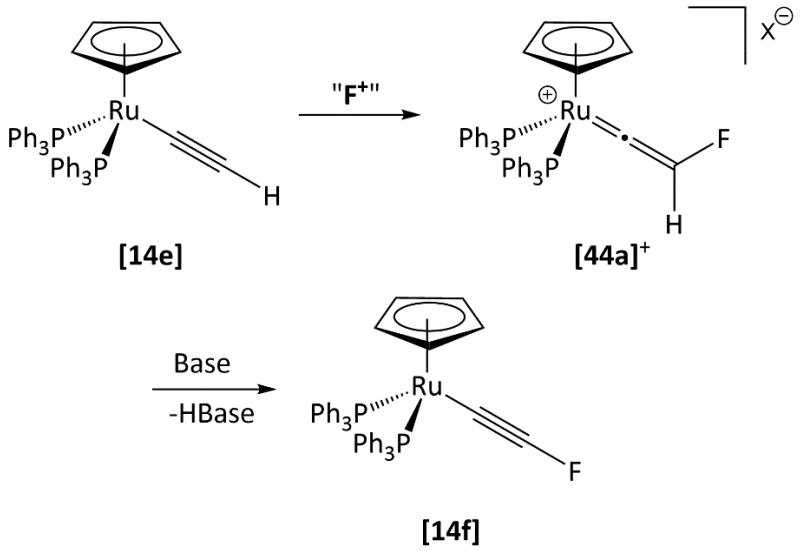

Scheme 110: Envisaged synthetic route for accessing ruthenium fluoroalkynyl complex [14f].

2.3.1 Continued Study of Fluorocyclobutenylidinium Complex [27]BF_4

Assignment of **[27]**$^+$ was proposed previously on the partial characterisation by NMR spectroscopy. The ^{19}F NMR spectrum of **[27]**BF_4 exhibited a doublet of doublets resonance at δ -137.4 with coupling of 58 and 13 Hz, which matched resonances in the ^1H NMR spectrum at δ 4.84 and 7.47 ppm with 58 and 13 Hz coupling respectively. The data were consistent with the presence a geminal proton and fluorine pair and alkenyl proton of a cyclobutenyl ligand. The ^1H-^{13}C HSQC and HMBC correlation experiments revealed short range coupling between the proton of the geminal pair and a carbon resonance at δ 109.1 with doublet coupling of 234 Hz to fluorine. Short range coupling was also observed between the alkenyl proton at δ 7.47 and a carbon resonance at δ 183.6. Finally, long range coupling was observed to a low field carbon environment at δ 250.9 which is consistent with a metal bound carbon with multiple bond character. The mass spectrum revealed a species with the m/z of two alkynyl complexes and one fluorine atom, consistent with the assignment.

The structure of **[27]**$^+$ has now been confirmed by X-ray crystallography as the hexafluorophosphate salt. The crystals were grown by slow diffusion of pentane into a dichloromethane solution of **[27]**PF_6. The cyclobutenylidinium ligand forms as a 1:1 ratio of two stereoisomers, both of which occupy two possible orientations in the lattice equally (Figure 6). Additionally, half of the phosphine-phenyl rings occupied two possible positions

with 3:2 occupancy. The β-carbon, C(7), displays increased disorder due to slight rotations of the ring in the lattice and the overlapping electron density of the C(sp^2) and C(sp^3) carbons. The cyclobutenyl ligand is coordinated to the two ruthenium centres at distorted angles of 129.0(2)° (Ru-C(6)-C(7)) and 142.6(3)° (Ru-C(6)-(C(7')) in both isomers and is in good agreement with the BP86-S(V)P geometry optimised structure (127.9° and 144.6° respectively). The remaining angle around the α- carbon of the cyclobutenyl ring (C(7A)-C(6)-C(7A)) was measured at 88.3(3)° and consistent with the calculated value (87.6°). The bond angle between C(6)-C(7)-C(6) was measured at 91.7(3)°, approximately half way between the two calculated angles of 87.6° and 97.1° as would be expected with equal occupancy of the C(sp^2) and C(sp^3) carbons. The C(6)-C(7)-F(1) bond angle, recorded between 116.9(18)° and 122.9(18)°, was statistically identical over the four sites, and distorted away from the ideal C(sp^3) geometry.

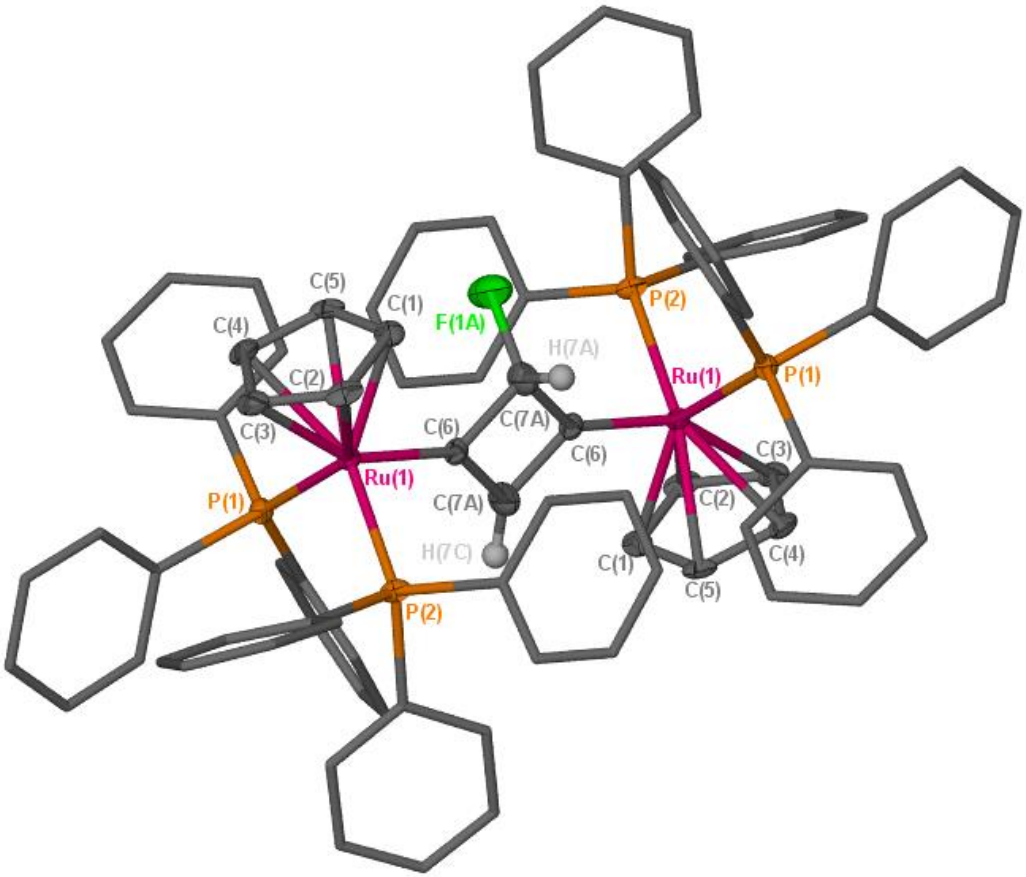

Figure 6: Crystal structure of [27]PF_6. Hydrogens (with the exception of H(7A) and H(7C)), counterion, and solvent of crystallisation omitted for clarity; thermal ellipsoids are shown with 50% probability level. Hydrogens 7A and 7C were fixed with 1.2 U_{iso}.

2.3.2 Alternating Reaction Conditions and Formation of Fluorovinylidene Complex, [44a]$^+$

It was shown previously that conducting the reaction under low temperature conditions (176 K) failed to inhibit or suppress the formation of **[27]**$^+$ with NFSI, [FTMP]BF_4, or Selectfluor. To determine whether cyclisation occurs through a photochemical [2+2] cycloaddition pathway, and attempt to inhibit this process, **[14e]** was reacted with NFSI, [FTMP]BF_4, and Selectfluor in the absence of light at room temperature. However, cyclisation was found to proceed regardless of the choice of fluorinating agent, suggesting that a traditional photochemically promoted [2+2] cycloaddition mechanism is not being observed. It is postulated that the formation of **[27]**$^+$ occurs *via* a step-wise mechanism (Scheme 111) in which **[44a]**$^+$ undergoes nucleophilic attack by the alkynyl complex (**A**), followed by the vinyl moiety attacking the newly formed vinylidene (**B**) to afford **[27]**$^+$.

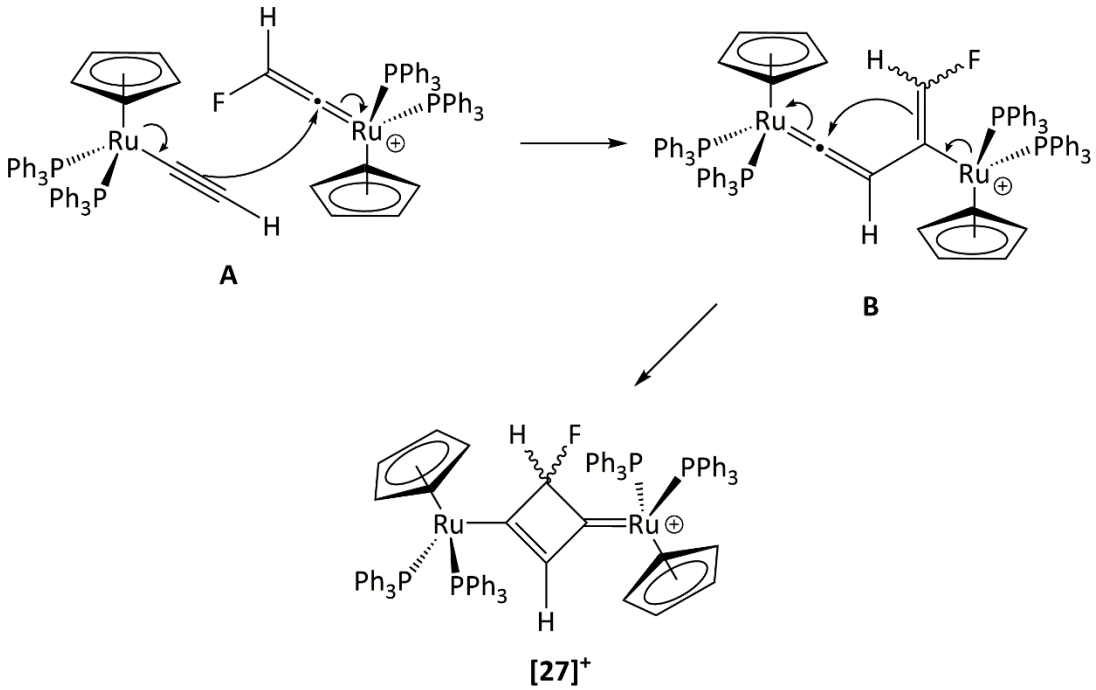

Scheme 111: Proposed mechanism for the cyclisation of [14e] and [44a]$^+$ by nucleophilic attack (A) and cyclisation (B) to afford [27]$^+$.

However, it was found that the suppression or complete absence of **[27]**$^+$ was observed while conducting the reaction in acetonitrile at room temperature in the presence of light. Under these conditions the fluorinating agents ([FTMP]BF_4, NFSI, and Selectfluor) are fully soluble while **[14e]** remains almost insoluble. The reaction of [FTMP]BF_4 with **[14e]** in acetonitrile, afforded the diprotio-vinylidene **[44b]**$^+$ as the major product through competing protonation. This observation was unsurprising given the acidic nature of the fluorinating

agent. Reaction of NFSI with **[14e]** afforded **[44a]**$^+$ as a mixture of products including small quantities of **[27]**$^+$ and **[44b]**$^+$. Additional species with inequivalent phosphorus environments and fluorine environments with high multiplicity, were also observed by NMR spectroscopy but were not identified.

In contrast, the addition of Selectfluor to a d^3-acetonitrile suspension of **[14e]** resulted in the formation of a new major organometallic phosphorus-containing product at δ 44.1, which was assigned to the formation of the desired product **[44a]**BF_4 (57 % conversion by $^{31}P\{^1H\}$ NMR spectroscopy). Additional minor products were also observed in the $^{31}P\{^1H\}$ NMR spectrum at δ 44.0, 41.9, 41.6, and 38.4, of which only **[44b]**BF_4 was identified at δ 44.0 (17 % conversion). Complex **[44a]**BF_4 in d^3-acetonitrile exhibited a doublet resonance at δ 8.27 in the ^1H NMR spectrum with 80 Hz coupling to a matching doublet resonance at δ -233.0 in the ^{19}F NMR spectrum. The size of the coupling is indicative of geminal H-F coupling and the fluorine chemical shift is consistent with previously reported fluoro-vinylidene complexes, **[15]**$^+$.[218] The mass spectrum displayed a m/z of 735.1334 corresponding to **[44a]**$^+$. Unfortunately, separation of **[44a]**BF_4 from **[44b]**BF_4 and the other minor species proved challenging and full characterisation of **[44a]**BF_4 could not be achieved due to complete decomposition within 16 hours.

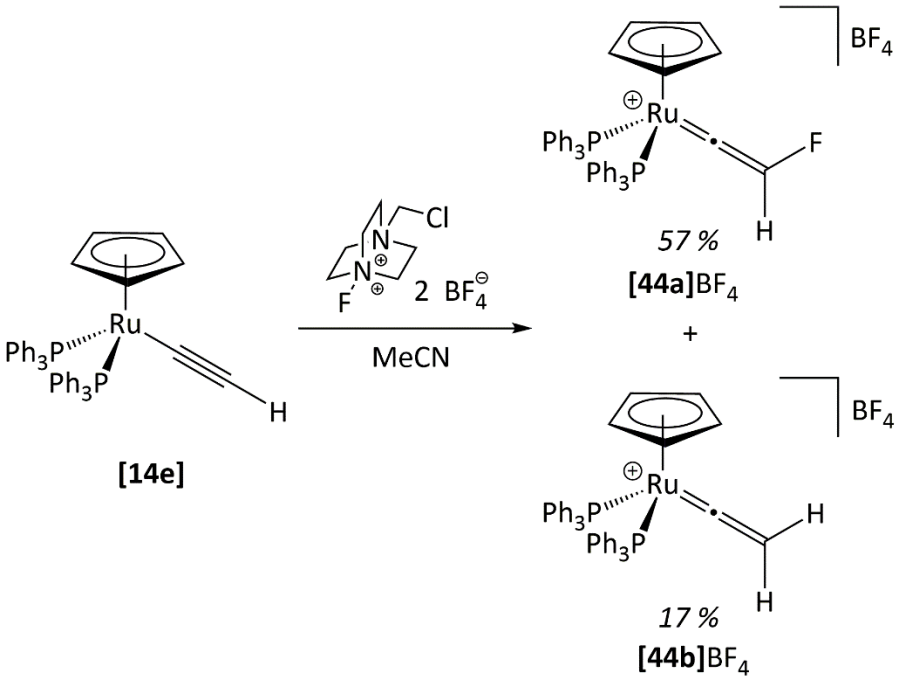

Scheme 112: Conducting the reaction of [14e] with Selectfluor in acetonitrile afforded a mixture of [44b]BF_4 and [44a]BF_4

The low concentration of **[14e]** in solution, enforced by poor solubility in acetonitrile, and the large concentration difference with respect to the fluorinating agent is believed to be the driving force in supressing or inhibiting formation for **[27]**$^+$. The formation of **[27]**$^+$ is not surprising given that **[27]**$^+$ is calculated to be lower in energy than the individual alkynyl and vinylidene complexes, **[14e]** and **[44a]**$^+$ respectively (ΔH_{298} = -153 kJ mol^{-1} , ΔG_{298} = -77 kJ mol^{-1} at the (RI-)BP86/SV(P)//PBE0/def2-TZVPP level).

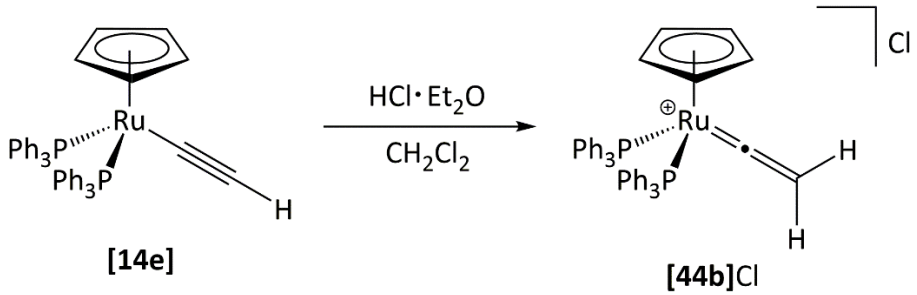

[14e] **[44b]**Cl

Scheme 113: Addition of a diethyl ether solution of hydrochloric acid to a dichloromethane solution of [14e] afforded [44b]Cl cleanly.

In comparison to the addition of a latent source of 'F$^+$', the addition of 'dry' hydrochloric acid to a dichloromethane solution of **[14e]** resulted in rapid protonation to yield only the diprotio-vinylidene complex **[44b]**Cl with no observation of the analogous protio-cyclobutenylidinium complex (Scheme 113). The formation of the protio-cyclobutenylidinium analogue was also predicted to be thermodynamically lower in energy than the constituent components by ΔH_{298} = -48 kJ mol^{-1} (ΔG_{298} = -4 kJ mol^{-1}), albeit less favourable than the formation of **[27]**$^+$. It is presumed that the rate of protonation is sufficiently high with respect to cyclisation to enable complete protonation of the starting material. Bruce *et al*.[235] reported the formation of an analogous cyclobutenylidinium complex **[47]**PF_6 over two hours through mixing the constituent alkynyl and vinylidene complexes (Scheme 114). This indicates that the cyclisation reaction with protio-substituents is significantly slow compared to the rate with fluorine-substituents. The presence of a fluorine-substituent significantly activates the vinylidene α-carbon to nucleophilic attack compared to the protio-analogue, resulting in different products being observed.

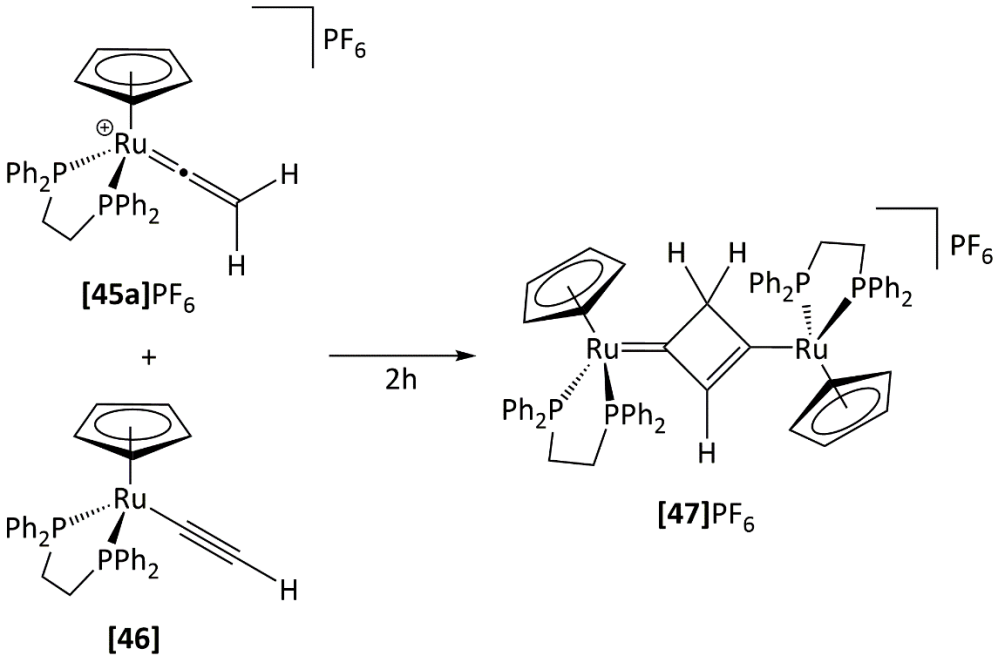

Scheme 114: Bruce *et al.* described formation of cyclobutenylidinium [47]PF_6 from the reaction of [45]PF_6 and [46] over two hours.

2.4 Fluorination of [Ru(η^5-C$_5$Me$_5$)(PPh$_3$)$_2$(-C≡C-R] Complexes

2.4.1 Optimised synthesis of Fluorovinylidene complex, [30a]$^+$

Previous efforts to synthesise **[30a]**$^+$ at room temperature afforded the product as a mixture of components which could not be separated by conventional means. Optimisation of the reaction found that addition of Selectfluor to a 1:1 dichloromethane: acetonitrile solution of **[28a]** at -78 °C ensured complete selectively for the fluorination pathway (Scheme 115). There was no evidence for competing formation of **[29]**BF_4 or **[31]**BF_4 according to NMR spectroscopy and elemental analysis.

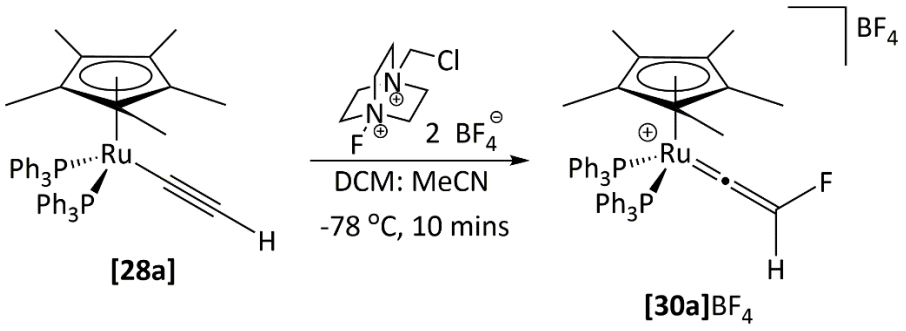

Scheme 115: Cold addition of the Selectfluor to [28a] afforded [30a]BF_4 selectively.

Formation of **[30a]**BF_4 was confirmed by the presence of the characteristic doublet resonances in the ^{1}H and ^{19}F NMR spectra at δ 8.63 and δ -234.8 respectively with 81 Hz geminal coupling. Synthesis of a pure product enabled the carbon resonances of the vinylidene ligand to be identified as two downfield signals in the ^{13}C{^{1}H} NMR spectrum. The α-carbon was observed as a doublet resonance at δ 368.0 with 39 Hz C-F coupling and the β-carbon a doublet resonance at δ 178.7 with 282 Hz C-F coupling.

2.4.2 Synthesis of the Fluoroalkynyl Complex, [28b]

It was envisaged that the addition of a strong base to **[30a]**$^+$ would enable the formation and isolation of the fluoro-alkynyl complex **[28b]**. Indeed, addition of lithium *bis*(trimethylsilyl)amide at -78 °C resulted in the isolation of a yellow solid which was identified as **[28b]** by NMR spectroscopy, albeit in low yield (19 %, Scheme 116). The fluorine substituent was observed as a triplet at δ -186.9 ppm (t, $^4J_{FP}$ = 5 Hz) in the ^{19}F NMR spectrum, coupling to the two phosphorus nuclei. The ^{31}P{^{1}H} NMR spectrum displayed a matching doublet resonance at δ 50.9 with 5 Hz coupling to fluorine; the chemical shift is indicative of a [Ru(η^5-C$_5$Me$_5$)(PPh$_3$)$_2$(C≡C-R)] complex.[236, 237] The β-carbon was observed by a ^{13}C-^{19}F HSQC NMR experiment at δ 94.2 with 271 Hz coupling to fluorine. The α-carbon could not be identified with confidence by either 1D or 2D carbon NMR experiments. Attempts to crystallise **[28b]** from pentane at -23 °C were unsuccessful.

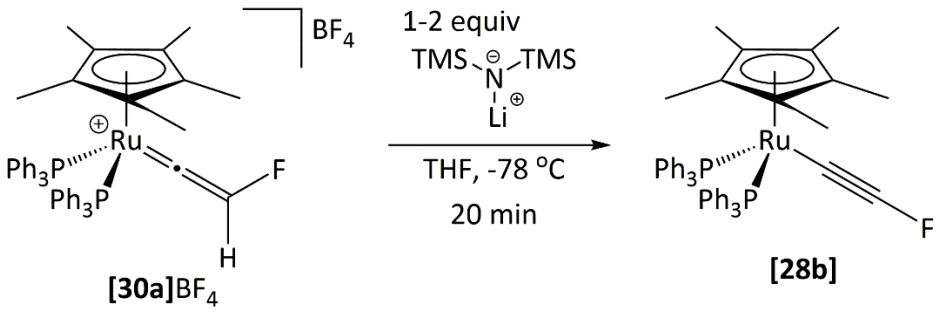

Scheme 116: Cold addition of lithium *bis*(trimethylsilyl)amide to [30a]BF$_4$ afforded the fluoroalkynyl complex [28b] as a minor product.

Although addition of base at -78 °C afforded the desired product, the major product was identified as the ortho-metallated phosphonium fluorovinyl complex **[48]**BF$_4$, formed through attack of the vinylidene ligand in **[30a]**BF$_4$ by triphenylphosphine (discussed in section 2.4.4). Separation of **[28b]** from **[48]**BF$_4$ was achieved by extraction of **[28b]** with pentane. However, separation of **[28b]** from HMDS and residual lithium HMDS was challenged by similar solubility and the decomposition of **[28b]** upon silica and alumina columns.

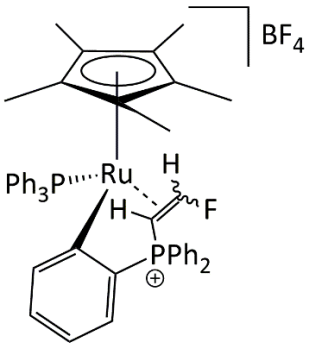

[48]BF_4

Figure 7: *Ortho*-metallated phosphonium fluorovinyl complex [48]BF_4.

Upon standing in CD_2Cl_2 for 16 hours, **[28b]** undergoes protonation to form **[30a]**BF_4, and after 1 week no alkynyl complex remained, only **[30a]**BF_4 and **[48]**BF_4. Nevertheless, **[28b]** is stable towards the oligomerisation pathway observed frequently with organic fluoroalkynes (Scheme 108).

The initial attempts at deprotonating **[30a]**BF_4 with the weaker base, 1,8-*bis*(dimethylamino)naphthalene (proton sponge, pK_a(THF)[238] = 11.1), did not afford **[28b]**. The decreased acidity of the vinylidene proton in **[30a]**BF_4 compared to **[29]**BF_4 can be rationalised by the electron-donating mesomeric effect of fluorine. Use of ^{n}BuLi was avoided due to the possible nucleophilicity of the butyl anion, and instead a sterically hindered amide base was chosen. Lithium *bis*(trimethylsilyl)amide (Li-HMDS) was chosen over lithium diisopropylamide for ease of storage and handling. Room temperature addition of Li-HMDS afforded **[28b]**, however, formal loss of 'F^+' was observed in addition to the formation of **[48]**BF_4.

2.4.3 Reactivity of [28b] with a Latent Source of 'F+'

To assess the reactivity of **[28b]** compared to the protio-analogue, **[28a]**, towards an electrophile, the reactivity of **[28b]** towards a latent source of 'F+' was investigated. The addition of NFSI to a d^6-benzene, or tetrahydrofuran, solution of **[28b]** at -78 °C afforded the expected difluorovinylidene complex, **[30b]**NSI, as the major product (Scheme 117a). Additional organic and organometallic by-products were also observed and are likely formed due to the presence of HMDS and/or unreacted lithium HMDS contained in the samples of **[28b]**. By-products that were identified by MS were **[48]**NSI and fluorocarbenes, **[49]**NSI and **[50]**NSI (Scheme 117b).

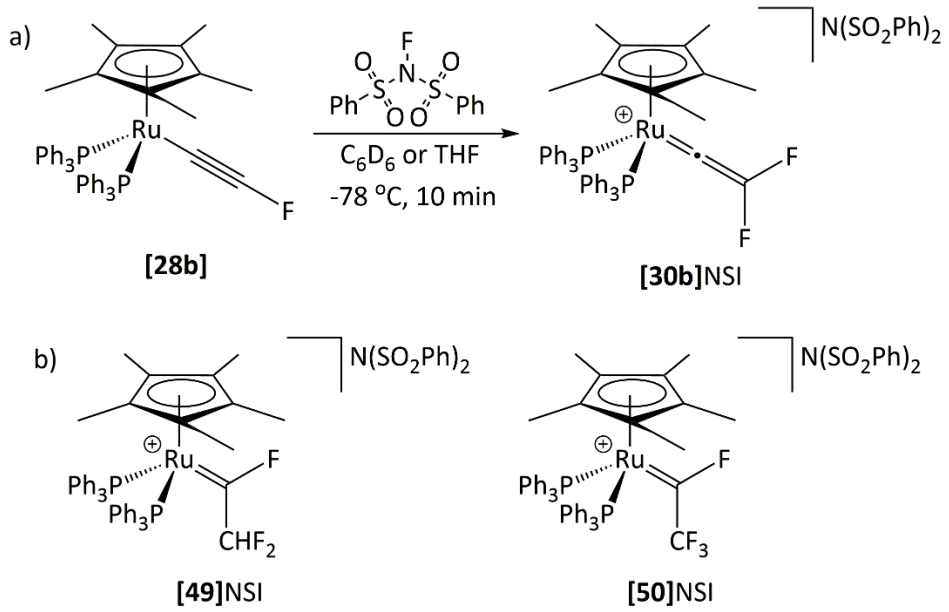

Scheme 117: a) Cold addition of NFSI to [28b] afforded [30b]NSI in a mixture of products; b) other products identified as fluorocarbene [58]NSI and [30a]NSI.

Despite the number of by-products, the difluoro-vinylidene complex **[30b]**BF_4 was identified by singlet resonances in the $^{31}P\{^1H\}$ and ^{19}F NMR spectra at δ 49.5 and -135.2 respectively. The ESI-mass spectrum revealed a species with a m/z of 823.1996 corresponding to the m/z of **[30b]**$^+$.

The initial attempt at fluorination with NFSI, conducted at room temperature in THF, resulted in complete protonation of **[28b]** back to **[29]**NSI and again demonstrated the need of cold conditions to supress protonation. Full characterisation of **[30b]**NSI was not achieved, or pursued further, due to the low yield and purity of the previous synthetic step. Instead, the use of an alternative metal fragment was investigated to overcome the synthetic challenges encountered with **[28b]** and subsequently **[30b]**NSI.

2.4.4 Identification and Formation of *Ortho*-Metallated Phosphonium Fluorovinyl Complex, [48]$^+$

The addition of lithium HMDS to a tetrahydrofuran solution of **[30a]**BF_4 at -78 °C resulted in the formation of **[48]**BF_4 as the major product (Scheme 116 and Figure 7). Alternatively, **[48]**BF_4 was formed by decomposition of **[30a]**BF_4 upon standing in a CD_2Cl_2 solution for at least one week. Complex **[48]**BF_4 was identified by the NMR spectroscopic parameters in Figure 8 and the presence of a species with the same m/z as **[30a]**BF_4 in the mass spectrum.

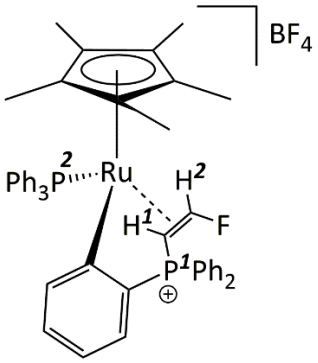

***Z*-[48]**BF_4

H^1
δ 2.80 (app. dtd, $^3J_{HF}$ = 21.5 Hz, $^2J_{HP}$ + $^3J_{HH}$ = 5.6 Hz, $^3J_{HP}$ = 2.2 Hz)

H^2
δ 5.99 (dddd, $^2J_{HF}$= 69.0 Hz, $^3J_{HP}$ = 23.1 Hz, $^3J_{HP}$ = 8.1 Hz, $^3J_{HH}$ = 5.6 Hz)

F
δ -164.1 (ddd, $^2J_{HF}$ = 69.1 Hz, $^3J_{HF}$ = 21.5 Hz, $^3J_{PF}$ =13.0 Hz)

P^1
δ 42.7 (dd, $^3J_{FP}$ = 12.8 Hz, $^3J_{PP}$ = 3.9 Hz)

P^2
δ 56.5 (d, $^3J_{PP}$ = 3.9 Hz)

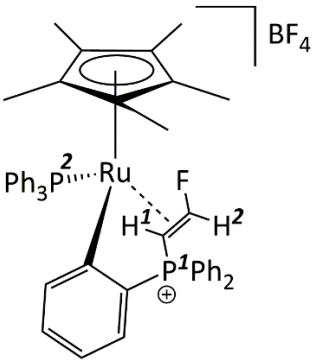

***E*-[48]**BF_4

H^1
δ 1.92 (dd, $^3J_{HF}$ = 12.6 Hz, $^3J_{HH}$ = 6.4 Hz)

H^2
δ 6.37 (dddd, $^2J_{HF}$ = 69.2 Hz, $^3J_{HP}$ = 11.3 Hz, $^3J_{HH}$ = 6.3 Hz, $^3J_{HP}$ = 1.9 Hz)

F
δ -165.12 (app. td, $^2J_{HF}$+$^3J_{PF}$ = 69.3 Hz, $^3J_{HH}$ = 12.2 Hz)

P^1
δ 48.7 (dd, $^3J_{FP}$ = 69.9 Hz, $^3J_{PP}$ = 4.9 Hz)

P^2
δ 41.3 (d, $^3J_{PP}$=4.9 Hz)

Figure 8: *E*- and *Z*- isomers of [48]BF_4 with accompanying NMR spectroscopic data.

The $^{31}P\{^{1}H\}$ NMR spectrum consisted of two pairs of mutually coupled environments. The first pair was observed as a doublet resonance at δ 41.3 ($^{3}J_{PP}$ = 5 Hz) coupling to a doublet of doublets resonance at δ 48.7 (showing an additional coupling of 70 Hz). The second pair of mutually coupled resonances was observed as a doublet resonance at δ 56.5 (4 Hz) coupling to a doublet of doublets resonance at δ 42.7 (with an additional doublet coupling of 12.8 Hz). The ^{19}F NMR spectrum consisted of two fluorine environments. The first resonance appears as an apparent triplet of doublets at δ -165.1 with 69 Hz apparent triplet coupling to one phosphorus and one proton environment and 5 Hz doublet coupling to another proton environment. The second signal was observed as a doublet of doublets of doublets resonance at δ -164.1 exhibiting doublet coupling of 13 Hz to phosphorus and two doublet couplings of 69 and 23 Hz to hydrogen. These data suggest the presence of a single organometallic species with inequivalent phosphine ligands, which forms two possible isomers where the fluorine and phosphorus nuclei are either mutually *trans* or *cis* to one another. The size of coupling indicates that the fluorine resonance at δ -165.1 is *trans* to the phosphorus environment at δ 48.7, while the fluorine resonance at δ -164.1 is *cis* to the phosphorus environment at δ 42.7 (Figure 8). The data are consistent with phosphine addition to the vinylidene ligand of **[30a]**BF_4 to form a fluorovinylphosphonium complex similar to **[18]**$^{+}$ and **[55a]**PF_6 reported by Milner[223] and Onitsuka *et al*.[239] respectively. The ^{1}H NMR spectrum revealed two pairs of mutually coupled proton resonances. One pair consisted of a doublet of doublets resonance at δ 1.92 ($^{3}J_{HF}$ = 12.6 Hz, $^{3}J_{HH}$ = 6.4 Hz) with 6.4 Hz *trans* coupling to the dddd resonance at δ 6.37 ($^{2}J_{HF}$ = 69.2 Hz, $^{3}J_{HP}$ = 11.3 Hz, $^{3}J_{HH}$ = 6.3 Hz, $^{3}J_{HP}$ = 1.9 Hz) corresponding to *E*-**[48]**BF_4. The other pair of proton resonances were observed as an apparent dtd at δ 2.80 ($^{3}J_{HF}$ = 21.5 Hz, $^{2}J_{HP}$ + $^{3}J_{HH}$ = 5.6 Hz, $^{3}J_{HP}$ = 2.2 Hz) with *cis* coupling of 5.6 Hz to the dddd resonance at δ 5.99 ($^{2}J_{HF}$= 69.0 Hz, $^{3}J_{HP}$ = 23.1 Hz, $^{3}J_{HP}$ = 8.1 Hz, $^{3}J_{HH}$ = 5.6 Hz) corresponding to *Z*-**[48]**BF_4. However, attempts to crystallise **[48]**$^{+}$ as either the tetrafluoroborate salt or the hexafluorophosphate salt failed yield crystals.

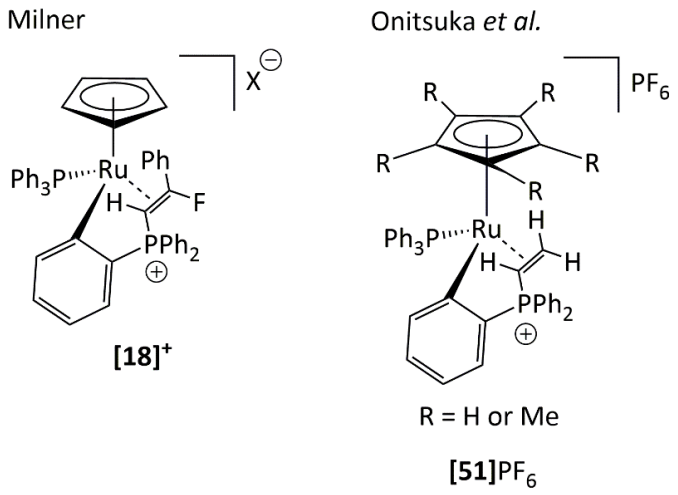

[18]$^+$ **[51]PF_6**

Figure 9: Literature examples of *ortho*-metallated phosphonium vinyl complexes, [18]$^+$ and [55a]PF_6.

Formation of **[48]**$^+$ is believed to proceed by the mechanism proposed by Onitsuka *et al*.[239] (Scheme 118), in which the vinylidene undergoes nucleophilic attack by free triphenylphosphine at the α-carbon affording the vinyl intermediate **[52]**$^+$. Dissociation of a metal-bound triphenylphosphine ligand generates a co-ordinately unsaturated metal centre enabling *ortho*-metallation of one of the alkenyl-phosphine's phenyl groups to afford ruthenium(IV) hydride intermediate **[53]**$^+$. Subsequent reductive elimination, or hydride insertion, affords **[48]**BF_4.

It is also possible for the mechanism to proceed by migratory insertion of a metal bound-phosphine into the ruthenium-carbon bond of **[30a]**$^+$ producing a co-ordinately unsaturated metal centre through which *ortho*-metallation affords **[53]**$^+$.[239]

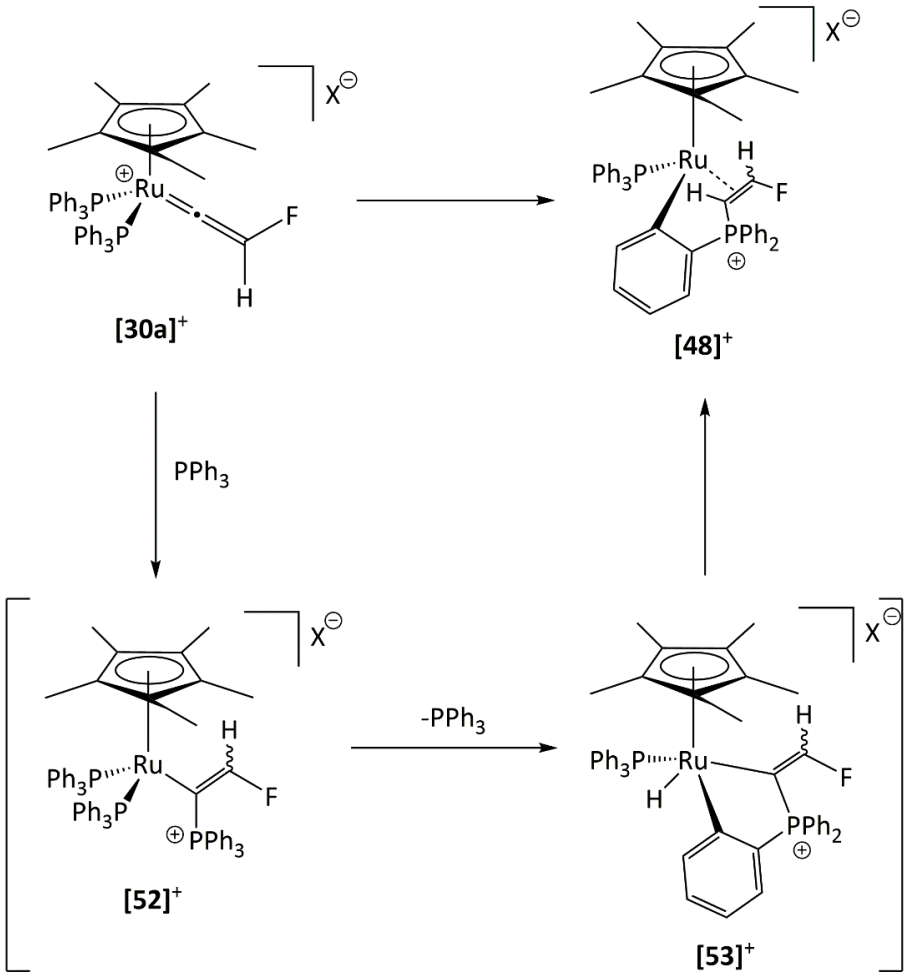

Scheme 118: Proposed mechanism for formation of [48]$^+$ *via* phosphonium vinyl [52]$^+$ and *ortho*-metallated ruthenium phosphonium vinyl [53]$^+$.

Despite *E*-**[48]**$^+$ being -24 kJ mol^{-1} (ΔH_{298}, or ΔG_{298} = -29 kJ mol^{-1}) lower in energy than *Z*-**[48]**$^+$ at the (RI-)PBE0/def2-TZVPP//BP86/SV(P) level, there is no preference for the formation of the more thermodynamically stable isomer. This indicates that there is no interconversion between isomers. In contrast, only the thermodynamically favoured *E*- isomer of **[18]**$^+$ was observed experimentally.[223] Similar to **[48]**$^+$, the isomers of **[18]**$^+$ are different by only 26 kJ mol^{-1} at the (RI-)PBE0-D3/def2-TZVPP//BP86/SV(P) level. The observation of a single isomer for **[18]**$^+$ can be rationalised by the steric difference between the phenyl and fluorine substituents of the vinylidene ligand. Phosphine attack would be expected to form the most sterically unhindered alkenyl intermediate, i.e. the phenyl group *trans*- to the phosphine. The steric discrimination between proton and fluorine is comparatively small with respect to fluorine and phenyl substituents, resulting in no clear preference for attack of the phosphine, hence mixture of isomers. Alternatively, under the thermal conditions used by Milner (50 °C for 16 hours),[223] the rotational barrier for isomerisation of the vinyl group could be accessible enabling isomerisation to give the thermodynamic product from a mixture of isomers.

2.5 Fluorination of [Ru(η^5-C$_5$Me$_5$)(dppe)(-C≡C-R] Complexes

Due to the loss of phosphine from the coordination sphere of the metal, or migration of phosphine, being an essential step in the formation of **[48]**$^+$, it was expected that a bidentate phosphine ligand would inhibit this pathway due to the chelate effect. Consequently, the two triphenylphosphine ligands were replaced with the 1,2-*bis*(diphenylphosphino)ethane (dppe) ligand.

2.5.1 Synthesis of Fluorovinylidene Complex, [54a]$^+$

The corresponding dppe alkynyl complex **[55a]** was subjected to fluorination at low temperature in order to supress any competing protonation, as observed for the fluorination of **[28a]** at room temperature.

The addition of NFSI to a toluene solution of **[55a]** at -78 °C resulted in a rapid colour change to the characteristic green colour of a fluoro-vinylidene complex (Scheme 119). The ^{19}F NMR spectrum of **[54a]**NSI in CD_2Cl_2 displayed a new doublet resonance at δ -235.8 with 80 Hz coupling to the geminal proton, matching the $^2J_{HF}$ coupling observed in **[30a]**$^+$. The ^{1}H NMR spectrum of **[54a]**NSI displayed the mutually coupling doublet resonance at δ 7.32 and was assigned to the proton-substituent of the vinylidene ligand. A new singlet resonance at δ 1.59 corresponding to the protons of the Cp* ligand and a set of multiplets at δ 2.70 and 2.94 corresponding to the protons of the backbone of dppe were also observed. These signals integrated to 15, 2 and 2 hydrogens respectively, with the resonance at δ 7.32 integrated to one. The ^{31}P{^{1}H} NMR spectrum displayed a new singlet resonance δ 76.4, which is indicative of a cationic [Ru(η^5-C$_5$Me$_5$)(dppe)] fragment.[240, 241] These data, along with the mass spectrum which displayed a species with the correct m/z for **[54a]**$^+$, are consistent with the formation of **[54a]**NSI (Scheme 119). Upon standing in solution, there was no evidence for attack of the vinylidene ligand by the phosphine ligand or the formation of the analogous *ortho*-metallated fluorovinyl phosphonium complex similar to **[48]**$^+$.

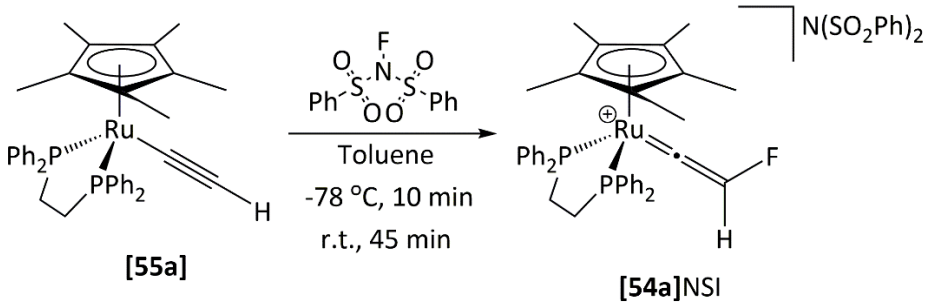

Scheme 119: Fluorination of [55a] afforded the expected fluorovinylidene [54a]NSI, with no evidence of an analogous ortho-metallated fluorovinyl phosphonium complex being formed.

Crystallisation of **[54a]**$^+$ as the hexafluorophosphate salt yielded two polymorphs, one green (Figure 10) and the other orange with **[54a]**PF_6 co-crystallised with dichloromethane. Similar to **[30a]PF_6**, both crystals of **[54a]**PF_6 consisted of a mixture of two vinylidene rotamers. The green polymorph consisted of a rotamer ratio (A:B) of 67:33 and the orange polymorph a ratio of 85:15.

In both rotamers, the vinylidene ligand is orientated such that the substituent in closest proximity to the dppe backbone is positioned slightly towards the pentamethylcyclopentadienyl ring, presumably to minimise steric interactions. The green crystalline form consisted mainly of rotamer A, whereby the fluorine (F1A) is orientated at an angle towards the Cp* ligand (Figure 10), while the orange crystal was mainly populated by the rotamer in which the fluorine substituent is pointed away from the Cp* ligand. The difference in the C1-C2-F1 bond angle is not statistically significant, however, the difference between the C2-F1 bond length is, with the C-F bond length being longer in rotamer A (A: 1.329(5) Å; B: 1.218(7) Å). The difference in bond length could arise from a change in orbital overlap. The smallest P-Ru---C_β-F torsion angle for rotamer A (major) of the green crystalline form is measured at 68.3° while smallest torsion angle for the minor rotamer (B) is measured at 31.3°. In the orange crystalline form, the smallest P-Ru---C_β-F torsion angle for rotamer A (minor) and B (major) is measured at 69.7° and 40.6° respectively. In both crystalline forms the torsion angle of the CHF group with respect to the metal-ligand framework is similar.

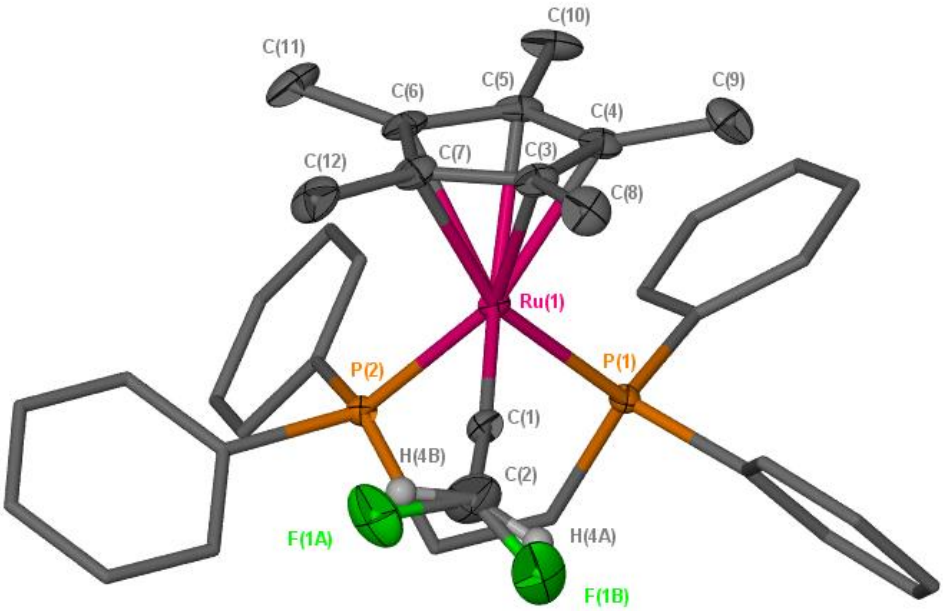

Figure 10: Crystal structure of [54a]PF_6 in the green crystalline form. Hydrogens and counterion omitted for clarity; thermal ellipsoids are shown with 50% probability level. Rotamer A (F(1A) and H(4A)) dominant (67:33); hydrogens fixed at 1.2 Uiso. Selected bond lengths / Å: Ru1-C1 = 1.836(3); C1-C2 = 1.300(5); C2-F1A = 1.329(5); C2-F1B = 1.218(7); Ru1-P1 = 2.3161(8); Ru1-P2 = 2.2999(8); Ru1-C(η^5-C_5Me_5) = 2.262 average. Selected bond angles / ° : Ru1-C1-C2 = 169.3(3); C1-C2-F1A = 126.7(4); C1-C2-F1B = 130.3(5); P1-Ru1-P2 = 81.78(3).

The observation of rotamers could be rationalised by the poor steric discrimination between the hydrogen and fluorine substituents of the vinylidene ligand. This is exaggerated by the compressed P1-Ru-P2 (96.57(2)° to 81.78(3)°) and widened P-Ru-C_α bond angles (89.69(7)° and 91.24(7)° to 84.62(11)° and 93.21°) upon substitution of PPh_3 with dppe respectively, allowing each substituent to reside in either position.

The significant difference in visual appearance for the two crystalline forms could be rationalised by the same argument made for the crystalline appearances of **[15b]**PF_6, whereby the low energy HOMO→LUMO transition for the orange form undergoes a bathochromic shift into the near IR (> 700 nm), which is outside the visual range of wavelengths distinguishable to human eye.[223]

Solution phase UV-Vis spectroscopy of **[54a]**PF_6 in dichloromethane revealed an absorption band at λ_{max}= 601 nm with a molar absorption coefficient of ε = 5.5 mol^{-1} m^2. The magnitude of the molar absorption coefficient is indicative of a d-d spin allowed transition. Time-dependent density functional theory (TD-DFT) predicts that the band corresponds to the HOMO→LUMO transition (Figure 11). The bathochromic shift is induced by the

incorporation of a π-donor, resulting in the HOMO being increased in energy, reducing the energy gap between the ground state HOMO and excited state LUMO.

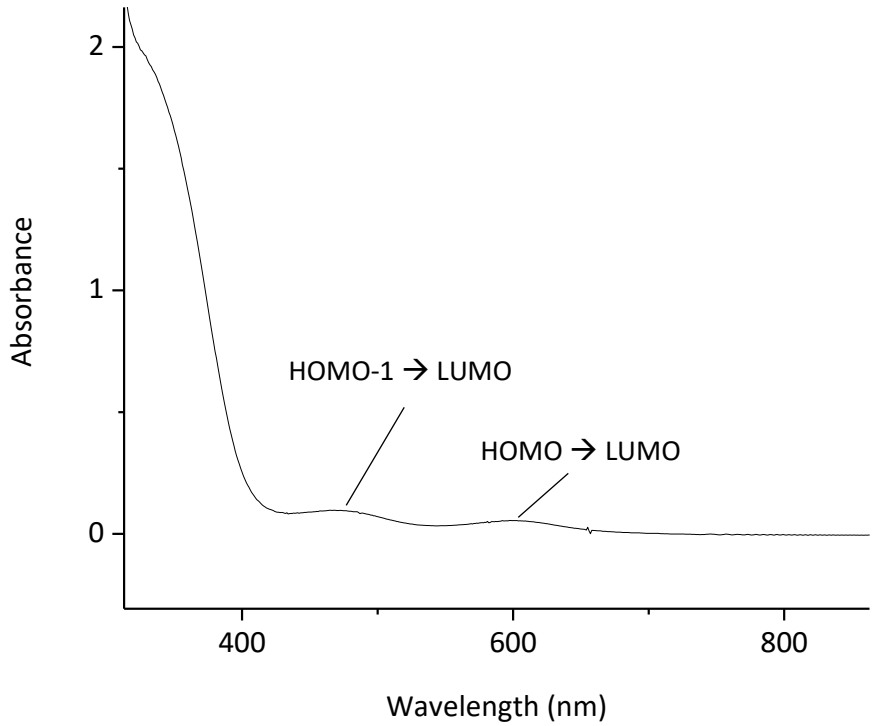

Figure 11: UV-Vis absorption spectrum for [54a]PF_6 at 1 mmol dm^{-3} in dichloromethane with 1 cm pathlength.

The HOMO consists of a π-bonding interaction between the two vinylidene carbons, which are themselves π-antibonding with respect to ruthenium and fluorine (Figure 12). The LUMO appears similar to the HOMO in the sense that the ruthenium is antibonding with respect to the vinylidene α-carbon. There is a possible weak π-bonding interaction between the two vinylidene carbons and a weak antibonding interaction with fluorine. The magnitude of the molar absorption coefficient is indicative of a d-d spin allowed transition.

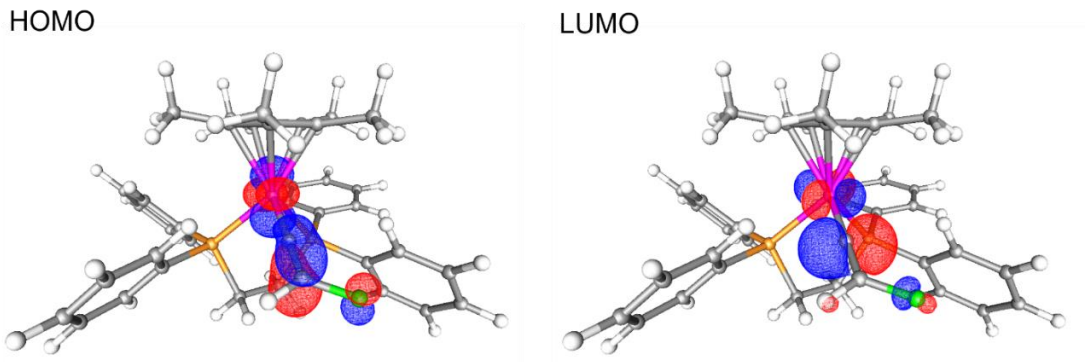

Figure 12: Predicted HOMO and LUMO orbitals of [54a]$^+$; both the HOMO and LUMO consist of orbitals on the metal and vinylidene ligand. The p-orbital of fluorine is antibonding with respect to the π-system of the C-C fragment. The C-C π-systemis itself π-antibonding with respect to the metal d-orbital.

A second absorption band at λ = 465 nm was observed, similar to that observed for **[15b]**$^+$. TD-DFT predicts the band is dominated by the HOMO-1 → LUMO transition. The HOMO-1 orbital (Figure 13) resides predominantly on the symmetry adapted dorbital of ruthenium and the π-system of the Cp* ring, and to a lesser extent the vinylidene ligand.

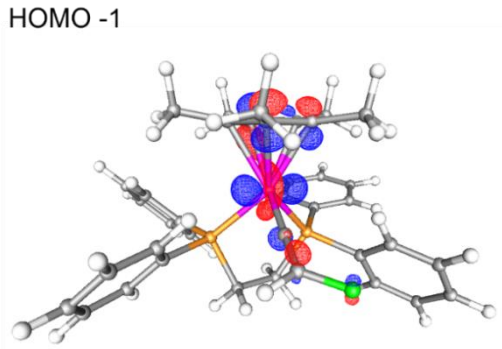

Figure 13: Predicted HOMO-1 orbital of [54a]$^+$ based predominantly on the ruthenium and Cp* ligand, and to a lesser extent the vinylidene ligand .

Dissolution of the orange and green crystals resulted in the formation of a green solution with identical NMR spectroscopic data to the reaction mixture, suggesting the orange and green crystals interconvert to the same structure in solution.

The calculated HOMO of **[54a]**$^+$ is very similar in appearance to the classical representation of the HOMO of a metal vinylidene fragment (Chapter 1, Scheme 76) except there is an additional antibonding interaction between the fluorine substituent and the C=C π-system. In contrast, the LUMO of fluorovinylidene complexes (e.g. **[54a]**$^+$) differ significantly to that of the classical LUMO representation. Instead of the there being no interaction between the C_α and C_β atoms of the vinylidene ligand, as in the classical representation, the presence of a

strongly polarising fluorine substituent results in the formation of a weak π-bonding interaction between C_α and C_β, and a weak antibonding interaction between the C_β atom and the fluorine substituent. This suggests that the generic MO diagram (Chapter 1, Scheme 76) for metal vinylidene complexes is not entirely suitable for describing fluorovinylidene ligands.

2.5.2 Formation of Fluoroalkynyl Complex [55b]

The formation of the first metal fluoro-alkynyl complex, **[28b]**, was only synthesised as a minor product, even upon addition of lithium *bis*(trimethylsilyl)amide to **[30a]**BF_4 at -78 ˚C (Scheme 116). The addition of lithium *bis*(trimethylsilyl)amide to a tetrahydrofuran solution of **[54a]**NSI at -78 ˚C resulted in the rapid formation of a yellow solution. Extraction of the yellow residue with pentane yielded **[55b]** as a yellow solid upon removal of the solvent in less than 19 % yield (Scheme 120). The ^{1}H NMR spectrum of **[55b]** in C_6D_6 contained two multiplet signals at δ 1.86 and 2.58 ppm which correspond to the protons of the dppe backbone. A triplet resonance at 1.63 ppm with 1.4 Hz coupling to phosphorus corresponds to the methyl groups of the Cp* ligand. The ^{19}F NMR spectrum displayed a triplet resonance at δ -189.4 with 5 Hz coupling to the doublet resonance at δ 81.9 in the $^{31}P\{^1H\}$ NMR spectrum. The multiplicity of the mutually coupled resonances indicates that a single fluorine substituent is present along with two equivalent phosphorus environments, consistent with the formation of **[55b]**. The LIFDI mass spectrum revealed the formation of a species with the correct m/z for **[55b]**. Similar to **[28b]**, separation of **[55b]** from HMDS and any residual Li HMDS could not be achieved through column chromatography due to protonation and decomposition. Separation could only be achieved through crystal picking.

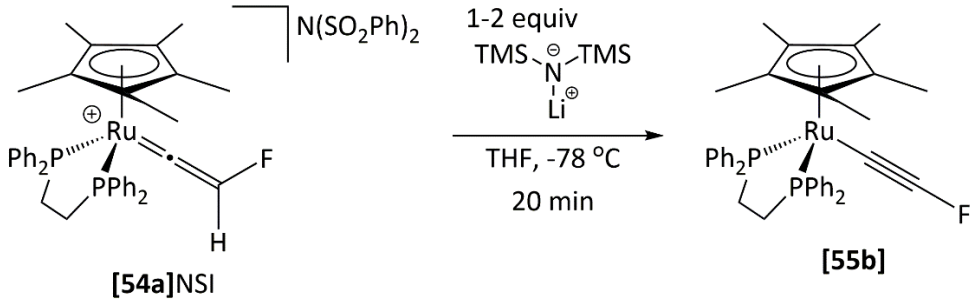

Scheme 120: Deprotonation of [54a]NSI using excess lithium HMDS at -78 °C yielded [55b].

The structure of **[55b]** was confirmed by X-ray crystallography from yellow crystals grown by slow evaporation of a pentane solution of **[55b]** (Figure 14). The alkynyl ligand shows distortion away from the ideal geometry of 180˚ (Ru-C≡C, 171.8(3)˚; C≡C-F, 177.2(4)˚), which

is more pronounced than the distortion of the alkynyl ligand in **[55a]**. The C-F bond length, 1.324(4) Å, is in good agreement with the calculated gas-phase value, 1.31 Å. The C-F bond length is shorter than the typical range of C-F bond length, 1.35-1.43 Å,[242] as expected for a fluorine bonded to a *sp* hybridised carbon with high *s* character, leading to greater orbital overlap.

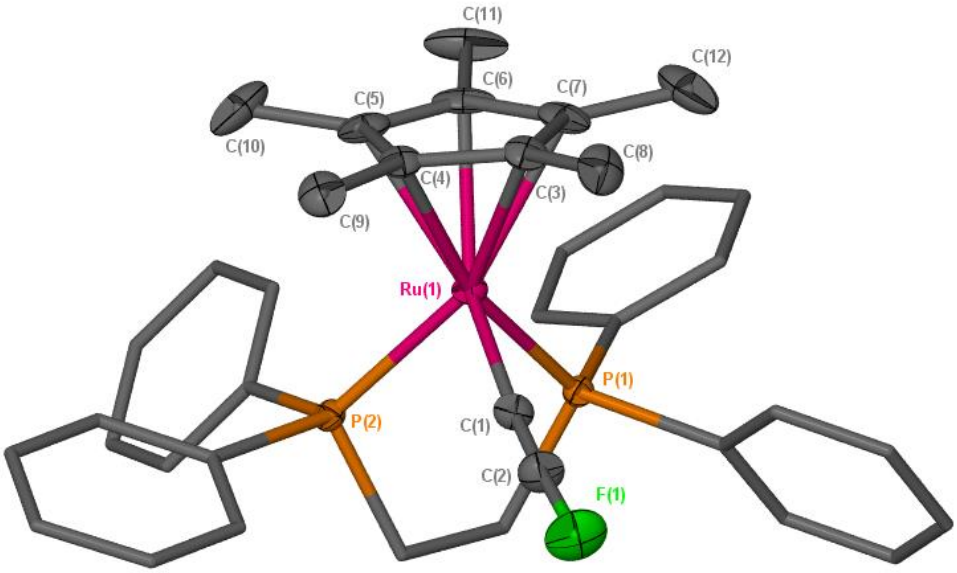

Figure 14: Crystal structure of [55b]; hydrogens were omitted for clarity and thermal ellipsoids displayed at 50 % probability level. Selected bond lengths / Å: Ru1-C1 = 2.036(3); C1-C2 = 1.187(4), C2-F1 = 1.324(4); Ru1-P1 = 2.2677(7); Ru1-P2 = 2.2570(7); Ru1-C(η^5-C_5Me_5) = 2.2408 average. Selected bond angles / ° : Ru1-C1-C2 = 171.8(3); C1-C2-F1 = 177.2(4); P1-Ru1-P2 = 82.56(3).

The UV-Vis spectrum of **[55b]** in THF at 1 mM (Figure 15) displays a shoulder at 396 nm and closely matches the spectrum observed for **[55a]**. TD-DFT predicts the absorption band is dominated by the HOMO → LUMO transition. The HOMO (Figure 16) is based predominantly on the metal and alkynyl ligand, consisting of a π-bonding interaction between the p-orbitals of the carbons. The HOMO displays π-antibonding interactions between the metal-centred orbital and the π-system of the alkynyl ligand and between the fluorine lone pair and the π-system of the alkynyl ligand. The LUMO is based on the symmetry-adapted metal d-orbital and partially on the rear facing phenyl groups of the dppe ligand. The transition appears a mixture of inter-metal, ligand-to-metal, and ligand-to-ligand charge transfer.

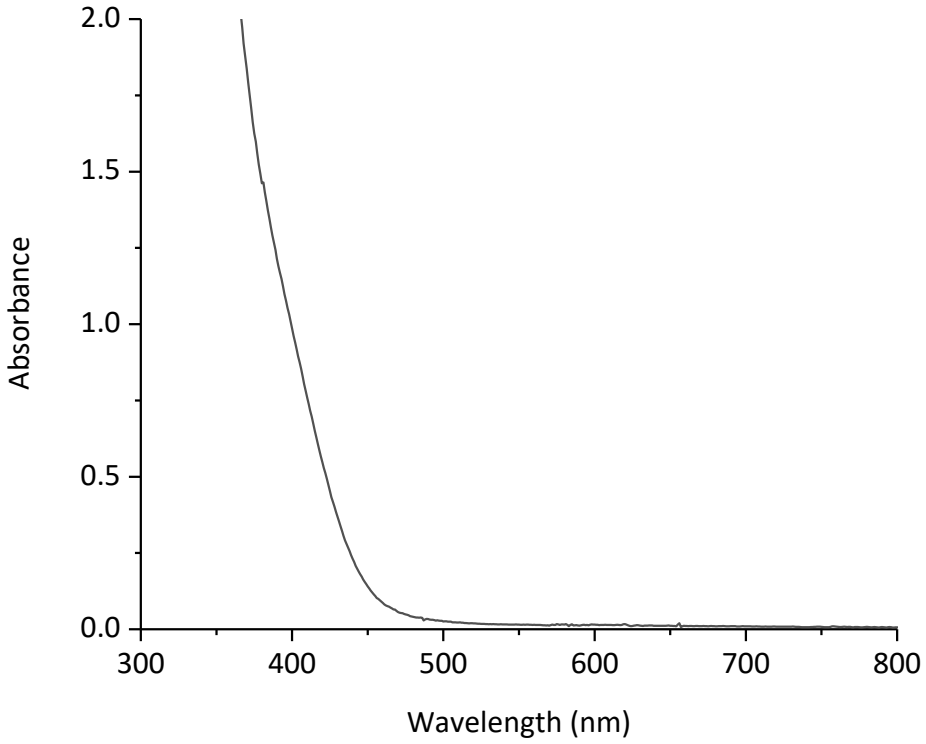

Figure 15: UV-Vis spectrum of [55b] at 1 mM in THF displaying.

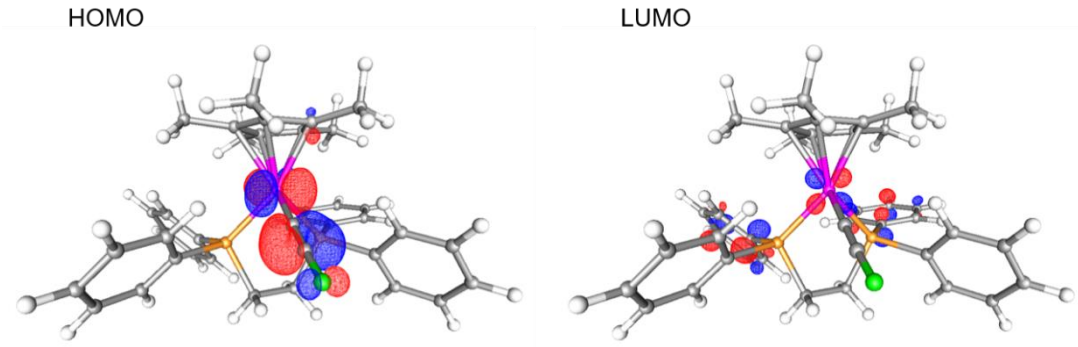

Figure 16: Calculated HOMO and LUMO for [55b] at (RI-)BP86/SV(P)//PBE0/def2-TZVPP.

2.5.3 Reactivity of the Fluoroalkynyl Complex [55b] with a Latent Source of 'F⁺'

The isolation of **[55b]** enabled the reactivity of fluoroalkynyl complexes to be investigated with an electrophile. In the same manner as before, the addition of NFSI at -78 °C to **[55b]** led to the rapid formation of a green solution, which slowly darkened upon warming to room temperature to afford **[54b]**NSI as a red/brown solution (Scheme 121). The ^{19}F NMR spectrum of **[54b]**NSI displayed a new singlet resonance at δ -134.0, while the $^{31}P\{^{1}H\}$ NMR spectrum displayed a singlet resonance at δ 75.2, indicative of a cationic species.[241] The ^{1}H NMR spectrum consisted of a singlet resonance at δ 1.56, corresponding to the methyl groups of the Cp* ring. Two multiplet resonances at δ 2.72 and 2.82 correspond to the protons of the dppe backbone. Two deshielded carbons environments, observed at δ 366.7 and δ 231.3, in the ^{13}C NMR spectrum were assigned to the α- and β-carbons of the vinylidene ligand respectively. These are consistent with the deshielded chemical shifts observed for **[54a]⁺**. The mass spectrum displayed a m/z of 697.1545 corresponding to the m/z of the expected difluoro-vinylidene complex. The structure of **[54b]**NSI was confirmed by X-ray crystallography (Figure 17).

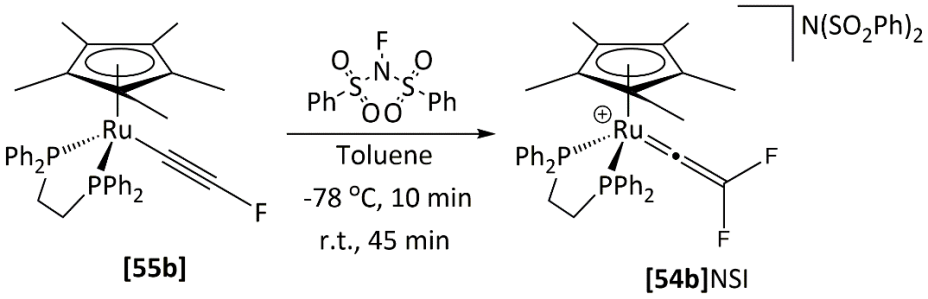

[55b] **[54b]**NSI

Scheme 121: Fluorination of [55b] with NFSI at -78 °C afforded [54b]NSI as dark red/purple solid.

The hexafluorophosphate salt of **[54b]⁺**, formed by ion metathesis, crystallised as purple plates from a dichloromethane: pentane solvent system (Figure 17). Despite increased steric effects and lone pair repulsion, the incorporation of a second fluorine substituent results in further compression of the R-C-R bond angle (where R = F or H), from 119.3° to 116.7(4)° to 107.9(2)˚ for **[56]**PF_6, **[54a]**PF_6, and **[54b]**PF_6 respectively. The torsion angles for the CF_2 group of the vinylidene ligand with respect to metal-ligand framework (P_1-Ru---C_β-F_1, 69.2° ; P_2- Ru---C_β-F_2, 39.4°) are similar to those measured for the two crystalline forms of **[54a]**PF_6. Further discussion of the crystallographic data can be found in section 2.7.4.1.

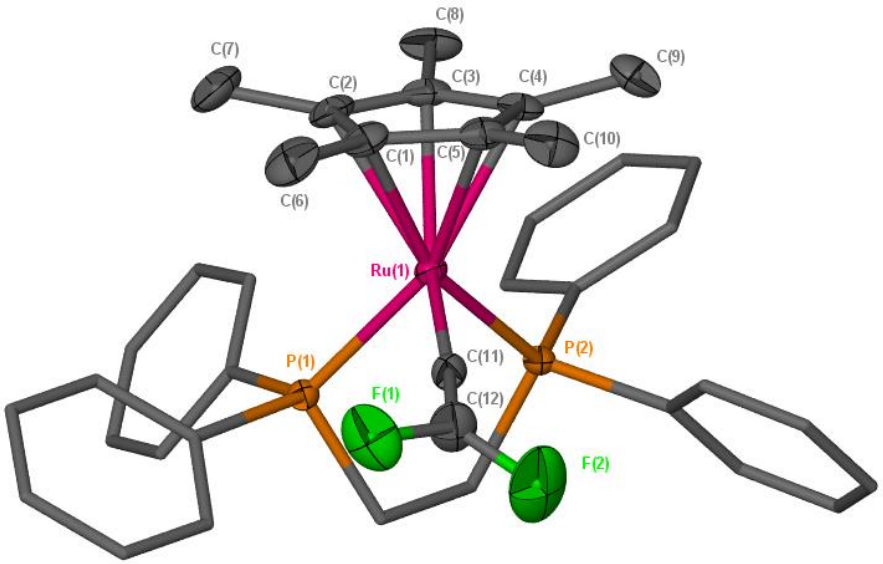

Figure 17: Crystal structure of [54b]PF_6; hydrogens and hexafluorophosphate counterion were omitted for clarity and thermal ellipsoids displayed with 50 % probability level. Selected bond lengths / Å: Ru1-C11 = 1.840(2); C11-C12 = 1.307(4); C12-F1 = 1.340(4); C12-F2 = 1.316(3); Ru1-P1 = 2.3060(6); Ru1-P2 = 2.3277(6); Ru1-C(η^5-C_5Me_5) = 2.272 average. Selected bond angles / ° : Ru1-C11-C12 = 167.3(2); C11-C12-F1 = 126.4(3); C11-C12-F2 = 125.6(3); F1-C12-F2 = 107.9(2); P1-Ru1-P2 = 81.65(2).

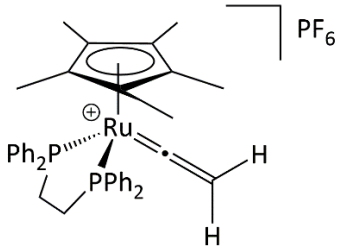

[56]PF_6

The UV-Vis absorption spectrum of **[54b]**NSI in dichloromethane displays a large bathochromic shift in the lowest energy absorption band from 609 nm to 693 nm upon substitution of hydrogen for a second fluorine substituent (Figure 18). TD-DFT predicts this transition also arises from a pure HOMO → LUMO transition, whereby the HOMO and LUMO consist of significant orbital contributions from both the ligand and metal. The HOMO (Figure 19) displays a π-antibonding interaction between the fluorine substituents and the π-system of the vinylidene, which is itself antibonding with respect to the metal. The LUMO displays a weak π-bonding interaction between the carbon atoms of the vinylidene ligand. Two antibonding interactions are predicted between the p-orbitals of the fluorine substituents and the carbon atoms of the vinylidene ligand. The α-carbon is π-antibonding with respect to the metal.

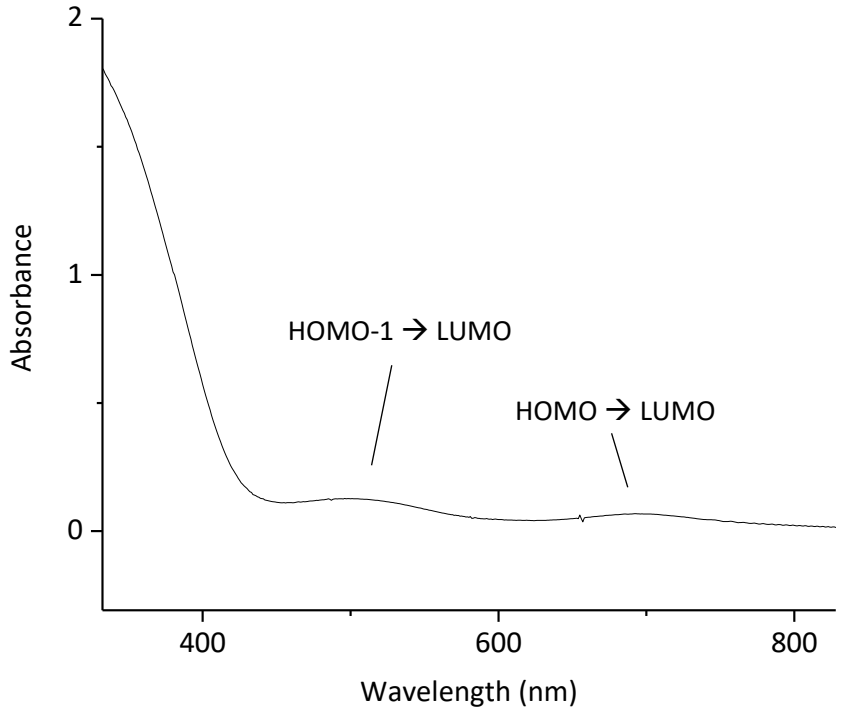

Figure 18: UV-Vis absorption spectrum of [54b]NSI at 1 mmol dm^{-3} concentration in dichloromethane with a pathlength of 1 cm.

An additional band in the UV-Vis spectrum of **[54b]**NSI was observed at 500 nm and is predicted to arise primarily from the HOMO-1 → LUMO transition. The HOMO-1 is dominated by the antibonding interaction between the metal-based orbital and the π-system of the Cp* ligand. A weak π-antibonding interaction is also predicted between the symmetry adapted d-orbital of the metal and the vinylidene ligand, similar to the HOMO-1 predicted for **[54a]**$^{+}$.

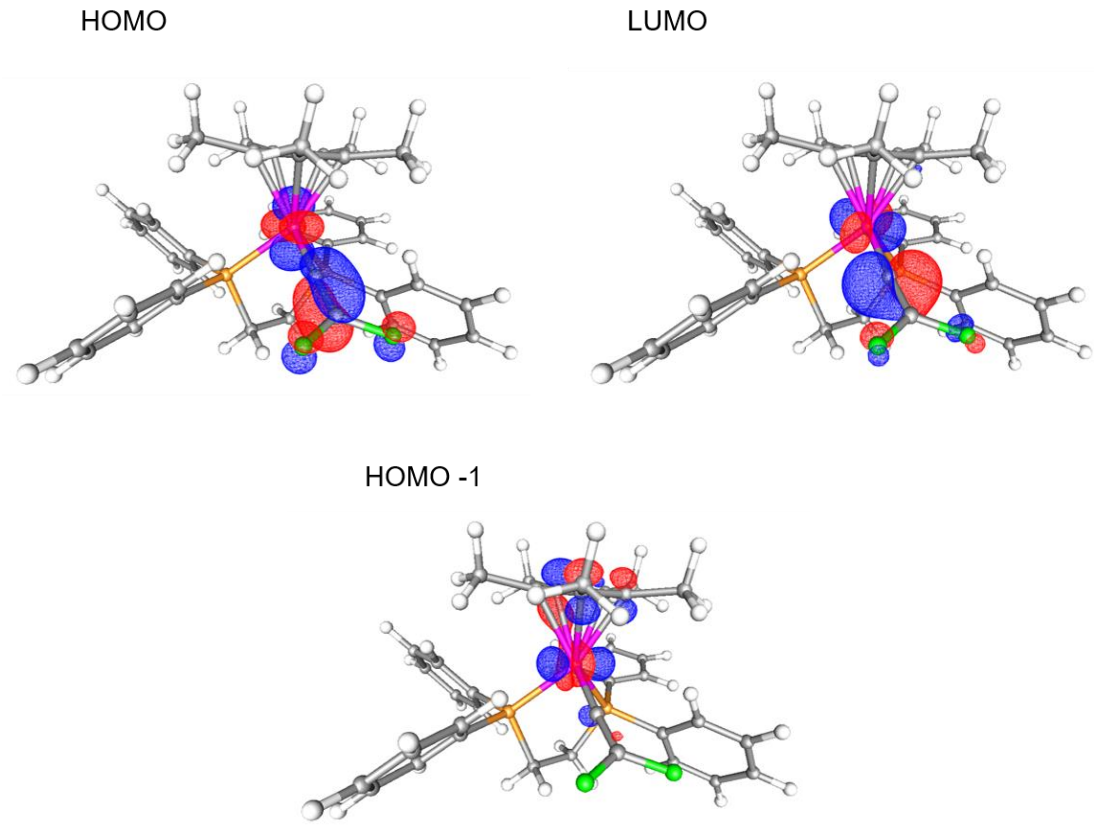

Figure 19: The HOMO-1, HOMO, and LUMO for [54b]$^+$ calculated at the (RI-)BP86/SV(P)//PBE0/def2-TZVPP level.

2.6 Fluorination of [ClRu(dppe)$_2$(-C≡C-R)] Complexes

To demonstrate the wider application of the OSEF-deprotonation strategy, which has successfully afforded ruthenium half-sandwich fluoroalkynyl complexes **[28b]** and **[55b]**, a new metal fragment was sought. The ruthenium *bis*-dppe chloride fragment was identified as a new target to investigate due to the stability afforded by the two bulky bidentate bidentate phosphines.

2.6.1 Synthesis of Fluorovinylidene Complex [58a]$^+$

In addition to the fluorination of half-sandwich alkynyl complexes, the protio-alkynyl complex **[57a]** also underwent fluorination in the presence of Selectfluor (Scheme 122). Addition of Selectfluor to a dichloromethane: acetonitrile solution of **[57a]** at -78 °C resulted in the formation of the desired fluorinated vinylidene **[58a]**BF_4 as a characteristic green solution after 5 minutes, which became paler over 20 minutes.

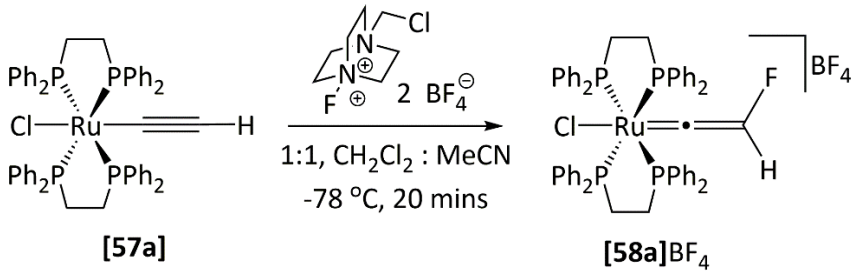

Scheme 122: Addition of Selectfluor to [57a] at -78 °C afforded the fluorovinylidene complex [58a]BF_4.

The ^{19}F NMR spectrum of **[58a]**BF_4 in CD_2Cl_2 displayed a doublet resonance at δ –242.6 with a geminal H-F coupling of 81 Hz (Figure 20). The corresponding proton was observed at δ 6.14 as a doublet of quintets with 2.7 Hz quintet coupling to the four phosphorus nuclei in the ^1H NMR spectrum (Figure 21) and confirmed by a ^1H-^{19}F HMBC experiment (Figure 22). The $^1H\{^{31}P\}$ NMR experiment (Figure 23) simplifies the multiplicity of signals corresponding to protons coupled to phosphorus environments, e.g. the backbone protons and the aromatic *ortho*-protons of the dppe ligands. The β-carbon of the vinylidene ligand was observed at δ 176.5 with doublet C-F coupling of 230 Hz in the $^{13}C\{^1H\}$ NMR spectrum (Figure 25). The α-carbon could not be observed directly in the 1D $^{13}C[^1H\}$ NMR spectrum presumably due to the high multiplicity. However, the α-carbon was observed at δ 382.4 *via* a ^{13}C-^{19}F HSQC NMR experiment (Figure 26). As observed with the other fluorovinylidene complexes reported here and previously,[218] both the α- and β-carbon resonances undergo significant down field shifts compared to the protio-analogue (see 2.7.1.4). The deshielding of the carbon nuclei is

not surprising due to the incorporation of more electronegative atoms, however, the magnitude of deshielding, *ca.* 30 and 70 ppm for the α- and β-carbon respectively compared to the protio-analogue, warrants further investigation.

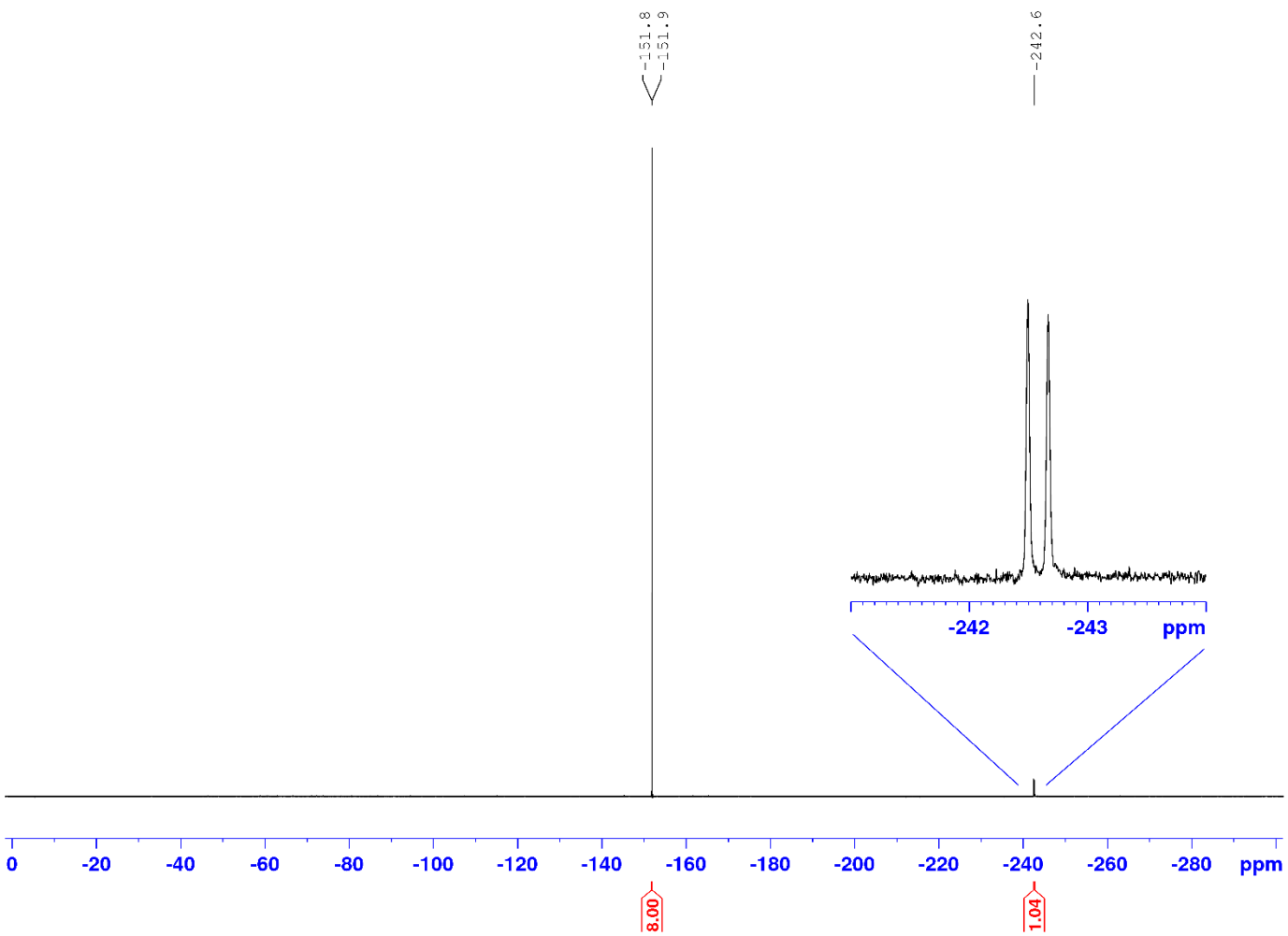

Figure 20: ^{19}F NMR spectrum of [58a]BF_4 with 1:1 1-chloromethyl-1,4-diazoniabicyclo[2.2.2]octane BF_4 in CD_2Cl_2.

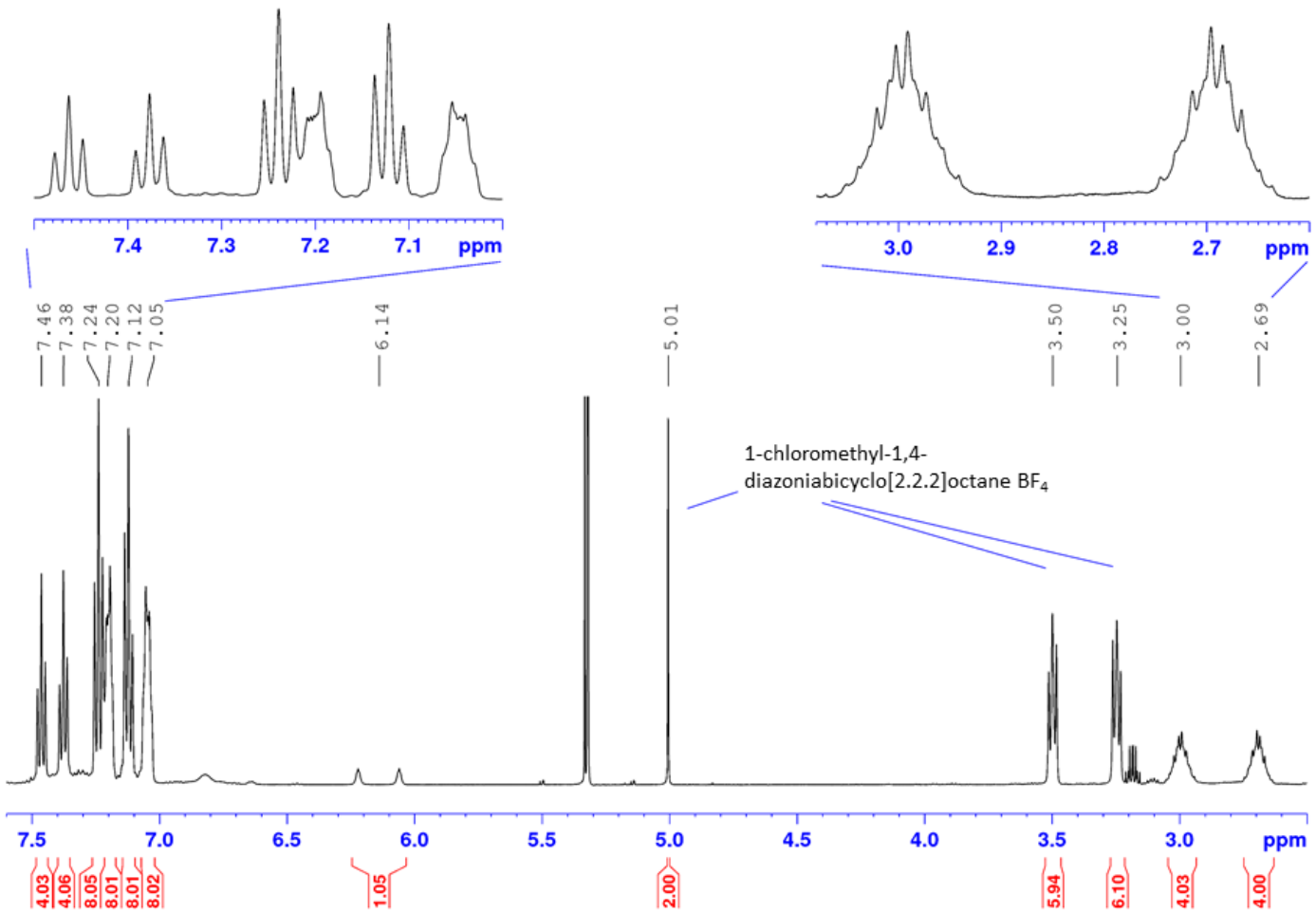

Figure 21: ^{1}H NMR spectrum of [58a]BF_4 with 1:1 1-chloromethyl-1,4-diazoniabicyclo[2.2.2]octane BF_4 in CD_2Cl_2.

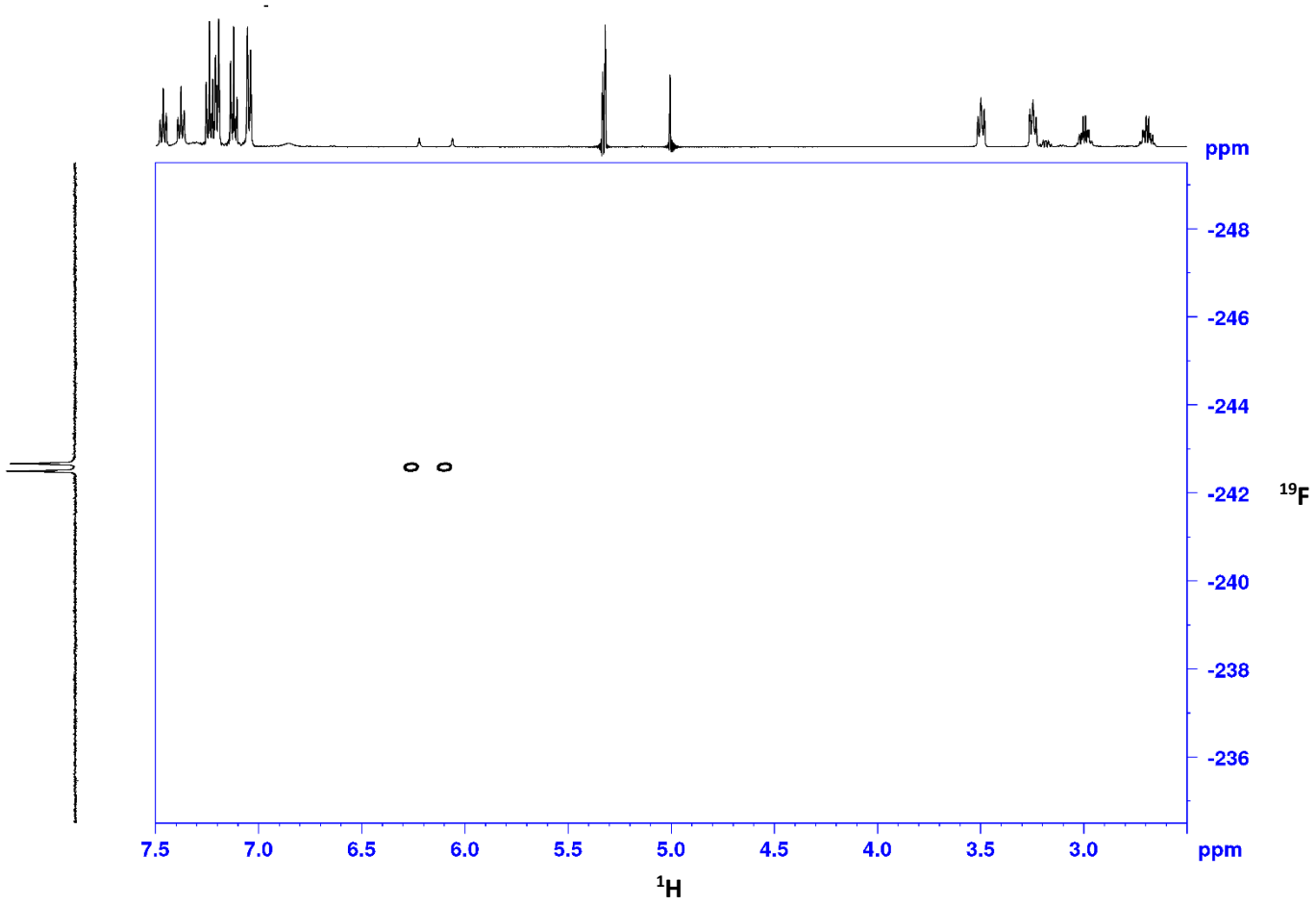

Figure 22: ^{1}H-^{19}F HMBC NMR spectrum of [58a]BF_4 with 1-chloromethyl-1,4-diazoniabicyclo[2.2.2]octane BF_4 in CD_2Cl_2.

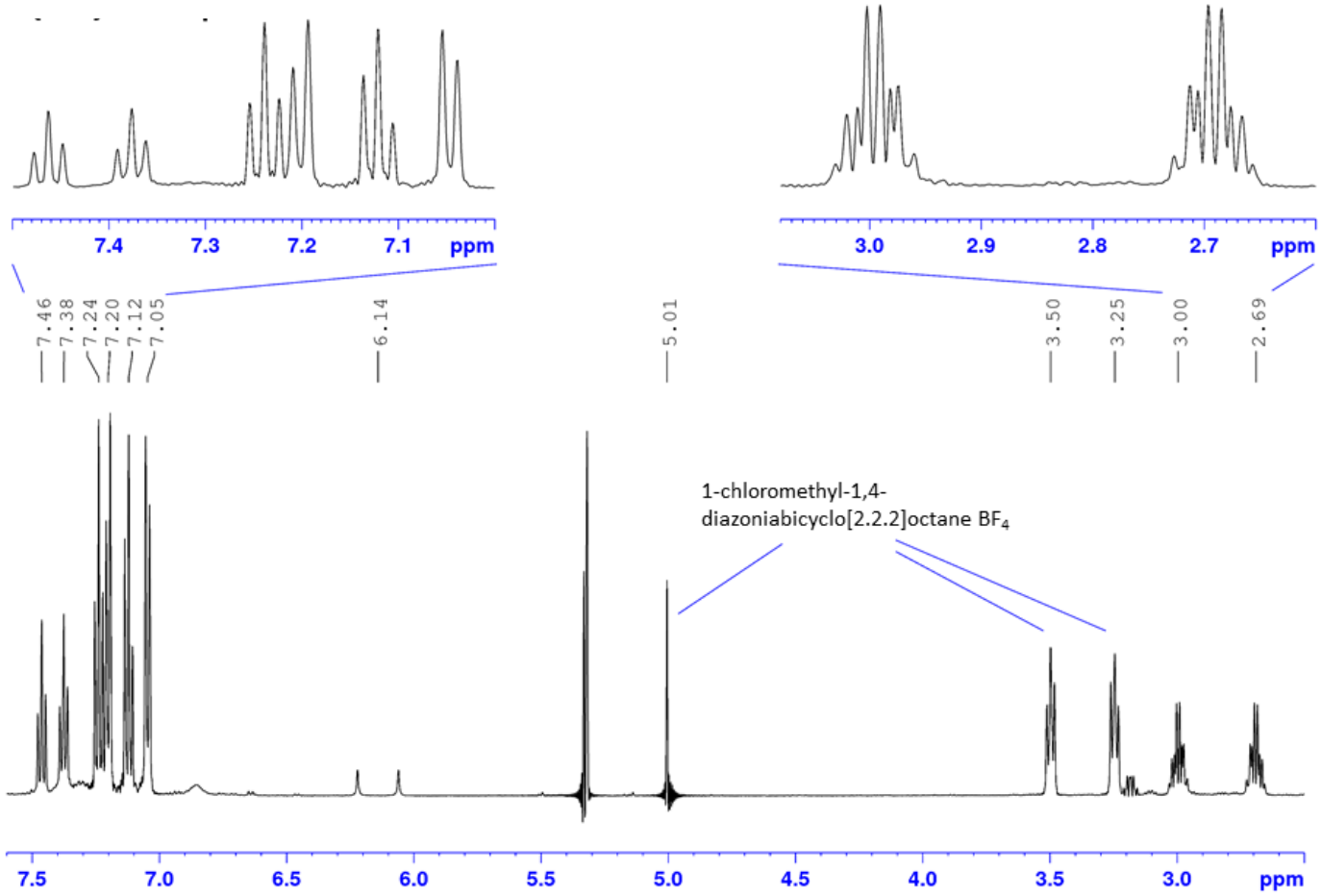

Figure 23: $^{1}H\{^{31}P\}$ NMR spectrum of [58a]BF_4 with 1-chloromethyl-1,4-diazoniabicyclo[2.2.2]octane BF_4 in CD_2Cl_2. Note that the signals corresponding to the protons of the *ortho* position and backbone of the dppe are less complex with phosphorus decoupling compared to the ^{1}H NMR spectrum with phosphorus coupling (Figure 21).

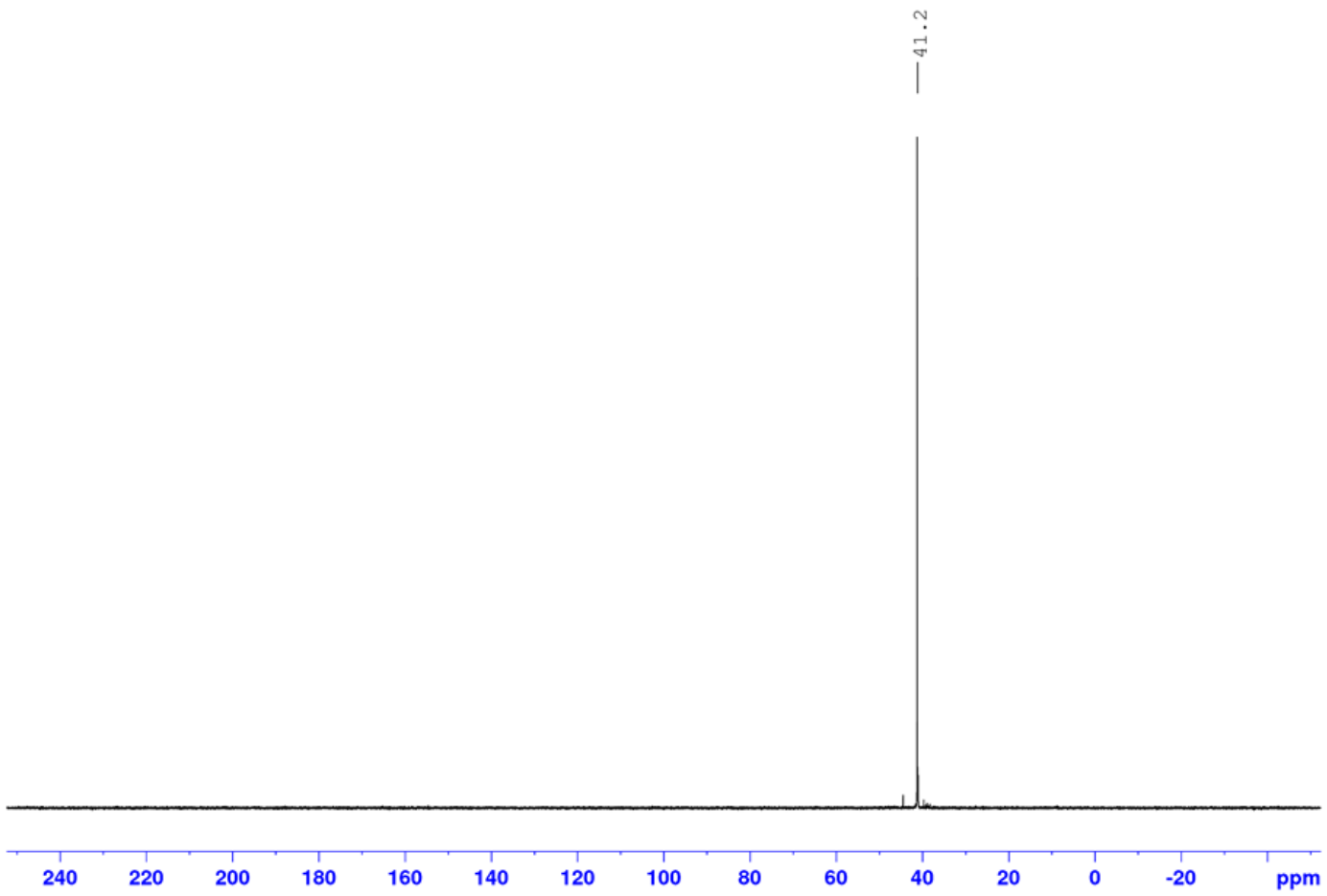

Figure 24: $^{31}P\{^{1}H\}$ NMR spectrum of [58a]BF_4 with 1-chloromethyl-1,4-diazoniabicyclo[2.2.2]octane BF_4.

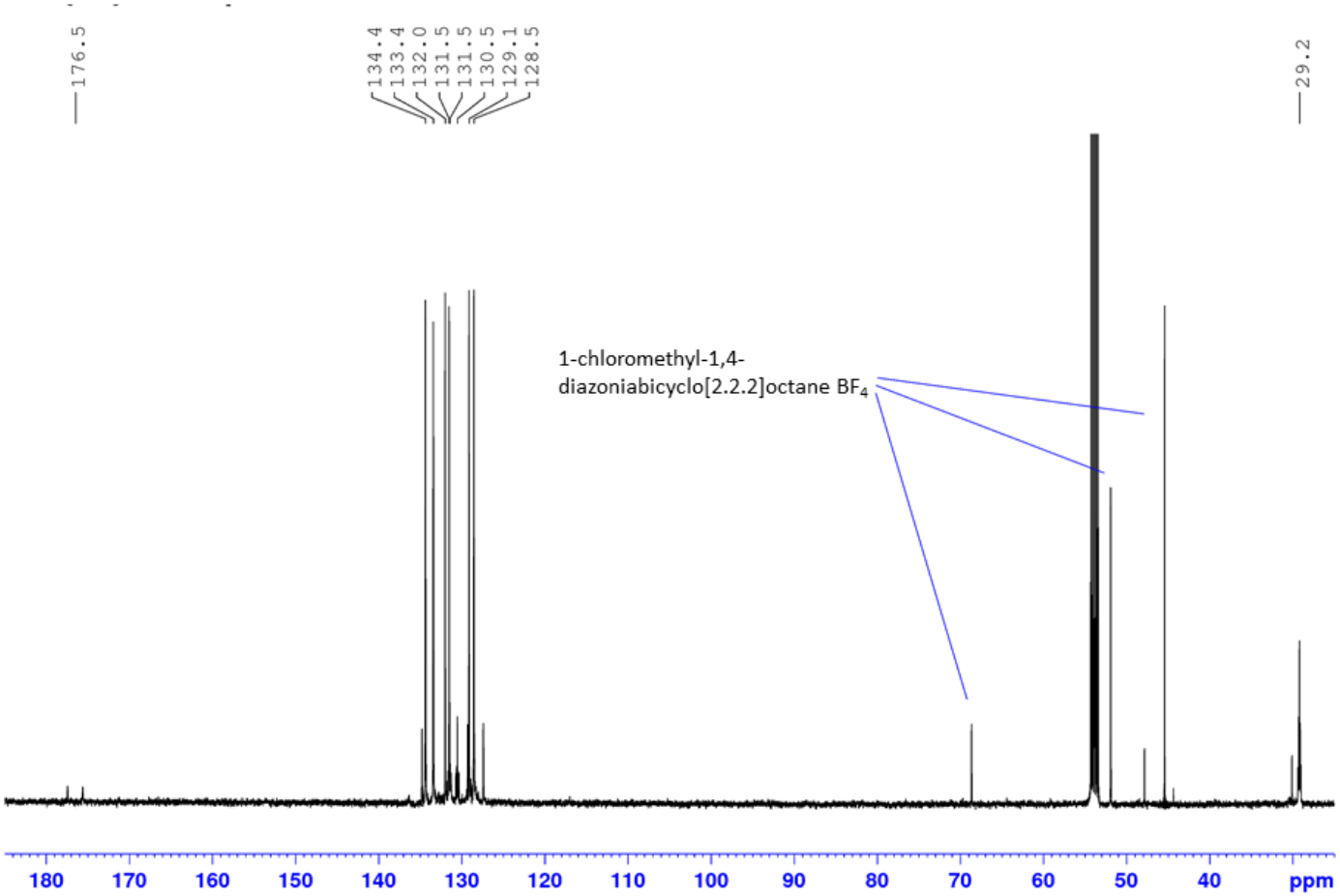

Figure 25: $^{13}C\{1H\}$ NMR spectrum of [58a]BF_4 with 1-chloromethyl-1,4-diazoniabicyclo[2.2.2]octane BF_4.

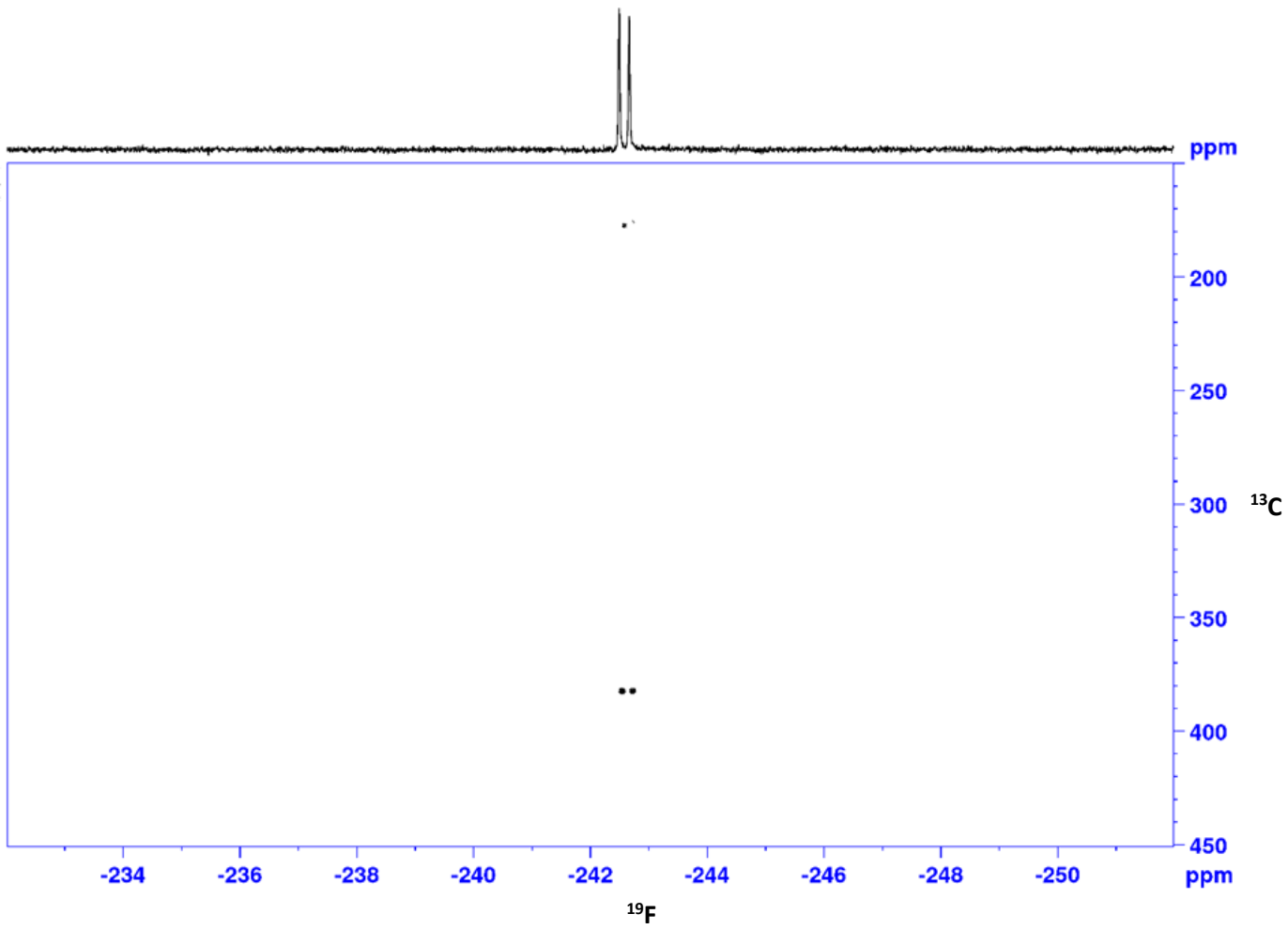

Figure 26: ^{13}C-^{19}F HSQC NMR spectrum of [58a]BF_4 with 1-chloromethyl-1,4-diazoniabicyclo[2.2.2]octane BF_4.

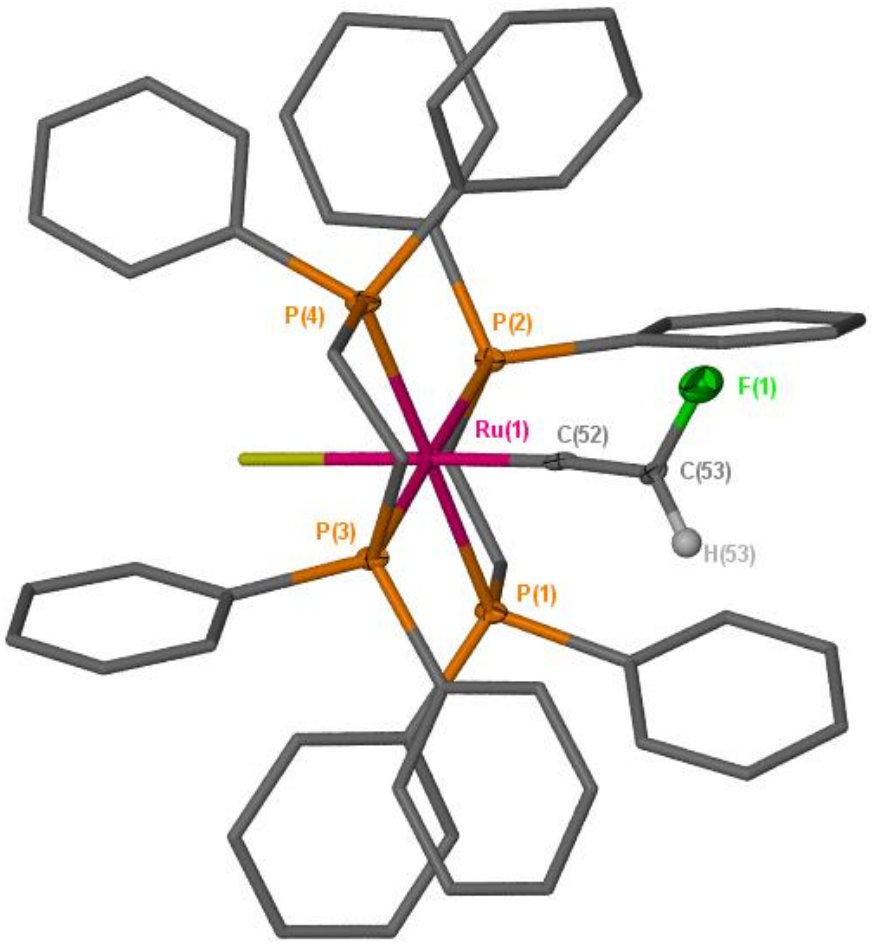

Figure 27: Crystal structure of [58a]PF_6; hydrogens (with the exception of H(53)) and hexafluorophosphate counterion were omitted for clarity and thermal ellipsoids displayed with 50 % probability level. H53 displayed with 1.2 U_{iso}.

The structure of **[58a]**$^+$ was confirmed by single crystal X-ray crystallography with suitable crystals of the hexafluorophosphate salt (Figure 27). The hexafluorophosphate salt was obtained through stirring **[58a]**BF_4 with *ca*. 20 equivalents of sodium hexafluorophosphate for one hour in dichloromethane. The crystallographic data for **[58a]**PF_6 reveals a distorted octahedral geometry of the ligands around the ruthenium centre. The *trans*-P-Ru-P bond angles were determined at 178.80(5)° and 178.44(5)°, with the chloride and vinylidene ligand being colinear with respect to one another (Cl-Ru=C_α, 178.5(2)°) but are distorted away from the ideal geometry (90°) with respect to the phosphorus atoms (Cl-Ru-P and C_α-Ru-P bond angles). Unlike the half sandwich complexes **[30a]**PF_6 and **[54a]**PF_6, there was no evidence for rotational isomers of the vinylidene ligand in the crystal lattice. Despite the poor steric discrimination between the fluorine and proton atoms, the orientation of the vinylidene is well defined. This could be due to increased steric crowding around the ligand as a consequence of the bulkier dppe ligand with respect to a pentamethylcyclopentadienyl

ligand, confining the substituents of the vinylidene ligand into a smaller spatial pocket. The smallest P-Ru---C_β-F torsion angle for the major and minor (distorted) forms in the crystal are is measured at 26.5° and 40.3° respectively. The smallest torsion angle between the CHF group of the vinylidene and the metal-ligand framework is significantly different in the two forms observed in the crystal. However, it is not clear why the torsional angles are different with the exception of packing effects.

The positions of the vinylidene and chloride ligands about the ruthenium are reversed in 20 % of unit cells of the crystal. The octahedral geometry is further distorted in this disordered form, with the P-Ru-C_α angles determined at 93.3(7)°, 81.5(8)°, 99.7(3)°, and 85.3(7)°. Additionally, the Cl-Ru=C_α bond angle is distorted further away from linearity in the more disordered form from 178.5(2)° to 175.2(8)°. The Ru-C_α-C_β and C_α-C_β-F bond angles of the vinylidene remain statistically identical to the angles observed in the major component. The Ru=C_α, C_α=C_β, and C_β-F bond lengths of the vinylidene also remain statistically the same, however, the Ru-Cl bond undergoes elongation from 2.5125(19) Å to 2.567(10) Å in the minor component.

Unlike the UV-Vis absorption spectra for **[54a]**$^+$ and **[54b]**$^+$ (Figure 11 and Figure 18), the UV-Vis spectrum for **[58a]**$^+$ does not display a noticeable low energy absorption band corresponding to the HOMO→LUMO transition (Figure 28). Small absorption bands from 446 nm onwards arise from trace quantities of stable radical species which form during the reaction with Selectfluor (see Chapter 4). Trace radical species are easily observable by UV-Vis due to their high molar absoprtion coefficients.[243] The HOMO-LUMO transition is calculated by TD-DFT to be observed at around 670 nm, but it cannot be observed clearly due to overlapping bands from trace contaminants.

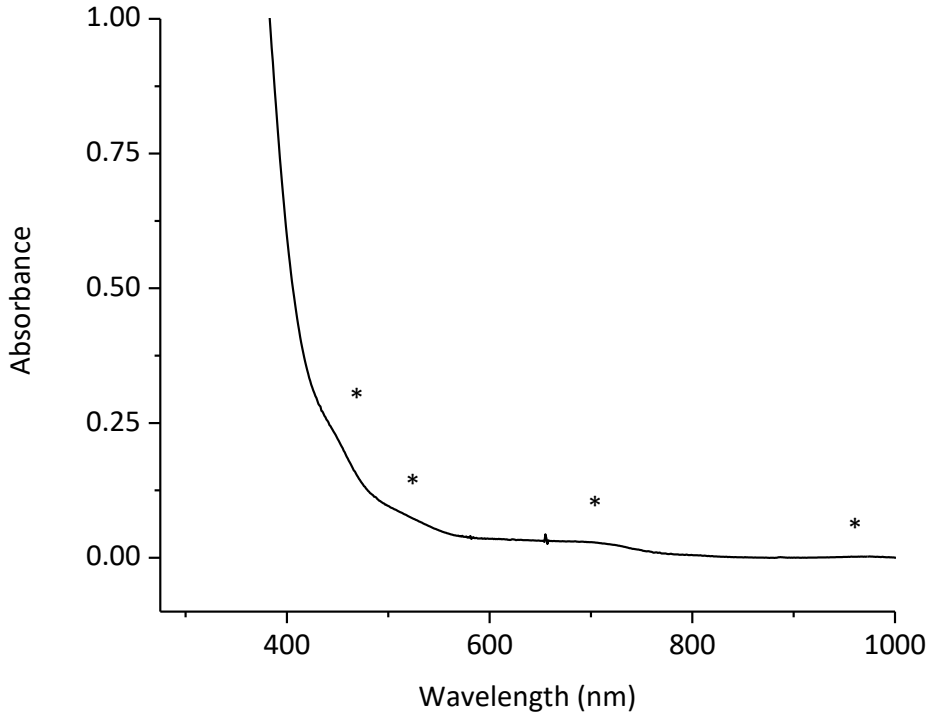

Figure 28: UV-Vis absorption spectrum for [58a]BF_4 in dichloromethane at 1 mmol dm^{-3} concentration with a pathlength of 1 cm. Asterisks denote absorption bands from trace radical impurities.

2.6.2 Synthesis of Fluoroalkynyl Complex, [57b]

Addition of lithium *bis*(trimethylsilyl)amide to a tetrahydrofuran solution of **[58a]**$^{+}$ at -78 °C afforded the desired fluoroalkynyl complex **[57b]** in excellent yield (82 %, Scheme 123). Due to the solubility differences of **[57b]** to that of Li-HMDS and HMDS, purification of **[57b]** proved significantly easier than the purification of **[28b]** and **[55b]**.

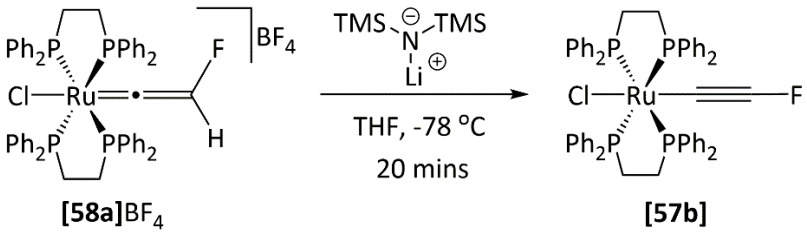

[58a]BF_4 **[57b]**

Scheme 123: Cold addition of Li-HMDS to [58a]BF_4 afforded fluoroalkynyl complex, [57b].

Similar to **[28b]** and **[55b]**, the ^{19}F NMR spectrum for **[57b]** in C_6D_6 displayed a new resonance at δ -182.1 with 4 Hz quintet coupling to phosphorus and consistent with 4-bond coupling. The $^{31}P\{^{1}H\}$ NMR spectrum exhibited a doublet resonance at δ 49.7 with matching coupling. The chemical shift of the phosphorus nuclei is indicative of a neutral complex and consistent with alkynyl complexes of this fragment.[244-246] The observation and size of the P-F coupling agrees with the observed spectroscopic data for the fluoroalkynyl **[55b]**. The β-carbon of the alkynyl ligand was observed at δ 111.5 as a doublet resonance with C-F coupling of 326 Hz, while the α-carbon was observed at δ 36.7 as a doublet resonance with C-F coupling of 36 Hz. Both assignments were confirmed by a ^{13}C-^{19}F HSQC NMR experiment. The LIFDI-MS spectrum displayed a peak at 976.10 m/z corresponding to the m/z of **[55b]**. Single crystal X-ray crystallography unambiguously confirmed the presence of the fluorinated alkynyl ligand (Figure 29).

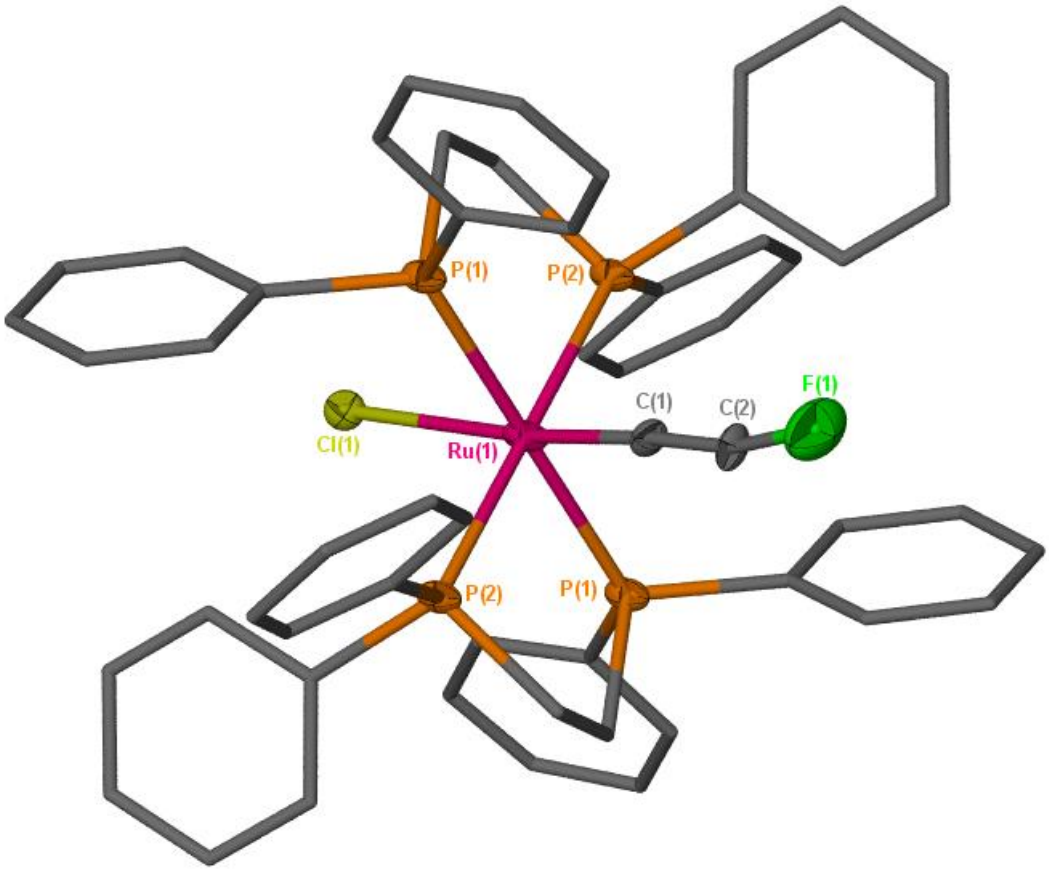

Figure 29: Crystal structure of [57b]; hydrogens were omitted for clarity and thermal ellipsoids displayed with 50 % probability level.

The structure of the fluoroalkynyl complex **[57b]** displays a distorted octahedral coordination environment in which the *trans*-chloride and alkynyl ligand are disordered over opposite sites in the crystal lattice with 50 % occupancy. This is presumably due to poor steric discrimination between the two ligands. The alkynyl ligand shows considerable distortion with the Cl-Ru-C_α and Ru-C_α-C_β angles being distorted away from linearity at 173.22(18)° and 175.8(5)° respectively, with the C_α-C_β-F angle being significantly distorted further from ideal at 166.1(9)°. The Ru-C_α, C_α-C_β, and C_β-F bond lengths were measured at 1.854(7) Å, 1.251(9) Å, and 1.300(8) Å respectively.

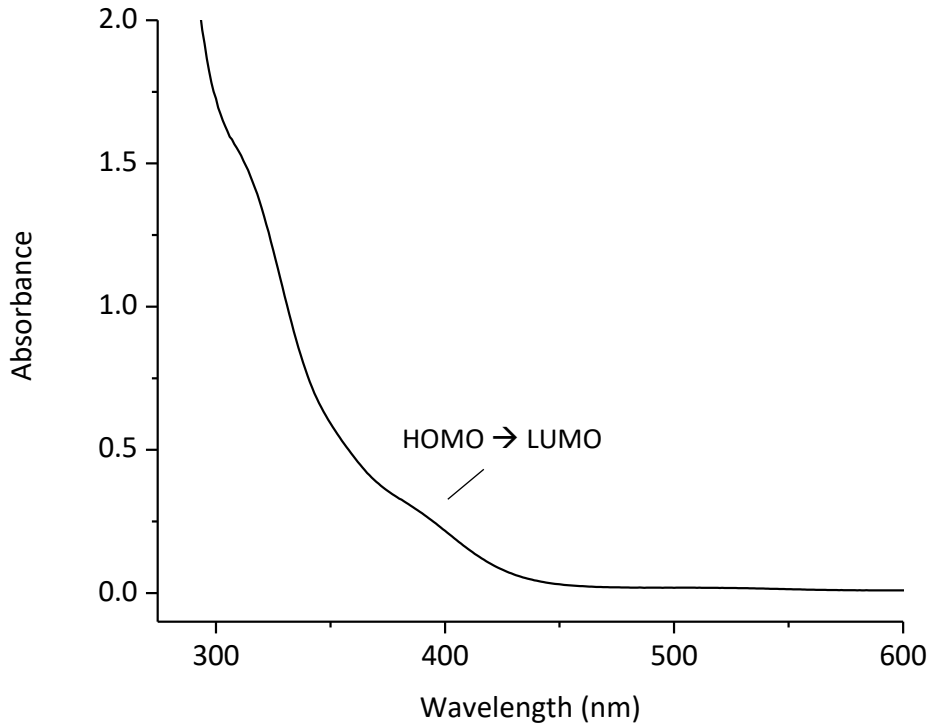

Figure 30: UV-Vis absorption spectrum for [57b] in dichloromethane at 0.5 mmol dm^{-3} concentration with a pathlength of 1 cm.

The UV-Vis spectrum of **[57b]** (Figure 30) displays two shoulders at 309 and 382 nm. The lowest energy band is believed to arise from the HOMO-LUMO transition while the band at 309 nm is believed to arise from a number of different transitions based on the TD-DFT calculation at (RI-)BP86/SV(P)//PBE0/def2-TZVPP level.

2.6.3 Fluorination of Fluoroalkynyl Complex [57b]

The reactivity of **[57b]** was comparable to that of **[57a]** and the other fluoroalkynyl complexes **[28b]** and **[55b]**, when subjected to a latent source of "F^+". Addition of Selectfluor to a dichloromethane: acetonitrile solution of **[57b]** at -78 °C resulted in the formation of a green solution after one minute. The solution changed colour to afford a dark yellow-brown solution after 20 minutes of stirring. The resultant product was identified as the desired difluoro-vinylidene complex **[58b]**$^+$ by NMR spectroscopy, MS and single crystal crystallography (Scheme 124).

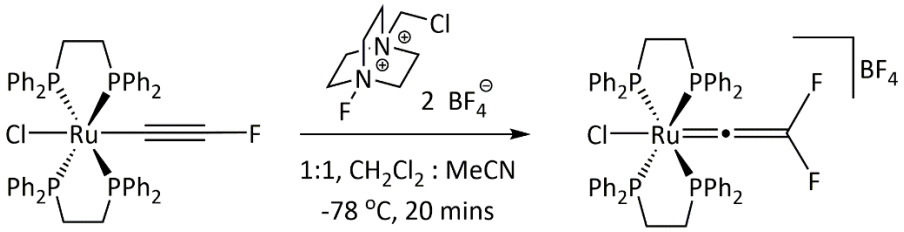

[57b] **[58b]**BF_4

Scheme 124: Cold addition of Selectfluor to [57b] afforded difluoro-vinylidene complex, [58b]BF_4.

The ^{19}F NMR spectrum of **[58b]**BF_4 in CD_2Cl_2 displayed a new singlet resonance at δ -145.2 while the $^{31}P\{^1H\}$ NMR spectrum displayed a singlet resonance at δ 39.7. The fluorine substituent was observed at a similar chemical shift as the fluorine substituents in **[30b]**$^+$ and **[54b]**$^+$, while the phosphorus chemical shift is within the range observed for vinylidene complexes of the type $[ClRu(dppe)_2(=C=CR^1R^2]^+$.[244, 245] The β-carbon of the vinylidene ligand was identified as a doublet resonance at δ 349 in the ^{13}C NMR spectrum with 270 Hz coupling to the adjacent fluorine nucleus. The α-carbon could not be identified in the 1D ^{13}C NMR spectrum but was detected in the ^{13}C-^{19}F HSQC experiment at δ 408. High resolution ESI-MS detected a species at 995.1437 m/z which corresponds to the expected m/z for **[58b]**$^+$. Suitable crystals of the hexafluorophosphate salt for X-ray diffraction were obtained by slow diffusion of a dichloromethane solution **[58b]**PF_6 into pentane. X-ray crystallography unambiguously confirmed the structure of **[58b]**PF_6.

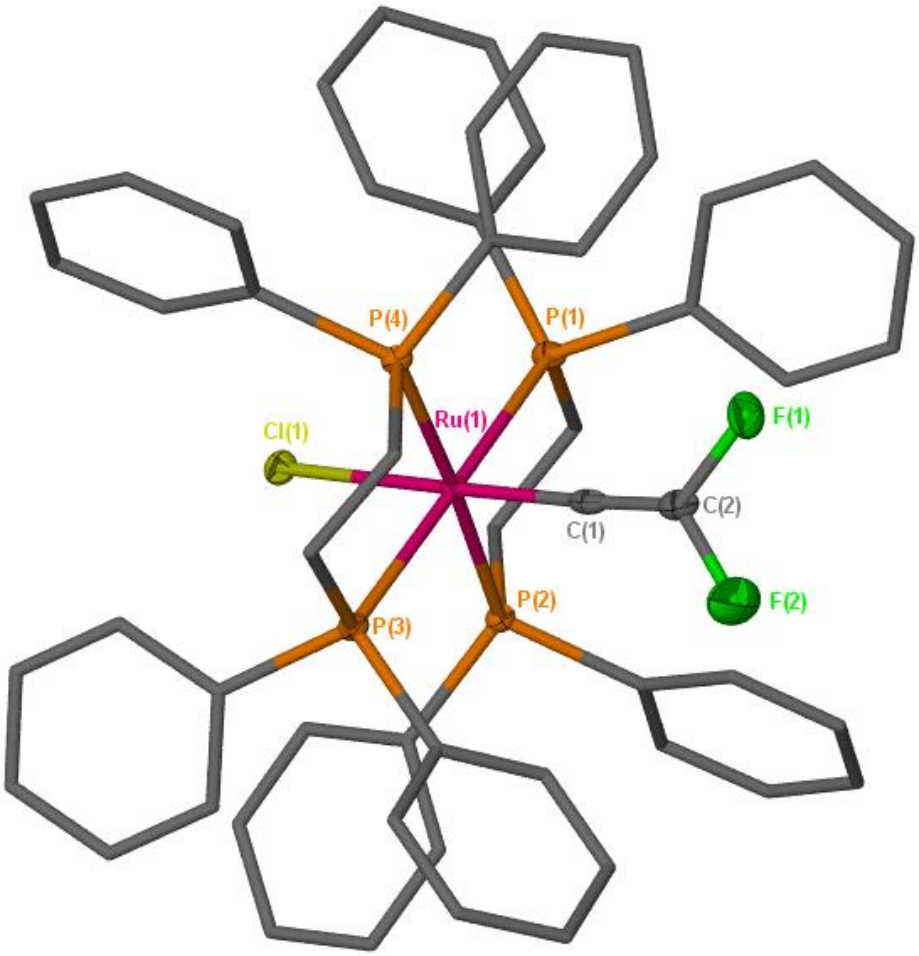

Figure 31: Crystal structure of [58b]PF_6; hydrogens and hexafluorophosphate counterions were omitted for clarity and thermal ellipsoids displayed with 50 % probability level.

As with **[58a]**PF_6, **[58b]**PF_6 has a distorted octahedral coordination geometry with the *trans*-phosphorus atoms displaying distortion away from linearity (P(1)-Ru-P(3) measured at 177.006(18)° and P(2)-Ru-P(4) at 177.074(17)°). The chloride and vinylidene ligand are also distorted from linearity (Cl-Ru=C_α, 178.35(6)°) and are distorted away from perpendicularity with respect to the phosphine ligands (i.e. Cl-Ru-P and C_α-Ru-P ≠ 90°). In contrast to **[58a]**PF_6, the vinylidene and chloride ligands are only observed in a single position in the crystal lattice rather than disordered over two sites, indicating there is sufficient steric discrimination between the chloride and vinylidene ligand in **[58b]**PF_6 but not in **[58a]**PF_6. This is likely due to changes in the spatial pocket surrounding the vinylidene and chloride ligand in which the steric crowing around the chloride is increased as a consequence of the second fluorine substituent, enforcing discrimination between the two ligands. The vinylidene Ru-C_α and C_α-C_β bond lengths were determined at 1.853(2) Å and 1.259(3) Å respectively. The two C_β-F bonds were determined to be statistically identical at 1.348(2) Å and 1.356(2) Å, as predicted for the gas-phase structure. The bond angles of the vinylidene are distorted away from ideal

with the Ru-C_α-C_β angle non-linear at 176.69(17)°. The C_α-C_β-F bond angles are statistically same at 127.42(19)° and 126.38(19)°, however significant compression of F-C_β-F bond angle is observed from the ideal 120° to 105.93(17)°.

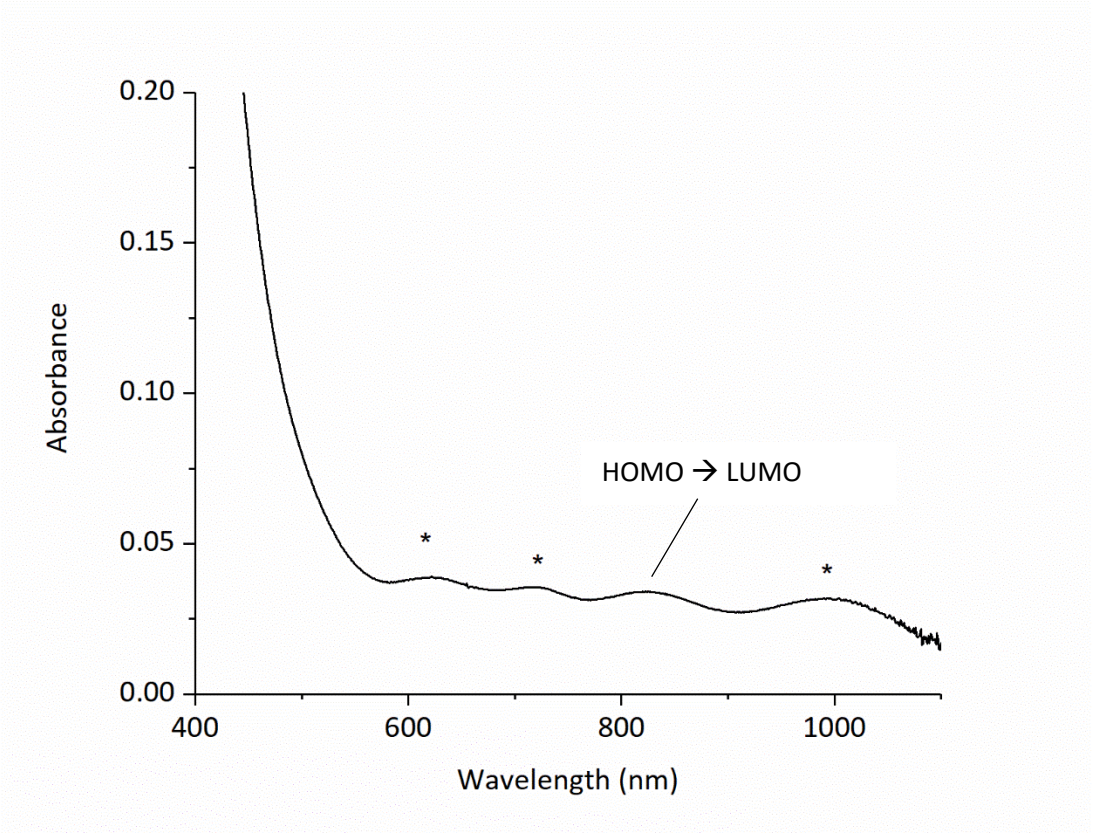

Figure 32: UV-Vis absorption spectrum of [58b]PF_6 at 1 mmol dm^{-3} in dichloromethane with a pathlength of 1 cm; asterisks denote absorption bands from trace radical contaminants.

The UV-Vis absorption spectrum of **[58b]**PF_6 (Figure 32) consists of a broad shoulder at around 380 nm and four exceptionally weak absorption bands at 623, 717, 823, and 1000 nm. The observed absorption bands at 623, 717, and 1000 nm are believed to arise from to trace quantities of stable radical contaminants observed in the reaction of **[57a]** with Selectfluor (see Chapter 4), despite the UV-Vis absorption spectrum being obtained from crystalline **[58b]**PF_6 which passed elemental analysis. These trace contaminants are observed due to their high molar absorption coefficients. The weak band at 823 nm is believed to correspond to the HOMO-LUMO transition based on the TD-DFT calculation for **[58b]**$^+$ which predicts a low energy absorption band at 823 nm a small oscillator strength (f-value of 0.21 $x10^{-4}$). The next lowest transition, calculated at 434 nm, could not be observed. The predicted HOMO (Figure 33) consists of a symmetry adapted ruthenium d-orbital with π-antibonding interactions with the chloride p-orbital and vinylidene π-system. The vinylidene carbons are π-bonding with respect to one another, with the β-carbon being π-antibonding with respect

to the fluorine substituents. The LUMO also consists of a π-antibonding interaction between the symmetry adapted ruthenium d-orbital and the p-orbital of the α- carbon. A weak π-bonding interaction is predicted between the vinylidene carbons as a consequence of the fluorine substituents, which are themselves antibonding with respect to the vinylidene π-system.

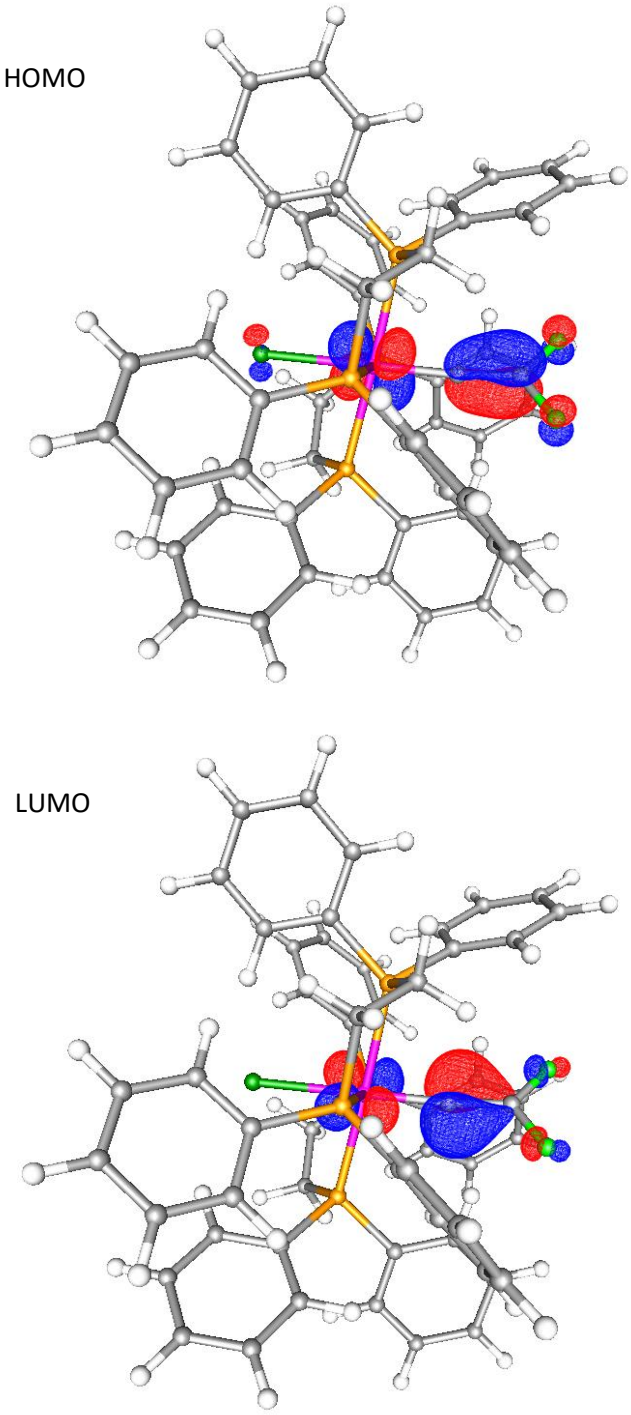

Figure 33: Orbital representation of the HOMO and LUMO of [58b]$^{+}$.

2.7 Substituent/fluorine effect within the series

2.7.1 Discussion of NMR Spectroscopic parameters

2.7.1.1 [Ru(η^5-C$_5$H$_5$)(PPh$_3$)$_2$(=C=CR^{1}R^2)]$^+$ Complexes

Table 1: Table of selected chemical shifts for [Ru(η^5-C$_5$H$_5$)(PPh$_3$)$_2$(=C=CR^{1}R^2)]$^+$ vinylidene complexes where R = H or F.

	^{1}H NMR δ / ppm	^{19}F NMR δ / ppm	^{31}P{^{1}H} NMR δ / ppm
[Ru(η^5-C$_5$H$_5$)(PPh$_3$)$_2$(CCH$_2$)]$^+$, **[44b]$^+$**	4.26	-	47.5
[Ru(η^5-C$_5$H$_5$)(PPh$_3$)$_2$(CCHF)]$^+$, **[44a]$^+$**	8.51	-235.3	43.8

Replacement of the hydrogen-substituent of the vinylidene ligand with fluorine results in a downfield shift of the phosphorus resonance from δ 47.5 in **[44b]$^+$** to δ 43.8 in **[44a]$^+$** (Table 1). The proton chemical shift undergoes a significant downfield shift from δ 4.26 in **[44b]$^+$** to δ 8.51 in **[44a]$^+$**. The deshielding of the proton resonance in **[44a]$^+$** can be rationalised by the presence of a highly electronegative nature of fluorine. The shielding of the phosphorus environments can be rationalised by the electron-donating mesomeric effect provided by the fluorine substituent.

2.7.1.2 [Ru(η⁵-C₅Me₅)(PPh₃)₂(=C=CR¹R²)]⁺ Complexes

Table 2: Table of selected chemical shifts for [Ru(η⁵-C₅Me₅)(PPh₃)₂(=C=CR¹R²)]⁺ vinylidene complexes where R = H or F.

			^{1}H NMR	^{19}F NMR	^{31}P{^{1}H} NMR	^{13}C{^{1}H} NMR δ / ppm	
	R^1	R^2	δ / ppm	δ / ppm	δ /ppm	C_α	C_β
[29]⁺	H	H	4.36	-	47.8	349.3[190]	104.7[190]
[30a]⁺	F	H	8.6	-236.1	51.5	367.9	178.7
[30b]⁺	F	F	-	-135.2	49.5	-	-

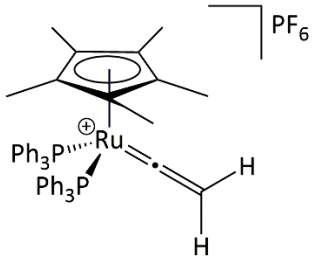

[29]PF_6

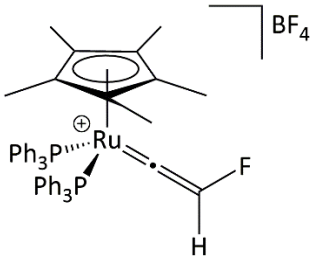

[30a]BF_4

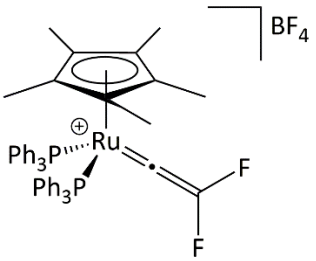

[30b]BF_4

Substitution of hydrogen with fluorine in the [Ru(η⁵-C₅Me₅)(PPh₃)₂(=C=CR₂)]⁺ vinylidene series results in the deshielding of the proton environment from δ 4.26 in the diprotio-vinylidene complex, **[29]⁺**, to δ 8.60 in the monofluoro-vinylidene complex, **[30a]⁺**, as observed with fluorination of **[44b]⁺** to **[44a]⁺**. Significant deshielding of the fluorine resonance is observed from δ -236.1 in **[30a]⁺** to δ -135.2 in **[30b]⁺**(Table 2). Large downfield shifts of 19 and 74 ppm are observed for the vinylidene α- and β-carbon chemical shifts respectively with replacement of one hydrogen substituent with fluorine.

Upon sequential replacement of the hydrogen substituents with fluorine, the phosphorus resonances display a varying trend. The first substitution results in the deshielding of the phosphorus resonance from δ 47.5 in **[29]⁺** to δ 51.5 in **[30a]⁺**, while the second substitution results in shielding of the phosphorus resonance to δ 49.5 in **[30b]⁺**.

The more shielded phosphorus resonances of **[29]⁺** and **[30b]⁺** compared to **[30a]⁺** could be highlighting the importance of orbital symmetry and its relation to chemical shielding tensors through magnetic mixing of orbitals in the presence of a magnetic field. A consistent trend in the phosphorus chemical shift would be expected based on the electronic properties of fluorine alone.[193, 194] Nevertheless, the deshielding of the proton and fluorine chemical shifts can be again rationalised by strong electron-withdrawing inductive effect of fluorine. The

incorporation of a second fluorine substituent reduces the electron density available to both fluorine substituents resulting in deshielding effect.

2.7.1.3 [Ru(η⁵-C₅Me₅)(dppe)(=C=CR¹R²)]⁺ Complexes

The same trend in NMR spectroscopic data was observed with the [Ru(η⁵-C_5Me_5)(dppe)(=C=CR_2)]⁺ vinylidene complexes when sequentially replacing the hydrogen substituents of the vinylidene ligand with fluorine (Table 3).

Table 3: Table of selected chemical shifts for [Ru(η⁵-C_5Me_5)(dppe)(=C=CR^1R^2)]⁺ vinylidene complexes where R = H or F.

			^{1}H NMR	^{19}F NMR	^{31}P{^{1}H} NMR	^{13}C{^{1}H} NMR δ / ppm	
	R^1	R^2	δ / ppm	δ / ppm	δ / ppm	C_α	C_β
[56]⁺	H	H	2.99	-	77.3	344.2[241]	102.7[241]
[54a]⁺	F	H	7.32	-235.8	76.4	362.8	173.9
[54b]⁺	F	F	-	-134.0	75.2	366.7	231.3

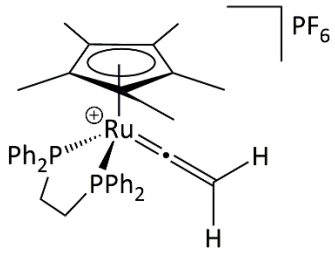

[56]PF_6

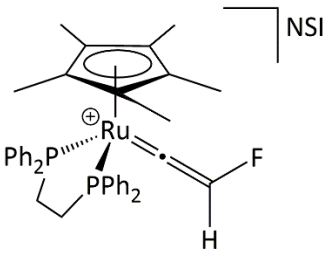

[54a]NSI

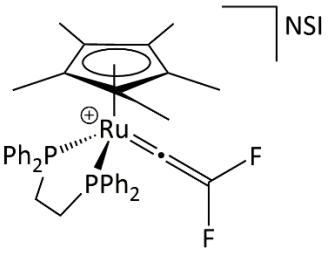

[54b]NSI

After substitution of the first hydrogen substituent with fluorine (**[56]⁺** to **[54a]⁺**) a large downfield shift is observed for the remaining proton resonance from δ 2.99 to δ 7.32. Similarly, the fluorine resonance undergoes deshielding upon the second substitution from δ -235.8 in **[54a]⁺** to δ -134.0 in **[54b]⁺**, due to the two fluorine substituents competing with one another for electron density.

A downfield shift of 19 and 71 ppm is observed in the α- and β-carbon resonances, respectively, from **[56]⁺** to **[54a]⁺**. However, after the second substitution, only the β-carbon resonance of the vinylidene undergoes a significant downfield shift (57.4 ppm), while the α-carbon of **[54b]⁺** undergoes a modest downfield shift of 4 ppm but otherwise remains unperturbed. It is unclear without further investigation why this is the case.

In contrast to the varying trend in phosphorus chemical shifts observed for the [Ru(η⁵-C_5Me_5)(PPh_3)₂(=C=CR_2)]⁺ vinylidene complexes, the phosphorus chemical shifts of the dppe

analogues undergo consistent deshielding with sequential fluorine incorporation, from δ 77.3 to δ 76.4 to δ 75.2 in **[56]**$^+$, **[54a]**$^+$, and **[54b]**$^+$ respectively.

2.7.1.4 [ClRu(dppe)$_2$(=C=CR^{1}R^2)]$^+$ Complexes

Table 4: Table of selected chemical shifts for [ClRu(dppe)$_2$(=C=CR^{1}R^2)]$^+$ vinylidene complexes where R = H or F.

			^{1}H NMR	^{19}F NMR	^{31}P{^{1}H} NMR	^{13}C{^{1}H} NMR δ / ppm	
	R^1	R^2	δ / ppm	δ / ppm	δ /ppm	C_α	C_β
[59]$^+$	H	H	2.43	-	41.5	349.9[244]	92.4[244]
[58a]$^+$	F	H	6.14	-242.6	41.2	382.4	176.5
[58b]$^+$	F	F	-	-145.2	39.7	408.2	249.4

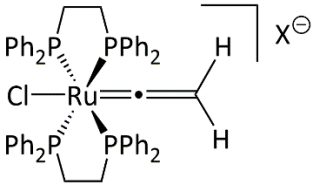

[59]$^+$

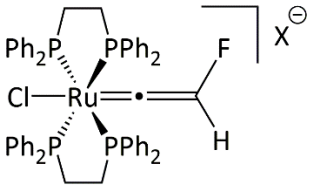

[58a]$^+$

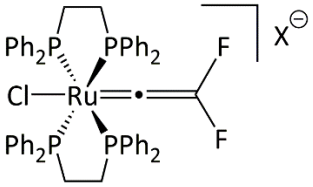

[58b]$^+$

As observed throughout the half-sandwich vinylidene series, incorporation of fluorine into *trans*-[ClRu(dppe)$_2$(=C=CR$_2$)]$^+$ vinylidene complexes results in deshielding of the vinylidene's carbon, proton, and fluorine resonances. The vinylidene proton environment undergoes deshielding from δ 2.43 in **[59]**$^+$ to δ 6.14 in **[58a]**$^+$ while the fluorine substituent undergoes deshielding from δ -242.6 in **[58a]**$^+$ to δ -145.2 in **[58b]**$^+$ (Table 4). Sequential incorporation of the fluorine results in deshielding of the α- and β-carbons of the vinylidene. The α- carbon resonance undergoes a 32.5 ppm and 25.8 ppm downfield shift upon the first and second substitution with fluorine respectively. The deshielding of the β-carbon resonance is more pronounced, displaying an 84.1 ppm and 117.9 ppm downfield shift upon the first and second substitution with fluorine respectively.

The phosphorus resonances appear to follow the same trend as observed with the [Ru(η^5-C$_5$Me$_5$)(dppe)(=C=CR$_2$)]$^+$ vinylidene complexes, in which there is a general shielding of the phosphine environments upon incorporation of fluorine. The phosphorus chemical shift undergoes a small upfield shift upon incorporation of the first fluorine (δ 41.5 to δ 41.2) and subsequently another upfield shift of 1.5 ppm after the second incorporation of fluorine.

As would be expected for organic molecules, the incorporation of fluorine results in strong deshielding of the adjacent atoms when considering the vinylidene ligand. Across the four series, deshielding of the carbon, proton and fluorine resonances is generally observed. The general trend could be rationalised simply by the strong electron-withdrawing inductive effect of fluorine which reduces the electron density residing around the adjacent atoms resulting in chemical shift deshielding. The β-carbon experiences greater deshielding than the α- carbon as would be expected due to the diminishing inductive effect with distance. The mesomeric effect would counteract the inductive effect to a certain degree and provide electron-donating contribution over a greater distance, which would reinforce the observation of the α-carbon being deshielded to a lesser extent than the β-carbon, and the general shielding of the phosphorus environments.

A more accurate rationale for the deshielding of the vinylidene environments would be the enhancement in paramagnetic shielding from increased MO mixing upon incorporation of a π-donor. Generally, the MO contributions to chemical shielding are proportional to the MO mixing coefficients and inversely proportional to the energy gap between orbitals. A reduction in the MO energy gaps upon incorporation of fluorine, signified by the bathochromic shift of the HOMO-LUMO transition in the UV-Vis spectra, would enable increased mixing of the MOs in an external magnetic field. This results in increased paramagnetic shielding which is nearly always deshielding.[193, 194]

The relatively small magnitude of deshielding observed for the α- carbon chemical shift of **[54b]**$^{+}$ was unexpected given the large deshielding observed for the β-carbon and fluorine resonances and also the large deshielding of the α- carbon in **[58b]**$^{+}$. Without investigation of the complexes by solid-state NMR and understanding the origin for the changes in the shielding tensors, it is unclear why this complex bucks the trend.

The phosphorus chemical shifts across the series do not show a pronounced trend except for a small upfield shift that is observed in all but one case upon sequential fluorine incorporation. The mesomeric effect of fluorine could provide a simple rationale, however, it is clear that a simple consideration of the electronic effects cannot describe fully the observed chemical shifts in these metal complexes. The shielding of phosphorus resonances is more likely the result of enhanced paramagnetic shielding through changes to the molecular orbitals induced by incorporation of a π-donor.

2.7.1.5 The Deshielding Influence of Fluorine.

A comparison of chemical shift changes reveals that incorporation of fluorine does not have the same deshielding effect across each ruthenium fragment series (Table 5). Comparing the effect of fluorine incorporation on the $[Ru(\eta^5\text{-}C_5H_5)(PPh_3)_2(=C=CR^1R^2)]^+$ series with the $[Ru(\eta^5\text{-}C_5Me_5)(PPh_3)_2(=C=CR^1R^2)]^+$ series reveals the proton chemical shifts undergo the same *ca.* 4.25 ppm downfield shift. Fluorine incorporation into **[56]**$^+$ results in a similar downfield shift in the proton resonance by 4.33 ppm. This indicates that changes to chemical shielding of the hydrogen substituent are similar across all the half-sandwich complexes, with increased deshielding being observed in the $[Ru(\eta^5\text{-}C_5Me_5)(dppe)]$ fragment. Comparison of the α- and β-carbon chemical shift changes in the $[Ru(\eta^5\text{-}C_5Me_5)(PPh_3)]$ and $[Ru(\eta^5\text{-}C_5Me_5)(dppe)]$ series reveals the deshielding effect of fluorine is identical for the α-carbon but slightly diminished in the later series for the β-carbon. The deshielding influence of fluorine varies when considering the phosphorus chemical shift changes and it is unclear without further investigation what the cause of this is.

The changes in proton chemical shift reveal that fluorine has a reduced deshielding effect on the proton substituent in the $[ClRu(dppe_2)]$ series compared to the half-sandwich series. Incorporation of a second fluorine induces the same *ca.* 100 ppm downfield shift in the fluorine chemical shift across all series reported, indicating the degree of deshielding fluorine induces between each fragment remains essentially the same, although the deshielding effect is slightly diminished in the $[ClRu(dppe_2)]$ fragment.

Conversely a greater deshielding effect is observed for the α- and β-carbon environments with incorporation of either one or two fluorine substituents in the $[ClRu(dppe_2)]$ series compared to the half-sandwich series. As with the $[Ru(\eta^5\text{-}C_5Me_5)(dppe)]$ fragment, the deshielding of the vinylidene carbon environments is diminished with the second substitution compared to the first substitution. The reduced deshielding effect observed after the second fluorine substituent is introduced could be rationalised by the reduced magnitude of the HOMO-LUMO energy gap. However, the smaller MO energy gaps do not account for the reduced deshielding observed for the hydrogen and fluorine substituents in the $[ClRu(dppe_2)]$ series compared to the half-sandwich series. When comparing $[ClRu(dppe_2)]$ with the half-sandwich complexes, the replacement of 1,2,3,4,5-pentamethylcyclopentadienyl with dppe and a chloride ligand will obviously have a significant effect on the symmetry and energies of the MOs and consequently the chemical shielding tensors.

The observed changes in the deshielding ability of fluorine stands to highlight the importance of how orbital angular momentum and overlap in complexes as a whole influences chemical shielding.[193, 194] A more thorough approach to rationalising the observed chemical shifts through understanding how the directional diamagnetic and paramagnetic shielding tensors relates to the molecular orbital structure of the complexes is needed. The significant changes in the ancillary ligands of the metal will have a profound effect upon the molecular orbitals of the system, despite the similarities in the frontier orbitals. Although a reduction in the HOMO-LUMO energy is typically expected to result in an increase of the paramagnetic shielding tensors due to increased MO contributions, it is clear from the observed chemical shifts that the magnitude of the MO mixing coefficients play an important role. This is due to the MO contributions to chemical shielding being proportional to both the MO mixing coefficients and inversely proportional to the energy gap between MOs, and it's the contributions from all the MOs that define the total shielding experienced by each nucleus individually.[193, 194]

Table 5: Table of selected chemical shift differences for incorporation of fluorine into a ruthenium vinylidene complex. A positive value denotes a downfield shift.

Fluorination			^{1}H NMR Δδ /ppm	^{19}F NMR Δδ /ppm	^{31}P{^{1}H} NMR Δδ /ppm	^{13}C{^{1}H} NMR Δδ/ ppm C_α	C_β
$[Ru(\eta^5\text{-}C_5H_5)(PPh_3)_2(=C=CH_2]^+$	→	$[Ru(\eta^5\text{-}C_5H_5)(PPh_3)_2(=C=CHF]^+$	4.25	-	-3.7	-	-
$[Ru(\eta^5\text{-}C_5Me_5)(PPh_3)_2(=C=CH_2]^+$	→	$[Ru(\eta^5\text{-}C_5Me_5)(PPh_3)_2(=C=CHF]^+$	4.24	-	3.7	18.6	74.0
$[Ru(\eta^5\text{-}C_5Me_5)(PPh_3)_2(=C=CHF]^+$	→	$[Ru(\eta^5\text{-}C_5Me_5)(PPh_3)_2(=C=CF_2]^+$	-	100.9	-2.0	-	-
$[Ru(\eta^5\text{-}C_5Me_5)(dppe)(=C=CH_2]^+$	→	$[Ru(\eta^5\text{-}C_5Me_5)(dppe)(=C=CHF]^+$	4.33	-	-0.9	18.6	71.2
$[Ru(\eta^5\text{-}C_5Me_5)(dppe)(=C=CHF]^+$	→	$[Ru(\eta^5\text{-}C_5Me_5)(dppe)(=C=CF_2]^+$	-	101.8	-1.2	3.9	57.4
$[ClRu(dppe)_2(=C=CH_2]^+$	→	$[ClRu(dppe)_2(=C=CHF]^+$	3.71	-	-0.3	32.5	84.1
$[ClRu(dppe)_2(=C=CHF]^+$	→	$[ClRu(dppe)_2(=C=CF_2]^+$	-	97.4	-1.5	25.8	72.9

2.7.2 Discussion of UV-Vis Spectroscopic Data

The lowest energy absorption bands observed in the UV-Vis absorption spectra across the different ruthenium fluorovinylidene series correspond to the HOMO → LUMO transition (Table 6). These absorption bands undergo a bathochromic shift upon sequential substitution of the proton substituents of the vinylidene with fluorine.

Table 6: Table of observed and calculated lowest energy absorption bands for [Ru(η^5-C_5Me_5)(dppe)(=C=CR^1R^2)]$^+$ and [ClRu(dppe)$_2$(=C=CR^1R^2)]$^+$ vinylidene complexes where R = H or F.

Complex	λ / nm Experimental	λ / nm Calculated
[Ru(η^5-C_5Me_5)(dppe)(CCH_2)]$^+$, **[56]$^+$**	355	378
[Ru(η^5-C_5Me_5)(dppe)(CCHF)]$^+$, **[54a]$^+$**	601	580
[Ru(η^5-C_5Me_5)(dppe)(CCF_2)]$^+$, **[54b]$^+$**	693	698
[ClRu(dppe)$_2$(CCHF)]$^+$, **[58a]$^+$**	-	660
[ClRu(dppe)$_2$(CCF_2)]$^+$, **[58b]$^+$**	823	823

Lowest energy transitions calculated by TD-DFT at the (RI-)BP86/SV(P)//PBE0/def2-TZVPP

Despite discrepancies between the calculated and experimental UV-Vis absorption bands, the shift appears systematic and correctly predicts a bathochromic shift with fluorine incorporation. This suggests the choice of functional and basis set is providing a good approximation for these complexes. The trends observed experimentally agree with the predicted energies from the TD-DFT vertical excitation calculations, giving confidence that the trend applies across all series despite the absence of experimental data for **[58a]$^+$**.

The bathochromic shift upon incorporation of fluorine can be rationalised by the effect a π-donor substituent has on increasing the energy of the HOMO, thus reducing the HOMO-LUMO transition energy. The incorporation of a second fluorine substituent further raises the energy of the HOMO, reducing the HOMO-LUMO transition energy further.

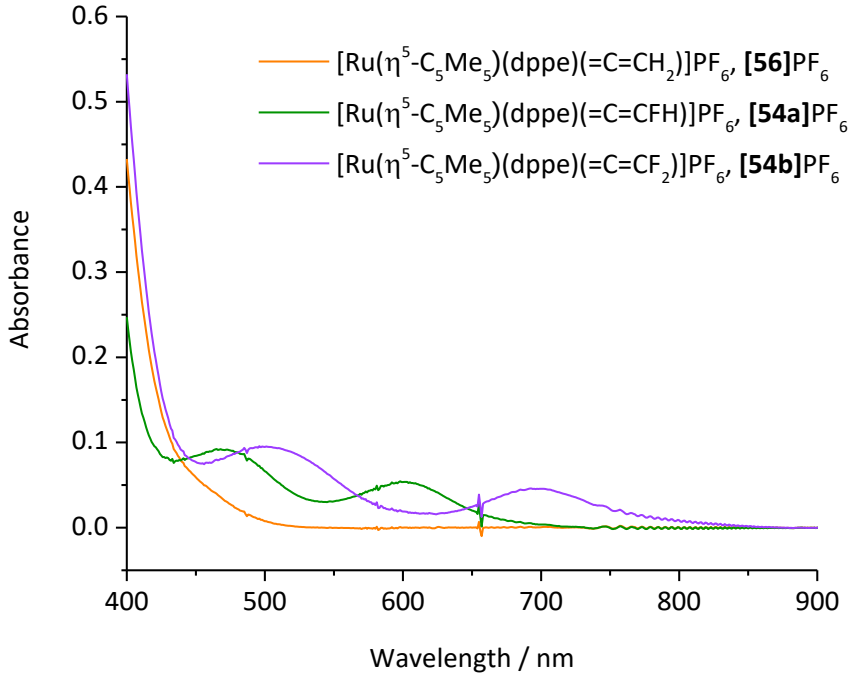

Figure 34: Stacked UV-Vis absorption spectra of $[Ru(\eta^5\text{-}C_5Me_5)(dppe)(=C=CR^1R^2)]^+$ vinylidene complexes (where R = H or F) at 1 mmol dm^{-3} in dichloromethane with a pathlength of 1 cm.

The same trend is observed for the second lowest energy absorption bands of **[54a]**$^+$ and **[54b]**$^+$ (Figure 34). Again, the bathochromic shift can be rationalised by the increased energy of the HOMO-1 through incorporation of a better π-donor ligand, i.e. the second π-donor fluorine substituent results in a better π-donor vinylidene.

The molar absorption coefficient for the lowest energy transition in **[58b]**$^+$ (ε = 0.7 m^2 mol^{-1}) is *ca.* ten-fold smaller than the lowest energy transitions in the half-sandwich complexes (ε = 5.5 and 6.8 m^2 mol^{-1} for **[54a]**$^+$ and **[54b]**$^+$ respectively). The magnitude of the molar absorption coefficients are indicative of d-d transitions for octahedral complexes. The inability to identify the HOMO-LUMO transition of **[58a]**$^+$ in the UV-Vis absorption spectrum over the trace radical contaminants suggests the molar absorption coefficient is comparable in size to that of **[58b]**$^+$.

Replacing the two triphenylphosphine ligands with dppe results in a hypsochromic shift in the dominant transition from 638 nm in **[44a]**$^+$ to 601 nm in **[54a]**$^+$. The replacement of two phenyl substituents with an ethyl backbone upon substitution of the phosphines should result in an increase in the σ-donor, and decreased π-acceptor, ability. Consequently, a reduction in the HOMO-LUMO transition energy, observed as a bathochromic shift in the absorption band, would be expected going from **[44a]**$^+$ to **[54a]**$^+$. Instead we observe an increase in the HOMO-LUMO transition energy contrary to what is expected from a purely

electronic stand point. The observation could again be rationalised by the changes/distortions in the geometry of the coordination sphere of the metal enforced by the bidentate phosphine ligand. Changes in geometry will have an impact on orbital overlap and energy, which in these complexes is sufficiently significant that the HOMO-LUMO transition energy increases despite the change in the electronic nature of the phosphine ligand.

2.7.3 Discussion of Vibrational Stretching Frequencies

Table 7: Table of C=C vibrational stretching frequencies for ruthenium fluorovinylidene complexes bearing hydrogen or fluorine substituents.

Compound	ν C=C / cm^{-1}
$[Ru(\eta^5\text{-}C_5Me_5)(PPh_3)_2(=C=CH_2)]^+$, **[29]**$^+$	1628[190]
	1649
$[Ru(\eta^5\text{-}C_5Me_5)(PPh_3)_2(=C=CHF)]^+$, **[30a]**$^+$	1644
	1661
$[Ru(\eta^5\text{-}C_5Me_5)(dppe)(=C=CH_2)]^+$, **[56]**$^+$	1621[241]
	1664
$[Ru(\eta^5\text{-}C_5Me_5)(dppe)(=C=CHF)]^+$, **[54a]**$^+$	1652
	1675
$[Ru(\eta^5\text{-}C_5Me_5)(dppe)(=C=CF_2)]^+$, **[54b]**$^+$	1725
	1741
$[ClRu(dppe)_2(=C=CH_2)]^+$, **[59]**$^+$	1619[244]
	1649
$[ClRu(dppe)_2(=C=CHF)]^+$, **[58a]**$^+$	1614
	1670
$[ClRu(dppe)_2(=C=CF_2)]^+$, **[58b]**$^+$	1723
	1731

Calculates values at the (RI-)BP86/SV(P) level in italics.

The IR spectroscopic data (Table 7) reveals the vibrational stretching frequency of the vinylidene C=C bond generally increases upon sequential fluorine substitution. This trend is observed across all three metal vinylidene fragments with the exception of **[59]**$^+$ and **[58a]**$^+$ which have essentially the same stretching frequency. However, the gas phase calculation predicts the C=C vibrational frequency should be greater in **[59]**$^+$ than **[58a]**$^+$ as observed in the other complexes. Due to the mechanical coupling of vibrational modes it is non-trivial to determine the force constants and thus changes in bond strength.

2.7.4 Discussion of Crystallographic Data

2.7.4.1 [Ru(η^5-C$_5$Me$_5$)(dppe)(=C=CR^{1}R^2)]$^+$ Complexes

Despite the differences in the chemical shifts observed for incorporation of fluorine into the vinylidene ligand, the crystal structures of **[56]**PF_6, **[54a]**PF_6, and **[54b]**PF_6 do not reveal many statistically significant differences.

Table 8: Table of selected bond lengths and bond angles for [Ru(η^5-C$_5$Me$_5$)(dppe)(=C=CR^{1}R^2)]PF$_6$ vinylidene complexes, where R = H or F.

Bond Length / Å	**[56]**PF_6[241]	**[54a]**PF_6 Orange Polymorph	**[54a]**PF_6 Green Polymorph	**[54b]**PF_6
Ru-C_α	1.85(1)/ 1.84(1)	1.835(4)	1.836(3)	1.840(2)
	1.846	*1.847*	*1.847*	*1.854*
C_α-C_β	1.31/ 1.29(2)	1.302(5)	1.300(5)	1.307(4)
	1.327	*1.338*	*1.338*	*1.339*
C_β-F1	-	1.340(5)/ 1.336(6)	1.329(5)/ 1.218(7)	1.340(4)
		1.358	*1.358*	*1.339*
C_β-F2	-	-	-	1.316(4)
				1.338
Ru-P1	2.2966(5)	2.2974(7)	2.2974(7)	2.3060(6)
	2.344	*2.350*	*2.350*	*2.354*
Ru-P2	2.2975(6)	2.3212(8)	2.3212(8)	2.3277(6)
	2.349	*2.353*	*2.353*	*2.354*
Ru-C(Cp*)	2.248-2.286(2)	2.223-2.306(3)	2.240-2.334(4)	2.230-2.306(2)
Bond Angle / °				
Ru-C_α-C_β	172.9(9)/ 172(1)	169.3(3)	170.2(3)	167.3(2)
	177.0	*175.3*	*175.3*	*174.7*
C_α-C_β-F1	-	126.7(4)/ 130.3(5)	123.7(4)/ 136.3(8)	126.4(3)
		123.7	*123.7*	*124.64*
C_α-C_β-F2	-	-	-	125.6(3)
				124.55
F1-C_α-F2	-	-	-	107.9(2)

				101.80
C_α-Ru-P1	83.5(3)/ 84.5(3)	84.36(11)	84.62(11)	86.06(8)
	87.40	*87.81*	*87.81*	*88.60*
C_α-Ru-P2	92.8(3)/ 92.3(4)	94.14(10)	93.21(11)	96.07(8)
	88.60	*89.35*	*89.35*	*89.40*
P1-Ru-P2	82.75(9)/ 83.6(1)	81.78(3)	82.34(3)	81.65(2)
	84.22	*83.87*	*83.87*	*83.54*

Calculated values at (RI-)BP86/SV(P) level in italics.

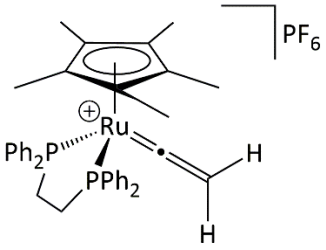

[56]PF_6

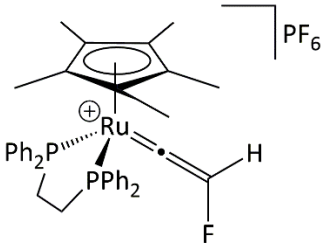

[54a]PF_6

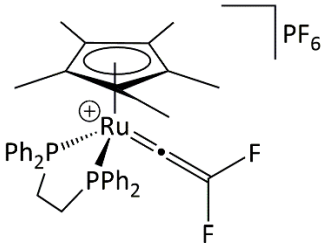

[54b]PF_6

The orange and green polymorphs of **[54a]**PF_6 are statistically identical in terms of bond lengths and most bond angles, however, the C_α-Ru-P2 bond angle is more compressed in the green polymorph while the P1-Ru-P2 is widened as a consequence of crystal packing differences. Additionally, the C_α-C_β-F1 bond angles are statistically different when comparing the two rotamers of each polymorph with one another, demonstrating the range of distortion which can be enforced by crystal-packing effects.

Comparison of **[56]**PF_6 and the two polymorphs of **[54a]**PF_6 do not reveal any statistical differences in the vinylidene Ru-C_α and C_α-C_β bond lengths or the Ru-C_α-C_β bond angle. The DFT gas-phase structure predicts the C=C bond of the vinylidene should undergo elongation upon fluorination while the Ru-C_α is predicted to remain essentially the same.

When comparing the structures of **[54a]**PF_6 and **[54b]**PF_6, the second fluorine substituent increases the distortion of the Ru-C_α-C_β bond angle further away from the ideal geometry. However, the size of distortion in the crystal structure appears to be pronounced by crystal packing effects based on the gas-phase calculations. On the other hand, the C_α-C_β-F angle is statistically identical between **[54a]**PF_6 and **[54b]**PF_6, although increased distortion of the angle is expected by DFT calculations.

It is unclear from the frontier orbitals why the vinylidene ligands undergo increased distortion upon incorporation of fluorine substituents. It is possible that distortion of the

fluorinated vinylidene ligand enhances orbital overlap and mixing, which lowers the energy of the MOs. Alternatively, distortion could arise from the fluorine substituent forming stabilising interactions with neighbouring C-H groups, however only long contacts with neighbouring molecules are observed in the crystal structures. Additionally, the incorporation of a second fluorine substituent would be expected to reduce distortion as both substituents are capable of forming stabilising interactions, and/or are equal in size.

The ruthenium-phosphorus bonds of **[54a]**PF_6 elongate upon substitution of a proton with fluorine from 2.2966(5) Å and 2.2975(6) Å in **[56]**PF_6, to 2.2974(7) Å and 2.3093(8) Å in **[54a]**PF_6. However the observed changes are barely significant. Interestingly, the two ruthenium-phosphorus bonds in both polymorphs of **[54a]** are statistically different in length whereas the same bonds in **[56]**PF_6 are identical. Comparison of the crystallographic data with the data for the gas-phase structure, calculated at the (RI-)BP86/SV(P) level, suggests that the inequivalence of the Ru-P bonds observed in **[54a]**PF_6 is not expected.

Similarly, the ruthenium-phosphorus bond lengths are not equivalent in **[54b]**$^+$ and are elongated compared to the Ru-P bonds in **[54a]**PF_6, from 2.2974(7) Å and 2.3212(8) Å in **[54a]**PF_6 to 2.3060(6) Å and 2.3277(6) Å in **[54b]**PF_6. The P_1-Ru-P_2 bond angle undergoes further compression from 82.34° to 81.65°, while the P_1-Ru=C_α and P_2-Ru=C_α bond angles widen from 84.62° and 93.21° to 86.06° and 96.07° respectively in comparing the green polymorph of **[54a]**PF_6 to **[54b]**PF_6. The same trend is observed in comparing the orange polymorph of **[54a]**PF_6 to **[54b]**PF_6, however the P1-Ru-P2 bond angle remains statistically the same. Comparison of the gas-phase structures again suggests the elongation and inequivalence of the Ru-P bonds are primarily the result of crystal-packing effects. However, the general trend in bond angles observed by X-ray crystallography are supported by the computational values. The P-R bond lengths of the dppe ligand in **[54a]**PF_6 and **[54b]**PF_6 do not undergo statistically significant changes.

2.7.4.2 [ClRu(dppe)$_2$(=C=CR^{1}R^2)]$^+$ Complexes

In contrast to the [Ru(η^5-C$_5$Me$_5$)(dppe)(=C=CR^{1}R^2]$^+$ complexes, the incorporation of fluorine into the [ClRu(dppe)$_2$(=C=CR^{1}R^2)]$^+$ complexes induces statistically significant changes in the bond metrics of the vinylidene ligand according to X-ray crystallography.

Table 9: Table of selected bond lengths and bond angles for [ClRu(dppe)$_2$(=C=CR^{1}R^2)]$^+$ vinylidene complexes, where R = H or F.

Bond Length / Å	**[59]B**F$_4$	**[58a]**PF$_6$	**[58b]**PF$_6$
Ru-C$_\alpha$	1.816 (10)	1.771 (9)/ 1.77 (3)	1.853 (2)
	1.831	*1.833*	*1.844*
C$_\alpha$-C$_\beta$	1.310 (11)	1.327 (11)/ 1.31 (4)	1.259 (3)
	1.329	*1.340*	*1.342*
C$_\beta$-F1	-	1.347 (12)/ 1.28 (4)	1.348 (2)
		1.340	*1.341*
C$_\beta$-F2	-	-	1.356 (2)
			1.341
Ru-P1	2.4179 (7)	2.4158 (11)	2.4143 (5)
	2.454	*2.433*	*2.441*
Ru-P2	2.4251 (7)	2.4342 (12)	2.4337 (5)
	2.462	*2.469*	*2.474*
Ru-P3	2.4179 (7)	2.4205 (12)	2.4242 (5)
	2.467	*2.462*	*2.472*
Ru-P4	2.4251 (7)	2.4289 (12)	2.4341 (5)
	2.433	*2.469*	*2.475*
Ru-Cl	2.476 (3)	2.5125 (19)/ 2.567 (10)	2.4478 (5)
	2.509	*2.502*	*2.492*
Bond Angle / °			
Ru-C$_\alpha$-C$_\beta$	176.8 (11)	173.1 (8)/ 174 (2)	176.69 (17)
	176.31	*173.94*	*174.558*
C$_\alpha$-C$_\beta$-F1	-	121.0 (9)/ 115 (3)	127.42 (19)
		123.46	*125.23*
C$_\alpha$-C$_\beta$-F2	-	-	126.38 (19)
			124.195

F1-C_β-F2	-	-	105.93 (17)
			110.422
Cl-Ru-C_α	178.9 (3)	178.5 (2)/ 175.2 (8)	178.35 (6)
	178.166	*178.89*	*179.826*
C_α-Ru-P1	90.1 (3)	88.6 (2)/ 93.3 (7)	90.06 (6)
	97.129	*92.847*	*92.934*
C_α-Ru-P2	97.6 (3)	96.9 (2)/ 81.5 (8)	99.56 (6)
	98.600	*99.092*	*99.813*
C_α-Ru-P3	89.9 (3)	81.9 (2)/ 99.7 (3)	92.32 (6)
	90.630	*82.532*	*95.729*
C_α-Ru-P4	82.4 (3)	92.8 (2)/ 85.3 (7)	83.13 (6)
	82.616	*94.669*	*82.175*

Calculated values at (RI-)BP86/SV(P) level in italics.

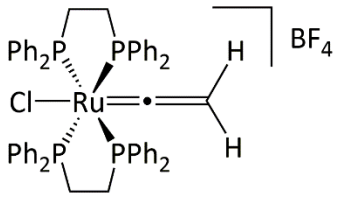

[59]BF_4

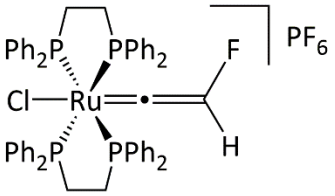

[58a]PF_6

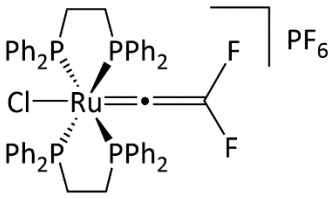

[58b]PF_6

Substitution of one hydrogen in **[59]**$^+$ for fluorine does not result in any statistical changes to the vinylidene or metal-ligand bond lengths, except for the Ru-Cl bond which elongates from 2.476(3) Å to 2.5125(19)/ 2.567(10) Å. Likewise the Ru-C_α-C_β and Cl-Ru-C_α bond angles remains statistically unperturbed.

Upon incorporation of a second fluorine substituent, the Ru-C_α bond length elongates considerably from 1.771(9) to 1.853(2) Å, while the vinylidene C_α-C_β bond shortens from 1.327(11) Å to 1.259(3) Å, in contrast to the trends observed between **[59]**BF_4 and **[58b]**PF_6. However, the Ru-C_α and C_α-C_β bond lengths of the more disordered form of **[58b]**PF_6 (1.77 (3) Å and 1.31 (4) Å respectively) are statistically identical to the same bonds in **[59]**BF_4 due to larger standard deviations in the data. Elongation of the Ru-C_α bond and shortening C_α-C_β bond is also observed in comparing **[59]**BF_4 with **[58b]**PF_6, although these changes in bond metrics are believed to be pronounced by crystal packing effects based on the gas-phase structures. The C-F bond lengths, as observed with **[54b]**PF_6, remain statistically identical between **[58a]**PF_6 and **[58b]**PF_6. However, the DFT-gas-phase structures predict that an elongation C_α-C_β bond is expected, contrary to the observed experimental evidence. This

trend is also observed in the calculated gas-phase structures of **[56]**PF_6, **[54a]**PF_6, and **[54b]**PF_6. It is not readily apparent why the predicted bond lengths differs significantly from the experimental values. The changes in bond length upon incorporation of fluorine substituent is not expected to arise from crystal packing effects due to the higher energy required versus distortion of bond angles.

The C_α-C_β-F bond angle in **[58a]**PF_6 widens from 121.0(9)°/ 115(3)° to 127.42(19)° and 126.38(19)° upon incorporation of the second fluorine substituent, as supported by the gas-phase calculations. The widening of the angle is likely the result of enhancing orbital overlap and mixing through changes to the hybridisation of the β-carbon. This is supported by a compressed F-C-F vinylidene bond angle of 105.93(17)° which indicates increased p-character of the C-F bonds.

As with **[59]**BF_4 and **[58a]**PF_6, the Ru-P bond lengths of **[58b]**PF_6 remain statistically identical suggesting the synergic bonding between the metal and the phosphines remains unperturbed.

The shortening of the Ru-Cl bond from 2.5125(19)/ 2.567(10) Å in **[58a]**PF_6 to 2.4478(5) Å in **[58b]**PF_6 is supported by the computational data. The compression can be rationalised by the enhanced π-acceptor ability of the vinylidene ligand with the incorporation of a fluorine substituent, as such there is greater donation from the π-donor chloride.

2.7.4.3 Comparison of Crystallographic Data Between Fragments [54b]PF_6 and [58b]PF_6

A compression of the geminal F-C-F angle is observed in both **[54b]**PF_6 (107.9°) and **[58b]**PF_6 (105.93°) which is consistent with the compression observed for various geminal-difluoro groups including the F-C-F angle in the diiron difluoro-vinylidene complex **[5]** (106.2°).[219] On the basis of electrostatic repulsion, a widening of the F-C-F angle would be expected, instead compression of the angle to that of a higher p-character hybridisation is observed. Organic sp^2 F-C-F bond angles tend toward the ideal sp^3-hydridised angle as a consequence of increased p-character of the C-F bond giving rise to the '*gem*-difluoro effect'.[247, 248] The change in hybridisation is more pronounced with the incorporation of a metal centre. However, compression of the R-C-R bond angle observed in the crystallographic data of **[54b]**PF_6 and **[58b]**PF_6 appears extenuated by crystal-packing effects on the basis of the gas-phase calculations. In both cases compression is predicted at 101.8 and 110.4° respectively.

2.8 Comparison of the Ruthenium Fluoroalkynyl Complexes

In stark contrast to the ready oligomerisation of organic fluoroalkynes, the ruthenium fluoroalkynyl complexes **[28b]**, **[55b]**, and **[57b]** show prolonged stability in the condensed phase. Complexes **[55b]** and **[57b]** exhibited high stability as solids in air or under nitrogen and in solution under an inert atmosphere for up to two months, with only minor decomposition being observed in the case of **[55b]**. To better understand the origin of this stability and assess the differences in structure and bonding between the metal fluoroalkynyl complexes and the organic fluoroalkynes, spectroscopic, crystallographic, and computational approaches have been explored.

2.8.1 Energies of Dimerisation

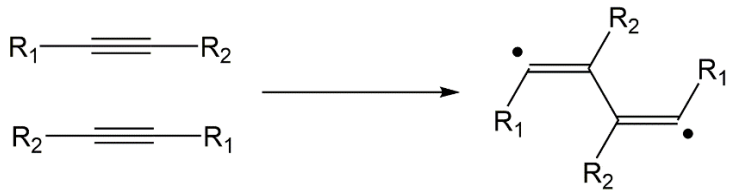

Table 10: Table of free energies for formation of diradical dimer from alkynes.

R_1	R_2	ΔG_{298} / kJ mol^{-1}
H	H	+128
F	H	+14
F	F	-86
[55a], Ru(η^5-C_5Me_5)(dppe)	H	+131
[55b], Ru(η^5-C_5Me_5)(dppe)	F	-18

Free energies calculated at the ((RI-)PBE0-D3/def2-TZVPP//(RI-)BP86/SV(P) level by Dr John Slattery.

The spontaneous oligomerisation of fluoroalkynes is attributed to a readily accessible low-lying diradical intermediate formed through dimerisation of two fluoroalkyne molecules. The diradical product is calculated to be thermodynamically more stable than the individual fluoroalkyne molecules for 1,2-difluoroethyne (ΔG_{298} = -86 kJ mol^{-1}), and slightly thermodynamically less stable for fluoroethyne (ΔG_{298} = +14 kJ mol^{-1}) at the ((RI-)PBE0-D3/def2-TZVPP//(RI-)BP86/SV(P) level. Although higher in energy for fluoroethyne, the diradical product is readily accessible at room temperature. In contrast the diradical product formed by dimerisation of ethyne is significantly unfavourable thermodynamically compared to the fluoroalkynes (ΔG_{298} = +128 kJ mol^{-1}). The thermodynamic unfavorability of

dimerisation in the absence of a fluorine substituent rationalises the stability of other alkynes toward oligomerisation. As mirrored by the organic alkynes, ethyne, 1-fluoroethyne and 1,2-difluoroethyne, the dimerisation of **[55a]** is calculated to be thermodynamically disfavoured (ΔG_{298} = +131 kJ mol^{-1}) while the dimerisation of **[55b]** is predicted to be thermodynamically favoured (ΔG_{298} = -18 kJ mol^{-1}). These calculations predict that the metal fluoroalkynyl complex should, from a thermodynamic argument, undergo dimerisation. This suggests that the sterically bulky Cp* and dppe ancillary ligands provide sufficient kinetic stability to the alkynyl ligand to inhibit the dimerisation pathway. It is believed for the same reasons that **[28b]** and **[57b]** do not undergo dimerisation.

The barrier to dimerisation in the simplified fluoroalkynyl complex, [Ru(η^5-C_5Me_5)($H_2PCH_2CH_2PH_2$)(C≡CF)], is predicted to be similar in energy to the barrier for 1,2-difluoroethyne ($\Delta G_{298}^{\ddagger}$ = + 80 kJ mol^{-1} vs + 68 kJ mol^{-1} respectively). Incorporation of the full dppe ligand further increases the barrier to dimerisation by *ca.* 50 kJ mol^{-1} according to the potential energy surface scan at the PBE0/def2-TZVPP//BP86/SV(P) level.

2.8.2 Discussion of NMR Spectroscopic Data

As reported previously for **[55b]**, the fluorine chemical shifts observed for **[28b]** and **[57b]** (Table 12) are more in line with the observed fluorine chemical shift for difluoroethyne (δ_F -261.3),[228] 1-chloro-2-fluoroethyne (δ -219),[229] and perfluoropropyne (δ -203)[230] than the fluorine resonances of the fluorocarbynes complexes **[60]** (δ 78.15)[249] and **[61]**$CHB_{11}Cl_{11}$ (δ 66.2)[250] which are reported at significantly downfield chemical shifts (Figure 35).

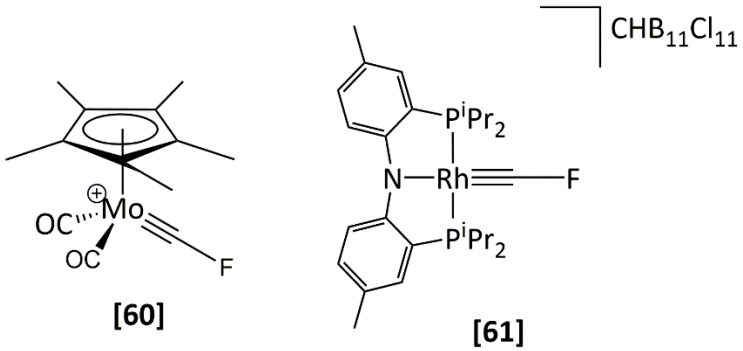

[60] **[61]**

Figure 35: Two examples of metal fluorocarbyne complexes.

Remarkably substitution of proton or carbon substituents with fluorine in ruthenium alkynyl complexes results in a significant upfield shift of *ca.* 70 ppm in the α-carbon resonances of the alkynyl ligands. This is in stark contrast to carbon resonances observed for the fluorovinylidene complexes whereby a large downfield shift is observed compared to the

protiovinylidene analogues. It is evident that substitution with fluorine results in a significant change to the shielding tensors, resulting in a large variation in the isotropic chemical shift compared to other ruthenium alkynyl complexes.

On the other hand, the β-carbon resonances of the fluoroalkynyl ligands are observed at similar chemical shifts to the protio- and carbon-analogues. This observation would be unexpected given the general observation that carbons adjacent to more electronegative nuclei display deshielded chemical shifts. However, given the significant upfield shift of the α-carbon resonances it is clear this generalised rule does not apply to these complexes. The similarity in the β-carbon chemical shifts for the fluorine-substituted alkynyl ligands compared to other substituted alkynyl ligands suggest the magnetic environment around the β-carbon is relatively similar, whereas the magnetic environment surrounding the α- carbon is significantly different.

The carbon chemical shifts of the alkynyl ligands appear to be insensitive to the electronic properties of the metal fragment they are coordinated to. The α- carbon chemical shifts for **[55b]** and **[57b]** are observed around δ 37, while the β-carbon chemical shifts for **[28b]**, **[55b]**, and **[57b]**, are observed at around δ 112 in the ^{13}C NMR spectra. Despite the clear differences in the magnetic environment around the fluoroalkynyl ligands with respect to the protioalkynyl ligands, it appears that magnetic environments experienced within the fluoroalkynyl series are essentially identical. This further supports the argument that the metal fragments provide kinetic stabilisation rather than electronic stabilisation to the ligand.

To the best of our knowledge, ^{13}C NMR spectroscopic data for organic 1-fluoroalkynes have not been reported, meaning comparison or comment on the unusual α- carbon chemical shifts of **[55b]** and **[57b]** cannot be made at present. However, three examples of fluoro-ynamides, **[62]**, have recently been reported bearing fluoroethyne substituents. The chemical shifts for the α- and β-carbons, with respect to the nitrogen substituent, were reported at *ca.* δ 98 and 162 respectively (Table 11). These chemical shifts are significantly different to those observed for **[28b]**, **[55b]** and **[57b]**, being *ca.* 60 and 50 ppm downfield to our reported α- and β-carbon resonances respectively. Furthermore, the fluorine chemical shifts of the ynamides are reported at *ca.* δ -90, which are again significantly shifted compared to the fluorine environments observed for our fluoroalkynyl complexes (*ca*. δ -180) and, more importantly, difluoroethyne (δ -261) and 1-chloro-2-fluoroethyne (δ -218). The chemical shifts reported by Meiresonne *et al*.[251] are more typical of fluoroalkenes.

However, due to the limited examples of fluoroalkynes and the different electronic nature of the halogen, nitrogen, and ruthenium substituent, the nature of the carbon chemical shifts cannot be compared with confidence.

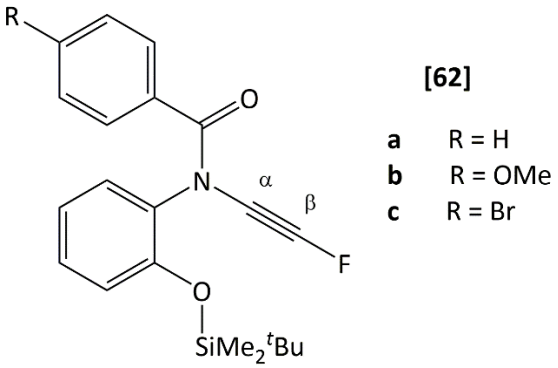

Figure 36: Three examples of fluoroynamides reported by Meiresonne *et al*.[251]

Table 11: NMR spectroscopic parameters for ynamides ligand of [62]

	$^{13}C\{^{1}H\}$ NMR / ppm		^{19}F NMR
	α	β	/ ppm
[62a]	98.5	162.8	-89.8
	(d, *J* = 55 Hz)	(d, *J* = 275 Hz)	
[62b]	98.7	162.4	-89.9
	(d, *J* = 54 Hz)	(d, *J* = 274 Hz)	
[62c]	89.5	162.5	-89.5
	(d, *J* = 55 Hz)	(d, *J* = 274Hz)	

Table 12: Table of selected chemical shifts for organic and organometallic 1-fluoroalkynes.

Compound	^{1}H NMR / ppm	^{19}F NMR / ppm	^{31}P{^{1}H} NMR / ppm	^{13}C{^{1}H} NMR C_α / ppm	^{13}C{^{1}H} NMR C_β / ppm
F-C≡C-F	-	-261.3, (287 Hz)[228]	-	-	-
Cl-C≡C-F	-	-219[252]	-	-	-
CF_3-C≡C-F	-	-203.0, (259 Hz)[229]	-	-	-
[Ru(η^5-C_5Me_5)(PPh_3)$_2$(C≡CH)], **[28a]**	2.20	-	50.5	119.8[237]	96.7[237]
[Ru(η^5-C_5Me_5)(PPh_3)$_2$(C≡CF)], **[28b]**	-	-186.9	50.9	*Not identified*	113.5 (336 Hz)
[Ru(η^5-C_5Me_5)(dppe)(C≡CH)], **[55a]**	1.57	-	82.2	120.6[241]	93.0[241]
[Ru(η^5-C_5Me_5)(dppe)(C≡CF)], **[55b]**	-	-189.4	81.9	36.8 (42 Hz)	111.4 (332 Hz)
trans-[ClRu(dppe)$_2$(C≡CH)], **[57a]**	1.30	-	49.2	131.1[244]	100.6[244]
trans-[ClRu(dppe)$_2$(C≡CF)], **[57b]**	-	-182.1	49.7	36.7 (36 Hz)	111.5 (327 Hz)

C-F Coupling in parentheses.

2.8.3 Discussion of UV-Vis Spectroscopic Data

Table 13: Table of observed and calculated lowest energy absorption bands.

Compound	Observed λ / nm	Calc. λ / nm
[Ru(η^5-C$_5$Me$_5$)(dppe)(C≡CH)], **[55a]**	398	428
[Ru(η^5-C$_5$Me$_5$)(dppe)(C≡CF)], **[55b]**	396	434
trans-[ClRu(dppe)$_2$(C≡CH)], **[57a]**	376	413
trans-[ClRu(dppe)$_2$(C≡CF)], **[57b]**	382	419

Lowest energy transitions calculated by TD-DFT at the (RI-)BP86/SV(P)//PBE0/def2-TZVPP. Measurements taken at 1 mM concentration in dichloromethane.

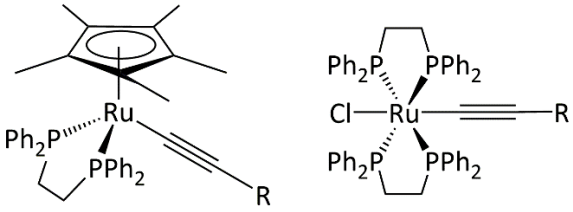

[55]
a, R = H
b, R = F

[57]
a, R = H
b, R = F

The similar wavelengths observed for the UV-Vis absorption bands of **[55a]** and **[55b]** (Table 13) indicates that the fluorine substituent does not significantly affect the HOMO-LUMO transition energy with respect to the protio-analogue. This is surprising given the significantly different electronic properties of hydrogen compared to fluorine. The presence of a π-donor would be expected to raise the energy of the HOMO thus lowering the HOMO-LUMO transition energy, resulting in a bathochromic shift.

The lowest energy transitions of **[57a]** and **[57b]**, observed at 376 nm and 382 nm respectively, show a similar trend to the [Ru(η^5-C$_5$Me$_5$)(dppe)] complexes. While a bathochromic shift is observed, the small magnitude of this shift (*ca.* 6 nm) indicates fluorine has a minor effect on raising the energy of the HOMO comparative to the marked effect fluorine has on the transition energy of fluorovinylidene complexes. Additionally, the similar absorption wavelength observed for the HOMO-LUMO transitions of **[55b]** and **[57b]** indicate that the electronic nature of the metal fragment does not have a significant impact on the HOMO-LUMO transition energy.

The substantial mixing of the MOs, as a consequence of the low symmetry of the metal alkynyl complexes, will significantly alter the MO contributions to chemical shielding

compared to the organic fluoroalkynes. Ramsey's model arbitrarily splits chemical shielding into a diamagnetic contribution and a paramagnetic contribution. The diamagnetic contribution is the shielding induced by an external field in the ground state only and is often insensitive to changes of environment around the nucleus (dominated by core atomic orbitals). The paramagnetic contribution arises from mixing of the ground state with different excited states and is nearly always deshielding. The contribution each MO provides to the shielding of the molecule is dominated by the energy difference between the mixing pair. Consequently, the largest contributions to paramagnetic shielding are observed between mixing MOs with the smallest energy difference, i.e. it is approximated that the paramagnetic contribution is inversely proportional to the HOMO-LUMO energy gap when considering occupied-virtual MO mixing. In the case of the fluorovinylidene complexes, in which significant deshielding of the α- and β-carbon chemical shifts is observed, this rule appears true. Incorporation of fluorine raises the energy of the HOMO, lowering the HOMO-LUMO energy gap, as observed in UV-Vis spectroscopy, enhancing the paramagnetic contribution from mixing MOs.[193, 194]

The small bathochromic shift of the HOMO-LUMO absorption bands for **[55b]** and **[57b]** (observed experimentally and expected computationally) should result in deshielding of the alkynyl ligand based on the assumption that a smaller HOMO-LUMO energy gap leads to enhance paramagnetic shielding. However, in the ruthenium fluoroalkynyl complexes, the α-carbon chemical shift undergoes significant shielding compared to the protio-analogues, while the β-carbon chemical shift remains unperturbed. This would instead imply an increase in the HOMO-LUMO energy gap due to reduced paramagnetic contribution. It is clear that this approximation cannot be applied to rationalise the observed chemical shifts in **[55b]** and **[57b]**. It is possible that the shielding contributions from occupied-occupied MO mixing are of increased significance in these complexes than the occupied-virtual MO mixing which are more sensitive to HOMO-LUMO transition energy changes.[193, 194]

2.8.4 Discussion of Vibrational Frequencies and Crystallographic Data

Table 14: Table of vibrational frequencies for organic and organometallic fluoroalkynes

Compound	ν C≡C / cm^{-1}	ν C-H or C-F / cm^{-1}
H-C≡C-H[253]	1974	3374 and 3287
	2085	*3525 and 3421*
H-C≡C-F[254]	2240	3358, 1057, 856, and 583
	2357	*3450, 1119, and 651*
F-C≡C-F[255]	2437	1349 and 794
	2591	*1419 and 820*
[Ru(η^5-C_5Me_5)(PPh_3)$_2$(C≡CH)], **[28a]**[237]	1925	-
	1948	-
[Ru(η^5-C_5Me_5)(PPh_3)$_2$(C≡CF)], **[28b]**	2148	1054
	2176	*1049*
[Ru(η^5-C_5Me_5)(dppe)(C≡CH)], **[55a]**[241]	1925	3269
	2056	*3489*
[Ru(η^5-C_5Me_5)(dppe)(C≡CF)], **[55b]**	2148	1068
	2307	*1115*
trans-[ClRu(dppe)$_2$(C≡CH)], **[57a]**[244]	1932	3280
	1950	*3360*
trans-[ClRu(dppe)$_2$(C≡CF)], **[57b]**	1970	1034
	2184	*1050*

Calculated values at the (RI-)PBE0/SV(P) level noted in italics

The vibrational frequency of the C≡C bond of the organic 1-fluoroalkynes increases upon incorporation of fluorine. However, it is unclear whether this corresponds to an increase in bond strength due to the mechanical coupling between vibrational modes.[256, 257] This trend is mimicked in the metal fluoroalkynyl complexes suggesting that the fluorine induces the same changes in bonding as in the organic alkynes. The C-F vibrational frequencies in the metal fluoroalkynyl complexes are similar to the C-F stretch in the organic fluoroalkynes.

Table 15: Table of selected bond lengths (Å) and bond angles (°) for [Ru(η^5-C$_5$Me$_5$)(dppe)(C≡CR)] alkynyl complexes, where R = H or F.

	[Ru(η^5-C$_5$Me$_5$)(dppe)(C≡CH)] **[55a]**[241]	[Ru(η^5-C$_5$Me$_5$)(dppe)(C≡CF)] **[55b]**
Ru-C$_\alpha$	2.015 (2)	2.036 (3)
	2.002	*2.021*
C$_\alpha$-C$_\beta$	1.202 (3)	1.187 (4)
	1.243	*1.239*
C$_\beta$-F	-	1.324 (4)
		1.31
Ru-P1	2.2649 (5)	2.2677 (7)
	2.303	*2.301*
Ru-P2	2.2592 (6)	2.2570 (7)
	2.297	*2.296*
Ru-C(Cp*)	2.215-2.269 (2)	2.210-2.264 (3)
	2.264-2.309	*2.262.301*
Ru-C$_\alpha$-C$_\beta$	173.7 (2)	171.8 (3)
	176.82	*178.115*
C$_\alpha$-C$_\beta$-F	-	177.2 (4)
		178.079
C$_\alpha$-Ru-P1	87.50 (6)	87.72 (8)
	86.02	*85.59*
C$_\alpha$-Ru-P2	85.27 (6)	86.40 (9)
	84.97	*84.66*
P1-Ru-P2	82.71 (2)	82.56 (3)
	84.45	*84.56*

Calculated values at the (RI-)BP86/SV(P) level in italics.

Comparison of the crystal structures for **[55a]** and **[55b]** reveals that substituting hydrogen with fluorine results in the elongation of the Ru-C bond length from 2.015(2) Å in **[55a]** to 2.036(3) Å in **[55b]**. This is supported by the gas phase structures optimised at the (RI)-BP86/SV(P) level. The C≡C bond lengths of the alkynyl complexes are statistically indistinguishable upon substitution of hydrogen with fluorine, while the gas phase calculations predict that a shortening of the C-C bond is expected.

As observed in the fluorovinylidene complexes, the Ru-C_α-C_β bond angle undergoes increased distortion from 173.2(2)° in **[55a]** to 171.8(3)° in **[55b]** upon substitution with fluorine. The distortion of the alkynyl ligand could be rationalised by crystal packing effects due to the larger Van der Waals' radius of fluorine (Rowland, 1.46 Å), coupled with the ability of fluorine to form weak contacts with neighbouring C-H groups within the crystal lattice. Analysis of the packing in the crystal of **[55b]** reveals two possible long-range contacts (2.668 and 2.681 Å) between the fluorine substituent and neighbouring protons of the phenyl rings.

Although the gas-phase calculations predict that the Ru-C_α-C_β and C_α-C_β-R bond angles should be more linear than the crystallographic values, increased distortion upon fluorination is still predicted. This suggests the electronic effects of fluorine play an important role. Distortion of the alkynyl ligand could improve orbital overlap or mixing between the π-system and the lone pairs of fluorine, due to the directionality of the p-orbitals compared to the s-orbital of hydrogen.

The ruthenium-phosphorus bond lengths in **[55a]** are statistically inequivalent with respect to one another and is also true for the Ru-P bond lengths in **[55b]**. However, comparing the Ru-P bonds in **[55a]** and **[55b]** with each other reveals that they are statistically identical. The P_1-Ru-P_2 and P-Ru-C_α bond angles remain statistically the same, along with the Ru-C(Cp*) bond lengths. This indicates that the fluorine substituent does not significantly alter the ability of ruthenium to back-bond.

Synergic back-bonding from the ruthenium to the alkynyl fragment is expected to be minimal due to the high energy of the π-antibonding orbitals of the alkynyl fragment. As such, the apparent lack of change in the C≡C bond length can be rationalised by the fact that increased back-bonding, due to the π-donating ability of fluorine, is not expected to result in geometric changes to the alkynyl ligand.

The strong electron-withdrawing inductive effect will reduce the C-C π-bonding interaction and subsequently reduce, to a lesser extent, the Ru-C π-antibonding interaction of the HOMO. This would manifest as a compression of the Ru-C bond and elongation of the C-C bond upon fluorination.

Table 16: Table of selected bond lengths (Å) and bond angles (°) for [ClRu(dppe)$_2$(C≡CR)] alkynyl complexes, where R = H or F.

	trans-[ClRu(dppe)$_2$(C≡CH)], **[57a]**[258]	*trans*-[ClRu(dppe)$_2$(C≡CF)], **[57b]**
Ru-C_α	1.936 (5)	1.854 (7)
	1.990	*2.011*
C_α-C_β	1.190 (5)	1.251 (9)
	1.245	*1.240*
C_β-F	-	1.300 (8)
		1.312
Ru-P1	2.3769 (4)	2.3747 (5)
	2.409	*2.404*
Ru-P2	2.3575 (4)	2.3545 (5)
	2.377	*2.375*
Ru-P3	2.3769 (4)	2.3746 (5)
	2.399	*2.398*
Ru-P4	2.3575 (4)	2.3546 (5)
	2.399	*2.395*
Ru-Cl	2.5838 (14)	2.605 (2)
	2.548	*2.539*
Ru-C_α-C_β	177.7 (4)	175.8 (5)
	175.86	*174.17*
C_α-C_β-F	-	166.1 (9)
		174.72
C_α-Ru-Cl	175.57 (12)	173.22 (18)
	178.8	*179.4*
C_α-Ru-P1	94.78 (11)	87.39 (15)
	94.98	*88.65*
C_α-Ru-P2	85.22 (11)	87.38 (14)
	79.09	*80.16*
C_α-Ru-P3	94.78 (11)	92.62 (15)
	97.99	*98.04*
C_α-Ru-P4	85.22 (11)	92.62 (14)
	88.25	*94.48*

Calculated values at the (RI-)BP86/SV(P) level in italics.

A comparison of the crystallographic data for **[57a]** and **[57b]** reveals the opposite trend in changes to bond lengths, whereby the Ru-C bond shortens from 1.936(5) Å to 1.854(7) Å and the C-C bond elongates from 1.190(5) Å to 1.251(9) Å upon fluorination. The bond metrics in the [Ru(η^5-C_5Me_5)(dppe)] and [ClRu(dppe)$_2$] fragments would have been expected to show the same trend, considering the pentamethylcyclopentadienyl ligand and the combination of a dppe and chloride ligand are isoelectronic fragments, in so far as a negatively charged 6 electron donor is replaced with a negatively charged 2 electron donor and neutral 4 electron donor. It is possible that the electronic structure is significantly perturbed upon fluorination that the opposite trend is observed. However, the similarity in the fluorine and α- and β-carbon chemical shifts of **[55b]** and **[57b]** suggests that the chemical shielding, and to an extent the electronic structure, should be comparable when considering the alkynyl ligand. The gas-phase structure calculated at the (RI)-BP86/SV(P) level predicts an elongation of the Ru-C bond and shortening of the C-C bond is expected with a fluorine substituent, in contrast to the experimentally observed changes. These changes are again unlikely to arise from crystal packing effects given bond angle distortions are expected to be lower in energy than changes in bond length (bending modes in IR spectroscopy are observed at lower energy frequencies than stretching modes).

Interestingly the Ru-C-C bond angles in **[57a]** and **[57b]** are more linear than the same bond angles in **[55a]** and **[55b].** This again is likely the result of crystal packing as the gas-phase calculations predict a greater similarity in the Ru-C-C bond angle across the series. The C-C-F bond angle of **[57b]** is significantly distorted at 166.1(9)° compared to the calculated gas-phase structure (174.7°) and **[55b]** (177.2(4)°). The significant distortion is believed to be result of crystal packing effects. Inspection of the crystal structure of **[57b]** reveals two contacts between the alkynyl fluorine and neighbouring C-H groups at *ca.* 2.377 Å and 2.358 Å away, which are considerably shorter contacts compared to those observed in the crystal structure of **[55b]**. This, coupled with the increased steric demand of the dppe ligands in **[57b]**, provides a rationale for the observed changes to the alkynyl ligand in the crystal structure.

The ruthenium-chloride bond length undergoes elongation upon incorporation of fluorine from 2.5838(14) Å to 2.605(2) Å. However, the gas-phase structure predicts that a shortening of the Ru-Cl bond is expected, indicating the observed change could again be an effect of crystal packing.

2.8.5 Discussion of Protio- and Fluoro-alkyne Frontier Orbitals

To rationalise the observed changes in the geometric and spectroscopic data upon incorporation of fluorine, a computational evaluation of the molecular frontier orbitals for ethyne, 1-fluoroethyne, 1,2-difluoroethyne, **[55a]** and **[55b]** was conducted. In collaboration with Dr. David Tew, the electronic structures were optimised using explicitly correlated Brueckner coupled cluster theory (BCCD(T)-F12), and Kohn-Sham DFT at the (RI)-PBE0/def2-TZVPP level independently. Due to the high computational cost of the *ab initio* calculations, the pentamethylcyclopentadienyl and dppe ligands were replaced with the simpler cyclopentadienyl and *bis*-phosphine (PH_3) ligands respectively. Although the Brueckner orbitals (BOs) derived from BCCD(T)-F12 were qualitatively similar to the Kohn-Sham orbitals, the calculated wavefunction from the *ab initio* approach is believed to be modelling the electronic structure more accurately based on the calculated BO energies being closer to the experimental data from photoelectron spectroscopy. The Brueckner orbitals for the organic alkynes, ethyne, fluoroethyne, and 1,2-difluoroethyne, and complexes **[55a]** and **[55b]** are shown below.

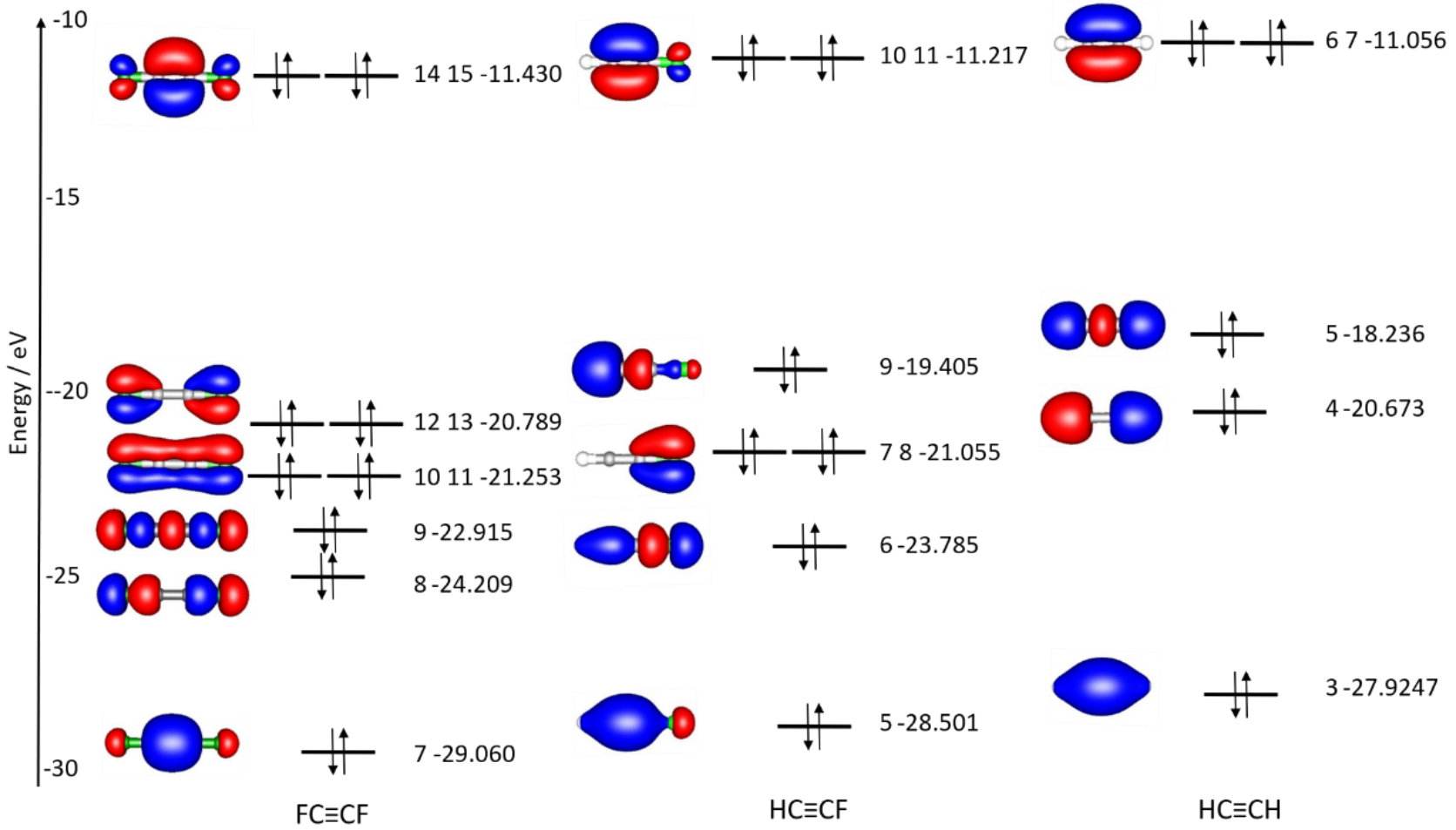

Figure 37: Brueckner orbitals of ethyne, fluoroethyne, and difluoroethyne derived from the optimised electronic structures using explicitly correlated Brueckner coupled cluster theory (BCCD(T)-F12).

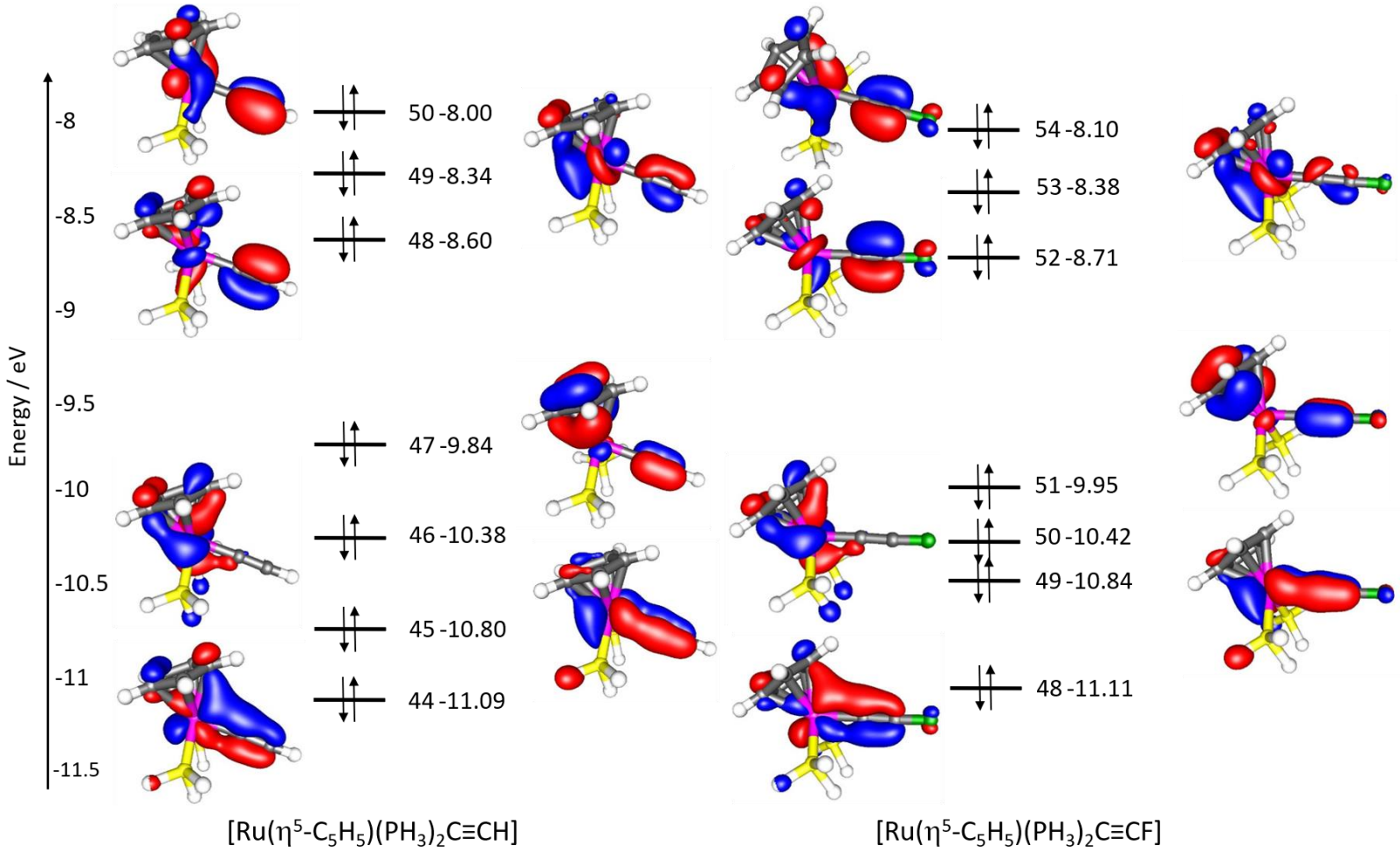

Figure 38: Brueckner orbitals of ethyne, fluoroethyne, and difluoroethyne derived from the optimised electronic structures using explicitly correlated Brueckner coupled cluster theory (BCCD(T)-F12).

Firstly, consideration of the frontier orbitals for ethyne, 1-fluoroethyne, and 1,2-fluoroethyne reveals the highest occupied orbitals consist of C-F π-antibonding and C-C π-bonding interactions. These C-F π-antibonding interactions provide a rationale for the weaker than expected C-F bond of sp-hybridised systems compared to sp^2- and sp^3-hybridised systems.

Orbitals 10 and 11 of 1,2-difluoroethyne are fully π-bonding between the two fluorine and two carbon atoms, while orbitals 7 and 8 of 1-fluoroethyne consist of only the single C-F π-bonding interaction. The weakening of the C-F bonds in 1,2-difluoroethyne can be rationalised by the electron density being shared across the C-C bond in these π-orbitals, whereas this additional C-C interaction is not present in 1-fluoroethyne. The additional C-C π-bonding interactions of orbitals 10 and 11 of 1,2-difluoroethyne are compensated by the two π-antibonding interactions of orbitals 12 and 13. Consequently, of the twelve π electrons (orbitals 10-15), four electrons are involved in C-C antibonding interactions, resulting in an expected net π-bond order of 2. However, the C-C π-antibonding orbitals, 10 and 11, are largely based on the fluorine substituents which are C-F π-bonding. This would be expected to diminish the effect of these orbitals on the C-C bond order, resulting in a shortening of the C≡C bond in the fluoroalkynes compared to the protioalkynes.

Although substantial mixing of the orbitals and loss of π-degeneracy is observed due to low symmetry, the frontier orbitals for [Ru(η^5-C_5H_5)$(PH_3)_2$(C≡C-H)] and [Ru(η^5-C_5H_5)$(PH_3)_2$(C≡C-F)] broadly resemble the orbitals for 1-fluoroethyne and 1,2-difluoroethyne respectively. Notably orbitals 48-50 of [Ru(η^5-C_5H_5)$(PH_3)_2$(C≡C-H)] and orbitals 52-54 of [Ru(η^5-C_5H_5)$(PH_3)_2$(C≡C-F) which display π-antibonding interactions between the d-orbitals of ruthenium and π-system of the alkynyl ligand, along with the same C-F π-antibonding interactions in the later complex. Therefore, the rationalisation for the strengthening of the C≡C bond in the organic fluoroalkynes could be applied to the metal alkynyl complexes to rationalise the changes in the alkynyl ligands.

2.8.6 Bond-dissociation Energies

To further assess the thermodynamic nature of the C-F bond in **[28b]**, **[55b]**, and **[57b]** the bond dissociation energies (BDEs) for C-F and C-H bonds across sp, sp^2, and sp^3 hybridised systems were calculated in conjunction with Dr. Jason Lynam using a modified methodology to that reported by Perutz and Eisenstein.[259, 260] The BDEs were calculated at the (RI-)PBE0/def2-TZVPP level, with the exception of the ruthenium complexes whose geometries and frequencies were optimised at the (RI-)PBE0/SV(P) level and a subsequent single point calculation performed at the (RI-)PBE0/def2-TZVPP level. The results were verified by comparison of the calculated BDES, at both the G4 and (RI-)PBE0/def2-TZVPP level, with available experimental data. Calibration was conducted using simple hydrocarbons, fluorocarbons and species displaying significant electron correlation, e.g. dihalogens and peroxide, as expected in fluoroalkynes. Both the G4 and (RI-)PBE0/def2-TZVPP BDEs are in good agreement with one another and fit the experimental data well (see accompanying CD).

Table 17: Table of calculated sp, sp^2, and sp^3 C-F and C-H bond dissociation energies (kJ mol^{-1}).

Hybridisation	Molecule	R = H	R = F
sp^3	H_3C-R	419	444
	$MeCH_2$-R	398	452
	$PhCH_2$-R	355	398
	$H_2C=CHCH_2$-R	341	385
sp^2	$H_2C=CH$-R	439	505
	$H_2C=C(Me)$-R	423	503
	E-MeCH=CH-R	443	507
	Z-MeCH=CH-R	445	507
	Ph-R	449	517
	Me-C_6H_4-4-R	450	518
	NO_2-C_6H_4-4-R	452	519
	MeC(O)-R	353	497
sp	HC≡C-R	544	547
	MeC≡C-R	544	541
	PhC≡C-R	522	520
	CF_3C≡C-R	550	554
	[Ru(η^5-C_5Me_5)(PPh_3)$_2$(C≡C-R)]	481	476
	[Ru(η^5-C_5Me_5)(dppe)(C≡C-R)]	519	517
	Trans-[ClRu(dppe)$_2$(C≡C-R)]	458	456

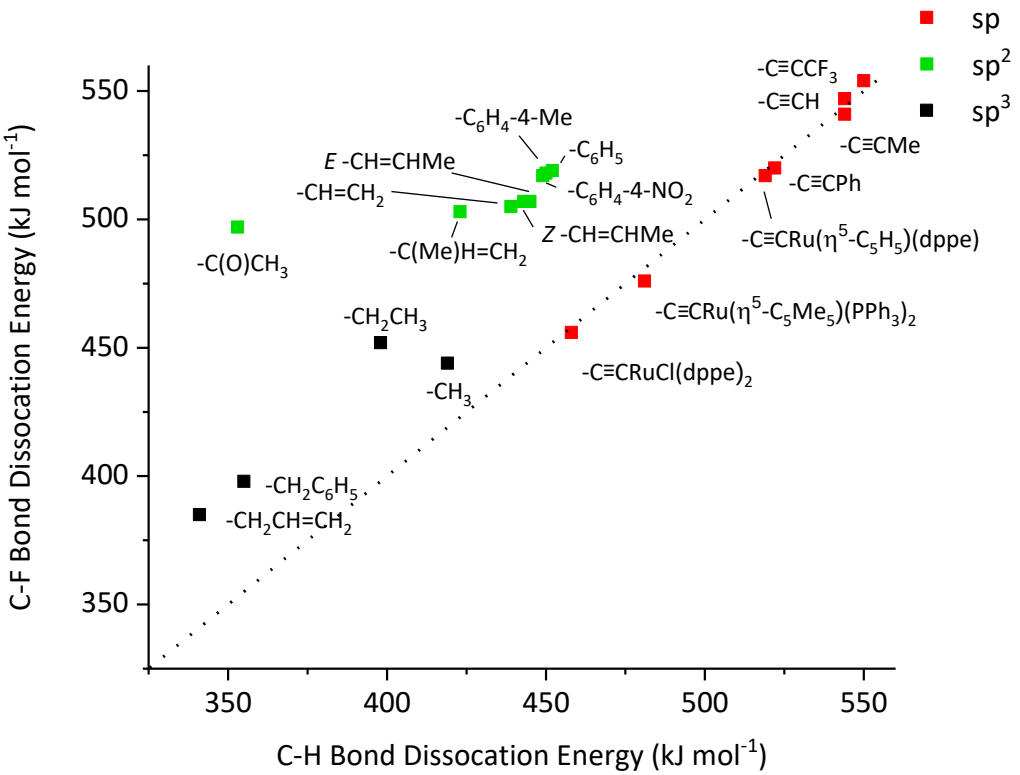

Figure 39: Plot of calculated sp (red), sp² (green), and sp³ (black) C-H and C-F bond dissociation energies. Dotted line denotes 1:1 relationship between C-H and C-F BDEs.

As shown in Table 17 and Figure 39, sp^2- and sp^3-hybridised C-F bonds are stronger than the corresponding C-H bonds, as expected due to the strong ionic character of the C-F bond. In contrast, the strength of the C(sp)-F bond does not follow the same trend, instead the BDEs for C(sp)-F bonds are weaker than expected, being almost of equal strength to the corresponding C(sp)-H bond. The calculated BDEs for **[55a]** and **[55b]** are essentially the same, as observed for the BDEs of the other sp-hybridised compounds. Likewise, the BDEs for the C-F bond in **[28b]** and **[57b]** are similar to the BDEs of the analogous C-H bond in **[28a]** and **[57a]**, respectively. This gives confidence, in conjunction with the spectroscopic data and BOs, that the stability afforded to the ruthenium fluoroalkynyl complexes is not electronic in nature but kinetic and should therefore provide good models to further explore the reactivity of fluoroalkynes.

2.9 Conclusion

The application of OSEF for the synthesis of mono- and difluoro-vinylidene complexes has been demonstrated for both monodentate and bidentate phosphine bearing ruthenium half-sandwich fragments and extended to the chloro-*bis*-dppe ruthenium fragment. Fluorination induces significant changes in the electronic properties of the vinylidene complexes, which manifest as large changes in the NMR, UV-Vis, and IR spectroscopic data compared to the diprotio-vinylidene analogues. Further shifts in the spectroscopic data are observed upon incorporation of a second fluorine substituent on the vinylidene ligand.

Fluorination induces significant deshielding of the carbon, hydrogen, and fluorine resonances of the vinylidene ligand. A bathochromic shift in the UV-Vis absorption spectra and a hypsochromic shift in the C=C vibrational stretching frequency is also observed. Changes in the electronic structure did not manifest in many statistically significant changes in the bond metrics according to single crystal X-ray diffraction. The most consistent change upon fluorination was increased distortion of the vinylidene ligand.

In contrast to the fluorination of [Ru(η^5-C_5Me_5)(PPh_3)$_2$(C≡CR], [Ru(η^5-C_5Me_5)(dppe)(C≡CR], and *trans*-[ClRu(dppe)$_2$(C≡CR)], fluorination of **[14e]** was shown previously to afford the fluorinated cyclobutenylidinium complex, **[27]**$^+$. Even at low temperatures or under dark conditions, fluorination resulted in the formation of **[27]**$^+$. Formation of **[44a]**$^+$ was only observed with the addition of Selectfluor or NFSI in neat acetonitrile, where the a high concentration difference between **[14e]** and the fluorinating agent was maintained.

Synthesis of fluoro-protio vinylidene complexes enabled access to, and isolation of, the first examples of transition-metal fluoroalkynyl complexes (**[28b]**, **[55b]**, and **[57b]**) through deprotonation with lithium HMDS. Unlike reported examples of organic fluoroalkynes, the ruthenium fluoroalkynyl complexes demonstrated complete stability toward oligomerisation, with **[55b]** and **[57b]** displaying high stability as a solid or in solution for long periods of time. While **[28b]** is significantly more stable than organic examples of fluoroalkynes, the synthetic route was challenged by a competing phosphine activation pathway to form an *ortho*-metallated fluorovinylphosphonium complex **[48]**$^+$, and yielded only small quantities of the desired fluoroalkynyl complex, making further study difficult.

Introduction of fluorine into the alkynyl ligand does not induce a large bathochromic shift in the observed absorption bands, in contrast to fluoro-vinylidene complexes. Additionally, the β-carbon resonance of fluoroalkynyl ligands compared to protioalkynyl ligands remain

unperturbed while significant shielding of the α-carbon resonance is observed upon fluorine incorporation. To better understand the changes in chemical shielding introduced by incorporation of fluorine into a vinylidene or alkynyl ligand, future work should focus on analysing the chemical shielding tensors from the anisotropic chemical shifts obtained by solid-state NMR spectroscopy and correlating these tensors to the electronic structures of the complexes.

Experimental and computational evidence suggest that the ruthenium fragments of **[28b]**, **[55b]**, and **[57b]** are best viewed as exotic substituents which provide kinetic, rather than electronic, stabilisation to the alkyne. Preliminary reactivity indicates that the ruthenium fluoroalkynyl complexes react with electrophiles in the same manner as other metal alkynyl complexes. Addition of a latent source of 'F^+' afford the difluoro-vinylidene complexes **[30b]**$^+$, **[54b]**$^+$, and **[58b]**$^+$. Both **[55b]** and **[57b]** have the potential to act as synthetically viable models for organic fluoroalkynes. As such additional future work should focus on optimising scale-up and investigating the reactivity of these complexes compared to other alkynes and metal alkynyl complexes.

Chapter 3. Reactivity Study of Ruthenium Fluorovinylidene Complexes

3.1 Attempted Liberation of Fluoroalkynes

Haloalkynes are an important class of highly versatile building blocks which have been employed in a variety of synthetic reactions, such as cross-coupling and cycloaddition reactions, to access complex and challenging halogenated products.[234] However, haloalkynes employed in synthesis are restricted to chloro-, bromo-, and iodo-substituted alkynes. Despite the high demand for fluorination strategies and the success of using other 1-haloalkynes, 1-fluoroalkynes are absent from synthetic chemistry due to the harsh and impractical conditions required to access this class of compound (see the introduction of Chapter 2). Therefore, establishing facile methods for accessing synthetically useful 1-fluoroalkynes is vitally important and highly desirable. This section details attempts made to liberate fluoroalkynes from the coordination sphere of ruthenium.

3.1.1 Previous Work

Liberation of terminal alkynes from ruthenium indenyl vinylidene complexes **[63]**PF_6 has been demonstrated by thermal activation in acetonitrile to afford the alkyne and the solvated product **[64]**PF_6 (Scheme 125).[261-263] Based on the kinetic investigation,[261] it is believed tautomerisation occurs by 1,2-hydrogen shift to form the η^2-alkyne complex **[65]**PF_6 transiently and affords the uncoordinated alkyne by displacement by acetonitrile. The barrier to tautomerisation for the phenyl substituted vinylidene complex was experimentally determined at $\Delta H^{\ddagger}$ = 100 kJ mol^{-1} and $\Delta S^{\ddagger}$ = -13 kJ mol^{-1} and accessible at 36-54 °C.[261]

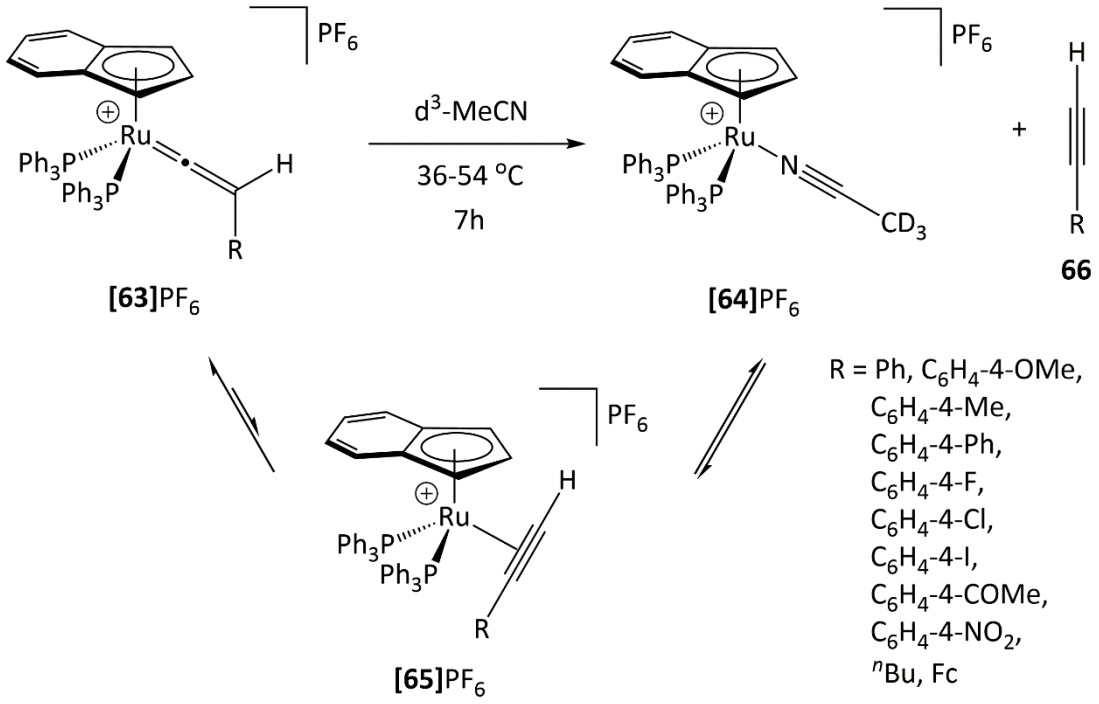

Scheme 125: Thermal activation of [63]PF_6 in d^3-acetonitrile affords [64]PF_6 and terminal alkynes 66 *via* [65]PF_6.

Previous work in the Lynam and Slattery groups demonstrated that attempts to liberate 1-fluoro-2-phenylethyne by heating **[15b]**BF_4 in acetonitrile at 50 °C did not result in the formation of the fluoroalkyne or cyclotrimers on heating for two weeks. Instead, **[18]**BF_4 was generated, presumably by activation of a triphenyl phosphine ligand (Scheme 126).[218]

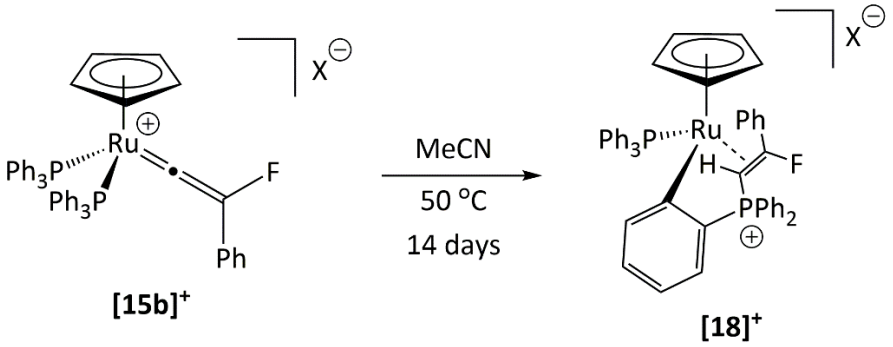

Scheme 126: Heating $[15b]^+$ in d^3-MeCN at 50 °C for 14 days did not afford an organic product but $[18]^+$. X^- = BF_4 or NSI.

This activation pathway can be circumvented by use of bidentate phosphines. However, heating **[19]**NSI in acetonitrile at 100 °C for two weeks resulted in no observable change in the spectroscopic data (Scheme 127). According to DFT calculations (Figure 40) conducted as part of this thesis, the η^2-alkyne complex was only calculated to be 49 kJ mol^{-1} (ΔG_{298}) higher in energy than **[19]**NSI. Displacement of the fluorinated alkyne by acetonitrile is

thermodynamically favourable (ΔG_{298} = -92 kJ mol^{-1}). This suggests the barrier to the η^2-alkyne complex must be significantly higher than the barrier to tautomerisation for the protio-analogue and is not accessible under the conditions used. Attempts to calculate the barrier through 1,2-migration of the fluorine or phenyl substituent were unsuccessful.

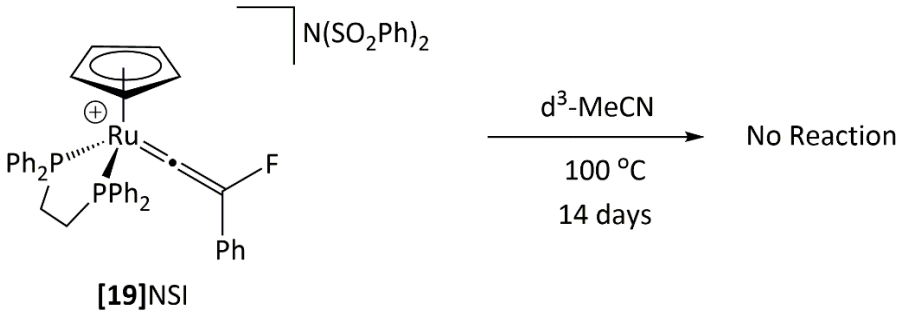

[19]NSI

Scheme 127: Heating [19]NSI in d^3-MeCN at 100 °C for 14 days did not result in any reaction being observed.

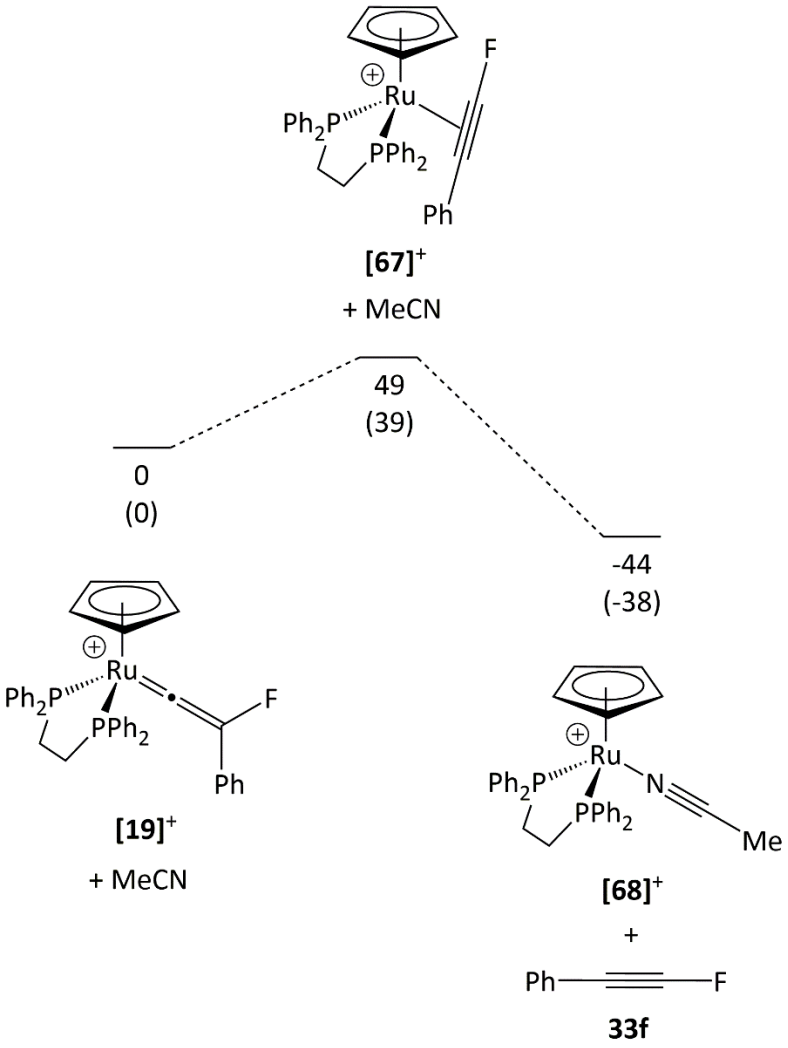

Figure 40: Relative Gibbs free energies of the η^2-alkyne complex, $[67]^+$, acetonitrile complex, $[68]^+$ and fluoroalkyne, 33f, with respect to $[91]^+$ and acetonitrile All energies were calculated at the (RI-)BP86/SV(P)//(RI-)PBE0/def2-TZVPP level with d3-dispersion and dichloromethane solvent correction. The values in parenthesis are the relative electronic energies with zero-point energy, dispersion and solvation (dichloromethane) corrections.

3.1.2 Heating Fluorovinylidene Complexes in Acetonitrile

3.1.2.1 Heating [54a]NSI in Acetonitrile

With access to vinylidene complexes with only hydrogen and fluorine substituents, **[54a]**NSI and **[58a]**BF_4, the barrier to hydrogen migration was expected to be significantly smaller compared to phenyl migration in **[15b]**BF_4 and **[19]**NSI.[261-265] Heating **[54a]**NSI in rigorously anhydrous acetonitrile at 50 °C for five days did not reveal any evidence for the formation of fluoroethyne or its cyclotrimerised products, nor was there any evidence for decomposition of **[54a]**NSI or formation of the acetonitrile complex, **[71]**NSI (Scheme 127).

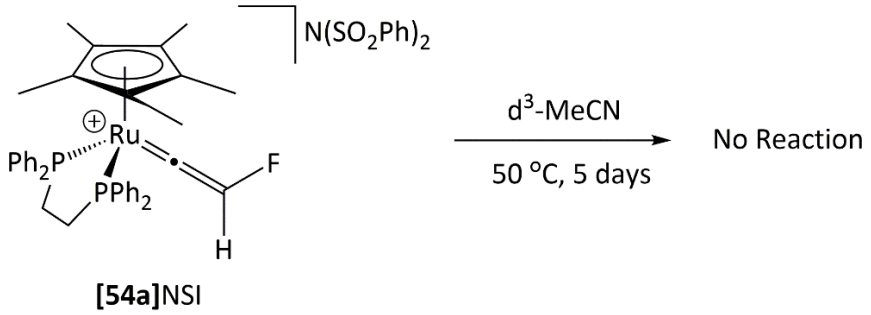

[54a]NSI

Scheme 128: Heating [54a]NSI in d^3-MeCN for five days at 50 °C did not result in any reaction being observed.

The η^2-alkyne complex, **[70b]**$^+$, is calculated to be (ΔG_{298}) 48 kJ mol^{-1} higher in energy than **[54a]**$^+$, with the barrier to proton migration being calculated at ($\Delta G_{298}^{\ddagger}$) 159 kJ mol^{-1}. Both the barrier to proton migration and the relative energy of the η^2-alkyne complex are similar compared to the protio-analogues (ΔG_{298} = 148 and 52 kJ mol^{-1} respectively). The high energy barrier to proton migration may not be accessible under the conditions used and would account for the lack of fluoroalkyne liberation despite being thermodynamically favourable compared to **[54a]**$^+$ (ΔG_{298} = -470 kJ mol^{-1}). Under more forcing conditions the barrier to proton migration might be accessible and warrants further investigation.

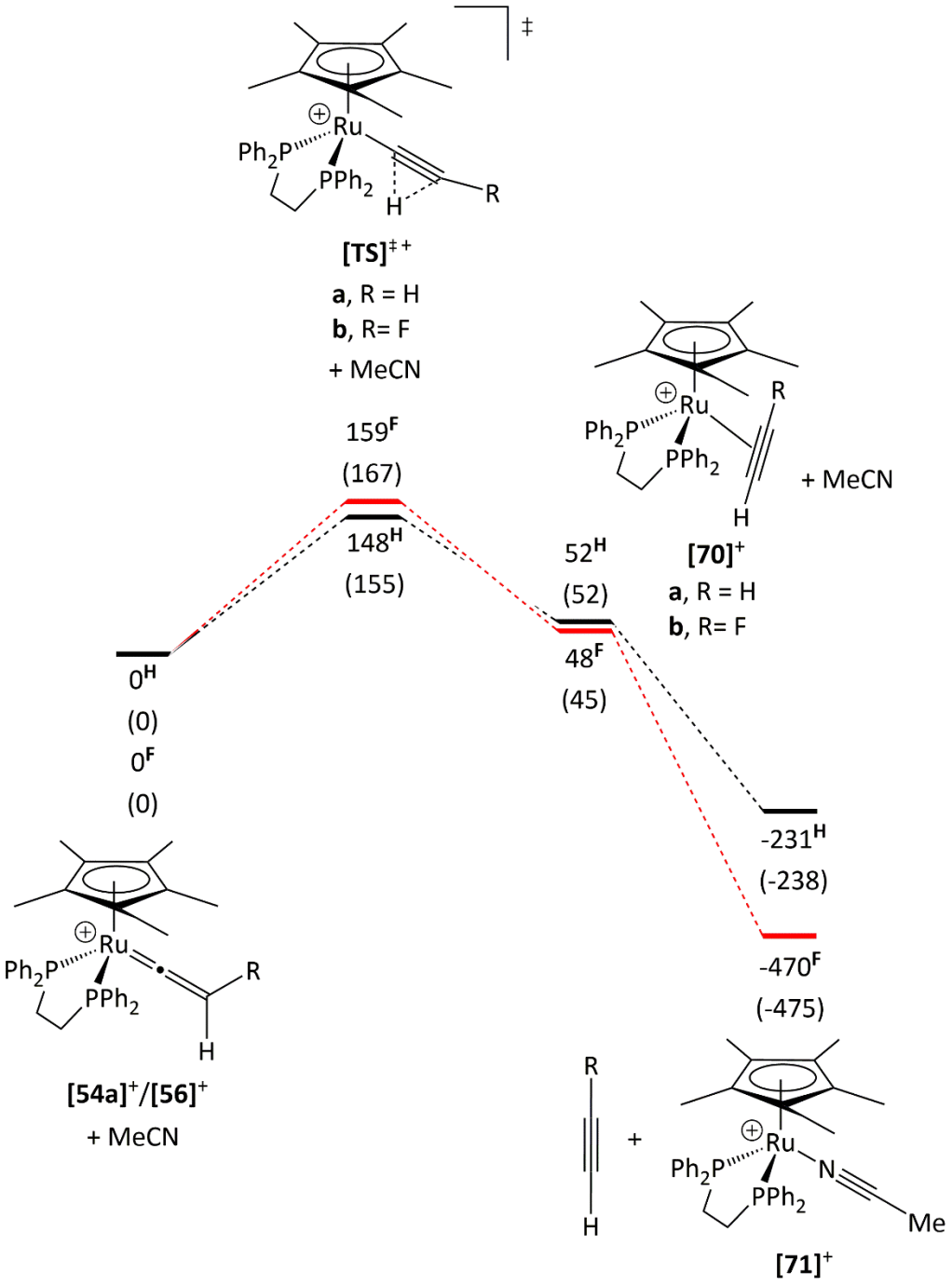

Figure 41: Gibbs free energies (in kJ mol^{-1}) for the barrier to proton migration from the vinylidene complexes, [56]$^+$ and [54a]$^+$, to the corresponding η^2-alkyne complex, as well as the formation of the respective alkyne and acetonitrile complex [71]$^+$. All energies were calculated at the (RI-)BP86/SV(P)//(RI-)PBE0/def2-TZVPP level with d3-dispersion and dichloromethane solvent correction. The values in parenthesis are the relative electronic energies with zero-point energy, dispersion and solvation (dichloromethane) corrections.

3.1.2.2 Heating [58a]BF_4 in Acetonitrile

In a similar manner, a d^3-acetonitrile solution of **[58a]**BF_4 was heated at 70 °C in the hope of liberating fluoroethyne or an isomer of trifluorobenzene. After heating at 70 °C for three days complete conversion of **[58a]**BF_4 to new organometallic species with complex NMR spectra was observed. However, there was no evidence for the displacement of fluoroethyne or the products from cyclotrimerisation. The $^{31}P\{^1H\}$ NMR spectrum in d^3-acetonitrile was complex with the major product consisting of four inequivalent phosphorus resonances with high multiplicity, indicating an organometallic species without a plane of symmetry. The phosphorus resonances are tabulated in Table 18.

Table 18: $^{31}P\{^1H\}$ NMR parameters observed from heating [58a]BF_4 in a d^3-acetonitrile solution.

$^{31}P\{^1H\}$ NMR / ppm	Multiplicity	Coupling *J* / Hz
62.6	dd	25, 18
41.4	ddd	311, 23, 18
27.5	dd	114, 19
23.4	ddd	311, 25, 19

The ^{19}F NMR spectrum consisted of one major resonance at δ -45.4 ppm which appears as a doublet of doublet of doublets with one or more smaller couplings which could not be resolved. The resonance exhibited coupling of 114 and 23 Hz to the phosphorus resonances at δ 27.5 and 41.4 respectively. The remaining coupling of 99 Hz is to hydrogen. Nucleophilic attack of the vinylidene ligand by one of the phosphines would afford a species with inequivalent phosphorus environment such as **[72]**BF_4 (Scheme 129), which is consistent with the observed NMR spectra. The mutually coupled proton environment was observed at δ 6.68 as a doublet-of-doublet resonance in the ^1H NMR spectrum with 99 Hz coupling to fluorine and 14 Hz coupling, presumably to phosphorus.

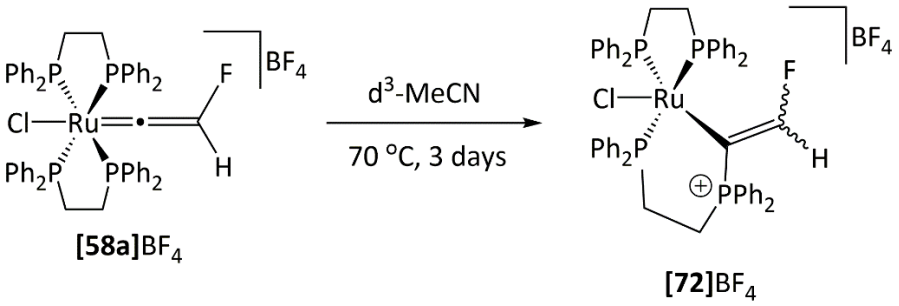

[58a]BF_4 **[72]**BF_4

Scheme 129: Heating [58a]BF_4 in d^3-MeCN for three days at 70 °C did not liberate a fluoroalkyne but a new major organometallic complex. The NMR parameters are consistent with the structure of [72]BF_4.

The appearance of a minor species with complex resonances at similar chemical shifts in the ^{19}F and $^{31}P\{^1H\}$ NMR spectra is indicative of the other isomer of **[72]**BF_4. The LIFDI and ESI mass spectra revealed the species observed has the same mass as **[58a]**$^+$, supporting the hypothesis that phosphine attack of the vinylidene ligand has occurred and the minor species is an isomer of the major species. Due to the tethering of the phosphines, *ortho*-metallation of one of the phenyl groups of the alkenyl-phosphonium is not possible.

3.1.3 Heating [15b]BF_4, [19]BF_4, and [30a]BF_4 in the Presence of Triphenylphosphine

Dissociation of disubstituted alkynes from the corresponding vinylidene complexes by triphenylphosphine has been demonstrated by Ishii *et al*.[187, 264, 265] for complexes **[73]**BAr^F_4 and **[1-307]**BAr^F_4 (Scheme 130). Based on the kinetic and isotope labelling experiments, and supported by a DFT study, tautomerisation was proposed to proceed by a 1,2-migration of the phenyl substituent.[265] It was therefore envisaged that the reaction of **[15b]**BF_4 or **[19]**NSI with triphenylphosphine under the same reaction conditions would afford 1-fluoro-2-phenylethyne.

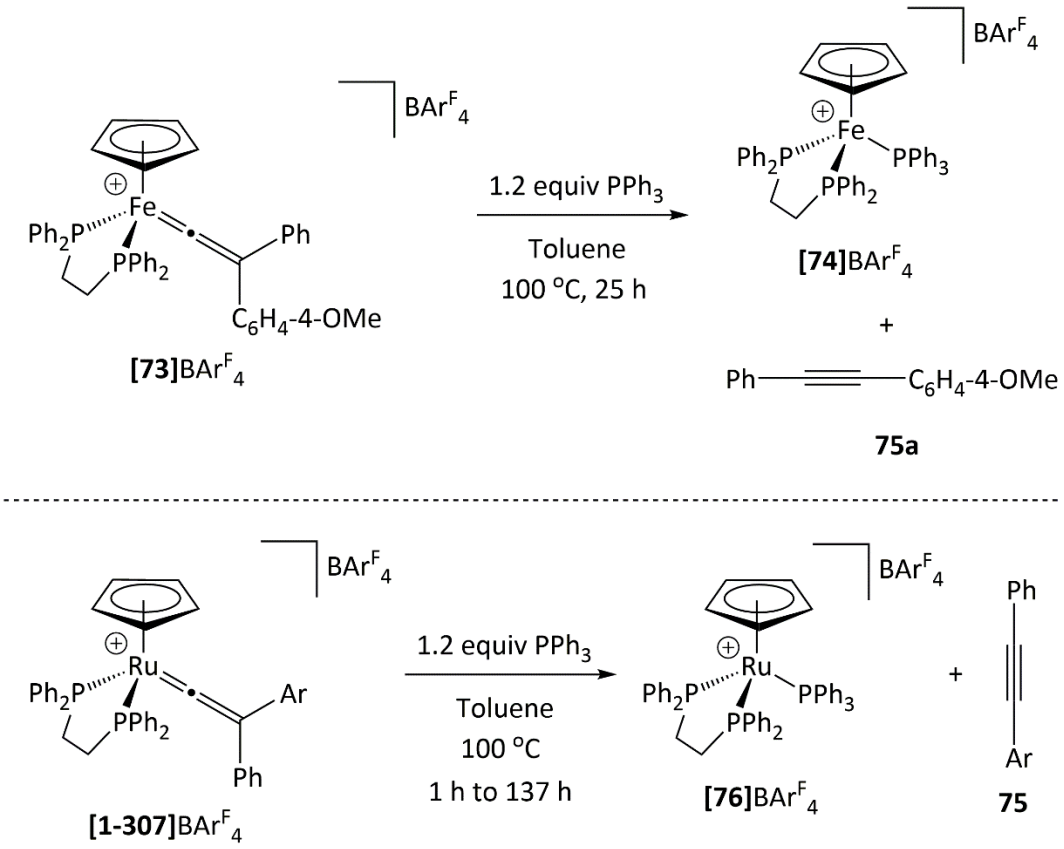

Ar = Ph, C_6H_4-4-Me, C_6H_4-4-OMe, C_6H_4-4-Cl, C_6H_4-4-CO_2Et

Scheme 130: Heating [73]BAr^F_4 and [1-307]Bar^F_4 in toluene with 1.2 equivalents of triphenylphosphine affords [74]BAr^F_4 and [76]BAr^F_4 respectively and the corresponding disubstituted alkenes (75).

Heating a toluene solution of **[15b]**BF_4 with 1.2 equivalents of triphenylphosphine for 16 hours in an FEP lined Youngs' NMR tube resulted in formal loss of 'F^{+}' (Scheme 131) according to NMR spectroscopy and ESI-MS. The $^{31}P\{^1H\}$ NMR spectrum in toluene indicated the disappearance of the resonance at δ 42.1 for **[15b]**BF_4 and the appearance of **[14b]** at δ 50.8.

The ^{19}F NMR spectrum displayed the resonance for the tetrafluoroborate anion at δ 152.8. The ESI mass spectrum supported the appearance of **[14b]**.

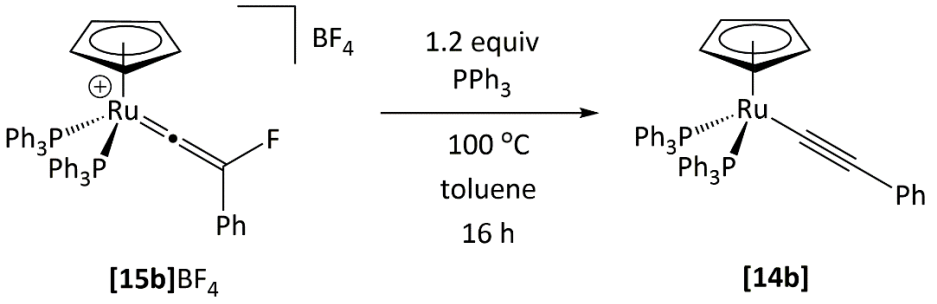

[15b]BF_4 **[14b]**

Scheme 131: Heating a toluene solution of [15b]BF_4 with triphenylphosphine at 100 °C for 16 hours resulted in formal loss of 'F^+' to afford [14b].

As with **[15b]**BF_4, heating **[19]**NSI in toluene with triphenylphosphine at 110 °C for 6 hours did not result in any observable changes to the NMR spectra or mass spectrum. Heating for a further four days at 110 °C resulted in the appearance of four new resonances in the ^{19}F NMR spectrum. The ^{19}F NMR spectrum of the mixture in toluene exhibited two mutually coupled resonances, a doublet of triplets at δ -83.2 and a doublet at δ -147.6. This corresponds to the formation of *Z*-**[23a]** through fluoride attack of **[19]**BF_4, conversion could not be calculated due to poor solubility of **[19]**BF_4. The other two new resonances at δ -41.5 (d, J_{PF} = 666 Hz) and -138.4 (s, ^{29}Si-^{19}F satellites not observable due to low intensity) correspond to the formation of difluorotriphenylphosphine[266] and pentafluorosiliconate[267] respectively. There was no evidence for the formation of a fluoroalkyne or fluorinated arene in the ^{19}F NMR spectrum.

The major resonance in the $^{31}P\{^1H\}$ NMR spectrum was triphenylphosphine at δ -6.9 and also displayed the resonance for triphenylphosphine oxide (δ 23.5). However, the resonance for difluorotriphenylphosphine could not be identified (expected at δ -55 with 666 Hz triplet coupling). The $^{31}P\{^1H\}$ NMR spectrum also displayed a doublet-of-doublet resonance at δ 91.6 corresponding to *Z*-**[23a]**,[223] as well as a mutually coupled doublet and triplet resonance at δ 66.2 and 42.3 respectively with 34 Hz coupling corresponding to the formation of **[76]**BF_4.[264] Singlet resonances at δ 78.9 and 84.6 correspond to unreacted **[19]**BF_4 and **[77]**, formed through formal loss of 'F^+' from **[19]**BF_4. Despite the appearance of **[76]**BF_4, the ESI and EI mass spectra did not provide any evidence for the formation of a fluoroalkyne or trimerised products, supporting the finding from the ^{19}F NMR spectrum. The ESI mass spectrum revealed the presence of species with the correct accurate masses for **[19]**BF_4, **[23a]**+H^+, **[76]**$^+$, and **[77]**+H^+. Complex **[76]**BF_4 may form through displacement of the vinylidene ligand,

or by displacement of the hydrolysed vinylidene ligand in the presence of adventitious water. It is clear that heating **[19]**BF_4 in toluene does not afford the expected fluoroalkyne or trimer products but rather formal loss of 'F^+' or fluoride addition (Scheme 132). Decomposition of the tetrafluoroborate anion is most likely the source of fluoride for the formation of *Z*-**[23a]**, as fluoride attack is not observed upon heating **[19]**NSI in acetonitrile at 100 °C.

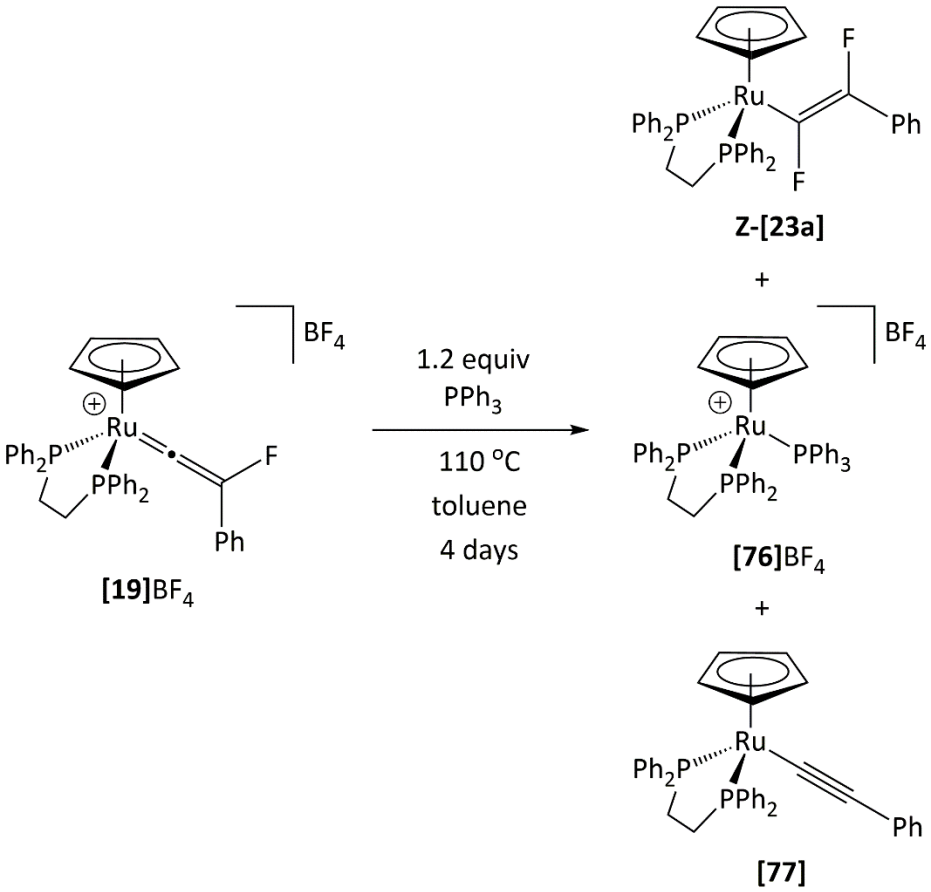

Scheme 132: Heating a toluene solution of [19]BF_4 with triphenylphosphine at 110 °C for four days resulted in fluoride addition to afford [23a], or formal loss of 'F^+' to afford [77]. Additionally, the formation of [76]BF_4 was observed after four days.

3.1.3.1 Heating [30a]BF_4 with triphenylphosphine

To determine whether the approach demonstrated by Ishii *et al.* (Scheme 130) could also be applied to vinylidene complexes with only fluorine and hydrogen substituents, **[54a]** was reacted with triphenylphosphine under the same reaction conditions. Although this approach did not afford a fluoroalkyne product when applied to complexes **[15b]**BF_4 and **[19]**BF_4, it was envisaged that the reaction with **[30a]**BF_4 under the same conditions may enable a fluoroalkyne to be liberated due a lower activation barrier for migration of hydrogen.

Heating a toluene solution of **[30a]**BF_4 at 110 °C with triphenylphosphine for 6 hours did not result in any observable resonances in the $^{31}P\{^1H\}$ NMR spectrum, with the exception of triphenylphosphine, due to the low solubility of **[30a]**BF_4 in toluene. Additionally, there was no evidence for the fluorinated alkyne or trimerised products according to the ^{19}F NMR and EI-mass spectra. Heating the suspension for a further three days at 110 °C resulted in the formation of an orange solution but there no evidence for the displacement of fluoroethyne or trimerised products according to the ^{19}F NMR spectroscopy and ESI-MS. The $^{31}P\{^1H\}$ NMR spectrum exhibited a resonance for triphenylphosphine and triphenylphosphine oxide. ESI-MS detected the presence of species at 785.2033 m/z, corresponding to the m/z of **[30a]**$^+$-HF, and a species at 821.1795 m/z which could not identified. It is clear that heating **[30a]**BF_4 with triphenylphosphine at 110 °C for four days does not result in the displacement of fluoroethyne.

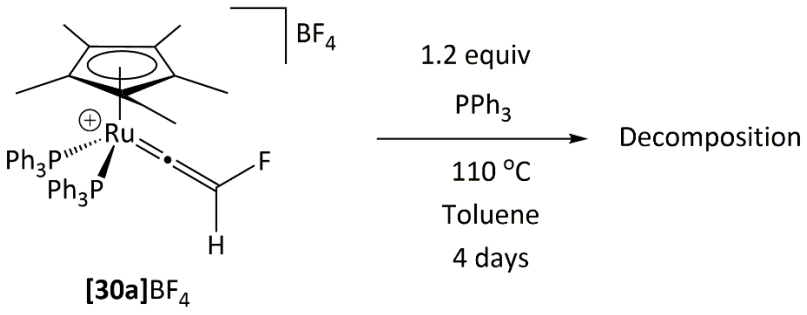

Scheme 133: Heating [30a]BF_4 with triphenylphosphine in toluene at 110 °C for four days did not result in the liberation of a fluoroalkyne.

3.1.4 Irradiation of Fluorovinylidene Complexes with Broadband UV Light

3.1.4.1 Irradiation of [30a]BF_4

To determine whether tautomerisation to an η^2-alkyne complex (e.g. **[65]**) and liberation of the alkyne could be observed upon irradiation with broadband UV light, d^3-acetonitrile solutions of **[30a]**BF_4, **[54a]**NSI, and **[19]**BF_4 were irradiated with broadband UV light for two and five hours.

Irradiation of a d^3-acetonitrile solution of **[30a]**BF_4 with broadband UV for two hours resulted in the appearance of a singlet resonance at δ 48.2 in the $^{31}P\{^1H\}$ NMR spectrum which is unlikely to correspond to the acetonitrile complex (δ 45.3). After five hours of irradiation, multiple new signals were observed in the $^{31}P\{^1H\}$ NMR spectrum. After two hours of irradiation, the ^{19}F NMR spectrum exhibited a small reduction in intensity of the resonance at δ -237.5 for **[30a]**BF_4 and the displayed the appearance of a broad signal at δ -238.0 and a new P-F species at δ -38.3 (d, $^1J_{PF}$ = 656 Hz). After irradiating the sample for two and five hours, the ^1H NMR spectra exhibited a reduction in intensity of the doublet resonance at δ 8.96 for **[30a]**BF_4 and the appearance of a doublet resonance at δ 0.19 with 7.9 Hz coupling. However, there was no clear evidence for the appearance of a new resonance for the cyclopentadienyl protons of a new organometallic species. The GC-EI mass spectrum did not detect any evidence for the formation of any alkyne or arene products.

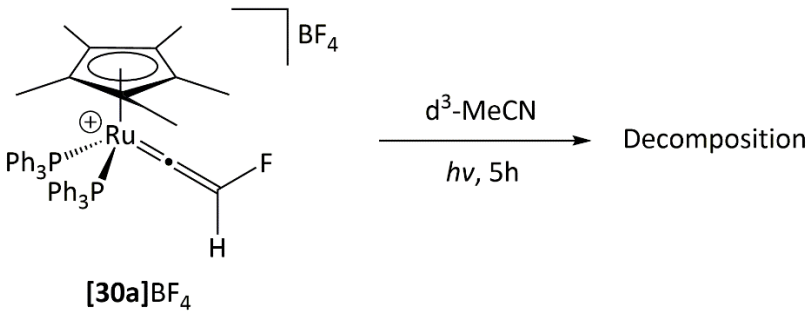

[30a]BF_4

Scheme 134: Irradiation of [30a]BF_4 with broadband UV light for 5 hours in d^3-acetonitrile did not afford fluoroethyne but resulted in decomposition.

Irradiation of **[30a]**BF_4 with broadband UV-light did not result in the formation of fluoroethyne or an isomer of trifluorobenzene according to NMR spectroscopy and mass spectrometry. Although a reduction in the signal intensity for **[30a]**BF_4 was observed by NMR spectroscopy, it appears broadband UV irradiation predominantly results in decomposition (Scheme 134).

3.1.4.2 Irradiation of [54a]NSI

Under the same conditions, a d^3-acetonitrile solution of **[54a]**NSI was irradiated with broadband UV light for two and five hours. The initial $^{31}P\{^1H\}$ NMR spectrum in d^3-acetonitrile exhibited the appearance of **[71]**NSI at δ 75.7 (28 % of initial composition)[268] which presumably forms through hydrolysis of **[54a]**NSI with adventitious water. The resonance for **[71]**NSI grows over the course of five hours of irradiation to 64 % conversion. The ^{19}F NMR spectrum displayed a reduction in the doublet resonance for **[54a]**NSI at δ -238.1 over five hours. There was no evidence for the formation of any new fluorine-containing products, suggesting the formation of hydrogen fluoride and other fluorides with its reaction with the glass. The ^1H NMR spectrum exhibited a reduction in the resonance at δ 1.55 for the Cp* protons of **[54a]**BF_4 and the growth of a resonance at δ 1.39 which corresponds to the Cp* protons of the **[71]**NSI.

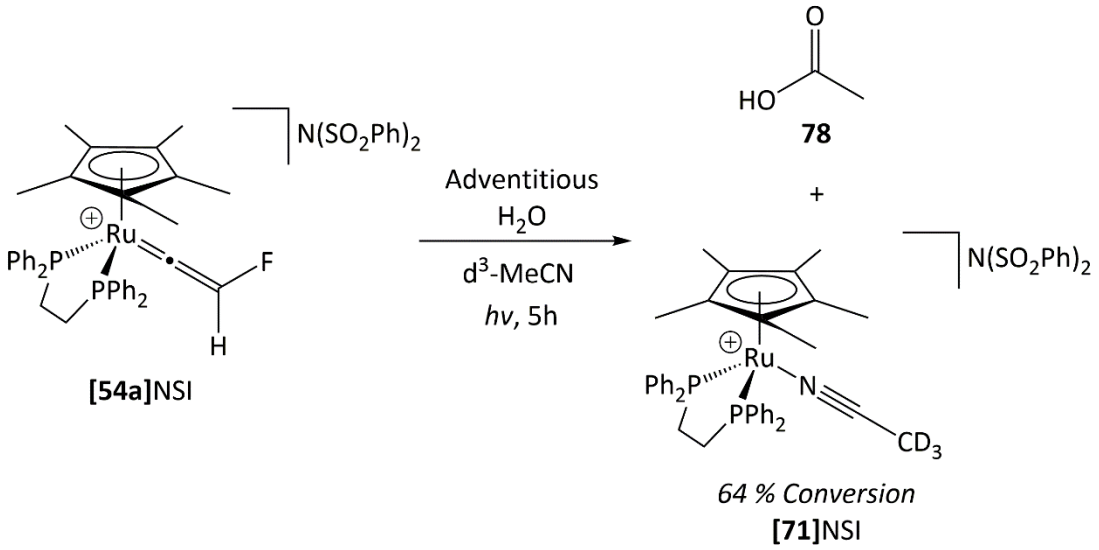

Scheme 135: UV irradiation of an d^3-acetonitrile solution of [54a]NSI afforded [71]NSI and 78 due to the presence of adventitious water.

The resonance for acetic acid, **78**, was also observed at δ 1.94 in the ^1H NMR spectrum along with a broad signal at δ 2.12 which could not be identified.[269] The data suggests hydrolysis of **[54a]**NSI occurs with adventitious water in the acetonitrile to afford **[71]**NSI and **79** initially. Fluoroaldehydes are reported to undergo rearrangement to the thermodynamically favoured acyl fluorides and has been demonstrated to occur by formal fluorine migration through isotope labelling experiments by Milner *et al*.[218] for fluoro(phenyl)acetaldehyde. It is therefore believed that **79** undergoes rearrangement to **80** and further hydrolysis to afford **78** and hydrogen fluoride (Scheme 136). There was no evidence for the formation of

fluoroethyne or trifluorobenzene according to NMR spectroscopy and GC-EI MS. It is unclear whether hydrolysis of **[54a]**BF_4 and/or **80** is thermally or photochemically promoted under these conditions. However, based on thermal hydrolysis of **[54a]** in section 3.2, hydrolysis could be accelerated under UV conditions.

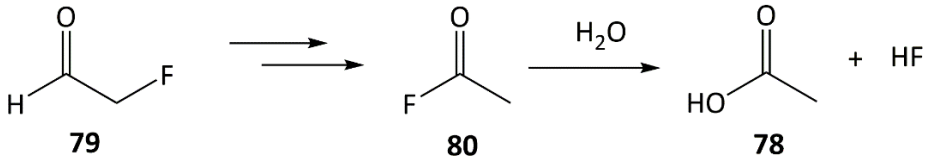

Scheme 136: Rearrangement of 79 affords fluoroacyl 80 which can undergo further hydrolysis to afford 78 and hydrogen fluoride.

3.1.4.3 Irradiation of [19]BF_4

In contrast to the broadband UV irradiation of **[30a]**BF_4 and **[54a]**NSI which underwent decomposition and/or hydrolysis, irradiation of a d^3-acetonitrile solution of **[19]**BF_4 for two and five hours did not result in any appreciable changes to the NMR spectra. After five hours of UV irradiation, the $^{31}P\{^1H\}$ NMR spectrum exhibited the appearance of two small signals at δ 77.2 and 79.8 corresponding to the formation of **[44c]**BF_4 (8 % conversion)[270] and **[68]**BF_4 (4 % conversion; Scheme 137)[271]. There was no apparent change in the ^{19}F NMR spectrum after irradiation for two and five hours. The ^1H NMR spectrum displayed a small reduction in the resonances for **[19]**BF_4 and the appearance of two small singlet resonances at δ 4.70 and 5.66 corresponding to the Cp protons of **[44c]**BF_4 and **[68]**BF_4. There was again no evidence for the expected fluoroalkyne or its cyclotrimerised products by NMR spectroscopy or GC-EI MS.

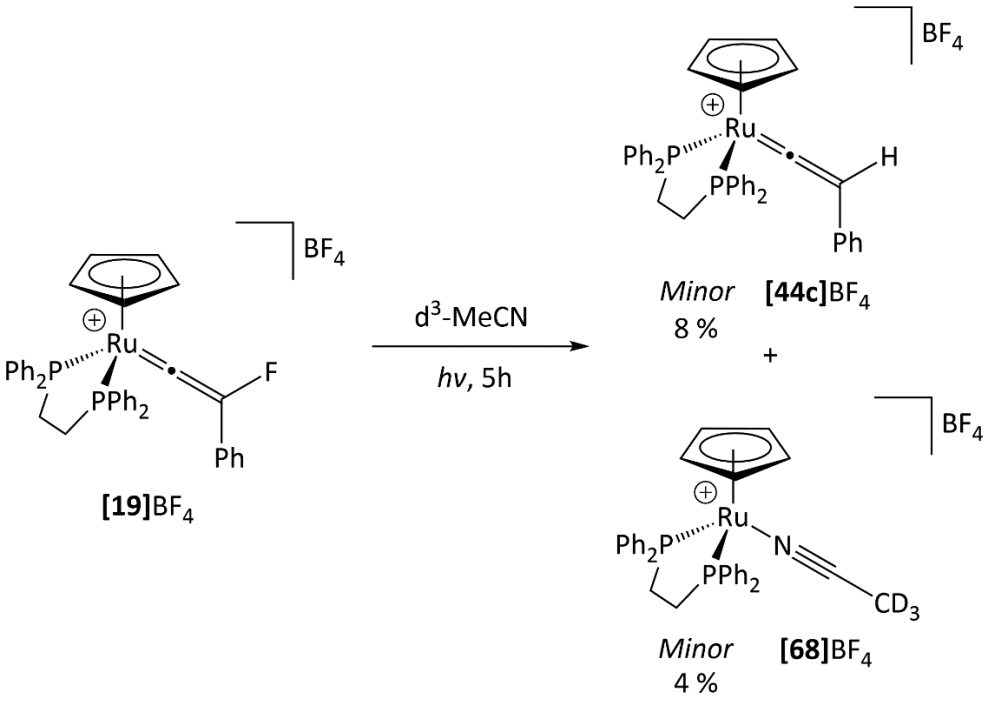

Scheme 137: UV irradiation of a d^3-acetonitrile solution of [19]BF_4 for 5 hours afforded [44c]BF_4 and [68]BF_4 as minor products but predominantly remains unreacted. There was no evidence for the formation of the fluoroalkyne or its trimers.

It is evident that irradiation of acetonitrile solutions of fluorovinylidene complexes with broadband UV light does not result in liberation of the corresponding fluoroalkyne. The irradiation results in hydrolysis in the presence of adventitious water, as well as formal loss of 'F^+' from **[19]**BF_4 and subsequent protonation to afford **[44c]**BF_4. However, complex **[19]**BF_4 remains predominantly unreacted under these conditions (Scheme 137).

3.1.5 Fluorination of [Ru(η^5-C$_5$H$_5$)(P(OMe)$_3$)$_2$(CCPh)]

Due to the unsuccessful attempts of liberating fluoroalkynes from the coordination sphere of phosphine containing fluorovinylidene complexes, presumably due to the strength of the Ru=C bond, an alternative ligand set around the metal was sought. It was hypothesised that the use of phosphite ligands, being poorer electron donor ligands compared to phosphines, may more readily enable access to the alkyne tautomer and subsequently an organic product. As such the bis-trimethylphosphite alkynyl complex **[81]** was synthesised and treated with a source of electrophilic fluorine.

The addition of stoichiometric NFSI to a toluene solution of **[81]** afforded a light green-blue solution over the course of approximately 30 seconds. The reaction afforded a green oil which was identified as the desired fluorovinylidene complex **[82]**NSI by NMR spectroscopy and ESI-MS. The reaction was also found to proceed by addition of FTMP BF_4 or Selectfluor in place of NFSI.

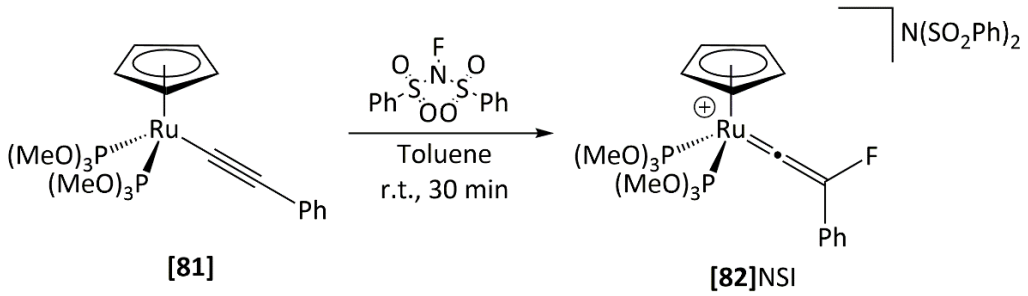

[81] **[82]**NSI

Scheme 138: Addition of NFSI to [81] afforded [82]NSI as a green oil.

The $^{31}P\{^1H\}$ NMR spectrum of **[82]**NSI in d^2-dichloromethane exhibited a doublet resonance at δ 168.7 with 7 Hz coupling to fluorine. The mutually coupled fluorine environment was observed as a triplet resonance at δ -213.9 with 7 Hz in the ^{19}F NMR spectrum. A ^{13}C-^{19}F HSQC experiment revealed the fluorine environment couples to two carbon environments at δ 193.3 and 398.6, which are at chemical shifts typical of fluorovinylidene complexes. The β-carbon of the vinylidene ligand was observed as a doublet resonance at δ 193.3 with 223 Hz coupling to fluorine, however, the α-carbon of the vinylidene ligand at δ 398.6 could not be observed directly in $^{13}C\{^1H\}$ NMR spectrum. The ESI-MS detected a species with the correct m/z for **[82]**$^+$.

In addition to the formation of **[82]**NSI, several other organometallic species were also formed. Complex **[82]**NSI was found to undergo rapid decomposition when exposed to air or left for three days under an inert atmosphere to form a red oil. The ESI-MS and $^{31}P\{^1H\}$

NMR spectrum revealed the formation of **[83]**$^{+}$ as the major product,[272] suggesting the fluorovinylidene ligand is highly susceptible to oxidative cleavage in the presence of oxygen or other decomposition pathways. The ^{19}F NMR spectrum revealed that decomposition afforded numerous fluorine-containing species between δ -25 and -113, although there was no evidence of any fluoroacyl species.

In order to determine whether reverse vinylidene-η^2-alkynyl isomerisation was possible, a d^3-acetonitrile solution of **[82]**NSI was heated at 70 °C for 24 hours. Rapid decomposition of **[82]**NSI was observed after one hour of heating to form numerous organometallic products (Scheme 139). Complete decomposition of **[82]**NSI was observed after 24 hours to produce a major phosphorus-containing species at δ 155.1 ppm and several minor species. In addition, the ^{19}F NMR spectrum displayed numerous fluorine-containing species between δ -60 and -150 which could correspond to fluorinated organic products but have not been identified so far. The ESI-MS displayed the presence of **[83]** (443.0053 m/z) and **[84]** (459.0451 m/z). The presence of the acetonitrile complex could indicate the liberation of fluorinated organic product. However, the ^{19}F NMR does not suggest formation of the fluoroalkyne or its trimerised form.

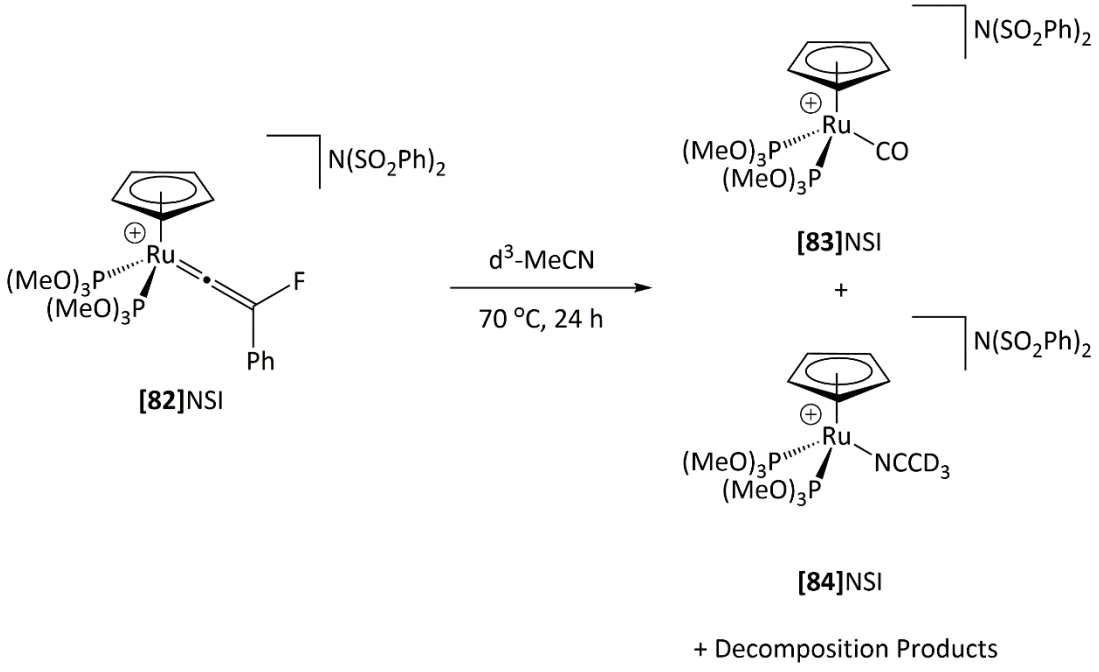

Scheme 139: Heating [82]NSI in d^3-acetonitrile at 70 °C resulted in the formation of numerous products including [83]NSI and [84]NSI.

3.2 Hydrolysis of [54a]NSI

The initial attempt to liberate fluoroethyne from **[54a]**NSI by heating **[54a]**NSI in d^3-acetonitrile at 50 °C for five days resulted in the appearance of two singlet resonances at δ 75.7 and 72.2 in the $^{31}P\{^1H\}$ NMR spectrum. These resonances corresponded to the formation of **[71]**NSI (37 %)[273] and **[85]**NSI (11 %)[274] respectively according to the literature data (Scheme 140). The ^1H NMR spectrum revealed the appearance of a small doublet resonance at δ 4.85 with 48 Hz coupling which matches the data for the formation of **79**, however, the aldehyde proton and fluorine resonance could not be observed. The ^{19}F NMR spectrum, after five days of heating, displayed the appearance of a singlet at δ -138.3 with two satellites (J_{SiF} = 144 Hz) corresponding to the formation of SiF_5^-, as well as the growth of the resonance at -151.7 for BF_4^-. The data suggested partial hydrolysis of **[54a]**NSI by adventitious water in the d^3-acetonitrile, similar to the results obtained from irradiating **[54a]**NSI in d^3-acetonitrile (section 3.1.4.2).

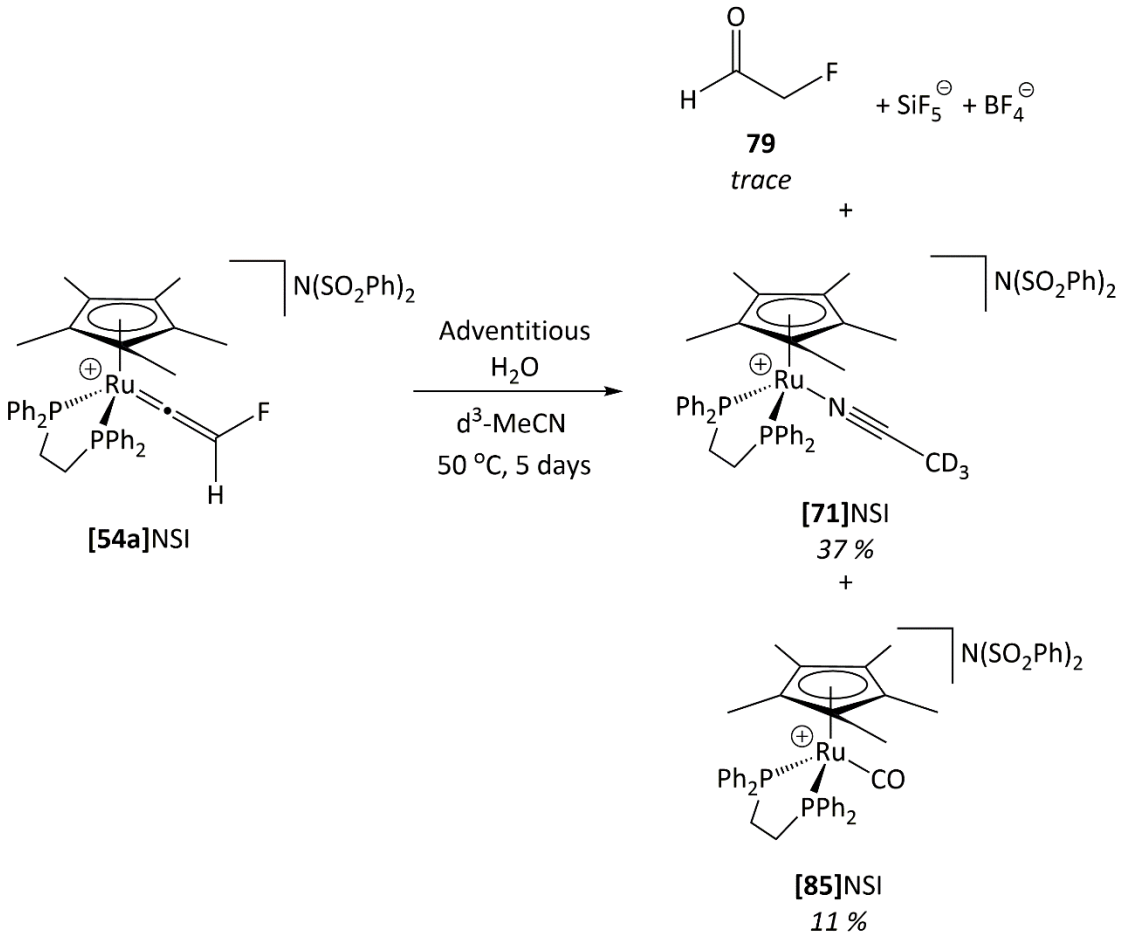

Scheme 140: Partial hydrolysis of [54a]NSI was observed upon heating the sample in d^3-actonitrile containing adventitious water to afford [71]NSI, [85]NSI and 79.

To confirm hydrolysis affords the reactivity observed above, one equivalent of water was added to a rigorously dried acetonitrile-d^3 solution of **[54a]**NSI and heated at 50 °C for 36 hours. The reaction was conducted in an FEP lined Youngs NMR tube to prevent etching of the glass by any hydrogen fluoride produced as part of the reaction. There was no evidence of hydrolysis according to the NMR spectra. An additional four equivalents of water were added and the reaction heated at 70 °C for two weeks.

After one day of heating, the ^{19}F NMR spectrum revealed the appearance of a small broad signal at δ -181.5 which corresponded to the formation of hydrogen fluoride (ca. 4% by ^{19}F NMR). There was no evidence for the formation of **79** or **80** as a result of hydrolysis. The $^{31}P\{^1H\}$ NMR spectrum revealed the appearance of **[71]**NSI and **[85]**NSI at δ 75.7 and 72.2 respectively (7 % conversion for each). The ^1H NMR spectrum supported both the ^{19}F and $^{31}P\{^1H\}$ NMR spectra, displaying the appearance of the Cp* proton resonance for both **[71]**NSI and **[85]**NSI at δ 1.39 and 1.55 respectively; there was no evidence for the formation of **79** or **80**. Over the course of one week 79 % of **[54a]**NSI undergoes conversion to **[71]**NSI (60 %) and **[85]**NSI (19 %) according to the $^{31}P\{^1H\}$ NMR spectra. The ^{19}F NMR spectra revealed consumption of **[54a]**NSI and growth of hydrogen fluoride (87 % after seven days). There was again no evidence for formation of **79** or **80**. The ^1H NMR spectrum confirmed the observations made from the ^{19}F and $^{31}P\{^1H\}$ NMR spectra. After two days the ^1H NMR spectrum exhibited a trace doublet resonance at δ 4.85 with 47 Hz coupling, which matched the literature data for the CH_2F moiety of **79**,[275, 276] however the aldehyde proton could not be identified.[275] The resonance for **79** did not significantly change over the course of two weeks. After seven days the ^1H NMR spectrum revealed the clear appearance of a singlet resonance at δ 1.93 which corresponds to the formation of acetic acid, **78**.[269] After two weeks the $^{31}P\{^1H\}$ NMR spectrum revealed further conversion of **[54a]**NSI to **[71]**NSI (73 % conversion) while the ^{19}F NMR spectrum revealed further conversion of **[54a]**NSI to hydrogen fluoride (95 % conversion). Due to the use of a non-fluorinated counterion or solvent, the fluorine can only originate from the vinylidene ligand of **[54a]**NSI.

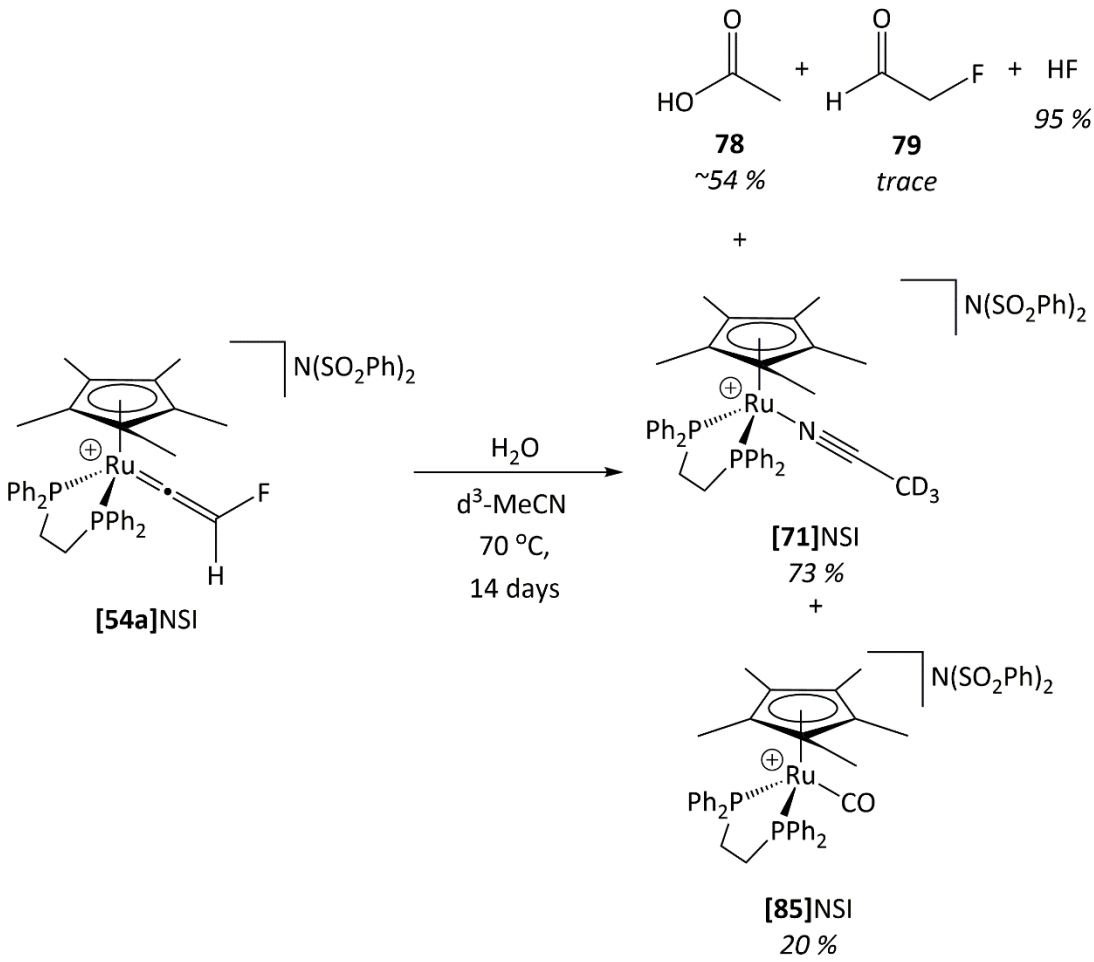

Scheme 141: Reaction of [54a]NSI with water afforded 78, hydrogen fluoride and [71]NSI after heating in d^3-acetontirile at 70°C for 14 days. Fluoroaldehyde 79 was observed as a trace product while fluoroacyl 80 was not observed due to rapid hydrolysis to afforded hydrogen fluoride.

The data are consistent with initial hydrolysis of **[54a]**NSI to afford **[71]**NSI and **79**, followed by rapid rearrangement of **79** to **80** and subsequent hydrolysis of **80**. This would afford the observed products, acetic acid and hydrogen fluoride (Scheme 136). Although there was no direct observation of **80** by the NMR spectroscopy over the 14 days, the formation of hydrogen fluoride and acetic acid **78** is suggestive that rearrangement of **79** to **80** does occur. This observation also suggests that fluoroacyl hydrolysis proceeds at a faster rate than the rate of fluoroacyl formation, and likewise, fluoroaldehyde-to-fluoroacyl rearrangement must occur at a faster rate than hydrolysis of **[54a]**NSI. It appears that **[54a]**BF_4 and **80** are highly susceptible to hydrolysis compared to hydrolysis of **[19]**NSI.[218] The observation of **[85]**NSI could indicate the presence of adventitious oxygen in the degassed water.

3.3 Reactions of [15b]$^+$

3.3.1 Addition of Allyl Alcohol

Trost *et al*.[277] demonstrated that the ruthenium vinylidene complex, **[45c]**PF_6, was capable reacting with allyl alcohol to afford a mixture of enone products, **86a** and **87a** (Scheme 142). It was envisaged that the reaction of a fluorinated vinylidene complex would enable access to the analogous fluorinated enones **86b** and **87b**.

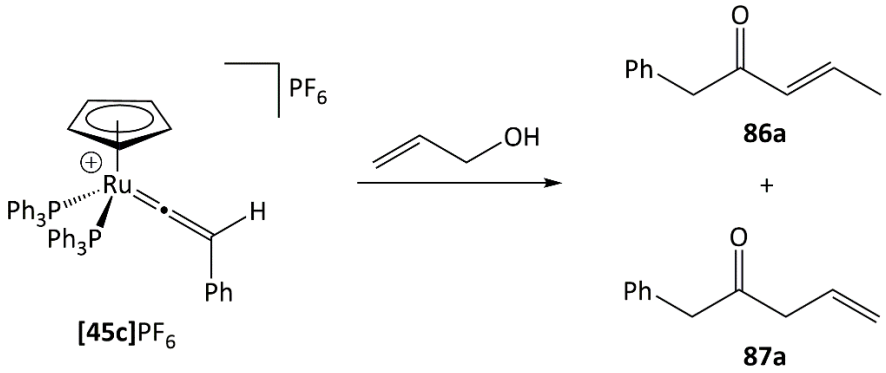

[45c]PF_6

Scheme 142: Trost *et al*.[277] demonstrated the reaction of allyl alcohol with [45c]PF_6 to afford enones 86a and 87a.

Although **[15b]**BF_4 is susceptible to phosphine activation to form *ortho*-metallated fluorovinylphosphonium complex **[18]**BF_4, the need for a coordinatively unsaturated centre to bind allyl alcohol requires the use of monodentate phosphines that can dissociate from the metal centre. It was envisaged that addition of allyl alcohol to **[15b]**BF_4 would compete with phosphine attack to afford a mixture of fluorinated enones **86b** and **87b**, analogous to the reaction of **[45c]**PF_6 with allyl alcohol to afford **86a** and **87a** (Scheme 142).[277] However, heating a d^3-acetonitrile solution of **[15b]**BF_4 and allyl alcohol for 3 days at 50°C did not result in the formation of any enone products, only the formation of **[18]**BF_4 was observed (Scheme 143).

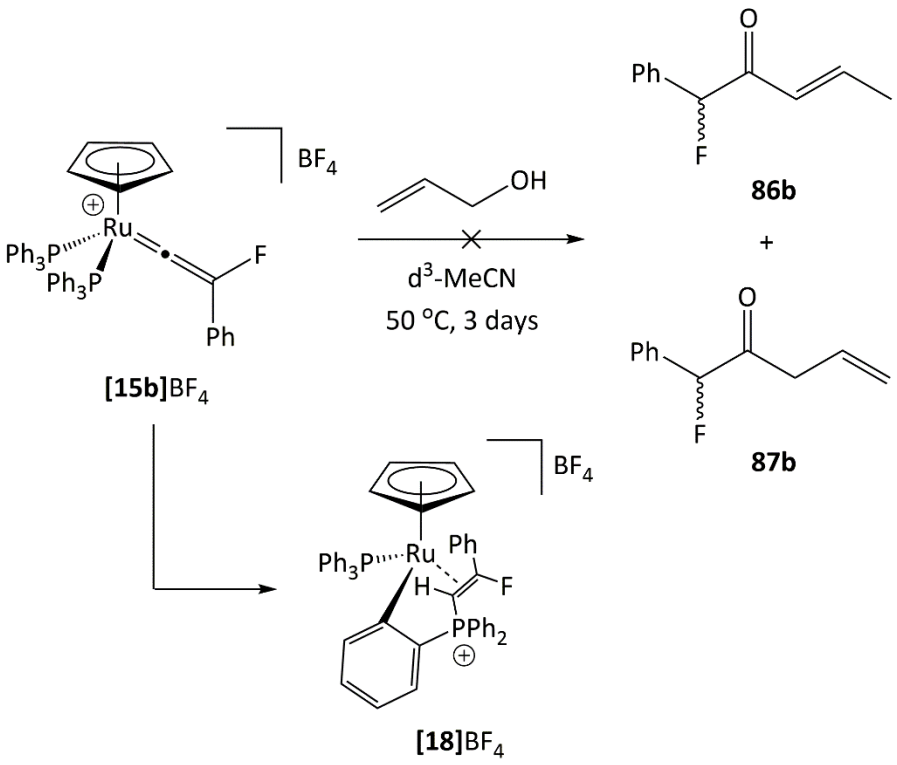

Scheme 143: The reaction of [15b]BF_4 with allyl alcohol was envisaged to afford 86b or 87b. However, heating allyl alcohol with [15b]BF_4 at 50 °C for 3 days in d^3-acetonitrile afforded [18]BF_4.

3.3.2 Addition of Styrene

Murakami *et al*.[210] demonstrated ruthenium catalysed coupling of unactivated alkenes and alkynes through a vinylidene intermediate. The reaction of **[45c]**$^+$ with oct-1-ene afforded a mixture of linear and branched diene products through loss of a phosphine and coordination of the alkene (Scheme 144).

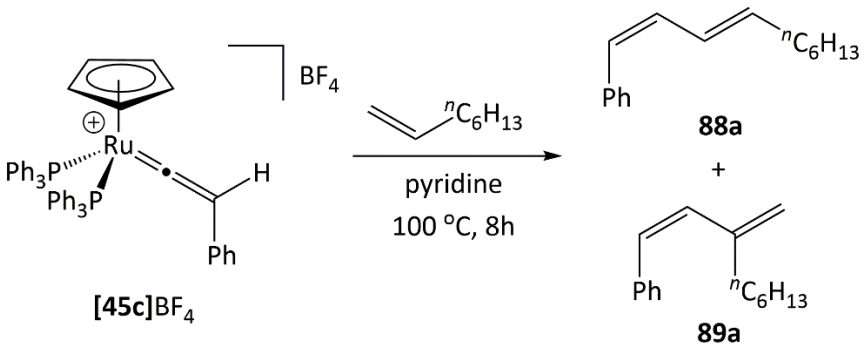

Scheme 144: Murakami *et al.*[210] reported the coupling of [45c]BF_4 with oct-1-ene in pyridine to afford 88a and 89a.

It was envisaged the addition of styrene to **[15b]**BF_4 would afford fluorinated dienes, **16** and **17**. However, heating a d^3-acetonitrile solution of **[15b]**BF_4 with styrene at 50 °C afforded only **[18]**BF_4, indicating phosphine attack is faster than alkene-vinylidene coupling (Scheme 145).

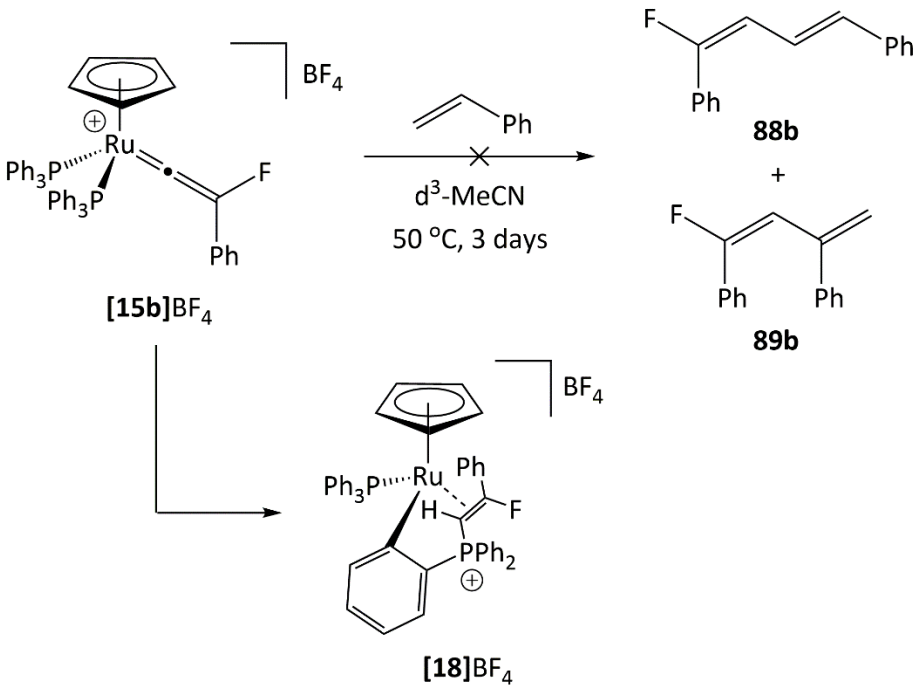

Scheme 145: The reaction of [15b]BF_4 with styrene was envisaged to afford 88b or 89b. However, heating styrene with [15b]BF_4 at 50 °C for 3 days in d^3-acetonitrile afforded [18]BF_4.

3.3.3 Addition of Ethynyltrimethylsilane

The addition of ethynyltrimethylsilane to **[15b]**BF_4 was predicted to form either the enyne complex **[90]**, through coupling of the alkyne and vinylidene ligand, and/or **[91]**BF_4, through defluoro-desilylation. However, heating **[15b]**BF_4 in the presence of ethnyltrimethylsilane only afford **[18]**BF_4 with no evidence to suggest the formation of either **[90]** or **[91]**BF_4 (Scheme 146).

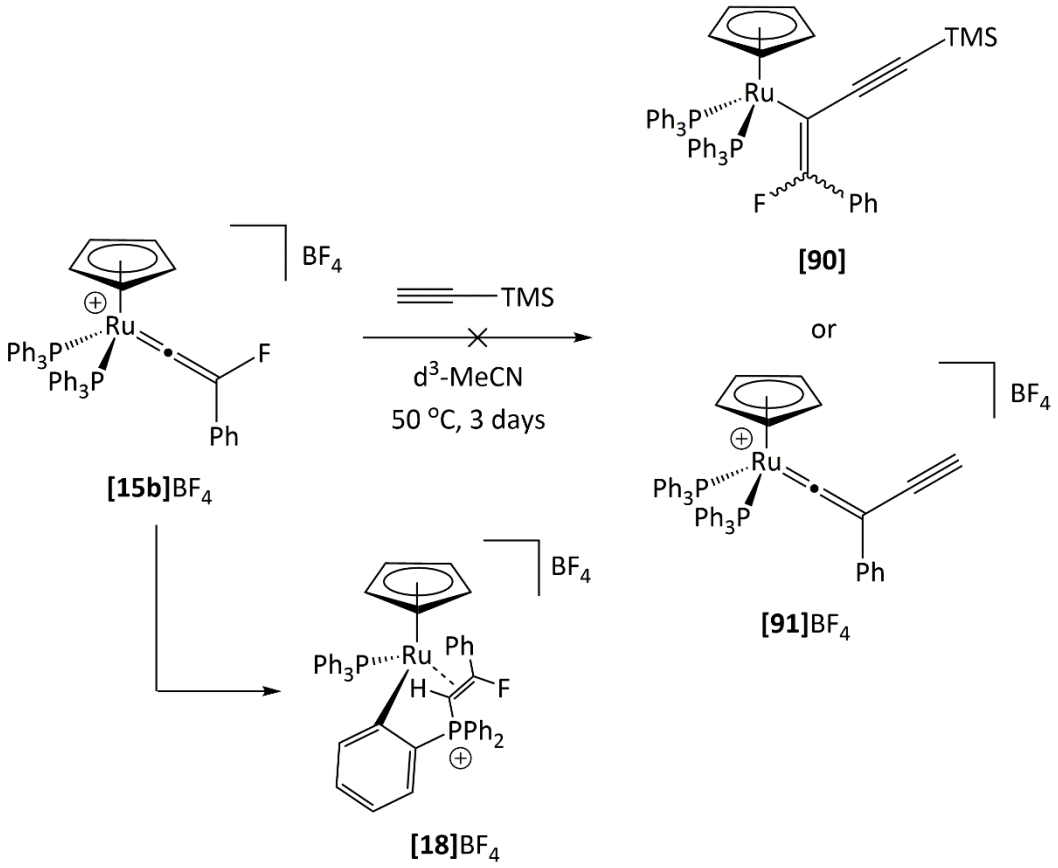

Scheme 146: The reaction of [15b]BF_4 with ethynyltrimethylsilane was envisaged to afford [90] or [91]BF_4. However, heating ethynyltrimethylsilane with [15b]BF_4 at 50 °C for 3 days in d^3-acetonitrile afforded [18]BF_4.

3.3.4 Addition of an Oxygen Atmosphere to [15b]BF_4

To determine whether fluorovinylidene complexes are capable of undergoing oxygenation across the C=C bond of the vinylidene ligand to afford an alternative method of accessing organic fluoroacyls directly, **[15b]**BF_4 was exposed to an oxygen atmosphere. It was envisaged that oxidative cleave of the vinylidene C=C bond would afford the fluoroacyl, **93**, and the carbonyl complex, **[92]**BF_4 (Scheme 147).

A d^2-dichloromethane solution of **[15b]**BF_4 was degassed by three freeze-pump-thaw cycles and the atmosphere was replaced with oxygen. Over the course of two weeks at room temperature, the ^{19}F NMR spectrum of the reaction mixture in d^2-dichloromethane displayed a small reduction in the resonance at δ -208.3 for **[15b]**BF_4 and the appearance of a small singlet resonance at δ 17.4 which matches the literature data for benzoyl fluoride **93** (Scheme 147).[278] The $^{31}P\{^1H\}$ NMR spectrum revealed the appearance of a small signal at δ 42.4 corresponding to **[92]**BF_4. The ESI-MS did not detect the presence of **93** but its hydrolysis product, benzoic acid, was detected supporting the formation of **93**. However, the reaction

was slow with only 10 % of **[15b]**BF_4 reacting over two weeks according to the ^{19}F NMR spectrum.

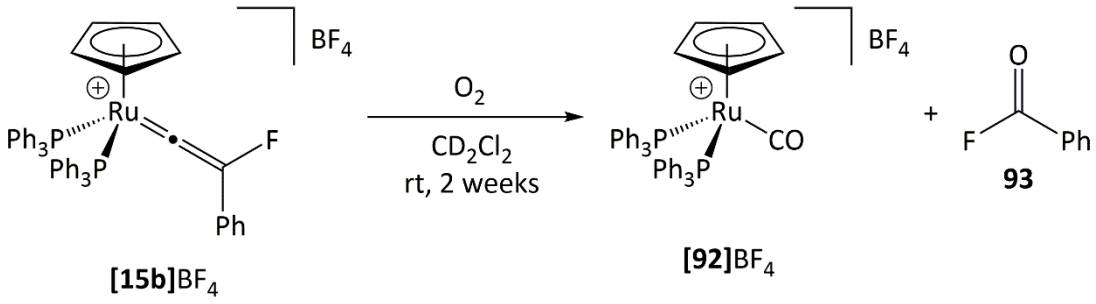

[15b]BF_4 **[92]**BF_4

Scheme 147: Under an atmosphere of oxygen, [15b]BF_4 undergoes oxidative cleavage of the vinylidene C=C to afford [92]BF_4 and 93.

3.4 Reactions of [54a]NSI

3.4.1 Addition of an Oxygen Atmosphere

It was shown in section 3.3.4 that exposing **[15b]**BF_4 to an atmosphere of oxygen resulted in the oxidative cleavage of the vinylidene C=C bond to afford **93**. To determine whether the oxidative cleavage of the vinylidene C=C bond occurs with other fluorovinylidene complexes, **[54a]**NSI was subjected to an oxygen atmosphere.

A d^2-dichloromethane solution of **[54a]**NSI was degassed by three freeze-pump-thaw cycles and the atmosphere was replaced with oxygen. After 16 hours at room temperature the ^{19}F NMR spectrum of **[54a]**NSI displayed the gradual appearance of a doublet resonance at δ 46.2 (J = 182 Hz) corresponding to the formation of **94** (3 % conversion by ^{19}F NMR; Scheme 148). However, the mutually coupled proton resonance could not be identified in the ^1H NMR spectrum.[279] The $^{31}P\{^1H\}$ NMR spectrum displayed a decrease in the resonance at δ 76.4 corresponding to **[54a]**NSI and the appearance of **[85]** at δ 72.2 (11 % conversion by $^{31}P\{^1H\}$ NMR). The ^1H NMR spectrum displayed the appearance of a triplet resonance at δ 1.57 with 1.7 Hz coupling to phosphorus, corresponding to the proton environments of the Cp* ligand of **[85]**NSI (11 % conversion); the proton resonance for **94** could not be observed.

Over 5 days the ^{19}F NMR spectrum displayed further conversion of **[54a]**NSI to **94** (26 %) along with the appearance, and growth, of resonances at δ -139.3 (15 %) and -153.0 (2 %) corresponding to SiF_5^- and BF_4^- respectively. The formation of SiF_5^- and BF_4^- presumably occurs through hydrolysis of **94** by adventitious water to afford hydrogen fluoride which subsequently reacts with the siliconborate glass. The $^{31}P\{^1H\}$ NMR spectrum of the solution exhibited a growth in the resonance for **[85]**NSI at δ 72.2, while the ^1H NMR spectrum displayed decay of the Cp* and dppe resonances for **[54a]**NSI and concomitant growth of **[85]**NSI corresponding to 47 % conversion. Again, the proton resonance for **94** could not be observed. After a further 11 days at room temperature, further oxygenation of the vinylidene C=C bond in **[54a]**NSI was observed according to the NMR spectroscopy (31 % by ^{19}F NMR). The ^{19}F NMR spectrum after 11 days revealed the quantity of **94** present in solution decreased (22 %) while the resonances for SiF_5^- (36 %) and BF_4^- (11 %) grew. It is believed that **94** undergoes hydrolysis in the presence of adventitious water to afford hydrogen fluoride which subsequently reacts with the glass of the NMR tube to afford SiF_5^- and BF_4^-. The vinylidene C=C bond in **[54a]**NSI appears to be more susceptible to oxidative cleavage compared to the vinylidene C=C bond in **[15b]**BF_4.

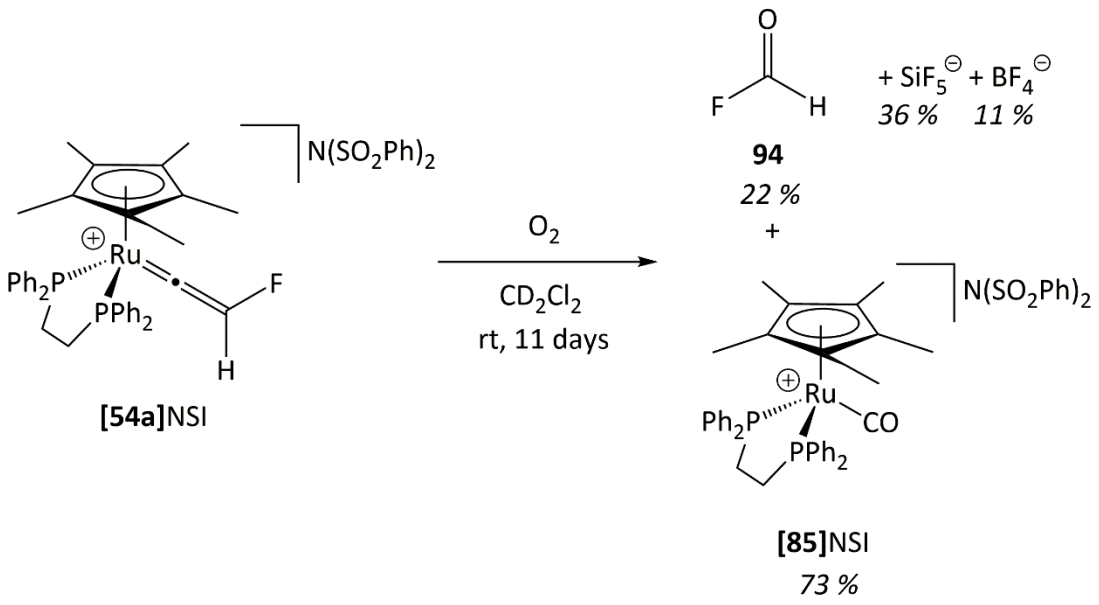

Scheme 148: Under an atmosphere of oxygen, [54a]NSI undergoes oxidative cleavage of the vinylidene C=C to afford 94 and [85]NSI; 94 also undergoes hydrolysis which subsequently affords inorganic fluorides SiF_5^- and BF_4^-.

3.4.2 Addition of a Carbon Monoxide Atmosphere

It was envisaged that under an atmosphere of carbon monoxide displacement of the vinylidene ligand would occur to afford **[85]**, fluoroethyne and its cyclotrimers, or insertion of carbon monoxide into the vinylidene ligand of **[54a]**NSI (Scheme 149).

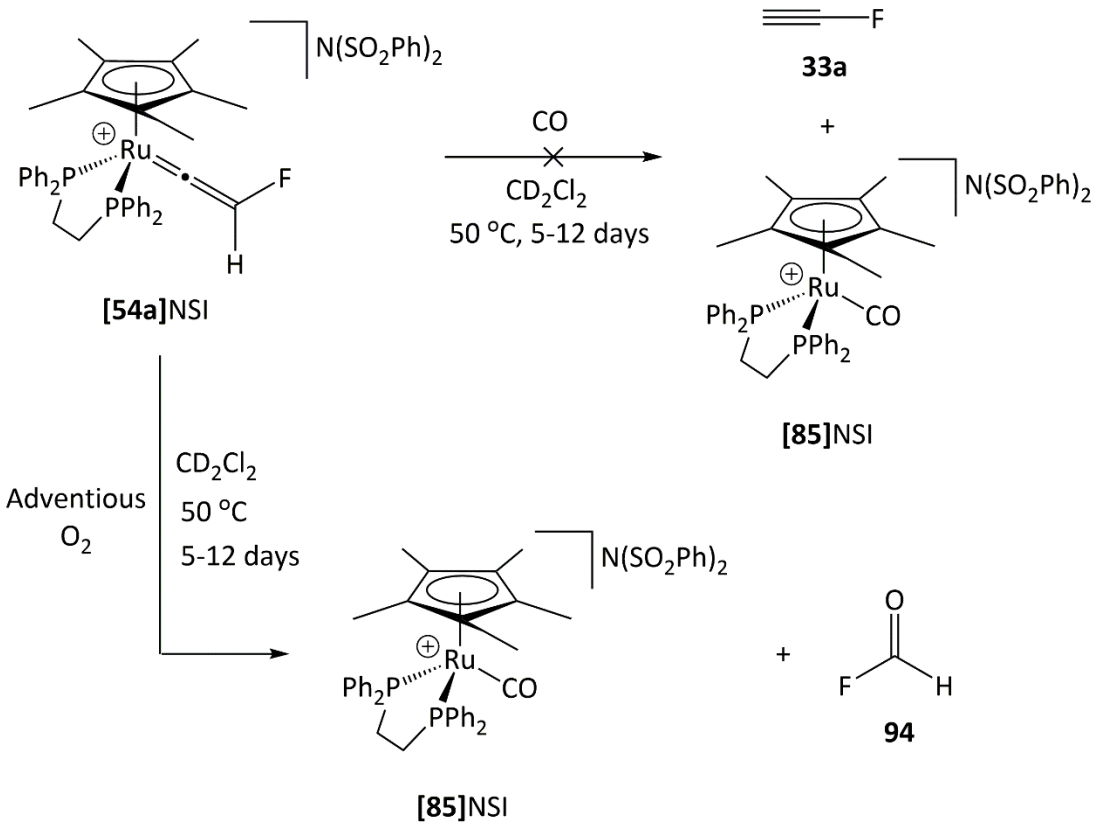

Scheme 149: Heating a dichloromethane solution of [54a]NSI at 50 °C under an atmosphere of carbon monoxide was envisaged to displace 33a and afford [85]NSI; however, oxidative cleavage of the vinylidene C=C bond by adventitious oxygen afforded 94 and [85]NSI over 5-12 days.

Heating a d^2-dichloromethane solution of **[54a]**NSI in a fluorinated ethylene polymer (FEP) lined Youngs NMR tube under a carbon monoxide atmosphere for seven days at 50 °C resulted in the partial conversion of **[54a]**NSI to **[85]**NSI according to the $^{31}P\{^1H\}$ NMR spectra. The spectra after seven days displayed depletion of the singlet resonance at δ 76.4 and the growth of the resonance at δ 72.2, corresponding to **[85]**NSI (8 % conversion). However, the ^{19}F NMR spectrum did not provide any evidence for the formation of fluoroethyne or trimerisation products, instead a small broad signal at δ -175.5 was observed (8 % conversion). This resonance is believed to correspond to the formation of hydrogen fluoride or a product from a reaction with hydrogen fluoride; it is highly unlikely to correspond to the formation of fluoroethyne given rapid trimerisation occurs above -80 °C. The ^1H NMR spectrum displayed the appearance of shoulders at δ 1.56 and 2.57 which correspond to the formation of **[85]**NSI. Heating the reaction for a further five days at 50 °C resulted in an additional 5 % conversion of **[54a]**NSI to **[85]**NSI (13 % total). No new species could be observed by NMR spectroscopy and it appears the reaction of **[54a]**NSI with carbon monoxide does not result in displacement of the alkyne.

The reaction was repeated without an FEP liner to determine whether there was any difference in the reactivity observed. Heating a d^2-dichloromethane solution of **[54a]**NSI under a carbon monoxide atmosphere for five days at 50 °C resulted in the reaction proceeding the same as it did in the FEP liner. The only difference was that hydrogen fluoride was not observed in the ^{19}F NMR spectrum, but instead, SiF_5^- and BF_4^- were observed at δ -139.4, and -153.2 respectively due to the reaction of hydrogen fluoride with the borosilicate glass of the NMR tube. The observations suggest that carbon monoxide does not react with **[54a]**NSI, but adventitious oxygen in the carbon monoxide atmosphere reacts with **[54a]**NSI to afford **94**.

3.4.3 Addition of a Hydrogen Atmosphere

It was envisaged that heating **[54a]**NSI under an atmosphere of hydrogen would afford **95a** or **[96]** *via* hydrogenation. However heating **[54a]**NSI in the solid state at 50 °C for 11 days under an atmosphere of hydrogen did not result in the formation of fluoroethene or **[96]** (Scheme 150). The $^{31}P\{^1H\}$ NMR spectrum after 11 days in d^2-dichloromethane was dominated by **[54a]**NSI at δ 76.4 with trace quantities of a number of phosphorus-containing organometallics that could not be identified. The ^{19}F NMR spectrum was dominated by unreacted **[54a]**NSI and displayed the appearance of resonances at δ -139.4 and -152.3 corresponding to SiF_5^- and BF_4^- respectively indicating that formation of hydrogen fluoride occurs during the reaction. The lack of reactivity could be rationalised by the need for a coordinatively unsaturated metal centre to bind hydrogen which is unfavourable using dppe.

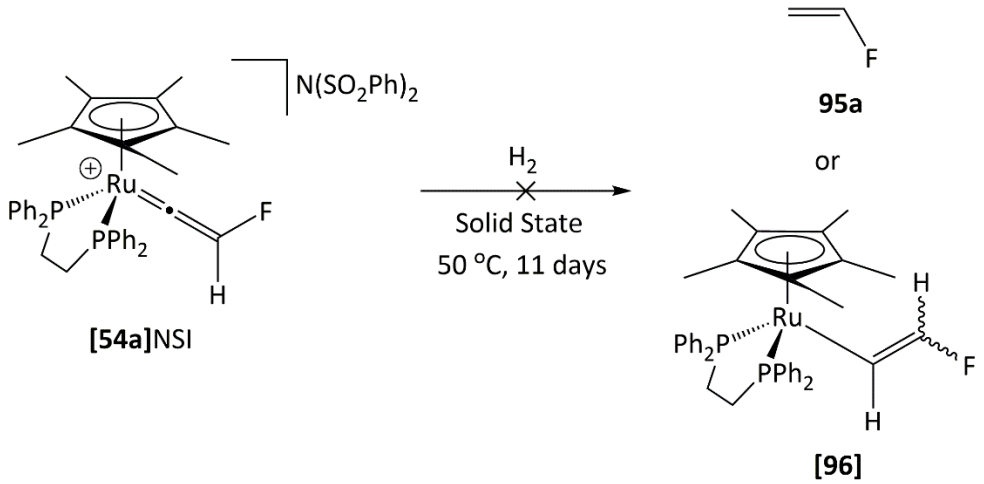

Scheme 150: Heating [54a]NSI at 50 °C under an atmosphere of hydrogen for 11 days was envisaged to displace 95a or form [96]NSI.

3.5 Attempts to Synthesise Fluorocarbene, [31]BF_4

During the early attempt to fluorinate **[28a]** with Selectfluor at room temperature (Scheme 151), the formation of fluorocarbene complex **[31]**BF_4 was observed as a minor product, presumably through sequential addition of fluoride and fluorenium ('F^+') to **[30a]**BF_4.[226]

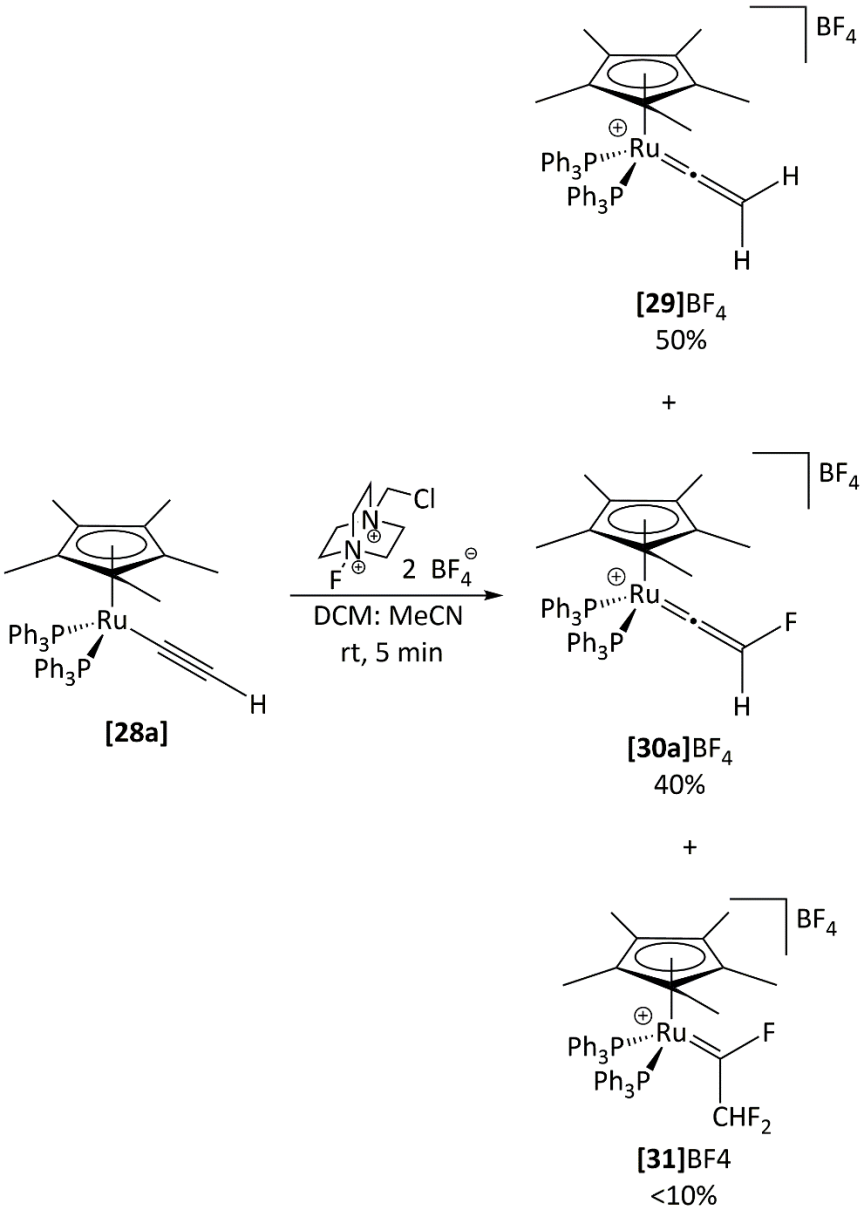

Scheme 151: Reaction of [28a] with Selectfluor at room temperature afforded a mixture of products including fluorocarbene complex [31]BF_4 as a minor product.

Due to the small number of fluorocarbene complexes reported in the literature[280-285] and the growing interest in using these carbene complexes in cross-metathesis reactions to generate novel fluoroalkenes,[283, 284, 286-290] the logical synthesis of **[31]**BF_4 was attempted to provide an alternative method for accessing this class of ligand and enable their reactivity to be

explored. The literature complexes are limited to difluoro- and fluoro-trifluoromethyl carbene ligands but have been synthesised with various metal centres (M = Mo, Co, Ru, Ir, and Ni).[280-285] Preparation of these fluorocarbene ligands are restricted to defluorination of perfluorinated ligands (Scheme 152). In contrast to the literature examples and procedures, the synthesis of fluorocarbene complexes here will be achieved through selective fluorination with electrophilic and nucleophilic sources of fluorine, and will enable a wider variety of fluorocarbene ligands to become accessible.

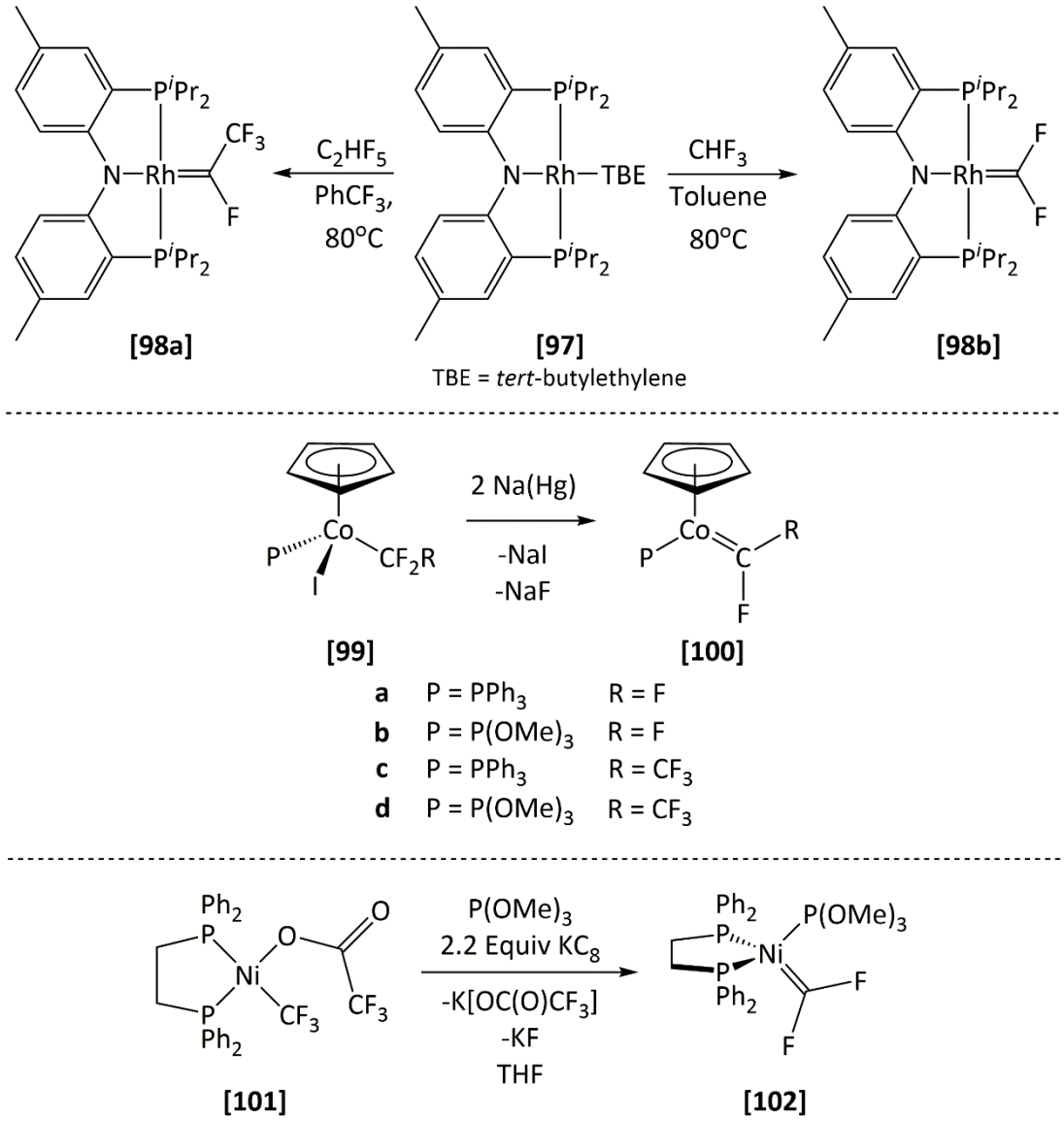

Scheme 152: Examples of fluorocarbene complexes of rhodium, cobalt, and nickel.

Room temperature fluorination of **[2-29]** with Selectfluor afforded fluorocarbene **[31]**BF_4 as a by-product. In an attempt to synthesise **[31]**$^+$ *via* **[103]**, **[30a]**BF_4 was reacted with tetramethylammonium fluoride in tetrahydrofuran. Instead of affording **[103]**, addition of

fluoride was found to facilitate the formation of the ortho-metallated fluorovinylphosphonium complex **[48]** over 36 hours (Scheme 153).

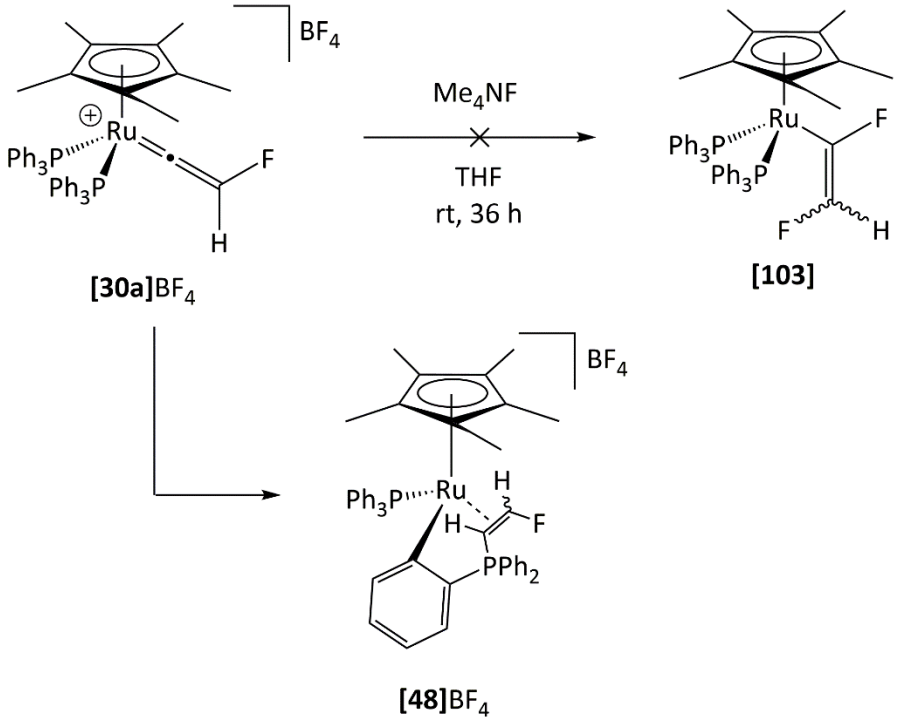

Scheme 153: The addition of tetramethylammonium fluoride to a tetrahydrofuran solution of [30a]BF_4 was envisaged to afford [103]. However, addition of fluoride afforded [4]BF_4 over 36 hours.

It is possible fluoride is acting as a base rather than a nucleophile, since addition of LiHMDS to **[30a]** was found to form **[48]** as the major product. However, it is also possible that in tetrahydrofuran loss of triphenylphosphine is favoured over fluoride attack presumably due to the insolubility of anhydrous tetramethylammonium fluoride. Milner also reported the phosphine activation pathway being favoured in the reaction of **[15b]**BF_4 with tetramethylammonium fluoride. Although the addition of triethylamine-trihydrogen fluoride (TREAT-HF) to **[15b]** was found to reduce the formation of the phosphine activation product, the addition of TREAT-HF to **[19]** was found to be selective due to the circumvention of phosphine activation using dppe. Consequently, the formation of fluorocarbenes complexes was instead studied with complexes of the type [Ru(η^5-C_5H_5)(dppe)(CFCFR)] (section 3.6).

3.6 Reactions of [23a]

Due to the effective competition of the phosphine activation pathway observed in the reactions of bis-triphenylphosphine half sandwich complexes, (e.g. **[30a]**BF_4), the formation and reactivity of ruthenium fluorocarbene complexes was explored using the [Ru(η^5-C_5H_5)(dppe)] fragment.

3.6.1 Formation of [23a]

Milner reported the synthesis of **[23a]** through treatment of a d^8-tetrahydrofuran solution of **[19]**NSI with TREAT-HF to afford **[23a]** as the *Z*-isomer selectively.[223] Instead, the synthesis of **[23a]** through addition of two equivalents of anhydrous TMAF to a tetrahydrofuran solution of **[19]**NSI reported here, afforded **[23a]** after twenty minutes sonication as a mixture of *E*- and *Z*- isomers (1:1). Presumably, the poor solubility of TMAF prevents or slows isomerisation to the *Z*-isomer.

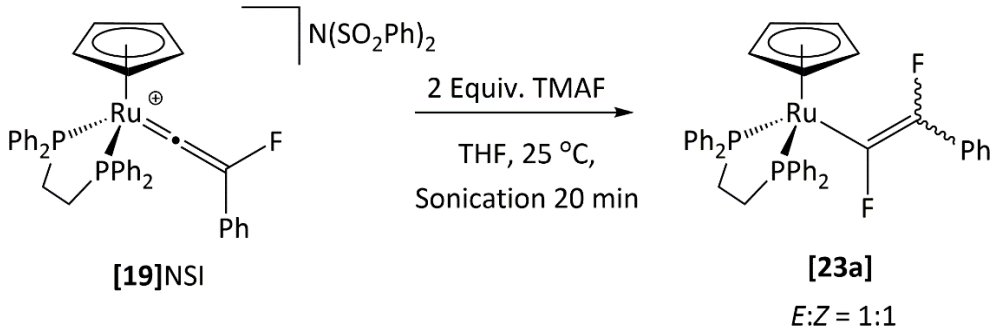

[19]NSI

[23a]

E:*Z* = 1:1

Scheme 154: Treatment of [19]NSI with TMAF in THF afforded a mixture of *E*-/*Z*- isomers of [23a].

The *Z*-isomer of **[23a]** is observed in the ^{19}F NMR spectrum in d^2-dichloromethane as a pair of mutually coupled resonances. The doublet-of-triplets resonance at δ -83.0 displays 28 Hz triplet coupling to phosphorus and 113 Hz doublet coupling to the doublet resonance at δ -107.3. The $^{31}P\{^1H\}$ NMR spectrum displayed a doublet-of-doublets resonance at δ 92.8 with 28 Hz and 3 Hz coupling to the fluorine substituents of the vinyl ligand. The α-carbon of the vinyl ligand was observed at δ 188.2 in the $^{13}C\{^1H\}$ NMR spectrum as a ddt resonance displaying doublet coupling of 294 Hz and 89 Hz coupling to fluorine substituents and triplet coupling of 19 Hz to phosphorus. The β-carbon was observed at δ 158.8 as a doublet-of-doublets resonance with 198 Hz and 51 Hz to fluorine. The data are consistent with the parameters reported by Milner.[223]

The *E*-isomer of **[23a]** is also observed in the ^{19}F NMR spectrum in d^2-dichloromethane as a pair of mutually coupled resonances at δ -67.8 and -107.3. The triplet-of-doublets resonance at δ -67.8 displayed a triplet coupling of 37 Hz to phosphorus and doublet coupling of 10 Hz to the doublet resonance at δ -103.8. The $^{31}P\{^1H\}$ NMR spectrum displayed a doublet resonance at δ 90.4 with a 37 Hz coupling to fluorine, the 3 Hz coupling to fluorine could not be distinguished. The carbon resonances α- and β-carbons of the vinyl ligand were observed at δ 173.0 and 151.2 respectively.

3.6.2 Reaction of [23a] with Hydrogen chloride in Dichloromethane

Addition of dry hydrogen chloridehydrogen chloride to a d^2-dichloromethane solution of **[23a]** resulted in rapid protonation to afford **[104a]**Cl within five minutes (Scheme 155). The $^{31}P\{^1H\}$ NMR spectrum revealed the symmetry of the complex had been broken and exhibited two doublet-of-doublets resonances at δ 84.6 and 89.5 with 19 Hz mutual coupling. The resonances displayed secondary doublet coupling of 27 Hz and 43 Hz respectively to a fluorine resonance at δ 115.9 in the ^{19}F NMR spectrum. This fluorine resonance is observed with dddd multiplicity, displaying $^3J_{FF}$ doublet coupling of 46 Hz to the adjacent the fluorine environment and $^3J_{HF}$ doublet coupling of 8 Hz to the adjacent proton environment, in addition to the two doublet couplings to phosphorus. The resonance corresponds to the α-fluorine substituent of the carbene ligand. The ^{19}F NMR spectrum also displayed an apparent triplet resonance at δ -162.9 in which the doublet coupling to the *geminal*-hydrogen and doublet coupling to fluorine are both 46 Hz, giving rise to a triplet multiplicity in the spectrum. The resonance was assigned to the fluorine substituent of the carbene β-carbon. The matching proton resonance was observed at δ 4.56 in the proton spectrum as a doublet of doublets with 46 Hz coupling to the *geminal* fluorine and 8 Hz to the adjacent fluorine. The α- and β-carbon chemical shifts of the carbene ligand were assigned to resonances at δ 299.0 and 103.4 in the $^{13}C\{^1H\}$ NMR spectrum according to a ^{13}C-^{19}F HSQC NMR experiment. The α-carbon resonance could not be observed directly but did display 388 Hz coupling to fluorine in the 2D experiment. The β-carbon of the carbene ligand could be observed directly in the $^{13}C\{^1H\}$ NMR spectrum as a doublet-of-doublets resonance with 45 and 185 Hz coupling to fluorine. The ESI mass spectrum revealed the presence of the desired complex at 705.1226 m/z and supported the crystallographic data which confirmed the structure of **[104a]**PF_6. Suitable crystals were obtained as a mixture of the desired carbene **[104a]**PF_6, and **[19]**PF_6 in a ratio of 75:25 (Figure 42), the latter complex formed through formal loss of hydrogen

fluoride. The loss of hydrogen fluoride was not observed in the initial NMR spectra, revealing the process is slow.

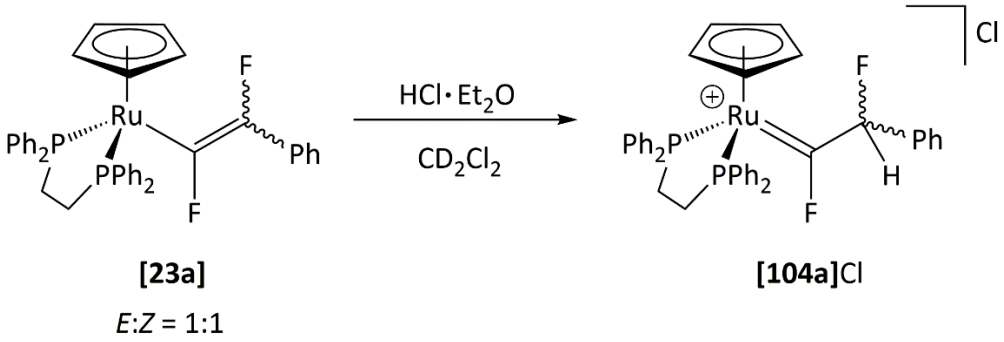

[23a]

E:*Z* = 1:1

[104a]Cl

Scheme 155: Addition of hydrogen chloride to a dichloromethane solution of [23a] afforded [104a]Cl.

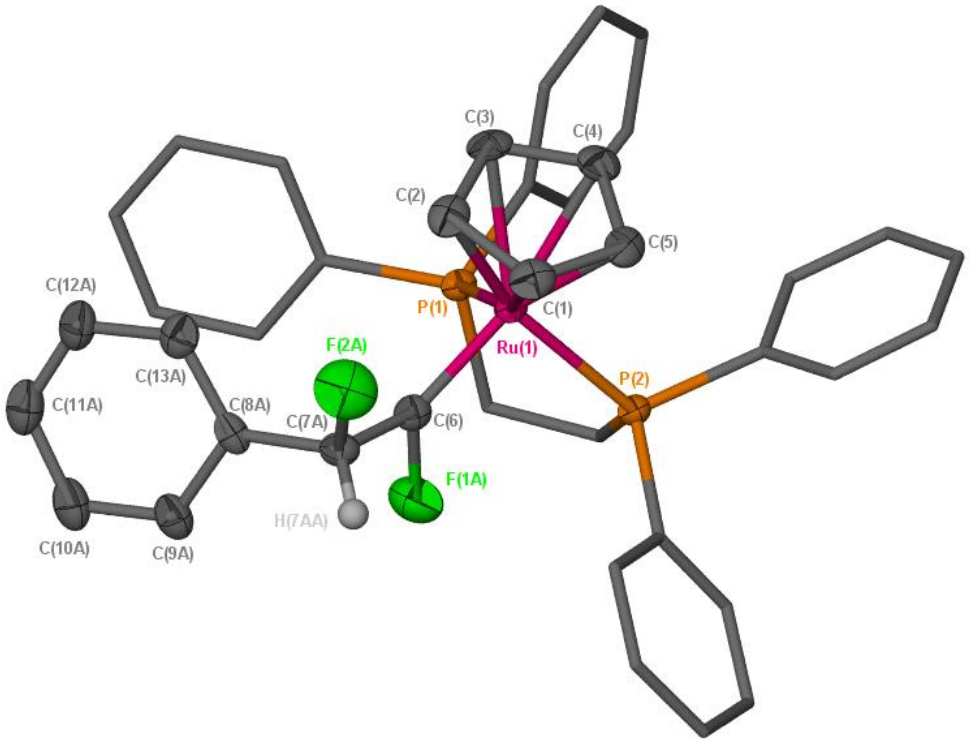

Figure 42: Crystal structure of [104a]PF_6. Hexafluorophosphate counter-ion, overlapping [15b]PF6, and hydrogens (with the exception H(7AA), have been omitted for clarity; H(7AA) fixed with 1.2 U_{iso}. Selected bond lengths (Å): Ru(1)-C(6), 1.8416(3); C(6)-C(7A), 1.371(13); C(6)-F(1A), 1.462(10); C(7A)-F(2A), 1.47(2); Ru(1)-P(1), 2.2992(7); Ru(1)-P(2), 2.2997(7); Ru(1)-C(Cp ring), 2.27 average. Selected bond angles (°): Ru(1)-C(6)-C(7A), 137.4(6); Ru(1)-C(6)-F(1A), 121.2(4); C(6)-C(7A)-F(2A), 109.5(11); C(7A)-C(6)-F(1A), 100.0(7); P(1)-Ru(1)-C(6), 85.80(9); P(2)-Ru(1)-C(6), 94.01(10); P(1)-Ru(1)-P(2), 81.57(3).

The highly deshielded chemical shift of the α-fluorine, observed at δ 115.9 in the ^{19}F NMR spectrum, is within the wide range observed for other metal fluorocarbene complexes (δ 13.6 (Co) up to δ 143.3 (Mo)). Complexes **[98b]** (δ 95.6) and **[108]**OTf (δ 99.6 and 109.2 respectively) display the closest fluorine chemical shifts to that observed for **[104a]**Cl.

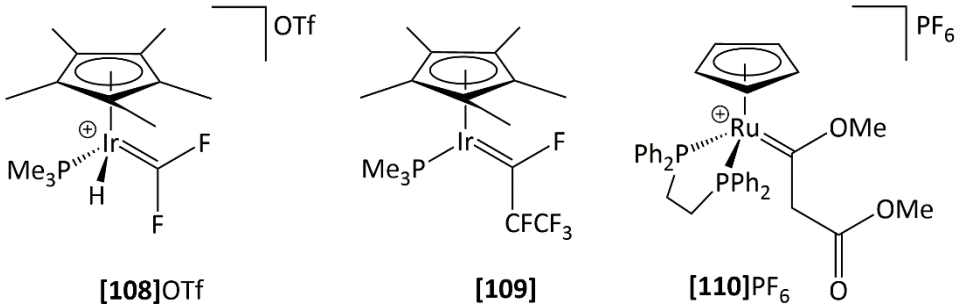

[108]OTf **[109]** **[110]**PF_6

Figure 43: Examples of fluorocarbene complexes

The Ru=C and =C-F bond lengths of **[104a]**PF_6 were measured at 1.8416(3) Å and 1.462(10) Å respectively and are within the range observed for other metal fluorocarbene complexes. The M=C and =C-F bond lengths are most similar to those in [Ir(η^5-C_5Me_5)(PMe_3)(=$CFCF_3$)], **[109]**, which were reported at 1.845(10) Å and 1.467(13) Å respectively. The Ru=C-F bond angle is statistically ideal for the bond angle around an sp^2-hybridised carbon at 121.2(4)°. The Ru=C-C and F-C-C bond angles were significantly distorted away from ideal at 137.4(6)° and 100.0(7)° respectively. The widening of the Ru=C-C bond angle would be expected in order to reduce the steric interaction of the carbene substituent with the neighbouring ligands. Significant compression of the F-C-R bond angle is a common feature observed in the other metal fluorocarbene complexes (98.2(11)° to 104.3(9)°), and also in the analogous bond angle in fluorovinylidene complexes reported in Chapter 2.

Compared to a similar Fischer-type ruthenium carbene complex, [Ru(η^5-C_5H_5)(dppe)(=C(OMe)CH_2C(O)OMe)]PF_6, **[110]**PF_6 which exhibited a Ru=C bond length of 1.933(4) Å,[235] **[104a]**PF_6 displays a significantly shorter Ru=C bond length. This can be rationalised by the difference in electronic properties between the methoxy and fluorine substituents of the carbene ligand. The methoxy group is an effective π-donor which competes with ruthenium in populating the vacant 2p orbital of the metal-bound carbon, resulting in less effective π-bonding between the ruthenium and carbene ligand and subsequently a longer than expected Ru=C bond length. Fluorine, while also a π-donor substituent, is less donating in comparison due it its high electronegativity. This leads to less effective competition between fluorine and ruthenium for donation into the 2p orbital of the

carbene carbon, and subsequently results in a stronger π-interaction between the ruthenium and carbene ligand and a shorter Ru=C bond. Such a large difference in metal-carbene bond lengths was also remarked upon by Baker *et al*.[283] for cobalt fluorocarbene complexes compared to other Fischer-type carbene complexes.

3.6.3 Reaction of [23a] with Hydrogen chloride in Tetrahydrofuran

In contrast to the reaction of **[23a]** with hydrogen chloride in dichloromethane, conducting the reaction in tetrahydrofuran did not afford **[104a]**Cl. Instead rapid formation of **[1-306]** was observed within ten minutes of hydrogen chloride (3 equivalents) addition. The $^{31}P\{^{1}H\}$ NMR spectrum revealed the disappearance of the phosphorus resonances for **[23a]** and the appearance of a singlet resonance at δ 72.2 for **[1-306]** (Scheme 156). The ^{19}F NMR spectrum displayed the appearance of two major doublet-of-doublet resonances at δ -170.5 and -177.6 matching the literature data for *E*-**105a**.[291] The resonance at δ -170.5 exhibited doublet coupling of 6 Hz to hydrogen and 125 Hz to fluorine, consistent with the fluorine being *cis*- to hydrogen and *trans*- to fluorine. The resonance at δ -177.6 exhibited the matching 125 Hz *trans*-coupling to fluorine and 75 Hz coupling to hydrogen consistent with *geminal*- HF coupling. The formation of **[1-306]** and *E*-**105a** implies the formal protonation of the metal bound carbon of **[23a]**. There was no evidence for the formation of **[104a]**Cl by NMR spectroscopy or ESI-mass spectrometry.

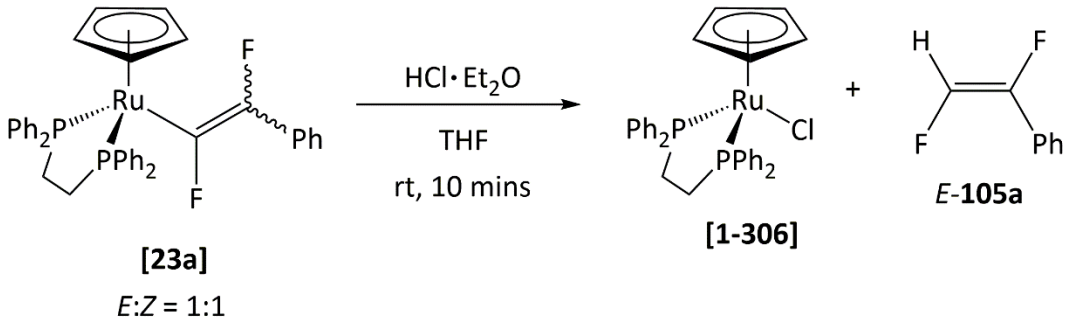

[23a]
E:*Z* = 1:1

[1-306]

E-**105a**

Scheme 156: Addition of hydrogen chloride to a tetrahydrofuran solution of [23a] afforded [1-306] and *E*-105a after 10 minutes.

To probe the relationship between **[104a]**Cl and *E*-**105a**, **[104a]**Cl was dissolved in tetrahydrofuran and the resulting reaction monitored by NMR spectroscopy. It was postulated that addition of tetrahydrofuran to **[104a]**Cl would afford **[1-306]** and *E*-**105a** if the carbene was a potential intermediate.

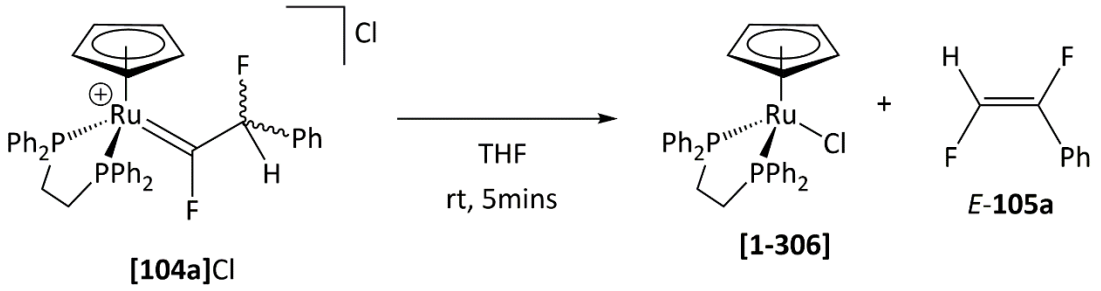

[104a]Cl **[1-306]** *E*-**105a**

Scheme 157: Dissolution of [104a]Cl in tetrahydrofuran afforded [1-306] and *E*-105a within five minutes.

The NMR spectroscopic data revealed that rapid and complete conversion of **[104a]**Cl to **[1-306]** and *E*-**105a** proceeded within five minutes (Scheme 157). The data imply that a formal 1,2-hydrogen shift must occur from **[104a]**Cl to afford **[106]** which, through formal displacement by chloride, affords the observed products, **[1-306]** and *E*-**105a**. The stereo-selective formation of the kinetic *E*- isomer is consistent with protonation of the α-carbon of **[23a]** to afford *E*-**[106]**.

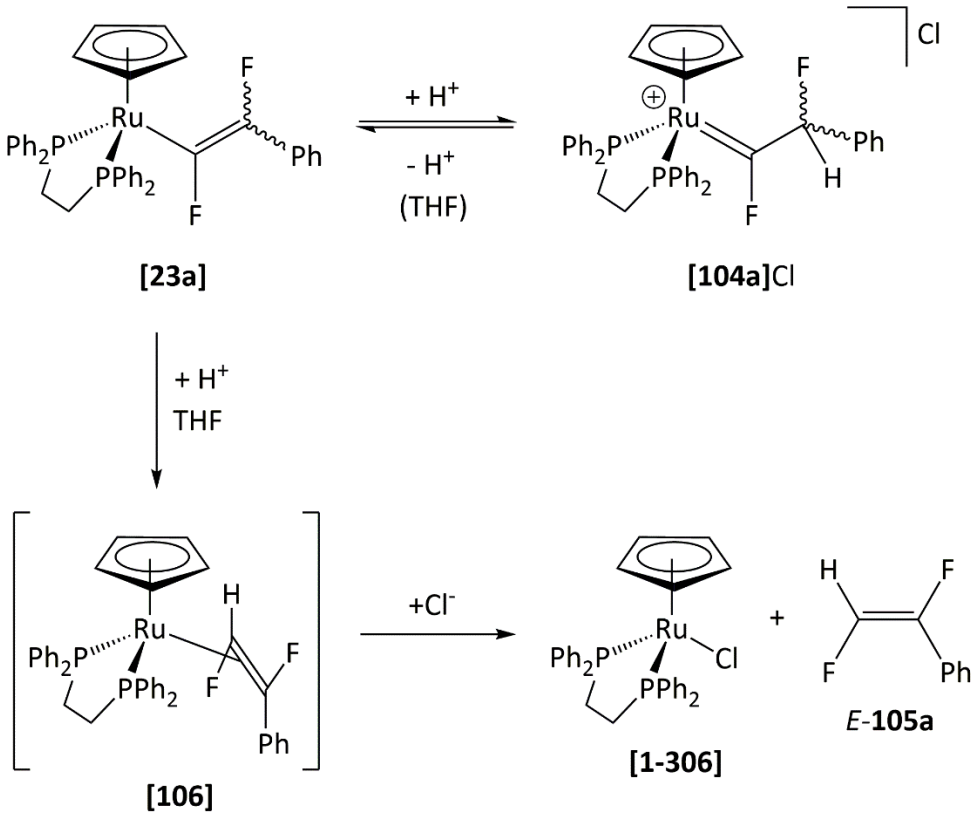

[23a] **[104a]**Cl **[106]** **[1-306]** *E*-**105a**

Scheme 158: Protonation of [23a] is believed to afford [104a]Cl as the kinetic product which undergoes deprotonation-protonation in tetrahydrofuran to afford [106] transiently and affords *E*-105a by displacement by chloride.

It is therefore proposed that protonation initially affords **[104a]**Cl as the kinetic product which undergoes solvent-assisted deprotonation-protonation in tetrahydrofuran to afford the thermodynamic product *E*-**[106]** transiently *in situ*. *E*-**105a** is rapidly displaced by chloride to afford **[1-306]** (Scheme 158). The combination of both chloride and THF appear to be important in the formation of the fluoroalkene product. The coordinating ability of tetrahydrofuran may assist in the displacement of the alkene by initially coordinating to the ruthenium prior to chloride attack, whereas this is not likely with a non-coordinating solvent such as dichloromethane.

Conversion of **[104a]**Cl to *E*-**[106]** may also proceed *via* a hydride intermediate rather than a deprotonation-protonation mechanism. However, the formation of such an intermediate would require dissociation of one of the tethered phosphines from the metal which would be unlikely.

3.6.4 Reaction of [23a] with Tetrafluoroboric Acid

To ensure protonation is not limited to hydrogen chloride and confirm the role played by the chloride anion, **[23a]** was reacted with tetrafluoroboric acid. Addition of tetrafluoroboric acid to a dichloromethane solution of **[23a]** resulted in the formation of **[104a]**BF_4 *via* protonation of the β-position. This is supported by the appearance of the characteristic fluorine and phosphorus resonances observed in the NMR spectra for **[104a]**Cl (Scheme 159).

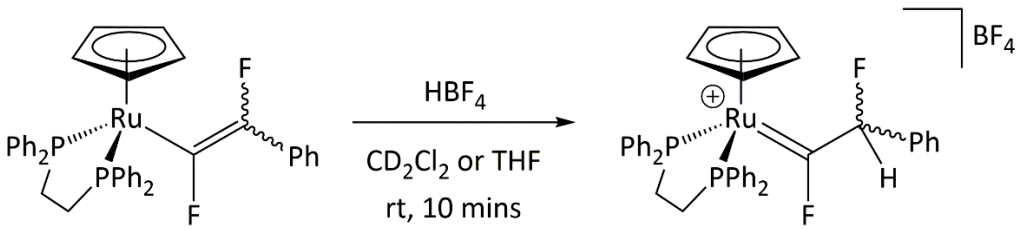

[23a]
E:*Z* = 1:1

[104a]BF_4

Scheme 159: [23a] undergoes protonation in both dichloromethane and THF by addition of tetrafluoroboric acid to afford [104a]BF_4.

It was found that addition of tetrafluoroboric acid to **[23a]** in tetrahydrofuran also afforded the β-protonated product **[104a]**BF_4, with no evidence for the formation of **[1-306]** or *E*-**105a** by NMR spectroscopy. Neither was there any evidence to suggest the formation of **[106]**. The data are consistent with the need for a chloride source to displace the alkene ligand and

supportive that the formation of **[106]** is transient and in equilibrium with **[104a]**BF_4 as there was no evidence of deprotonation-protonation in tetrahydrofuran.

3.6.5 Addition of Tetrabutylammonium Chloride to [104a]BF_4

To provide further evidence for the need of chloride in the displacement of the alkene from the coordination sphere of the metal, a chloride salt was added to **[104a]**BF_4. Tetrabutylammonium chloride was added to a d^8-tetrahydrofuran solution of **[104a]**BF_4, generated by addition of HBF_4 to **[23a]** and analysed by NMR spectroscopy. The $^{31}P\{^1H\}$ NMR spectrum revealed that addition of chloride to **[104a]**BF_4 afforded **[1-306]**, while the ^{19}F NMR spectrum revealed the formation of *E*-**[105a]** (Scheme 160). The experiments confirm the necessity of chloride anions in the displacement of *E*-**[105a]**.

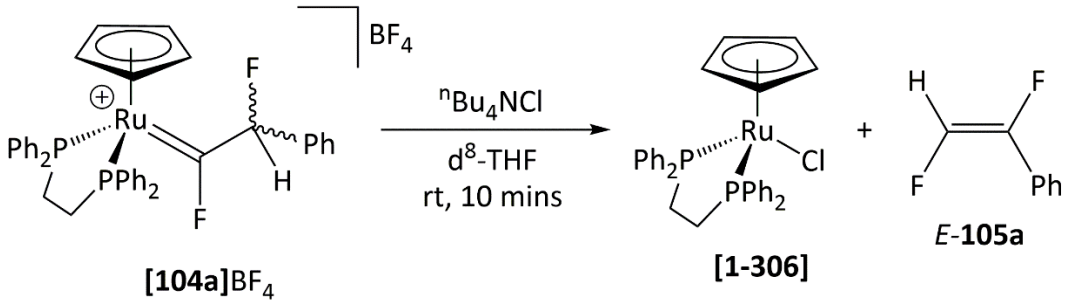

Scheme 160: Addition of tetrabutylammonium chloride to a d^8-tetrahydrofuran solution of [104a]BF_4 affords [1-306] and *E*-105a.

3.6.6 Reaction of [23a] with NFSI

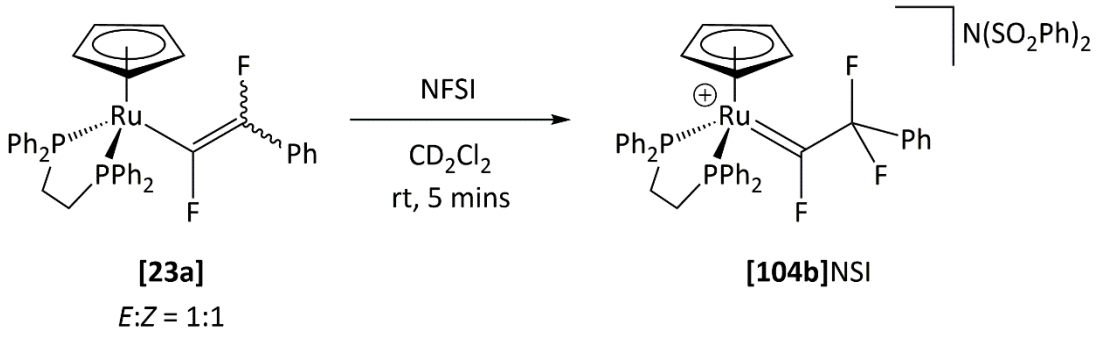

Scheme 161: Fluorination of [23a] by NFSI in dichloromethane rapidly afforded [104b]NSI within five minutes.

Addition of stoichiometric NFSI to a dichloromethane solution of **[23a]** resulted in rapid conversion to **[104b]**NSI within five minutes (Scheme 161). The $^{31}P\{^1H\}$ NMR spectrum of **[104b]**NSI in d^2-dichloromethane displayed the disappearance of the two resonances at

δ 92.8 and δ 90.4 corresponding to *Z*- and *E*-**[23a]** respectively and the appearance of a resonance at δ 85.5 with 33 Hz coupling to the α-fluorine of the carbene ligand. The ^{19}F NMR spectrum revealed the disappearance of the two pairs of fluorine resonances for **[23a]** and the appearance of two new resonances at δ 113.6 and -90.3 for **[104b]**NSI. The triplet-of-triplets resonance at δ 113.6 exhibited 33 Hz triplet coupling to the two phosphine substituents and 12 Hz triplet coupling to the two adjacent fluorine substituents. The doublet resonance at δ -90.3 exhibited the matching 12 Hz coupling to the adjacent fluorine substituent. A ^{13}C-^{19}F HSQC NMR spectrum displayed two cross peaks at δ 119.3 and 284.6 in the ^{13}C{^{1}H} NMR spectrum coupling to the fluorine signal at δ -90.3. The low field resonance at δ 284.6 corresponds to the metal bound carbon of the carbene ligand while the resonance at δ 119.3 corresponds to the β-carbon. These resonances could not be observed directly in the 1D ^{13}C{^{1}H} NMR experiment due to low intensity as a consequence of the high multiplicity. The ESI mass spectrum confirmed the presence of a species with the correct m/z for **[104b]**$^{+}$ and X-ray crystallography confirmed the structure (Figure 44).

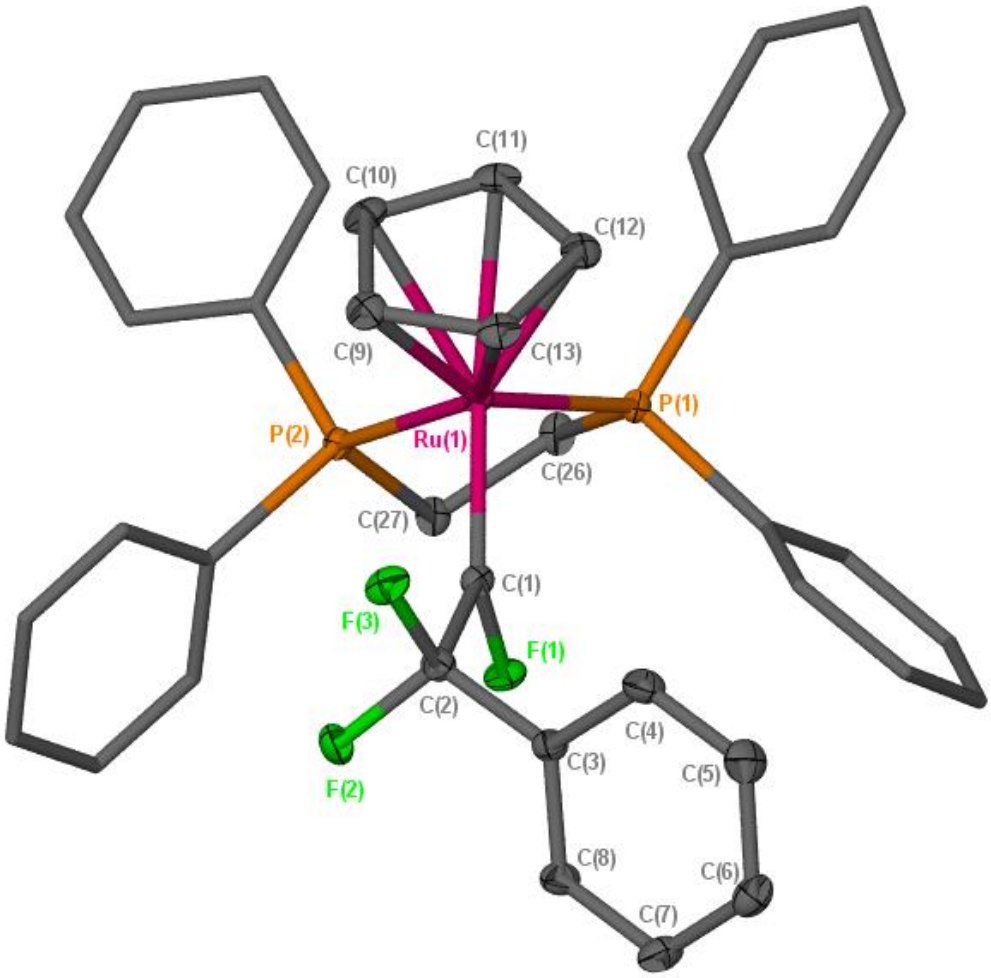

Figure 44: Crystal structure of [104b]PF_6. Hexafluorophosphate counter-ion and hydrogens have been omitted for clarity. Selected bond lengths (Å): Ru(1)-C(1), 1.872(2); C(1)-C(2), 1.540(3); C(1)-F(1A), 1.370(3); C(2)-F(2), 1.373(2); C(2)-F(3), 1.367(2); Ru(1)-P(1), 2.3057(5); Ru(1)-P(2), 2.3007(5); Ru(1)-C(Cp ring), 2.27 average. Selected bond angles (°): Ru(1)-C(1)-C(2), 132.25(26); Ru(1)-C(1)-F(1), 125.40(15); C(1)-C(2)-F(2), 107.02(17); C(1)-C(2)-F(3), 109.99(17); C(2)-C(1)-F(2), 102.21(17); F(2)-C(2)-F(3), 105.40(17); P(1)-Ru(1)-C(1), 94.98(7); P(2)-Ru(1)-C(1), 85.41(7); P(1)-Ru(1)-P(2), 83.233(19)

The α-fluorine substituent of **[104b]**NSI (δ 113.6) is observed at a similar chemical shift to the fluorine substituent in **[104a]**Cl (δ 115.9) suggesting there is not much difference in the local environment upon replacing the β-hydrogen of the carbene with fluorine. In contrast, the fluorine chemical shift of the β-fluorine in **[104a]**Cl (δ -162.9) undergoes significant deshielding upon replacing the *geminal*-hydrogen with fluorine in **[104b]**NSI (δ -90.3). This can be rationalised by an increase in competition for the electron density around the β-carbon by incorporation of a second fluorine substituent.

The Ru=C bond length of **[104b]**PF_6 was measured at 1.872(2) Å which appears elongated in comparison to **[104a]**PF_4 (1.8416(3) Å), but still significantly shorter than other Fischer carbene complexes.[283] The =C-F bond length, measured at 1.380(3) Å, was significantly

shorter than the analogous bond in **[104a]**PF_6 (1.462(10) Å). In contrast, the =C-C bond length in **[104b]**PF_6, measured at 1.540(3) Å, was significantly elongated compared to **[104a]**PF_6 (1.371(13) Å). However, it should be noted thatdifferences are observed between the Ru=C and =C-F bond lengths in the experimental data and the gas-phase structures calculated at the (RI-)BP86/SV(P) level. It is believed the presence of **[19]**PF_6 in the crystals obtained for **[104a]**PF_6 may be the cause for differences in bond lengths between the experimental and calculated data. Similar to **[104a]**PF_6 the bond angles around the carbene carbon are distorted away from the ideal geometry, with the F-C-C bond angle compressed at 107.01(17)°.

3.6.7 Attempt to Liberate a Fluoroalkene from [104b]NSI

In an attempt to displace alkene **105b** from **[104b]**NSI by chloride, a d^8-tetrahydrofuran solution of **[104b]**NSI was heated at 70 °C in the presence of tetrabutylammonium chloride for 6 days. However, there was no evidence for the formation of **105b** or **[1-306]** according to NMR spectroscopy (Scheme 162). After two days of heating, the $^{31}P\{^1H\}$ NMR spectrum displayed a significant reduction in intensity of the doublet resonance at δ 86.1 for **[104b]**NSI and the appearance of a singlet resonance at δ 96.3 (83 % conversion) which was assigned to **[107]**NSI. The ^{19}F NMR spectrum displayed the appearance of a resonance for hydrogen fluoride at δ -190.2 as a broad resonance, as well as the appearance of BF_4^- and SiF_5^- at δ -152.3 and -138.5 respectively. The other major species observed in the ^{19}F NMR spectrum was a singlet resonance at δ -92.3. This species may correspond to the formation of TBAF, which is observed at similar chemical shifts;[55] decomposition of **[104b]** by the adventitious water in the tetrabutylammonium chloride salt may result in the formation of **[107]**$^+$ along with the formation of fluoride. The LIFDI mass spectrum displayed the m/z for tetrabutylammonium cation, **[107]**$^+$ and unreacted **[104b]**$^+$. The LIFDI mass spectrum also exhibited an organic species with an m/z of 571.60 which could not be identified. Heating for an additional four days did not result in any change in the NMR spectra. The addition of a source of chloride did not result in the liberation of **105b** but rather decomposition to form hydrogen fluoride and other fluoride species according to the ^{19}F NMR spectra.

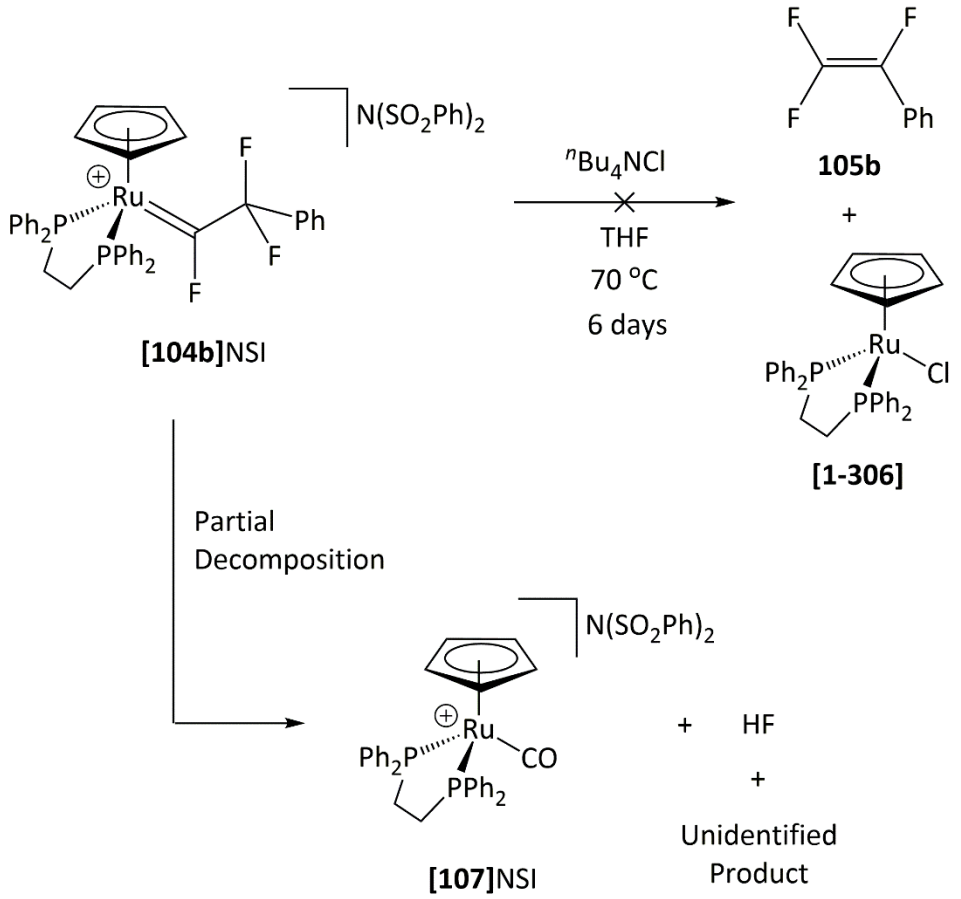

Scheme 162: It was envisaged heating tetrabutylammonium chloride with [104a]NSI in tetrahydrofuran would afford 105b and [1-306]. However no reaction was observed when [104b]NSI was heated at 70 °C for 6 days, only decomposition to afford HF and [107]NSI along with an unidentified fluorinated product.

3.6.8 Irradiation of [23a]

In a further attempt to liberate an organic product from **[23a]**, a sample in d^2-dichloromethane was subjected to irradiation with light with a wavelength greater than 412 nm. Irradiation for one hour did not result in any observable change in the NMR spectra. However, irradiation with broadband UV light for two hours resulted in a colour change from yellow to green (Scheme 163). The $^{31}P\{^1H\}$ NMR spectrum in d^2-dichloromethane revealed complete consumption of **[23a]** and the appearance of several new phosphorus-containing organometallic species at δ 93.7 (d, *J* = 25 Hz), 93.4 (d, *J* = 28 Hz), and 81.0 (s), in addition multiple species between δ 78.1-78.5. Only the singlet resonance at δ 81.0 could be identified and corresponds to the formation of **[1-306]**. Despite the complex nature of the ^{19}F NMR spectrum, two fluorinated alkenes were identified out of the numerous resonances. The appearance of two doublet resonances at δ -148.1 and -118.3 with 127 Hz coupling matches the literature data for *Z*-**105c**.[292] The *E*-isomer was also observed at δ -132.0

and -102.1 as doublet resonances with 11 Hz coupling; the isomers were formed in a 2:1 ratio *Z*/*E*. In addition to the formation of **105c**, **105b** was also identified by the three doublet of doublet resonances at δ -177.1 (*J* = 32, 110 Hz), -114.8 (*J* = 72, 110 Hz), and -100.0 (*J* = 32, 72 Hz).[293] Accurate integration was difficult due to the low intensity of the signals but it appears to be a minor product. The formation of **105c** and **[1-306]** requires a source of chloride which can only originate from the solvent. Therefore, under UV irradiation, **[23a]** must undergo a reaction with dichloromethane to afford chlorinated products.

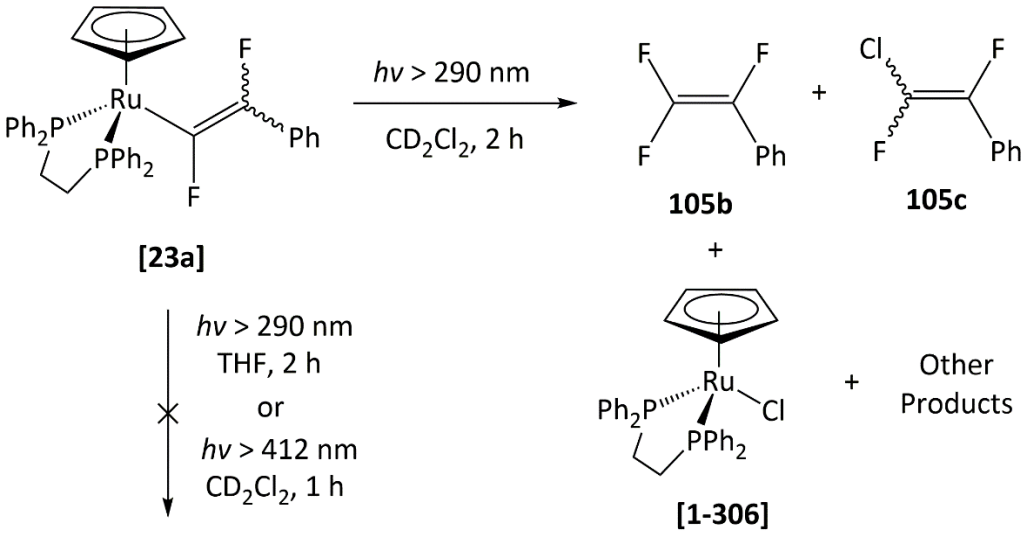

Scheme 163: Irradiation of [23a] with broadband UV light in dichloromethane afforded numerous products including alkenes 105b and 105c. However, irradiation of [23a] in tetrahydrofuran did not result in any reactivity being observed by NMR spectroscopy.

In contrast, irradiation of **[23a]** with broadband UV light in tetrahydrofuran for 2 hours did not afford any new products according to NMR spectroscopy (Scheme 163), supporting the hypothesis that **105c** is generated from the reaction of **[23a]** with dichloromethane under UV conditions.

The formation of trifluorostyrene, **105b**, in dichloromethane indicates that fluorine abstraction from **[23a]** occurs upon exposure to UV light. In an attempt to liberate **105b** by photodissociation, a tetrahydrofuran solution of **[23a]** was irradiated with broadband UV light in the presence of tetramethylammonium fluoride for one hour. However there no evidence of any alkene products or reactivity according to NMR spectroscopy (Scheme 164), implying that fluoride abstraction is the result of decomposition of dichloromethane under UV irradiation.

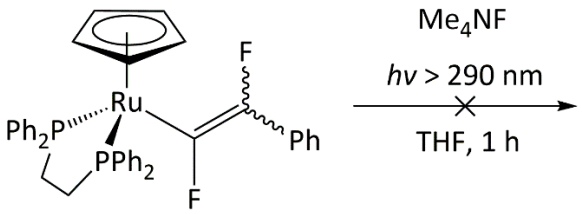

[23a]

Scheme 164: Irradiation of [23a] in the presence of tetramethylammonium fluoride did not result in any reactivity being observed by NMR spectroscopy.

Although chloro-fluorinated alkenes have been liberated, the complex nature of the ^{13}F and $^{31}P\{^{1}H\}$ NMR spectra indicate that broadband UV irradiation is not a selective or clean strategy for liberating alkene products from **[23a]**.

3.7 Reactions of $[19]^+$

3.7.1 Reaction of $[19]BF_4$ with Hydrochloric Aid

The addition of three equivalents of dry hydrogen chloride, as a 2 M solution in diethyl ether, to a d^2-dichloromethane solution of **[19]**BF_4 resulted in a gradual change in colour from green to yellow over one hour. The ^{19}F NMR spectrum of the reaction mixture in d^2-dichloromethane revealed complete consumption of **[19]**BF_4 and the appearance of a doublet signal at δ -130.2 with 48 Hz coupling. The ^1H NMR spectrum displayed a matching doublet resonance at δ 5.04 with 48 Hz coupling, consistent with *geminal* H-F coupling and protonation of the β-carbon. The $^{31}P\{^1H\}$ NMR spectrum, which is consistent with the ^{19}F NMR spectrum, revealed the disappearance of the singlet signal at δ -77.9 for **[19]**BF_4 and the appearance of a pair of mutually coupled doublet resonances at δ 89.6 and δ 93.8 with 16 Hz coupling indicating the symmetry of the complex is broken by addition of HCl. The $^{13}C\{^1H\}$ NMR spectrum displayed a low field resonance at δ 292.3 with doublet of triplets multiplicity consistent with the metal-bound carbon of the carbene ligand. The resonance displayed 48 Hz doublet coupling to fluorine and 10 Hz apparent triplet coupling to the phosphines. The β-carbon was observed as a doublet resonance at δ 109.5 with large $^1J_{CF}$ doublet coupling of 191 Hz. The NMR spectroscopic data are consistent with the formation of $[111]^+$ (Scheme 165).

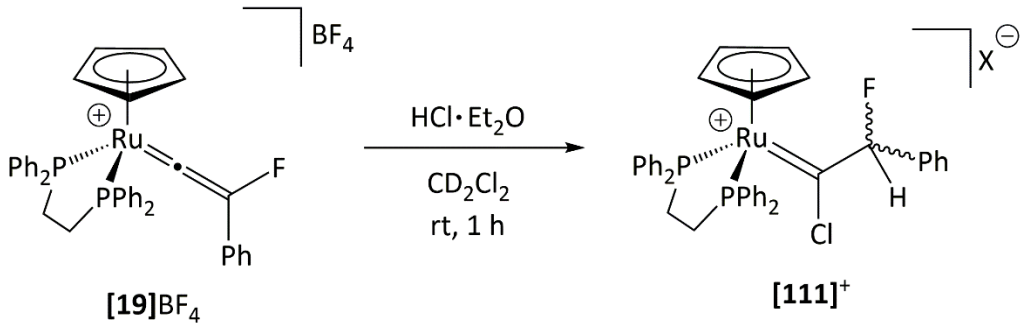

[19]BF_4 $[111]^+$

Scheme 165: Addition of hydrogen chloride to a dichloromethane solution of $[19]BF_4$ resulted in the formation of $[111]^+$ over one hour.

Attempts to isolate $[111]^+$ by removal of solvent *in vacuo* or precipitation with diethyl ether afforded green solids corresponding to $[19]^+$ formed through loss of HCl; $[111]^+$ can be regenerated by addition of hydrogen chloride. Attempted crystallisation through slow diffusion of pentane into a dichloromethane solution of $[111]^+$ failed to afford suitable crystals for X-ray crystallography.

In contrast to **[104a]**Cl, **[111]**$^{+}$ is highly unstable in the solid state and undergoes rapid loss of HCl unless in solution. Although formation of hydrogen fluoride is thermodynamically more favourable than formation of hydrogen chloride, kinetic stability afforded by the greater strength of the C-F bond compared to the C-Cl bond can be used to rationalise the contrasting stability of **[104a]**Cl compared to **[111]**$^{+}$.

It is unclear whether **[111]**$^{+}$ forms through concerted addition of hydrogen chloride to **[19]**BF_4, protonation first to form a carbyne complex and subsequent chloride attack, or nucleophilic attack of chloride first to form a vinyl complex and then protonation. However, initial protonation of a cationic vinylidene complex to afford a dicationic carbyne complex is unlikely. The formation of carbyne complexes in the literature have been limited to protonation of neutral vinylidene complexes rather than cationic vinylidene complexes. Therefore, it is believed that chloride attacks the α-carbon first followed by protonation of the β-carbon, or chloride and proton addition occur concertedly. This nucleophilic attack of the vinylidene ligand was proposed by Milner *et al*.[218] to occur first in the hydration of **[19]**BF_4.

The choice of solvent played a fundamental role in determining the products observed in the reaction of **[23a]** with hydrogen chloride (sections 3.6.2 and 3.6.3). Addition of hydrogen chloride in dichloromethane afforded the carbene **[104a]**Cl but in tetrahydrofuran afforded **105a** and **[2-25]**. In an attempt to liberate a chloro-fluorinated alkene, **[19]**BF_4 was reacted with hydrogen chloride in tetrahydrofuran.

Addition of three equivalents of hydrogen chloride to a d^8-tetrahydrofuran solution of **[19]**BF_4 resulted in the gradual colour change from green to yellow over the course of 30 mins. The $^{31}P\{^1H\}$ NMR spectrum after one hour revealed the disappearance of the resonance at δ -77.9 for **[19]**BF_4 and the appearance of a signal at δ 81.0 corresponding to **[1-306]**. The formation of **[1-306]** implies the dissociation of a fluorinated organic product. The ^{19}F NMR spectrum displayed the disappearance of the resonance at δ -208.3 for **[19]**BF_4 and the appearance of a doublet resonance at δ -111.2 with 13 Hz coupling and minor doublet resonance at δ -131.3 with 48 Hz coupling which integrates in a ratio of 3:1 respectively. The latter signal corresponds to the formation of **[111]**$^{+}$, while the chemical shift of the major resonance at δ -111.2 is consistent with an alkenyl fluorine environment. The ^1H NMR spectrum displayed a doublet resonance at δ 6.48 with the matching coupling of 13 Hz. The size of the coupling indicates that the fluorine and proton resonances are mutually *cis* to one another and the data are consistent with the literature data for *E*-**105c** (Scheme 166).[294] The

NMR spectra after three hours revealed complete disappearance of the resonances for **[111]**$^{+}$ and growth of the ^{19}F and ^{1}H resonances for *E*-**105c**, indicating **[111]**$^{+}$ is capable of undergoing rearrangement.

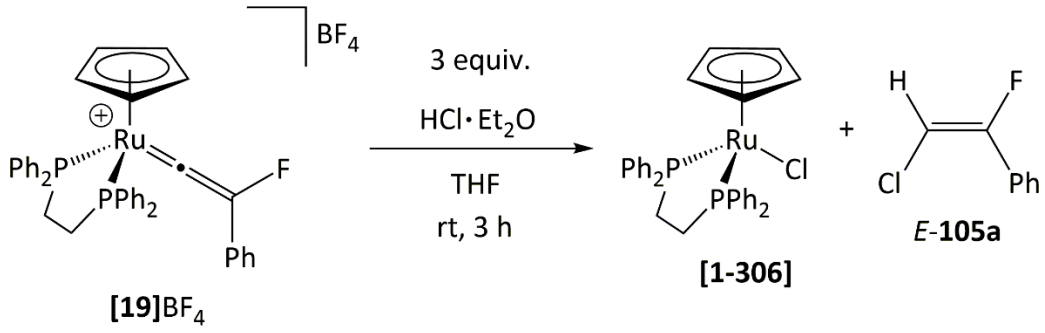

Scheme 166: Addition of excess hydrogen chloride to a tetrahydrofuran solution of [19]BF_4 afforded [1-306] and *E*-105c over 3 hours.

To confirm that **[111]**$^{+}$ is a potential intermediate in the formation of *E*-**105c**, tetrahydrofuran (*ca.* 100 μL) was added to a dichloromethane solution of **[111]**$^{+}$ (generated *in situ*. by addition of hydrogen chloride to **[19]**BF_4). Three days after addition of tetrahydrofuran, complete consumption of **[111]**$^{+}$ had occurred according to the ^{1}H, ^{19}F and ^{31}P{^{1}H} NMR spectra (Scheme 167). The ^{1}H NMR spectrum revealed the appearance of a doublet resonance at δ 6.36 with 13 Hz coupling corresponding to *E*-**105c** and resonances at δ 2.62, δ 2.42 and δ 4.57 corresponding to the two proton environments of the dppe backbone and protons of the Cp respectively of **[1-306]**. The ^{19}F NMR spectrum displayed the appearance of a doublet resonance at δ -110.7 with 13 Hz coupling corresponding to *E*-**105c**. The ^{31}P{^{1}H} NMR spectrum did not reveal the appearance of any phosphorus containing species except for a broad baseline between δ 77 and δ 82. However, the formation of **[1-306]** was confirmed by ^{1}H NMR spectroscopy and LIFDI MS.

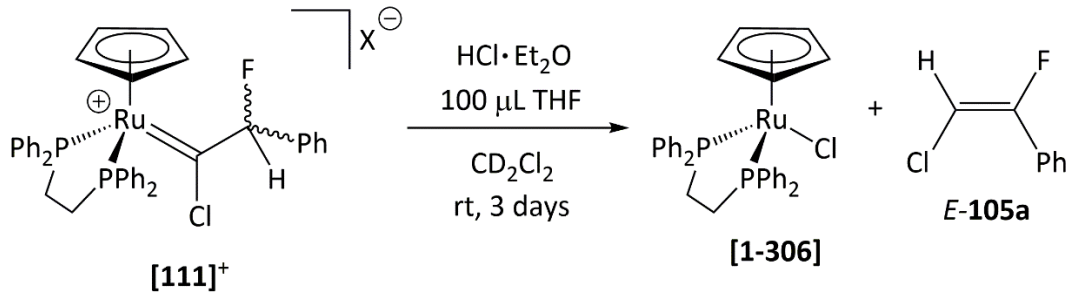

Scheme 167: Addition of tetrahydrofuran to a dichloromethane solution of [111]$^{+}$ afforded [1-306] and *E*-105c over 3 days in the presence of hydrogen chloride.

The data are consistent with the observed reactivity of **[23a]** and suggests protonation affords the carbene **[111]**$^+$ first as the kinetic product which then undergoes deprotonation-protonation in tetrahydrofuran to afford the alkene through the η^2-alkene complex.

3.7.2 Reaction of [19]NSI with Hydride

Addition of one and a half equivalents of an ethanol solution of sodium borohydride to a tetrahydrofuran solution of **[19]**NSI at -78 °C resulted in a gradual colour from green to yellow upon warming to room temperature. This resulted in the formation of two major products, **[23b]** (24 %) and **[77]** (58 %) according to NMR spectroscopy (Scheme 168).

The ^{19}F NMR spectrum of the reaction mixture in d^2-dichloromethane exhibited a doublet resonance at δ -99.9 with 71 Hz *trans*- coupling to the hydrogen substituent of *Z*-**[23b]**. The hydrogen substituent of the vinyl ligand of *Z*-**[23b]** was assigned to the doublet-of-triplets resonance at δ 5.61 in the ^{1}H NMR spectrum according to a ^{1}H-^{19}F HSQC NMR correlation experiment. The resonance displayed the matching 71 Hz *trans*-doublet coupling to fluorine and triplet coupling of 8 Hz to the two phosphines. The proton environments of the Cp ligand were assigned to a singlet resonance at δ 4.84. The ^{31}P{^{1}H} NMR spectrum displayed a singlet resonance at δ 89.7 which was assigned to formation of *Z*-**[23b]**. The metal bound α-carbon of the vinyl ligand was observed at δ 118.4 as a doublet-of-triplets resonance with 46 Hz doublet coupling to fluorine and 18 Hz triplet coupling to the phosphines. The β-carbon was observed as a doublet resonance at δ 161.1 with 227 Hz coupling to fluorine. The ESI mass spectrum displayed a signal at 686.1249 m/z corresponding to the radical cation of *Z*-**[23b]**, supporting the assignment. Attempts to crystallise *Z*-**[23b]** by slow diffusion of a dichloromethane solution into pentane were unsuccessful.

The ^{31}P{^{1}H} NMR spectrum of the reaction mixture also displayed a singlet resonance at δ 85.7 which was assigned to the formation of **[77]** based on the literature data and two unknown minor species observed at δ 90.9 and 91.2. The proton environments of the Cp ligand of **[77]** were observed at δ 4.80 in the ^{1}H NMR spectrum matching the literature data. The formation of **[77]** occurs through formal loss of F^+ from **[19]**BF_4.

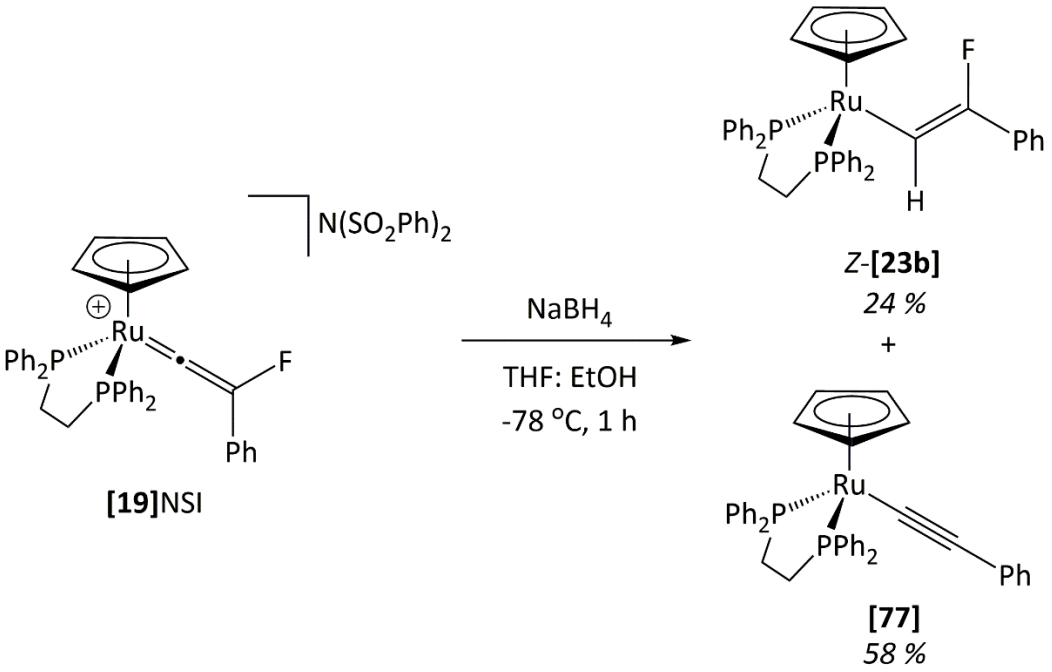

Scheme 168: Addition of an ethanol solution of sodium borohydride to a tetrahydrofuran solution of [19]NSI afforded a mixture of [23b] and [77].

The formation of a mixture of *Z*-**[23b]** and **[77]** suggests that hydride attack affords a mixture of *E*- and *Z*-**[23b]** initially, with the *E*- isomer undergoing reductive elimination of hydrogen fluoride to afford **[77]**. Alternatively, hydride addition may be in competition with fluorine abstraction. This would require the racemic mixture of **[77]** to undergo isomerisation to the thermodynamic *Z*- isomer through rotation of the C=C bond at room temperature.

3.7.3 Addition of a Hydrogen Atmosphere to [19]NSI

Exposing **[19]**NSI to an atmosphere of hydrogen for 11 days at 50 °C in the solid state was envisaged to afford 1-fluoro-styrene or **[23b]** through hydrogenation. However, only the partial reaction of **[19]**NSI with hydrogen was observed to afford numerous products (*ca*. 25 % conversion according the $^{31}P\{^{1}H\}$ NMR spectrum, Scheme 169). The $^{31}P\{^{1}H\}$ NMR spectrum of the reaction mixture in d^2-dichloromethane was dominated by unreacted starting material at δ 76.3, along with over nine minor phosphorus containing species. The ^{19}F NMR spectrum was also dominated by the starting material at δ -209.6 and also displayed the resonance for SiF_5^-, indicating the formation of hydrogen fluoride. Four additional resonances were observed at δ -90.2, -99.8, -100.1, and -103.4, corresponding to *ca.* 10 % of the fluorine containing species. These could not be identified but are unlikely to correspond to alkene products due to the singlet multiplicities. The ^{1}H NMR spectrum was complex and could not be assigned with the exception of the starting material which dominated the range for Cp

protons. It is clear that **[19]** does not react with hydrogen cleanly or afford the expected products.

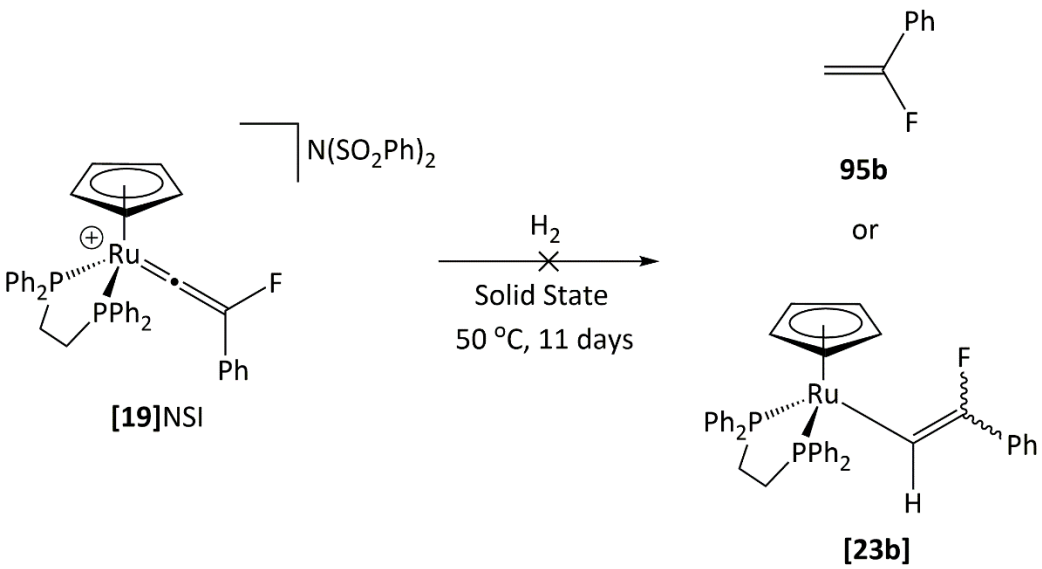

Scheme 169: Heating [19]NSI at 50 °C under an atmosphere of hydrogen for 11 days was envisaged to displace 95b or form [23b]NSI.

3.8 Reaction of [15b]BF_4 with Hydrogen chloride

Addition of three equivalents of hydrogen chloride to a dichloromethane solution of **[15b]**BF_4 was proposed by Milner to result in concomitant addition of chloride and proton across the vinylidene C=C bond to afford **[112]**$^+$ as a minor product (approximately 6 % conversion). Due to the successful liberation of alkene products through addition of hydrogen chloride to tetrahydrofuran solutions of **[19]** and **[23a]** in sections 3.4 and 3.6.2, the reaction **[15b]**BF_4 with hydrogen chloride was reinvestigated.

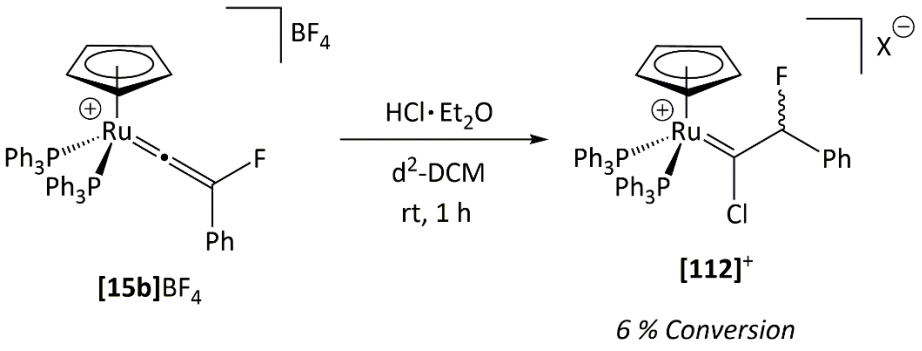

[15b]BF_4 **[112]**$^+$

6 % Conversion

Scheme 170: Addition of hydrogen chloride to [15b]BF_4 was proposed to afford [112]$^+$ with only 6% conversion according to Milner.

Addition of three equivalents of hydrogen chloride to a d^8-tetrahydrofuran solution of **[15b]**BF_4 resulted in the slow conversion to **[2-25]** over five days according to NMR spectroscopy (Scheme 171). At this time the $^{31}P\{^1H\}$ NMR spectrum showed a reduction in intensity of the resonance for **[15b]**BF_4 at δ 41.3 and the appearance of **[2-25]** at δ 39.6 along with the formation of **[18]**$^+$ and **[92]** as minor products. There was no evidence for the formation of the carbene intermediate **[112]**$^+$. The ^{19}F NMR spectrum at this time also displayed a reduction in the intensity of the resonance for **[15b]**BF_4 at δ -208.3 and the appearance of resonances at δ -111.2 (d, *J* = 14 Hz), -114.5 (d, *J* = 39 Hz), and -115.8 (d, *J* = 25 Hz). The doublet resonance at δ -111.2 with 14 Hz coupling to hydrogen corresponds to *E*-**105c**,[294] with the mutually coupled proton resonance observed at δ 6.45 in the ^1H NMR spectrum. The remaining doublet resonance at δ -115.8 (*J* = 25 Hz) corresponds to the formation of *Z*-**105c** which forms in a ratio of 1:5 (*Z:E*).[295] Over ten days **[15b]**BF_4 undergoes further conversion to **[2-25]** and **105c**. An additional doublet resonance was observed in the ^{19}F NMR spectrum at δ -114.5 with 39 Hz coupling to the doublet resonance at δ 5.88 in the ^1H NMR spectrum. The chemical shift and coupling suggest the unidentified product could be a fluorinated alkene.

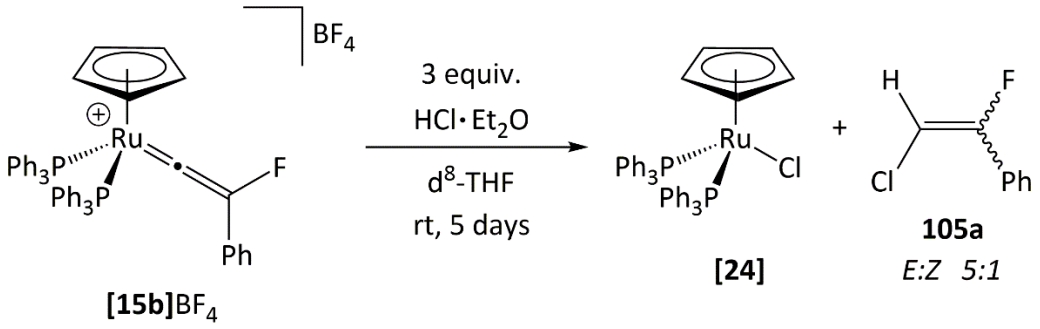

[15b]BF_4 **[24]** **105a** *E:Z 5:1*

Scheme 171: Addition of excess hydrogen chloride to a d^8-tetrahydrofuran solution of [15b]BF_4 afforded 105c (*E:Z,* 5:1) and [2-25] over five days.

The slow conversion of **[15b]**BF_4 to **105c** with no observation of the η^2-alkyne complex or **[112]**$^+$ suggests addition of hydrogen chloride to **[19]** is rate determining in this system. The formation of both isomers of **105c** indicates that displacement of the alkene from the metal is sufficiently slow for isomerisation to the thermodynamic isomer to occur. The lack of reactivity in dichloromethane indicates solvent choice remains crucial to the mechanism. This may imply a deprotonation-protonation mechanism as suggested for the reaction of **[23a]** and **[19]** with hydrogen chloride. The lability of the triphenylphosphine ligands could also mean a hydride mechanism is possible assuming protonation affords **[112]**$^+$ initially. A computational study into the possible mechanisms may help identify the most plausible pathway.

3.9 Conclusion

Attempts to liberate the fluoroalkyne from the coordination sphere of the metal through heating protio-fluorovinylidene complexes **[54a]**NSI and **[58a]**BF_4 in acetonitrile did not succeed. The reaction of **[58a]**BF_4 with acetonitrile is believed to result in phosphine attack of the vinylidene complex. Likewise attempts to liberate fluoroalkynes by displacement with triphenylphosphine also failed to achieve the desired result, instead formal loss of 'F^+', hydrolysis and/or decomposition was observed.

Irradiation of **[30a]**BF_4, **[54a]**BF_4, and **[19]**NSI with broadband UV light led to the minor consumption of the vinylidene complexes, however, no fluorinated alkyne or arene products were detected by NMR spectroscopy and ESI/EI mass spectrometry. Irradiation resulted in minor decomposition or hydrolysis in the presence of adventitious water.

The fluorovinylidene complex **[82]**BF_4 bearing phosphite ligands was synthesised in an attempt to generate a more electron-deficient metal centre and consequently enable the η^2-alkyne tautomer to be more readily accessible. However, **[82]** was found to be highly unstable and readily decomposed upon exposure to air or when left under an inert atmosphere for 16 hours. Heating **[82]** in d^3-acetonitrile for 24 hours at 70 °C resulted in complete decomposition to numerous unidentified species.

Under an atmosphere of oxygen the vinylidene C=C bond of **[54a]**NSI undergoes oxidative cleavage to afford **94**. No reaction was observed between **[19]**NSI, or **[54a]**NSI and an atmosphere of hydrogen. The addition of a carbon monoxide atmosphere to **[54a]**NSI resulted in partial conversion to **94** due to the presence of contaminant oxygen. Under a hydrogen atmosphere, **[54a]**NSI and **[19]**NSI failed to react.

The fluorovinylidene complex, **[15b]**BF_4, was found to be unreactive toward unsaturated reagents, styrene, ethynyltrimethylsilane, and allyl alcohol. Instead of affording fluorinated organic products, decomposition to the *ortho*-metallated phosphoniumvinyl complex, **[18]**BF_4, was observed.

Fluorovinylidene complexes have been shown to undergo nucleophilic attack by fluoride and hydride sources to afford the corresponding vinyl complexes. Addition of hydrogen chloride to **[19]**BF_4 in dichloromethane resulted in concomitant chloride addition and protonation to afford **[111]**$^+$. Addition of hydrogen chloride to **[23a]** in dichloromethane resulted in

protonation and afforded the analogous carbene **[104a]**Cl, while addition of NFSI resulted in fluorination to afford **[104b]**NSI.

Liberation of fluoroalkenes, *E*-**105a** and *E*-**105c**, was achieved by addition of tetrahydrofuran to **[104a]**Cl and **[111]**$^+$ respectively in the presence of chloride. This is essentially the formal addition of chlorofluoride or difluorine across the triple bond of a terminal alkene. Alternatively, formation of *E*-**105c** could be achieved directly from **[15b]**BF_4 and **[19]**BF_4 by addition of three equivalents of hydrogen chloride in tetrahydrofuran. It is believed that initial protonation of the respective vinyl complexes in dichloromethane affords the corresponding carbene complexes as the kinetic product. This can undergo deprotonation-protonation in the presence of tetrahydrofuran to presumably afford the η^2-alkene complex as a transient species, which affords the alkene by displacement with chloride. The absence of any alkene products from treatment of **[104b]**NSI with hydrogen chloride or tetrabutylammonium chloride implies deprotonation or migration is a crucial step. Future work would entail a DFT study into the mechanism of alkene displacement in the reaction of hydrogen chloride with **[15b]**BF_4, **[19]**BF_4, **[23a]** to provide detail on the favourability of a deprotonation-protonation or reductive elimination pathway for the conversion of the carbene complexes into the corresponding alkenes. Additionally, future work would entail the preparation of fluorinated alkenes catalytically and incorporation of more synthetically useful nucleophiles.

Attempts to liberate **95b** from **[104b]**NSI through addition tetrabutylammonium chloride, or by irradiation of **[14]** with tetramethylammonium fluoride, did not result in any reaction being observed.

The liberation of fluorinated organic products from fluorovinylidene complexes has now been expanded to include alkenes directly from the vinylidene complex or *via* a vinyl intermediate. Future work would focus on developing the stoichiometric reactions into catalytic ones. The main challenges to overcome are the generation of the alkynyl complexes *in situ* without the need of base and subsequent selective fluorination in the presence of acid.

Chapter 4. Exploring the Fluorination of *trans*-[ClRu(dppe)$_2$(C≡CR)] Complexes

4.1 Formation and Characterisation of Fluorovinylidene Complexes, [58]BF$_4$

Previous work within the Lynam and Slattery groups was focused on exploring the electrophilic fluorination of ruthenium half-sandwich complexes (Scheme 172).[218, 223, 226] Fluorination of complexes of the type *trans*-[ClRu(dppe)$_2$(C≡CR)], **[57]**, were investigated in order to expand the scope of OSEF. The ligand set was chosen due to the kinetic stability afforded by the two dppe ligands, as demonstrated in Chapter 2 for the fluorination of **[57a]** and **[57b]**, as well as the large number of reported alkynyl complexes of this type in the literature.[243-245] This chapter explores the reactivity of these *trans*-[ClRu(dppe)$_2$(C≡CR)] complexes towards Selectfluor, [FTMP]BF$_4$, and NFSI, the spectroscopic parameters of the corresponding fluorovinylidene complexes, **[58]**BF$_4$, and the potential mechanism(s) of fluorination. Alkynyl complexes bearing a range of electron-donating and withdrawing aryl substituents were studied from the strongly electron-donating dimethylaniline substituent to the strongly electron-withdrawing nitrobenzene substituent. This section, 4.1, discusses the characterisation of **[58]**BF$_4$ and the trends in spectroscopic data.

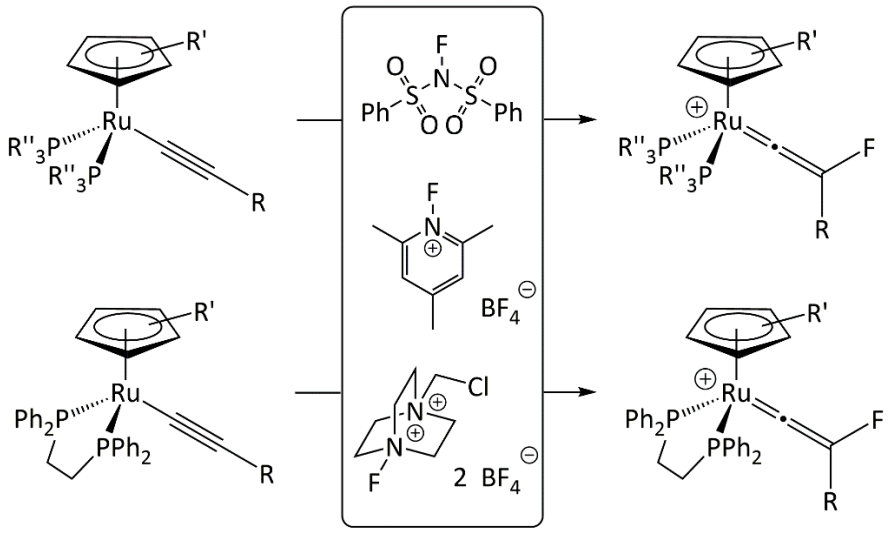

R = H, F, ^{t}Bu, C_6H_5, C_6H_4-4-OMe, C_6H_4-4-CF_3
R' = H, Me
R'' = Ph, OMe

Scheme 172: Fluorination of a variety of ruthenium half-sandwich alkynyl complexes with Selectfluor, [FTMP]BF_4 and NFSI afforded the respective fluorovinylidene complexes.

4.1.1 Fluorination of [57c] by Selectfluor

Treatment of a dichloromethane solution of **[57c]** with an acetonitrile solution of Selectfluor at -78 °C afforded a green solution upon warming to room temperature. Precipitation with pentane afforded a green-yellow solid which was identified as the desired fluorinated vinylidene complex, **[58c]**BF_4 (Scheme 173).

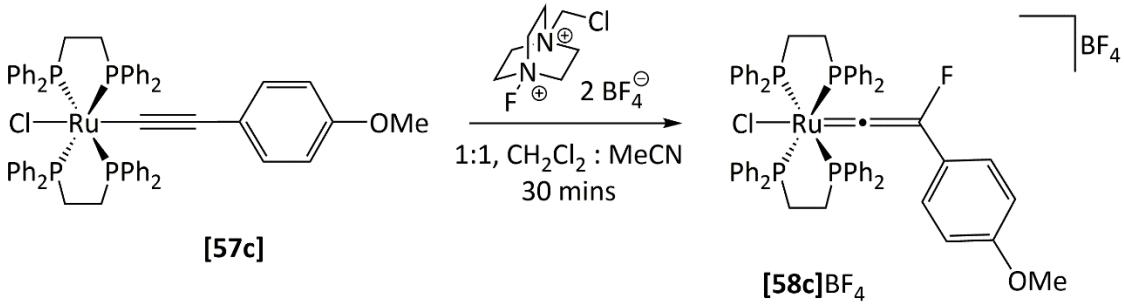

Scheme 173: The reaction of [57c] with Selectfluor in 1:1 dichloromethane: acetonitrile afforded the fluorovinylidene complex, [58c]BF_4.

The ^{19}F NMR spectrum for **[58c]**BF_4 in d^2-dichloromethane exhibited a singlet resonance at δ -229.6 corresponding to the fluorine substituent of the vinylidene ligand. The $^{31}P\{^{1}H\}$ NMR spectrum exhibited a singlet resonance at δ 34.1 signifying the formation of a cationic *trans*-$[ClRu(dppe)_2(=C=CR^1R^2)]^+$ complex[244] with four equivalent phosphorus environments. The ^{1}H

NMR spectrum displayed two new multiplet resonances centred at δ 2.62 and 2.94 corresponding to the four protons of the dppe backbone. The singlet resonance observed at δ 3.67 integrated to three protons and was assigned to the methoxy group of the anisole substituent. The aromatic protons of the anisole substituent were observed at δ 5.72 and 6.82, integrating to two protons each. The resonances between δ 7.06 and δ 7.15 were assigned to the *ortho*- and *meta*-aromatic protons of the two dppe ligands based on the ^{1}H-^{13}C HSQC 2D NMR experiment, while the resonances between δ 7.31 and δ 7.39 were assigned to the *para*-aromatic protons of the dppe ligands; each region integrated to 32 and 8 protons respectively.

The ^{13}C{^{1}H} NMR spectrum displayed a low field doublet resonance at δ 201.0 with 210 Hz coupling to fluorine and corresponds to the β-carbon of the vinylidene ligand. The metal bound α-carbon of the vinylidene ligand was observed as a cross-peak at δ 412.8 in the ^{13}C-^{19}F HSQC NMR experiment but could not be observed directly in the 1D ^{13}C{^{1}H} NMR experiment presumably due to multiple coupling decreasing the signal height. The backbone carbons of the dppe ligands were observed as a virtual quintet resonance at δ 29.2 with 11 Hz coupling to the four phosphorus nuclei. The methoxy carbon of the anisole substituent was observed as a singlet resonance at δ 55.6, while the aromatic carbons were identified by the HSQC and HMBC experiments and observed between δ 113.9 and 160.0.

The ESI mass spectrum displayed a species with a m/z of 1083.1954 corresponding to the m/z of **[58c]**$^{+}$. The structure of **[58c]**PF_6 was confirmed by X-ray crystallography with crystals grown by slow diffusion of pentane into a dichloromethane solution of **[58c]**PF_6.

The crystallographic data for **[58c]**PF_6 reveals a distorted octahedral geometry of the ligands around the ruthenium centre (Figure 45), with the vinylidene ligand observed in a single orientation unlike the vinylidene ligands in the crystal structures for **[58a]**BF_4 and **[58b]**BF_4. The *trans*-P-Ru-P bond angles were found to be inequivalent and significantly distorted at 169.66(2)° and 175.74(2)°, with the chloride and vinylidene ligand also being distorted away from linearity (Cl-Ru=C_α, 175.29(8)°). The *trans*-P1-Ru-P4 angle appears significantly distorted due to the steric interaction of the anisole substituent of the vinylidene ligand with P(1) (Figure 45). Likewise, the P-Ru-C_α angles are distorted away from the ideal geometry (90°) at 85.45(8)°, 91.38(8)°, 98.91(8)°, and 99.02(8)°. The Ru-C_α-C_β, C_α-C_β-F and C_α-C_β-C_{Ar} bond angles of the vinylidene ligand are also distorted away from ideal at 171.9(2)°, 115.6(2)°, and 131.2(2)° respectively. Distortion again appears to minimise the steric interaction between the anisole substituent of the vinylidene ligand and the neighbouring

dppe ligand. The gas phase structure of **[58c]**$^{+}$, calculated at the (RI-)BP86/SV(P) level, is predicted to show significant distortion of the octahedral geometry and vinylidene metrics. This suggests that the distortion is not the result of crystal packing effects (Table 19).

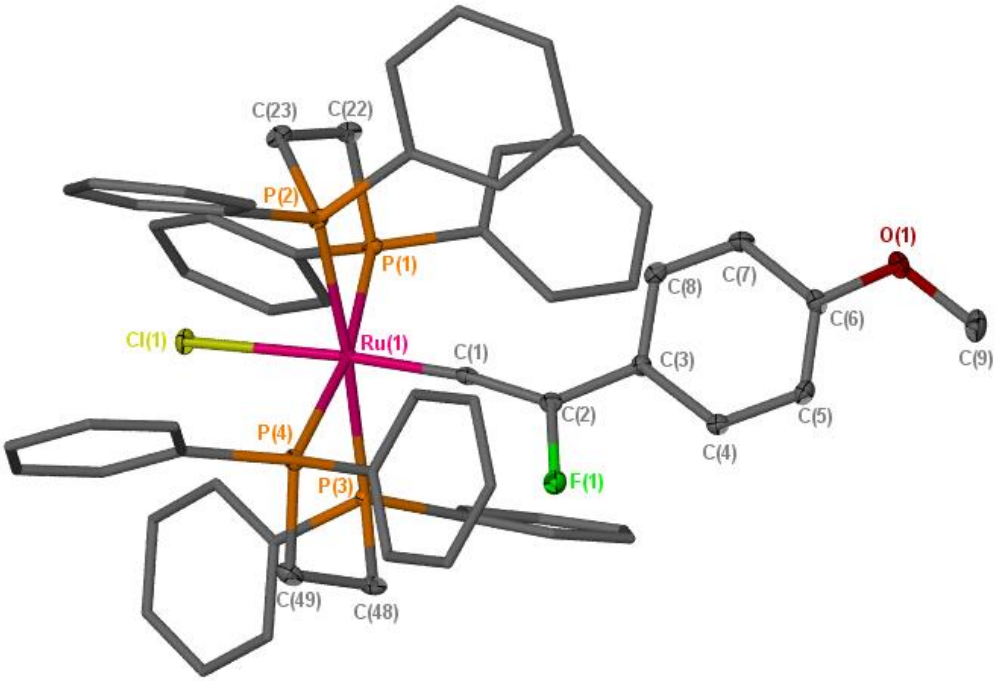

Figure 45: Crystal structure of [58c]PF_6; the hexafluorophosphate anion, dichloromethane (solvent of crystallisation) and hydrogens are omitted for clarity and thermal ellipsoids are displayed with 50 % probability level.

Table 19: Selected bond lengths and bond angles from the crystal structure of [58c]PF_6 with the calculated values at the (RI-)BP86/SV(P) level in italics.

Bond Length / Å	**[58c]**PF_6	Bond Angle / °	**[58c]**PF_6
Ru-C_α	1.831 (3) *1.841*	Ru-C_α-C_β	171.9 (2) *176.418*
C_α-C_β	1.333 (3) *1.355*	C_α-C_β-F	115.6 (2) *113.608*
C_β-F	1.386 (6) *1.388*	C_α-C_β-R	131.2 (2) *133.528*
C_β-R	1.460 (3) *1.469*	F-C_β-R	113.1 (2) *112.782*
Ru-P1	2.4359 (7) *2.496*	Cl-Ru-C_α	175.29 (8) *176.354*
Ru-P2	2.4359 (7) *2.473*	C_α-Ru-P1	98.91 (8) *96.646*
Ru-P3	2.4315 (7) *2.465*	C_α-Ru-P2	99.02 (8) *98.439*
Ru-P4	2.4179 (7) *2.443*	C_α-Ru-P3	85.45 (8) *84.845*
Ru-Cl	2.4391 (6) *2.498*	C_α-Ru-P4	91.38 (8) *92.965*
		trans-P-Ru-P	169.66(2) 175.74(2) *168.40* *177.69*

The UV-Vis absorption spectrum of **[58c]**BF_4 in dichloromethane exhibited a low energy absorption band at 820 nm (Figure 46) corresponding to the HOMO → LUMO transition according to TD-DFT at the (RI-)BP86/SV(P)//PBE0/def2-TZVPP level. The HOMO (Figure 47) is predicted to consist of a symmetry-adapted ruthenium d-orbital which is π-antibonding with respect to the α- and β-carbons of the vinylidene ligand, which are π-bonding. These atoms also exhibit π-antibonding interactions with the fluorine and anisole substituents. The LUMO (Figure 48) is dominated by a π-antibonding interaction between the symmetry adapted d-orbital of ruthenium and the vacant p-orbital of the α-carbon; the β-carbon appears to make only a minor contribution, with a weak π-bonding interaction with the α-

carbon and weak π-antibonding interaction with fluorine. The magnitude of the molar absorption coefficient (21.7 m^2 mol^{-1}) is indicative of a d-d spin allowed transition.

It was noted in Chapter 2 (section 2.5.1) that the LUMO of **[54a]**$^+$ differs from the LUMO of a generic metal-vinylidene fragment (Chapter 1, Scheme 76). The HOMO of **[54a]**$^+$ appeared similar to the generic HOMO, in particular they both display a smaller orbital coefficient on the α-carbon of the vinylidene ligand compared to the β-carbon. The orbital coefficients of the α- and β-carbon atoms of the vinylidene ligand in the HOMO of **[58c]**$^+$ (Figure 40) appear roughly equivalent. The LUMO again appears different to the generic representation seen in Scheme 76 in which the α- and β-carbon atoms are expected to be non-bonding. Instead, the LUMO of **[58c]**$^+$ appears to show polarisation of the α-carbon p-orbital or a weak π-bonding interaction between the α- and β-carbon atoms, due to the strong polarising nature of fluorine. Qualitatively, this could suggest that the generic MO diagram used to describe metal-vinylidene fragments is not suitable for describing the HOMO and LUMO of fluorovinylidene complexes. However, the differences mentioned above appear to be subtle and a quantitative approach, such as NBO analysis, would be required to fully assess the validity of the generic MO scheme with respect to fluorovinylidene complexes. The HOMO-LUMO transition for fluorovinylidene complexes appears similar to the HOMO-LUMO transition for a generic metal-vinylidene fragment, despite the subtle differences in the fluorovinylidene MOs. Although a large energy difference is observed for the HOMO-LUMO transition between protio- and fluoro-substituted vinylidene complexes, this energy difference is primarily due to a π-antibonding interaction between the fluorine and C=C π-system destabilising the HOMO, rather than the nature of the HOMO-LUMO transition changing.

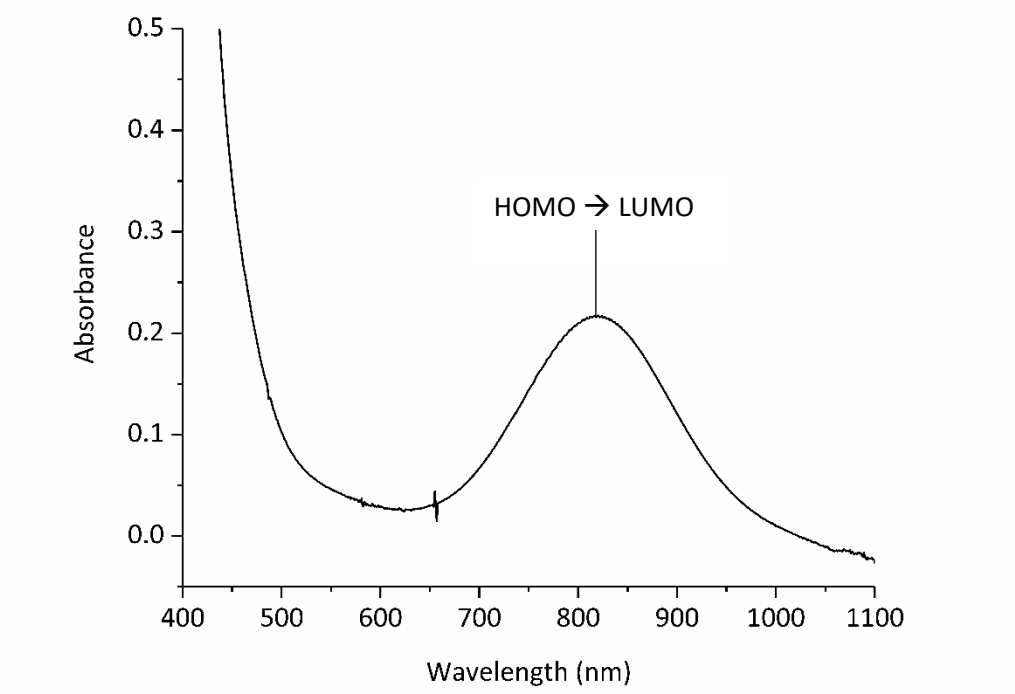

Figure 46: UV-Vis absorption spectrum of [58c]BF_4 at 1 mM concentration in dichloromethane with a pathlength of 1 cm. ε = 21.7 m^2 mol^{-1}.

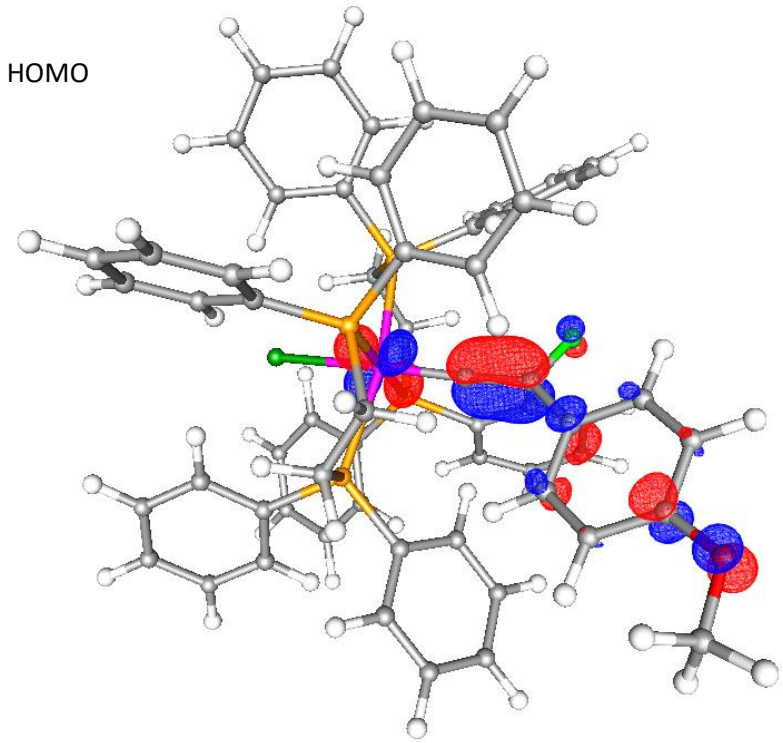

Figure 47: Predicted HOMO of $[58c]^+$ displaying a π-bonding interaction between the vinylidene α- and β-carbons which are π-antibonding with respect to the metal, fluorine and anisole substituents.

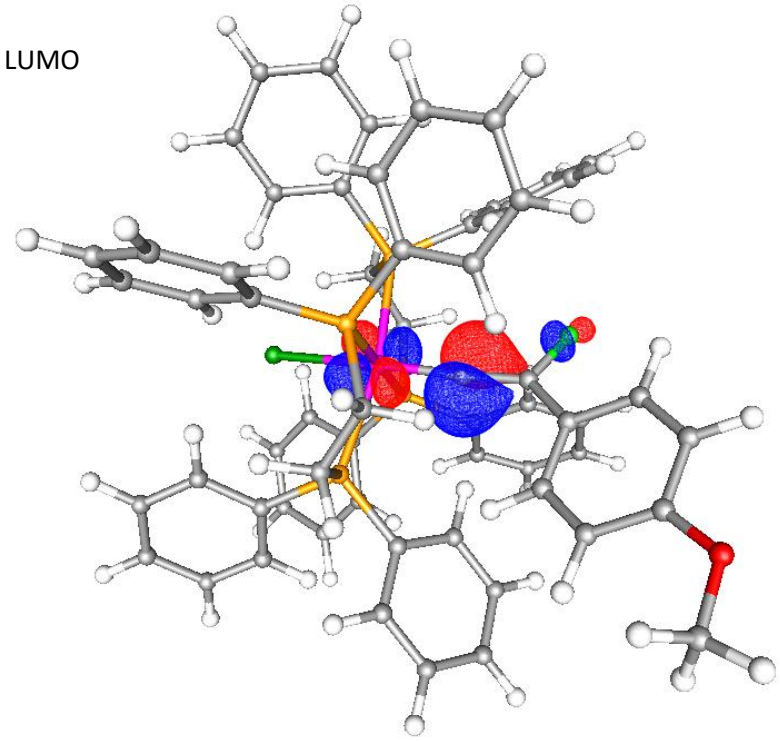

Figure 48: Predicted LUMO of [58c]$^{+}$ displaying a π-antibonding interaction between the metal and α-carbon of the vinylidene. The β-carbon is weakly π-bonding with respect to the β-carbon and π-antibonding with respect to the fluorine.

4.1.2 Characterisation Data for [58]BF_4 and Corresponding Trends

Addition of acetonitrile solutions of Selectfluor to dichloromethane solutions of aryl substituted alkynyl complexes **[57d-f]** also resulted in the formation of green solutions at either room temperature, or upon warming from -78 °C. Precipitation with pentane yielded yellow-green solids which were identified as the corresponding fluorovinylidene complexes, **[58]**BF_4, according to NMR spectroscopy, mass spectrometry, and X-ray crystallography (Scheme 174). The NMR, IR and UV-Vis spectroscopic data are summarised in Table 20, while the crystallographic data are summarised in Table 22 and discussed in section 4.1.4.

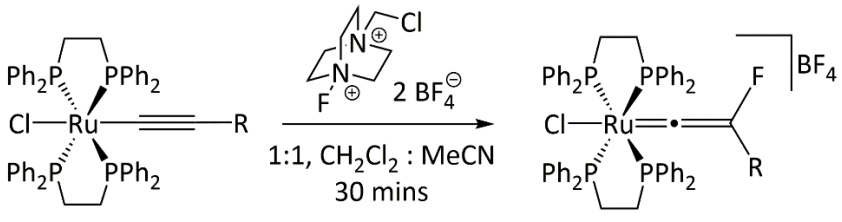

c = C_6H_4-4-OMe
d = C_6H_5
e = C_6H_4-4-C(O)OMe
f = C_6H_4-4-C(O)Me
g = C_6H_4-4-CF_3
h = C_6H_4-4-NO_2

Scheme 174: Addition of Selectfluor to [57c-h] in 1:1 dichloromethane: acetonitrile afforded the corresponding fluorovinylidene complexes [58e-h]BF_4.

The NMR spectroscopic parameters for **[58]**BF_4 (Table 20) display a general upfield shift in the fluorine, phosphorus and the vinylidene α- and β-carbon chemical shifts as the electronic property of the arene substituent becomes more electron-withdrawing. The α-carbon chemical shift of the vinylidene ligand is more susceptible to electronic changes in the aryl substituent than the β-carbon chemical shift, with the α-carbon chemical shift being observed over a 21.3 ppm range compared to a 3.4 ppm range for the β-carbon between **[58c]**BF_4 and **[58h]**BF_4. Likewise, the fluorine substituent of the vinylidene ligand and the four phosphorus nuclei undergo modest shielding of 5.2 and 3.0 ppm respectively upon changing the anisole substituent in **[58c]**BF_4 to nitrobenzene in **[58h]**BF_4.

Table 20: Selected NMR, IR and UV-Vis spectroscopic data for fluorinated vinylidenes, [58]BF_4

	[58]BF_4	$^{13}C\{^1H\}$ NMR ($^1J_{CF}$)/ ppm		^{19}F NMR / ppm	$^{31}P\{^1H\}$ NMR / ppm	IR ν / cm^{-1}	UV-Vis λ / nm	
		C_α	C_β			C=C	Observed	Calculated
c	R = C_6H_4-4-OMe	412.8	201.0 (210 Hz)	-229.6	34.1	1603 (*1632*)	820	856
d	R = C_6H_5	408.6	201.3 (209 Hz)	-235.4	33.4	1622 (*1605*)	793	790
e	R = C_6H_4-4-COOMe	400.3	199.2 (192 Hz)	-236.4	32.3	1598 (*1629*)	794	770
f	R = C_6H_4-4-COMe	399.8	199.0 (209 Hz)	-236.1	32.1	1626 (*1624*)	791	768
g	R = C_6H_4-4-CF_3	398.9	199.3 (214 Hz)	-236.1	31.7	1609 (*1624*)	790	764
h	R = C_6H_4-4-NO_2	391.5	197.6 (195 Hz)	-234.8	31.4	1618 (*1623*)	781	744

$^1J_{CF}$ coupling in parentheses. Calculated vibrational frequencies at the (RI-)BP86/SV(P) level denoted in italics and parentheses. The calculated UV-Vis absorption bands for the HOMO-LUMO transition were calculated by TD-DFT at the (RI-)BP86/SV(P)//PBE0/def2-TZVPP level.

The UV-Vis absorption data for **[58]** display low energy absorption bands between 781 nm and 820 nm corresponding to the HOMO-LUMO transition according to TD-DFT at the (RI-)BP86/SV(P)//PBE0/def2-TZVPP level. As the arene substituent of the vinylidene becomes more electron-withdrawing, the HOMO is lowered in energy and the HOMO-LUMO transition undergoes a hypsochromic shift to a higher energy (Figure 49). The molar absorption coefficients are of the magnitude of 10^1 m^2 mol^{-1} which are consistent with d-d spin allowed transitions.

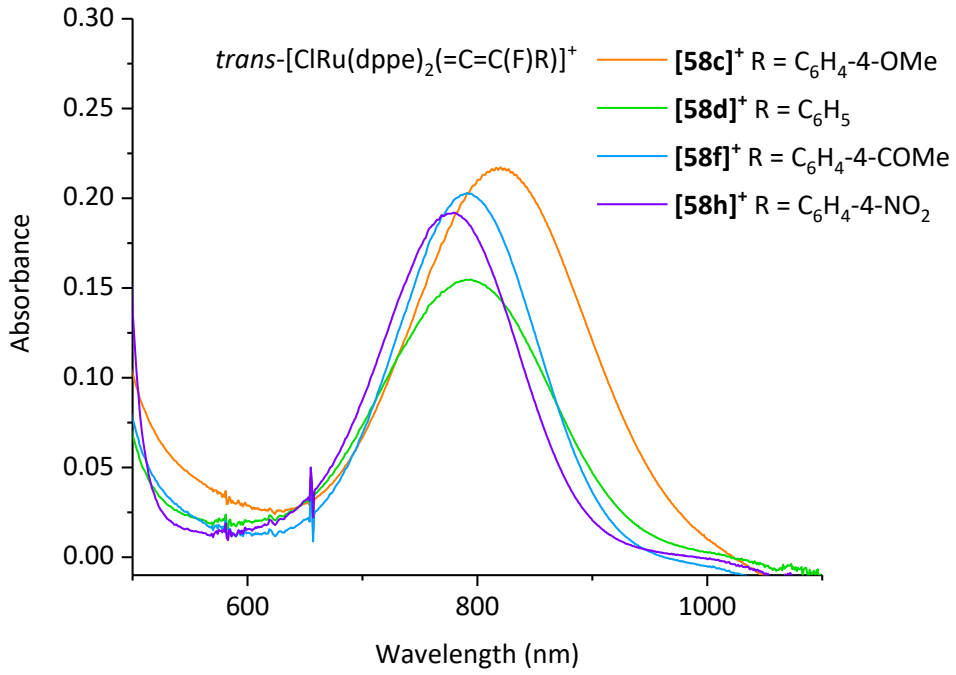

Figure 49: Overlay of the UV-Vis spectra for $[58c]^+$, $[58d]^+$, $[58f]^+$, and $[58h]^+$, displaying the change in the HOMO-LUMO band of each complex at 1 mM in dichloromethane with a pathlength of 1 cm. The molar absorption coefficients were determined at 21.7, 15.4, 20.3, and 19.2 m^2 mol^{-1} respectively.

The chemical shielding of the phosphorus and vinylidene fluorine, α- and β-carbon nuclei can be rationalised by the enhanced mixing of the MOs involved in chemical shielding with increasing electron-donating ability of the aryl substituent. As mentioned in Chapter 2, the paramagnetic contribution to chemical shielding, which is nearly always deshielding, is inversely proportional to the energy gap between the mixing MOs in an external magnetic field.[193] An increase in the HOMO-LUMO transition energy, e.g. **[58c]**$^+$ to **[58h]**$^+$, is therefore expected to result in a reduction of the paramagnetic shielding, giving rise to more shielded chemical shifts with more electron withdrawing vinylidene substituents.

In contrast to the NMR and UV-Vis spectroscopic parameters, the vinylidene C=C stretching frequencies for **[58]**BF_4 do not appear to follow any particular trend with respect to the

substitution patterns. The calculated vibrational frequencies at the (RI-)BP86/SV(P) level do not display a consistent trend either, supporting the observed experimental values.

4.1.3 Comparison of the Spectroscopic Data Between [58]PF_6 and [59]BF_4

The shielding of the resonances in **[58]**BF_4 with more electron-withdrawing substituents is also replicated in the reported phosphorus and vinylidene α- and β-carbon chemical shifts for the protio-vinylidene complexes **[59]** (Table 21). As noted in Chapter 2 for **[59]**BF_4, **[58a]**BF_4, **[58b]**BF_4 incorporation of fluorine into the vinylidene ligand of *trans*-[ClRu(dppe)$_2$(=C=CR^1R^2)]$^+$ complexes induces significant deshielding of the α- and β-carbon resonances of the vinylidene ligand. This trend also applies to the aryl substituted vinylidene complexes, **[58]**BF_4 and **[59]**PF_6. Upon fluorination the vinylidene β-carbon resonances undergo the largest upfield shifts of 91.8 ppm and 88.3 ppm for the anisole and nitrobenzene substituted vinylidene complexes respectively. The vinylidene α-carbon resonances undergo upfield shifts of 55.4 ppm and 40.8 ppm for the anisole and nitrobenzene substituted vinylidenes respectively. The phosphorus chemical shifts also undergo deshielding upon fluorination, however the magnitude of deshielding is much smaller (6.4 ppm and 8.5 ppm for the anisole and nitrobenzene substituted vinylidene complexes respectively).

The deshielding influence of fluorine on the chemical shifts of **[58]**BF_4 is not identical across the series, as noted before in section 2.7.1.5. Fluorine's deshielding effect on the vinylidene α- and β-carbons is diminished the more electron-withdrawing the arene substituent becomes. In contrast fluorine induces a greater deshielding effect on the phosphine resonances the more electron withdrawing the arene substituent becomes.

Table 21: Comparison of selected NMR parameters and IR stretching frequencies for protio- and fluorovinylidene complexes of the type $[ClRu(dppe)_2(=C=CRAr)]^+$

Compound	$^{13}C\{^1H\}$ NMR / ppm		$^{31}P\{^1H\}$ NMR / ppm	IR / cm^{-1}
	C_α	C_β		ν C=C
$Ru([dppe)_2Cl(CC(H)C_6H_4$-4-OMe)]$^+$, **[59c]$^+$** [a]	357.4	109.2	40.5	1637 (*1661*)
$[Ru(dppe)_2Cl(CC(F)C_6H_4$-4-OMe)]$^+$, **[58c]$^+$**	412.8	201.0	34.1	1603 (*1632*)
Δ	55.4	91.8	-6.4	-34 (*-29*)
$[Ru(dppe)_2Cl(CC(H)C_6H_5)]^+$, **[59d]$^+$** [a]	354.5	109.7	40.2	1628 (*1656*)
$[Ru(dppe)_2Cl(CC(F)C_6H_5)]^+$, **[58d]$^+$**	408.6	201.3	33.4	1622 (*1605*)
Δ	54.1	91.6	-6.8	-6 (*-51*)
$[Ru(dppe)_2Cl(CC(H)C_6H_4$-4-$NO_2)]^+$, **[59h]$^+$** [a]	350.7	109.3	39.9	1630 (*1643*)
$[Ru(dppe)_2Cl(CC(F)\ C_6H_4$-4-$NO_2)]^+$, **[58h]$^+$**	391.5	197.6	31.4	1618 (*1623*)
Δ	40.8	88.3	-8.5	-12 (*-20*)

NMR spectroscopic parameters reported in CD_2Cl_2; calculated C=C stretching frequencies at the (RI-)BP86/SV(P) level in italics; [a] data reported by Touchard et al.[244]

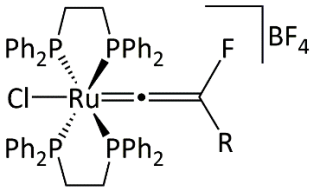

[58]BF_4

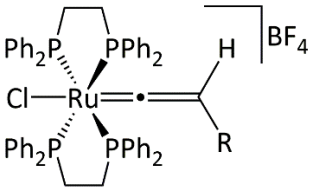

[59]BF_4

The vibrational stretching frequency of the vinylidene C=C bond undergoes a shift to a lower energy frequency upon incorporation of fluorine. This is supported by the calculated stretching frequencies of the C=C bond at the (RI-)BP86/SV(P) level and is reflected in the C=C stretch of the ruthenium half-sandwich complexes in Chapter 2.

4.1.4 Crystallographic Data for [58]PF_6

The slow diffusion of pentane into dichloromethane solutions of **[58]**PF_6 yielded suitable yellow and green crystals for X-ray crystallography; the crystallographic data for **[58]**PF_6 are summarised in Table 22.

Compounds **[58d]**PF_6, **[58f]**PF_6, and **[58h]**PF_6, co-crystallised with two molecules of dichloromethane per vinylidene complex, while **[58c]**PF_6 co-crystallised with one molecule of dichloromethane.

Crystallisation of **[58d]**PF_6 afforded two molecules of **[58d]**PF_6 per asymmetric unit (structure A and B), both of which displayed a distorted octahedral geometry about the ruthenium centre (Figure 50). The two structures displayed statistically identical bond metrics except for the vinylidene Ru-C_α (1.810(3) Å and 1.836(2) Å) and Ru-Cl (2.4141(8) and 2.4325(6)Å) bond lengths. Likewise the corresponding Ru-C_α-C_β (177.7(3)° and 173.4(2)°) and Cl-Ru-C_α (173.08(11)° and 177.49(7)°) bond angles were statistically different.

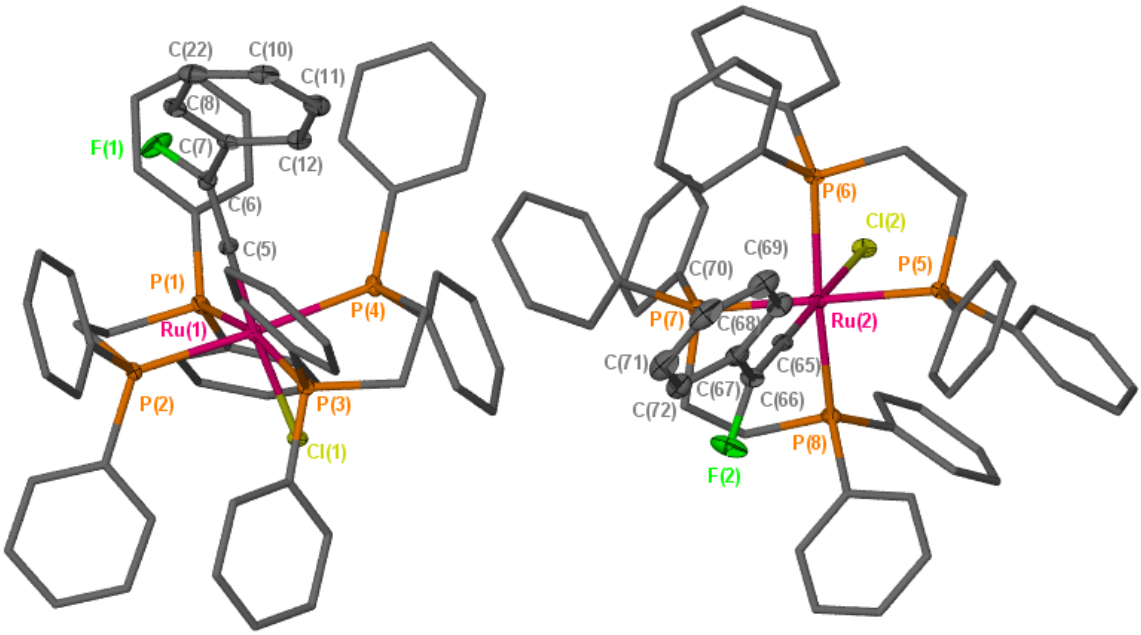

Figure 50: Crystal structure of [58d]PF_6; the hexafluorophosphate counterions, dichloromethane (solvent of crystallisation) and hydrogens are omitted for clarity and thermal ellipsoids are displayed with 50 % probability level.

Table 22: Crystallographic data for selected bond lengths and angles of [58]PF_6; calculated values at the (RI-)BP86/SV(P) level in italics.

Bond Length / Å	**[58c]**BF_4	**[58d]**BF_4 -A	**[58d]**BF_4- B	**[58e]**BF_4	**[58f]**BF_4	**[58g]**BF_4	**[58h]**BF_4
Ru-C_α	1.831 (3) *1.841*	1.810 (3) *1.836*	1.836 (2) *1.836*	1.8217(16) *1.832*	1.857 (10) *1.831*	1.828(3) *1.832*	1.839 (6) *1.827*
C_α-C_β	1.333 (3) *1.355*	1.374 (3) *1.356*	1.375 (4) *1.356*	1.335(2) *1.358*	1.279 (13) *1.359*	1.319(4) *1.358*	1.327 (8) *1.360*
C_β-F	1.386 (6) *1.388*	1.374 (3) *1.386*	1.384 (4) *1.386*	1.3899(17) *1.386*	1.382 (10) *1.385*	1.363(3) *1.386*	1.386 (6) *1.384*
C_β-R	1.460 (3) *1.469*	1.466 (4) *1.469*	1.461 (4) *1.469*	1.454(2) *1.464*	1.482 (13) *1.463*	1.465(4) *1.465*	1.450 (8) *1.461*
Ru-P1	2.4359 (7) *2.496*	2.4463 (6) *2.497*	2.4325 (6) *2.497*	2.4542(4) *2.482*	2.431 (2) *2.477*	2.4192(6) *2.472*	2.4542 (13) *2.485*
Ru-P2	2.4359 (7) *2.473*	2.4298 (6) *2.471*	2.4290 (6) *2.471*	2.4075(4) *2.498*	2.398 (2) *2.448*	2.4071(6) *2.446*	2.4290 (14) *2.501*
Ru-P3	2.4315 (7) *2.465*	2.4159 (6) *2.444*	2.4165 (6) *2.444*	2.4500(4) *2.448*	2.4453 (18) *2.499*	2.4469(6) *2.497*	2.4008 (15) *2.485*
Ru-P4	2.4179 (7) *2.443*	2.4342 (6) *2.48*	2.4474 (6) *2.48*	2.4334(4) *2.475*	2.433 (2) *2.482*	2.4388(6) *2.482*	2.4382 (14) *2.452*
Ru-Cl	2.4391 (6) *2.498*	2.4141 (8) *2.497*	2.4325 (6) *2.497*	2.4180(4) *2.496*	2.442 (2) *2.495*	2.4477(6) *2.496*	2.4324 (14) *2.493*

Bond Angle / °	**[58c]**BF_4	**[58d]**BF_4 -A	**[58d]**BF_4- B	**[58e]**BF_4	**[58f]**BF_4	**[58g]**BF_4	**[58h]**BF_4
Ru-C_α-C_β	171.9 (2) *176.418*	177.7 (3) *176.095*	173.4 (2) *176.095*	170.95(13) *175.914*	178.5 (8) *176.028*	177.7(2) *175.950*	179.1 (5) *175.627*
C_α-C_β-F	115.6 (2) *113.608*	115.9 (3) *113.40*	115.8 (2) *113.40*	115.11(14) *113.421*	116.3 (9) *113.522*	116.7(2) *113.356*	115.4 (5) *113.703*
C_α-C_β-R	131.2 (2) *133.528*	130.4 (3) *133.546*	130.6 (2) *133.546*	132.16(15) *133.335*	130.9 (9) *133.149*	129.3(3) *133.653*	129.9 (5) *132.94*
F-C_β-R	113.1 (2) *112.782*	113.6 (3) *113.013*	113.5 (2) *113.013*	112.66(13) *113.199*	112.8 (8) *113.292*	114.0(2) *112.968*	114.58 (5) *113.332*
Cl-Ru-C_α	175.29 (8) *176.354*	173.08 (11) *175.492*	177.49 (7) *175.492*	175.10(5) *175.379*	177.3 (3) *175.272*	177.92(8) *175.752*	177.92 (17) *174.749*
C_α-Ru-P1	98.91 (8) *96.646*	92.68 (11) *95.492*	96.48 (8) *95.492*	100.21(5) *98.937*	91.0 (3) *93.891*	95.57(7) *93.403*	93.21 (17) *98.77*
C_α-Ru-P2	99.02 (8) *98.439*	86.51 (11) *93.688*	97.79 (7) *93.688*	96.83(5) *95.405*	96.6 (3) *85.714*	93.86(8) *85.307*	89.79 (17) *94.728*
C_α-Ru-P3	85.45 (8) *84.845*	99.91 (11) *85.268*	85.66 (8) *85.268*	90.93(5) *93.837*	93.1 (3) *95.374*	93.84(7) *96.009*	97.22 (17) *94.562*
C_α-Ru-P4	91.38 (8) *92.965*	89.00 (11) *99.081*	91.58 (7) *99.081*	85.65(5) *85.517*	89.0 (3) *98.951*	85.07(8) *99.012*	91.03 (17) *86.202*
trans-P-Ru-P	169.66(2) 175.74(2) *168.40* *177.69*	166.80 (2) 174.49(2) *166.99* *177.93*	170.62(2) 177.67(2) *166.99* *177.93*	168.859(15) 177.519(15) *166.98* *177.85*	170.25(8) 179.67(8) *166.91* *177.78*	170.58(2) 178.58(2) *167.38* *177.67*	169.55(5) 179.13(6) *166.39* *177.74*

As with the crystal structure of **[58c]**PF_6, the crystal structures of the other fluorovinylidene complexes displayed distorted octahedral geometries with one significantly distorted *trans*-P-Ru-P angle between 166.80(2)° and 170.62(2)° due to the steric interaction of the aryl substituent with the nearest phosphine group. The Ru-C_α-C_β bond angles are distorted away from linearity with the exception of **[58f]**PF_6 and **[58h]**PF_6 which are statistically linear. The C_α-C_β-F, C_α-C_β-C_{Ar}, and F-C_β-C_{Ar} vinylidene bond angles are all distorted away from the ideal 120° to reduce the steric interaction of the aryl groups with the neighbouring phosphines. The distorted octahedral geometry of the ligands around the metal further alleviates the steric interactions of the vinylidene with the phosphines.

Comparison of the crystallographic data in Table 22 does not reveal any obvious trend between the selected bond lengths and bond angles with the electronic properties of the arene substituent of the vinylidene ligand. The calculated gas-phase structures of **[58]**$^+$ at the (RI-)BP86/SV(P) level predicts that minor elongation of the C_α-C_β bond and compression of the Ru-Cl and Ru-C_α bond should be expected the more electron-withdrawing the arene substituent. The bond angles of the vinylidene ligand, and the angles between the ligands surrounding the metal centre, appear to be unaffected by the electronic properties. However, the gas-phase structures agree with the significant distortions away from ideal of the octahedral geometry and vinylidene bond angles of **[58]**PF_6.

Comparing the crystallographic data for **[58d]**PF_6, **[58f]**PF_6 and **[58g]**PF_6 with their protio-vinylidene analogues, **[59]**$^+$ (Table 23), reveals only a small number of statistically significant differences in bond metrics upon replacing hydrogen with fluorine.

The two structures of **[58d]**PF_6 display an elongation of the C_α-C_β bond compared to **[59d]**PF_6, while the Ru-Cl bond undergoes compression. The Ru-C_α bond in **[58d]**PF_6-A is statistically shorter than in **[59d]**PF_6, whereas it is statistically identical in **[58d]**PF_6-B. The gas phase structures at the (RI-)BP86/SV(P) level predict that the Ru-C_α bond length should remain virtually unperturbed upon fluorine incorporation, suggesting the compression observed in structure B of **[58d]**PF_6 is due to crystal packing effects. The changes observed in the Ru-Cl and C_α-C_β bond lengths agree with the trend in the gas phase structures. The Ru-C_α-C_β bond angle in structure A of **[58d]**PF_6 (177.7(3)°) is less distorted from ideal than in **[59d]**PF_6 (174.78(17)°), whereas the same bond in structure B is distorted further away from linearity (173.4(2)°). The same trend is observed in the Cl-Ru-C_α bond angle, with **[58d]**PF_6-A being more distorted, and **[58d]**PF_6-B less distorted, than **[59d]**PF_6.

Comparison of **[58f]**PF_6 with **[59f]**OTf[296] reveals that the Ru-Cl bond length is statistically different along with variations in the Ru-P bond lengths. The Ru-Cl bond length is compressed in **[58f]**PF_6 compared to **[59f]**OTf-A but elongated compared to **[59f]**OTf-B. The gas phase structures predict a compression of the Ru-Cl bond upon fluorine incorporation, indicating changes in bond metrics are distorted by crystal packing effects. Similarly one of the *trans*-P-Ru-P bond angles in **[58f]**PF_6 (179.67(8)°) is statistically identical to the same bond angle in **[59f]**OTf-A (179.86(2)°), but less distorted compared to **[59f]**OTf-B (175.58(2)°). The other *trans*-P-Ru-P bond angles in the two structures for **[59f]**OTf are statistically identical to one another and are less distorted compared to **[58f]**PF_6 (170.25(8)°). The gas phase structures agree with the observed distortion of the *trans*-P-Ru-P bond angles away from linearity with fluorine incorporation. The Cl-Ru-C_α bond angle in **[58f]**PF_6 is statistically identical to the bond angle in **[59f]**OTf-A and but less distorted compared to **[59f]**OTf-B. The two structures of **[59f]** in the unit cell experience different degrees of crystals packing effects.

Upon fluorine incorporation, the Ru-C_α and Ru-Cl bond lengths undergo compression from 1.859(8) Å and 2.460(2) Å in **[59g]**OTf, to 1.828(3) Å and 2.4477(6) Å in **[58g]**PF_6 respectively, while the C_α-C_β bond length undergoes elongation from 1.265(11) Å to 1.319(4) Å. The Ru-C_α-C_β, Cl-Ru-C_α, and *trans*-P-Ru-P bond angles undergo further distortion away from linearity with incorporation of fluorine. The gas phase structures agree with the observed experimental changes with the exception of the Ru-C_α bond length which is predicted to remain unperturbed; this suggests the compression observed is due to crystal packing effects.

The crystallographic data, as a whole, for the aryl substituted vinylidene complexes highlight the significant impact crystal packing can have on the bond metrics, making correlations between the crystal structure and the electronic effects of the substituents difficult and unreliable.

Table 23: Selected crystallographic data for fluoro- and protio-vinylidene complexes, [58c]$^+$ and [59]$^+$ respectively; calculated values at the (RI-)BP86/SV(P) level in italics.

Bond Length / Å	**[59d]**PF_6	**[58d]**PF_6-A	**[58d]**PF_6-B	**[59f]**OTf-A[296]	**[59f]**OTf-B[296]	**[58f]**PF_6	**[59g]**PF_6	**[58g]**PF_6
Ru-C_α	1.836(2)	1.810 (3)	1.836 (2)	1.836(2)	1.835(2)	1.857 (10)	1.859(8)	1.828(3)
	1.837	*1.836*	*1.836*	*1.832*	*1.832*	*1.831*	*1.832*	*1.832*
C_α-C_β	1.311(3)	1.374 (3)	1.375 (4)	1.313(3)	1.312(3)	1.279 (13)	1.265(11)	1.319(4)
	1.339	*1.356*	*1.356*	*1.342*	*1.342*	*1.359*	*1.341*	*1.358*
C_β-R	1.483(8) / 1.480(14)	1.466 (4)	1.461 (4)	1.465(3)	1.470(3)	1.482 (13)	1.485(12)	1.465(4)
	1.47	*1.469*	*1.469*	*1.465*	*1.465*	*1.463*	*1.466*	*1.465*
Ru-P1	2.4019(5)	2.4463 (6)	2.4325 (6)	2.4533(5)	2.4319(6)	2.431 (2)	2.410(2)	2.4192(6)
	2.437	*2.497*	*2.497*	*2.473*	*2.473*	*2.477*	*2.438*	*2.472*
Ru-P2	2.4091(5)	2.4298 (6)	2.4290 (6)	2.4430(6)	2.4175(6)	2.398 (2)	2.411(2)	2.4071(6)
	2.449	*2.471*	*2.471*	*2.461*	*2.461*	*2.448*	*2.455*	*2.446*
Ru-P3	2.4403(5)	2.4159 (6)	2.4165 (6)	2.4175(6)	2.4185(6)	2.4453 (18)	2.440(2)	2.4469(6)
	2.471	*2.444*	*2.444*	*2.452*	*2.452*	*2.499*	*2.471*	*2.497*
Ru-P4	2.4292(5)	2.4342 (6)	2.4474 (6)	2.4003(6)	2.3958(6)	2.433 (2)	2.423(2)	2.4388(6)
	2.547	*2.48*	*2.48*	*2.439*	*2.439*	*2.482*	*2.462*	*2.482*
Ru-Cl	2.4622(5)	2.4141 (8)	2.4325 (6)	2.4533(5)	2.4666(6)	2.442 (2)	2.460(2)	2.4477(6)
	2.508	*2.497*	*2.497*	*2.507*	*2.507*	*2.495*	*2.506*	*2.496*

Bond Angle / °	**[59d]**PF_6	**[58d]**PF_6-A	**[58d]**PF_6-B	**[59f]**OTf-A[296]	**[59f]**OTf-B[296]	**[58f]**PF_6	**[59g]**PF_6	**[58g]**PF_6
Ru-C_α-C_β	174.78(17)	177.7 (3)	173.4 (2)	175.92(19)	177.43(18)	178.5 (8)	171.5(8)	177.7(2)
	170.497	*176.095*	*176.095*	*170.461*	*170.461*	*176.028*	*170.497*	*175.95*
C_α-C_β-R	131.3(5) / 128.4(8)	130.4 (3)	130.6 (2)	130.4(4)	129.1(2)	130.9 (9)	130.6(9)	129.3(3)
	135.618	*133.546*	*133.546*	*134.933*	*134.933*	*133.149*	*134.696*	*133.653*
Cl-Ru-C_α	176.29(6)	173.08 (11)	177.49 (7)	178.35(7)	174.78(6)	177.3 (3)	176.6(3)	177.92(8)
	177.748	*175.492*	*175.492*	*177.617*	*177.617*	*175.272*	*177.499*	*175.752*
C_α-Ru-P1	97.81(6)	92.68 (11)	96.48 (8)	89.15(7)	92.07(7)	91.0 (3)	96.7(3)	95.57(7)
	98.94	*95.492*	*95.492*	*82.473*	*82.473*	*93.891*	*94.877*	*93.403*
C_α-Ru-P2	92.78(6)	86.51 (11)	97.79 (7)	92.06(7)	85.76(7)	96.6 (3)	97.5(3)	93.86(8)
	94.752	*93.688*	*93.688*	*94.841*	*94.841*	*85.714*	*99.079*	*85.307*
C_α-Ru-P3	91.70(6)	99.91 (11)	85.66 (8)	90.78(7)	94.03(7)	93.1 (3)	84.3(3)	93.84(7)
	94.633	*85.268*	*85.268*	*94.697*	*94.697*	*95.374*	*82.409*	*96.009*
C_α-Ru-P4	84.41(6)	89.00 (11)	91.58 (7)	94.21(7)	93.12(7)	89.0 (3)	89.7(3)	85.07(8)
	82.305	*99.081*	*99.081*	*99.092*	*99.092*	*98.951*	*94.553*	*99.012*
trans-P-Ru-P	170.475(18)	166.80 (2)	170.62(2)	173.72(2)	173.58(2)	170.25(8)	172.74(8)	170.58(2)
	177.113(13)	174.49(2)	177.67(2)	179.86(2)	175.58(2)	179.67(8)	179.03(8)	178.58(2)
	170.61	*166.99*	*166.99*	*170.458*	*170.458*	*166.91*	*170.569*	*167.38*
	178.56	*177.93*	*177.93*	*178.298*	*178.298*	*177.78*	*178.398*	*177.67*

4.1.5 The Reaction of [57i] with Selectfluor

In contrast to the reactions of **[57c]** to **[57h]** with Selectfluor, addition of an acetonitrile solution of Selectfluor to a dichloromethane solution of **[57i]** afforded a blue solution upon warming from -78 °C. No signals were observed in the $^{31}P\{^{1}H\}$ NMR spectrum of the reaction mixture and the ^{1}H NMR spectrum consisted of broad resonances, which could be implying the presence of radical species. The ^{19}F NMR spectrum did not reveal the presence of any new fluorine signals indicting fluorination did not proceed as expected; the ESI mass spectrum did not provide any evidence for the formation of **[58i]**BF_4 either (Scheme 175).

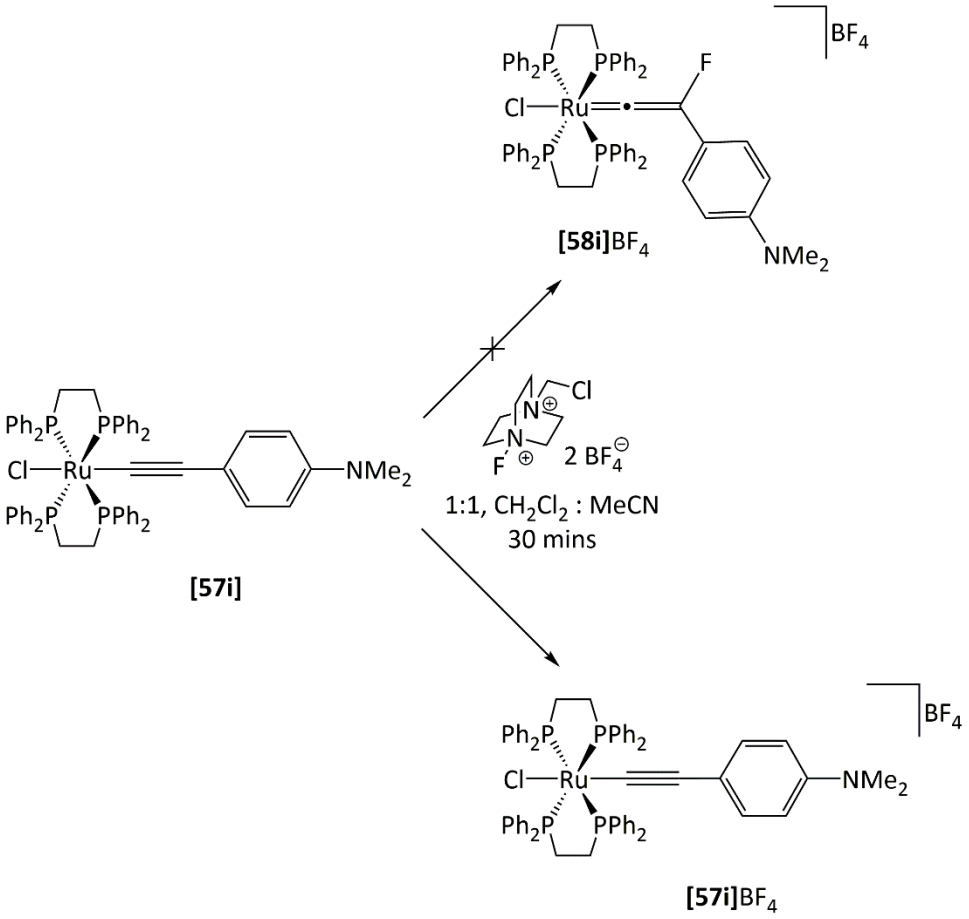

Scheme 175: Addition of Selectfluor to [57i] in 1:1 dichloromethane: acetonitrile did not afford [58i]BF_4 but rather the ruthenium(III) alkynyl complex [57i]BF_4.

Gauthier *et al*.[243] demonstrated that *trans*-[ClRu(dppe)$_2$(C≡CR)] complexes can undergo one-electron oxidation with a suitable oxidant to form quasi-stable ruthenium(III) alkynyl radicals. The radical alkynyl complexes exhibited characteristic low energy absorption bands in their UV-Vis spectra between *ca.* 800-1000 nm, with large molar absorption coefficients in the range of 5-15 x 10^3 M^{-1} cm^{-1}. In order to determine whether the addition of Selectfluor to

[57i] results in oxidation to **[57i]**BF_4, the UV-Vis spectrum of the reaction mixture in 1:1 dichloromethane: acetonitrile was recorded.

The UV-Vis absorption spectrum obtained from the reaction **[57i]** with Selectfluor in a 1:1 dichloromethane: acetonitrile solution (Figure 51) reveals the presence of four strongly absorbing bands and shoulders at 390, 421, 804 and 899 nm. The data are consistent with the values reported by Gauthier *et al.*[243] for **[57i]**BF_4 and also the spectrum recorded independently after mixing **[57i]** with ferrocenium hexafluorophosphate. This implies that instead of acting as a fluorinating agent, Selectfluor acts as an oxidant in the presence of **[57i]** to afford the one-electron oxidised product (Scheme 175). The band at 899 nm corresponds to a LMCT from the chloride ligand to ruthenium, while the shoulder at 804 nm is believed to correspond to a vibronic transition involving the C≡C stretch. The band at 421 nm corresponds to a MLCT from the ruthenium centre to the alkynyl ligand and the band at 390 nm likely corresponds to another vibronic transition.

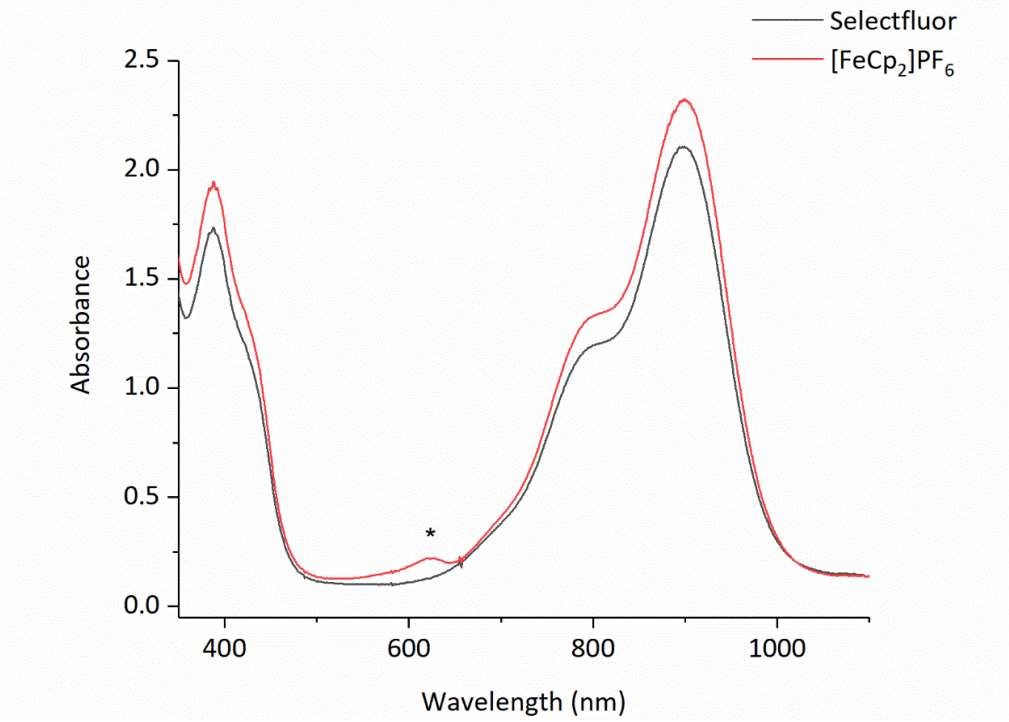

Figure 51: UV-Vis absorption spectrum obtained by the reaction of [57i] with Selectfluor (0.25 mM) and oxidation with ferrocenium hexafluorophosphate in 1:1 dichloromethane: acetonitrile. Asterisk denotes band arising from ferrocenium hexafluorophosphate.

Although the use of Selectfluor as an oxidant rather than a fluorinating agent is well documented in the literature,[297-303] the observation of oxidation rather than fluorination with **[57i]** is surprising given that fluorination is observed with complexes **[57c]** to **[57h]**, **[57a]** and **[57b]**, as well as ruthenium half-sandwich alkynyl complexes.

4.2 Monitoring the Reactions of [57] with Selectfluor by UV-Vis, IR, and EPR Spectroscopy

4.2.1 Monitoring the Reaction of [57] with Selectfluor by UV-Vis Spectroscopy

Due to the observation of one electron oxidation products in the reaction of **[57i]** with Selectfluor, the reactions of **[57c]** to **[57h]** with Selectfluor were monitored by UV-Vis, IR, and EPR spectroscopy, to ascertain whether oxidation products are also observed alongside C-F bond formation to give **[58]**BF_4.

The addition of Selectfluor to **[57c]** in 1:1 dichloromethane: acetonitrile resulted in the rapid growth of absorption bands at 835, 585, and 380 nm over two minutes (Figure 52) which corresponded to the formation of **[57c]**BF_4, indicating one electron oxidation occurs with the addition of Selectfluor. The band at 835 nm arises from a LMCT from the chloride ligand to the ruthenium centre. The band at 585 nm corresponds to a π to d_{Ru} transition from an MO distributed over the chloride-ruthenium-alkynyl ligands to the ruthenium, while the band at 380 nm arises from a MLCT from the ruthenium centre to the alkynyl ligand. After two minutes, the bands for **[57c]**BF_4 begin to decay and a new species grows in, as evidence by the observation of a band at 519 nm.

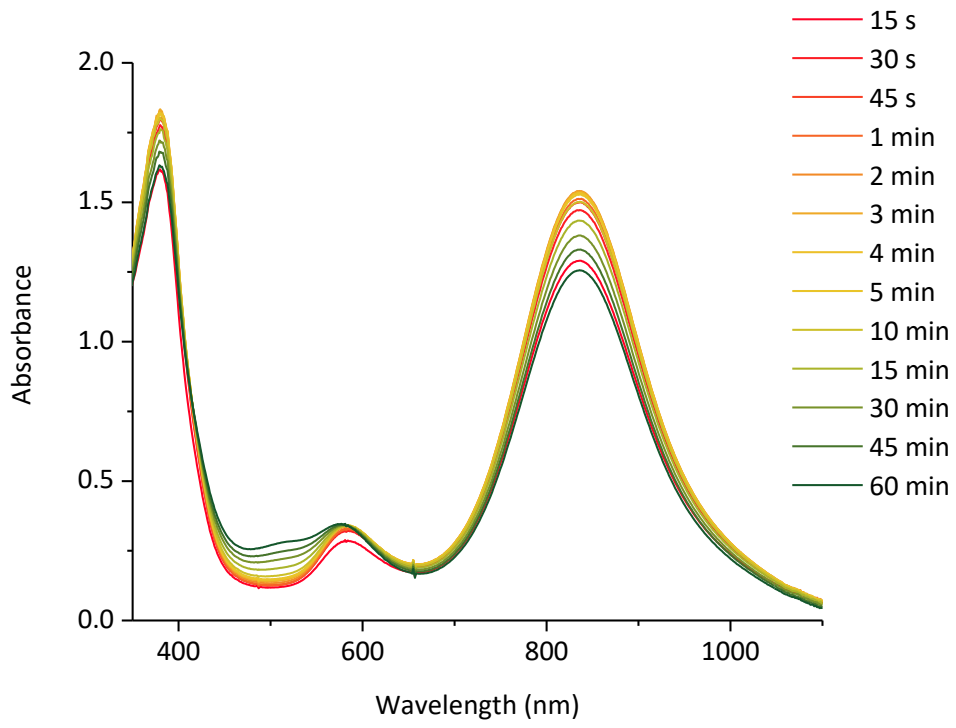

Figure 52: Overlaid UV-Vis spectra obtained from monitoring the reaction between [57c] and Selectfluor in 1:1 dichloromethane: acetonitrile at 0.25 mM

It is clear from the UV-Vis spectrum of **[58c]**BF_4 (Figure 53) that the band at 519 nm does not correspond to the formation of the fluorinated product **[58c]**BF_4. However, this band was only observable in the reaction of **[57c]** with Selectfluor and was not observed in the reactions of **[57c]** with [FTMP]BF_4, NFSI, ferrocenium hexafluorophosphate, or in any of the reactions of **[57d]** to **[57i]**. It was not possible to observe the direct formation of **[58c]**BF_4 due the low energy absorption band at 812 nm overlapping with the alkynyl radical at 835 nm and the two orders of magnitude difference between the molar absorption coefficient of **[58c]**PF_6 (ε = 25 m^2 mol^{-1}) and **[57c]**PF_6 (ε = 1240 m^2 mol^{-1}; Figure 53). Nevertheless UV-Vis spectroscopy has revealed that oxidation is observable in the reaction of **[57c]** with Selectfluor, alongside fluorination which is observed by NMR spectroscopy and synthetic studies.

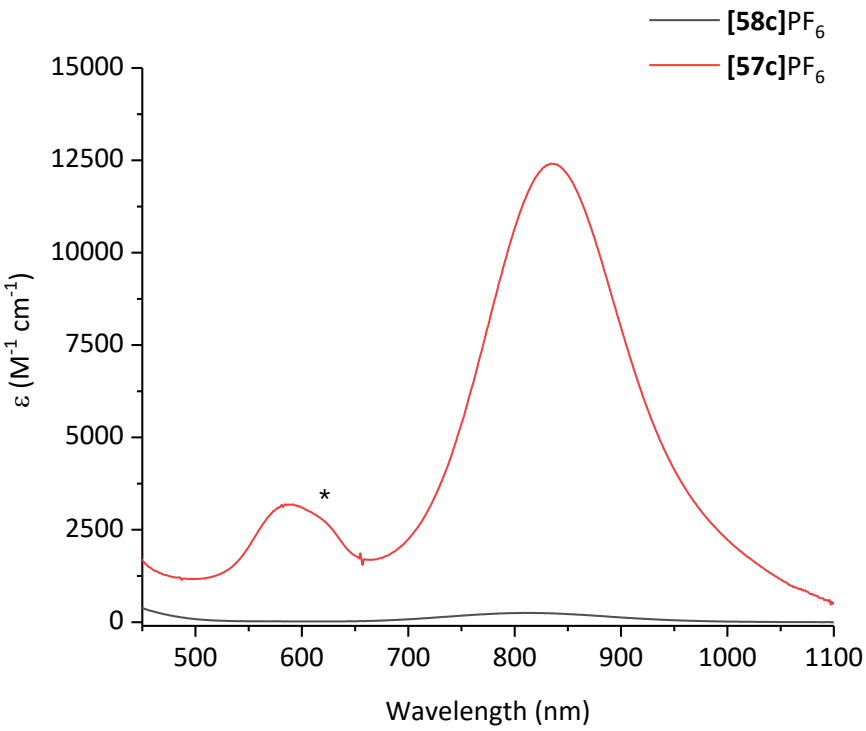

Figure 53: Overlaid UV-Vis spectra of [58c]PF_6 and [57c]PF_6 in 1:1 dichloromethane: acetonitrile; the asterisk denotes the band arising from unreacted ferrocenium hexafluorophosphate used to generate [57c]$^{\cdot}PF_6$.

The reaction of Selectfluor with complexes **[57d-h]** was monitored by UV-Vis spectroscopy in an analogous manner. One-electron oxidation of **[57d-h]** was observed in all cases, as well as decay of the respective radical cation. The UV-Vis spectra of **[57]**BF_4 all display characteristic bands around 800-900 nm (Cl→Ru LMCT) and around 600 nm ($\pi \rightarrow d_{Ru}$). However, the formation of a second species, such as that observed at 519 nm in the reaction of **[57c]** with Selectfluor, could not be observed. This suggests the species observed at 519

nm is unique to **[57c]** or that such species are hidden under the absorption bands for **[57]**BF_4. As observed with **[57c]**, the formation of the respective fluorovinylidene complexes could not be observed directly due to overlapping bands and the high molar absorption coefficients of the alkynyl radical complexes compared to the fluorovinylidene complexes. The observation of one-electron oxidation of **[57]** in these cases could imply that fluorination proceeds *via* a radical mechanism or that oxidation is a competing process to fluorination.

4.2.2 Attempted Deconvolution of UV-Vis Spectroscopic Data

The reactions of **[57c-h]** with Selectfluor were monitored by UV-Vis spectroscopy in an attempt to obtain kinetic data on the formation of **[57]**BF_4 and **[58]**BF_4 and determine the relationship between them. However, in all cases the formation of the fluorinated vinylidene complex could not be observed due to the overlapping bands of the alkynyl radical cation and the order of magnitude difference between the molar absorption coefficients. To determine whether the contributions of **[57]**BF_4 and **[58]**BF_4 could be approximated, deconvolution was performed on the UV-Vis spectra obtained from the reaction of **[57d]** with Selectfluor. Deconvolution was performed by fitting the spectra (Figure 54) to Gaussian functions with fixed peak widths and centre points based on the UV-Vis spectroscopic data obtained for the alkynyl radical cation and fluorinated vinylidene complex in 1:1 dichloromethane: acetonitrile independently. The reaction of **[57d]** with Selectfluor was chosen for devolution.

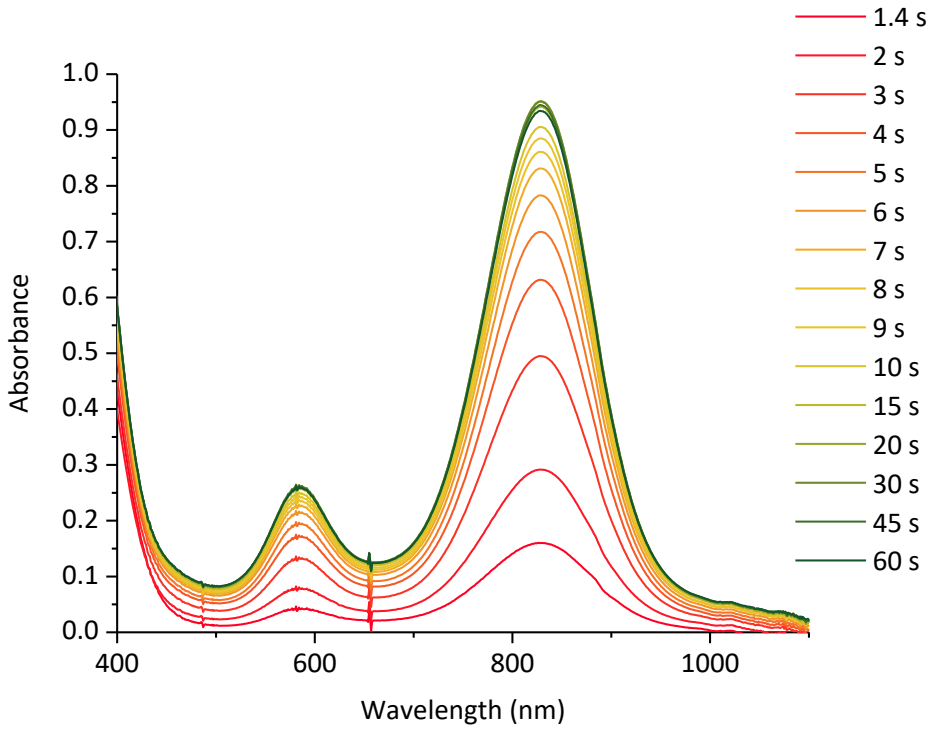

Figure 54: UV-Vis spectra for a 0.25 mM reaction mixture of [57d] and Selectfluor in 1:1 dichloromethane: acetonitrile over one minute.

The only background correction applied was zeroing all spectra at 1100 nm to correct for baseline drift; an example of deconvolution is displayed in Figure 55. The difference between the observed spectrum and the cumulative fit (dashed line, Figure 55) reveals the parameters used do not fully model the spectrum correctly. Nevertheless, comparing the observed spectrum to the Gaussian fits for **[57d]**BF_4 at 585 and 828 nm reveals that the low energy bands in the observed spectrum are approximately equal in absorbance to bands in the spectrum of **[57d]**BF_4 on its own. The concentration of **[57d]**BF_4 calculated from the observed spectrum was 0.17 mM while the concentration calculated form the fitted spectrum was 0.15 mM.

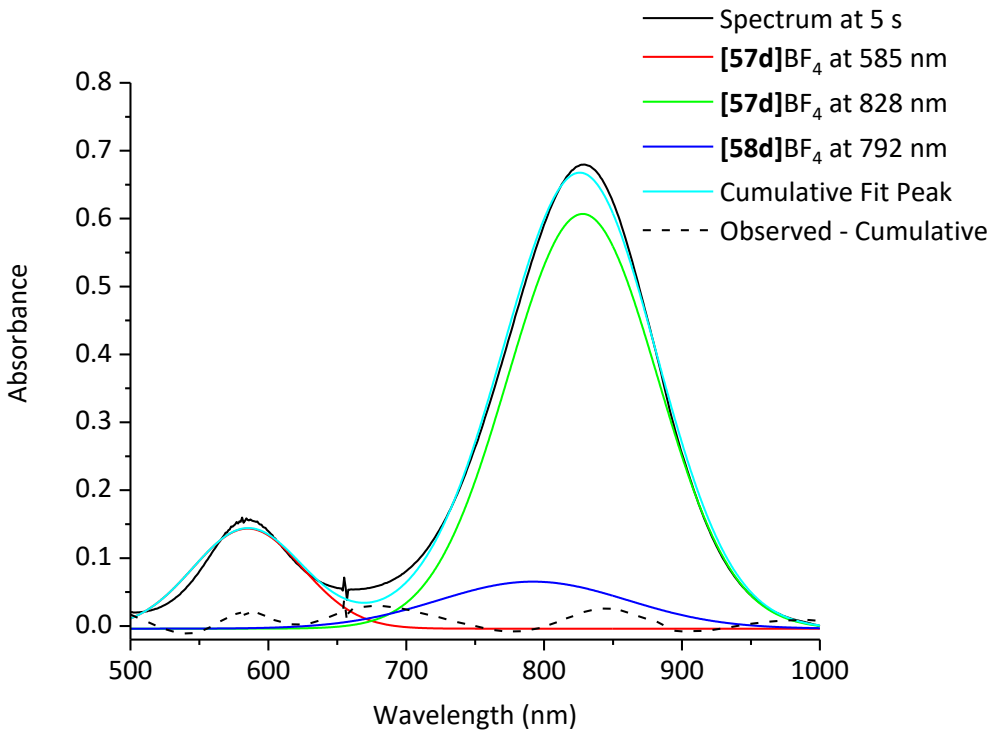

Figure 55: Example deconvolution of the UV-Vis spectrum five seconds after addition of Selectfluor to [57d] at 0.25 mM.

The concentration of the fluorovinylidene complexes **[58d]**BF_4 calculated from the fitting exceeded the maximum possible concentration (0.25 mM) indicating that deconvolution of the UV-Vis spectroscopic data could not provide absolute concentrations for **[58d]**BF_4. The contribution of **[58]**BF_4 to the UV-Vis spectra determined by deconvolution is therefore skewed by the large band for **[57d]**BF_4 and is unable to provide reliable kinetics for the formation of **[58d]**BF_4.

4.2.3 EPR Spectroscopic Data

In order to obtain further evidence for the formation of the ruthenium(III) alkynyl species, 0.5 mM reaction mixtures of **[57]** with Selectfluor were subjected to X-band EPR spectroscopy at *ca*. 140 K (Figure 56). The samples were prepared by immediately freezing a 1:1 dichloromethane: acetonitrile reaction mixture in liquid nitrogen after addition of Selectfluor or oxidant to **[57]**. Ferrocenium hexafluorophosphate was also used as the oxidant for **[57c]**, **[57d]**, and **[57i]**, while thianthrenium tetrafluoroborate, **[113]**BF_4 (1.26 V vs SCE in MeCN)[304] was used as the oxidant for **[57a]**, **[57b]**, **[57g]**, and **[57h]**.

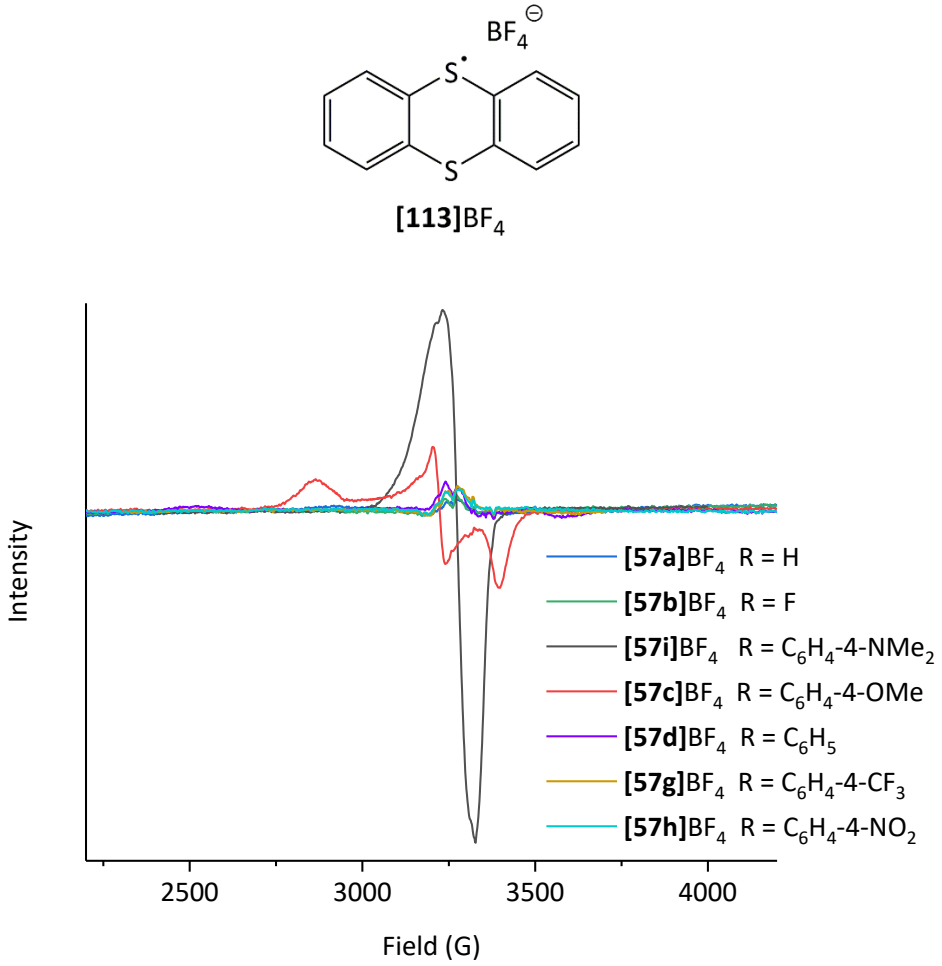

Figure 56: Overlaid EPR spectrum from the reaction of *trans*-[ClRu(dppe)$_2$(C≡CR)] with Selectfluor at 0.5 mM in 1:1 dichloromethane: acetonitrile. The signal denoted by the asterisk arises from artefacts of baseline correction and from radical species in the quartz EPR tube.

A strong radical signal could only be detected for complexes **[57i]** and **[57c]** which are the most easily oxidised alkynyl complexes. A weak signal was observable in the EPR spectrum with **[57d]** and Selectfluor, in which only the g_x and g_z components were observable; the g_y component was hidden under the background noise and quartz signal from the EPR tube

(Figure 56). In these three cases the signal observed was rhombic in character and suggestive of a ruthenium-centred radical based on literature.[243, 305]

No clear signal was observed in the samples of **[57a]**, **[57b]**, **[57g]**, and **[57h]** with Selectfluor (Figure 56). Only very weak signals for the g_x and g_z components were observable in the samples of **[57g]** and **[57h]** oxidised with **[113]**BF_4, indicating insufficient time had elapsed to allow an observable concentration of alkynyl radical to be generated, presumably due to the slower rate of oxidation (Table 26). Gauthier *et al.*[243] reported that excess oxidant was required to observe the radical alkynyl complexes of the most electron-withdrawing substituents by EPR spectroscopy, which also hints at a slower rate of oxidation. However, there was no observable radical after the samples with Selectfluor were allowed to warm to room temperature for five minutes and being refrozen in liquid nitrogen. With complexes **[57a]** and **[57b]**, no signal could be observed with the addition of thianthrenium tetrafluoroborate either. Based on the irreversible nature of oxidation and UV-Vis spectra mentioned later in the chapter (sections 4.7.1.3, 4.7.2.3, and 4.10), it is not surprising that a signal could not be observed due to their instability and reactivity. The decreasing intensity of radical signal with increased electron-withdrawing character of the aryl substituent observed in the 0.5 mM samples with Selectfluor reflects the ease of which the alkynyl complexes can be oxidised (Figure 56).

The EPR spectra for the reactions of **[57d]**, **[57g]** and **[57h]** with Selectfluor were re-recorded at a higher concentration (10 mM) in order to observe all three g-components. The EPR spectra at 142 K obtained immediately after mixing **[57d]** with Selectfluor displayed a rhombic signal with broad g_x, g_y, and g_z components (Figure 57). The spectra obtained ten minutes after addition of Selectfluor to **[57g]** and **[57h]** at a concentration of 10 mM exhibited weak signal in which the g_x and g_z components were observable. The g_x and g_z components matched the g-values obtained from oxidation of **[57g]** and **[57h]** by thianthrenium tetrafluoroborate, **[113]**BF_4. The g_y component was obscured by artefacts from the background correction due to the poor signal to noise ratio (Figure 57). However, one part of the g_y component is observed in both cases.

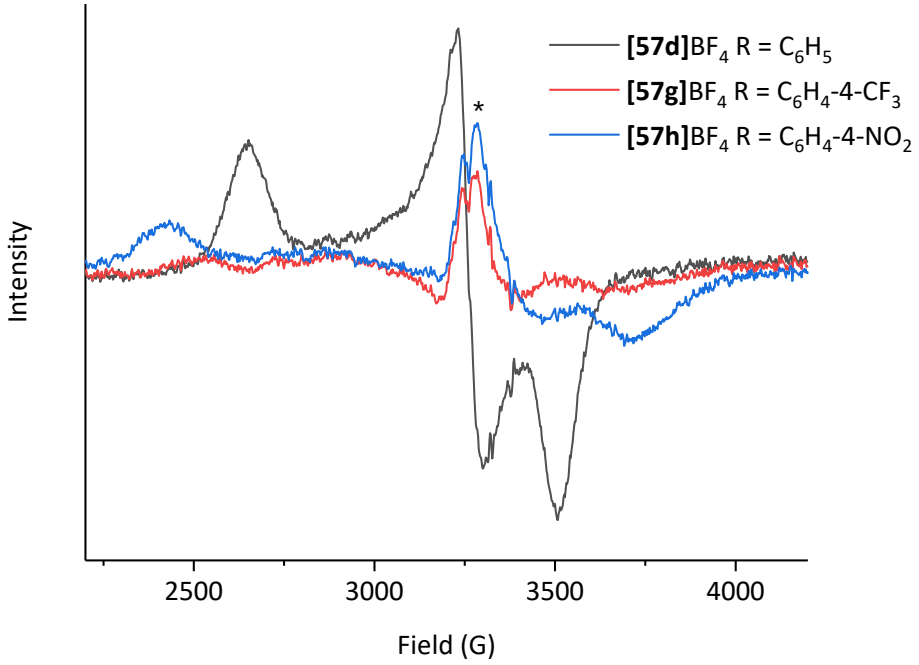

Figure 57: Overlaid EPR spectra obtained immediately after mixing Selectfluor with [57d], and ten minutes after mixing Selectfluor with [57g] and [57h] at 10 mM (recorded at *ca.* 140 K). Asterisk denotes artefacts from baseline correction.

The EPR spectra from the reactions of **[57c]**, **[57d]**, **[57g]**, **[57h]** and **[57i]** with Selectfluor were simulated with EasySpin in MATLAB, and afforded g-values which matched the g-values obtained from addition of an oxidant and/or reported by Gauthier *et al*.[243] (Table 24). An example of the fitting is shown in Figure 58 for the reaction of **[57d]** with Selectfluor at a concentration of 10 mM. Any hyper-fine structure was not observable or distinguishable from background noise and/or the quartz tube. Broad g-components with no discernible hyperfine structure were also observed by Gauthier *et al.*[243] and also noted for ruthenium(III) half-sandwich alkynyl complexes by Paul *et al.*[305] The g-values obtained from oxidation of **[57c]** and **[57h]** with Selectfluor and an oxidant were different to the values reported by Gauthier *et al.*[243] and are assumed to be the result of the spectra being recorded at different temperatures and solvent mixtures (77 or 80 K in 1:1 dichloromethane: 1,2-dichloroethane). Due to the limitations of the liquid nitrogen evaporator used, the spectra were only recorded at *ca.* 140 K.

Table 24: EPR spectroscopic data for radicals formed from reaction of Selectfluor with [57c], [57d], [57g], [57h] and [57i] in 1:1 dichloromethane: acetonitrile glass at *ca.* 140 K.

[ClRu(dppe)$_2$(C≡CR)] R =	g_x	g_y	g_z	‹g›	Δg
[57i]$^+$ C_6H_4-4-NMe_2	1.994	2.035	2.100	2.043	0.106
	1.994[a]	*2.035*[a]	*2.100*[a]	*2.043*[a]	*0.106*[a]
	1.993[c]	*2.037*[c]	*2.100*[c]	*2.043*[c]	*0.107*[c]
[57c]$^+$ C_6H_4-4-OMe	1.951	2.061	2.327	2.113	0.376
	1.951[a]	*2.061*[a]	*3.327*[a]	*2.113*[a]	*0.376*[a]
	1.958[c]	*2.039*[c]	*3.309*[c]	*2.109*[c]	*0.351*[c]
[57d]$^+$ C_6H_5	1.896	2.039	2.516	2.150	0.680
	1.896[a]	*2.039*[a]	*2.516*[a]	*2.150*[a]	*0.680*[a]
	1.896[c]	*2.039*[c]	*2.519*[c]	*2.151*[c]	*0.623*[c]
[57g]$^+$ C_6H_4-4-CF_3	1.827	-	2.671	-	0.844
	1.827[b]	*1.993*[b]	*2.671*[b]	*2.164*[b]	*0.844*[b]
[57h]$^+$ C_6H_4-4-NO_2	1.788	-	2.745	-	0.957
	1.788[b]	*1.963*[b]	*2.745*[b]	*2.165*[b]	*0.957*[b]
	1.766[c]	*1.955*[c]	*2.777*[c]	*2.166*[c]	*1.011*[c]

The g-values in italics were obtained by oxidation with [a] *$[FeCp_2]PF_6$ or* [b] ***[113]***BF_4 *at ca. 140 K, and* [c] *reported by Gauthier et al.*[243] *at 77 or 80 K in 1:1 dichloromethane: 1,2-dichloroethane.*

‹g› is defined as the average g-value while *Δg is defined as the difference between* g_x *and* g_z.

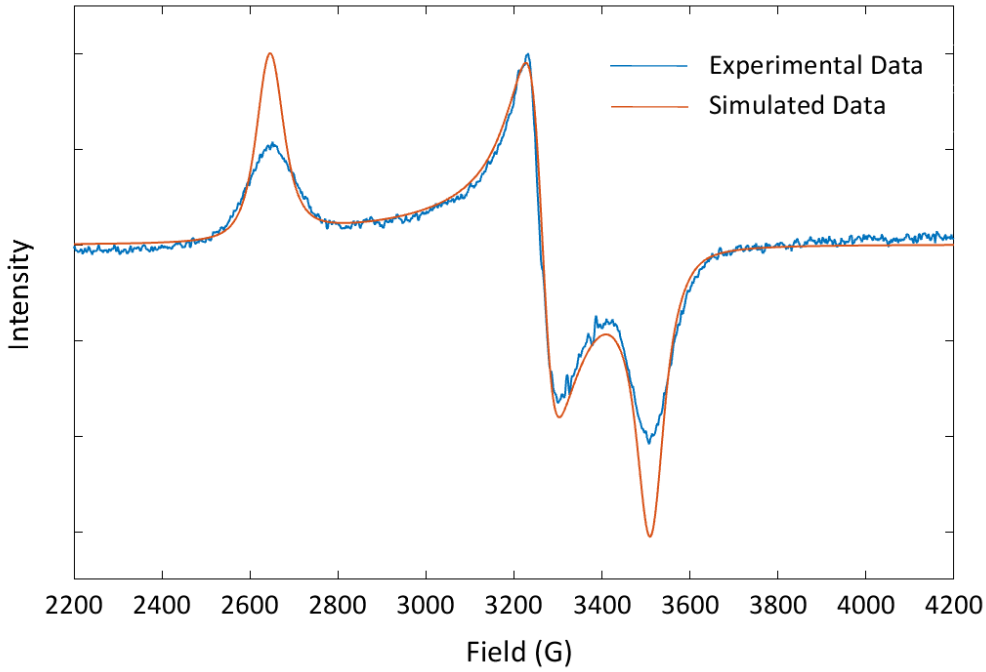

Figure 58: Experimental EPR data (blue) of [57d] with Selectfluor in 1:1 dichloromethane: acetonitrile at a concentration of 10 mM at 142 K and recorded at a frequency of 9.3186 MHz, overlaid with the simulated fit (red) with g_x = 1.896, g_y = 2.039, g_z = 2.516.

Nevertheless the principal objective of using EPR spectroscopy was to provide further evidence for the formation of ruthenium(III) alkynyl radical species. The aryl substituted alkynyl complexes **[57c]**, **[57d]**, **[57g]**, **[57h]** and **[57i]** all displayed evidence for the formation of the respective ruthenium(III) alkynyl complexes, **[57]**BF_4, with addition of Selectfluor. This supports the observations obtained by monitoring the reactions of **[57]** with Selectfluor by UV-Vis spectroscopy.

4.2.4 Combined UV-Vis-NMR Spectroscopic Experiments

An alternative approach to probing the relationship between the alkynyl radical and the fluorovinylidene complex involved monitoring the reactions of **[57c]**, **[57d]**, and **[57g]** with Selectfluor by UV-Vis spectroscopy over one hour, to determine the approximate changes in concentrations of the respective alkynyl radical. Then, immediately after one hour, obtaining a $^{31}P\{^{1}H\}$ NMR spectrum of the reaction mixture, with an internal reference, to approximate the conversion to the fluorovinylidene complex. The $^{31}P\{^{1}H\}$ NMR spectra of the alkynyl and reaction mixtures were recorded with a triphenylphosphine insert to enable conversion of **[57]** to **[58]**BF_4 to be calculated.

Monitoring the reaction of **[57d]** with Selectfluor in 1:1 dichloromethane: acetonitrile over the course of one hour (Figure 59) resulted in overall decay of the radical being observed (Figure 59). At maximum conversion, the alkynyl radical makes up approximately 63 % of the total composition of ruthenium species, assuming the contribution of **[58d]**BF_4 to the signal at 829 nm is negligible compared to the alkynyl radical (see section 4.2.3). The percentage of **[57d]**BF_4 drops to 51 % after one hour, corresponding to a decrease of 12 %.

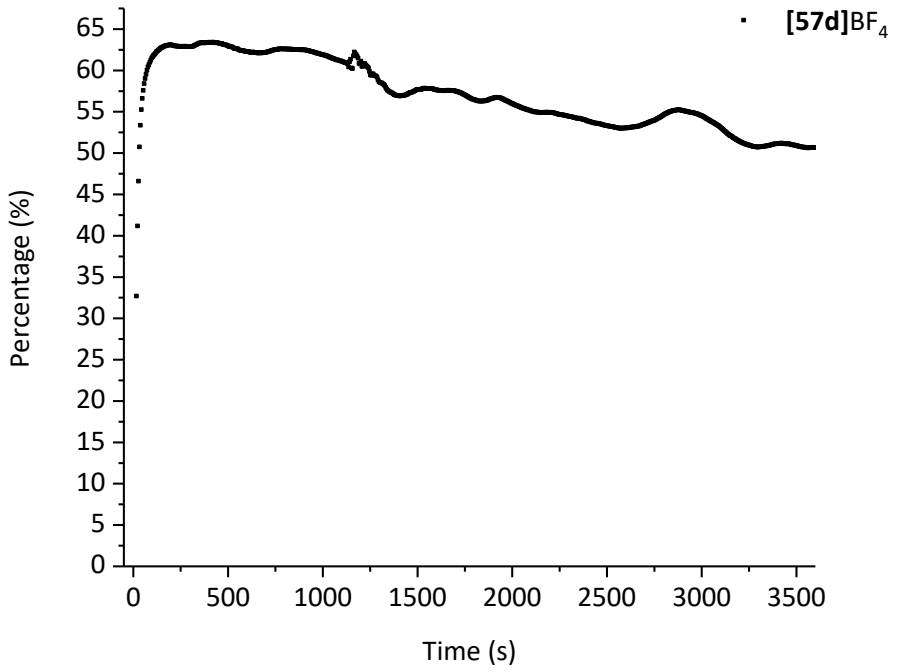

Figure 59: Percentage contribution of [57d]BF_4 to the total ruthenium content at 0.25 mM in 1:1 dichloromethane: acetonitrile.

The $^{31}P\{^{1}H\}$ NMR spectrum of the 1:1 dichloromethane: acetonitrile solution after one hour with a triphenylphosphine insert displayed a singlet resonance at δ 33.2 corresponding to **[58d]**BF_4 in the solvent mix and integrated to approximately 0.45 P with respect to the triphenylphosphine reference. Based on the integration of **[57d]** at the same concentration and solvent mix, **[58d]**BF_4 constitutes 53% of the total ruthenium content in solution (Table 25). In addition to **[58d]**BF_4 being observed, the $^{31}P\{^{1}H\}$ NMR spectrum displayed the appearance of a trace decomposition product at δ 50.3. It is believed that this species corresponds to formation of **[114d]**BF_4 on the basis of ESI-MS. Complex **[114d]**BF_4 is also observed upon standing **[57d]** in 1:1 dichloromethane: acetonitrile for three days or upon decay of **[57d]**BF_4 in the same solvent mix (discussed in section 4.6.1). The integration of this resonance could not be obtained accurately due to poor signal to noise ratio. The respective complexes **[114c]**BF_4 and **[114g]**BF_4 were also observed in the $^{31}P\{^{1}H\}$ NMR spectrum after one-hour with **[57c]** and **[57g]** respectively.

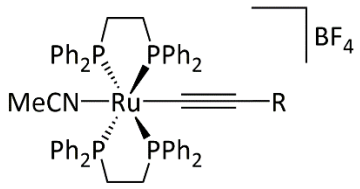

[114]BF_4

a R = H
b R = F
c R = C_6H_4-4-OMe
d R = C_6H_5
e R = C_6H_4-4-C(O)OMe
f R = C_6H_4-4-C(O)Me
g R = C_6H_4-4-CF_3
h R = C_6H_4-4-NO_2
i R = C_6H_4-4-NMe_2
j R = C_3H_5

Table 25: Contribution of [57]$^+BF_4$, [58]BF_4 and [114]BF_4 to the total composition of ruthenium species in solution one hour after addition of Selectfluor. The maximum percentage of radical alkynyl complex that is observed, and the time it at which it is reached, is also reported.

[Ru](C≡CR) R=	UV-Vis Spectroscopy			NMR Conversion	
	[57]$^+_{Max}$ / %	Time $_{max}$ / s	**[57]**$^+_{1h}$ / %	**[58]**$^+_{1h}$ / %	**[114]**$^+_{1h}$ / %
C_6H_4-4-OMe	50	182	41	25	15
C_6H_4	63	197	51	55	Trace
C_6H_4-4-CF_3	41	707	32	35	20

[Ru] = trans-[ClRu(dppe)$_2$]; NMR conversion reported to nearest 5 %.

The UV-Vis spectra recorded from the reaction of Selectfluor with **[57c]** and **[57g]** over one hour also displayed rapid growth of the respective radical alkynyl complex followed by slow

decay. In the case of **[57c]**, the maximum concentration of **[57c]**BF_4 is reached 182 seconds after addition of Selectfluor, with the radical contributing approximately 50 % to the total composition of ruthenium species. After one hour the radical decays by approximately 9 %, while the $^{31}P\{^1H\}$ NMR spectrum predicts approximately 25 % conversion of **[57c]** to **[58c]**BF_4. This was also supported by the same experiment with **[57g]** in which the radical alkynyl complex decays by approximately 9 % over the course of an hour, while the $^{31}P\{^1H\}$ NMR experiment afterwards indicates 33 % conversion of **[57g]** to **[58g]**BF_4.

As the percentage change in the alkynyl radical over one hour is less than the percentage growth of fluorovinylidene complex observed by NMR spectroscopy, the data suggest that decay of the ruthenium(III) alkynyl radical does not correspond to fluorination and that the radical alkynyl complex cannot be an intermediate. Instead, the data appear to indicate that **[57]**BF_4 and **[58]**BF_4 are formed *via* different pathways. The decay of **[57]**BF_4 observed in the UV-Vis spectra is believed to result in the formation of the acetonitrile complex **[114]**BF_4. Fluorination of **[57]** (with the exception of **[57i]**) on a 100-200 mg scale provided isolated yields between 59 % and 95 %. It is believed that the isolated product is a combination of both **[57]**BF_4 and **[58]**BF_4.

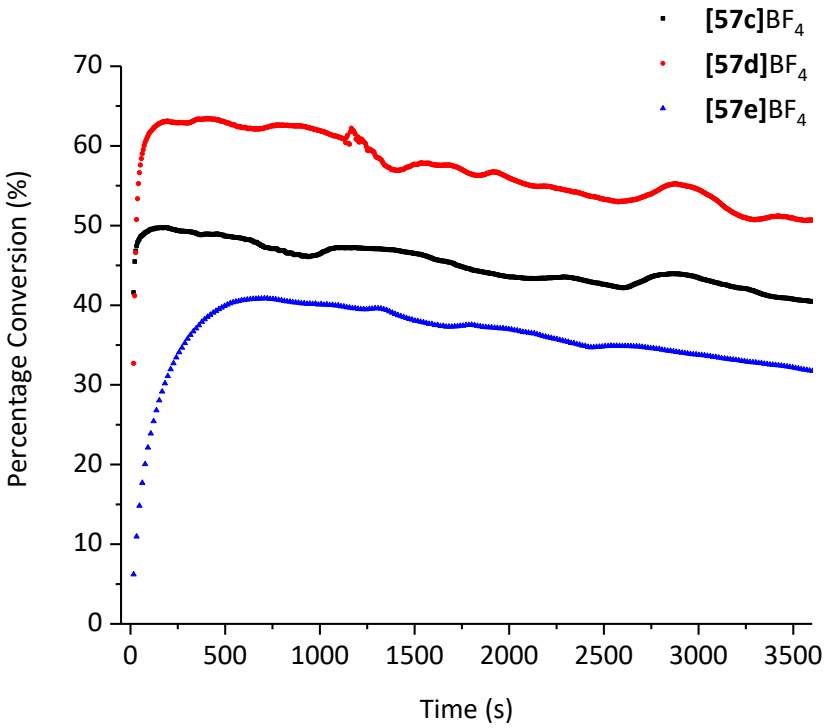

Figure 60: Overlaid percentage composition of alkynyl radicals [57c]BF_4, [57d]BF_4, and [57g]BF_4 with time.

Fluctuations in the decay period for **[57]**BF_4 in Figure 60 are believed to be artefacts from data collection. Smoothing with adjacent-averaging, Lowess and Loess methods could not eliminate the fluctuations and attempts to fit the decay to an exponential decay function failed using Levenberg Marquardt and orthogonal distance regression algorithms.

4.2.5 Probing Fluorination with IR Spectroscopy

Due to the difficulty observing **[57]**, **[57]**$^+$, and **[58]**$^+$ simultaneously, solution phase IR spectroscopy was explored as a possible technique with which to monitor all three species through their characteristic C≡C and C=C vibrational stretching modes. The IR data were obtained by mixing near saturated solutions of Selectfluor with **[57d]** in 1:1 dichloromethane: acetonitrile and immediately transferring the solution into an IR cell. The spectrum was recorded with one scan in order to acquire data as rapidly as possible after mixing to determine whether fluorination is observed on a short time scale (*ca.* 15-20 seconds from mixing to data acquisition).

The IR spectrum obtained *ca.* 20 seconds after mixing **[57d]** with Selectfluor displayed bands at 1622 cm^{-1} and 2069 cm^{-1} corresponding to **[58d]**BF_4 and unreacted **[57d]** respectively (Figure 61). The band corresponding to **[57d]**BF_4, reported at 1908 cm^{-1}, could not be observed. The observation of **[58d]**BF_4 indicates that fluorination occurs on a short timescale (< 20 s) and supports the conclusion drawn from UV-Vis-NMR experiments. However, the bands within the area of interest are weak compared to the vibrational bands elsewhere in the spectrum. Future work would entail the use of stopped-flow IR or *in situ* IR monitoring with ReactIR, in an attempt to obtain kinetic data on alkynyl consumption and vinylidene formation.

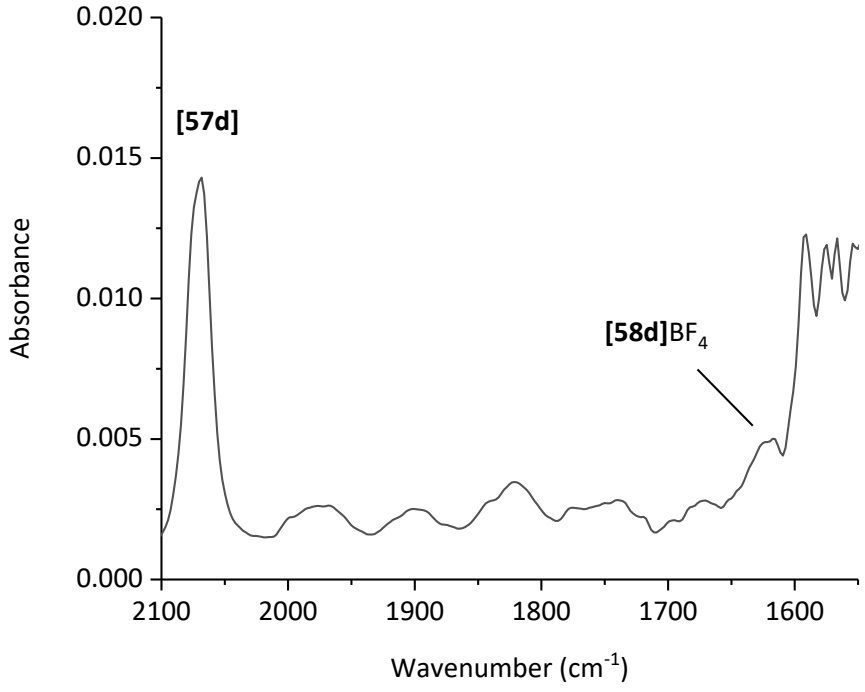

Figure 61: Solution phase IR spectrum recorded approximately 20 seconds after mixing Selectfluor and [57d].

4.3 Reactions of *trans*-[ClRu(dppe)$_2$(C≡CR)] with Selectfluor in the Presence of a Radical Trap

The observation of organometallic radicals by UV-Vis, EPR and IR spectroscopy in the reactions of **[57]** with Selectfluor could suggest the involvement of radicals in the fluorination pathway. To ascertain whether fluorination proceeds by a radical mechanism the reactions of **[57a]**, **[57c]**, **[57d]** and **[57g]** with Selectfluor were conducted in the presence of the radical trap, 2,2,6,6-tetramethyl-1-piperidinyloxyl (TEMPO), **115**. In addition, the reactions of **[57a]** and **[57c]** with Selectfluor were also conducted in the presence of 2,6-di-*tert*-butyl-4-methylphenol (BHT), **116**.

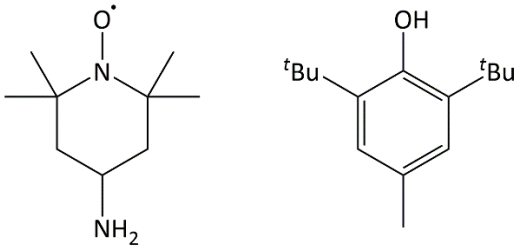

TEMPO **115** BHT **116**

Figure 62: TEMPO, 115, and BHT, 116.

4.3.1 Reactions of [57c], [57d], and [57g] with Selectfluor in the Presence of TEMPO

Dichloromethane solutions of **[57c]**, **[57d]**, and **[57g]** were prepared with three equivalents of TEMPO to which acetonitrile solutions of Selectfluor (1 equivalent) were added at room temperature (Scheme 176). In all three reactions fluorination to the respective fluorovinylidene complexes was observed by NMR spectroscopy and ESI-mass spectrometry.

In the reaction of **[57c]** with Selectfluor in the presence of TEMPO, the $^{31}P\{^1H\}$ NMR spectrum in 1:1 dichloromethane: acetonitrile was dominated by a resonance at δ 32.2 for **[58c]**BF_4, along with trace unreacted **[57c]**; no other species was observed in the spectrum. The ^{19}F NMR spectrum revealed **[58c]**BF_4 was the only fluorinated product afforded by the reaction of **[57c]** with Selectfluor in the presence of TEMPO. The observation of unreacted **[57c]** could have implied quenching of the radical alkynyl complex by TEMPO; however control experiments revealed that there was no observed quenching of **[57c]**$^+$ by TEMPO in the UV-Vis spectra (Figure 63). The controls also revealed there was no observed reactivity between

TEMPO and complexes **[57c]** or **[58c]**BF_4 (NMR spectroscopy). In contrast, addition of three equivalents of TEMPO to one equivalent of Selectfluor in d^3-acetonitrile was found to result in complete consumption of Selectfluor within 10 minutes of mixing according to the ^1H and ^{19}F NMR spectra. The reaction of Selectfluor with TEMPO implies it is capable of reacting *via* an SET mechanism as noted by Vincent *et al*.[306] The presence of unreacted **[57c]** is therefore believed to be the result of TEMPO deactivating Selectfluor rather than inhibition of any organometallic radicals, with the rate of fluorination is competitive with Selectfluor deactivation.

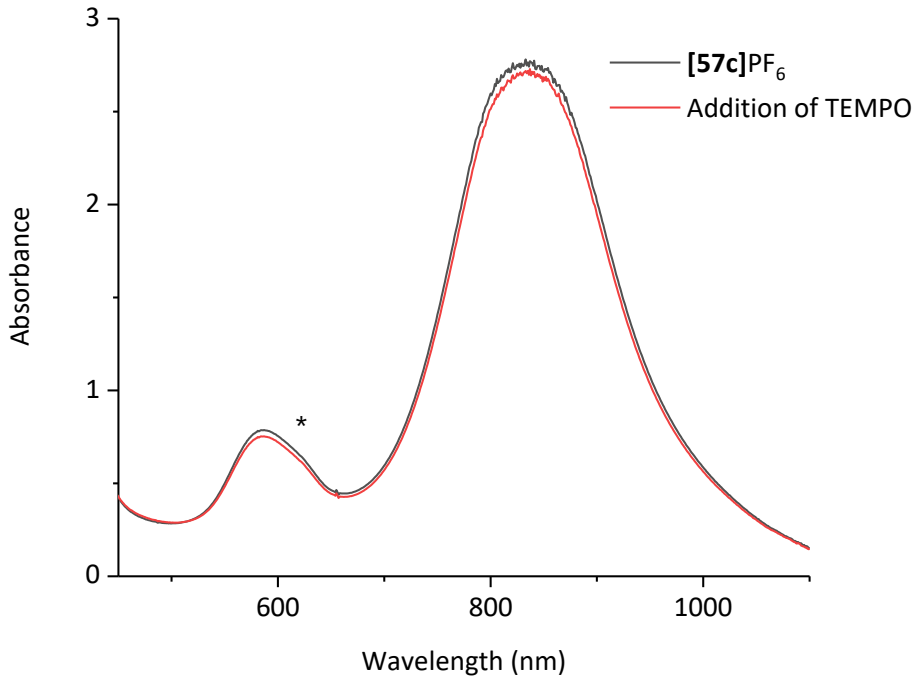

Figure 63: Overlaid UV-Vis spectra of [57c]PF_6 (generated by addition of ferrocenium hexafluorophosphate), and [57c]$^{\cdot}PF_6$ with addition of TEMPO at 0.25 mM. Asterisk denotes absorption band for ferrocenium hexafluorophosphate.

Similarly, the fluorination of both **[57d]** and **[57g]** was found to proceed in the presence of TEMPO, with **[58]**BF_4 forming as the major product according NMR spectroscopy (80 % and 81 % respectively by $^{31}P\{^1H\}$ NMR). Significant quantities of unreacted **[57]** were observed in both reactions (14 % and 12 % respectively by $^{31}P\{^1H\}$ NMR), presumably as a consequence of TEMPO competing with the alkynyl complexes for Selectfluor.

The $^{31}P\{^1H\}$ NMR spectrum from the reaction of **[57d]** with Selectfluor in the presence of TEMPO also displayed a minor product at δ 30.0 contributing 6 % to the species observed in the spectrum. It is unclear whether this species forms as a consequence of TEMPO inhibiting fluorination or from the alkynyl/ radical alkynyl complexes reacting with the products

produced from the reaction between TEMPO and Selectfluor. A trace product was also observed in $^{31}P\{^{1}H\}$ NMR spectrum from the reaction of **[57g]** with Selectfluor in the presence of TEMPO and contributed to 6% of phosphorus-containing species by NMR spectroscopy.

In the reaction of **[57g]** with Selectfluor in the presence of TEMPO, the ^{19}F NMR spectrum in 1:1 dichloromethane: acetonitrile reveals the presence of three minor trifluoromethyl environments at δ -64.7, -64.6, and -63.5, which integrate to 0.2, 0.3, and 0.1 F respectively against the trifluoromethyl environment for **[58g]**BF_4. The resonance at δ -63.5 corresponds to unreacted **[57g]**, however it is not clear what species the other two environments correspond to.

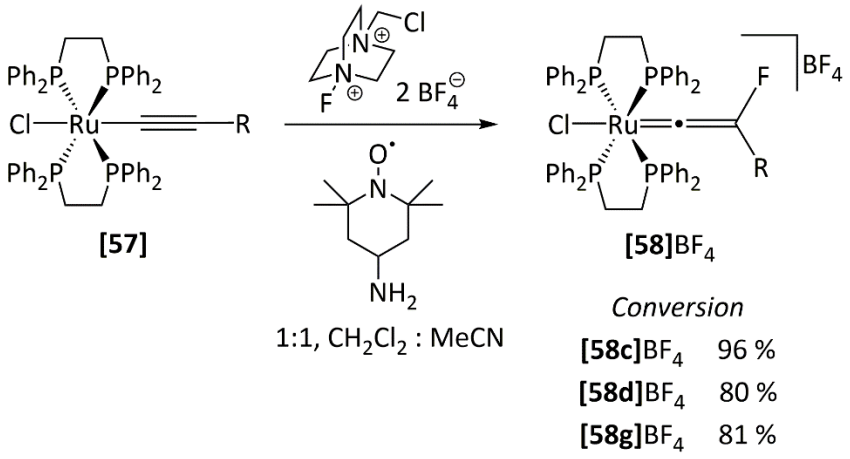

Scheme 176: Reaction of [57c], [57d], and [57g] with Selectfluor in the presence of TEMPO resulted in fluorination to [58]BF_4 still being observed, however TEMPO competed with [57] for Selectfluor resulting in unreacted [57] being observed. Conversion to [58]BF_4 based on integration from $^{31}P\{^{1}H\}$ NMR spectra.

4.3.2 Reaction of [57c] with Selectfluor in the Presence of BHT

Conducting the reaction of **[57c]** with Selectfluor in 1:1 dichloromethane: acetonitrile in the presence of three equivalents of BHT also resulted in the formation of the fluorinated product, **[58c]**BF_4, according to ESI-MS and NMR spectroscopy (Scheme 177). The $^{31}P\{^{1}H\}$ NMR spectrum revealed the presence of unreacted **[57c]** as a minor species due to the competing reaction between Selectfluor and BHT according to the control experiment. There was no evidence of any additional species being generated in the $^{31}P\{^{1}H\}$ or ^{19}F NMR spectra.

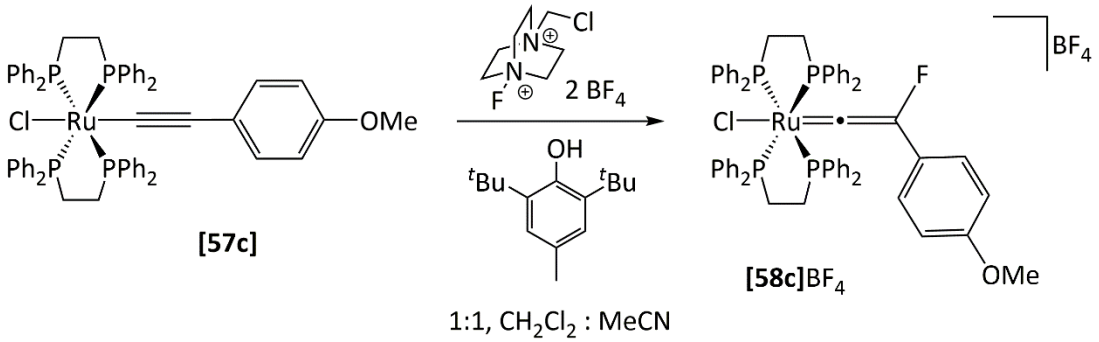

Scheme 177: Reaction of [57c] with Selectfluor in the presence of BHT resulted in fluorination to [58c]BF_4 still being observed, however BHT competed with [57c] for Selectfluor resulting in unreacted [57c] being observed.

It is evident that TEMPO or BHT to alter the ratio of fluorinated to radical products should be used with caution and rigorous control experiments to ensure any change is not the result of the radical trap reacting or quenching with reagents and products rather than intercepting radicals.[306, 307] For example, Vincent *et al*.[306] found that TEMPO completely inhibit the fluorination of glycals by Selectfluor but also demonstrated that TEMPO reacted independently with Selectfluor which may have accounted for observed inhibition. Likewise, addition of BHT was found to hinder fluorination but the control experiment also revealed BHT reacts slowly with Selectfluor, accounting for the reduced yield of fluorinated product.

4.3.3 Reaction of [57a] with Selectfluor in the Presence of TEMPO and BHT

The radical trapping experiments were also conducted with *trans*-[ClRu(dppe)$_2$(C≡CH)], **[57a]**, which displayed irreversible electrochemistry and underwent fluorination with NFSI, to determine whether fluorination proceeds by a different mechanism to the aryl substituted alkynyl complexes **[57c-h]**.

Addition of an acetonitrile solution of Selectfluor to a dichloromethane solution of **[57a]** with three equivalents of TEMPO did not inhibit fluorination. Complex **[58a]**BF_4 was the only fluorinated species observed in the ^{19}F NMR spectrum and was the major species observed in the $^{31}P\{^1H\}$ NMR spectrum (Scheme 178). The $^{31}P\{^1H\}$ NMR spectrum also displayed minor singlet resonances at δ 36.9 and δ 30.0, approximately integrating to 0.5 and 0.1 with respect to **[58a]**BF_4. The identities of these species could not be determined but do not correspond to the formation of a TEMPO adduct according to ESI-MS. The species at δ 30.0 is believed to correspond to the same species observed in the reactions of **[57c]** and **[57d]** with Selectfluor in the presence of TEMPO. However, as with the previous experiments, it is not

clear whether these additional species correspond to fluorination being inhibited or the result of the reaction between TEMPO and Selectfluor.

In contrast to the reactions with **[57c]**, **[57d]**, and **[57g]**, complete consumption of **[57a]** was observed which could suggest that **[57a]** is sufficiently reactive to outcompete TEMPO for Selectfluor. Alternatively, the products afforded by the reaction between Selectfluor and TEMPO may react with **[57a]**, contributing to the complete consumption of the starting material and may account for the formation of the species observed at δ 36.9 and 30.0 in the $^{31}P\{^{1}H\}$ NMR spectrum.

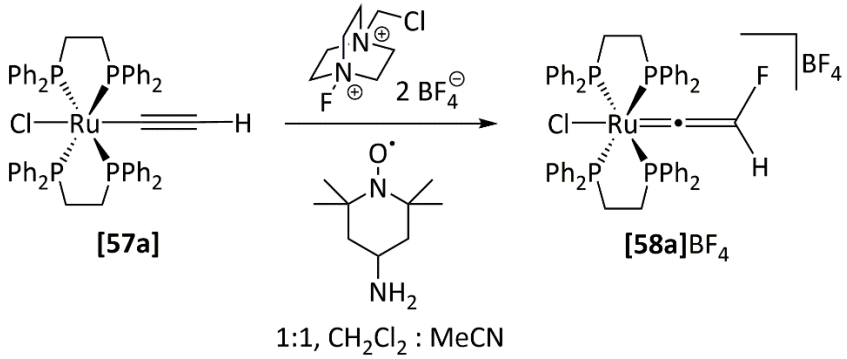

Scheme 178: Reaction of [57a] with Selectfluor in the presence of TEMPO still afforded [58a]BF_4 as the major product.

Repeating the reaction in the presence of BHT did not result in any inhibition of fluorination according to the $^{31}P\{^{1}H\}$ and ^{19}F NMR spectra.

4.4 Reaction of a Cyclopropyl-Substituted Alkynyl Complex with Selectfluor,

Employment of cyclopropyl-containing substrates is a common method of detecting the presence of radical intermediates, with ring-opened products signifying a radical mechanism, and closed-ring products an S_N2 mechanism.[139, 306, 308, 309] In order to probe the potential role and presence of radical complexes in the fluorination or oxidation of *trans*-[ClRu(dppe)$_2$(C≡CR)] complexes, the cyclopropyl-substituted alkynyl complex, **[57j]**, was synthesised. It was expected that the cyclopropyl group would ring-open upon oxidation to afford **[117]**$^+$ which would than abstract fluorine to afford **[118]**$^+$ (Scheme 179). Direct fluorination would be expected to give the fluorinated vinylidene complex **[58j]**$^+$ with no observation of ring opening.

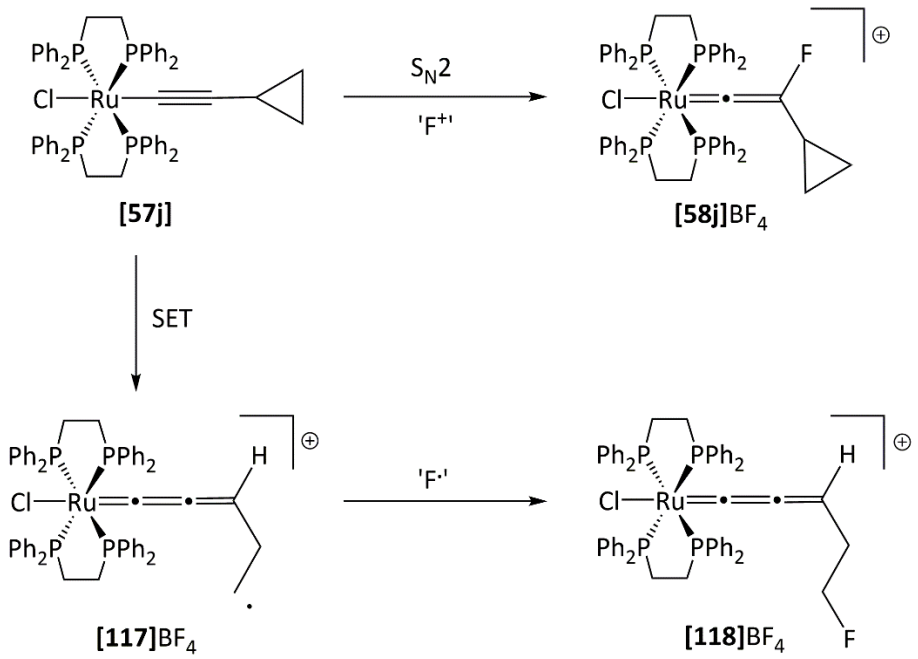

Scheme 179: S_N2 fluorination would be expected to afford [58j]BF_4 while an SET mechanism could result in ring-opening to afford [117]BF_4 with fluorine transfer affording [118]BF_4.

Addition of an acetonitrile solution of Selectfluor to a dichloromethane solution of **[57j]** at -78 °C resulted in the formation of a green solution upon warming. The ^{19}F NMR spectrum in d^2-dichloromethane exhibited a new singlet resonance at δ -249.0 which matches the chemical shifts observed for the fluorine substituents of **[58]**BF_4 rather than an alkyl-fluorine substituent, suggesting the formation of **[58j]**BF_4. The ^{31}P{^{1}H} NMR spectrum displayed a singlet resonance at δ 37.8 corresponding to the new organometallic species. The ^{1}H NMR spectrum displayed three multiplet resonances at δ 0.54, 0.60, and 0.74 integrating 2:1:2

protons respectively. The chemical shifts are indicative that the cyclopropyl ring remains intact. The ^{13}C-^{19}F HSQC 2D NMR experiment displayed cross peaks between the fluorine resonance at δ -249.0 with carbon resonances at δ 198.5 and 412.3 which is indicative of the β- and α-carbon atoms of a fluorinated vinylidene ligand (Table 20). The ESI mass spectrum displayed a species with the correct m/z for **[118]**BF_4 or **[58j]**BF_4. The NMR parameters are consistent with the formation of the fluorinated vinylidene complex, **[58j]**BF_4. Crystallisation by slow diffusion of pentane into a dichloromethane solution of the hexafluorophosphate salt yielded suitable crystals for X-ray crystallography. The structure obtained confirmed the formation of **[58j]**PF_6 (Figure 64); no evidence for any ring-opened products was obtained.

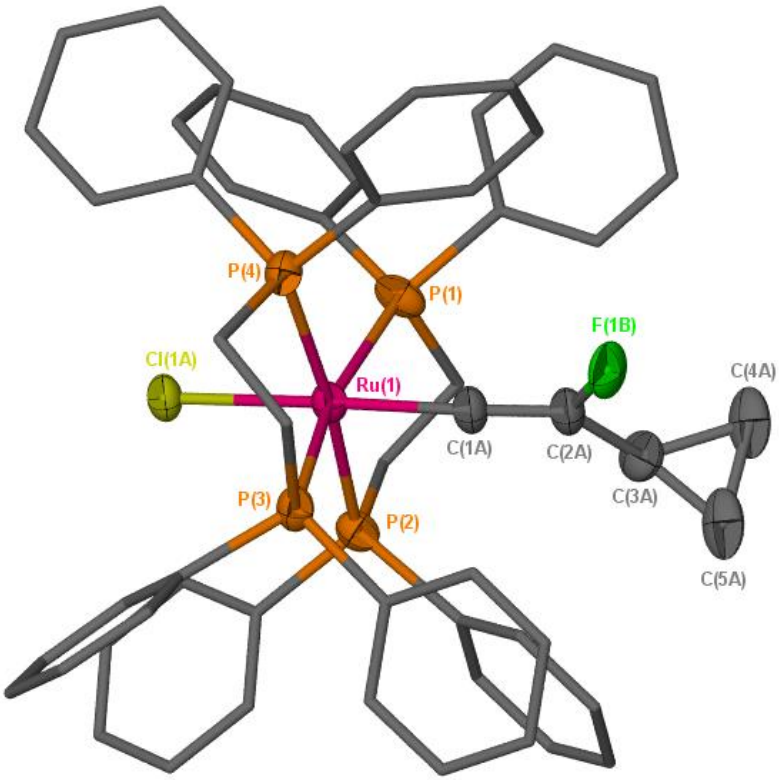

Figure 64: Crystal structure of [58j]PF_6; the hexafluorophosphate counterion, dichloromethane (solvent of crystallisation) and hydrogens are omitted for clarity and thermal ellipsoids are displayed with 50 % probability level.

A spin density calculation on the ruthenium(III) radical alkynyl complex, optimised at the (RI-)BP86/SV(P)//PBE0/def2-TZVPP level, does not show any significant spin density on the cyclopropyl ring. Instead the spin density is predicted to reside primarily on the ruthenium centre and the β-carbon of the alkynyl ligand (Figure 65). It is therefore unlikely for ring opening to occur in the alkynyl radical. Further support is provided by the cyclic-voltammogram of **[57j]** (Figure 66), which exhibits a quasi-reversible redox event at -0.08 V (vs $[FeCp_2]PF_6$ in 1:1 DCM: MeCN) or 0.34 V (vs SCE in DCM) similar to cyclic-voltammograms

of **[57c-h]**. If ring opening was to occur then an irreversible cyclic-voltammogram would be expected; however even at the lowest scan rate of 25 mVs^{-1} the reverse reduction peak of the alkynyl complex is still observed, indicating ring opening does not occur on a time scale of 30 seconds or less.

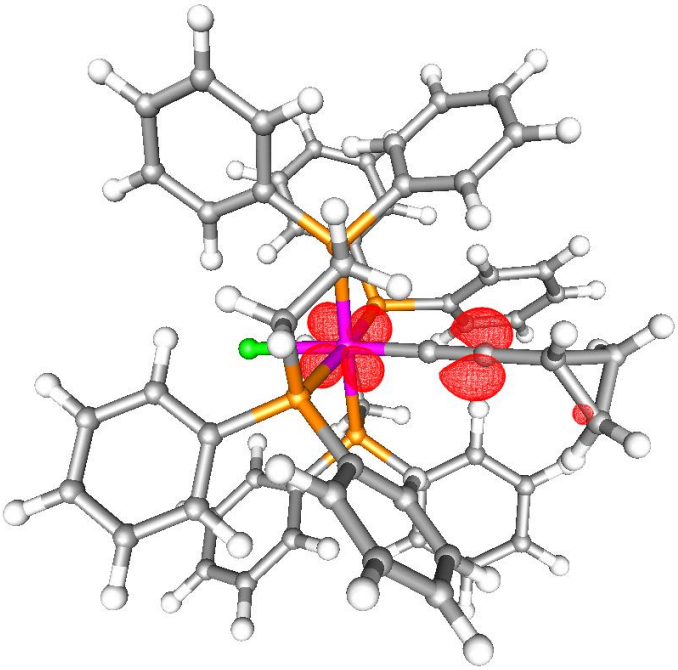

Figure 65: Calculated spin density map at the (RI-)BP86/SV(P)//PBE0/def2-TZVPP level for the radical cation $[57j]^+$.

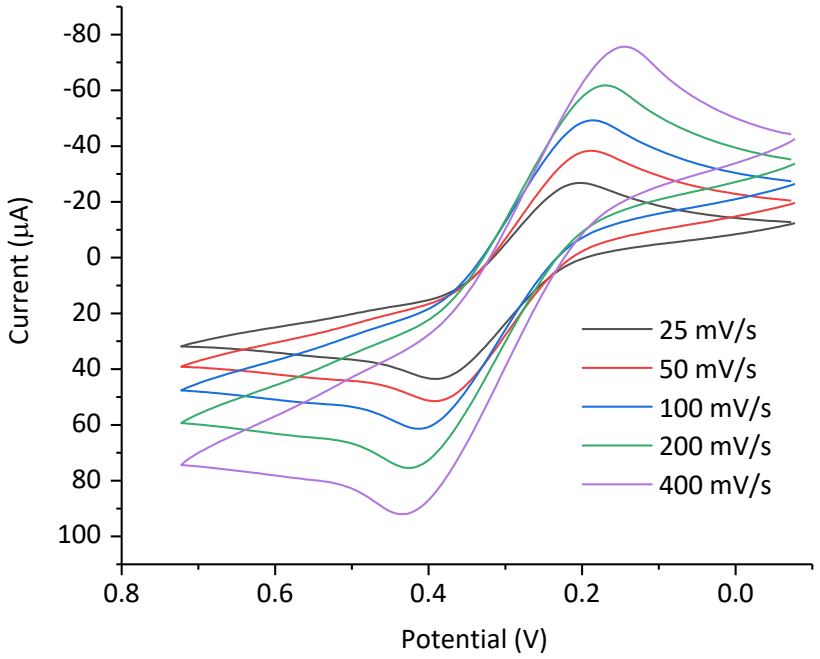

Figure 66: Cyclic-voltammogram of [57j] vs SCE at varying scan rates in dichloromethane with 0.1 M *tetra*-butylammonium hexafluorophosphate as supporting electrolyte and ferrocene as internal reference. A platinum disc was used as the working electrode, platinum wire for the counter electrode and silver wire for the pseudo reference.

4.5 Investigating the Reaction of [77] with Selectfluor by UV-Vis and EPR Spectroscopy

Given the observation of radicals in the reaction of *trans*-[ClRu(dppe)$_2$(C≡CR)] complexes with Selectfluor, the fluorination of **[77]** with Selectfluor (Scheme 181) was investigated by UV-Vis and EPR spectroscopy to determine whether radical species could be detected. The reactions between the half-sandwich alkynyl complexes and the three fluorinating agents have not been monitored before by a technique capable of observing radical species. Since the oxidation of [Ru(η^5-C$_5$Me$_5$)(dppe)(C≡CR)] and *trans*-[ClRu(dppe)$_2$(C≡CR)] complexes has been reported between 0.04-0.59 V (vs SCE in dichloromethane),[305, 310] and that **[14b]** and **[77]** oxidise in the presence of ferrocenium hexafluorophosphate, ruthenium half sandwich alkynyl complexes could in theory undergo oxidation in the presence of a fluorinating agent as observed with *trans*-[ClRu(dppe)$_2$(C≡CR)].

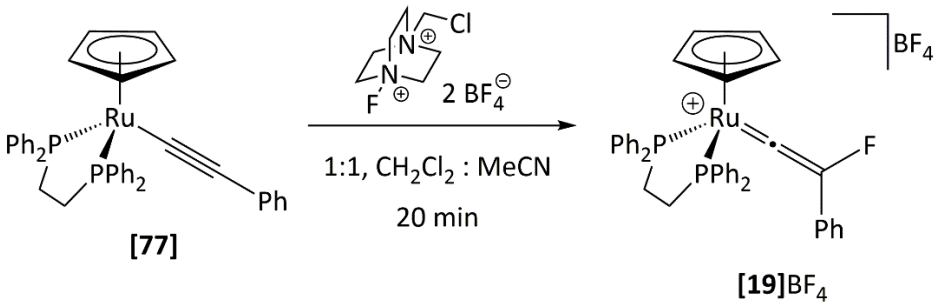

Scheme 180: Fluorination of [77] with Selectfluor affords [19]BF$_4$.

To determine whether there is any evidence for the formation of a radical alkynyl complex in the reaction of ruthenium half-sandwich alkynyl complexes with a fluorinating agent, the reaction of **[77]** with Selectfluor was monitored by UV-Vis spectroscopy in a 1:1 dichloromethane: acetonitrile solution. Upon addition of Selectfluor a single low energy absorption band at 644 nm grows in over ten seconds corresponding to the formation of **[19]**BF$_4$. However, there was no evidence for the appearance of absorption bands corresponding to the oxidation of **[77]** (shown in the blue spectrum of Figure 67). The peak shape of the absorption band at 644 nm appears symmetric and fits well to a single Gaussian function (Figure 68). The attempts to fit the absorption band to both the fluorovinylidene and radical alkynyl complexes failed. This suggests that either oxidation does not occur, the radical is too short lived or affords the alkynyl radical at concentrations too low to be observable by UV-Vis spectroscopy.

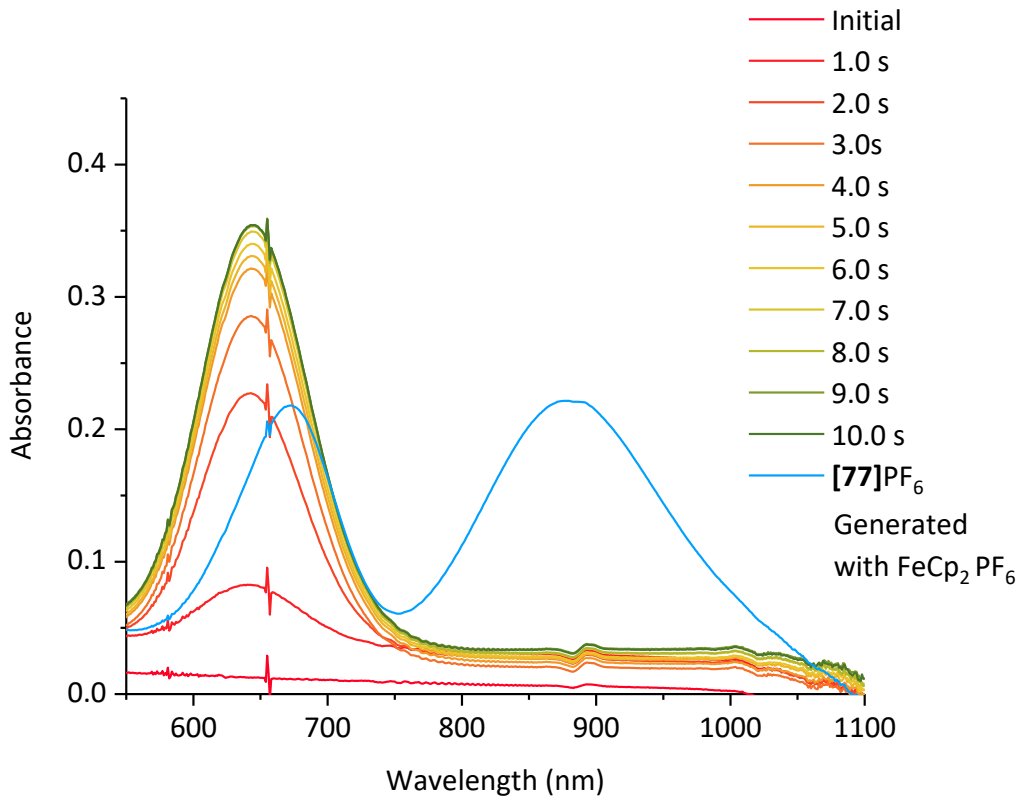

Figure 67: Overlaid UV-Vis spectra for the reaction of [77] with Selectfluor at 1 mM in 1:1 dichloromethane: acetonitrile. The blue UV-Vis spectrum was obtained from the oxidation of [77] with ferrocenium hexafluorophosphate and scaled down for clarity.

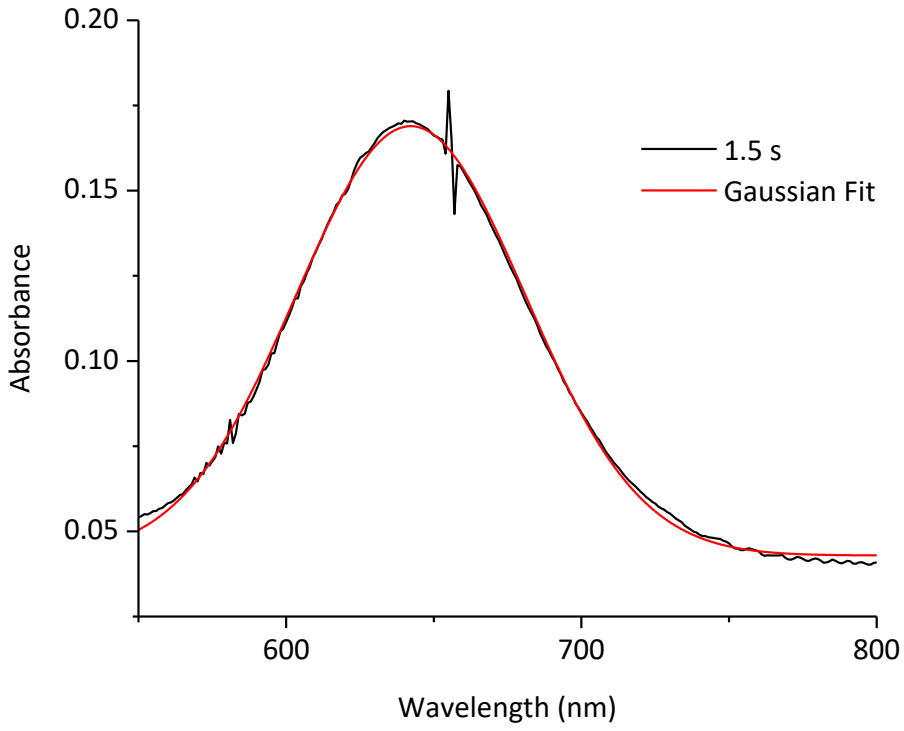

Figure 68: Gaussian fitting of the UV-Vis absorption band at 644 nm at 1.5 seconds after addition of Selectfluor to [77] at 1 mM in 1:1 dichloromethane: acetonitrile (R^2 = 0.998).

In another attempt to discern whether or not radical species could be detected in the reaction of Selectfluor with **[77]**, the reaction mixture, at a concentration of 20 mM, was frozen immediately after addition of Selectfluor and subjected to EPR spectroscopy (Figure 69). The EPR spectrum revealed the presence of a weak rhombic signal characteristic of a ruthenium-centred radical (approximate g-values; $g_x = 1.994$, $g_y = 2.075$, $g_z = 2.171$). Allowing the sample to stand at room temperature for five minutes then reacquiring the EPR spectrum resulted in a change to the spectrum; the signal appeared shifted compared to the initial spectrum obtained after mixing **[77]** with Selectfluor (black spectrum in Figure 69). The EPR spectrum of **[77]**PF_6 generated by addition of ferrocenium hexafluorophosphate produced a rhombic signal (approximate g-values; $g_x = 1.994$, $g_y = 2.063$, $g_z = 2.178$) which is similar in appearance to the spectrum acquired after 5 minutes at room temperature. However, in all cases the radical signal observed was weak with artefacts from baseline correction and the quartz EPR tube distorting the spectra. The data suggest that the competition between fluorination and oxidation is at best a minor.

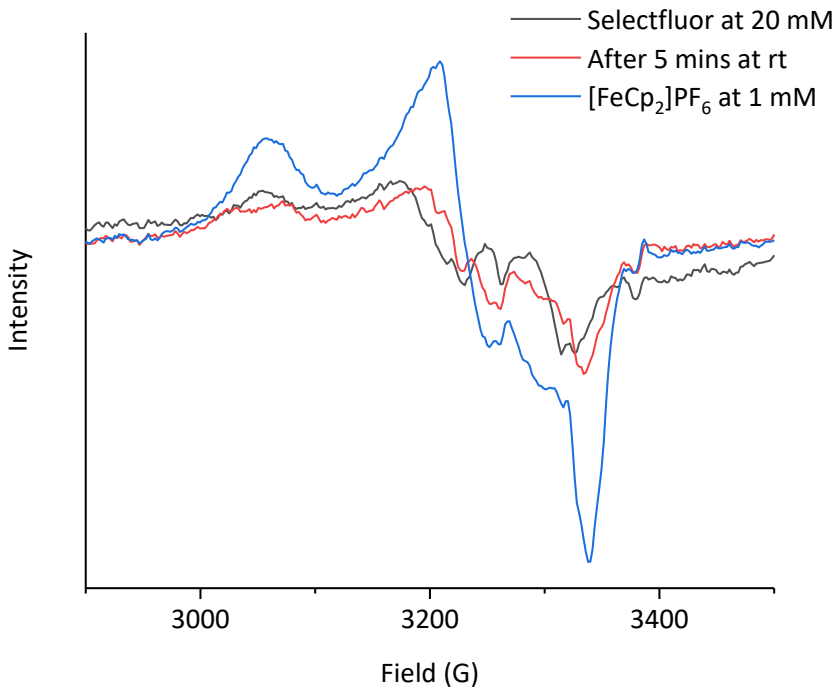

Figure 69: Overlaid EPR spectra from the reaction of [77] with Selectfluor at 20 mM in 1:1 dichloromethane: acetonitrile, immediately after addition (black), and after 5 minutes at room temperature (red). The EPR spectrum of [77]$^{\cdot}PF_6$, generated by addition of ferrocenium hexafluorophosphate is shown in blue.

Future work would entail studying the reaction of the other half-sandwich alkynyl complexes with all three fluorinating agents by UV-Vis and EPR spectroscopy to determine whether alkynyl radicals are also observed and conducting radical trap experiments.

4.6 Reaction of *trans*-[ClRu(dppe)$_2$(C≡CR)] with [FTMP]BF$_4$ and NFSI

Due to the unexpected oxidation, rather than fluorination, of **[57i]** with Selectfluor, the reactions of **[57a-i]** with NFSI and [FTMP]BF$_4$ were investigated to determine if there was any difference in behaviour between the three fluorinating agents. In particular to determine how the different fluorinating agents affect the balance between fluorination and oxidation.

4.6.1 Reaction of [57c] with NFSI

Addition of NFSI to a d^2-dichloromethane solution of **[57c]** resulted in the rapid formation of a blue solution over 5 minutes. In contrast to the reaction of **[57c]** with Selectfluor, there was no evidence of **[58c]**$^+$ by ESI-MS, instead the ESI mass spectrum revealed the presence of the radical cation **[57c]**$^+$ at 1064.1979 m/z. The ^{19}F NMR spectrum did not exhibit the resonance for **[58c]**$^+$, expected at δ -229.6, supporting the mass spectrum. Instead the spectrum displayed unreacted NFSI at δ -38.3 and the appearance of a singlet resonance at δ 65.4 corresponding to the formation of **119**,[311] formed through decomposition of NFSI, presumably by reaction with fluoride.[312] The ^{31}P{^{1}H} NMR spectrum exhibited one weak resonance at δ 35.0 which does not correspond to **[57c]**, **[58c]**NSI, or **[59c]**NSI.

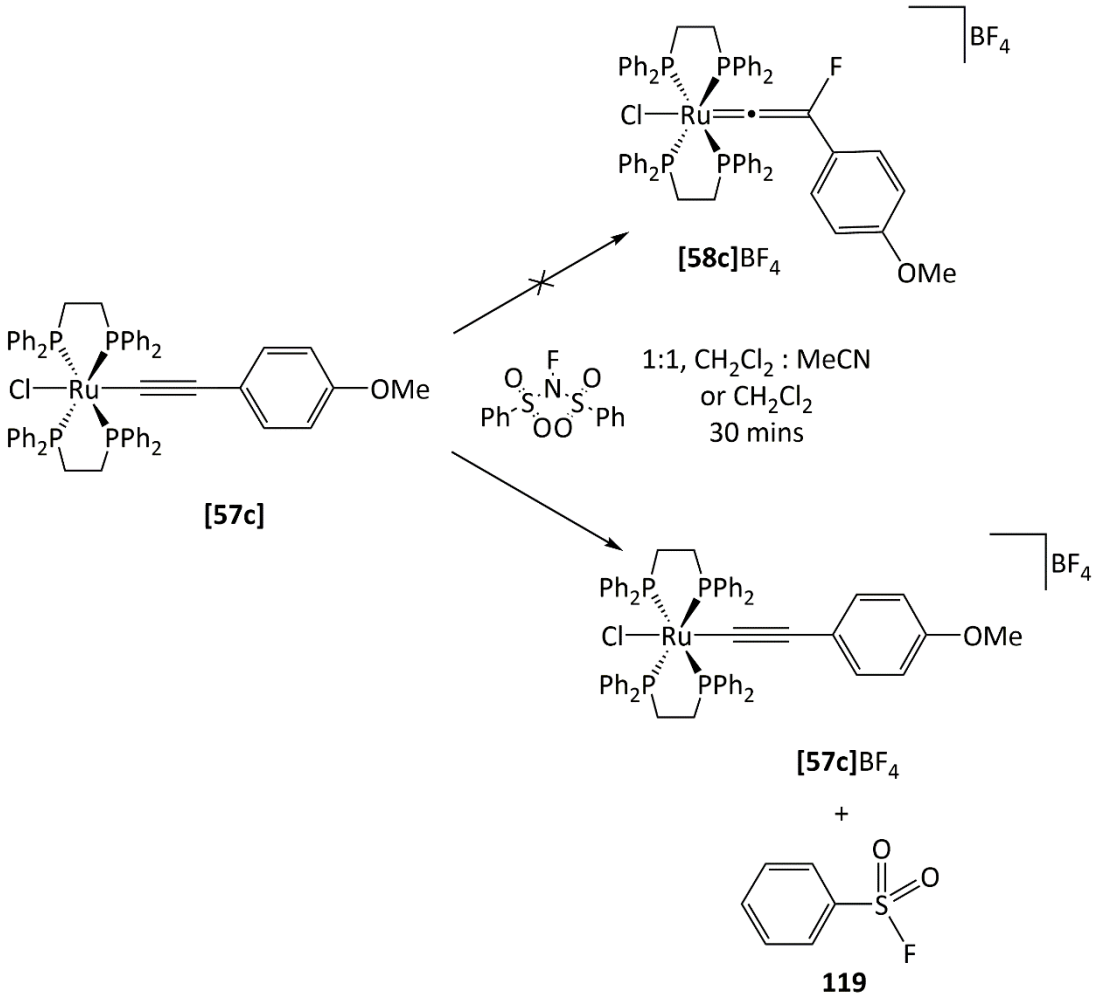

Scheme 181: Addition of NFSI to [57c] did not afford [58c]BF_4 but rather the one-electron oxidised product [57c]$^{\cdot}BF_4$ and decomposition product, 119, among other species.

The ^{1}H NMR spectrum displayed broad resonances in the aromatic region but did not exhibit any resonances for the anisole substituent of **[58c]**$^{+}$ (expected at δ 3.67, 4.72 and 6.36) or protons of the dppe backbone, neither was there any evidence for unreacted **[57c]**. The NMR and ESI-mass spectra reveal that **[57c]** does not undergo fluorination with NFSI but rather undergoes oxidation to form radical species (Scheme 181). This is in stark contrast to the reaction of ruthenium half-sandwich alkynyl complexes which undergo fluorination with NFSI, [FTMP]BF_4, and Selectfluor.

To determine whether the solvent choice was crucial for the observed fluorination with Selectfluor, the reaction was repeated in a 1:1 dichloromethane: acetonitrile solvent mixture. As observed with the reaction in neat dichloromethane, addition of NFSI resulted in the formation of a blue solution over five minutes. The $^{31}P\{^{1}H\}$ NMR spectrum in 1:1 dichloromethane: acetonitrile displayed only a singlet resonance for unreacted **[57c]** at δ 47.6. The ^{19}F NMR spectrum again displayed resonances for unreacted NFSI and a significant

quantity of **119** at δ 65.4. The tetrafluoroborate anion was also observed as a minor product presumably through the reaction of hydrogen fluoride with the siliconborate glass. It is presumed that reduction of NFSI affords hydrogen fluoride as a product through hydrogen abstraction by the putative fluorine radical. There was no evidence for the formation of **[58c]**NSI after addition of NFSI by NMR spectroscopy.

The reaction of **[57c]** with NFSI was monitored by UV-Vis spectroscopy in a 1:1 dichloromethane: acetonitrile solvent mixture (Figure 70). The spectra displayed the appearance of two absorption bands at 579 and 835 nm which correspond to **[57c]**$^{\cdot}$NSI according to the literature. The same absorption bands were also observed when **[57c]**$^{\cdot}BF_4$ was independently generated by addition of ferrocenium hexafluorophosphate to **[57c]**. Instead of acting as a fluorinating agent, NFSI acts an oxidant in the presence of **[57c]**, indicating the choice of solvent does not influence whether fluorination is observed or not.

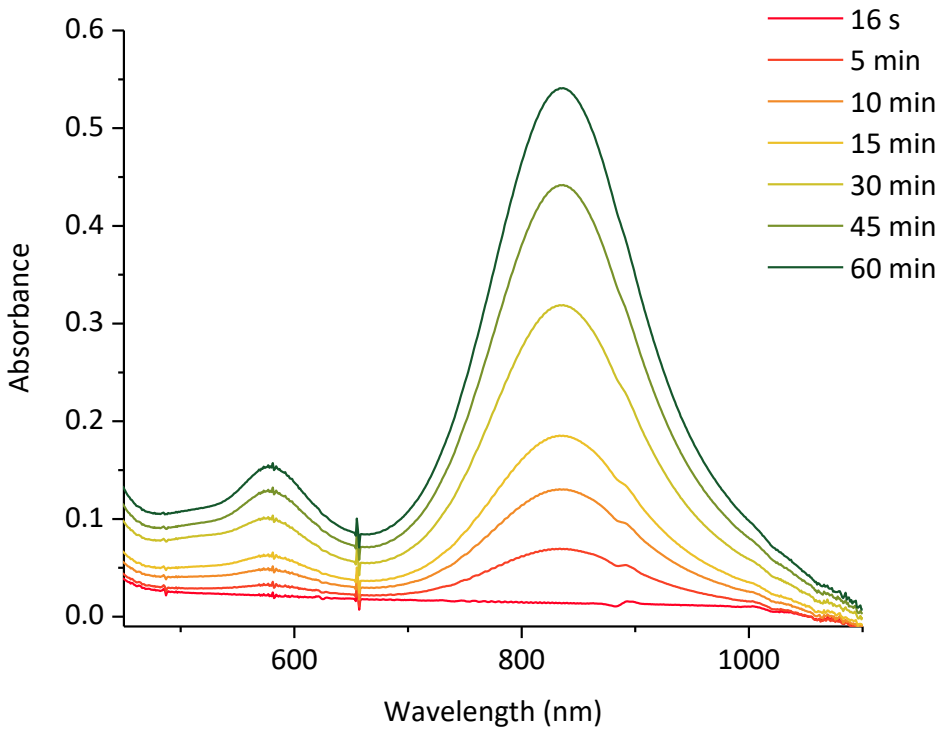

Figure 70: UV-Vis spectra of the reaction of [57c] with NFSI at 0.25 mM in 1:1 dichloromethane: acetonitrile with 1 cm pathlength.

After one week no **[58c]**NSI could be observed in $^{31}P\{^1H\}$ and ^{19}F NMR spectra, instead only further decomposition of NFSI to **119** is observed in the ^{19}F NMR spectrum. The spectrum was dominated by **119** and displayed the appearance of SiF_5^- and increased levels of BF_4^- indicating further formation of hydrogen fluoride and subsequent reaction with the glass.

The $^{31}P\{^{1}H\}$ NMR spectrum was dominated by a species at δ 49.5 which could correspond to the formation **[114c]**$^{+}$ through loss of chloride and coordination of acetonitrile. Such a species was detected by ESI-MS and the phosphorus resonance was observed at a similar chemical shift as **[120]**PF_6 and **[114k]**PF_6.[313, 314] A minor species is observed at δ 49.9 which could correspond to the alkynyl complex with loss of chloride or **[114c]** without acetonitrile coordinated. These species do not correspond to **[57c]** which is observed at δ 47.6 in the 1:1 solvent mix. A minor species is also observed at δ 33.6 whose identity could not be determined but does not correspond to the formation of **[58c]**NSI or **[59c]**NSI.

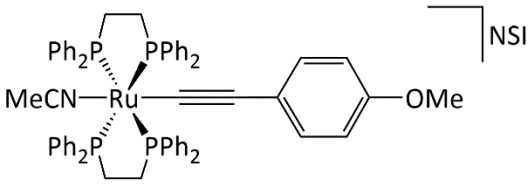

[114c]NSI

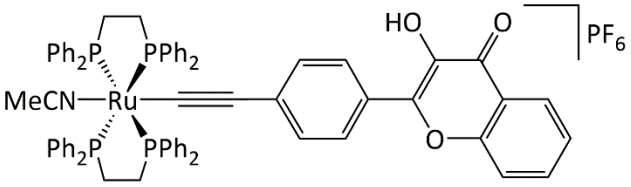

[114k]PF_6

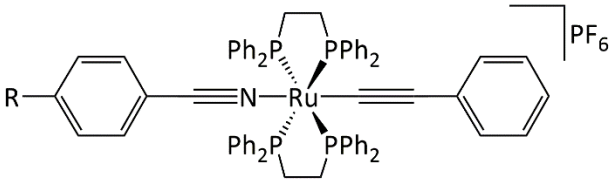

[120]PF_6 **;** **a** = H, **b** = CN

Scheme 182: Loss of chloride and coordination of acetonitrile would afford [114c]NSI. The chemical shift observed is similar to the those reported for [114k]PF_6 and [120]PF_6.

4.6.2 Reaction of [57c] with [FTMP]BF_4

Addition of [FTMP]BF_4 to a d^2-dichloromethane solution of **[57c]** also resulted in the formation of a blue solution after approximately five minutes. The $^{31}P\{^{1}H\}$ NMR spectrum exhibited two small resonances at δ 34.9 and 42.2, neither of which corresponds to the formation of **[58c]**BF_4. The ^{19}F NMR spectrum displayed resonances at δ 17.4 and -153.2 corresponding to unreacted [FTMP]BF_4 in addition to smaller resonances at δ -73.6 and -78.9 corresponding to hexafluorophosphate and triflate anions carried over from synthesis of **[57c]**. A small triplet resonance was observed at δ -219.1 with 48 Hz coupling corresponding

to the formation of **121** through formal loss of H^+ and fluoride migration from [FTMP]BF_4 (Scheme 184).[315] There was no evidence for the formation of **[58c]**BF_4 in either the $^{31}P\{^1H\}$ or ^{19}F NMR spectra (Scheme 183). The ^1H NMR spectrum, as with NFSI, displayed broad signals suggesting the presence of one or more radical species; there was no evidence for the proton resonances for the anisole substituent of **[57c]** or **[58c]**$^+$. The ESI-MS displayed a weak signal for a species with the same m/z as **[58c]**$^+$, however, there is no evidence for **[58c]**$^+$ by NMR spectroscopy. The mass spectrum also displayed signals for species with the m/z of **[57c]**-Cl, **[114c]**$^+$, and **[57c]**+Cl. The presence of **[57c]**+Cl in the mass spectrum could suggest the formation of a chlorinated vinylidene species, however, it is unclear whether this process occurs under the reaction conditions or in the mass spectrometer.

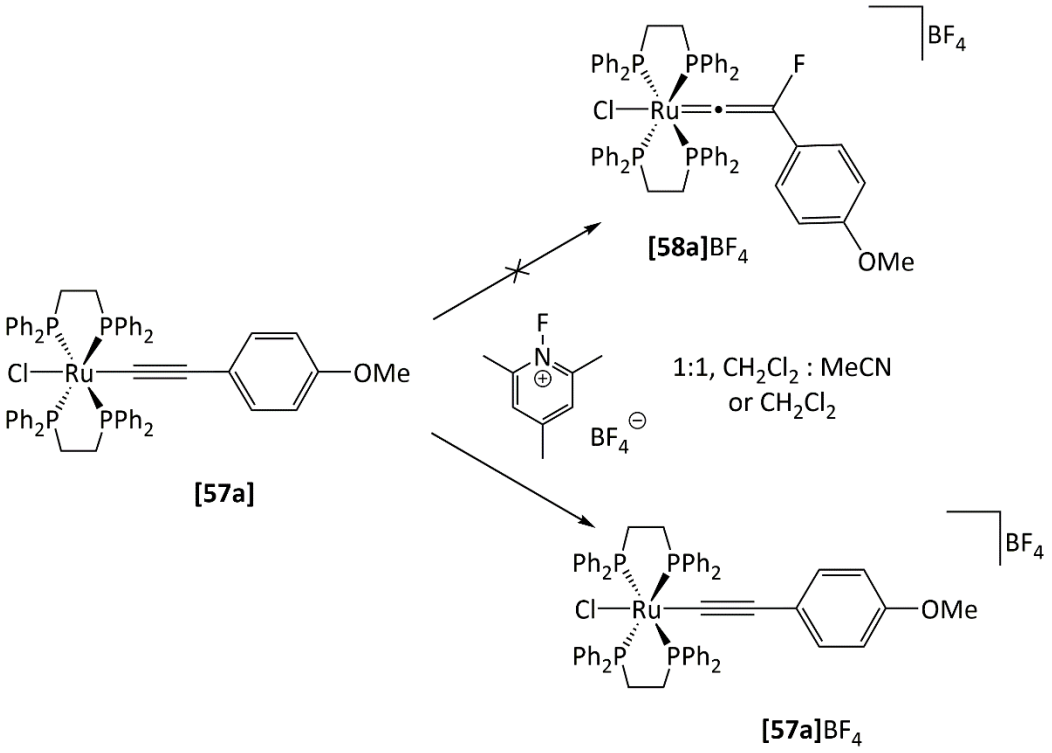

Scheme 183: As with NFSI, addition of [FTMP]BF_4 to [57c] in 1:1 dichloromethane: acetonitrile did not result in fluorination but one-electron oxidation.

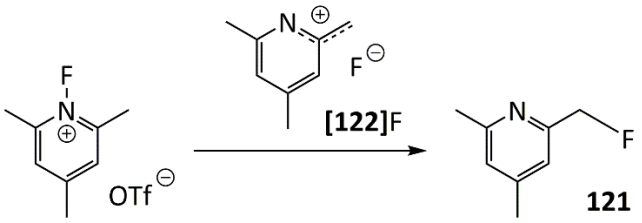

Scheme 184: Umemoto *et al.* observed decomposition of [FTMP]OTf to afford 121 which they proposed proceed *via* tight ion pair [122]F.[315]

The reaction of **[57c]** with [FTMP]BF_4 was repeated in a 1:1 dichloromethane: acetonitrile solvent mixture to again ensure solvent choice does not influence reactivity. Five minutes after addition of [FTMP]BF_4, the yellow solution turned blue as with NFSI. The $^{31}P\{^1H\}$ NMR spectrum in 1:1 dichloromethane: acetonitrile exhibited a weak singlet resonance at δ 49.5 which is believed to correspond to **[114c]**BF_4 as observed in the reaction of **[57c]** with NFSI in the same solvent mixture. The ^{19}F NMR spectrum displayed only the presence for unreacted [FTMP]BF_4 at δ 17.3 and -153.1. In contrast to the ESI mass spectrum of the reaction in d^2-dichloromethane, the mass spectrum in the solvent mixture did not display a species with the m/z of **[58c]**$^+$; instead the mass spectrum was dominated by the species with the m/z of **[114c]**$^+$ and also displayed species with m/z of **[57c]**$^+$, **[57c]**-Cl, **[57c]**+Cl. As with the reaction in dichloromethane, there was no evidence to suggest the formation of **[58c]**$^+$.

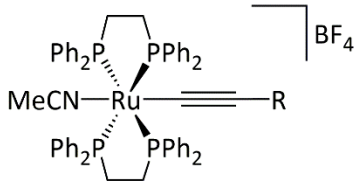

[114]BF_4

a R = H	**f** R = C_6H_4-4-C(O)Me
b R = F	**g** R = C_6H_4-4-CF_3
c R = C_6H_4-4-OMe	**h** R = C_6H_4-4-NO_2
d R = C_6H_5	**i** R = C_6H_4-4-NMe_2
e R = C_6H_4-4-C(O)OMe	**j** R = C_3H_5

After one week there was still no evidence for the formation of **[58c]**BF_4 in either the $^{31}P\{^1H\}$ or ^{19}F NMR spectra. The ^{19}F NMR spectrum displayed the appearance of broad resonances for SiF_5 and **121**, indicating further decomposition of [FTMP]BF_4. The $^{31}P\{^1H\}$ NMR spectrum was dominated by **[114c]**BF_4 at δ 49.5 but also displayed minor species at δ 33.6 and 38.3 which are believed to correspond to decomposition of the radical alkynyl complex, **[57c]**$^{\cdot}BF_4$. Again, the choice of solvent did not influence whether or not fluorination was observed with [FTMP]BF_4.

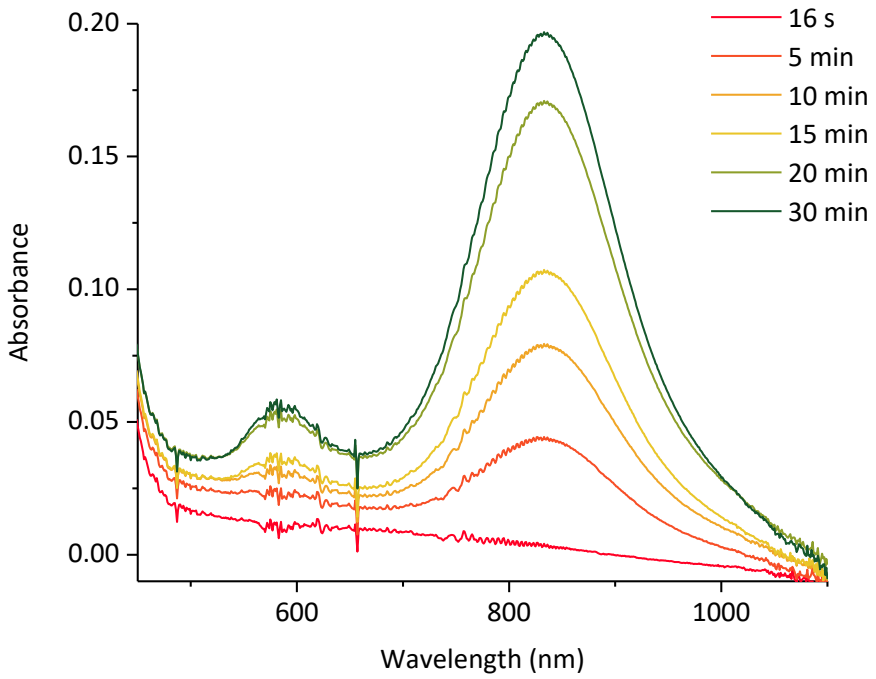

Figure 71: UV-Vis spectra of the reaction of [57c] with [FTMP]BF_4 at 0.25 mM in 1:1 dichloromethane: acetonitrile with 1 cm pathlength.

Monitoring the reaction of **[57c]** with [FTMP]BF_4 by UV-Vis spectroscopy (Figure 71) reveals the growth of two absorption bands at 579 and 835 nm corresponding to the formation of **[57c]**BF_4. The data are indicative that [FTMP]BF_4, like NFSI, acts as an oxidising agent rather than a fluorinating agent, with the species observed by MS and NMR spectroscopy formed through decomposition pathways.

4.6.3 Reactions of [57d] to [57h] with NFSI and [FTMP]BF_4

The reactions of **[57c-h]** with NFSI and [FTMP]BF_4, conducted in a 1:1 dichloromethane: acetonitrile solvent mixture, did not result in the formation of **[58c-h]**$^+$ according to NMR spectroscopy and mass spectrometry. Monitoring the reactions by UV-Vis absorption spectroscopy revealed the growth of low energy absorption bands which did not correspond to the formation of **[58]**$^+$**,** but rather **[57]**$^+$. The data are consistent with **[57c-h]** undergoing one-electron oxidation in the presence of [FTMP]BF_4 and NFSI, rather than fluorination (Scheme 185).

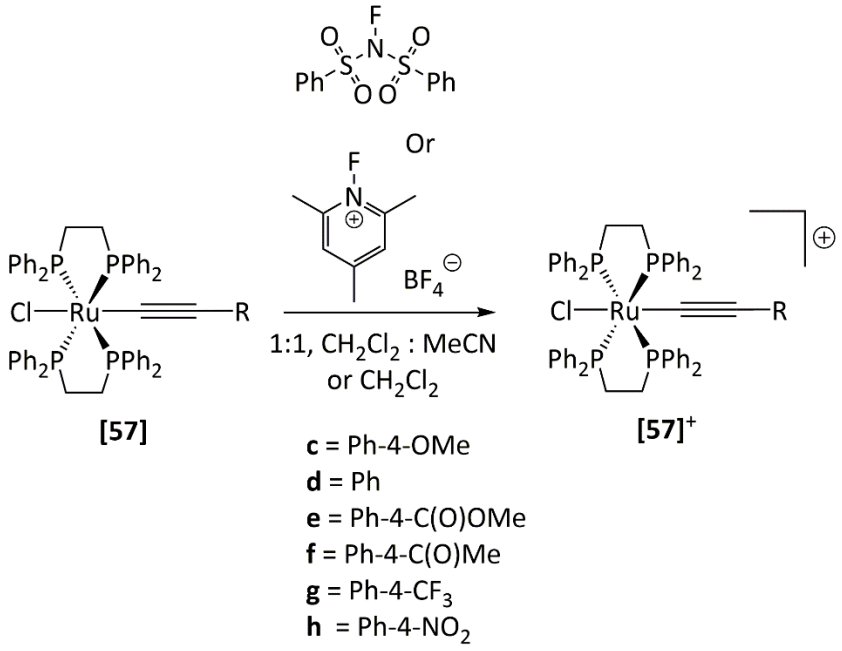

Scheme 185: Addition of either [FTMP]BF_4 or NFSI to [57] resulted in one-electron oxidation to afford [57]$^{\cdot+}$.

Even with the most electron-deficient alkynyl complex, **[57h]**, addition of [FTMP]BF_4 and NFSI still resulted in one-electron oxidation being observed according to UV-Vis spectroscopy. The UV-Vis spectra (Figure 72 and Figure 73) displayed the growth of an absorption band at 855 nm corresponding to **[57h]**BF_4. The data reveal that NFSI and [FTMP]BF_4 are sufficiently powerful to oxidise all complexes of **[57]**.

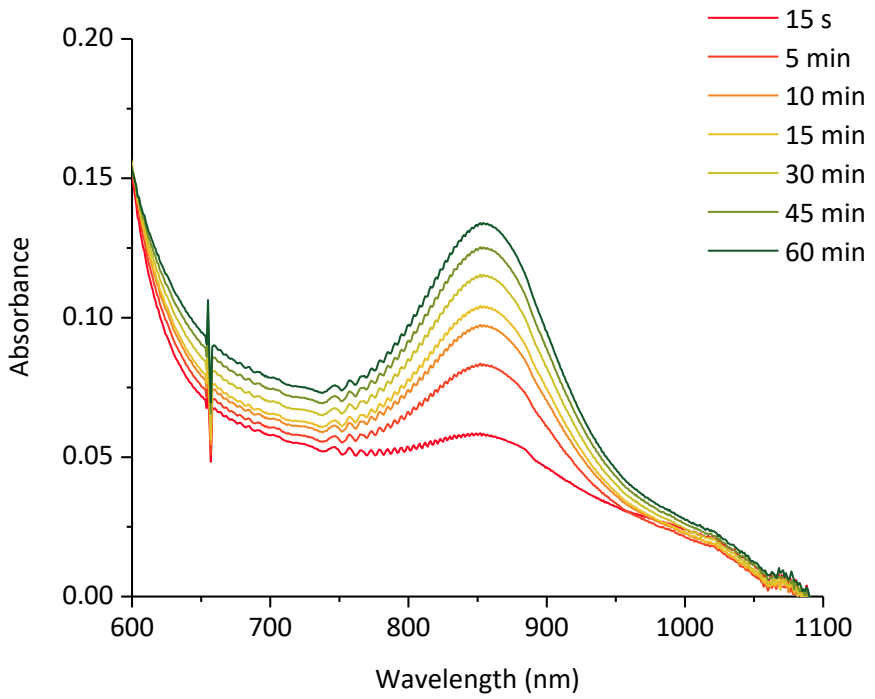

Figure 72: UV-Vis spectra of the reaction of [57h] with NFSI at 0.1 mM in 1:1 dichloromethane: acetonitrile with 1 cm pathlength.

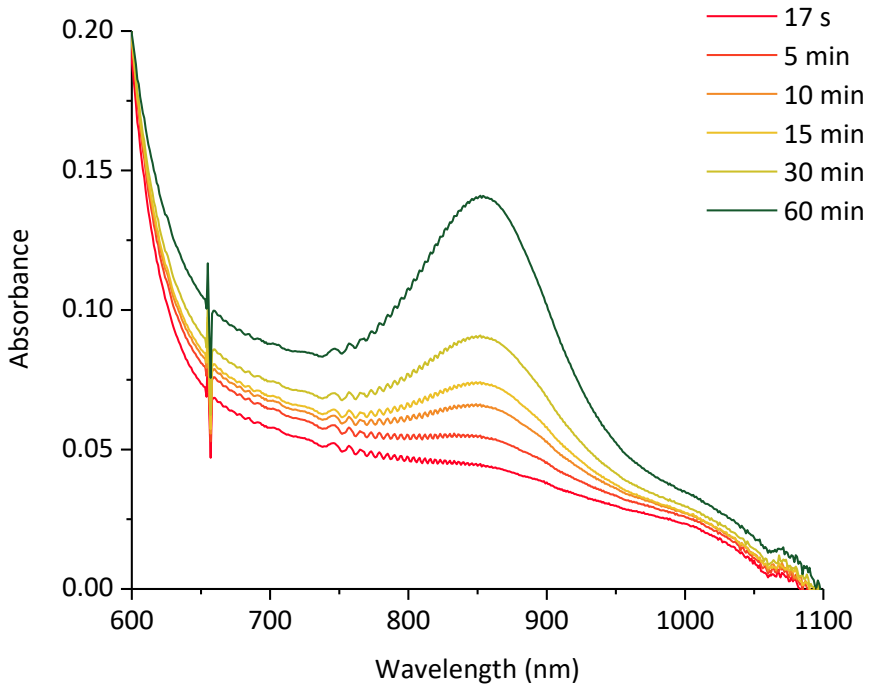

Figure 73: UV-Vis spectra of the reaction of [57h] with [FTMP]BF_4 at 0.25 mM in 1:1 dichloromethane: acetonitrile with 1 cm pathlength.

It was noted that addition of [FTMP]BF_4 and NFSI to **[57e]** resulted in the slow formation of green solutions, as observed upon fluorination of **[57]** with Selectfluor. However, the $^{31}P\{^{1}H\}$ NMR spectrum in 1:1 dichloromethane: acetonitrile displayed only a singlet resonance at δ

48.6 which corresponds to unreacted **[57e]**. There was no evidence for formation **[58e]**$^{+}$ in the $^{31}P\{^{1}H\}$ or ^{19}F NMR spectra. Similarly, the reaction of **[57f]** with [FTMP]BF_4 also afforded a green solution as observed in the reaction Selectfluor but there was again no evidence for **[58f]**BF_4. The observed change in colour arises from the slow oxidation of **[57e]** and **[57f]** to form the radical alkynyl complexes which make the solution green in lower concentrations. In contrast the reaction of **[57f]** with NFSI did not result in any obvious change to the colour of solution after ten minutes. Nevertheless, monitoring the reaction by UV-Vis spectroscopy over one hour resulted in the growth of absorption bands at 602 and 851 nm corresponding to the formation of **[57f]**$^{\cdot+}$ (Figure 74).

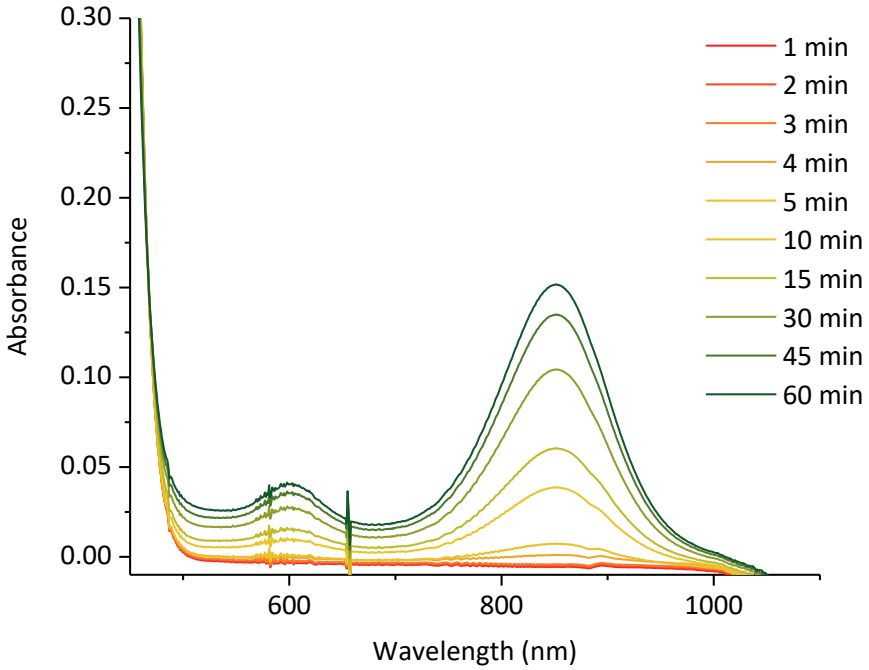

Figure 74: UV-Vis spectra of the reaction of [57f] with NFSI at 0.25 mM in 1:1 dichloromethane: acetonitrile with 1 cm pathlength.

The decay of the radical alkynyl complexes is not, below one hour, observed with NFSI and [FTMP]BF_4 (for example Figure 75), in contrast to the reaction with Selectfluor. However, if the rate of oxidation is slow with NFSI and [FTMP]BF_4, but still faster than decay of the radical alkynyl complexes, then slow growth of the radical alkynyl complexes would be observed in the UV-Vis spectra. This may explain why the decay process is not apparent in the UV-Vis spectra below one hour for the reactions with [FTMP]and NFSI.

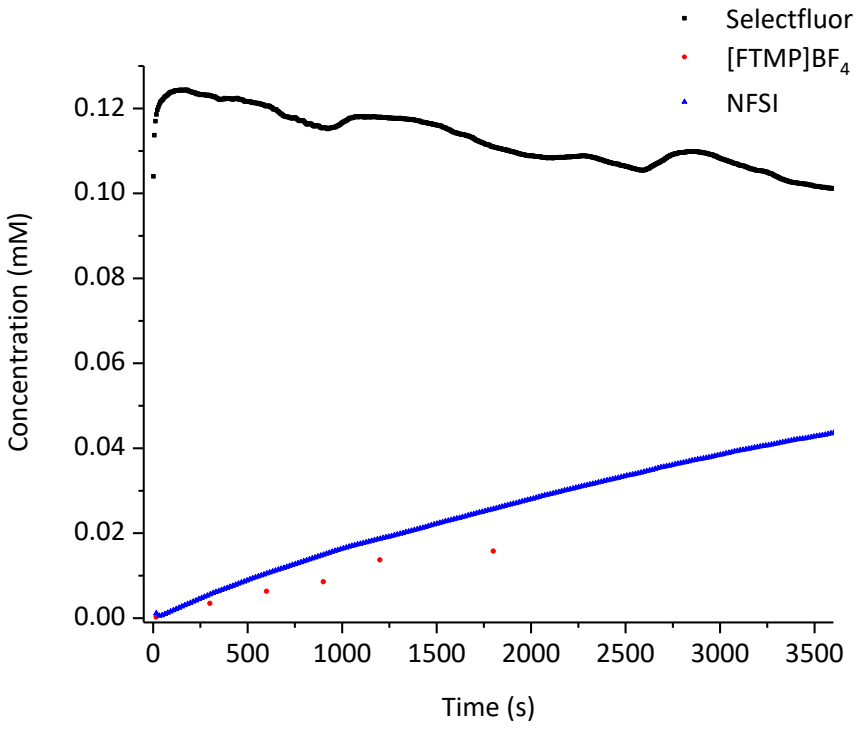

Figure 75: Overlaid time plots for reaction of [57c] with Selectfluor, [FTMP]BF_4, and NFSI at 0.25 mM in 1:1 dichloromethane: acetonitrile.

4.6.4 Observed Rate Constants for Oxidation of [57c-h]

The observed rate constants for oxidation were approximated through fitting the growth of the ruthenium(III) alkynyl complexes to an exponential expression. The concentration of alkynyl radical was approximated from the absorbance of the low energy absorption band around 800 nm on the assumption that the contribution from the fluorovinylidene complex was negligible due to the one or two orders of magnitude difference in molar absorption coefficients (Table 26). It was therefore assumed that the initial change in concentration for **[57]**$^+$ results solely from the oxidation of **[57]** by the fluorinating agent and fitting the initial growth to an exponential equation would provide the observed rate constant for the conversion of **[57]** to **[57]**$^+$. The concentration was fitted to a sequential exponential growth (oxidation) and decay (unknown reaction) equation used in Origin:

$$C = \begin{cases} C_0 + A_d + A_g\left(e^{-k_{obs}.t_c} - e^{-k_{obs}\cdot t}\right) & when\ t \leq t_c \\ C_0 + A_d e^{-k_d\cdot(t-t_c)} & when\ t > t_c \end{cases}$$

Where C is the concentration of **[57]**$^+$, C_0 is the initial concentration, A_g and A_d are the growth and decay amplitudes respectively, k_{obs} is the observed rate constant for growth (oxidation), k_d is the observed rate constant for decay, t_c is the time at which growth and decay are equal, and t is time. The top equation used to fit the exponential growth period while the bottom

equation is used to fit the decay period. Data fitting (to the equations above) was achieved with Origin using the Levenberg Marquardt algorithm. An example of exponential fitting to the oxidation of **[57g]** with Selectfluor in a 1:1 dichloromethane: acetonitrile solution is shown in Figure 76. Where decay was not observed over the course of the experiment (i.e. reactions using [FTMP]BF_4 and NFSI), the data was fitted to an exponential growth equation given by:

$$C = C_0 + Ae^{k_{obs} \cdot t}$$

Where C is the concentration of **[57]**$^+$, C_0 is the initial concentration, A is a constant, k_{obs} is the observed rate constant, and t is time.

Table 26: The observed rate constants for oxidation of [57c-h] by Selectfluor, [FTMP]BF_4, and NFSI.

trans-[ClRu(dppe)$_2$(C≡CR)]	k_{obs} / s^{-1}		
R =	Selectfluor	[FTMP]BF_4	NFSI
[57c] C_6H_4-4-OMe	(7.4 ± 1.0) x 10^{-2}	(4.1 ± 2.7) x 10^{-4}	(2.0 ± 0.3) x 10^{-4}
[57d] C_6H_5	(4.5 ± 0.3) x 10^{-2}	(1.3 ± 0.5) x 10^{-3}	(9.8 ± 2.6) x 10^{-4}
[57e] C_6H_4-4-COOMe	(1.4 ± 0.1) x 10^{-2}	(1.6 ± 0.1) x 10^{-3}	(3.9 ± 3.8) x 10^{-5}
[57f] C_6H_4-4-COMe	(1.1 ± 0.2) x 10^{-2}	(5.7 ± 0.3) x 10^{-4}	(5.4 ± 0.2) x 10^{-4}
[57g] C_6H_4-4-CF_3	(6.8 ± 0.1) x 10^{-3}	(1.5 ± 0.1) x 10^{-3}	(9.2 ± 0.2) x 10^{-4}
[57h] C_6H_4-4-NO_2	(3.4 ± 0.1) x 10^{-3}	(1.2 ± 0.1) x 10^{-3}	(2.0 ± 0.2) x 10^{-3}
[57j] C_3H_5	(1.7 ± 0.3) x 10^{-2}	(3.6 ± 0.3) x 10^{-3}	(2.7 ± 0.3) x 10^{-3}

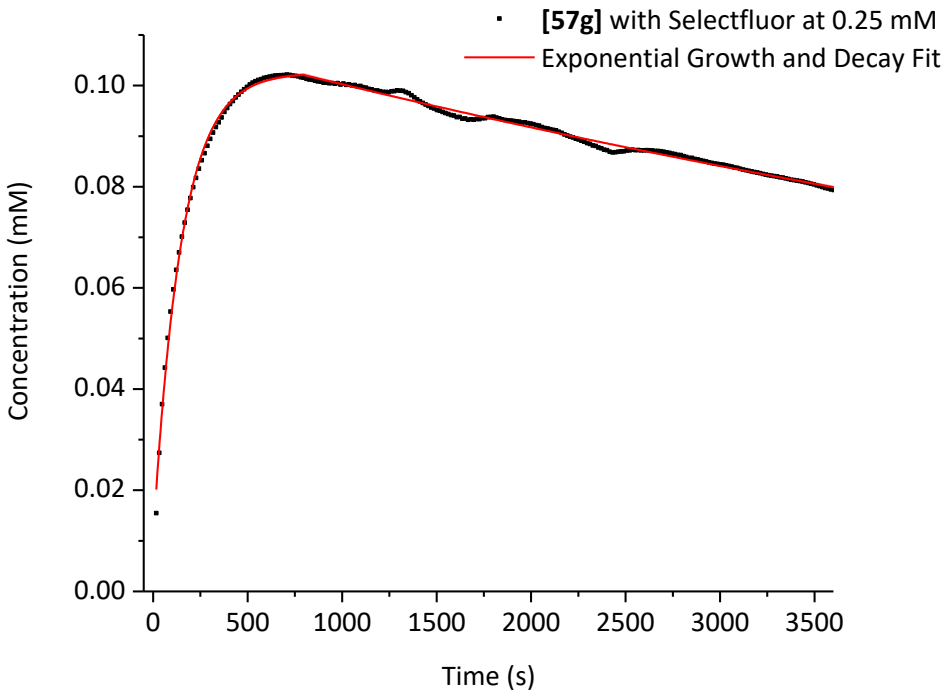

Figure 76: Example exponential fitting for oxidation of [57g] with Selectfluor 1:1 dichloromethane: acetonitrile at 0.25 mM.

The observed rate constants for oxidation of **[57c-h]** by Selectfluor reflect the change in oxidation potential and the electronic nature of the aryl substituent. The most electron-deficient alkynyl complex, **[57h]**, which is the hardest to oxidise at 0.630 V (vs SCE in DCM) had the smallest observed rate constant of (3.4 ± 0.1) x 10^{-3} s^{-1}. While **[57c]** which is more easily oxidised at 0.36 V (vs SCE in DCM)[243] had the largest observed rate constant of (7.4 ± 1.0) x 10^{-2} s^{-1}. The observed rate constants for **[57d]**, **[57e]**, and **[57f]** are statistically identical and can be rationalised by the identical oxidation potentials recorded for both complexes (0.55 V vs SCE in DCM)[243].

In contrast, the observed rate constants for oxidation of **[57c-h]** by NFSI and [FTMP]BF_4 do not appear to display a clear trend with respect to the electronic property of the alkynyl substituent. The difference in rate constants observed with NFSI and [FTMP]BF_4 for the same substituent is not consistent either. A higher observed rate constant was obtained for NFSI with **[57h]**, while a higher observed rate constant was obtained for oxidation of **[57e]** and **[57g]** with [FTMP]BF_4. In contrast, the observed rates constants for oxidation of **[57c]** and **[57f]** by [FTMP]BF_4 and NFSI were within the confidence limits of each other. Nevertheless, the observed rate constants for oxidation of **[57]** with Selectfluor are consistently higher than [FTMP]BF_4 and NFSI, indicating Selectfluor is the stronger oxidant.

4.6.5 Reaction of [57j] with [FTMP]BF_4 and NFSI

The addition of NFSI to **[57j]** in a 1:1 dichloromethane: acetonitrile solution resulted in the formation of a pale orange solution. The ^{19}F NMR spectrum of the reaction mixture did not contain any new fluorine environments and no evidence for **[58j]**NSI or **[118]**NSI was obtained (Scheme 186). The resonance for **[58j]**BF_4 was absent in the $^{31}P\{^1H\}$ NMR spectrum, instead the spectrum was dominated by unreacted **[57j]**. Two triplet resonances were observed as trace components at δ 36.0 and 45.5 with 18 Hz coupling, the identity of these species could not be determined. The ESI-mass spectrum displayed a small signal for a species with an m/z of **[58j]**$^+$ or **[118]**$^+$ but a fluorinated product could not be observed in the NMR spectra; other species detected included **[57j]**-Cl, **[57j]**-Cl+MeCN, and **[57j]** +Cl, one of which could correspond to the minor species in the $^{31}P\{^1H\}$ NMR spectrum.

The addition of [FTMP]BF_4 to **[57j]** in a 1:1 dichloromethane: acetonitrile solution afforded a blue solution within five minutes but again there was no evidence for the formation of **[58j]**BF_4 or any new fluorinated species according to the ESI-MS and ^{19}F NMR spectroscopy. The $^{31}P\{^1H\}$ NMR spectrum was dominated by unreacted **[57j]** and also contained minor species at δ 41.4, 40.4, 36.3, and 33.2 belonging to new organometallic species.

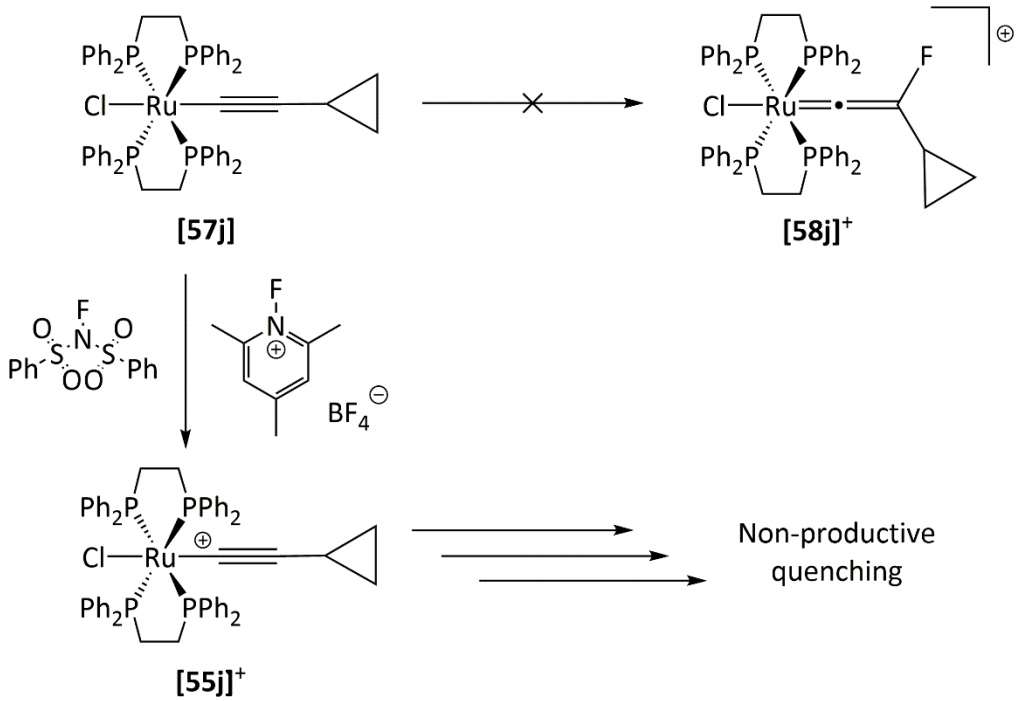

Scheme 186: Reaction of [57j] with NFSI and [FTMP]did not afford any fluorinated products instead oxidation and subsequent non-productive decay was observed.

The UV-Vis spectrum recorded of the radical alkynyl complex of **[57j]**, obtained by oxidation with ferrocenium hexafluorophosphate, displays two low energy absorption bands at 537 and 762 nm, matching the observed spectra obtained initially by addition of [FTMP]BF_4, NFSI, and Selectfluor to **[57j]**. This demonstrated that all three fluorinating agents are capable of oxidising **[57j]** (Figure 77). Fitting the change in absorption at wavelengths 537 and 762 nm with a sequential exponential growth and decay equation using Origin (see section 4.6.4) provides the observed rate constant for the oxidation of **[57j]** to **[57j]**$^+$, along with the observed rate constant for an unknown decay process.

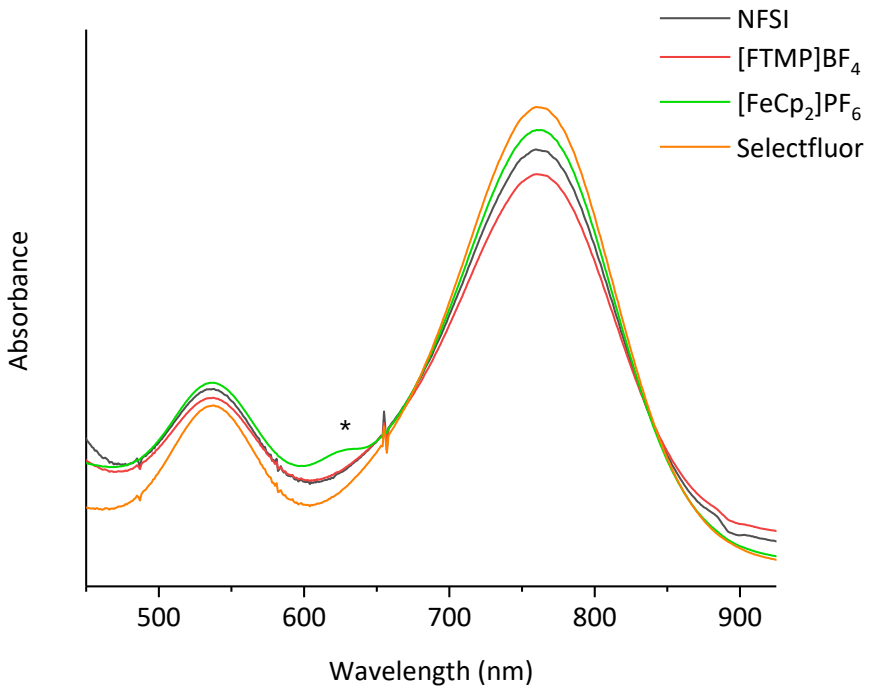

Figure 77: Overlaid UV-Vis spectra obtained by the reaction of [57j] with NFSI, [FTMP]BF_4, Selectfluor, and ferrocenium hexafluorophosphate which have been scaled for clarity. Asterisk denotes ferrocenium hexafluorophosphate.

As with the reactions of **[57]** with Selectfluor, the absorption band for the HOMO → LUMO transition of **[58j]**BF_4 at 757 nm could not be observed directly due to the strong overlapping absorption band for **[57j]**$^+$ at 762 nm (Figure 78). Oxidation of **[57j]** is observed with a rate constant of (1.7 ± 0.3) x 10^{-2} s^{-1} (Figure 79). After four minutes the absorption band at 762 nm for **[57j]**$^+$ begins to decay (k_{obs} = (2.4 ± 0.2) x 10^{-4} s^{-1}) and the band at 537 nm shifts to a higher energy wavelength; it is not known what species **[57j]** converts into.

In contrast, the reaction of **[57j]** with NFSI and [FTMP]BF_4 show markedly different UV-Vis spectra as time progresses. In the reaction with NFSI (Figure 80), the radical alkynyl complex grows in over 15 minutes (k_{obs} = (2.7 ± 0.3) x 10^{-3} s^{-1}) and then decays (k_{obs} = (6.0 ± 0.3) x 10^{-4}

s^{-1}). After 30 minutes a new absorption band at 471 nm grows in with a rate constant of (1.1 ± 0.1) x 10^{-3} s^{-1}. The rate constant for decay of **[57j]**NSI does not match the observed rate constant for growth of the species at 471 nm, suggesting the complexes do not share a common intermediate.

In the reaction of **[57j]** with [FTMP]BF_4 (Figure 82) in a 1:1 dichloromethane: acetonitrile solution, the oxidation of **[57j]** is observed over ten minutes with a rate constant of (3.6 ± 0.1) x 10^{-3} s^{-1} and decays away with an observed rate constant of (9.0 ± 0.8) x 10^{-3} s^{-1}; after ten minutes a new absorption band is observed at 684 nm.

The observed rate constant for oxidation of **[57j]** was greatest in the reaction with Selectfluor, which agrees with Selectfluor being reported as the most oxidising electrophilic fluorinating agent. The observed rate constant is similar in magnitude to those of **[57e]** and **[57f]** (Table 26). The observed rate constant for oxidation of **[57j]** by NFSI (k_{obs} = (2.7 ± 0.3) x 10^{-3} s^{-1}) was smallest out of the three reactions with **[57j]**. The observed rate constants are similar in magnitude to those observed for the reactions of **[57c-h]** with [FTMP]BF_4 and NFSI (Table 26). The observed rate constants for decay of **[57j]**$^+$ are of the same magnitude with any of the three electrophilic fluorinating agents used. The observed rate constant for decay of **[57j]**$^+$ was highest for [FTMP]BF_4 and smallest for Selectfluor.

The UV-Vis spectra indicate that **[57j]**$^+$ and/or products from decay of **[57j]**$^+$ react to form additional species depending on the fluorinating agent used. One or more of the new species observed with NFSI and [FTMP]BF_4 may correspond to a ring-opened species and/or addition of an organic fragment. It is clear that the fluorinating agents, or products from reduction, react differently with **[57j]** and or **[116]**$^+$, with fluorination only being observed with Selectfluor.

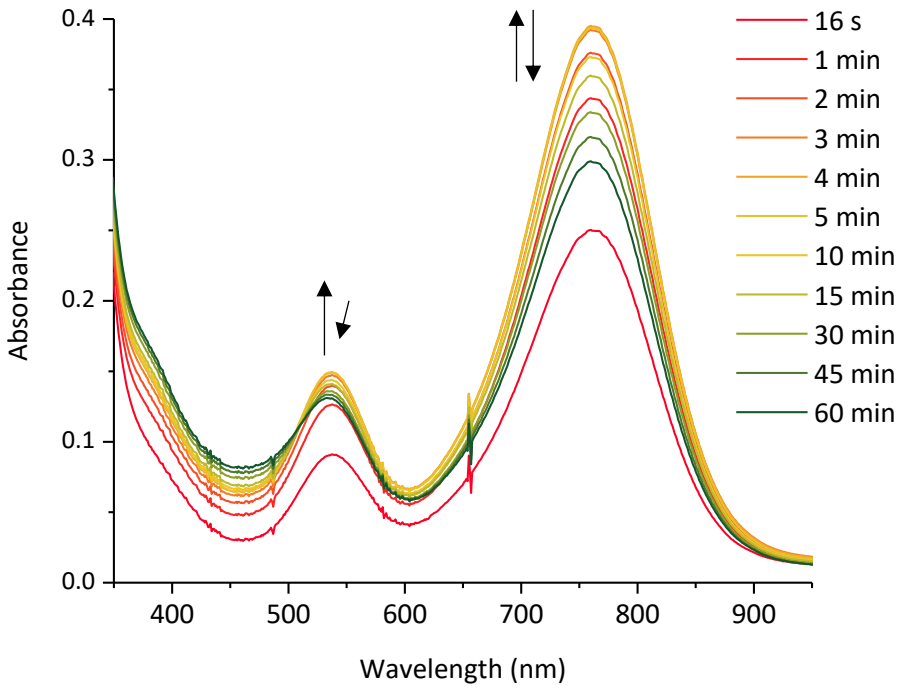

Figure 78: UV-Vis spectra recorded in the reaction of [57j] with Selectfluor at 0.25 mM in 1:1 dichloromethane: acetonitrile.

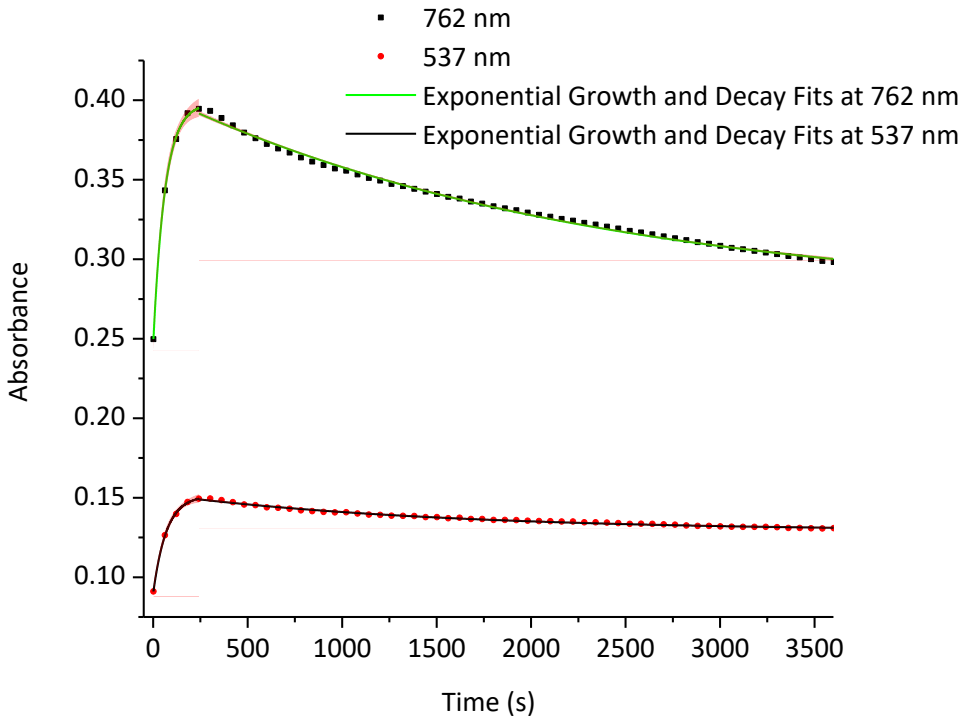

Figure 79: Time plot from the reaction of [57j] with Selectfluor in 1:1 dichloromethane: acetonitrile at 0.25 mM with exponential growth and decay fits shown with 95 % confidence limits.

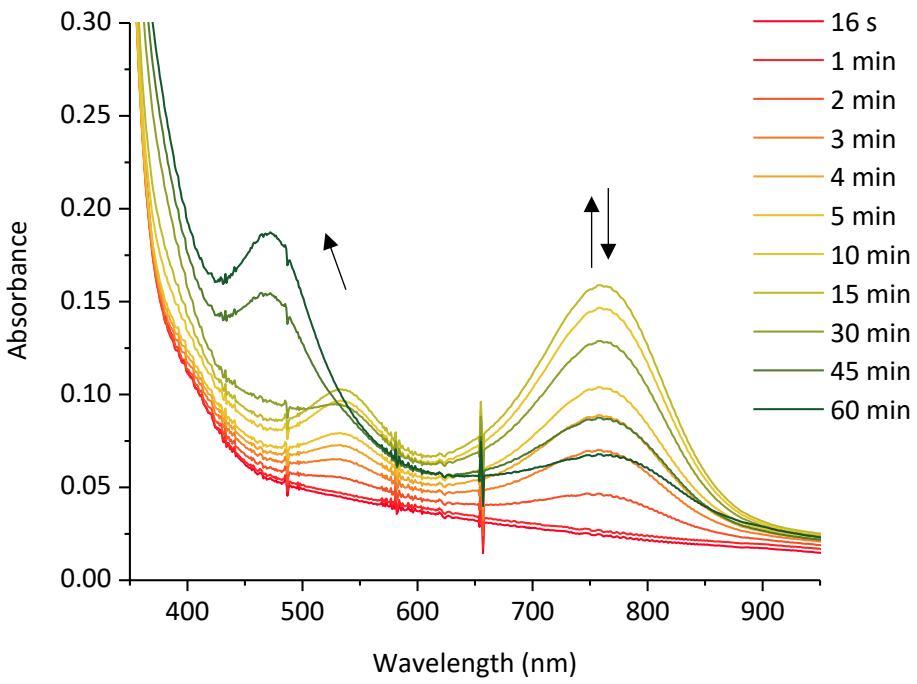

Figure 80: UV-Vis spectra recorded in the reaction of [57j] with NFSI at 0.25 mM in 1:1 dichloromethane: acetonitrile.

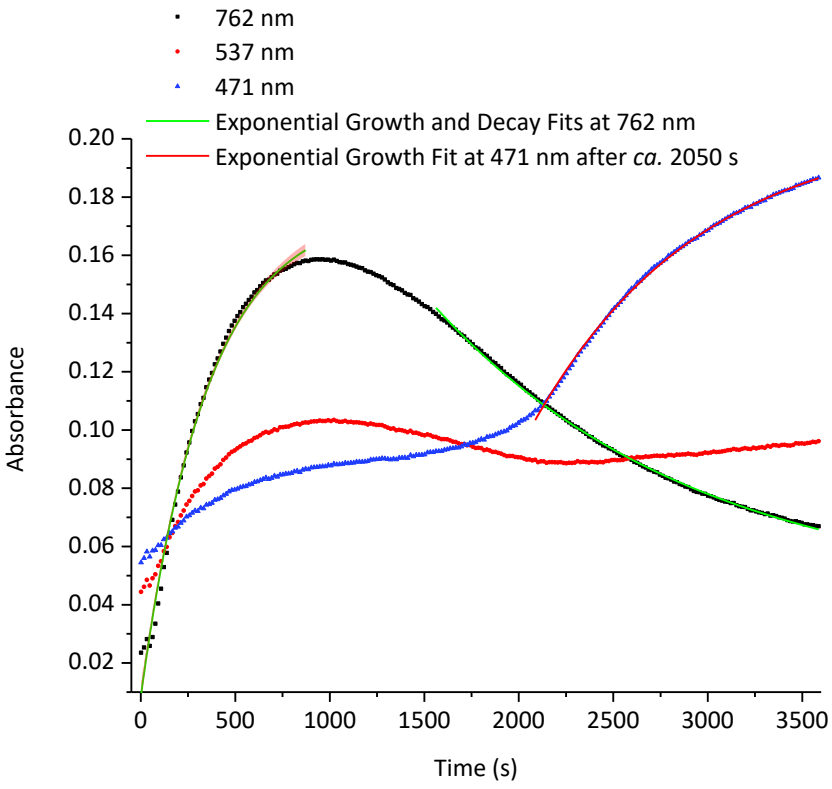

Figure 81: Time plot from the reaction of [57j] with NFSI in 1:1 dichloromethane: acetonitrile at 0.25 mM with exponential growth and decay fits shown with 95 % confidence limits.

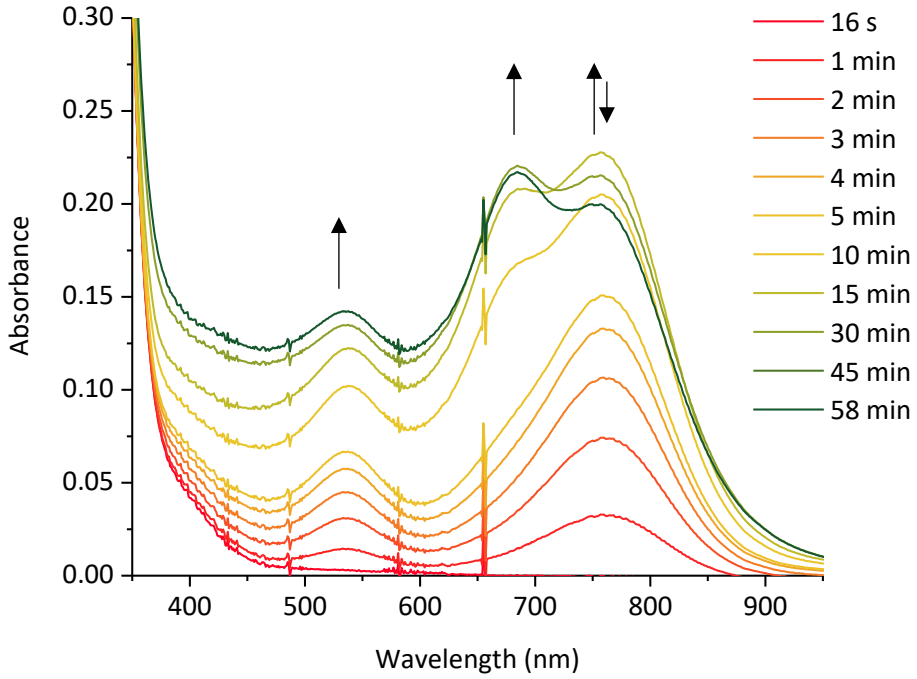

Figure 82: UV-Vis spectra recorded in the reaction of [57j] with [FTMP]BF_4 at 0.25 mM in 1:1 dichloromethane: acetonitrile.

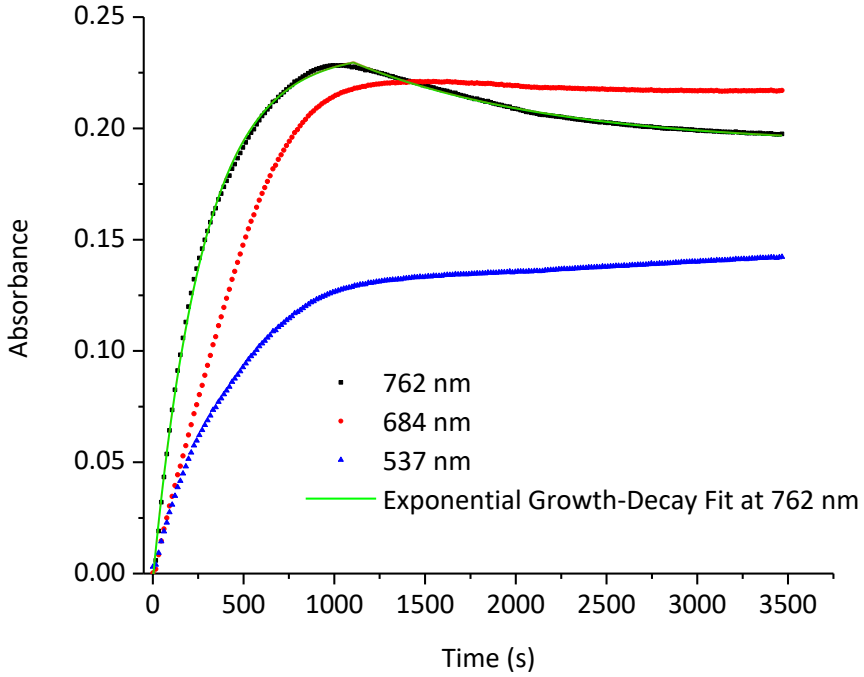

Figure 83: Time plot from the reaction of [57j] with [FTMP]BF_4 in 1:1 dichloromethane: acetonitrile at 0.25 mM with exponential growth-decay fit for [57j]BF_4 at 762 nm shown with 95 % confidence limits.

4.7 Reactions of [57a] and [57b] with NFSI and [FTMP]BF_4

As described in Chapter 2, addition of Selectfluor to **[57a]** and **[57b]** afforded fluorinated vinylidene complexes **[58a]**BF_4 and **[58b]**BF_4 respectively (Scheme 187). Complexes **[57a]** and **[57b]** were also reacted with NFSI and [FTMP]BF_4 in order to determine whether they exhibited the same reactivity as **[57c-h]**.

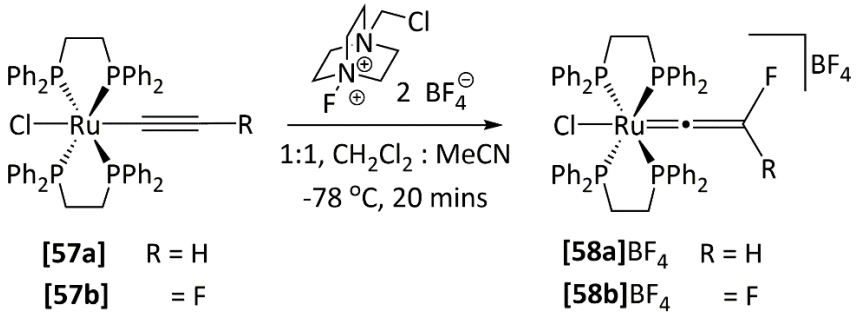

Scheme 187: Fluorination of [57a] and [57b] with Selectfluor afforded fluorovinylidene complexes [58a]BF_4 and [58b]BF_4 respectively.

4.7.1.1 Reaction of [57a] with [FTMP]BF_4

Addition of [FTMP]BF_4 to a d^2-dichloromethane solution of **[57a]** afforded a blue solution within five minutes. Although the ESI-MS detected trace quantities of **[58a]** or a species with the same mass, there was no evidence for the fluorovinylidene complex being formed in the ^1H, ^{19}F, and $^{31}P\{^1H\}$ NMR spectra. Instead the $^{31}P\{^1H\}$ NMR spectrum in dichloromethane-d^2 was dominated by a singlet resonance at δ 41.5 corresponding to the formation of **[59a]**BF_4, revealing protonation is favoured over fluorination (Scheme 188). Minor species were also observed at δ 42.8, 46.8, 50.0, 50.6, of which only unreacted **[57a]** was identified at δ 50.0. The ^1H NMR spectrum was dominated by the proton resonances for **[59a]**BF_4 along with a weak resonance for unreacted **[57a]**. The ^{19}F NMR spectrum displayed only resonances for unreacted [FTMP]BF_4 at δ 17.3 and -152.8, along with significant quantities the decomposition product, **121**, observed as a triplet resonance at δ -219.1 with 48 Hz coupling to hydrogen. Repeating the reaction of **[57a]** with [FTMP]BF_4 in 1:1 dichloromethane: acetonitrile did not result in the formation of **[58a]**BF_4 either, instead protonation was observed to afford **[59a]**BF_4 as in dichloromethane. The $^{31}P\{^1H\}$ NMR also revealed the presence of unreacted starting material at δ 46.4 and a decomposition product at δ 47.1 as minor species.

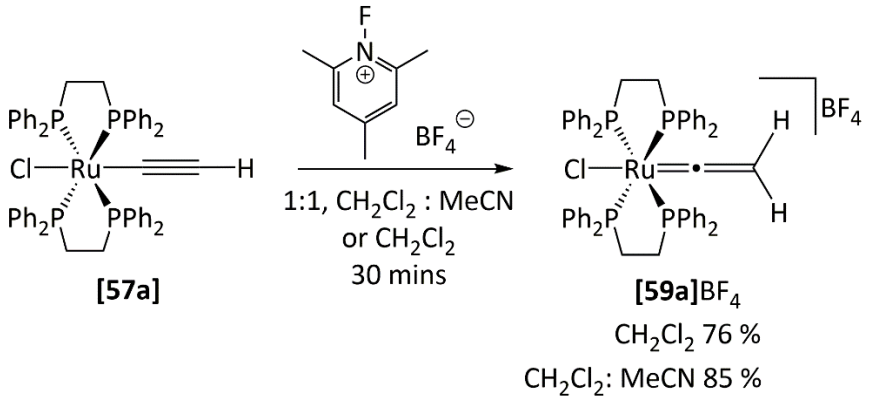

Scheme 188: Addition of [FTMP]BF_4 to [57a] did not afford fluorinated vinylidene [58a]BF_4 but rather [59a]BF_4 as a major product and numerous other minor species.

4.7.1.2 Reaction of [57a] with NFSI

In contrast to the reactivity of **[57c-h]**, addition of NFSI to a d^2-dichloromethane solution of **[57a]** resulted in the formation of the desired fluorovinylidene complex **[58a]**BF_4, along with **[59]**. The $^{31}P\{^1H\}$ NMR spectrum in d^2-dichloromethane was dominated by **[58a]**NSI at δ 41.7 along with a weaker resonance for **[59]**NSI at δ 41.5. Two minor species were also observed at δ 41.6 and 50.7 but could not be identified. The ^{19}F NMR spectrum consisted of unreacted NFSI and its decomposition product, **119**, at δ -37.8 and δ 65.4 respectively, along with the doublet resonance at δ -242.5 for **[58a]**NSI. The formation of **119** indicates the formation of hydrogen fluoride and is supported by the observation of trace quantities of the SiF_5^- anion. The ^1H NMR spectrum was dominated by the resonances for **[58a]**NSI, along with weaker resonances for **[59]**NSI. Integration of the hydrogen substituents of the vinylidene ligand at δ 6.10 (d, $^2J_{HF}$ = 48 Hz) and δ 3.58 (s) for **[58a]**NSI and **[59a]**NSI respectively, reveals a ratio of 1: 0.4 for **[58a]**NSI : **[59a]**NSI (Scheme 189).

Repeating the reaction of **[57a]** with NFSI in 1:1 dichloromethane: acetonitrile also afforded a mixture of **[58a]**NSI and **[59]**NSI. There was a slight increase in the ratio of protonation to fluorination, from 1: 0.4 in dichloromethane, to 1: 0.5 in the solvent mix for **[58a]**NSI: **[59a]**NSI according to the $^{31}P\{^1H\}$ NMR spectrum. In addition to **[59a]**NSI and **[58a]**NSI, the decomposition product observed at δ 47.1 was also observed as a significant product, integrating to approximately 0.8 P with respect to **[58a]**NSI. This same species is observed as a minor product in the reaction of **[57a]** with [FTMP]BF_4 in both solvent systems and in the reaction with NFSI carried out in dichloromethane (δ 50.7). The identity of this species is not known but is believed to be a product from decomposition of the radical alkynyl complex. The ESI-MS displays a species with an m/z of 923.1875 m/z in high intensity which may

correspond to the unknown ruthenium-containing species. However, it is unclear from the mass what this species may correspond to. Other than increased decomposition of the radical alkynyl complex, the choice of solvent was unimportant in determining whether NFSI can fluorinate complex **[57a]**.

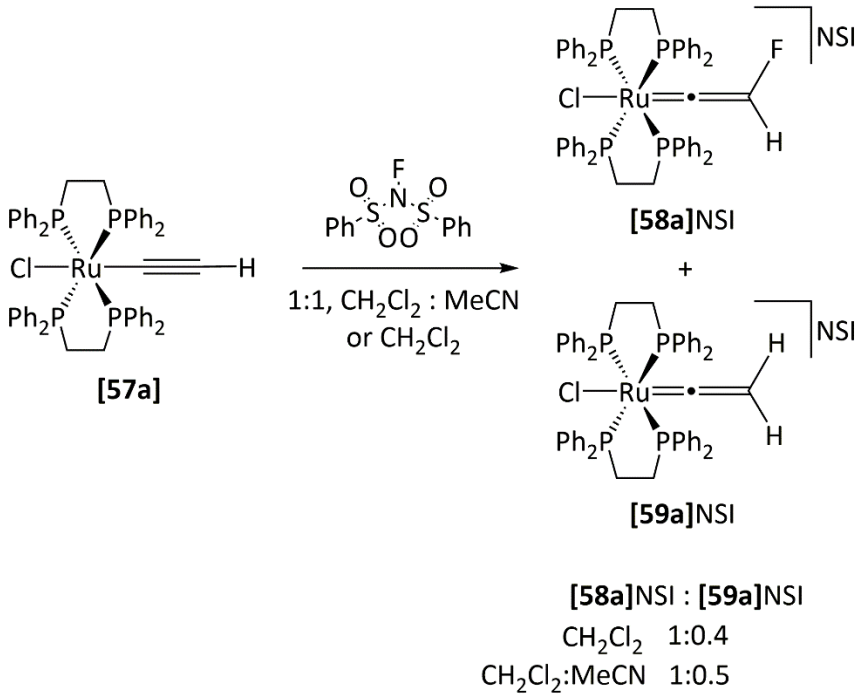

Scheme 189: In contrast to the reaction of [57c-h] with NFSI, [57a] reacts with NFSI to afford [58a]NSI as the major product, along with [59a]NSI as a minor product.

4.7.1.3 Monitoring the reactions of [57a] with Selectfluor, [FTMP]BF_4, and NFSI

The contrasting reactivity between **[57a]** and the three fluorinating agents is reflected in the UV-Vis spectra obtained from monitoring the reactions. Monitoring the reaction of **[59a]** with [FTMP]BF_4 by UV-Vis spectroscopy in 1:1 dichloromethane: acetonitrile resulted in the appearance of absorption bands at 440, 498, 575, 608, 634, 866, and 1021 nm over the course of 30 minutes (Figure 84). The large number of absorption bands suggests the addition of [FTMP]BF_4 results in one-electron oxidation of **[57a]** to afford an unstable radical cation which subsequently undergoes decomposition *via* numerous pathways to afford various products, none of which correspond to **[58a]**BF_4. This is supported by the irreversible electrochemistry observed in the cyclic-voltammograms of **[57a]** (see section 4.10).

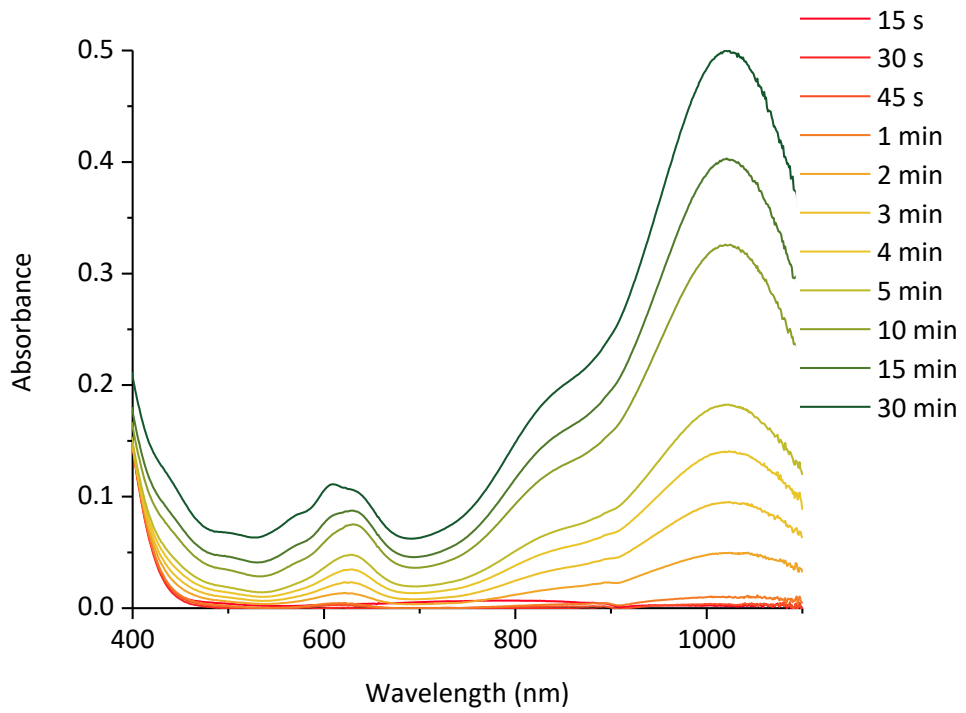

Figure 84: Overlaid UV-Vis spectra of the reaction of [57a] with [FTMP]BF_4 at 0.5 mM in 1:1 dichloromethane: acetonitrile.

The reaction of **[57a]** with NFSI in 1:1 dichloromethane: acetonitrile was monitored by UV-Vis spectroscopy at a concentration of 0.5 mM. The spectra revealed the growth of absorption bands at 614, 836, and 1000 nm over the course of 40 minutes. The spectra from this reaction were related in appearance to those obtained with [FTMP]BF_4 but had undergone a small in shift in wavelength. There was no evidence of the observed species undergoing decay within 30 minutes, suggesting they are not linked to the fluorination pathway, as fluorination was observed within approximately 15 mins of mixing by NMR spectroscopy.

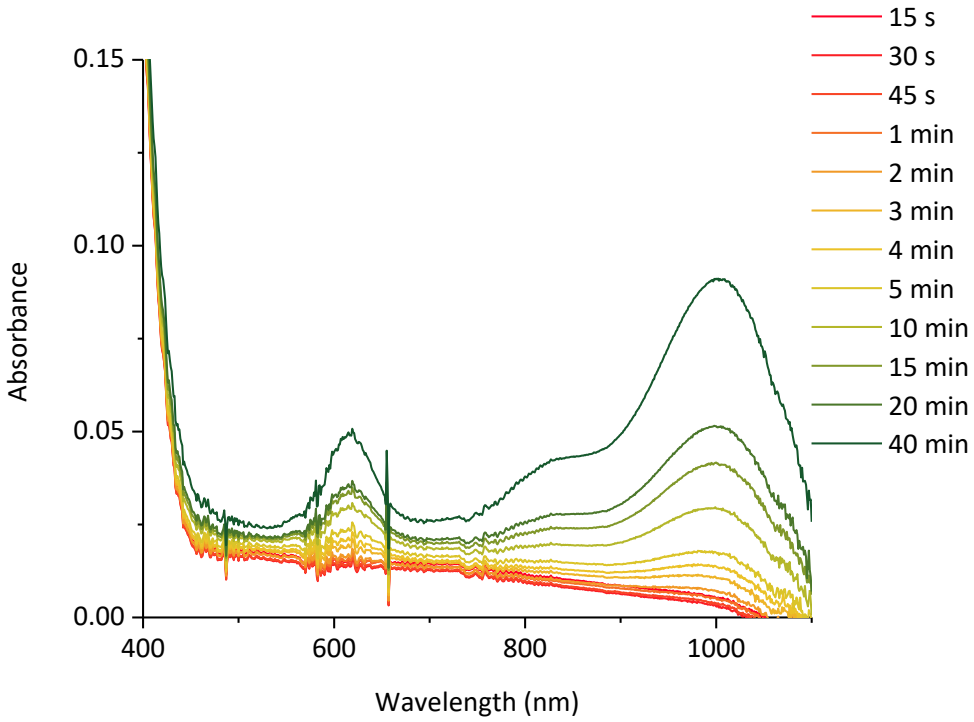

Figure 85: Overlaid UV-Vis spectra of the reaction of [57a] with NFSI at 0.5 mM in 1:1 dichloromethane: acetonitrile.

The UV-Vis spectra obtained from the reaction of **[57a]** with Selectfluor at a concentration of 0.5 mM in 1:1 dichloromethane: acetonitrile appears significantly different to the spectra obtained with NFSI and [FTMP]BF_4. The spectra display rapid growth of an absorption band at 612 nm over 45 seconds, which decays away with time (Figure 86). There is concurrent growth of new absorption bands at 446, 721 and 891 which mirrors the decay of the band at 612 nm, suggesting the latter is an intermediate. Although the identities of the species observed at 446, 612, 721, and 891 nm remain unknown, they are not due to **[58a]**BF_4. The absorption bands are unique to the reaction of **[57a]** with Selectfluor and not observed in the reactions of **[57a]** with [FTMP]BF_4 or NFSI.

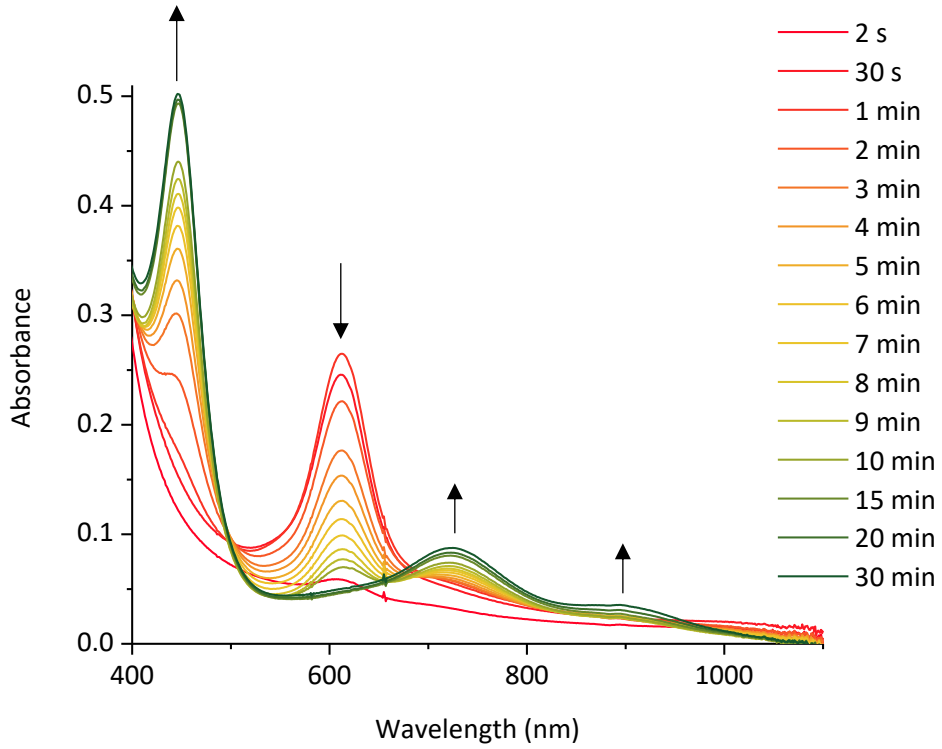

Figure 86: Overlaid UV-Vis spectra of the reaction of [57a] with Selectfluor at 0.5 mM in 1:1 dichloromethane: acetonitrile over ten minutes.

Attempts to obtain the UV-Vis spectrum of **[57a]**$^+$ by chemical oxidation, or by electrochemical oxidation in an OTTLE cell, resulted in the observation of different absorption bands (Figure 87). The observation of different absorption bands in UV-Vis spectra with addition of different fluorinating agents or oxidants reflects the high reactivity of **[57a]**$^+$ and can be rationalised by the irreversible nature of oxidation (see section 4.10).

The addition of ferrocenium hexafluorophosphate to a 1:1 dichloromethane solution of **[57a]** resulted in the growth of absorption bands at 1030, 863, and 576 nm in the UV-Vis spectrum (blue line in Figure 87). The UV-Vis spectrum was similar in appearance to the UV-Vis spectra obtained by the reaction of **[57a]** with [FTMP]BF_4 or NFSI, which could suggest the same or a similar species is observed in all three cases. The addition of thianthrenium tetrafluoroborate, **[113]**BF_4, to a 1:1 dichloromethane: acetonitrile solution of **[57a]**, resulted in the appearance of absorption bands at 1008 and 730 nm. The spectrum obtained by the reaction of **[57a]** with **[113]**BF_4 is believed to display the same species observed in the reaction of **[57a]** with [FTMP]BF_4 and NFSI. The additional band at 730 nm could correspond to further oxidation due to the disappearance of the absorption band at 1008 nm and growth of the absorption band at 730 nm with addition of excess **[113]**BF_4 to **[57a]** (red line in Figure 87). Similarly, the application of a 1.1 V potential to a 1:1 dichloromethane: acetonitrile

solution of **[57a]** in an OTTLE cell, resulted in the appearance of bands at 1008, 745 and 710 nm in the UV-Vis spectrum. Application of a 1.7 V potential resulted in the disappearance of the band at 1008 nm and growth of the bands at 710 and 745 nm.

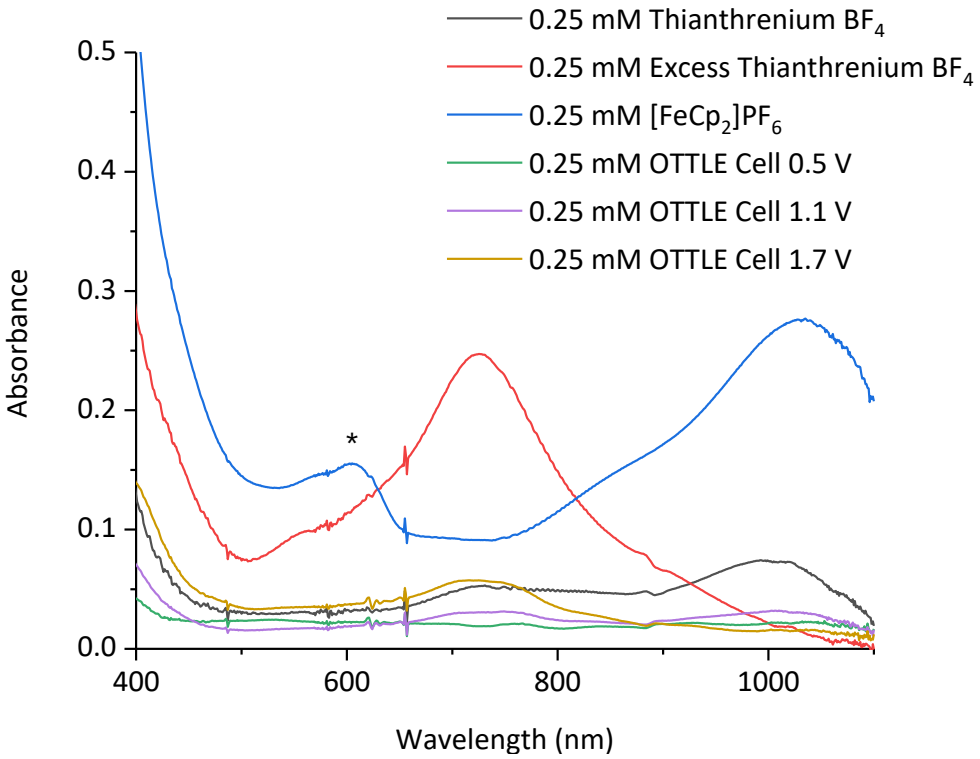

Figure 87: UV-Vis spectra obtained by chemical and electrochemical oxidation of [57a] at 0.25 mM in 1:1 dichloromethane: acetonitrile. Asterisk denotes band for ferrocenium hexafluorophosphate.

The species observed in the UV-Vis spectra obtained from the reaction of **[57a]** with [FTMP]BF_4, NFSI, and ferrocenium hexafluorophosphate is not believed to be **[57a]**BF_4 on the basis of the irreversible cyclic-voltammogram.

It has been shown that hydrogen-substituted metal alkynyl complexes can undergo dimerisation upon oxidation to form bridged vinylidene complexes and subsequently butadiyndiyl bridged complexes (e.g. **[124]**) upon deprotonation (where M = Ru,[241, 316] Fe,[316-318] Mo,[319] Os[320] and Re[321, 322]). The oxidised dimeric complexes are reported to show characteristic absorption bands in the region of 800-1000 nm.[241, 316, 323] Although, the corresponding *bis*-dppe dimeric complex **[123]** has not been reported, an analogous C_{12} bridged complex **[125]** was obtained by oxidation and deprotonation.[245] It is possible the species observed in the UV-Vis spectra obtained from the oxidation of **[57a]** with [FTMP]BF_4 or NFSI corresponds to **[123]**$^+$, which forms through radical dimerisation, deprotonation by **[57a]**$^+$, and oxidation by unreacted fluorinating agent. However, the ESI-MS did not detect such a species.

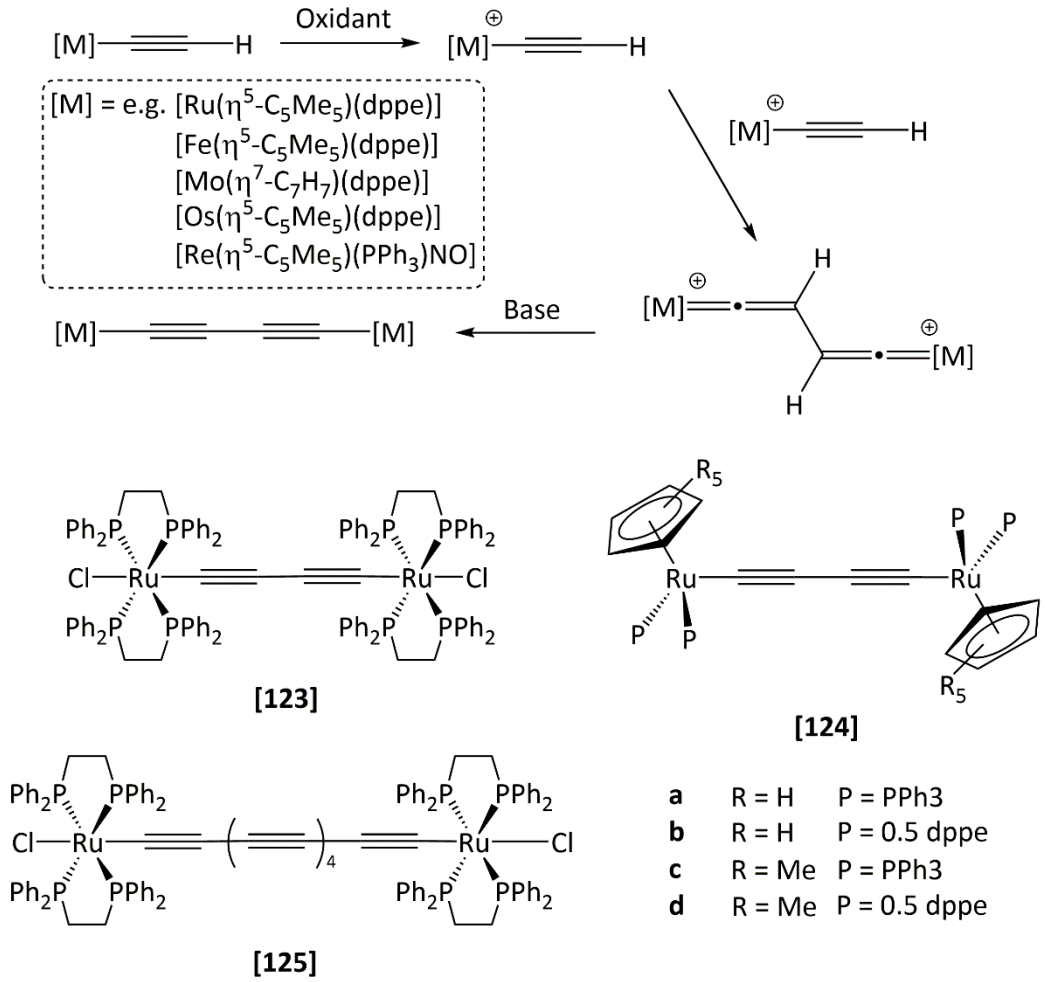

Figure 88: Metal protio-substituted alkynyl complexes are reported to form butadiyndiyl complexes (e.g. [124])[241, 316, 324, 325] through oxidation, radical combination, and deprotonation.[241] Complex [123] is analogous product which may form from oxidation-dimerisation of [57a].

4.7.2 Reaction of [57b] with [FTMP]BF_4 and [FTMP]BF_4

4.7.2.1 Reaction of [57b] with [FTMP]BF_4

The reaction of **[57b]** with [FTMP]BF_4 in a d^2-dichloromethane did not result in any noticeable change in the colour of solution, in contrast to the reactions of **[57a]** and **[57c-h]** which typically displayed a clear change in colour. The ESI-mass spectrum was dominated by a species with the mass of **[58a]**$^+$ with weak signals for species with m/z of **[58b]**$^+$ and **[59a]**$^+$. The $^{31}P\{^1H\}$ NMR spectrum was dominated by **[58a]**BF_4 at δ 41.8 revealing protonation is the favoured outcome of the reaction. However, despite the detection of a species with the m/z of **[58b]**BF_4 there was no observation of the phosphorus resonance for **[58b]**BF_4 (Scheme 190). Likewise, there was no evidence for the formation of **[58b]**BF_4 in the ^{19}F NMR spectrum. Instead the ^{19}F NMR spectrum exhibited resonances for unreacted [FTMP]BF_4, **121**, and

[58a]BF_4 along with small quantities of SiF_5^- through the reaction of the glass with hydrogen fluoride. The ^1H NMR spectrum was dominated by the resonances for **[58a]**BF_4 with no evidence for **[58b]**BF_4.

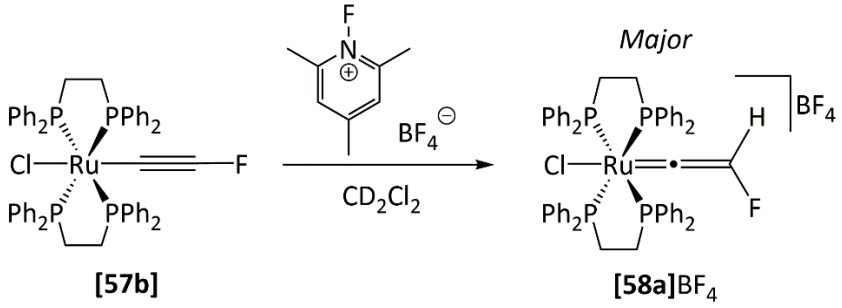

Scheme 190: Addition of [FTMP]BF_4 to [57b] resulted in protonation to afford [58a]BF_4 as the major product.

4.7.2.2 Reaction of [57b] with NFSI

The addition of NFSI to a d^2-dichloromethane solution of **[57b]** did not result in an obvious colour change. However, fluorination was observed by ESI-MS and NMR spectroscopy. In contrast to the reaction of **[57a]** with NFSI, the protonated product, **[58a]**NSI, was only observed as a trace product. The $^{31}P\{^1H\}$ NMR spectrum recorded approximately 15 minutes after addition of NFSI was dominated by **[58b]**NSI along with unreacted **[57b]** as a minor product. Integration of the dppe backbone protons in the ^1H NMR spectrum revealed that **[58b]**NSI and **[57b]** are present in a ratio of approximately 2:1. The presence of unreacted NFSI in the ^{19}F NMR spectrum suggests that **[57b]** reacts slower than **[57a]** with NFSI. The observation of **119** again indicates that hydrogen fluoride is being produced and supported by the appearance of BF_4^- in the ^{19}F NMR spectrum.

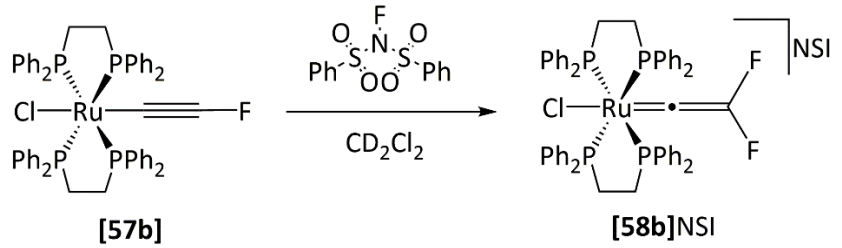

Scheme 191: Addition of NFSI to a d^2-dichloromethane solution of [57b] afforded [58b]NSI with [58a]NSI being observed as a trace component of the reaction mixture.

4.7.2.3 UV-Vis Spectra Obtained from the Reactions of [57b] with Selectfluor, [FTMP]BF_4 and NFSI

The UV-Vis spectra recorded after addition of Selectfluor, [FTMP]BF_4, and NFSI to **[57b]** in 1:1 dichloromethane: acetonitrile solution displayed different absorption bands depending on the fluorinating agent used. The UV-Vis spectra of **[57b]** with NFSI and [FTMP]BF_4 both displayed a weak low energy absorption band at 1001 nm and a higher energy absorption band at *ca.* 529 nm which were not observable after addition of Selectfluor. An absorption band at 695 nm was common with addition of Selectfluor or [FTMP]BF_4 and an absorption band at 840 nm observable after addition of NFSI and Selectfluor. The latter band at 840 nm may correspond to the formation of **[58b]**BF_4. It is unclear which, if any, of the absorption band(s) corresponds to the ruthenium(III) radical cation of **[57b]**. However, it is clear that the radical cation of **[57b]** is unstable and reactive due the irreversible oxidation observed by cyclic-voltammetry (see section 4.10) and is supported by the observation of multiple new species by UV-Vis spectroscopy (Figure 89).

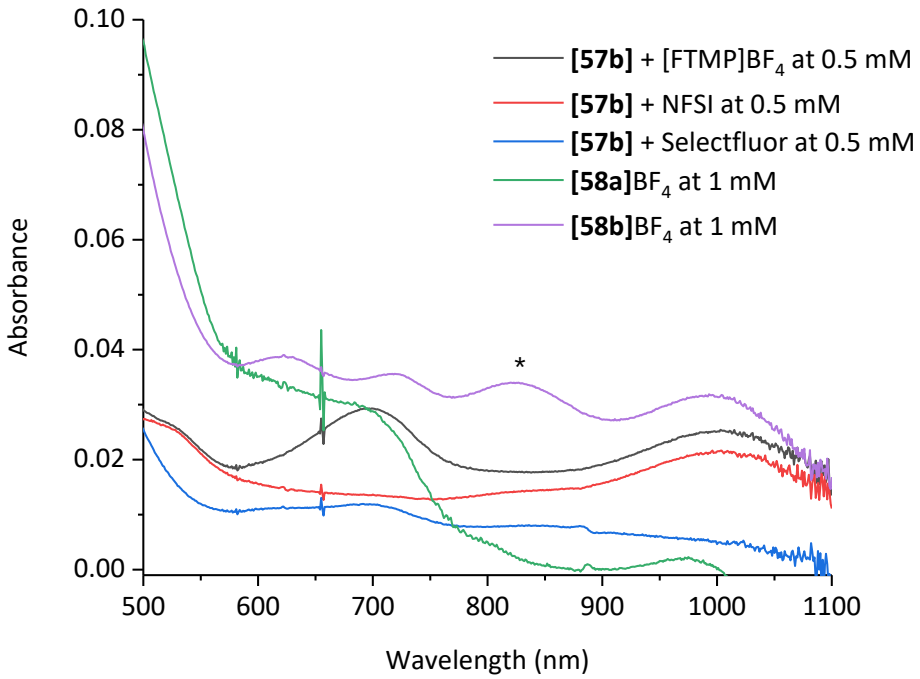

Figure 89: Overlaid UV-Vis spectra of [57b] after addition of [FTMP]BF_4, NFSI and Selectfluor at 0.5 mM in 1:1 dichloromethane: acetonitrile and [58a]BF_4 and [58b]BF_4 at 1 mM in dichloromethane with 1 cm pathlength. Asterisk denotes the absorption band for the HOMO→LUMO transition of [58b]BF_4.

4.8 Reaction of [57a] with NFSI in the presence of TEMPO and BHT

As a consequence of fluorination being observed in the reaction of **[57a]** with NFSI, the reaction was probed with radical traps, TEMPO and BHT, to determine whether there is any difference in the reactivity compared to the reaction with radical traps or the reaction of **[57a]** with Selectfluor.

In contrast to the reaction between **[57a]** and Selectfluor with TEMPO, near complete inhibition of the fluorination pathway was observed in the reaction of NFSI with **[57a]** in the presence of three equivalents of TEMPO in d^2-dichloromethane (Scheme 192). Instead of affording a mixture of **[58a]**BF_4 and **[59]**BF_4, the $^{31}P\{^1H\}$ NMR spectrum was complex, with a new organometallic species dominating the spectrum at δ 46.5, along with a minor species at δ 50.7 corresponding to a decomposition product observed in the absence of TEMPO. The new species observed at δ 46.5 does not correspond to the reaction of TEMPO with **[57a]** or **[58a]**NSI and is not observed in the reaction with Selectfluor; this could indicate the species is related to the inhibition of fluorination by TEMPO. Due to the irreversibility of one electron oxidation of **[57a]**, the species observed may be a product from decay of the alkynyl radical. However, the species is not observed in the absence of TEMPO and the ESI-MS indicates that it does not correspond to a TEMPO adduct. There was also no evidence for unreacted **[57a]** in the ^1H and $^{31}P\{^1H\}$ NMR spectra, suggesting all the starting material has undergone a reaction with NFSI and/or the products from the reaction of NFSI with TEMPO. Additional trace resonances were observed in $^{31}P\{^1H\}$ NMR spectrum at δ 49.1, 48.9, 47.8, 47.6, 41.8, and 41.7, with the resonance at 41.8 corresponding to **[58a]**NSI. The ^{19}F NMR spectrum exhibited resonances for unreacted NFSI, **119**, and a weak resonance for **[58a]**BF_4. Two minor resonances, observed at 26.7, and -97.4, could not be identified. The ^1H NMR spectrum displayed numerous resonances corresponding to different dppe backbone environments; the vinylidene proton of **[58a]**BF_4 was observable as a trace component of the spectrum. The control experiments reveal that TEMPO reacts slowly with NFSI to afford **119**, but unreacted NFSI was still observed after approximately 15 minutes. Again, there was no observation of unreacted **[57a]** in the ^1H and $^{31}P\{^1H\}$ NMR spectra, suggesting TEMPO is disrupting the fluorination of **[57a]** by NFSI.

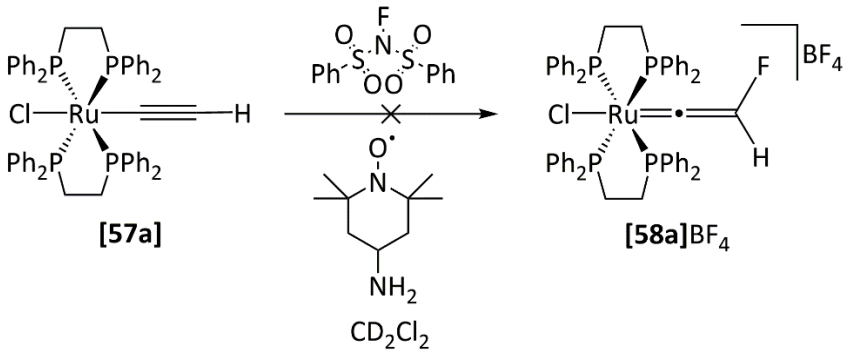

Scheme 192: Reaction of [57a] with NFSI in the presence of TEMPO was found to inhibit fluorination.

Repeating the reaction of NFSI with **[57a]** in the presence three equivalents of BHT did not completely inhibit fluorination, instead suppression of fluorination was observed in the ratio of **[58a]**NSI and **[59a]**NSI formed (Scheme 193). In the reaction without BHT the ratio of **[58a]**NSI to **[59a]**NSI was approximately 1: 0.5 while in the presence of BHT the ratio was 1: 1.3. This could indicate an SET mechanism is in effect. Although BHT reacts slowly with NFSI, there was no evidence for unreacted **[57a]** in the $^{31}P\{^{1}H\}$ and ^{1}H NMR spectrum, indicating **[57a]** is capable of reacting with NFSI before BHT. However, it cannot be ruled out that the increased proportion of protonation is not related to the fluorination pathway but rather a decomposition pathway.

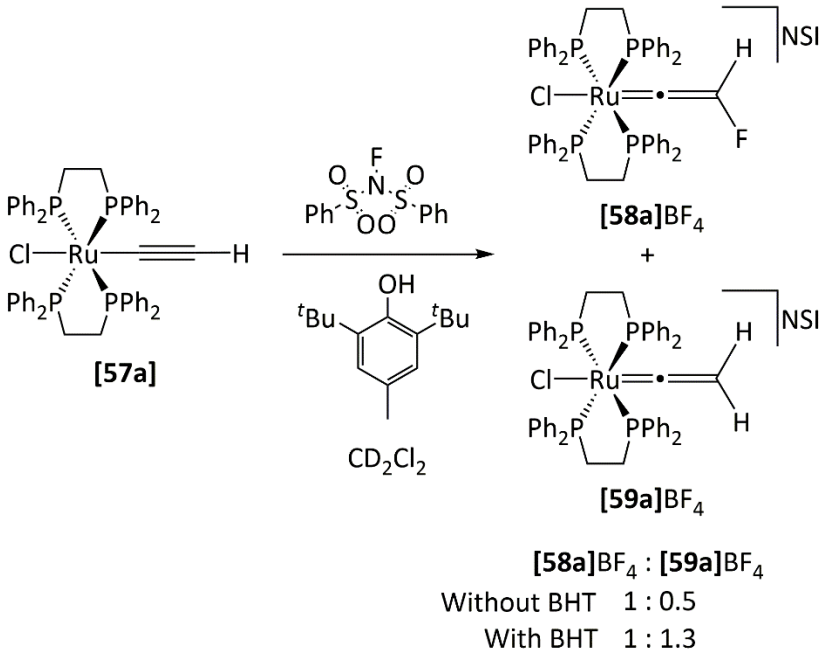

Scheme 193: Reactions of [57a] with NFSI in the presence of BHT afforded the protonated product [59a]BF_4 as the major product with [58a]BF_4 formed as the minor product.

4.9 Calculated Gibbs Free Energies of Fluorination for *trans*-[ClRu(dppe)$_2$(C≡CR)] Complexes

To determine whether fluorination is thermodynamically favourable or not with Selectfluor, NFSI and [FTMP]BF_4, the free energies of fluorination in dichloromethane were calculated by DFT at the (RI-)BP86/SV(P)//(RI-)PBE0(D3)/def2-TZVPP level with solvent correction applied with COSMO. The free energies were calculated based on the isodesmic reaction shown below in Scheme 194.

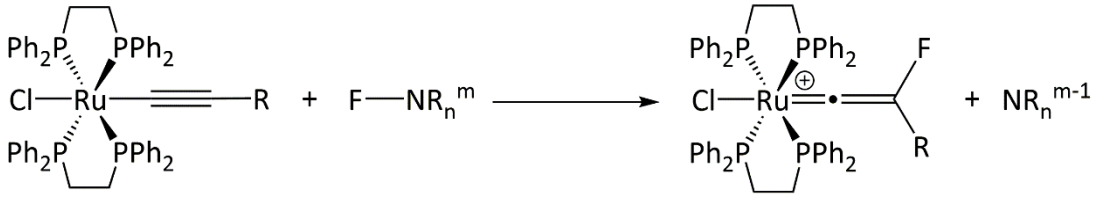

Scheme 194: Free energies of fluorination were calculated based on the isodesmic reaction between the fluorinating agent and alkynyl complex.

Table 27: Calculated free energies of fluorination for complexes of the type *trans*-[ClRu(dppe)$_2$(C≡CR)].

trans-[ClRu(dppe)$_2$(C≡CR)]	ΔG_{298} / kJ mol^{-1}		
R =	NFSI	FTMP	Selectfluor
[57i] C_6H_4-4-NMe_2	-189.5	-193.0	-301.1
[57c] C_6H_4-4-OMe	-183.6	-187.1	-295.3
[57d] C_6H_5	-179.6	-183.0	-291.2
[57e] C_6H_4-4-COOMe	-171.9	-175.4	-283.6
[57f] C_6H_4-4-COMe	-171.7	-175.2	-283.4
[57g] C_6H_4-4-CF_3	-173.7	-177.1	-285.3
[57h] C_6H_4-4-NO_2	-164.3	-167.8	-276.0
[57j] C_3H_5	-220.8	-224.3	-332.4
[57a] H	-223.2	-226.7	-334.8
[57b] F	-266.6	-270.0	-378.2

Calculated at the (RI-)BP86/SV(P)//(RI-)PBE0(D3)/def2-TZVPP level with COSMO correction for dichloromethane.

The enthalpy of fluorination for all substituents is energetically favourable regardless of the fluorinating agent employed; thus, it would be expected from a thermodynamic standpoint that fluorination could be observed with all three fluorinating agents. As the substituent

becomes more electron donating, fluorination becomes thermodynamically more favourable due to the increased nucleophilicity and ability to stabilise the positive charge of the vinylidene complex. Fluorination with Selectfluor is predicted to be thermodynamically more favourable than [FTMP]BF_4 and NFSI presumably due to the reduction of the dicationic charge to monocationic. The larger thermodynamic driving force (*ca.* 110 kJ mol^{-1}) for fluorination using Selectfluor could be one possible reason why fluorination is consistently observed with *trans*-[ClRu(dppe)$_2$(C≡CR)] complexes with the exception of **[57i]**. The free energies of fluorination with [FTMP]BF_4 and NFSI are essentially the same, which suggests that the fluorination of **[57a]** and **[57b]** with NFSI is not due to thermodynamic reasons but other factors. Likewise, the absence of fluorination in the reactions of **[57c-h]** and **[57j]** with [FTMP]BF_4 and NFSI must be the result of kinetic factors or a more thermodynamically favourable process. This must also be true for **[57i]** which has the largest thermodynamic driving force for fluorination of complexes **[57]**; the lack of fluorination with Selectfluor indicates that kinetic factors or a more thermodynamically favourable process prevents fluorination, e.g. reactivity of the radical alkynyl complex or competing oxidation.

4.10 Redox Potentials of the *trans*-[ClRu(dppe)$_2$(C≡CR)] Complexes and Fluorinating Agents

To understand the thermodynamic favourability of electron transfer between the three fluorinating agents and complexes **[57]**, the redox potentials were measured by cyclic voltammetry in the 1:1 dichloromethane: acetonitrile mix used in the fluorination procedure. The ruthenium alkynyl complexes were also measured in dichloromethane for comparison against SCE.

The redox potentials measured in 1:1 dichloromethane: acetonitrile are reported against the ferrocene couple due to the nontrivial nature of accurately using an aqueous standard reference electrode, e.g. the standard calomel electrode, to measure the ferrocene couple (Fc) in organic solvents. This is the result of large junction potentials being generated at the interface of the frit/membrane between the organic solution of the electrochemical cell and the aqueous solution of the electrode.[326]

Table 28: Redox potentials for complexes of the type *trans*-[ClRu(dppe)$_2$(C≡CR)] and fluorinating agents in dichloromethane (vs SCE), and 1:1 dichloromethane: acetonitrile (vs ferrocene).

trans-[ClRu(dppe)$_2$(C≡CR)] R =	$E_{1/2}$ / V vs Fc 1:1 DCM:MeCN	$E_{1/2}$ / V vs SCE DCM
[57c] C_6H_4-4-OMe	-0.07	0.36[a]
[57d] C_6H_5	-0.01	0.44[a]
[57e] C_6H_4-4-COOMe	0.12	0.55[a]
[57f] C_6H_4-4-COMe	0.12	0.55
[57g] C_6H_4-4-CF_3	0.14	0.57
[57h] C_6H_4-4-NO_2	0.20	0.63[a]
[57j] C_3H_5	-0.08	0.34
R =	$E_{p,\,o}$ / V	$E_{p,\,o}$ / V
[57a] H	0.14	0.56
[57b] F	0.10	0.52

Mix defined at 1:1 dichloromethane: acetonitrile; [a]data reported by Gauthier et al.[243]

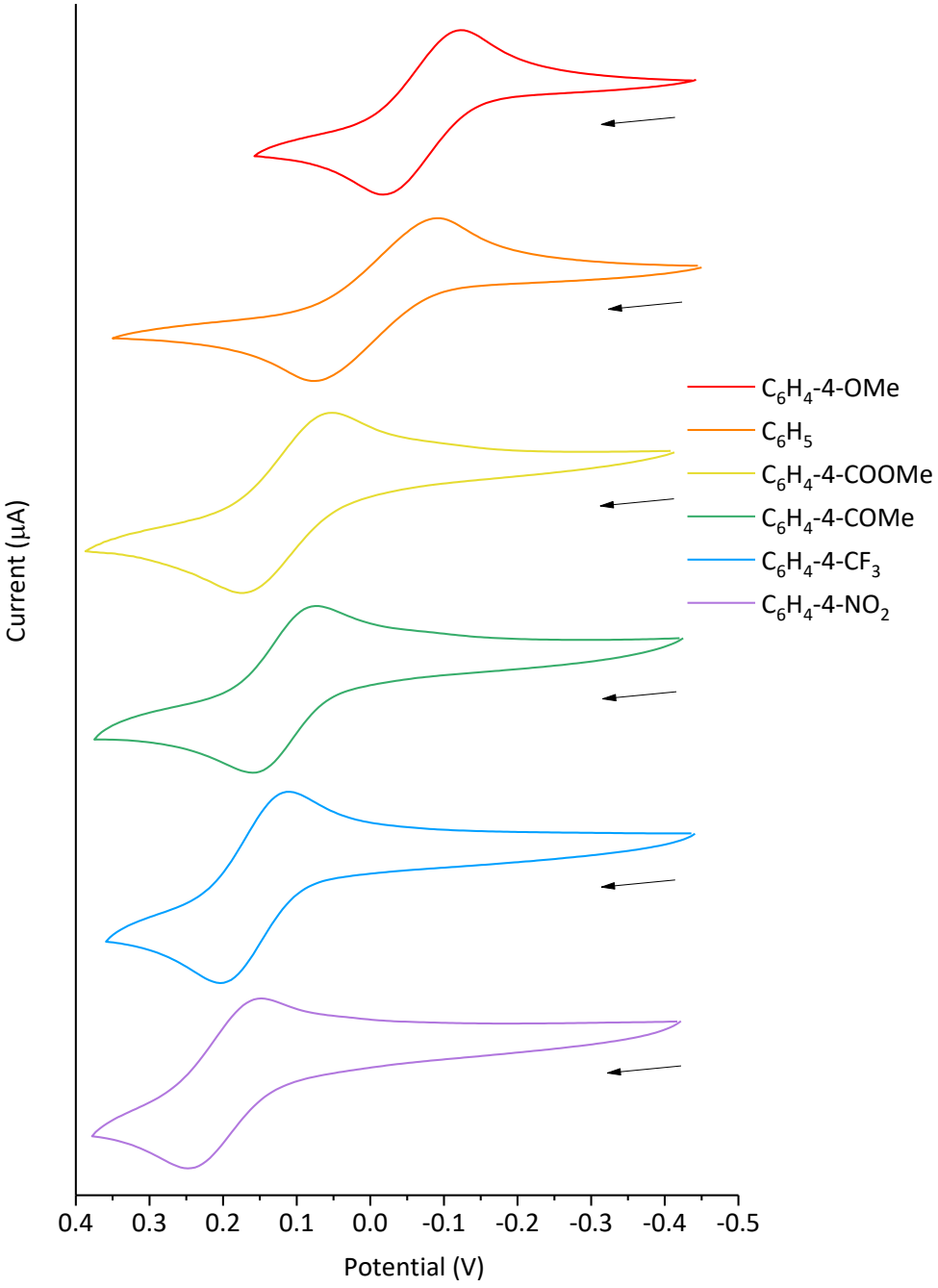

Figure 90: Overlaid cyclic-voltammograms of complexes [57] vs ferrocene in 1:1 dichloromethane: acetonitrile recorded at a scan rate of 50 mV/s with 0.1 mM tetrabutylammonium hexafluorophosphate as supporting electrolyte. A platinum disc was used as the working electrode, platinum wire for the counter electrode and silver wire for the pseudo reference. Peak heights were scaled for clarity.

In a study on the nature of *trans*-[ClRu(III)(dppe)$_2$(C≡CR)]$^{\cdot+}$ complexes by Gauthier *et al.*[243] the redox potentials of the **[57c]**, **[57d]**, **[57f]**, and **[57h]** in dichloromethane were reported between 0.36 V and 0.63 V vs SCE in dichloromethane and displayed quasi-reversible behaviour. Likewise, complexes **[57e]** and **[57g]** also displayed quasi-reversible behaviour as

noted by the increase in peak separation with increased scan rate, matching that of the other aryl-substituted alkynyl complexes. As the aryl-substituent becomes more electron-donating the oxidation potential shifts to a more negative (less oxidising) potential reflecting the ability to stabilise the radical cation. The same span in half-cell potentials observed in dichloromethane is also observed in the 1:1 dichloromethane: acetonitrile solvent mix, with the half-cell potential of **[57c]** measured at -0.07 V vs Fc, and **[57h]** at 0.20 V vs Fc.

In contrast to **[57c-h]**, the cyclic-voltammograms for **[57a]** (Figure 91) and **[57b]** (Figure 92) displayed irreversible behaviour as noted by the absence of a reduction peak, and in the case of **[57b]**, new species being observed as result of one or more chemical process. The cyclic-voltammogram of the analogous bis-dppm complex of **[57a]** is also reported to show complete irreversibility.[327] However, there was no discussion of the products afforded by oxidation.

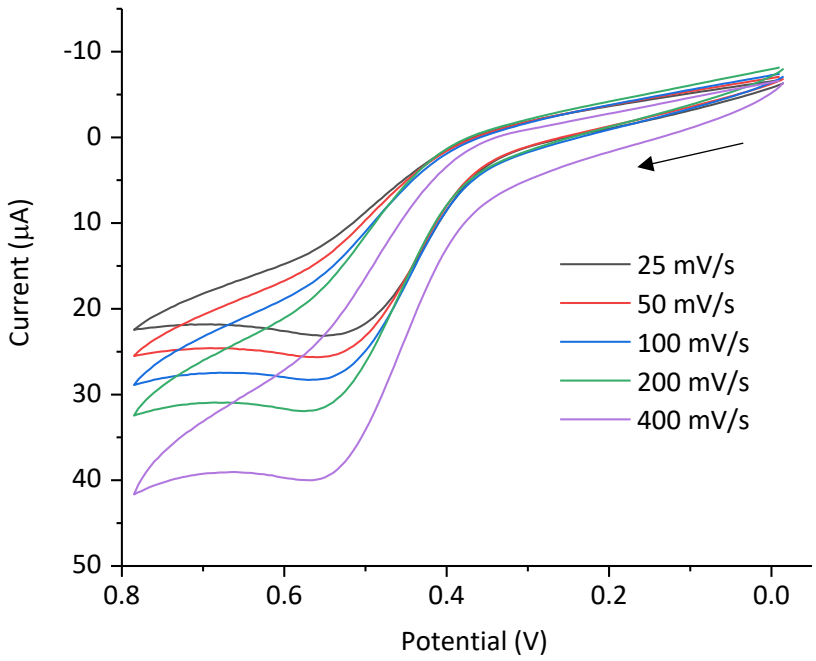

Figure 91: Cyclic-voltammogram of [57a] at varying scan rates vs SCE in dichloromethane with 0.1 M tetrabutylammonium hexafluorophosphate as supporting electrolyte; corrected to SCE using ferrocene as an internal reference. A platinum disc was used as the working electrode, platinum wire for the counter electrode and silver wire for the pseudo reference.

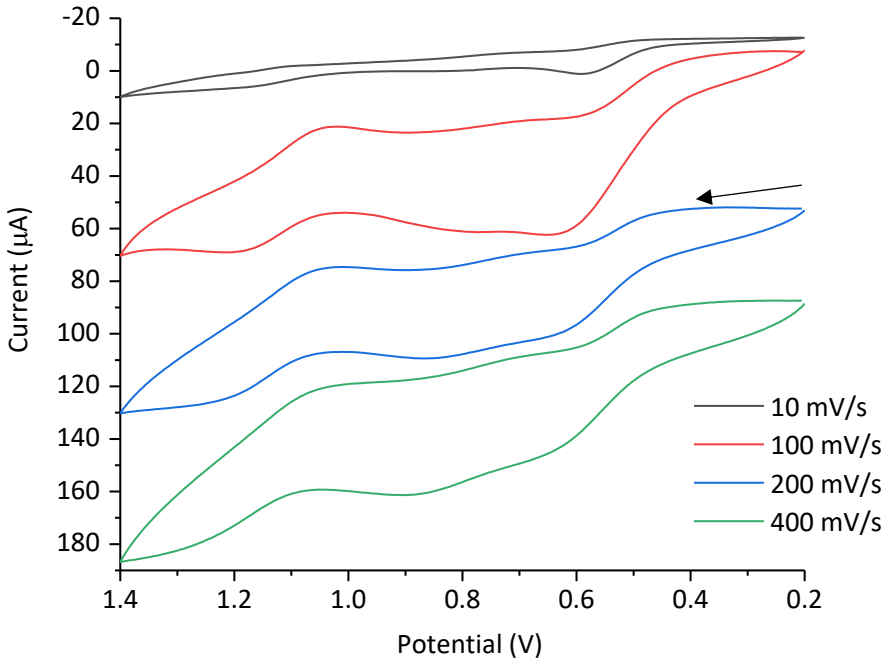

Figure 92: Cyclic-voltammogram of [57b] at varying scan rates vs ferrocene in 1:1 dichloromethane acetonitrile with 0.1 M tetrabutylammonium hexafluorophosphate as supporting electrolyte. A platinum disc was used as the working electrode, platinum wire for the counter electrode and silver wire for the pseudo reference.

The irreversible oxidation of **[57a]** and **[57b]** accounts for the observation of multiple species in the UV-Vis spectra of **[57a]** and **[57b]** when they are treated with Selectfluor, [FTMP]BF_4, and NFSI. The peak oxidation potential for **[57a]** is close to that of **[57e]** while the peak oxidation potential for **[57b]** is closest to that of **[57d]**.

The electrochemical data in the literature report various values for the peak reduction potentials of NFSI, [FTMP]BF_4, and Selectfluor but consistently displayed irreversible behaviour. The irreversible nature of reduction has been attributed to the cleavage of the N-F bond as demonstrated by Andrieux *et al*.[328] with the reduction of fluorosultam, **126**, which resulted in concerted elimination of fluoride and reduction of the organic fragment.

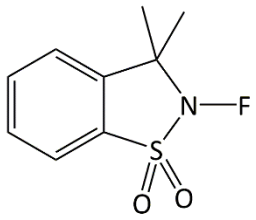

126

Figure 93: Fluorosultam, 126.[328]

Table 29: Measured and reported peak reduction and half-wave potentials for Selectfluor, NFSI, and [FTMP]BF_4

Fluorinating Agent	$E_{p,r}$ / V vs Fc DCM:MeCN	$E_{p,r}$ / V vs SCE MeCN[a]	$E_{p,r}$ / V vs SCE MeCN[b]	$E_{1/2}$ / V vs SCE MeCN[c]	$E_{1/2}$ / V vs SCE MeCN[d]
Selectfluor	-1.13	-0.04	-	-	0.33
[FTMP]X^-	-1.47[e]	-0.73[f]	-0.65[f]	-0.21[f]	-
NFSI	-1.85	-0.78	-0.54	0.16	-1.24

[a] Values reported by Gilicinski et al.[329] using Pt working electrode; [b] values reported by Differding and Bersier[330] using glassy carbon working electrode and [c] dropping mercury electrode; [d] values reported by Girina et al.[331] using a Pt rotating disc electrode at 1830 rpm; [e] X = BF_4; [f] X = OTf.

Gilicinski *et al.*[329] reported the peak reduction potentials of Selectfluor, [FTMP]OTf, and NFSI at -0.78 V, -0.73 V, and -0.04 V respectively against the saturated calomel electrode (SCE) in acetonitrile using a static platinum working electrode. Conversely Differding and Bersier[330] reported peak reduction potentials for [FTMP]OTf and NFSI at -0.65 and -0.54 V respectively vs SCE in acetonitrile with the same supporting electrolyte on a static glassy carbon electrode. The peak reduction potentials recorded showed a clear discrepancy between the different electrode material. Gilicinski *et al*.[329] also recorded cyclic-voltammograms for Selectfluor and *N*-fluoropyridinium triflate with gold and glassy carbon electrodes and observed a shift in the peak reduction potential with different electrode material. Differding and Bersier[330] were also able to measure the half-wave potentials using a dropping mercury electrode, observing a large shift to more positive (oxidising) potentials compared to the peak reduction potentials with the glassy carbon electrode. Nevertheless, the reported values for Selectfluor are consistently at the most positive peak reduction potential and consequently the most oxidising out of the three fluorinating agents in terms of thermodynamics.

Attempts to observe the reduction peaks of NFSI, [FTMP]BF_4, and Selectfluor above -0.45 V (vs Fc) in 1:1 dichloromethane: acetonitrile using the same electrochemical cell setup used to record the potentials for **[57]**, were not successful (Figure 94). There were no reduction peaks observed between 3.05 V and -0.45 V (vs Fc); however, at significantly more reducing potentials irreversible reduction processes were observed for all three fluorinating agents. Peak reduction potentials for Selectfluor, [FTMP]BF_4, and NFSI were observed at -1.13 V, -1.47 V, and -1.85 V vs Fc respectively in 1:1 dichloromethane: acetonitrile (Figure 95,

Table 29), with Selectfluor being reduced at a more positive (oxidising) potential and NFSI at a more negative (reducing) potential, agreeing with the general order reported by Gilicinski *et al.*[329]

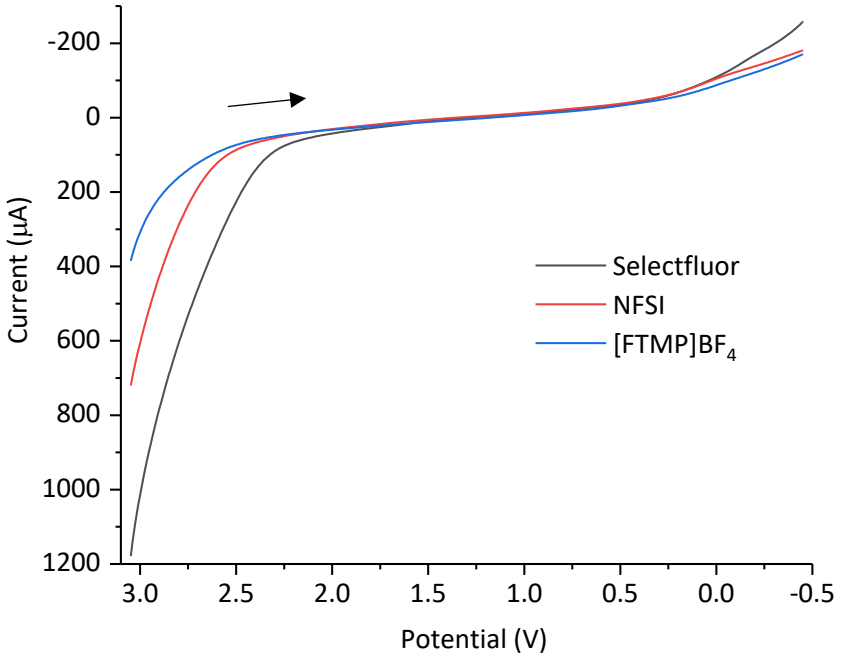

Figure 94: Overlaid linear voltammograms for Selectfluor, NFSI, and [FTMP]BF_4 between 3.05 V and -0.45 V vs ferrocene in 1:1 dichloromethane: acetonitrile with 0.1 M tetrabutylammonium hexafluorophosphate as supporting electrolyte. A platinum disc was used as the working electrode, platinum wire for the counter electrode and silver wire for the pseudo reference.

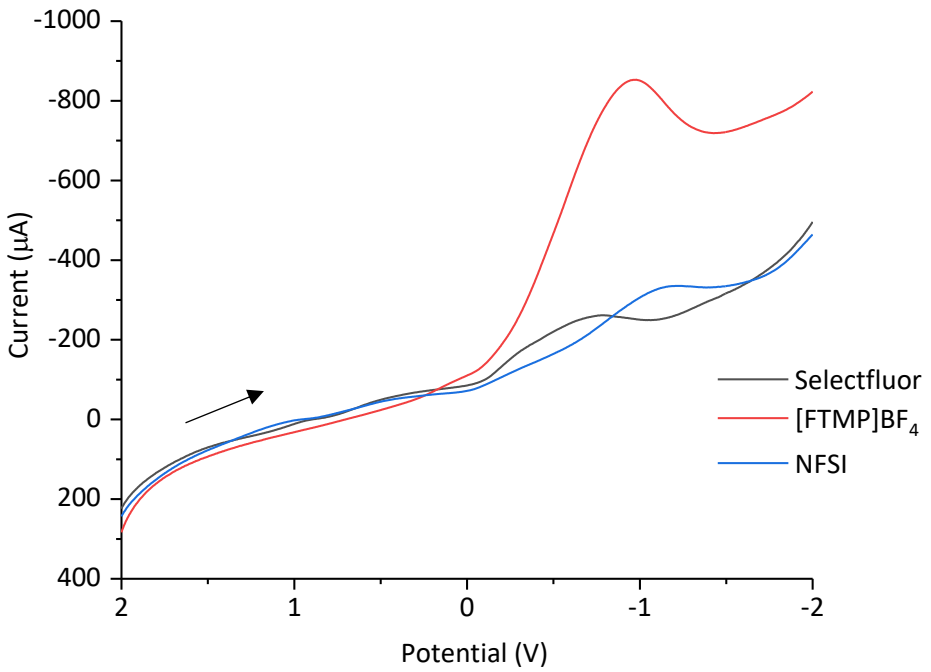

Figure 95: Overlaid linear voltammograms for Selectfluor, NFSI, and [FTMP]BF_4 between 2.0 V and -2.0 V vs ferrocene in 1:1 dichloromethane: acetonitrile with 0.1 M tetrabutylammonium hexafluorophosphate as supporting electrolyte. A platinum disc was used as the working electrode, platinum wire for the counter electrode and silver wire for the pseudo reference.

It is clear, based on the recorded potentials, that none of the fluorinating should be able to able to oxidise the alkynyl complexes, even considering the potential difference between **[57c]**, one of the easiest alkynyl complexes to oxidise, and Selectfluor, the strongest oxidising fluorinating agent, the cell potential will be negative (E_{cell}= $E_{reduction}$-$E_{oxidation}$), and oxidation of the alkynyl complex is not expected to be spontaneous given $\Delta G = -nFE_{cell}$ (where ΔG is the change in Gibbs free energy, n is the number of electrons transferred in the reaction, F is Faraday's constant, and E_{cell} is the cell potential):

$E_{cell} \approx -1.13\ V-(-0.07\ V) \approx -1.06\ V$

$\Delta G \approx -(1\ mol \cdot 96{,}485\ J\ V^{-1}\ mol^{-1} \cdot -1.06\ V) \approx 102\ kJ\ mol^{-1}$

Due to oxidation of the ruthenium alkynyl complexes being observed experimentally, electron transfer must be thermodynamically favourable indicating the thermodynamics of electron transfer in the electrochemical cell is not representative of the true thermodynamics of electron transfer in solution between the ruthenium alkynyl complexes and the fluorinating agents. As the measured potential does not correspond to the equilibrium potential, but rather the equilibrium potential plus the overpotential needed to drive electron transfer between the molecule of interest and the electrode, differences in

the overpotential can potentially provide false indications of favourability. In this case the overpotentials needed to drive the reduction of the fluorinating agents must be significantly different to the overpotentials required to drive the redox process for the metal alkynyl complexes, such that the recorded potentials indicate electron transfer is disfavoured thermodynamically. Differding and Bersier[330] observed significant shifts to more negative potentials for the peak reduction potentials of fluorinating agents measured on glassy carbon electrodes compared to the half-wave potentials measured with a dropping mercury electrode (as high as 1 V) due to large differences in overpotential. They attributed the large overpotential needed for irreversible reduction on the glassy carbon electrode to the cleavage of the N-F bond. The observations of Differding and Bersier[330] indicate that the large negative values recorded here are also the result of significant overpotentials being required to drive reduction and would account for the experimental observation of oxidation despite the measured redox potentials indicating otherwise. Gilicinski *et al*.[329] also noted that the equilibrium redox potential of Selectfluor must be significantly greater than the observed peak reduction potential, due to its ability to oxidise an aqueous bromide solution which has a redox potential of + 0.85 V vs SCE.

4.11 Oxidation of [57c] and Fluoride Addition

4.11.1 One-Electron Oxidation

To probe the possibility that fluorination of proceeds by the reaction of **[57]**$^+$ with fluoride to form **[58]**$^+$ upon oxidation (Scheme 195), the radical cation, **[57c]**PF_6, was generated *in situ* by addition of ferrocenium hexafluorophosphate and treated with one equivalent of tetrabutylammonium fluoride in 1:1 dichloromethane: acetonitrile.

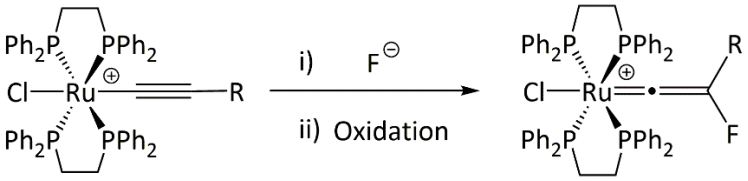

[57]BF_4 **[58]**BF_4

Scheme 195: A possible pathway to fluorination through reaction of [57]BF_4 with fluoride.

The reaction was monitored by UV-Vis and NMR spectroscopy. Addition of fluoride resulted in the slow decay of the ruthenium(III) alkynyl complex by UV-Vis spectroscopy (Figure 96). The $^{31}P\{^1H\}$ NMR spectrum in 1:1 dichloromethane: acetonitrile was dominated by a singlet resonance at δ 50.3 which is assigned to the formation of **[114c]**$^+$. Multiple trace resonances were also observed between δ 33-36 and δ 58-66. There was no evidence for the formation of **[58c]**$^+$ (Scheme 196). The ^{19}F NMR spectrum was dominated by the hexafluorophosphate anion but there was again no evidence for the formation of **[58c]**$^+$; this was supported by the absence of **[58c]**$^+$ in the ESI-MS. The ESI-MS was dominated by the m/z of **[114c]**$^+$-MeCN and also displayed the m/z of **[114c]**$^+$ with acetonitrile still bound. The decay of **[57c]**$^+$ observed in the UV-Vis spectra does not correspond to the formation of a fluorinated product according the NMR spectra. It is clear that fluorination of **[57c]** does not proceed through a stepwise oxidation-fluoride attack mechanism.

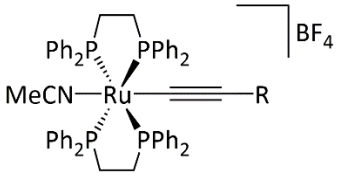

[114]BF_4

a R = H	**f** R = C_6H_4-4-C(O)Me
b R = F	**g** R = C_6H_4-4-CF_3
c R = C_6H_4-4-OMe	**h** R = C_6H_4-4-NO_2
d R = C_6H_5	**i** R = C_6H_4-4-NMe_2
e R = C_6H_4-4-C(O)OMe	**j** R = C_3H_5

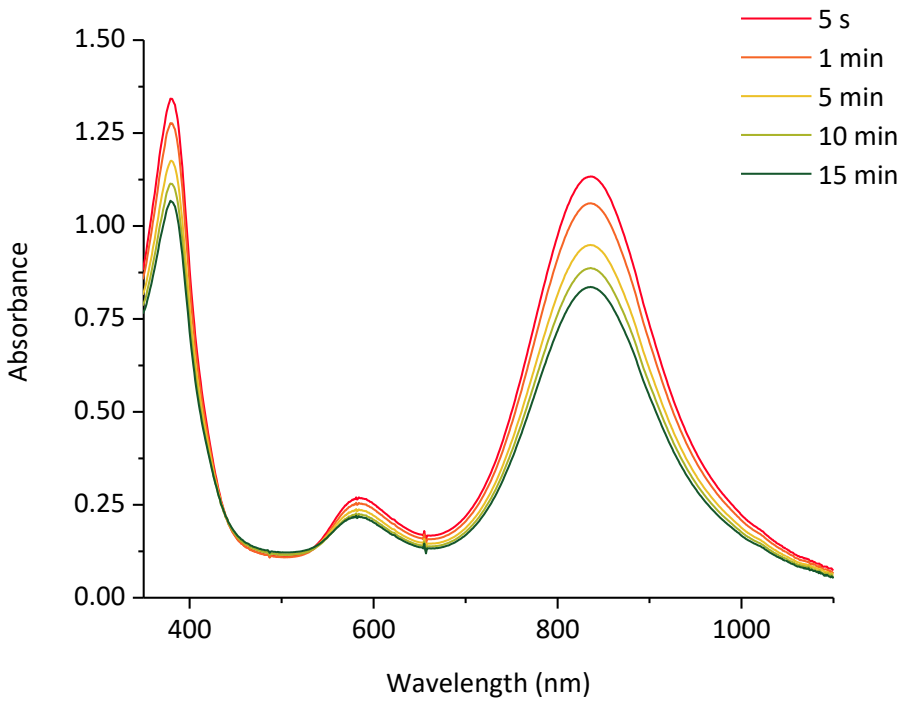

Figure 96: Overlaid UV-Vis spectra recorded after addition of TBAF to [57c]$^{+}$$PF_6^{-}$ in 1:1 dichloromethane: acetonitrile at 0.2 mM.

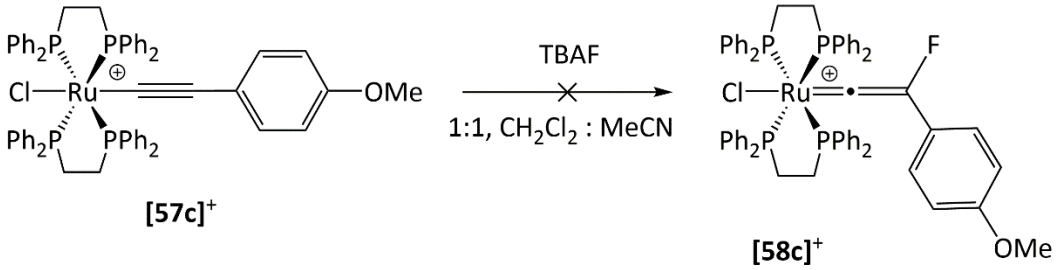

Scheme 196: Reaction of [57c]$^{+}$ with TBAF did not afford fluorovinylidene complex, [58c]$^{+}$.

4.11.2 Two-Electron Oxidation

An alternative mechanism to fluorination could be the double oxidation of **[57]** by the fluorinating agent to form a ruthenium(IV) complex, which subsequently undergoes fluoride attack to afford **[58]**$^{+}$ (Scheme 197).

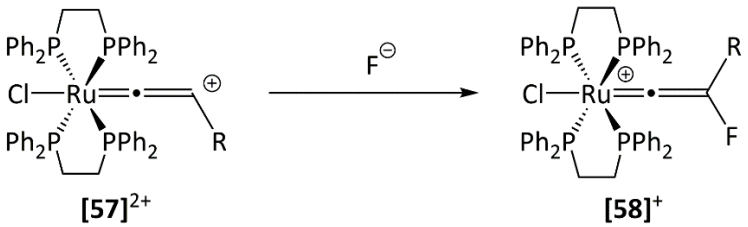

Scheme 197: A possible pathway to fluorination through reaction of [57]BF_4 with fluoride.

To probe the possibility of this pathway, one equivalent tetrabutylammonium fluoride was reacted with the Ru(IV) complex obtained by double oxidation of **[57c]**BF_4, with three equivalents of thianthrenium tetrafluoroborate in a 1:1 dichloromethane: acetonitrile solution. Thianthrenium tetrafluoroborate was chosen as the oxidant due to its strong oxidising capability (E^o = 1.26 V *vs* SCE in MeCN) which was sufficient to oxidise **[57c]** to ruthenium(IV) according to the appearance of new absorption bands at 356, 405, 736, and 810 nm (purple spectrum in Figure 97). It is not clear whether the bands arise directly from the Ru(IV) species or its decomposition species, but the data are indicative that a second oxidation step had taken place. The addition of one equivalent of tetrabutylammonium fluoride resulted in decay of the ruthenium(IV) species; however, there was no evidence for the formation of **[58c]**$^+$.

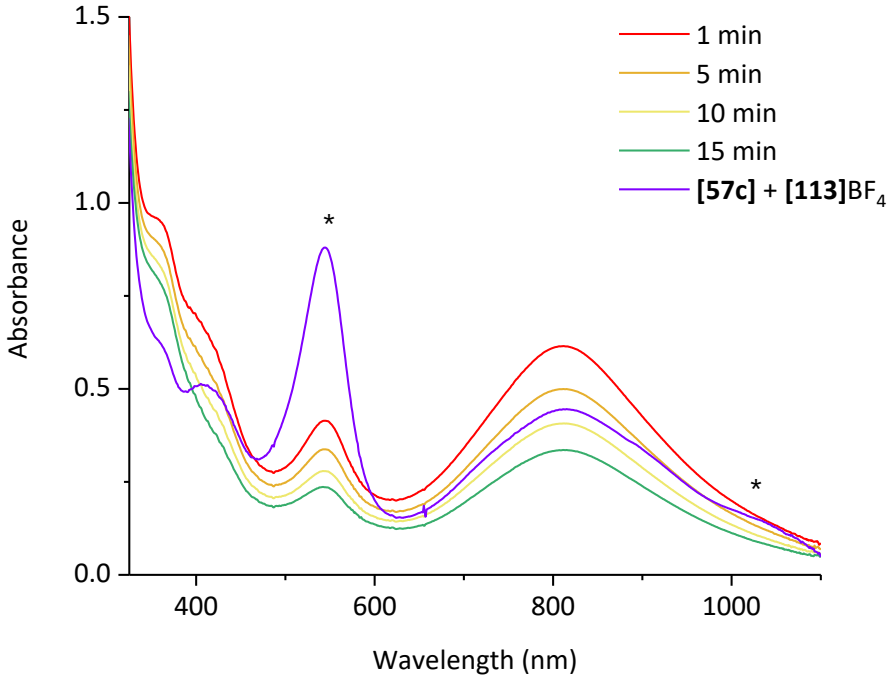

Figure 97: Overlaid obtained by addition of TBAF to doubly oxidised [57c] in 1:1 dichloromethane: acetonitrile at 0.2 mM; asterisks denote bands corresponding to excess thianthrenium tetrafluoroborate, [113]BF_4.

The $^{31}P\{^1H\}$ NMR spectrum of the reaction mixture in 1:1 dichloromethane: acetonitrile was complex exhibiting a large mixture of broad and sharp resonances between δ 10 and δ 70 with different multiplicity. However, there was no clear evidence that **[58c]**$^+$ was formed. The ^{19}F NMR spectrum displayed numerous weak resonances around δ -75, δ -140 to -150, and δ -180 but no resonance around δ -230 where **[58]**$^+$ is observed. The ESI-MS did not detect the presence of **[58c]**$^+$, supporting the NMR data (Scheme 198), instead the mass

spectrum was dominated by the m/z of **[57c]**-H. The data suggest that fluorination does not proceed by double oxidation of **[57]** and subsequent nucleophilic attack of the Ru(IV) species by fluoride.

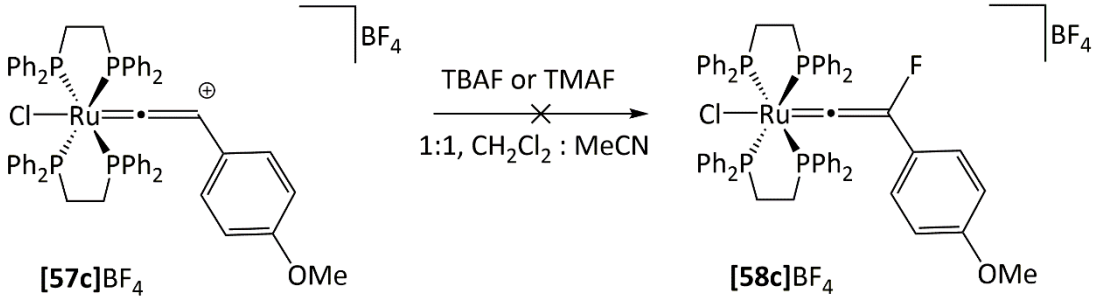

Scheme 198: Double oxidation of [57c] to ruthenium(IV) with thianthrenium tetrafluoroborate and subsequently reacting with fluoride did not afford [58c]BF_4.

4.12 Probing the Mechanism of Fluorination

Electrophilic fluorination has been proposed to proceed *via* two main mechanisms, a classical two-electron S_N2 mechanism and a single electron transfer (SET) mechanism, both of which have been debated over the years in the literature.

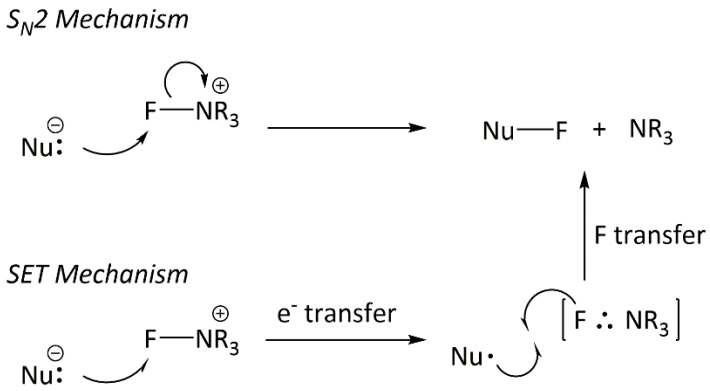

Scheme 199: Representation of an S_N2 and SET mechanism to electrophilic fluorination.

Umemoto *et al*.[332] attributed the reactivity of *N*-fluoropyridinium salts toward neutral and anionic nucleophiles to an SET mechanism due to the formation of alkyl fluorides with Grignard reagents, which were capable of reacting by SET mechanisms, but not the analogous organolithium reagents, which were thought to react by an S_N2 mechanism. However, Yamataka *et al*.[333] proposed organolithium regents were able to react through an SET mechanism but the electron transfer step is rate determining, while radical recombination is rate determining in the reaction of Grignard reagents. Holm and Crossland[334] also demonstrated that Grignard reagents were capable of reacting with electrophiles through an S_N2 mechanism, disproving the argument made by Umemoto *et al*. The other piece of evidence provided by Umemoto *et al*.[332] was the observed formation of a coloured solution upon addition of *N*-fluoropyridinium to 2-napthol which bleached as the reaction proceeded. Kochi *et al*.[335, 336] attributed the coloured species to the formation of a π-stacked charge transfer complex formed after SET between fluorinating agent and substrate (Scheme 200); such charge transfer complexes were observed with other substituted *N*-pyridinium salts. They also observed enhanced rates of fluorination upon irradiation of the sample with the wavelength the charge transfer band, suggesting the charge transfer species could be an intermediate in fluorination.

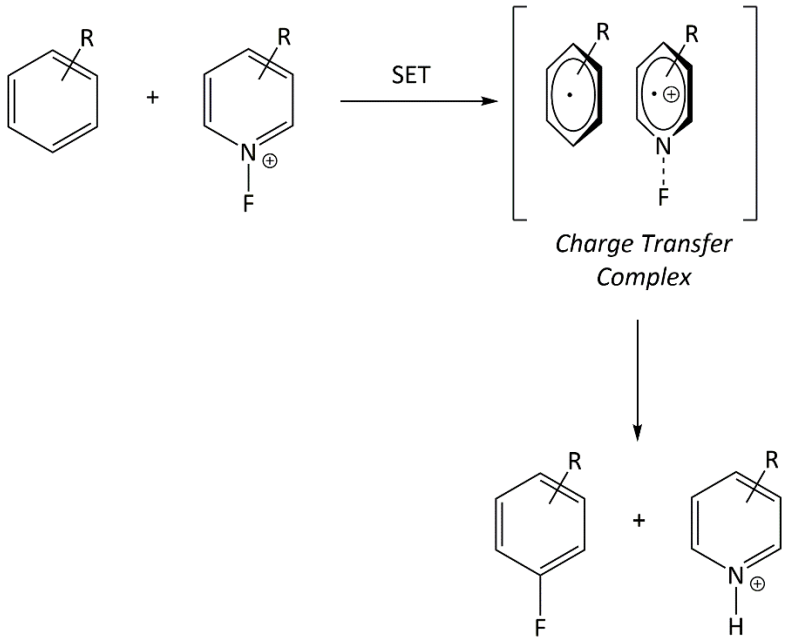

Scheme 200: Umemoto *et al*.[332] and Kochi *et al*.[335, 336] proposed the formation of coloured solutions during fluorination was due to SET and formation of a charge transfer complex.

The most commonly employed method for probing the possibility of a radical mechanism is the use of radical traps or clocks to either trap radical intermediates or produce mechanism dependent products.[308, 337, 338] The addition of radical traps, such as 2,6-di-*tert*-butyl-4-methylphenol (BHT) and 2,2,6,6-tetramethyl-1-piperidinyloxyl (TEMPO), may imply a radical mechanism through suppression or complete inhibition of fluorination by quenching radical intermediates through SET, protonation, or formation of adducts.[337, 339] Addition of substrates capable of undergoing ring-opening or ring-closing upon electron transfer (radical clocks), e.g. cyclopropyl-bearing substrates, provide different products depending on whether a radical intermediate is produced. Such an approach is only appropriate provided the rate of ring-opening or closing is faster than fluorine transfer.

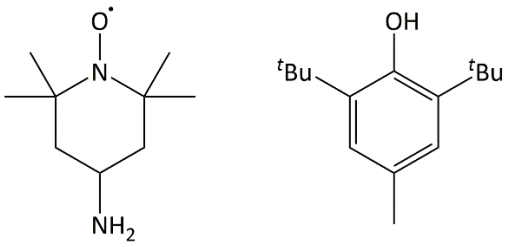

TEMPO
115

BHT
116

For example, Differding *et al*.[340] probed the fluorination of a citronellic ester enolate bearing a 5-hexenyl chain, **127**, whose radical would cyclise to give a cyclopentylmethyl radical if the

enolate underwent an electron transfer mechanism. Observation of ring-closed fluorinated products would suggest an SET mechanism. However, there was no evidence of ring-closed fluorinated products with any of the four fluorinating agents employed (including NFSI) which suggested fluorination proceeded by an S_N2 mechanism in all cases. The possibility of a fast 'in-cage' SET mechanism, which proceeds at a rate faster than ring-closing, could not be excluded. Due to the reaction of atomic fluorine with solvent having been recorded by laser flash photolysis[341] at a rate of between 1 x 10^9 and 1 x 10^{11} s^{-1} while the cyclisation of **127** had been recorded at a rate of approximately 1 x 10^5 s^{-1},[340] evidence for an SET mechanism by a fluorine radical would not be expected.

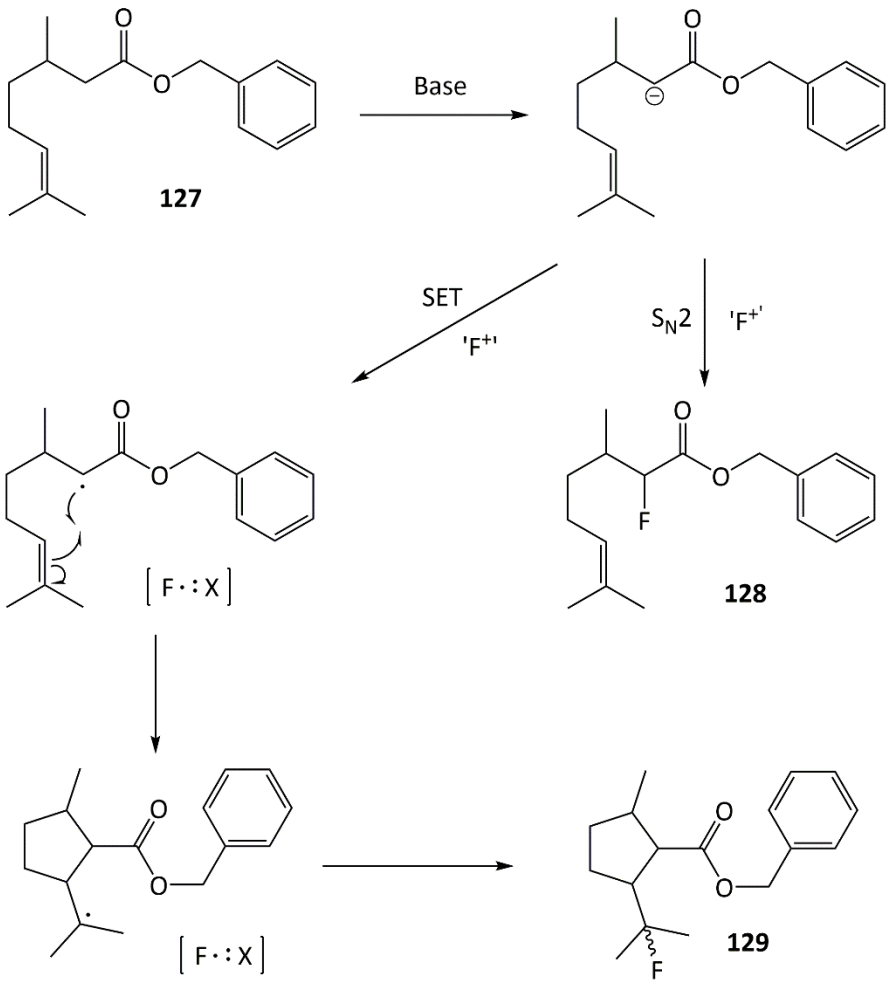

Scheme 201: Fluorination of [127] was proposed to form [128] in an S_N2 mechanism or [129] in an SET mechanism

In a different example, the fluorination of glycals was probed by the reaction of Selectfluor (triflate salt), NFSI, and xenon difluoride with a cyclopropyl radical trap, **127**,[306] whose analogues are capable of ring opening at rates as high as 10^{11} s^{-1}.[308, 338] The formation of the cyclopropyl fluorinated product **128** would imply an S_N2 mechanism while formation of **129**

would imply an SET mechanism (Scheme 202). The reaction of **127** with NFSI afforded a mixture of the ring-closed and ring-opened fluorinated products, implying fluorination proceeded through an SET mechanism. Xenon difluoride was also proposed to react through an SET mechanism due to the formation of numerous olefin products and the disappearance of the cyclopropyl group in the crude NMR spectrum. The reaction of **127** with Selectfluor, however, afforded only the ring-closed fluorinated product, **128**, which implied that fluorination proceeded by an S_N2 mechanism in contrast to fluorination by NFSI. Nevertheless, the reaction of TEMPO with Selectfluor in a control experiment revealed Selectfluor is capable of reacting in an SET manner.

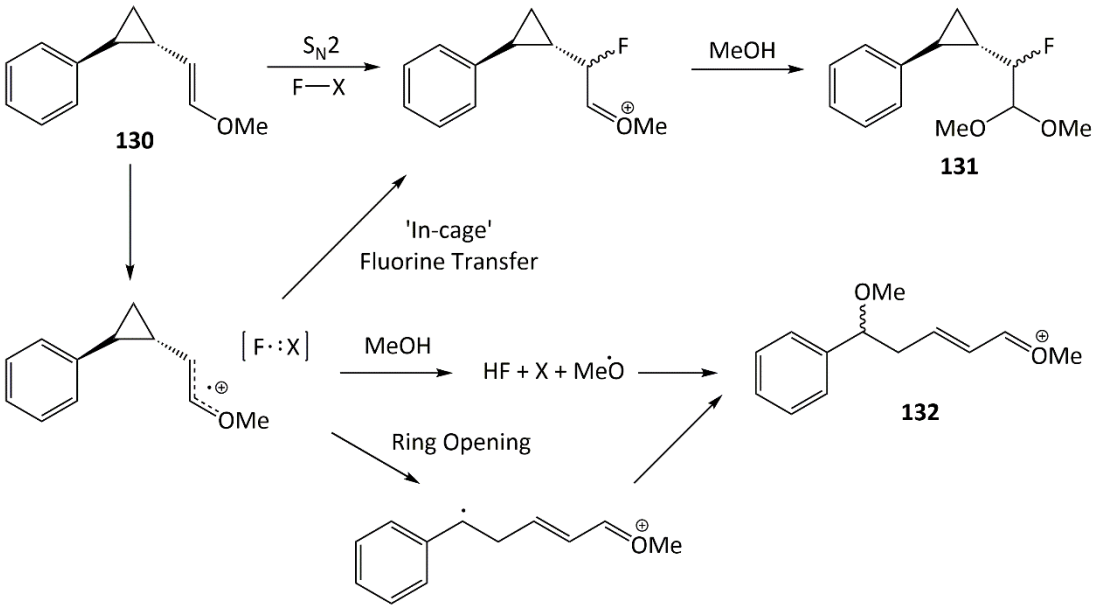

Scheme 202: Radical trap 130 was proposed to afford 131 through an S_N2 mechanism or 'in cage' SET mechanism or 132 through an SET mechanism.[306]

In a more recent example Zhang *et al*.[139] proposed the copper-catalysed fluoroamination of styrene with NFSI proceeded through an SET radical mechanism, due to the inhibition of the fluorination in the presence of radical traps BHT and TEMPO. The radical clock experiment with **130** as the substrate afforded the ring-opened fluorinated product indicating fluorination proceeded by a radical mechanism in which the alkyl radical abstracts fluorine from NFSI. The fluorination step of the mechanism was proposed to proceed by fluorine abstraction from NFSI *via* an alkyl radical.

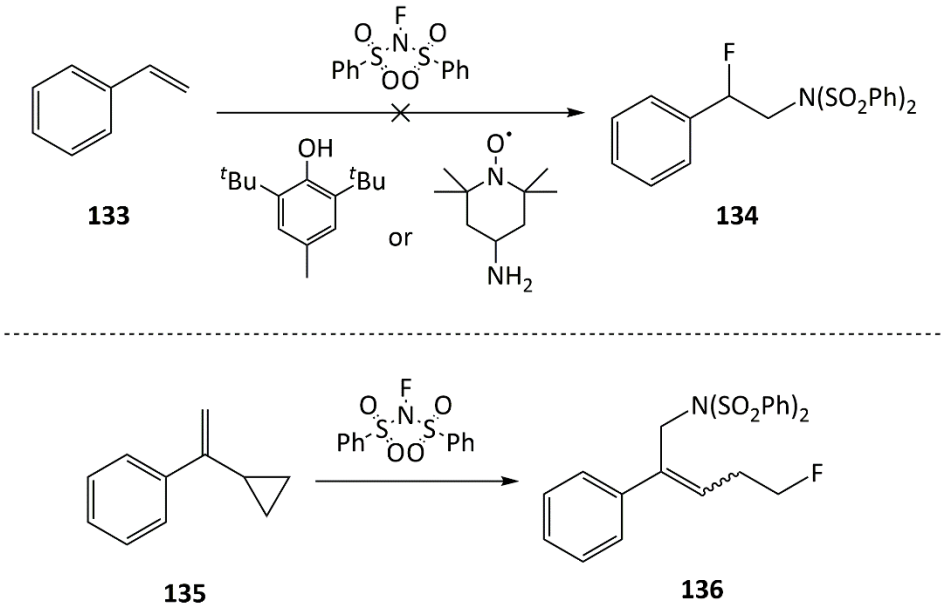

Scheme 203: Zhang *et al.* proposed fluoroamination of styrenes with NFSI through ring-opening fluorination of 135 and inhibition of fluorination with TEMPO and BHT.[306]

Despite the numerous examples in literature which invoke a radical mechanism for fluorination, few examples have been reported which invoke fluorine transfer between the putative radical formed by reduction of the fluorinating agent and the radical of the substrate. The palladium(III) catalysed fluorination of aryl boronic acid derivatives reported by Ritter *et al*.[98] is one example in which fluorination is proposed to proceed by radical fluorine transfer from the Selectfluor radical to the substrate (Scheme 204).

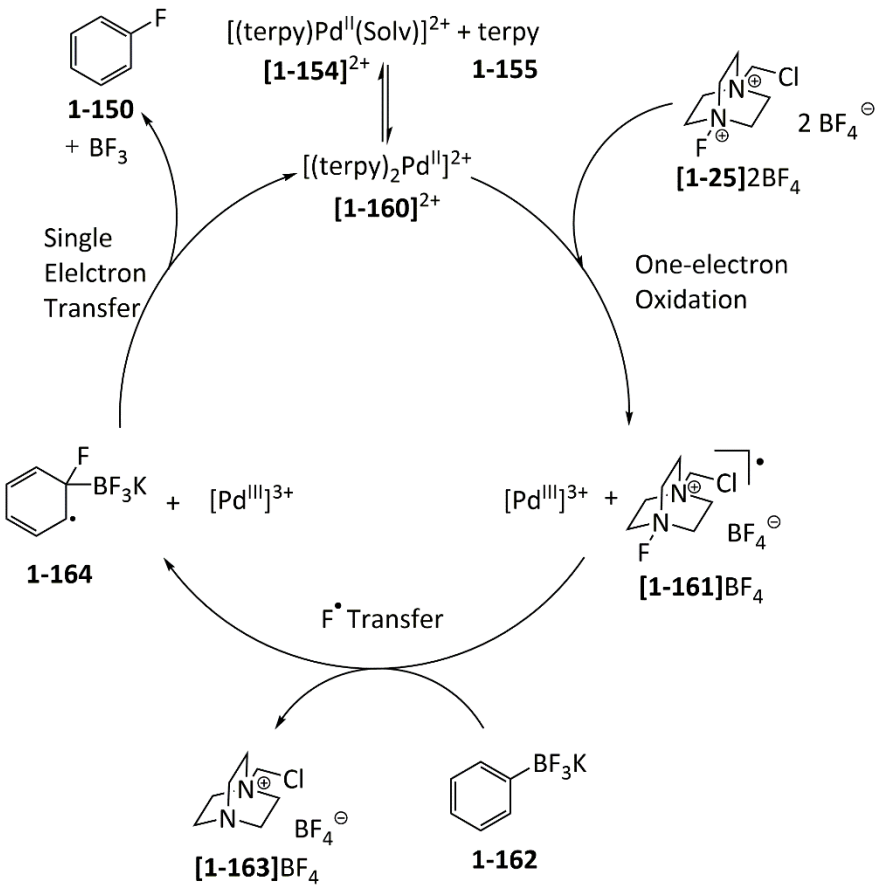

Scheme 204: Fluorination of aryl boronic acids was proposed to proceed through an SET mechanism in which radical fluorine transfer occurs between the substrate and reduced Selectfluor.[90]

In a more recent example Wu *et al*.[309] reported metal-free cyanofluorination of vinyl azides, in which Selectfluor was used as the oxidant to thermally generate cationic alkene radicals and provide a putative source of atomic fluorine. The addition of Selectfluor to aryl substituted vinyl azides afforded coloured solutions which were proposed to arise from the formation of an electron-donor-acceptor complex prior to electron transfer. The involvement of radicals was proposed on the inhibition of fluorination with TEMPO and ring-opening of a cyclopropyl substrate, **137**. The proposed mechanism consisted of SET from the alkene to Selectfluor in electron-donor-acceptor complex to afford the alkene radical and Selectfluor radical, which affords the fluorinated alkyl radical through in-cage fluorine transfer. However, it could not be ruled out that diffusion of the radical species away from one another is possible, with fluorination proceeding by fluorine abstraction from Selectfluor by the alkene radical in an out-of-cage pathway.

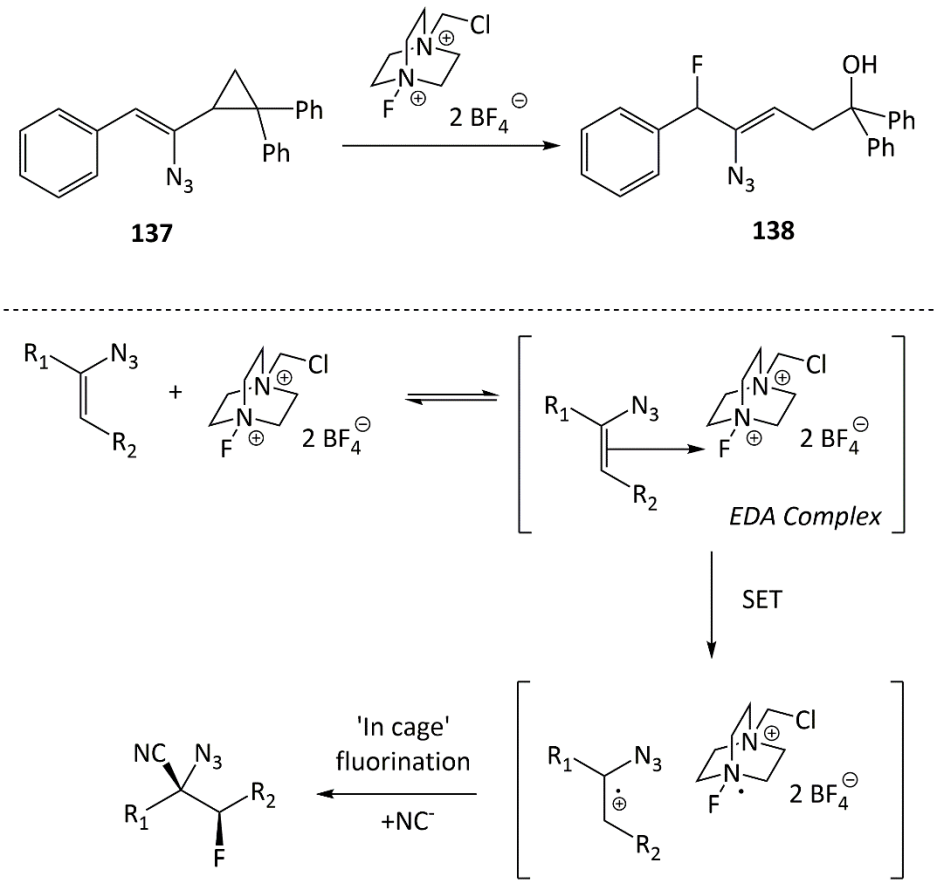

Scheme 205: An SET mechanism was proposed for *cis*-cyanofluorination based on the inhibition of fluorination with TEMPO and fluorination of 137 affording 138. Fluorination was proposed to proceed by formation of a EDA complex, SET and radical fluorine transfer in-cage.[309]

4.12.1 Potential Mechanisms for Fluorination

Based on the proposed mechanisms in the literature, fluorination of *trans*-[ClRu(dppe)$_2$(C≡CR)] complexes could proceed by two main mechanisms, S_N2 or SET. These mechanisms can be further separated into 'out of solvent cage' and 'in solvent cage' mechanisms (Scheme 206). The 'in cage' mechanisms involve fluorination occurring by a classic S_N2 (closed shell singlet) mechanism (Pathway A) or a rapid 'in cage' SET (short range diradical open shell) mechanism (Pathway B) in which oxidation of the alkynyl complex is indistinct from C-F bond formation. The S_N2 mechanism (Pathway A) proceeds by two-electron nucleophilic attack at the fluorinating agent by the ruthenium alkynyl complex. The fluorination pathway is independent of, and in competition with, the oxidation pathway. Pathway B proceeds *via* an SET between the alkynyl complex and the fluorinating agent to afford a putative fluorine radical which undergoes rapid radical recombination with the alkynyl radical within a solvent cage (i.e. putative fluorine radical reacts at a rate close to the diffusion limit) to afford the fluorovinylidene complex. Non-productive oxidation is proposed

to be the result of a long-range SET event in which the products from reduction of the fluorinating agents are not within proximity of the alkynyl ligand to react. Although the observation of ruthenium(III) alkynyl complexes experimentally could also arise from the species afforded by SET 'in-cage' diffusing apart rather than reacting, this scenario is believed to be unlikely given fluorine radicals are reported to react at rates nearing diffusion control (1×10^9 to 1×10^{11} s^{-1}).[341]

The 'out of cage' mechanisms (Pathways C and D, Scheme 206) involve oxidation and fluorination proceeding in distinct steps. In pathway C, reduction of the fluorinating agent affords a fluoride anion and the radical cation of the respective organic fragment, or a putative fluorine radical which is subsequently reduced to fluoride. Radical attack of fluoride by the ruthenium alkynyl radical and concurrent or concomitant oxidation affords the fluorovinylidene complex. Pathway D proceeds by two consecutive SETs to afford a ruthenium(IV) complex, fluoride, and the respective organic fragment. Nucleophilic attack of the ruthenium(IV) complex by fluoride generates the fluorovinylidene complex. Pathway E proceeds by non-productive oxidation of the alkynyl complex by the fluorinating agent to generate the ruthenium(III) alkynyl radical, which abstracts fluorine from unreacted fluorinating agents to afford the fluorovinylidene complex.

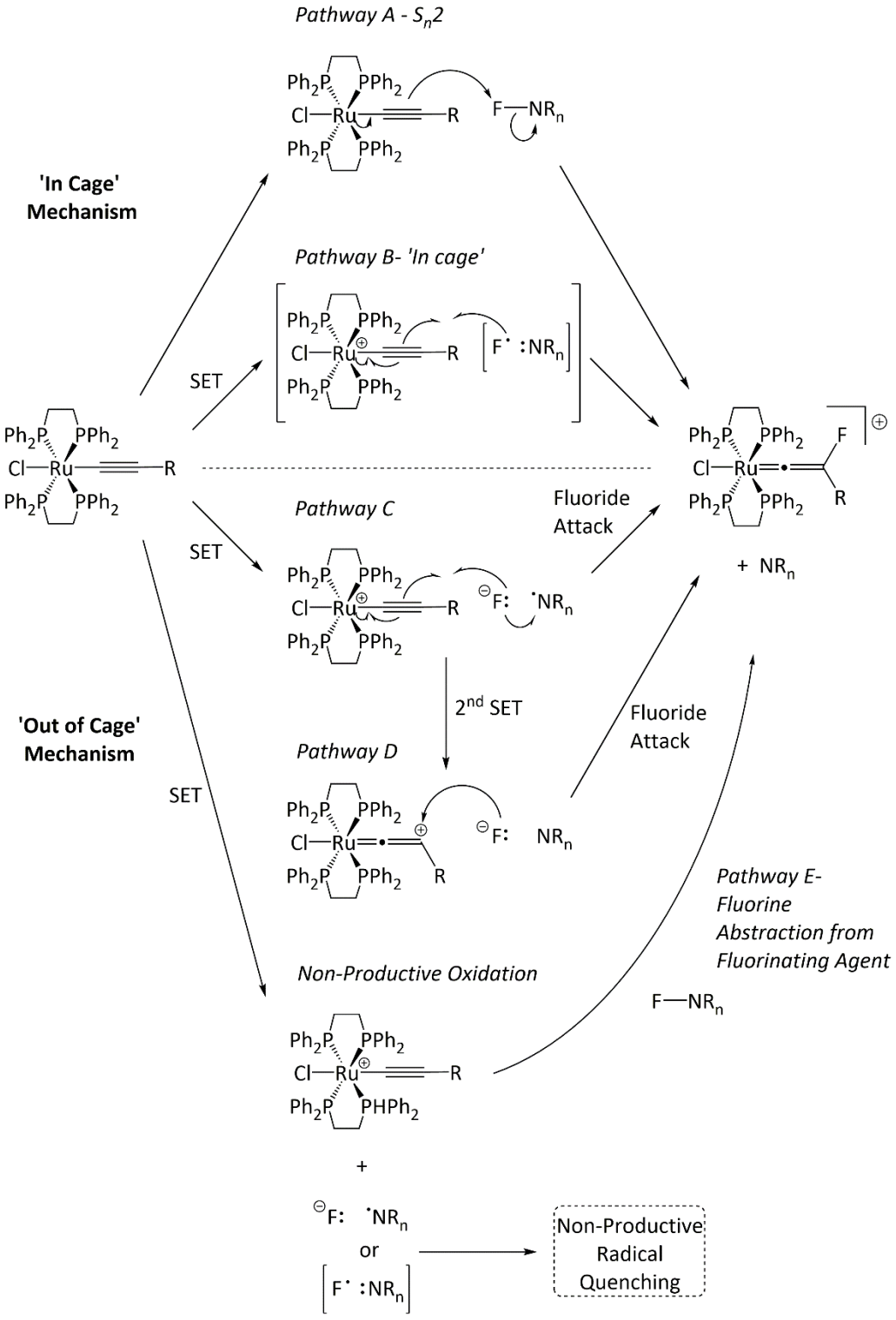

Scheme 206: Pathway A denotes a classic S_N2 mechanism in which the fluorinating agent undergoes nucleophilic attack by the ruthenium alkynyl complex with oxidation being a competing side-reaction. Pathways B-D denote SET mechanisms; pathway B proceeds by 'in-cage' radical recombination between the alkynyl radical and putative fluorine radical. Pathway C proceeds by reduction of the fluorinating agent to afford fluoride which reacts with the ruthenium(III) alkynyl radical to ultimately afford the fluorovinylidene complex. Pathway D proceeds by a second SET step which affords a ruthenium(IV) complex which undergoes nucleophilic attack by fluoride to afford the fluorinated product. Non-productive radical quenching or fluorination processes must occur to account for observation of ruthenium(III) alkynyl complexes.

4.12.2 Summary of Data and Mechanistic Discussion

The main experimental findings established from the work in this chapter are summarised below:

- Reactions of *trans*-[ClRu(dppe)$_2$(C≡CR)] (R = H, F, C_3H_5, C_6H_5, C_6H_4-4-OMe, C_6H_4-4-C(O)OMe, C_6H_4-4-C(O)Me, C_6H_4-4-NO_2) with Selectfluor in a 1:1 dichloromethane: acetonitrile solution gives **[57]**$^+$ and **[58]**$^+$.
- Reaction of **[57i]** with Selectfluor did not afford **[58i]**BF_4 but **[57i]**BF_4.
- Reactions of *trans*-[ClRu(dppe)$_2$(C≡CR)] (R = C_3H_5, C_6H_5, C_6H_4-4-NMe_2, C_6H_4-4-OMe, C_6H_4-4-C(O)OMe, C_6H_4-4-C(O)Me, C_6H_4-4-NO_2) with [FTMP]BF_4 or NFSI do not afford **[58]**$^+$, instead one electron oxidation to **[57]**$^+$ is observed.
- The reaction of **[57a]** and **[57b]** with NFSI afforded the fluorovinylidene complexes, **[58a]**NSI and **[58b]**NSI, respectively.
- The reaction of **[57a]** and **[57b]** with [FTMP]BF_4 does not result in fluorination but protonation and oxidation.
- The combined UV-Vis-NMR experiments reveal that decay of **[57c]**BF_4, **[57d]**BF_4, and **[57g]**BF_4, in the reaction of **[57]** with Selectfluor, does not correspond to formation of **[58]**BF_4.
- The IR spectra obtained after mixing **[57d]** with Selectfluor revealed fluorination occurs within *ca.* 15-20 seconds.
- The calculated Gibbs free energy for fluorination of **[57]** is thermodynamically favourable with all three fluorinating agents. But *ca.* 110 kJ mol^{-1} more favourable for fluorination by Selectfluor.
- Reaction of **[57c]**BF_4 with TBAF did not afford fluorovinylidene complex, **[58c]**$^+$.
- Reaction of **[57c]**$^{2+}$ with TBAF does not afford fluorovinylidene complex, **[58c]**$^+$.
- Fluorination of cyclopropyl-substituted alkynyl complex, **[57j]**, with Selectfluor afforded the fluorovinylidene complex, **[58j]**BF_4, with no evidence of ring-opening.
- Reaction of **[57c]**, **[57d]**, and **[57g]** with Selectfluor in the presence of the radical trap, TEMPO, still afforded **[58]**BF_4.
- Reaction of **[57c]** with Selectfluor in the presence BHT proceeded to form **[58c-h]**BF_4.
- The fluorination of **[57a]** by Selectfluor was not inhibited by addition of TEMPO or BHT.
- Fluorination was inhibited in the reaction of **[57a]** with NFSI in the presence of TEMPO and increased protonation observed with BHT.

It can be concluded from the reactions of the ruthenium(III) and ruthenium(IV) complexes of **[57c]** with fluoride, which did not exhibit fluorination, that out-of-cage pathways C and D are unlikely mechanisms for fluorination. Similarly, pathway E can be eliminated as the main mechanism for fluorination, as fluorination of **[57]** with 1.2 equivalents of Selectfluor affords the respective fluorinated vinylidene complexes in greater than 59 % in all cases. This narrows down the mechanism to either pathway A or pathway B.

The observation of fluorination with the most electron-deficient substrate **[57h]** by Selectfluor but not the most electron-rich substituent, **[57i]**, does not offer any clear evidence for either main mechanisms. If a two electron S_N2 mechanism was in effect, the most electron-rich substituent would be expected to be the most reactive toward an electrophile but also most easily oxidised, such that oxidation outcompetes fluorination. If an SET mechanism was in effect, the most electron-rich substituent would be expected to form the most stable, and therefore least reactive, radical alkynyl complex such that the products from SET diffuse away or react with neighbouring species, e.g. solvent or glass.

Further support for oxidation and fluorination being distinct processes was provided by monitoring the growth and decay of the radical alkynyl complexes of **[57c]**, **[57d]**, and **[57g]**, over one hour by UV-Vis spectroscopy and subsequently observing the conversion to the respective fluorovinylidene complex by NMR spectroscopy afterwards. The percentage change in the alkynyl radical over one hour was less than the percentage growth of fluorovinylidene complex observed by NMR spectroscopy. The experiments revealed that decay of the ruthenium(III) alkynyl radical does not correspond to fluorination, assuming a single mechanism for fluorination. The data suggests fluorination proceeds by an S_N2 or rapid SET mechanism (pathways A or B) and the radical alkynyl complex observed in the UV-Vis spectra corresponds to a competing side reaction.

Likewise, IR spectroscopy revealed that fluorination of **[57d]** had occurred within the 20 seconds of mixing the reagents and recording the spectra. This indicates that fluorination is fast relative to decay of the radical alkynyl complex and supports the conclusions made from the combined UV-Vis-NMR experiments. Stopped-flow IR spectroscopy may provide some kinetic data provided the alkynyl, alkynyl radical and fluorovinylidene complexes can be observed simultaneously which does not appear trivial by the preliminary investigation here.

The cyclopropyl-substituted alkynyl complex **[57j]** was found to fluorinate only with Selectfluor to afford **[58j]**BF_4. The absence of ring-opened fluorinated products could

indicate that an S_N2 mechanism is in effect, however the quasi-reversible nature of oxidation and lack of electron density on the cyclopropyl ring predicted by DFT indicate that ring opening is unlikely to occur on a short timescale. Consequently, mechanistic insight for fluorination is limited as evidence for a fast SET mechanism was unlikely to be observed.

Conducting the reactions of **[57c]**, **[57d]**, and **[57g]** with Selectfluor in the presence of TEMPO still enabled fluorination to be observed. Due to the competing reaction of TEMPO with Selectfluor, unreacted starting material was observed in addition to other minor species. The reaction of **[57c]** with Selectfluor in the presence of TEMPO or BHT afforded **[58c]**BF_4 as the only product, suggesting fluorination with Selectfluor proceeds by an S_N2 mechanism.

The reaction of **[57a]** with Selectfluor in the presence of TEMPO also afforded **[58a]**BF_4 along with additional minor species only observed with TEMPO. Again, it is difficult to draw a definitive conclusion on the mechanism since it is not known whether the minor products are produced from inhibition of fluorination or a side-reaction due to the reaction between TEMPO and Selectfluor. However, the reaction of **[57a]** with Selectfluor in the presence of BHT indicates that fluorination with Selectfluor proceeds by an S_N2 mechanism. In contrast, the fluorination of **[59]** with NFSI was almost completely inhibited by TEMPO and increased protonation was observed with BHT which could point toward an SET mechanism for NFSI.

Collectively the experiments suggest fluorination of *trans*-[ClRu(dppe)$_2$(C≡CR)] by Selectfluor proceeds by an S_N2 mechanism or a rapid 'in cage' SET mechanism which occurs too quickly to be observed with radical trapping experiments. Fluorination of **[57a]** with NFSI could proceed by an SET mechanism.

The formation of ruthenium(III) alkynyl complexes in the reaction with Selectfluor is therefore proposed to arise from long-range, non-productive, SET competing with fluorination. In the event of an 'in cage' SET mechanism, it is only when reduction of Selectfluor occurs in close proximity to the alkynyl ligand of the ruthenium complex does fluorination occur. Formation of alkynyl radicals are observed when reduction of Selectfluor does not occur in proximity of the alkynyl ligand and the putative fluorine radical quenches non-productively, e.g. proton abstraction.

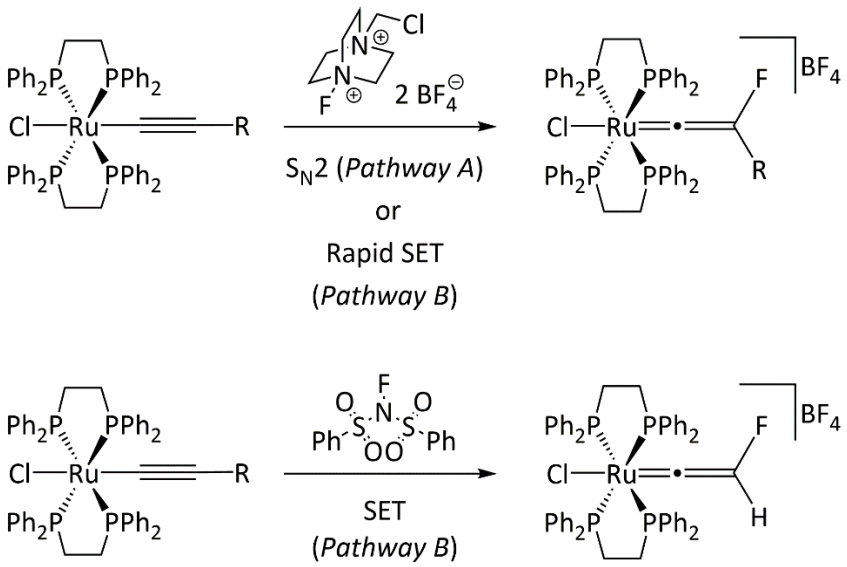

Scheme 207: Fluorination with Selectfluor is believed to proceed *via* an S_N2 mechanism or rapid SET mechanism while fluorination of [57a] with NFSI is believed to proceed by an SET mechanism.

It is unclear why different reactivity is observed between the use of Selectfluor, $[FTMP]BF_4$, or NFSI with *trans*-$[ClRu(dppe)_2(C{\equiv}CR)]$ complexes. The reactivity of fluorinating agents has previously been qualitatively attributed to their peak reduction potentials, due to the concerted cleavage of the N-F bond upon reduction; the more oxidising reagents being considered more reactive as demonstrated by their chemistry towards arenes. Therefore, Selectfluor would be expected to be the most reactive given it is most oxidising out of the three fluorinating agents used here. In this respect the argument stands true as fluorination of **[57b-h]** is only observed with Selectfluor. However, as reduction is associated with N-F bond cleavage this would also imply that fluorination should be expected with the use of $[FTMP]BF_4$ and NFSI, since oxidation of *trans*-$[ClRu(dppe)_2(C{\equiv}CR)]$ complexes is observed with both reagents.

In the case of **[57a]** and **[57b]**, fluorination is observed with NFSI but not $[FTMP]BF_4$; based on the peak reduction potentials recorded for $[FTMP]BF_4$ and NFSI (-1.47 V and -1.85 V, respectively, vs Fc in 1:1 DCM:MeCN), fluorination with $[FTMP]BF_4$ would have been expected if reactivity was proportional to oxidising ability only. The difference in oxidising power between the three electrophilic fluorinating agents appears unimportant for fluorination in this system.

The peak oxidation potentials of **[57a]** and **[57b]** overlap with the redox potentials for **[57d]**, **[57e]**, and **[57f]**. It therefore appears that the oxidation potential of the ruthenium alkynyl

complex does not, at least solely, explain differences in reactivity between complexes **[57c-j]** with NFSI compared to complexes **[57a]** and **[57b]**.

Thermodynamically, fluorination is calculated to be favourable for all *trans*-[ClRu(dppe)$_2$(C≡CR)] complexes studied here with all three electrophilic fluorinating agents. It is possible that the increased favourability of fluorination with Selectfluor compared to [FTMP]BF_4 and NFSI (*ca*. 110 kJ mol^{-1}) is a contributing factor for differences in reactivity.

Due to the radical trap experiments indicating fluorination of **[57a]** with NFSI may occur by an SET mechanism, the lack of fluorination in the reactions of NFSI with **[57c-j]** could be rationalised by the difference in reactivity between the ruthenium(III) alkynyl complexes. Unlike **[57a]**$^+$ and **[57b]**$^+$, protonation of **[57c-j]**$^+$ is not observed in the reactions with NFSI or [FTMP]BF_4, suggesting the radical cations of **[57c-j]** are less reactive compared to **[57a]**$^+$ and **[57b]**$^+$. This is further supported by their different electrochemical behaviour. However, given the high reactivity of fluorine radicals, the difference in reactivity of the ruthenium(III) alkynyl complexes is an unlikely reason for fluorination not being observed in the reaction of **[57c-j]** with NFSI. It is more likely the differences in reactivity between the three fluorinating agents and *trans*-[ClRu(dppe)$_2$(C≡CR)] complexes are due to steric factors as much as electronic factors. Given the β-carbons of the protio- and fluoro-substituted alkynyl ligands of **[57a]** and **[57b]** respectively, are less sterically shielded than the cyclopropyl- and aryl-substituted ligands of **[59c-j]**, it would be expected that **[57a]** and **[57b]** are more susceptible to attack.

It is surprising that [FTMP]BF_4 does not fluorinate the *trans*-[ClRu(dppe)$_2$(C≡CR)] complexes studied in this chapter given **[57a]** and **[57b]** were capable of being fluorinated by NFSI. Instead only protonation of **[57a]** and **[57b]** was observed with [FTMP]BF_4 by NMR spectroscopy. This may imply that the steric properties of the fluorinating agent are also an important factor in determining whether fluorination proceeds or not. The two *ortho*-methyl groups of [FTMP]BF_4 would be expected to hinder the ability to deliver fluorine close to the alkynyl ligand which, in the case of an S_N2 mechanism, would favour oxidation over fluorination, and in an SET mechanism, would increase the probability of non-productive SET. This may account for the absence of fluorinated products even with the least sterically encumbered alkynyl complexes, **[57a]** and **[57b]**.

The absence of fluorination in the reaction of **[57i]** with any three of the fluorinating agents could be rationalised by the ease with which the complex can be oxidised. In this instance the steric influence of the alkynyl ligand is unlikely to contribute significantly due to the fluorination of **[57e]** and **[57f]** being observed with Selectfluor. This fits with a mechanistic picture in which the balance between fluorination and one-electron oxidation is controlled by both the nature of the fluorinating agent and the alkynyl complex. It was noted by Differding and Wehrli that fluorination did not proceed in the reaction of **126** with tetramethylphenyldiamine, instead they observed only one electron oxidation.[342]

4.13 Conclusion

The fluorination of ruthenium alkynyl complexes has been expanded to include ruthenium(II) bis-dppe alkynyl complexes bearing cyclopropyl and both electron-donating and withdrawing aryl substituents, in addition to the fluorination of **[57a]** and **[57b]** demonstrated in Chapter 2. Fluorination proceeded with Selectfluor to afford the respective fluorovinylidene complexes, **[58]**BF_4, with the exception of **[57i]**, which was found to undergo one electron oxidation instead according to UV-Vis and EPR spectroscopy. The work highlights the duality of fluorinating agents acting both as oxidants and a source of electrophilic fluorine.

The NMR and UV-Vis spectroscopic data obtained for **[58]**BF_4 revealed trends that reflected the electronic property of the vinylidene substituent. The chemical shifts for the vinylidene α- and β-carbon atoms, as well as the phosphorus chemical shift, shifted downfield with more electron-withdrawing substituents. Likewise, the HOMO→LUMO transition shifts to higher energy wavelength the more electron-deficient the vinylidene is. In contrast the vinylidene C=C stretching frequency did not appear to follow any trend in electronic property and was reflected in the predicted values calculated by DFT. Similarly, the crystal-structures of **[58]**PF_6 did not display many statistically significant trends in bond metrics with differing electronic property of the aryl substituent due to crystal packing effects.

In contrast to the fluorination of ruthenium half-sandwich alkynyl complexes (e.g. **[14]** and **[77]**), which were capable of undergoing fluorination with the addition of NFSI, [FTMP]BF_4, or Selectfluor, the choice of fluorinating agent was significant in determining the reactivity with the *trans*-[ClRu(dppe)$_2$(C≡CR)] complexes. Fluorination of **[57a-h]** and **[57j]** was only observed spectroscopically with Selectfluor, while the reactions with [FTMP]BF_4 and NFSI resulted in one-electron oxidation rather than fluorination according to UV-Vis, EPR, and NMR spectroscopy. Fluorination of **[57a]** and **[57b]** was also achieved with NFSI, with competing protonation also being observed in the reaction with **[57a]**. The reaction of **[57a]** and **[57b]** with [FTMP]BF_4 afforded only the protonated products **[59]**BF_4 and **[58a]**BF_4 respectively. To identify the species observed in the UV-Vis spectra from the reaction of **[57a]** with NFSI and [FTMP]BF_4, the rational synthesis and characterisation of **[123]** needs to be undertaken.

Fluorination of **[57a-h]** with Selectfluor is believed to proceed by an S_N2 or rapid 'in cage' SET mechanism on the basis of the radical trap and UV-Vis-NMR experiments. The fluorination

of **[57a]** with NFSI in the presence of TEMPO and BHT suggests fluorination proceeds by an SET mechanism. Future work includes expanding the UV-Vis-NMR experiments to include the reactions of **[57a]**, and **[57b]** with Selectfluor and NFSI to confirm whether the radical trap experiments suggest the correct mechanisms for fluorination. Likewise, the reactions of *trans*-[ClRu(dppe)$_2$(C≡CR)] complexes with Selectfluor conducted with a radical trap should be monitored by a UV-Vis-NMR experiment to compare with the results obtained in the absence of a radical trap. Studying fluorination by stopped-flow IR spectroscopy or an *in-situ* IR probe, may provide kinetic data in which the mechanism can be elucidated.

Further work also includes conducting a mechanistic study on the fluorination of ruthenium half-sandwich alkynyl complexes such as **[77]** to determine whether fluorination proceeds by an S_N2 mechanism or an SET mechanism. Preliminary work found that a radical species was detected by EPR spectroscopy in the fluorination of **[77]** with Selectfluor, which could imply a radical mechanism. Unlike the fluorination of **[57]**, there was no clear evidence for radical alkynyl complex by UV-Vis spectroscopy indicating the radical either forms in concentrations too low to be detected on the scale of the reaction or is highly reactive and quickly quenches *via* either productive or non-productive pathways. Additional work involves studying the fluorination of **[77]** with NFSI and [FTMP]BF_4 by UV-Vis and EPR spectroscopy.

Distinguishing or obtaining direct evidence of fluorination proceeding by either a classical S_N2 or 'in cage' SET mechanism will be challenging experimentally, given that elemental fluorine reportedly reacts with solvent at a rate between 1 x 10^9 and 10^{11} s^{-1}.[341] Probing the fluorination of ruthenium alkynyl complex by DFT could provide valuable insight into the favourability of an S_N2 or closed shell mechanism, versus an 'in cage' SET or open shell mechanism.

Chapter 5. Computational Studies of the OSEF Mechanism in *trans*-[ClRu(dppe)$_2$(C≡CR)] Complexes

5.1 Introduction

The observation of one electron oxidation in the reaction of **[57]** with electrophilic fluorinating agents, discussed in Chapter 4, suggests that fluorination might proceed by an SET mechanism. As the experimental data did not allow distinction between an S_N2 or a rapid 'in-cage' SET mechanism in the fluorination of [ClRu(dppe)$_2$(C≡CR)] by Selectfluor, it was envisaged that DFT studies of this system might provide additional insight. Additionally, it was hoped that insight could be gained as to why fluorination is not observed with [FTMP]BF_4 or NFSI for the aryl substituted [ClRu(dppe)$_2$(C≡CR)] complexes.

As mentioned at the start of Chapter 2, Milner *et al*.[223, 225] reported the OSEF of a ruthenium metallocycle, **[16]**, which afforded the fluorinated product **[17a]**BF_4 (Figure 98). The formation of **[17a]**BF_4 could be rationalised by either the formation of a ruthenium fluoride intermediate or direct fluorination of the ligand. The DFT study conducted revealed that the formation of a ruthenium-fluoride intermediate was thermodynamically favourable ($\Delta E_{SCF+ZPE}$ = -158 kJ mol^{-1}) but the barrier to formation **[17a]**$^+$ was significantly high ($\Delta E_{SCF+ZPE}$ = 160 kJ mol^{-1}). In addition to calculating the energies of a ruthenium-fluoride pathway, Milner *et al*.[223, 225] used relaxed potential energy surface (PES) scans to study the barriers for direct fluorination of **[16]** along a single reaction coordinate. This reaction coordinate was defined as the distance between the fluorine of [FTMP]BF_4 and the 2-position of the ruthanindolizine ring in **[16]**. In addition to a closed-shell PES scan, representing S_N2-type attack of the fluorinating agent by the metallocycle, a singlet open-shell PES was also constructed, which relates to an SET-type mechanism whereby fluorination occurs *via* a diradical intermediate.

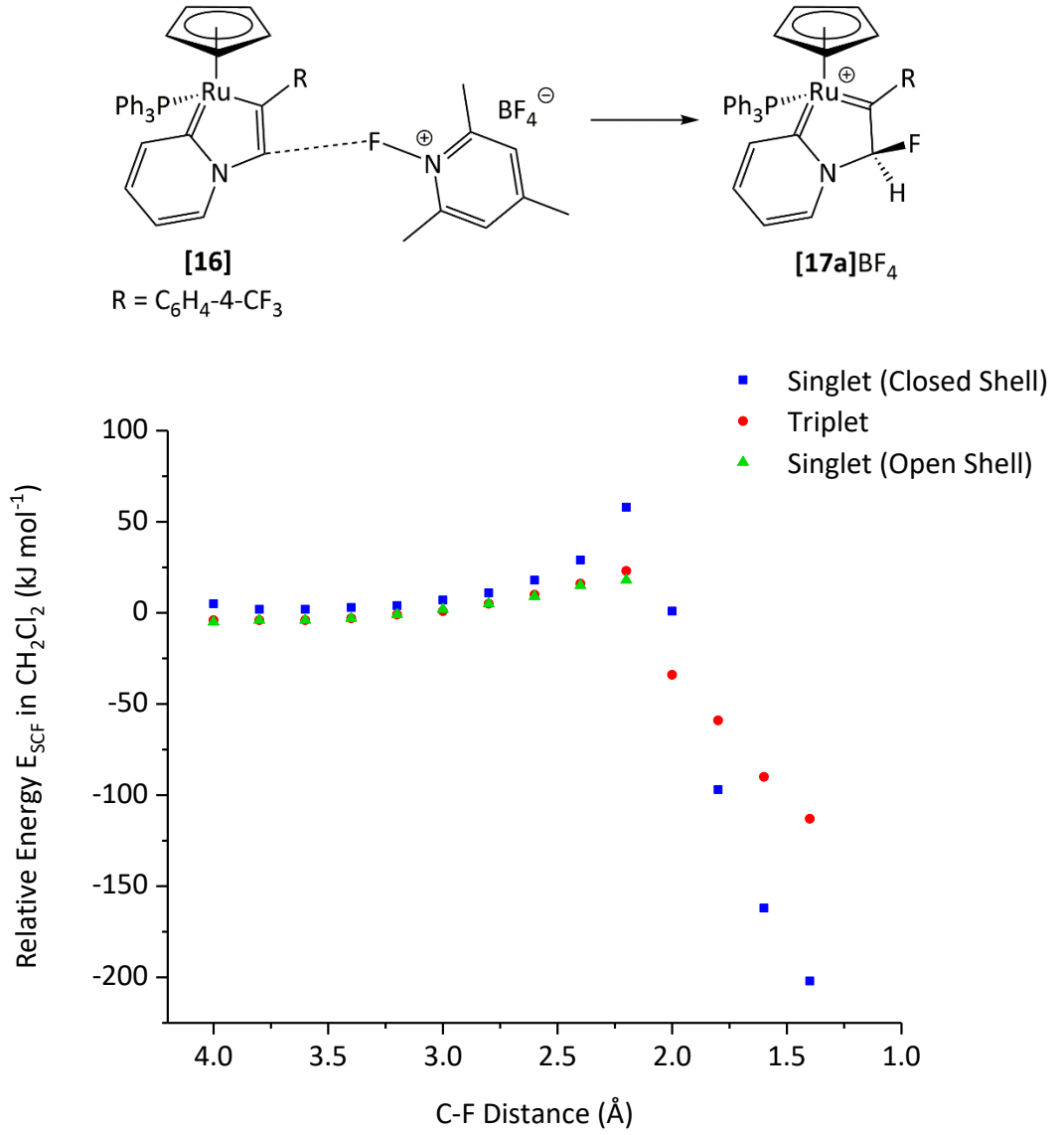

Figure 98: Relaxed PES scans reported by Milner *et al.*[225] for the direct fluorination of [16] by [FTMP]BF_4.

The low energy barriers ($\Delta E_{SCF\text{-}DCM}$ = 58 and 23 kJ mol^{-1} for the singlet closed-shell and singlet open-shell respectively) obtained from the PES scans supported the conclusion that fluorination occurs by direct attack of the ligand rather than formation of a ruthenium-fluoride intermediate. Additionally, the PES scans also suggested that the singlet diradical proceeded *via* a lower energy transition state than the singlet closed-shell configuration. This suggested that fluorination may occur by an SET mechanism.

It was envisaged that performing relaxed PES scans for the S_N2 and SET pathways for the fluorination of *trans*-[ClRu(dppe)$_2$(C≡CR)] complexes, using the approach employed by Milner *et al*., would provide insight into which mechanism of fluorination is favoured in this system. In addition, it was hoped that the relaxed PES scans could provide insight as to why

fluorination of aryl substituted alkynyl complexes only proceeds with Selectfluor and not with [FTMP]BF_4 or NFSI. The phenyl-substituted alkynyl complex, **[57b]**, was chosen as the model complex to be investigated, due to it being an electronic midpoint within the range of aryl substituted complexes of **[57]** studied experimentally (from C_6H_4-4-OMe to C_6H_4-4-NO_2).

5.2 Brief Introduction to Computational Chemistry

This first section provides a brief introduction to computational chemistry describing the fundamentals of the Hartree-Fock (HF) method, and density functional theory (DFT) methods.

5.2.1 The Schrödinger Equation and Born-Oppenheimer Approximation

The Schrödinger equation is a second-order differential equation from which the energy and wavefunction of a system can be calculated. The time-dependent Schrödinger equation involves differentiation with respect to both time and position and is given by:[343]

$$\hat{H}(\mathbf{r},\mathrm{t})\Psi(\mathbf{r},\mathrm{t}) = i\frac{\partial\Psi(\boldsymbol{r},t)}{\partial t}$$

Where the Hamiltonian, $\hat{H}$ is given by:

$$\hat{H}(\mathbf{r},\mathrm{t}) = \mathbf{T}(\mathbf{r}) + \mathbf{V}(\mathbf{r},\mathrm{t})$$

Where **T** is the kinetic energy term of all particles and **V** is the potential energy term containing all attractive and repulsive interactions between all particles. The time and position dependency of the time-dependent Schrödinger equation can be separated when the system is in a stationary state, at which point the potential energy operator is time independent. As result the Hamiltonian also becomes time independent, with the total energy of the system being constant and dependant on spatial variables only.[343] This affords the time independent Schrödinger equation:

$$\hat{H}(\mathbf{r})\Psi(\mathbf{r}) = E(\boldsymbol{r})\Psi(\boldsymbol{r})$$

The Hamiltonian operator, $\hat{H}$, contains the both the kinetic (**T**) and potential (**V**) energies of all particles (*N*) in the system.

$$\hat{H}(\mathbf{r}) = \mathbf{T}_{\boldsymbol{e}}(\mathbf{r}) + \mathbf{T}_{\boldsymbol{n}}(\mathbf{r}) + \mathbf{V}_{\boldsymbol{ee}}(\mathbf{r}) + \mathbf{V}_{\boldsymbol{nn}}(\mathbf{r}) + \mathbf{V}_{\boldsymbol{ne}}(\mathbf{r})$$

Where T_n is the nuclear kinetic energy, T_e is the electron kinetic energy, V_{ee} is the electron-electron repulsion potential, V_{nn} is the nucleus-nucleus repulsion potential, and V_{ne} is the nucleus-electron attraction potential.

In which the total kinetic energy is given by the sum of the individual kinetic energies of each nucleus and electron:

$$\mathbf{T_e} = -\sum_{i=1}^{n} \frac{1}{2m_i} \nabla_i^2$$

$$\mathbf{T_n} = -\sum_{A=1}^{N} \frac{1}{2M_A} \nabla_A^2$$

$$\nabla^2 = \left(\frac{\partial^2}{\partial x^2} + \frac{\partial^2}{\partial y^2} + \frac{\partial^2}{\partial z^2} \right)$$

Where the Laplace operator, or 'del' squared, is a second order deferential operator acting upon the coordinates of the particle. Likewise, the potential energy is defined as the summation of all potential energy terms acting on/between *N* particles; on the molecular level the potential energy is defined as the coulomb potential.

$$\mathbf{V_{ee}} = \sum_{i<j}^{n} \frac{1}{r_{ij}}$$

$$\mathbf{V_{nn}} = \sum_{A<B}^{N} \frac{Z_A Z_B}{R_{AB}}$$

$$\mathbf{V_{ne}} = -\sum_{A=1}^{N} \sum_{i=1}^{n} \frac{Z_A}{r_{iA}}$$

The large mass difference between nuclei and electrons indicate that nuclei move at velocities much slower than electrons and that electrons respond rapidly to changes in nuclear geometries. As such the nuclei are considered stationary from the electronic point and coupling between the electron and nuclear velocities (kinetic energies) is neglected. The electronic wavefunction depends on the position of the nuclei, but not their momentum; this is known as the Born-Oppenheimer approximation.[343]

$$\hat{H}_{tot} \Psi_{tot}(\mathbf{R}, \mathbf{r}) = E_{tot}(\mathbf{R}, \mathbf{r}) \Psi_{tot}(\mathbf{R}, \mathbf{r})$$

$$\widehat{H}_{tot} = \boldsymbol{H}_e + \boldsymbol{T}_n$$

$$\Psi_{tot}(\mathbf{R}, \mathbf{r}) = \Psi_e(\mathbf{R}, \mathbf{r})\Psi_n(\mathbf{R})$$

As such the electronic wavefunction can be separated from nuclear motion, allowing the Schrödinger equation to be simplified into the electronic Schrödinger equation:

$$\boldsymbol{H}_e\Psi_e(\mathbf{R}, \mathbf{r}) = E_e(\boldsymbol{R})\Psi_e(\mathbf{R}, \mathbf{r})$$

Where $\mathbf{H}_e$ is the electronic Hamiltonian given by the electron kinetic energy, nucleus-electron potential energy, electron-electron repulsion, and the nucleus-nucleus repulsion:

$$\boldsymbol{H}_e = \boldsymbol{T}_e + \boldsymbol{V}_{ne} + \boldsymbol{V}_{ee} + \boldsymbol{V}_{nn}$$

Thus, the electronic wavefunction Ψ_e, depends only on the position of the nuclei and not their kinetic energy ($\boldsymbol{T}_n$ becomes a constant). Solving the electronic Schrödinger equation affords the electronic energy. Reintroduction of the nuclear kinetic energy into the equation allows the total energy of the system to be determined, where the electronic energy becomes the potential energy:

$$(\boldsymbol{T}_n - \mathrm{E}_e(\mathbf{R}))\Psi_n(\mathbf{R}) = E_{tot}\Psi_n(\mathbf{R})$$

Solving the nuclear wavefunction Ψ_n allows the molecular rotational and vibrational energy levels to be calculated.[343]

5.2.2 Self-Consistent Field Theory

The Schrödinger equation can only be solved exactly for $H^{\cdot}$, H_2^+ and other one-electron systems, for an *N* body system the Schrödinger equation has to be solved numerically (approximately). One of the simplest methods of approximating the solution to the time-independent Schrödinger equation of an *N*-body system is by the Hartree-Fock method.[343]

To solve the electronic Schrödinger equation for an *N*-electron system by the Hartree-Fock method, the electronic wavefunction is assumed to be describable by a single determinant containing an *N* number of one electron wavefunctions or orbitals, known as a Slater determinant. The one-electron functions obtained from expansion of the Slater determinant describe the molecular orbitals (ϕ), or spin orbitals, which are the product of the spatial orbitals and a spin function (α or β).[343]

$$\Psi(1,2,\dots,N) = \frac{1}{\sqrt{N!}}\begin{bmatrix} \Phi_a^{\alpha}(1) & \Phi_a^{\beta}(1) & \cdots & \Phi_z^{\beta}(1) \\ \Phi_a^{\alpha}(2) & \Phi_a^{\beta}(2) & \cdots & \Phi_z^{\beta}(2) \\ \vdots & \vdots & \ddots & \vdots \\ \Phi_a^{\alpha}(N) & \Phi_a^{\beta}(N) & \cdots & \Phi_z^{\beta}(N) \end{bmatrix}$$

Expansion of the Slater determinant satisfies the antisymmetry requirement, since any two electrons occupying the same orbital with the same spin provide a value of zero (Pauli exclusion principle). A consequence of the wavefunction being described by a single Slater determinant is that the real electron-electron interaction is neglected. Instead each electron is assumed to move independently of each other and only experiences the average effect of all other electron. As such the Hartree-Fock method is considered a mean field theory or independent particle model.[343]

The Hartree-Fock method approximates solutions to the Schrödinger equation by the variation principle, which states that an approximate wavefunction affords an energy which is always equal to or greater than the true energy of the system. The true energy is only given by the exact wavefunction; varying the parameters to generate a better approximation of the wavefunction will afford an energy which is closer to the true energy and a wavefunction that is closer to the true wavefunction. Since the wavefunction can be described by the product of the one electron molecular orbitals, then the correct molecular orbitals are those that that minimise the energy. As such the optimised molecular orbitals must satisfy the Hartree-Fock equations, which are a modified version of the time independent Schrödinger equation:

$$\boldsymbol{F_i}\Phi_i = \varepsilon_i\Phi_i$$

The Fock operator ($\boldsymbol{F_i}$) acting on the molecular orbitals provides the orbital energies as elements in the matrix. The Fock operator itself is a single-electron energy operator describing the kinetic energy of an electron and the attraction to all nuclei ($\boldsymbol{T_i}$), as well as the repulsion to all other electrons ($\boldsymbol{J_{ij}}$-$\boldsymbol{K_{ij}}$). However, electron-electron repulsion is only considered as an average potential and electron correlation is neglected.[343]

$$\boldsymbol{F_i} = \boldsymbol{T_i} + \sum_{j}^{N_{elec}} (\boldsymbol{J}_{ij} - \boldsymbol{K}_{ij})$$

The total energy of the system is given by the sum of all the orbital energies, the nuclear-nuclear repulsion energy, and subtraction of the sum of all electron-electron repulsion, since electron-electron repulsion is given twice by summation of the orbital energies:

$$E = \sum_{i}^{N_{elec}} \varepsilon_i - \frac{1}{2} \sum_{ij}^{N_{elec}} (J_{ij} - K_{ij}) + V_{nn}$$

$$\varepsilon_i = T_i + \sum_{j}^{N_{elec}} (J_{ij} - K_{ij})$$

For small symmetric systems, molecular orbitals can be obtained by mapping orbitals onto a grid and integrating. Usually, however, molecular orbitals are expressed in terms of a linear combination of basis functions, or atomic orbitals, which are contained within a basis set.[343]

$$\Phi_i = \sum_{o}^{M_{basis}} c_{oi} \chi_o$$

Where the M_{basis} is the size of the basis set, c_{oi} are the MO coefficients, and χ_o are atomic orbitals.

A basis set containing an infinite number of functions is said to be complete and results in the closest approximation of the true wavefunction. In the case of Hartree-Fock this represents the best single-determinant wavefunction (as the wavefunction is assumed to be represented by a single Slater determinant) and known as the Hartree-Fock limit. A larger basis increases the number of basis functions, allowing the accuracy in which the molecular orbitals are described, and consequently the wavefunction, to be improved. However, a large basis set also increases the computational expense by a power of four for HF methods. This often means a comprise is made between basis set completeness and computational time. With a sufficiently large basis set the Hartree-Fock wavefunction can account for up to 99% of the total energy, with the remaining 1 % corresponding to the motion of interacting electrons (electron correlation energy). However, the remaining 1% is important for describing chemical processes. Post-Hartree-Fock methods, such as configuration interaction (CI), Möller-Plesset perturbation theory (MP2, MP3, MP4…), and coupled-cluster (CC), have been developed to approximate the electron-correlation energy of the system but with increased computational expense (Table 30).[343]

Table 30: Computational expense of wavefunction methods

Method	Cost
HF	N^4
MP2	N^5
MP3	N^6
CISD	N^6
CCSD(T)	N^7

The energy of the system is minimised by optimising the orbitals such that the energy of the Slater determinant is lowered. This is achieved by determining the orbital coefficients through formation of a Fock matrix and diagonalizing. However, construction of the Fock matrix requires all the MO coefficients to be known. Therefore, minimisation of the energy is an iterative process in which the coefficients from an initial guess (based on the same kind of analysis of the input geometry) are used to construct a Fock matrix from which new orbital coefficients can be obtained. These new coefficients are then used to form a new Fock matrix to generate better coefficients etc. Convergence is achieved when coefficients obtained from the Fock matrix are within the threshold value of the original coefficients used to construct the matrix, i.e. eigenvalues and are self-consistent, allowing the self-consistent field solution to the wavefunction to be determined (Figure 99).

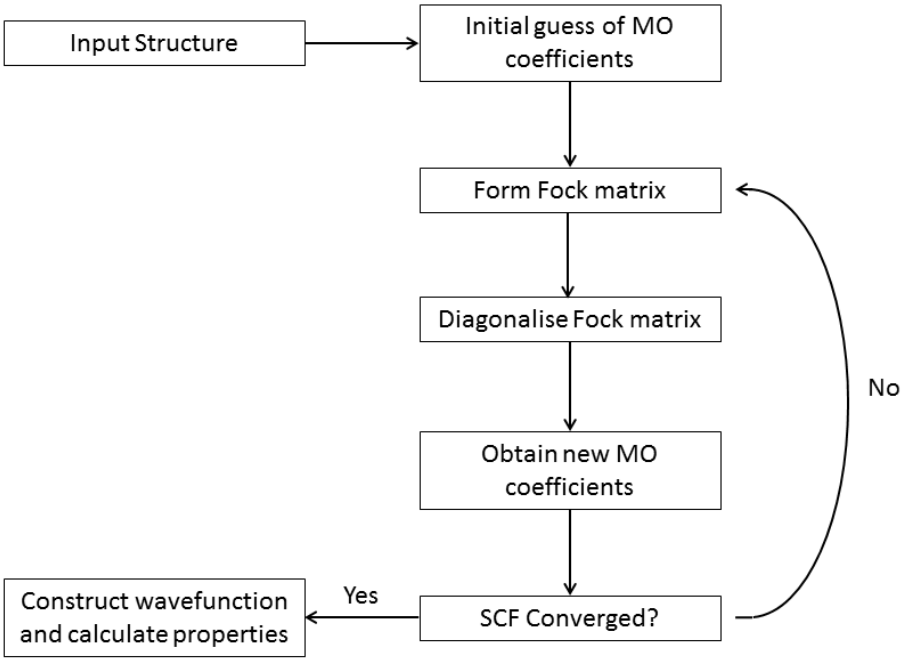

Figure 99: Illustration of SCF procedure.

The matrix form of the Hartree-Fock equations is given by the Roothaan-Hall equations:

$$\boldsymbol{FC} = \boldsymbol{SC\varepsilon}$$

Where **F** is the Fock matrix, **S**, is the matrix of overlay integrals, **C**, is the matrix formed from the orbital coefficients, and **ε** is the matrix of orbital energies.[343]

5.2.3 Restricted and Unrestricted Hartree-Fock

As mentioned above, the Slater determinant used to describe the wavefunction is written in terms of the spin-orbitals whereby one orbital is multiplied by a spin function to denote the α- and β- electrons occupying it. In a closed-shell system, where the number of electrons is even and has a singlet wavefunction, the restriction that each MO contains one α- and one β-electron is made; this scenario is referred to as a restricted Hartree-Fock (RHF) wavefunction.[343]

In an open-shell system, two types of wavefunctions can be used, a restricted open-shell Hartree-Fock (ROHF) wavefunction or an unrestricted Hartree-Fock (UHF) wavefunction. A restricted open-shell Hartree-Fock wavefunction restricts the doubly occupied spatial orbitals to be same. The unrestricted Hartree-Fock wavefunction places no restriction on spatial orbitals and allows different spatial orbitals to be used for α- and β- electrons (for example the UHF doublet in Figure 100). This is sometimes referred to as 'different orbital for different spins' (DODS). The UHF wavefunction provides different optimised α- and β-spin orbitals due to the unpaired electron(s), with a particular spin, interacting differently with the other α- and β- electrons. Since there is no restriction each one electron orbital is optimised individually. As a consequence, the UHF wavefunction is always lower, or equal to, in energy as the ROHF wavefunction.[343]

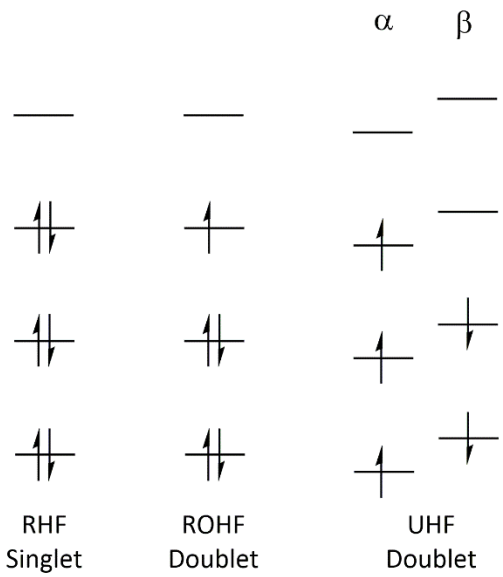

Figure 100: Representation of restricted Hartree-Fock singlet, restricted open-shell Hartree-Fock and unrestricted Hartree-Fock doublet state.

The drawback of using an UHF wavefunction is that it is not an eigenfunction of the spin operator squared, $\langle S^2 \rangle$ (where the operator evaluates the total spin of the system). Consequently, contributions from higher multiplicity states (e.g. triplets and quintets for singlet states; quartets and sextets for doublet states etc.) may be incorporated into the wavefunction, which is known as spin contamination. The amount of spin contamination is given by the deviation of the S^2 value from that of a pure spin state (S(S+1) i.e. 0 for a singlet state). The larger the deviation from the theoretical value the greater the spin contamination.[343]

5.2.4 Density Functional Theory

Density functional theory is based upon the proof of the Hohenburg-Kohn theorem that the electron density, ρ, of the system completely determines the ground state electronic energy, i.e. the energy is a functional of electron density.[344] The theorem showed that the integral of electron density defines the number of electrons and that the electron density defines nuclei position (cusps in the electron density) and charges (height of the cusps), thus the Hamiltonian operator can be determined. DFT methods use a functional (function of functions) to relate the electron density to the energy of the system. Knowing the exact energy functional allows the exact ground state energy of the system to be determined from the ground state electron density.[343]

In the wavefunction approach, e.g. Hartree-Fock theory, the wavefunction of an *N*-electron system depends on 4*N* variables, the three spatial and one spin coordinate per electron. The larger the system, the more complex the wavefunction becomes to approximate. In contrast, the electron density is dependant only on three spatial coordinates and is independent of the system size, which significantly reduces the dimensional complexity. However, earlier DFT methods provided poor approximations for the kinetic energy.[343] Instead modern DFT methods are based upon the inclusion of orbitals to more accurately calculate the kinetic energy, as suggested by Kohn-Sham.[345] This results in Kohn-Sham (KS) DFT methods being dependent on 3*N* variables rather than 3 for true DFT methods. However, these modern DFT methods are still less complicated than many-particle wavefunction methods (4*N*). Kohn-Sham DFT (referred to simply as DFT in this thesis) is similar to the Hartree-Fock method both conceptually and computationally; they both use identical formulae to calculate the kinetic, nuclear-electron and electron-electron coulomb energies, and are both solved iteratively to minimise energy. The main difference being that an exchange-correlation term is used in DFT, whereas correlation energy is neglected in the Hartree-Fock method.

Kohn-Sham DFT splits the true kinetic energy functional (T[ρ]) into two parts, one of which can be calculated exactly (as in Hartree-Fock with non-interacting electrons and the energy given by a single Slater determinant), $T_s[\rho]$, and the other a kinetic correlation energy correction ($T[\rho]$-$T_s[\rho]$) which is unknown and included in the exchange-correlation functional. The general energy expression in DFT is given by:

$$E_{DFT}[\rho] = T_S[\rho] + E_{ne}[\rho] + J[\rho] + E_{xc}[\rho]$$

Where $E_{DFT}[\rho]$ is the functional relating energy to electron density, $E_{ne}[\rho]$ is the functional for nuclear-electron attraction, $J[\rho]$ is the functional describing the electron-electron coulomb repulsion, and $E_{xc}[\rho]$ is the functional describing both the kinetic correlation energy and the potential correlation and exchange energies.

$$E_{xc}[\rho] = (T[\rho] - T_S[\rho]) + (E_{ee}[\rho] + J[\rho])$$

The exchange-correlation term of the energy functional is not known and has to be approximated by the use of an electron exchange-correlation functional.[343]

The electron density can be obtained by solving an *N* number of one-electron equations known as the Kohn-Sham equations, which are a set of pseudo-eigenvalue equations similar to the Hartree-Fock equations:

$$\hat{\mathrm{h}}_{ks}\Phi_i = \varepsilon_i\Phi_i$$

Where $\hat{\mathrm{h}}_{KS}$ a one-electron operator which contains the kinetic energy, $\frac{1}{2}\nabla^2$, and effective potential terms, V_{eff}. The effective potential consists of the nuclear contributions, the electron-electron repulsion and exchange correlation potentials.[343]

$$\hat{\mathrm{h}}_{hs} = \frac{1}{2}\nabla^2 + \hat{V}_{eff}$$

While ε_i is the one-electron energy and ϕ_i is the kohn-sham orbital, which is an expansion of the atomic orbitals in an M size basis set:

$$\Phi_i = \sum_{\alpha}^{M_{basis}} c_{\alpha i}\chi_i$$

The KS orbitals are constructed from a basis set of atomic orbitals in the same manner as the orbitals used in the Hartree-Fock method. The construction of the correct orbitals produces the closest approximation to the true electron-density (limited by the exchange-correlation functional), and consequently the lowest energy. As with the Hartree-Fock equations, the Kohn-Sham equations may be written in matrix form, which is used to expand across all possible permutations:

$$\boldsymbol{h}_{KS}\boldsymbol{C} = \boldsymbol{SC\varepsilon}$$

The $\hat{\mathrm{h}}_{KS}$ matrix contains elements similar to those in the Fock matrix. Because the correlation term requires the electron density to be known, DFT methods solves the equations iteratively. The **S** and **C** matrices are again the matrices for the orbital spins and orbital coefficients respectively. DFT requires the electron density to be self-consistent with the initial density, within a threshold, for the calculation to be considered converged, similar to the Hartree-Fock method. An initial guess is constructed from the superposition of atomic electron densities and a set of orbitals generated from the Kohn-Sham equations and initial structure. These orbitals are used to evaluate the electron density and the process is repeated until the threshold criteria is reached. From the converged electron density, the energy and other properties of the system can be calculated.[343]

5.2.4.1 Exchange-Correlation Functionals

Since the exchange-correlation functional is unknown it has be approximated and there are a wide range of different functionals that can be used to approximate this. The choice of

functional is system dependant with no one functional being suitable for all systems. Early functionals used the Local Density Approximation (LDA), which treated the local electron density as a uniform electron gas and is very limited in its application. An improvement on LDA functionals was the development of Generalised-Gradient-Approximations (GGA) which make the exchange and correlation energies dependent on both the electron density and its derivatives (i.e. non-uniform density). Examples of GGA functionals include B88, BLYP, PBE, and BP86. A further improvement has been made through hybrid GGA functionals (or hyper GGA) which incorporates exact exchange energy from Hartree-Fock theory. The optimum percentage of HF exchange energy is dependent on the system and calculated property of interest; examples of hybrid functionals include B3LYP (20 % HF exchange) and PEB0 (25 % HF exchange).[346] Hybrid-meta GGA functionals, such as M06, are similar to hybrid GGA functionals and contain both HF exchange energy and an additional term for the second derivative (Laplacian) of the electron density. However, these hybrid-meta GGA functionals are also highly parameterised through empirical fitting[347] and as such, they can perform significantly better than other functionals in areas which they have been parameterised for.[348-350] However, there are cases when hybrid-meta GGA functionals also perform worse than other functional types.[351-353] There is currently no golden functional which outperforms all other functionals in all areas. Instead, the functional of choice is dependent on the system and properties of interest.[343]

5.2.4.2 Broken Symmetry DFT

Calculating exchange energies becomes a major problem in systems with unpaired, interacting, electrons situated on different sites (e.g. ions or fragments). Although systems with ferromagnetically aligned spins (for example a triplet state) can be described well by a single Slater determinant, antiferromagnetically aligned spins (e.g. singlet diradical) require several determinants to describe the system correctly. Although antiferromagnetically coupled systems can be described using multireference *ab initio* approaches, the computational expensive required to calculate the correlation effects makes these approaches less practical. A more practical approach is the use of broken-symmetry DFT which enables antiferromagnetically coupled systems to be described by a single determinant.[354, 355]

Broken-symmetry DFT generates an initial guess from a single determinant wavefunction which describes the singlet open-shell state but with the 'wrong' spin symmetry. In this sense there are regions for positive and negative spin density (around the different sites where the

unpaired electrons reside) which gives zero when integrated over all space. However, a true singlet wavefunction has zero spin density at any point in space. Using the variational principle, the orbitals generated in the initial guess are optimised to find the true broken-symmetry wavefunction. The optimised orbitals are usually less localised than the initial orbitals due to the energy gained by partial delocalisation.[354, 355]

5.2.4.3 Some Considerations of DFT Methods

DFT methods are known to poorly describe dispersion forces, such as van der Waals interactions, often underestimating or displaying a repulsive interaction depending on the functional used. However, empirical attraction terms can be used to compensate for the poor description by DFT (*see 5.2.4.4*).[343, 355-357]

DFT methods employing GGA functionals often predict systems involving radical cations and anions, as well as three-centre four electron bonds, as being too stable. Similarly, the poor performance of GGA functionals in broken symmetry DFT, compared to hybrid functionals, is primarily due to the overdelocalisation of spin density across the electronic structure and consequently overestimates the exchange-correlation energy. The tendency of HF exchange to over localise spin density offsets the overdelocalisation of DFT exchange-correlation, which enables hybrid functionals to provide values closer to the experimental values. Likewise transition states are often calculated to be too stable, with barrier energies being underestimated. However, the use of hybrid functionals was found to provide better approximations for energy than the GGA functionals.[343, 355-357]

Studying excited states with DFT is difficult since it is a method for studying the ground state of the system. Describing an excited state is easier if the spatial or spin symmetry is different to the ground state but not if they are same. However, it is possible to calculate excited state properties, such as excitation energies, from the ground-state through linear response time-dependent density functional theory (TD-DFT). This method applies a small external perturbation (external potential) on the ground state electronic structure and calculates the response on the electron density without changing the ground-state structure.[343, 355-357]

DFT methods are unsuitable for describing charge-transfer systems whereby electron transfer occurs over long distances, since the exchange-correlation functional is only dependent on density at a given point.[343]

5.2.4.4 Dispersion Correction

The poor description of dispersive force by DFT methods can be overcome, or improved upon, by the use of empirical dispersion correction methods, such as these proposed by S. Grimme *et al*.[358-360] for DFT. These can be added onto the total energy calculated from Kohn-Sham DFT. The dispersion correction is calculated by the summation of all two- and three-body dispersion energies, which are dependent on atomic distances between the respective pairs or groups. The most recent correction, DFT-D3, improves upon older versions by calculating some parameters from first principles.[360]

Dispersion corrected energy is given by:

$$E_{D3\ Corr} = E_{KS} + E_{Disp}$$

Where $E_{D3\ Corr}$ denotes the dispersion corrected total energy, and E_{KS} the self-consistent Kohn-Sham energy from Kohn-Sham DFT. The dispersion energy from DFT-D3, E_{Disp}, given by:

$$E_{Disp} = E^{(2)} + E^{(3)}$$

Where $E^{(2)}$ denotes the dispersion energy between two-bodies in the system, and $E^{(3)}$ the dispersion energy between three-bodies in the system.

5.2.4.5 Solvation Methods

The time independent Schrödinger equation is typically solved for a system in the gas-phase due to the computational expense for solving the equation for the same system in solution or the solid-state. The computational expense arises from the increased system size needed to replicate the interacting components of the system. However, it is highly desirable to approximate the energy of a system in a non-gaseous state for many chemical problems. To reduce the computational expense, a correction can be applied to the gas-phase energy to account for the interaction of solvent with the molecule(s) (i.e. solute).[343]

For solution-state calculations, a solvation method can be applied to approximate the interaction of the molecule with solvent. Due to computational expense of explicit models, in which solvation is described by modelling the individual solvent molecules, implicit solvation methods, such as the conductor-like screening model (COSMO),[361-363] are most commonly used in mechanistic organometallic chemistry. In implicit solvation, or continuum solvation, the solvent is described as a continuous medium with uniform polarisability given by the dielectric constant, ε, of the solvent of interest. The solute forms a cavity in the

medium which causes a destabilising effect (due to entropic factors and loss of solvent-solvent interactions), while the dispersion forces and electrostatic stabilisation, from charge distribution between the solvent and solute, generate a stabilising effect.[343] The total energies provide a correction to approximate the energy of system in solution:

$$E_{Solu} = E_{KS} + E_{Solvation}$$

Where E_{Solu} is the energy of the system in solution, E_{Ks} is the self-consistent Kohn-Sham energy calculated for the molecule in the gas phase, and $E_{Solvation}$ is the solvation correction energy given by:

$$E_{Solvation} = E_{Cavity} + E_{Disp} + E_{Elec}$$

Where E_{Cavity} is the energy required to create the solute cavity, E_{disp} is the dispersion energy between the solute and solvent, and E_{elec} is the energy of the electrostatic forces between the solute and solvent.[343]

In COSMO solvation, the solute cavity is defined by a van der Waals surface which is constructed from atom-centred spheres with radii equal to the van der Waals radius multiplied by a suitable factor, typically 1.2. The atomic charges and dipoles of the molecule are used to determine the charge distribution over the molecule in order to create the charged surface of the solute. From this the energy of the solute and solvent interactions can be calculated and subsequently the energy of a solvated system approximated.[361-363]

5.3 Methodology

The relaxed PES scans for direct fluorination of **[57b]** were calculated at the (RI-)PBE0/def2-TZVPP//(RI-)PBE0/SV(P) level with COSMO correction for dichloromethane (ε = 8.93). A hybrid functional was chosen due to the GGA functional BP86 being unable to describe the geometries near to the transition state in the work by Milner *et al*.[225] It has been observed in other systems that hybrid functionals perform reasonably well, and much better than GGA functionals, when studying both transition states and radical systems.[355, 356] In this case the PBE0 functional, which was used by Milner *et al.,* was chosen due to the similarity of the systems and to ensure that the results could be directly compared.[225]

The distances between the fluorine atom of the fluorinating agent and the β-carbon of the alkynyl ligand were constrained between 4.0 Å and 1.4 Å, with 0.1 Å steps from 3.0 Å to 1.4 Å. Each geometry was optimised for the closed-shell singlet, triplet, and open-shell (diradical) singlet electronic configurations. Other than the constraint on the C-F distance, all atoms

were allowed to move freely to enable an energy minimum to be reached for each C-F distance. The open-shell singlet, or broken symmetry singlet diradical, structures were generated using the triplet state structures as the starting point. Spin flipping one of the α-spin orbitals (representing one of the unpaired electrons) to a β-spin orbital enables the initial molecular-orbitals of the broken symmetry singlet to be formed. This was achieved by localisation of the occupied valance orbitals through turbomole's 'flip' function. An extra localised alpha valence electron was consistently generated on the ruthenium atom and consequently all spin flips were performed on one of the ruthenium localised alpha valence electrons. The alpha electron with contributions to the d-orbital functions which did not match any of the beta-analogues was chosen as the electron to spin flip in each singlet open-shell calculation. In order to prevent the spin state generated from being immediately destroyed to a closed-shell configuration, the optimisation criterion was relaxed by starting with a large SCF dampening and increasing SCF orbital shift (allows closed-shell MOs to be shifted to a lower energy).

After optimisation of the singlet diradical structures, Mulliken population analysis was performed and the unpaired electron densities were checked to ensure the structures did correspond to a diradical singlet state or if the system had optimised from the open-shell initial guess to a closed-shell singlet. All points on the diradical singlet PES scans which converged back to a singlet-closed-shell state are not displayed for clarity. The PES scans are displayed in relative solvated (dichloromethane) electronic energies referenced to the singlet closed-shell geometry at a C-F distance of 4.0 Å, where it was assumed that there was little or no interaction between the two fragments.

5.4 PES Scans for Fluorination of *trans*-[ClRu(dppe)$_2$(C≡CPh)], [57b] by NFSI

The relaxed PES scans for the singlet closed-shell and triplet states are shown below in Figure 101. All attempts at generating singlet diradical states from the triplet states resulted in singlet closed-shell states being obtained after optimisation. It is clear from the PES scans that the triplet 'pathway' is significantly higher in energy, *ca.* 200 kJ mol^{-1}, than the closed-shell singlet pathway. Presumably the diradical singlet states converged back to the closed-shell singlet states due to the high stability of the closed-shell configuration. The closed-shell singlet pathway has a barrier to fluorination corresponding to a value of around 110 kJ mol^{-1}.

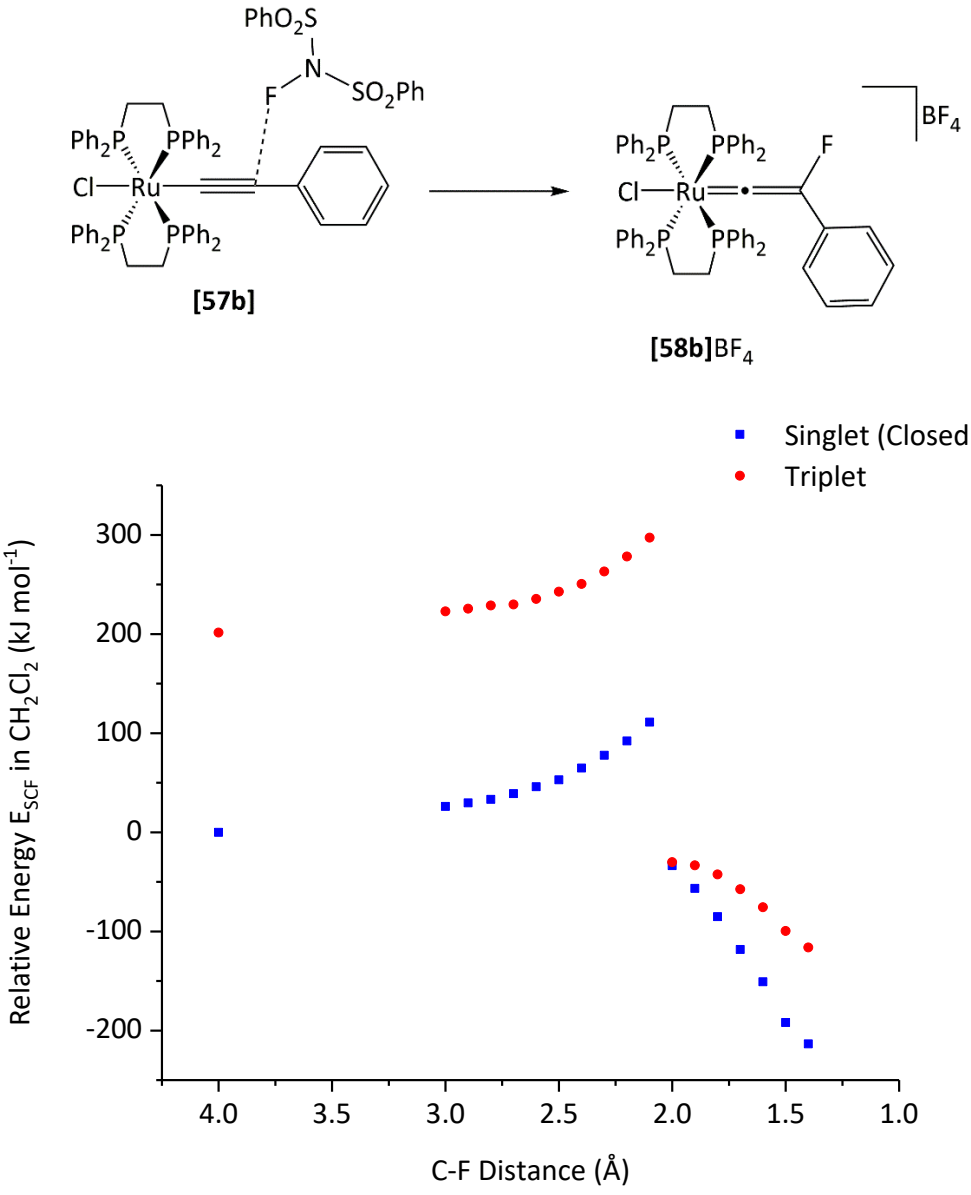

Figure 101: The relaxed PES scans for the fluorination of the alkynyl ligand of [57b] by NFSI at the (RI-)PBE0/def2-TZVPP//(RI-)PBE0/SV(P) level with COSMO solvation for dichloromethane.

The large, sharp, drop in energy between 2.1 and 2.0 Å corresponds to a large change in geometry (Figure 102) whereby the N-F bond is broken and the C-F bond is formed. The N-F distance increases significantly from 1.42 Å to 3.87 Å. The formation of the C-F bond is indicated by the compression of the Ru-C_α bond (2.00 Å to 1.83 Å) and elongation of the C_α-C_β bond (1.25 Å to 1.30 Å) i.e. conversion of the alkynyl ligand to the vinylidene ligand. Smooth PES scans were not obtained as a consequence of the optimisation algorithms used. The structures were optimised with only one constraint, the C-F distance. Therefore, optimisation was performed by finding the lowest energy structure on any potential surface accessible under the criteria set. This does not necessarily correspond to finding the lowest

energy structures along a single PES. In the case above (Figure 101) the PES being tracked changes to a lower energy PES upon changing the C-F distance from 2.1 Å to 2.0 Å.

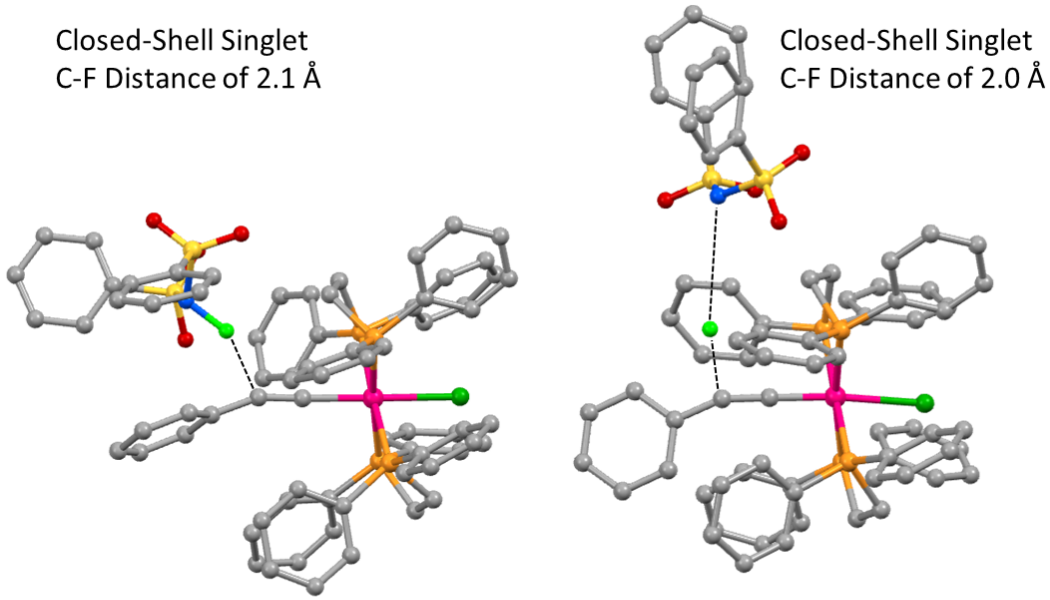

Bond	Bond Length / Å	
	Closed-shell Singlet	Closed-Shell Singlet
C_β-F	2.10	2.00
Ru-C_α	2.00	1.83
C_α-C_β	1.25	1.30
N-F	1.42	3.87

Figure 102: Closed-shell singlet optimised geometries at C-F distances of 2.1 and 2.0 Å calculated at the (RI-)PBE0/SV(P) level. Hydrogens are omitted for clarity. The reduction in energy from a C-F distance of 2.1 to 2.0 Å corresponds to the breakage of the N-F bond and formation of the vinylidene complex on the basis of the change in Ru-C_α and C_α-C_β bond lengths.

5.5 PES Scans for Fluorination of [57b] by [FTMP]BF_4

In contrast to the PES scans for fluorination of **[57b]** by NFSI, the closed-shell singlet, triplet and diradical singlet PES scans for [FTMP]BF_4 are similar in energy to one another (Figure 103).

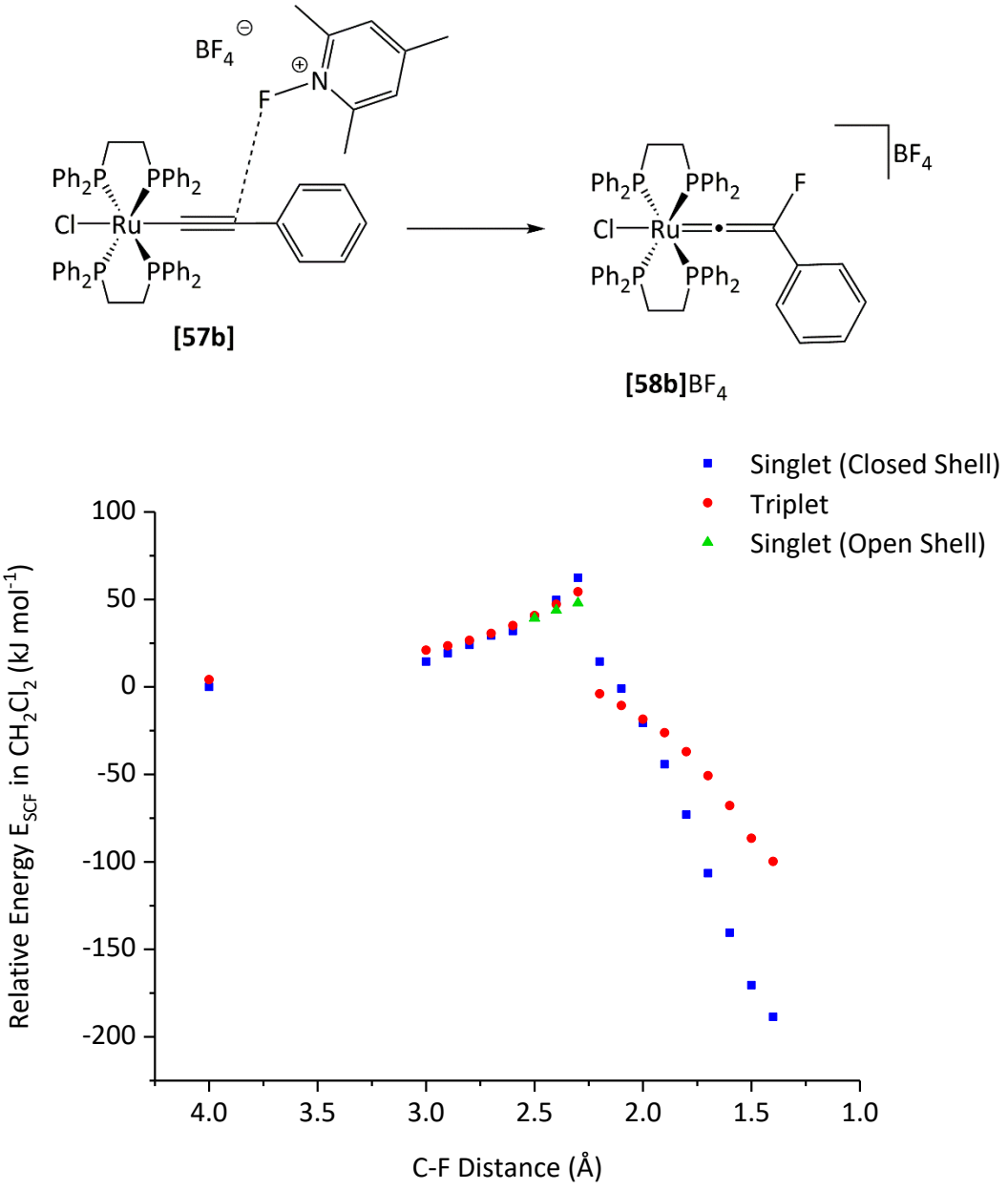

Figure 103: The relaxed PES scans for the fluorination of the alkynyl ligand of [57b] by [FTMP]BF_4 at the (RI-)PBE0/def2-TZVPP//(RI-)PBE0/SV(P) level with COSMO solvation for dichloromethane.

The barrier to C-F bond formation at 2.3 Å on the closed-shell singlet scan was calculated at ($\Delta E_{SCF\text{-}DCM}$) 62 kJ mol^{-1}. The triplet scan closely tracks the singlet closed-shell scan with geometries close to the transition state being slightly lower in energy than the closed-shell singlet geometries, although the energy differences are not likely to be significant at this

level of theory. The diradical singlet scan reveals that diradical states can be optimised between a C-F distances of 2.5 Å to 2.3 Å. These open-shell singlet geometries were calculated to be lower in energy than the closed-shell singlet geometries by 1, 6 and 14 kJ mol^{-1} ($\Delta E_{SCF\text{-}DCM}$) at C-F distances of 2.5, 2.4 and 2.3 Å respectfully. The barrier to C-F bond formation on the diradical singlet PES was calculated to be slightly lower in energy ($\Delta E_{SCF\text{-}DCM}$ = 48 kJ mol^{-1}) compared the closed-shell singlet PES.

The large drop in energy between 2.3 Å and 2.2 Å again corresponds to large structural changes as a result of N-F bond breakage and C-F bond formation (Figure 104). As observed in the PES scans with NFSI, formation of the C-F bond is indicated by formation of a vinylidene ligand (compression of the Ru-C_α bond from 1.91 Å to 1.83 Å and elongation of the C_α-C_β bond from 1.26 to 1.30 Å).

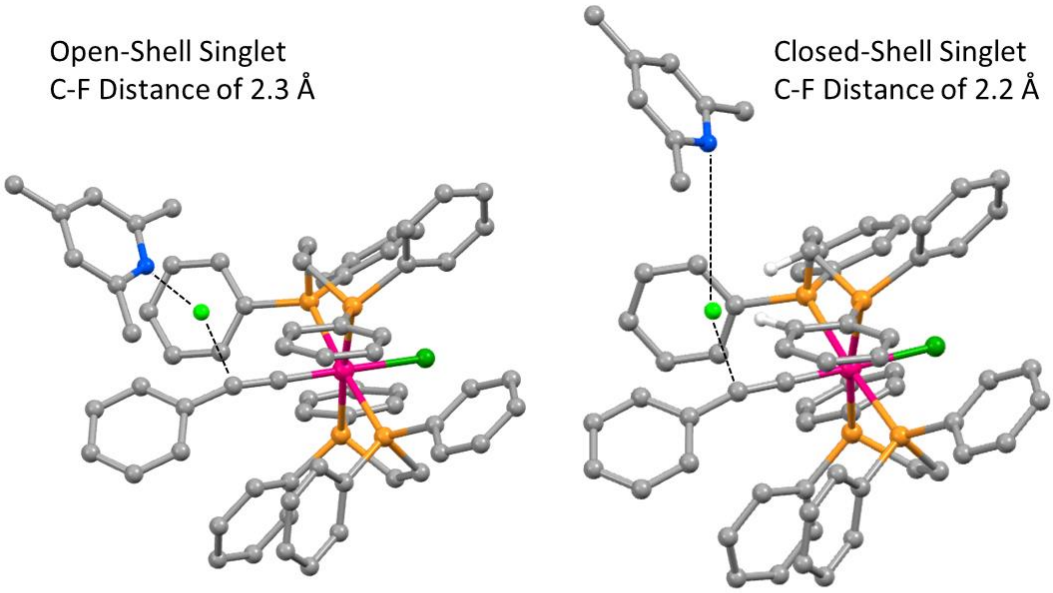

Bond	Bond Length / Å	
	Open-shell Singlet	Closed-Shell Singlet
C_β-F	2.30	2.20
Ru-C_α	1.91	1.83
C_α-C_β	1.26	1.30
N-F	2.05	4.55

Figure 104: Optimised structures for the open-shell singlet at a C-F distance of 2.3 Å (prior to C-F bond formation) and the closed-shell singlet at a C-F distance of 2.2 Å (after C-F bond formation) calculated at the (RI-)PBE0/SV(P) level. Hydrogens are omitted for clarity. The large drop in energy from a C-F distance of 2.3 to 2.2 Å corresponds to the breakage of the N-F bond and formation of the vinylidene complex.

Mulliken population analysis reveals that the optimised diradical singlet states exhibit unpaired α-spin density on both the ruthenium centre and the alkynyl β-carbon, while unpaired β-spin density resides on the nitrogen and fluorine atoms of the fluorinating agent (for example see Figure 105). The open-shell singlet geometries at 2.5, 2.4, and 2.3 Å represent the system after SET occurs between **[57b]** and [FTMP]BF_4 to form the ruthenium (III) alkynyl radical and $FTMP^{\cdot+}$.

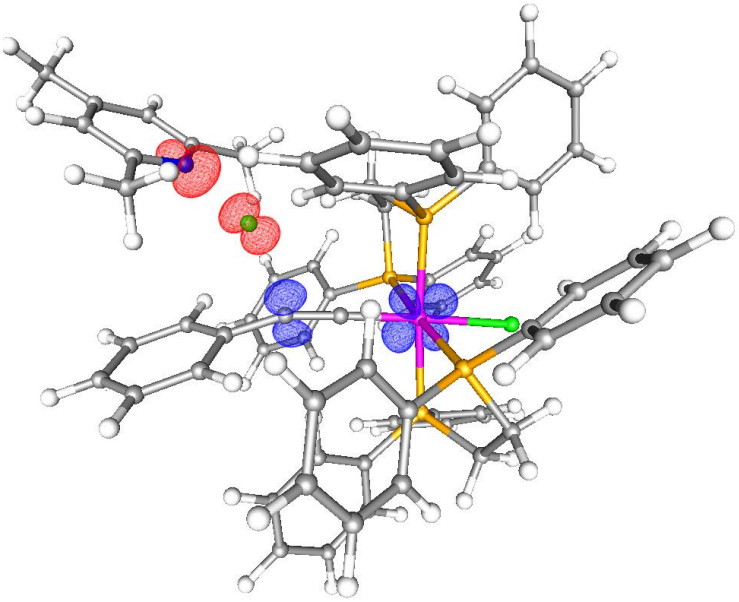

Figure 105: Spin density map overlaid on the open-shell singlet geometry at the C-F distance of 2.3 Å. Alpha spin density resides on the alkynyl β-carbon and ruthenium of the metal fragment and beta spin density resides on the fluorine and nitrogen of the fluorinating agent.

The significant differences between the open-shell singlet and closed-shell singlet geometries (representing before and after SET) are the elongation of the N-F and Ru-C_α bonds (Figure 106). For example, at a C-F distance of 2.3 Å the N-F bond is significantly elongated from 1.37 Å in the closed-shell singlet structure to 2.05 Å in the open-shell singlet structure. The Ru-C_α bond is elongated from 1.91 Å to 1.99 Å for the singlet diradical and closed-shell singlet structures respectively. As a result of these changes in geometry and electronic structure upon SET, the barrier to C-F bond formation is lowered.

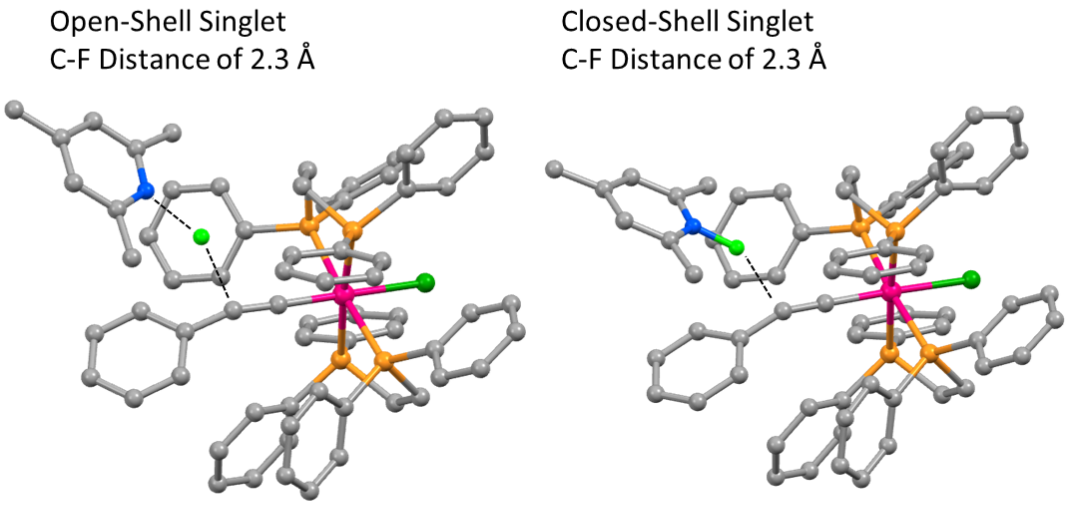

Bond	Bond Length / Å	
	Open-shell Singlet	Closed-Shell Singlet
C_β-F	2.30	2.30
Ru-C_α	1.91	1.99
C_α-C_β	1.26	1.25
N-F	2.05	1.37

Figure 106: Optimised structures for the open-shell singlet and closed-shell singlet at a C-F distance of 2.3 Å calculated at the (RI-)PBE0/SV(P) level. Hydrogens are omitted for clarity.

5.6 PES Scans for Fluorination of [57b] by Selectfluor

In order to describe the geometries used in the relaxed PES scans with Selectfluor correctly, geometry optimisations had to be carried out with COSMO solvation, rather than performing geometry optimisations in the gas phase and correcting for solvent effects on the electronic energies after optimisation. COSMO solvation was required to generate realistic structures presumably due to Selectfluor being highly charged and some degree of charge stabilisation being gained with solvation. The relaxed PES scans obtained are shown below in Figure 107.

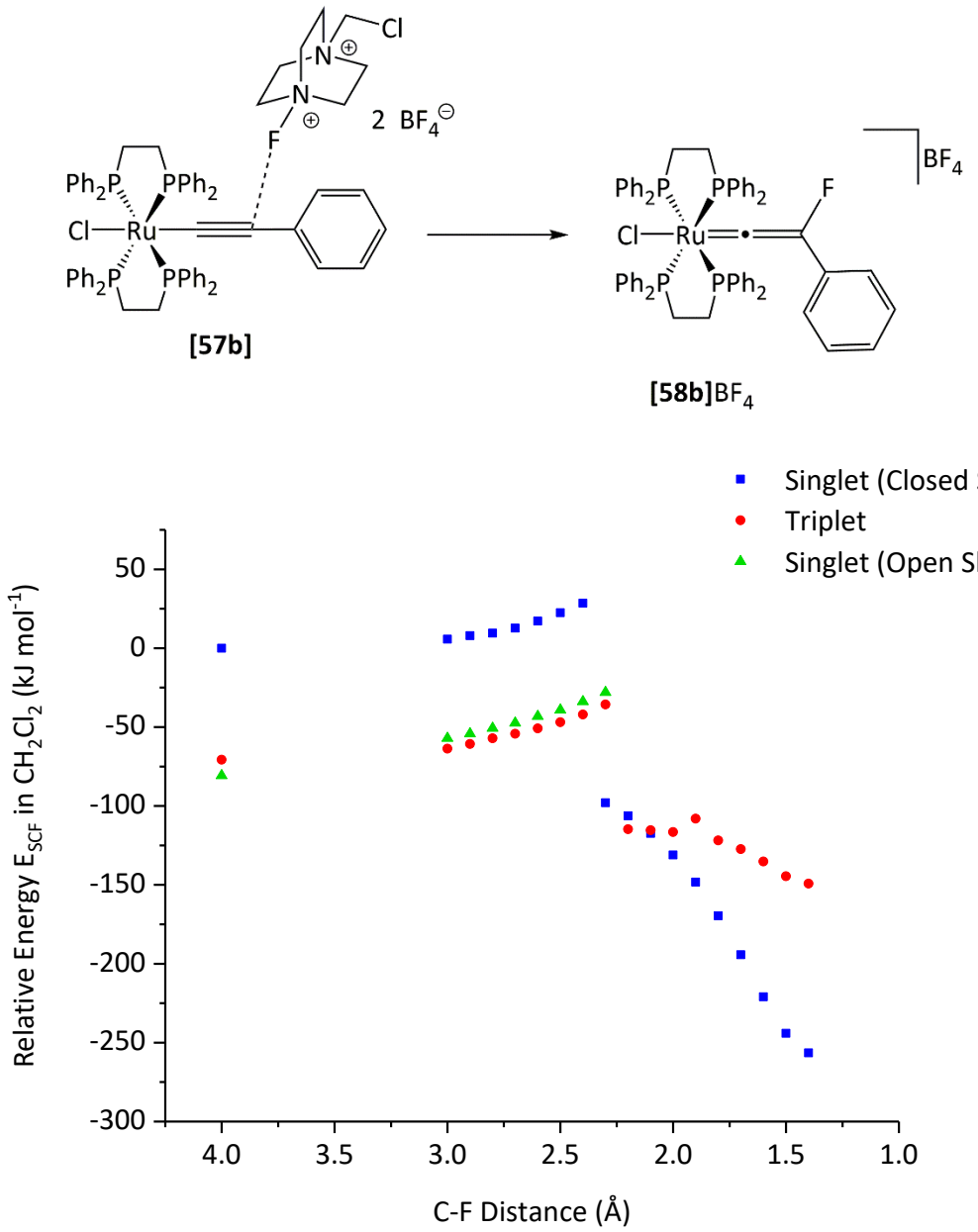

Figure 107: The relaxed PES scans for the fluorination of the alkynyl ligand of [57b] by Selectfluor at the (RI-)PBE0/def2-TZVPP//(RI-)PBE0/SV(P) level optimised with COSMO solvation for dichloromethane.

The most notable feature of the PES scans for fluorination of **[57b]** by Selectfluor is that the triplet and diradical singlet PES are both significantly lower in energy than the singlet closed-shell PES scan prior to C-F bond formation (between 62-81 kJ mol^{-1} lower in energy between 4.0 Å and 2.4 Å; see Appendix I). The barrier to fluorination *via* the closed-shell singlet was calculated at around 110 kJ mol^{-1} while the barrier for the open-shell singlet PES was calculated at around 55 kJ mol^{-1}. The larger drop in energy between the C-F distances of 2.4 Å and 2.3 Å for the closed-shell singlet PES, and 2.3 Å to 2.2 Å for the open-shell singlet PES, again correspond to the formation of the C-F bond and breakage of the N-F bond (Figure

108). As observed before large structural changes accompany the drop in energy as the PES slips onto the PES for the vinylidene complex as noted by the compression of the Ru-C_α bond from 2.30 Å to 2.20 Å.

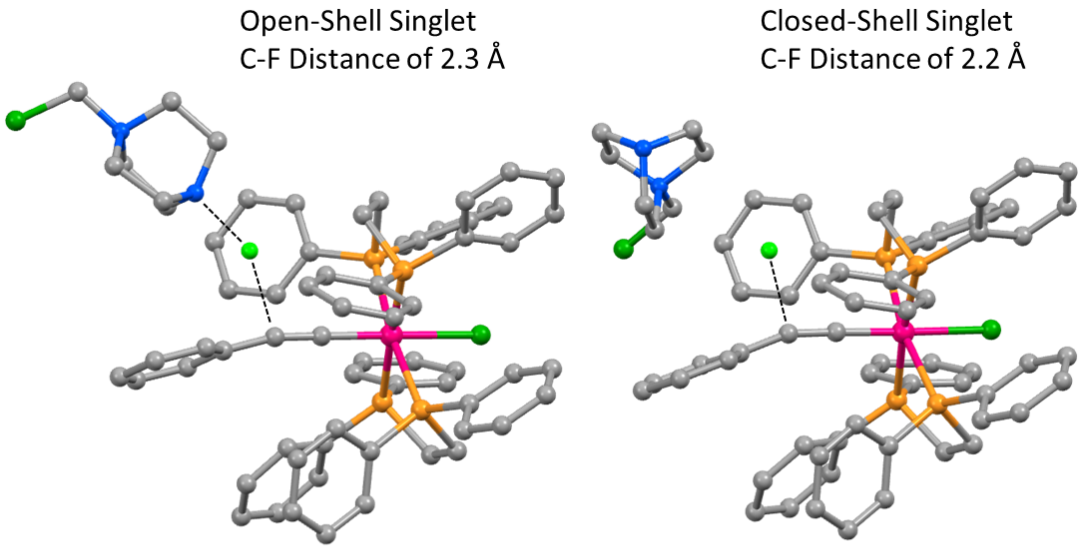

Bond	Bond Length / Å	
	Open-shell Singlet	Closed-Shell Singlet
C_β-F	2.30	2.20
Ru-C_α	1.90	1.83
C_α-C_β	1.26	1.25
N-F	1.97	4.80

Figure 108: Optimised structures for the open-shell singlet at a C-F distance of 2.3 Å (prior to C-F bond formation) and the closed-shell singlet at a C-F distance of 2.2 Å (after C-F bond formation) calculated at the (RI-)PBE0/SV(P) level. Hydrogens are omitted for clarity.

Mulliken population analysis (Table 31) reveals that the unpaired electron density in the optimised structures of the diradical singlet PES, between 4.0 and 2.3 Å, reside predominately on the ruthenium and the alkynyl α- and β-carbons of **[57b]**, as well as the fluorine and (fluorine-bound) nitrogen atoms of Selectfluor (see Figure 109 and Figure 110 for the spin densities on the singlet diradical structure at C-F distances of 4.0 Å and 2.3 Å respectively). The spin densities in both structures are localised on the same nuclei, with the exception that increased beta-spin density was expected on the alkynyl α-carbon at the C-F distance of 2.3 Å than at 4.0 Å.

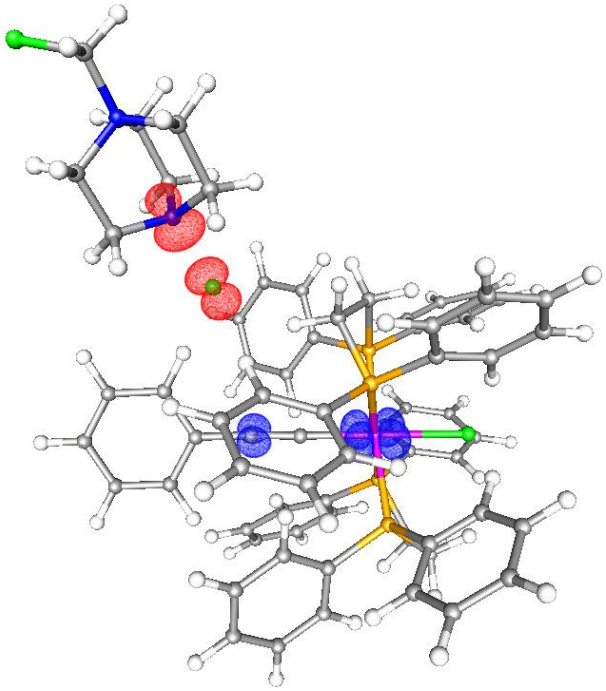

Figure 109: Unpaired spin density mapped onto the open-shell singlet geometry at 4.0 Å

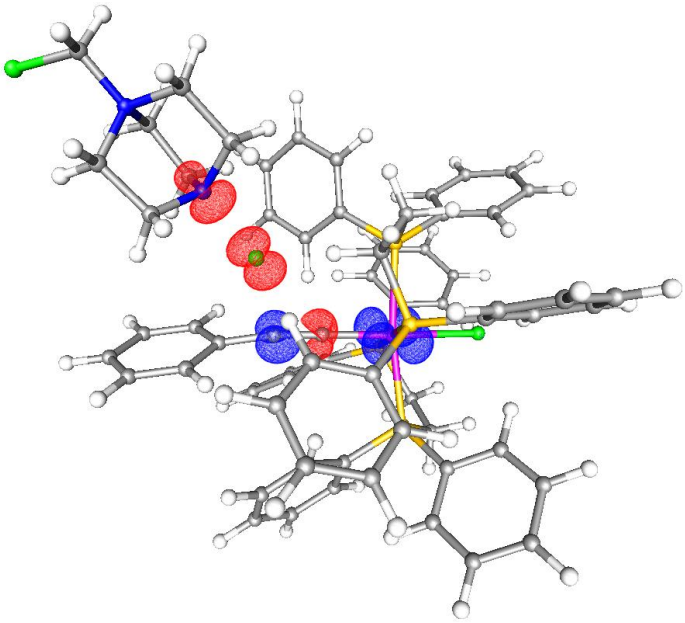

Figure 110: Unpaired spin density mapped onto the open-shell singlet geometry at 2.3 Å.

Table 31: Major spin density contributions from population analysis of the open-shell singlet structures at C-F distances of 2.3 Å and 4.0 Å.

		Total Spin Density (α - β)	
	Atom	2.3 Å	4.0 Å
Metal Fragment	Ru	-0.7720	-0.7188
	C_α	-0.3475	-0.3089
	C_β	0.3397	0.12815
Selectfluor	N	0.2678	0.43873
	F	0.4671	0.51239

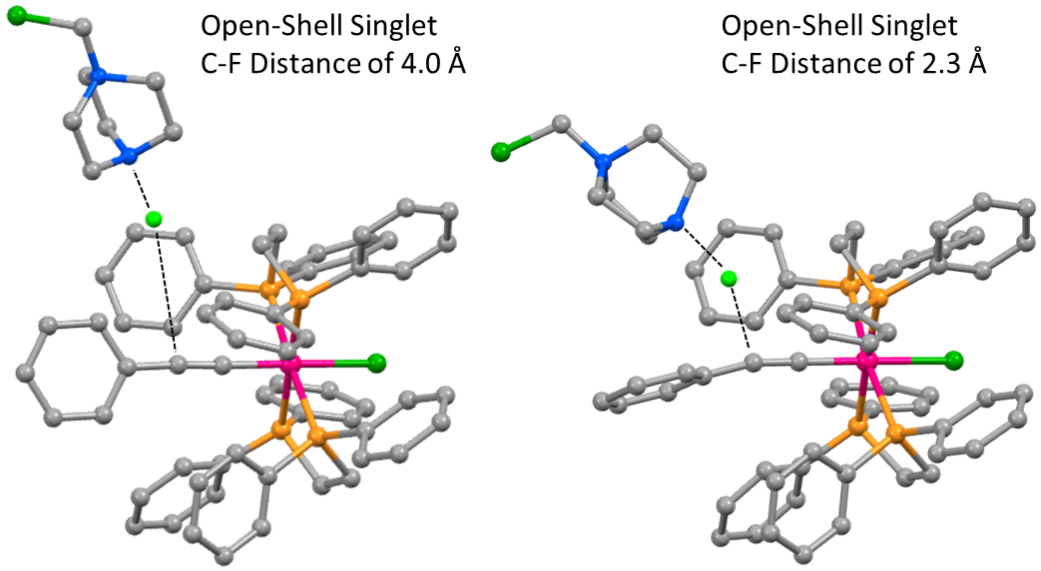

	Bond Length / Å	
Bond	Open-shell Singlet	Closed-Shell Singlet
C_β-F	4.00	2.30
Ru-C_α	1.91	1.90
C_α-C_β	1.25	1.30
N-F	1.97	4.55

Figure 111: Optimised structures for the open-shell singlet at a C-F distances of 4.0 and 2.3 Å calculated at the (RI-)PBE0/SV(P) level. Hydrogens are omitted for clarity

The population analysis (Table 31) and optimised structures reveal that the diradical singlet geometries (Figure 111) represent the system after SET has occurred between **[57b]** and Selectfluor. The PES scans suggest that even at long distances (at least up to a C-F distance of 4.0 Å) SET is thermodynamically favoured to form radical cations of **[57b]** and Selectfluor.

Assuming free interconversion between the closed-shell singlet and open-shell singlet PES, there would be no population of the closed-shell singlet between 4.0 Å and 2.4 Å since the open shell PES are lower in energy. Consequently, the barrier to fluorination at 2.4 Å for the singlet closed-shell PES is expected to be around 110 kJ mol^{-1}. In contrast, the barrier to fluorination at 2.3 Å for open-shell singlet PES is expected to be significantly lower in energy at around 55 kJ mol^{-1}. It would therefore be expected that fluorination of **[57b]** would proceed *via* the singlet diradical pathway.

5.7 Conclusion

The PES scans for the fluorination of **[57b]** by Selectfluor (Figure 107) appears to suggest that one-electron oxidation is thermodynamically favoured even at long distances (at least up to 4.0 Å), which supports the experimental observations of **[57]**$^{\cdot}BF_4$ made in Chapter 4. In addition to fluorination, one electron oxidation of **[57b]** was observed experimentally by UV-Vis and EPR spectroscopy when reacted with Selectfluor. The experiments used to probe the mechanism of fluorination could not distinguish between a closed-shell S_N2 mechanism and an open-shell 'in cage' SET mechanism.

The barrier to fluorination *via* a singlet closed-shell pathway was calculated to be approximately 55 kJ mol^{-1} higher in energy than that of the singlet open-shell pathway (Table 32), assuming free interconversion between the closed-shell singlet and the open-shell singlet states. Although interconversion between the two states will not be a zero energy process in reality, the barriers obtained suggest that fluorination of **[57b]** with Selectfluor is expected to proceed *via* a singlet open-shell 'in cage' SET mechanism rather than a closed-shell S_N2 mechanism.

Table 32: The approximate barriers to C-F bond formation to the nearest 5 kJ mol^{-1} for the fluorination of [57b] by the three fluorinating agents.

$\Delta E_{SCF-DCM}$/ kJ mol^{-1}	Singlet Closed-shell	Triplet	Diradical Singlet
NFSI	110	95	-
$[FTMP]BF_4$	60	55	50
Selectfluor[a]	110	45	55

[a]*Assuming free interconversion between the singlet closed-shell and the singlet open-shell.*

The PES scans with Selectfluor (Figure 107) are markedly different to the PES scans with NFSI (Figure 101). The main differences are that the triplet surface, used as a starting point for the

open-shell singlet, is around 200 kJ mol^{-1} higher in energy than the singlet closed-shell PES. The broken symmetry calculations for the open-shell singlet optimised back to the closed-shell singlet. The barrier to fluorination could only be calculated for the closed-shell singlet pathway and is significantly higher in energy ($\Delta E_{SCF\text{-}DCM}$ = 110 kJ mol^{-1}) compared to the singlet open-shell barrier to fluorination with Selectfluor. This large difference in activation energy could rationalise why fluorination is not observed when attempting to fluorinate **[57b]** at room temperature with NFSI. Experimentally, one-electron oxidation of **[57b]** is observed upon addition of NFSI. However, the PES scans for NFSI suggest that SET is not thermodynamically favoured. This indicates that oxidation of **[57b]** by NFSI is being thermodynamically driven by another process, such as the formation of fluoride. To determine whether fluorination of **[57b]** with NFSI could be hampered by the higher activation barriers, fluorination should be attempted at temperatures above ambient.

It is less clear from the PES scans why fluorination of **[57b]** is not observed when [FTMP]BF_4 is used, since the barrier to fluorination, *via* either a closed-shell singlet ($\Delta E_{SCF\text{-}DCM}$ = 60 kJ mol^{-1}) or open-shell singlet ($\Delta E_{SCF\text{-}DCM}$ = 50 kJ mol^{-1}), are similar in energy to the open-shell singlet barrier with Selectfluor ($\Delta E_{SCF\text{-}DCM}$ = 55 kJ mol^{-1}). Fluorination would be expected on this basis. It is important to remember that the PES scans only explore the fluorination of **[57b]** along a single trajectory and is it not possible to compare the PES scans to other mechanistic pathways that are competing with it. The experimental observation of one-electron oxidation, coupled with the calculated barriers to fluorination, suggests that an alternate pathway is being favoured over fluorination of **[57b]** by [FTMP]BF_4.

The difference in energy between the barriers to (non-productive) one-electron oxidation and fluorination ($\Delta\Delta G^{‡}$) could rationalise the observed balance between the two processes (Figure 112). With Selectfluor, the value of $\Delta\Delta G^{‡}$ is such that both fluorination and oxidation is observed experimentally. While for [FTMP]BF_4, the value for $\Delta\Delta G^{‡}$ is larger such that only oxidation is observed experimentally despite the barriers to fluorination of **[57d]** being similar in energy with both Selectfluor and [FTMP]BF_4 ($\Delta E_{SCF\text{-}DCM}$ = 55 kJ mol^{-1} and 50 kJ mol^{-1} respectively). Due to the barriers to fluorination being similar, the barrier to oxidation with [FTMP]BF_4 must be lower than the barrier to oxidation with Selectfluor. With NFSI, $\Delta\Delta G^{‡}$ must be sufficiently large to account for the observation of oxidation. It is clear from the PES scans that the barrier to fluorination with NFSI is significantly higher in energy than the other two fluorinating agents and would favour oxidation, even if the barrier to oxidation is higher than with Selectfluor.

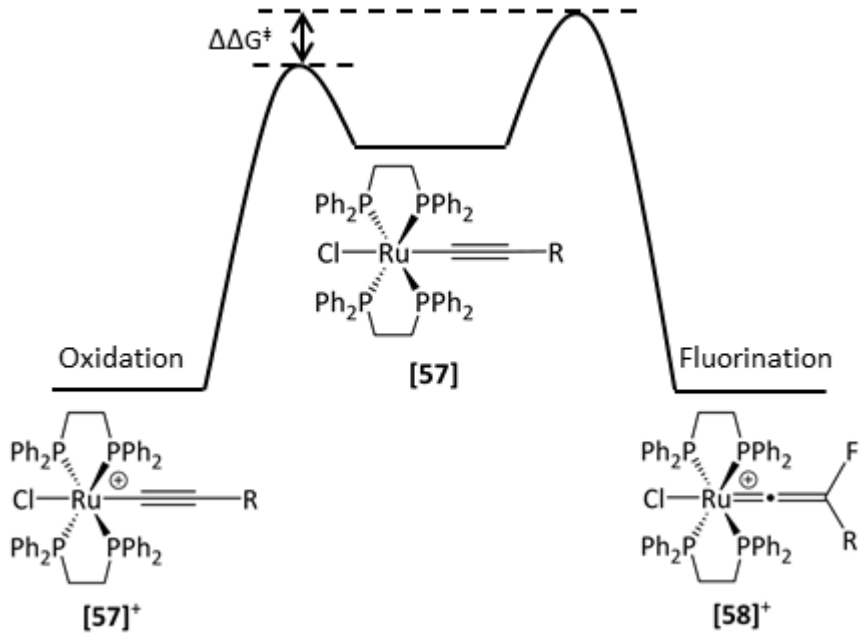

Figure 112: A schematic representation of difference energy barriers to fluorination and oxidation.

Due to the fluorination of **[57a]** and **[57b]** being observed with NFSI, future work would include constructing relaxed PES scans for the fluorination of both complexes with all three fluorinating agents. This might offer mechanistic insight into why NFSI is capable of fluorinating **[57a]** and **[57b]** but not **[57c-j]**. Additionally, it will allow the PES scans with Selectfluor and [FTMP]BF_4 to be compared with PES scans reported here. Similarly calculating the PES scans for the fluorination of the dimethylaniline substituted alkynyl complex, **[57g]**, may provide insight into why fluorination is not observed with Selectfluor.

Chapter 6. Conclusions

6.1 Exploration of Electrophilic Fluorination of Unsubstituted Ruthenium Acetylide Complexes and Synthesis of Fluoroalkynyl Complexes (Chapter 2)

Application of OSEF has enabled mono- and di-fluorinated ruthenium vinylidene complexes to be synthesised from the corresponding protio- and fluoro- substituted alkynyl complexes. Incorporation of fluorine into the vinylidene ligand induces significant deshielding of the carbon, hydrogen and fluorine nuclei across the various ruthenium fragments. The HOMO-LUMO electronic transition undergoes a bathochromic shift in the UV-Vis spectra with a fluorine substituent, while the vinylidene C=C stretching frequency undergoes a hypsochromic shift. The crystallographic data reveals that the incorporation of fluorine consistently induces increased distortion in the vinylidene ligand.

Access to the first mono-fluorinated vinylidene complexes has enabled stable fluoroalkynyl complexes to be obtained by deprotonation with lithium *bis*(trimethylsilyl)amide. The ruthenium fluoroalkyne complexes, **[28b]**, **[55b]**, and **[57b]**, were found to be stable towards alkyne dimerisation, unlike most organic fluoroalkynes reported in the literature.[227, 230, 231, 233] The calculated Brueckner orbitals, bond dissociation energies, energies of dimerisation suggest that the ruthenium fluoroalkynyl complexes are best viewed as alkynes with an exotic substituent which provides kinetic stability to the C≡C-F bond.

Substitution of the hydrogen substituent of the alkynyl ligand with fluorine does not induce a large bathochromic shift in the lowest energy absorption bands. The carbon chemical shift of the alkynyl β-carbon remains relatively unperturbed when the hydrogen substituent is replaced with fluorine. In contrast the alkynyl α-carbon undergoes significant shielding in the presence of a fluorine substituent.

To better understand the influence of fluorine on the chemical shifts of the vinylidene and alkynyl ligands, the chemical shielding tensors need to be obtained from solid-state NMR experiments. Correlating the tensors with the electronic structures of the fluorinated vinylidene and alkynyl complexes will provide insight into the observed chemical shifts. Furthermore, the reactivity of fluoroalkynyl complexes needs to be expanded and contrasted to the reactivity of analogous ruthenium alkynyl complexes.

6.2 Reactivity Study of Ruthenium Fluorovinylidene Complexes (Chapter 3)

The reactivity of ruthenium fluorovinylidene complexes, first investigated by Milner *et al*.,[218, 223] has been explored further. Attempts to liberate fluoroethyne from the coordination sphere of protio-fluorovinylidene complexes by heating the complex in a coordinating solvent were unsuccessful. Likewise attempts to displace fluoroalkynes by heating fluorovinylidene complexes in the presence of triphenylphosphine, which proved successful for disubstituted vinylidene complexes,[264] also failed.

The reaction of fluorovinylidene complexes with an oxygen atmosphere results in oxidative cleavage of the vinylidene C=C bond to afford fluoroacyls, RC(O)F. Attempts to liberate organic species under a carbon monoxide or hydrogen atmosphere were unsuccessful. The data indicate that the isomerisation of fluorovinylidene complexes to the η^2-alkyne complex is irreversible under the conditions used. More enforcing conditions are required to overcome the barrier to isomerisation.

Reaction of **[15b]**BF_4 with unsaturated reagents, styrene, ethynyltrimethylsilane, and allyl alcohol, did not result in the expected formation of fluorinated organic products, but rather the formation of the decomposition product, **[18]**BF_4. Complex **[18]**BF_4 is formed *via* initial attack of the vinylidene α-carbon by triphenylphosphine and is favoured over the coordination of the unsaturated reagents.

Greater success was achieved with nucleophilic addition to the fluorovinylidene ligand; hydride addition to **[19]**BF_4 afforded vinyl complex *Z*-**[23b]**, while addition of hydrochloric acid in dichloromethane afforded the mixed halogenated carbene complex **[111]**$^+$. The difluorinated vinyl complex, **[23a]** was found to undergo electrophilic fluorination to afford the fluorinated carbene **[104b]**NSI; alternatively protonation of **[23a]** with tetrafluoroboric acid, or hydrochloric acid afforded, carbene complex **[104a]**$^+$. Fluoroalkenes *E*-**105a** and *E*-**105c**, could be displaced from the carbene complexes **[104a]**$^+$ and **[111]**$^+$ respectively, in the presence of a chloride source and tetrahydrofuran. Displacement of the fluoroalkenes was not observed in dichloromethane, with the combination of tetrahydrofuran and a source of chloride being crucial. Similarly, **105c** was afforded by the reaction of **[15b]**BF_4 with hydrochloric acid in tetrahydrofuran. Attempts to liberate trifluorostyrene by reacting **[104b]**NSI with tetrabutylammonium chloride or irradiation of **[23a]** in the presence of tetramethylammonium fluoride were unsuccessful, except as a trace product. The liberation of alkene products from a carbene complex requires a sufficiently labile substituent to enable

isomerisation from the carbene complex to the η^2-alkenyl complex. In the case of **[104b]**NSI, the fluorine and phenyl substituents are unable to undergo migration presumably due to the high barriers involved.

Future work would include studying the mechanism of alkene displacement from **[104a]**$^+$, **[104b]**$^+$, and **[111]**$^+$ by DFT to understand the importance of solvent choice, the favourability of alkene displacement, and the favourability of a deprotonation-protonation or a reductive elimination pathway in conversion of the carbene complexes into the η^2-alkene intermediates. Further work would also include developing a catalytic method to synthesise fluoroalkenes and attempting to synthesise other fluorocarbene complexes in order to expand the range of fluoroalkene products that can be obtained by this method.

6.3 Exploring the Fluorination of *trans*-[ClRu(dppe)$_2$(C≡CR)] Complexes (Chapter 4)

A range of *trans*-[ClRu(dppe)$_2$(C≡CR)] complexes bearing both electron-donating and electron-withdrawing aryl substituents have been successfully fluorinated with Selectfluor. The UV-Vis and NMR spectroscopic parameters obtained for the fluorovinylidene complexes, **[58]**BF_4, reflect the electronic property of the aryl substituent. More electron-donating substituents resulted in a bathochromic shift of the lowest energy absorption band, and deshielding of the vinylidene α- and β-carbon atoms as well as the phosphorus chemical shifts. There was no apparent trend in the vinylidene C=C vibrational frequencies, and neither were there many statistically significant differences in bond metrics from the crystal structures.

The reaction of **[57]** with NFSI and [FTMP]BF_4 was found to result in one-electron oxidation; however, fluorination was not observed in the presence of either fluorinating agent. Furthermore, the dimethylaniline substituted alkynyl complex, **[57g]**, did not undergo fluorination with Selectfluor, NFSI, or [FTMP]BF_4. Monitoring the reactions of **[57]** with Selectfluor by EPR and UV-Vis spectroscopy revealed that one-electron oxidation is also observed in addition to fluorination.

The reaction of the protio- and fluoro-substituted alkynyl complexes, **[57a]** and **[57b]**, with NFSI resulted in fluorination being observed; however, their reactions with [FTMP]BF_4 resulted in protonation rather than fluorination.

Fluorination of a cyclopropyl bearing alkynyl complex, **[57j]**, was found to undergo fluorination, with Selectfluor only, to afford the fluorovinylidene complex **[58j]**BF_4 with no evidence for the cyclopropyl substituent having ring-opened.

The Gibbs free energies of fluorination for **[57]**, with the three fluorinating agents, were calculated by DFT. The calculations revealed that fluorination is thermodynamically favourable in all cases.

The possibility of an open-shell SET or a closed-shell S_N2 mechanism was probed with radical trap experiments and combined UV-Vis-NMR experiments. The radical trap experiments with TEMPO and BHT suggest that fluorination by Selectfluor occurs *via* an S_N2 or rapid 'in-cage' SET mechanism. The fluorination of **[57a]** by NFSI was found to be inhibited by TEMPO suggesting the possibility of an SET mechanism. The combined NMR-UV-Vis experiments revealed that oxidation observed experimentally is in competition with fluorination, and that fluorination of **[57]** by Selectfluor does not occur *via* the ruthenium(III) alkynyl complex reacting with a long lived fluorine species (e.g. fluoride, unreacted fluorinating agent, or other source of fluorine).

The reaction of **[77]** with Selectfluor was investigated by UV-Vis and EPR spectroscopy. The EPR spectrum obtained revealed the presence of a radical species which matched the spectrum obtained for **[77]**$^{\cdot+}$, and could suggest fluorination of ruthenium half-sandwich alkynyl complexes occurs by a radical mechanism.

Future work includes expanding the combined UV-Vis-NMR experiments to include the fluorination of **[57a]**, and **[57b]** with Selectfluor and NFSI to confirm the observations from the radical trap experiments. In addition, the UV-Vis-NMR experiments should be used to monitor the reactions of *trans*-[ClRu(dppe)$_2$(C≡CR)] complexes with Selectfluor in the presence of TEMPO in order to ensure the correct conclusions have been drawn from the radical trap experiments. Studying the fluorination reactions by stopped-flow IR spectroscopy or an *in-situ* IR probe, may provide kinetic data in which the mechanism can be elucidated.

To determine whether oxidation is also observed in the reaction of **[77]** with NFSI and [FTMP]BF_4, the reactions need to be monitored by EPR and UV-Vis spectroscopy. The fluorination of other half-sandwich alkynyl complexes will also need to be investigated by UV-Vis and EPR spectroscopy, in order to determine whether oxidation is observed. In

addition, fluorination should be conducted in the presence of radical traps to probe the possibility of an SET mechanism.

6.4 Probing Fluorination through Relaxed Potential Energy Surface (PES) Scans (Chapter 5)

The relaxed PES scans for the fluorination of **[57b]** by Selectfluor revealed that both a closed-shell S_N2 and an open-shell SET mechanism are feasible. The PES scans revealed that the formation of a diradical singlet system was thermodynamically favourable over a singlet closed-shell system along the entirety of the reaction coordinate studied. This suggests that long-range oxidation is thermodynamically favoured and accounts for the observation of oxidation experimentally. The scans also revealed that the barrier to fluorination is lowered with a singlet diradical configuration compared to the singlet closed-shell barrier ($\Delta E_{SCF\text{-}DCM}$ = 55 kJ mol^{-1} vs 110 kJ mol^{-1} respectively). Coupled with the experimental data from Chapter 4, the data collectively suggests that fluorination proceeds by a rapid 'in-cage' SET the mechanism rather than an S_N2 mechanism.

The relaxed PES scans for the fluorination of **[57b]** by NFSI suggests that fluorination is not observed due to the significantly higher barrier to fluorination ($\Delta E_{SCF\text{-}DCM}$ = 111 kJ mol^{-1} at a C-F distance of 2.1 Å). A diradical singlet scan could not be obtained, presumably due to the greater stability of the closed-shell singlet (the triplet scan was *ca*. 200 kJ mol^{-1} higher in energy).

The barriers to fluorination of **[57b]** with [FTMP]BF_4 are similar in energy for both the singlet closed-shell ($\Delta E_{SCF\text{-}DCM}$ = 60 kJ mol^{-1}) and singlet open shell ($\Delta E_{SCF\text{-}DCM}$ = 50 kJ mol^{-1}) scans. Fluorination would be expected considering the barrier to fluorination with Selectfluor *via* a singlet diradical pathway is approximately 55 kJ mol^{-1}. The experimental observation of one electron oxidation indicates that the oxidation pathway with [FTMP]BF_4 must be lower in energy than the fluorination pathway.

Constructing relaxed PES scans for the fluorination of **[57a]** and **[57b]** may provide insight into why fluorination is observed with either Selectfluor or NFSI but not [FTMP]BF_4. Similarly, construction of PES scans for the fluorination of **[57g]** may provide a possible explanation for why fluorination is not observed with any of the three fluorinating agents used. Applying this approach to the fluorination of ruthenium half-sandwich complexes could allow the feasibility of an SET mechanism to be determined.

Chapter 7. Experimental

7.1 General Considerations

All experimental procedures were performed under an atmosphere of dinitrogen using standard Schlenk Line and Glove Box techniques unless otherwise stated. Dichloromethane, pentane, hexane, tetrahydrofuran, methanol, ethanol, and diethyl ether were purified with the aid of an Innovative Technologies anhydrous solvent engineering system or distilled over sodium (under argon) before use. The d^2-dichloromethane, d^3-acetonitrile, and d^8-tetrahydrofuran used for NMR experiments were dried over CaH_2 (C_6D_6 was dried over sodium metal) and degassed with three freeze-pump-thaw cycles, then used in the glovebox under a nitrogen atmosphere or directly transferred to NMR tubes fitted with PTFE Young's taps under vacuum. [$RuCl_3 \cdot 3H_2O$] was purchased from Precious Metals Online, and [$Ru(\eta^5\text{-}C_5H_5)Cl_2]_n$ was purchased from Sigma Aldrich.

NMR spectra were acquired on either a Jeol ECS400 (Operating frequencies; ^1H 399.78 MHz, ^{13}C 100.53 MHz, ^{19}F 376.17 MHz, ^{31}P 162 MHz), a Bruker AVANCE III 500 (Operating Frequencies; ^1H 500.23 MHz, ^{13}C 125.77 MHz, ^{19}F 470.68 MHz, ^{31}P 202.50 MHz). ^{31}P and ^{13}C spectra were recorded with proton decoupling. Assignments were completed with the aid of ^1H COSY, ^{19}F COSY, ^1H-^{13}C HSQC, ^{13}C-^{19}F HSQC, ^1H-^{13}C HMBC, ^{13}C-^{19}F HMBC and/or ^{19}F-^{31}P HMBC experiments. NMR experiments were performed in 5 mm NMR tubes fitted with PTFE J. Young's taps typically using ca. 5-20 mg of material in 0.55 mL of the appropriate solvent.

Mass spectrometry measurements were performed on a either a Bruker microTOF MS (ESI) or a Waters GCT Premier Acceleration TOF MS (LIFDI) instrument. IR spectra were acquired on a Bruker Alpha FT-IR spectrometer with ATR and solution cell modules (solution phase IR recorded in CsCl solution cells). Elemental analyses were performed using an Exeter Analytical Inc. CE-440 analyser.

UV−visible absorption spectra were measured using an Agilent 8453 spectrometer with a DH-2000-BAL Deuterium/Helium light source (200-1100 nm). All UV-Vis spectra were recorded under an atmosphere of dinitrogen using a Youngs Tap quartz UV cuvette with a pathlength of 1 cm. Broadband UV irradiation (λ >290 nm) was carried out using a Philips HPK 125 W medium pressure mercury lamp with water filter in front of lamp output.

All EPR spectra were recorded on a Brucker using a continuous wave (X-band) Bruker EMX Micro spectrometer at about 9.3 GHz and a modulating frequency of 100 kHz at 148 K. Cyclic

voltammograms were recorded using a PalmSens EmStat^{3+} potentiostat in dichloromethane or 1:1 dichloromethane: acetonitrile solvent mix, using tetrabutylammonium hexafluorophosphate as a supporting electrolyte (0.1 M $[NBu_4][PF_6]$). All cyclic voltammograms were recorded at room temperature under dinitrogen in a glovebox. A platinum disc was used as the working electrode, with a platinum wire as counter and a silver wire as the reference electrode. Ferrocene and diacetylferrocene were used as internal calibrants.

7.2 Synthesis of $[Ru(\eta^5\text{-}C_5Me_5)(PPh_3)_2Cl]$

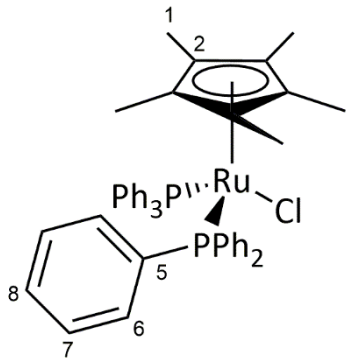

Prepared as described in the literature.[237]

$[Ru(\eta^5\text{-}C_5Me_5)Cl_2]_n$ (450 mg, 1.46 mmol) was suspended in absolute ethanol (50 mL) and triphenylphosphine (2.20 g, 8.39 mmol) was then added as a solid. The mixture was heated under reflux for 24 hours and allowed to cool to room temperature. The mixture was filtered in air and washed with absolute ethanol (10 mL) and hexanes (2x 10 mL), to afford an orange solid. Yield = 755 mg, 72 %.

^{1}H NMR (400 MHz, CD_2Cl_2, 295 K): δ 0.98 (t, $^4J_{HP}$ = 1.6 Hz, 15 H, H_1), 7.00-7.08 (m, 12 H, $H_{6/7}$), 7.12-7.18 (m, 6 H, H_8), 7.38-7.47 (m, 12 H, $H_{6/7}$).

^{31}P{^{1}H} NMR (162 MHz, CD_2Cl_2, 295 K): δ 41.0 (s, PPh_3).

7.3 Synthesis of [Ru(η^5-C$_5$Me$_5$)(dppe)Cl]

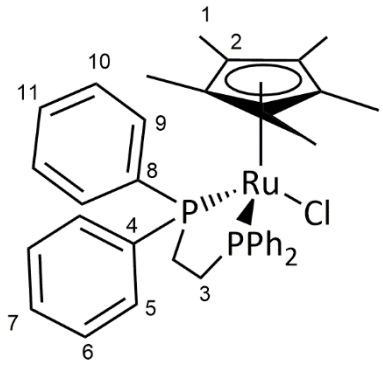

Prepared as described in the literature.[364]

[Ru(η^5-C$_5$Me$_5$)Cl$_2$]$_n$ (250 mg, 0.81 mmol) and 1,2-*bis*(diphenylphosphino)ethane (388 mg, 0.97 mmol) were added to an oven dried Schlenk tube and suspended in ethanol (*ca.* 30 mL). The reaction mixture was heated under reflux for 24 hours and the solvent removed *in vacuo* once cooled. The orange solid was purified by column chromatography (alumina), and an orange band eluted using dichloromethane. Removal of solvent *in vacuo* yield desired product. Yield = 267 mg, 49 %.

^{1}H NMR (CD_2Cl_2, 400 MHz, 295 K): δ 1.39 (15H, H_1), 2.02-2.16 (m, 2H, $H_{3a/b}$), 2.51-2.65 (m, 2H, $H_{3a/b}$), 7.16 (t, $^2J_{HH}$ = 7.2 Hz, 4H, $H_{5/6/9/10}$), 7.26-7.34 (m, 12H, $H_{5\text{-}7/9\text{-}11}$), 7.62-7.66 (m, 4H, $H_{5/6/9/10}$).

^{31}P{^{1}H} NMR (CD_2Cl_2, 162 MHz, 295 K): δ 75.8 (s).

7.4 Synthesis of $[Ru(\eta^5\text{-}C_5H_5)(P(OMe)_3)_2Cl]$

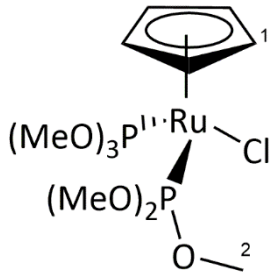

Prepared as described in the literature.[272]

An oven dried Schlenk tube charged with a solution of $[Ru(\eta^5\text{-}C_5H_5)(PPh_3)_2Cl]$ (1.00 g, 1.83 mmol) and trimethylphosphite (500 mg, 4.00 mmol) in xylene (30 mL) was heated at reflux for 4 hours. The solution was allowed to cool and the solvent removed *in vacuo*. The product was extracted with dichloromethane and purified by column chromatography on alumina. The excess phosphite and xylene was eluted with 4:1 light petroleum: dichloromethane. The product was eluted with dichloromethane and crystallised by addition of light petroleum. Yield 563 mg, 91 %.

^{1}H NMR (CD_2Cl_2, 400 MHz, 295 K): δ 3.60 (m, $^3J_{HP} + {}^5J_{HP}$ = 11.6 Hz, 18H, H_2) 4.79 (t, $^4J_{HP}$ = 0.8 Hz, 15 H, H_1).

^{31}P{^{1}H} NMR (CD_2Cl_2, 162 MHz, 295 K): δ 159.2 (s).

7.5 Synthesis of [$Ru(PPh_3)_3Cl_2$]

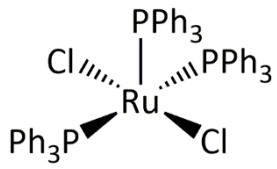

Prepared as described in the literature.[310]

An oven dried Schlenk tube charged with a suspension of $RuCl_3{\cdot}nH_2O$ (1.00 g, 3.83 mmol for n = 3) and triphenylphosphine (6.00 g, 22.9 mmol) in methanol (50 mL) was heated at reflux for 4 hours. The brown solid that precipitated was collected by filtration, washed with diethyl ether and dried in air to give $RuCl_2(PPh_3)_3$ as a dark brown powder. Yield = 3.59 g, 98 %.

$^{31}P\{^1H\}$ NMR (CD_2Cl_2, 202 MHz, 295 K): δ 30.2 (s, PPh_2).

7.6 Synthesis of [*trans*-$Ru(dppe)_2Cl_2$]

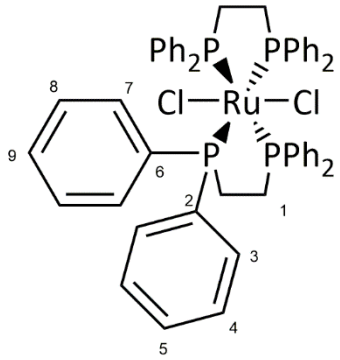

Prepared as described in the literature.[246]

An oven dried round bottom flask was purged with nitrogen and charged with $RuCl_2(PPh_3)_3$ (3.59 g, 3.75 mmol) and dppe (3.14 g, 7.89 mmol) in degassed acetone (40 mL) was stirred for 1 hour at room temperature. The resulting yellow precipitate was collected by filtration, washed with acetone and dried in air to afford [*trans*-$Ru(dppe)_2Cl_2$]. Yield 3.40 g, 99%.

^1H NMR (CD_2Cl_2, 400 MHz, 295 K): δ 2.75 (m, 8H, H_1), 6.99 (m, 16H, H_{4+8}), 7.17-7.25 (m, 24H, $H_{3+5+7+9}$).

$^{31}P\{^1H\}$ NMR (CD_2Cl_2, 202 MHz, 295 K): δ 44.6 (s, PPh_2).

7.7 Synthesis of [Ru(dppe)$_2$Cl][OTf]

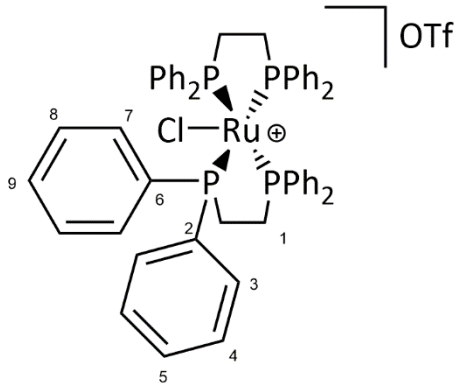

Prepared as described in the literature.[246]

An oven dried round bottom flask was purged with nitrogen and charged with a suspension of [*trans*-Ru(dppe)$_2$Cl$_2$] (3.40 g, 3.51 mmol) and AgOTf (0.90 g, 3.51 mmol) in dichloromethane (40 ml) was stirred 1 h. The resulting dark red solution was filtered through Celite to remove the precipitated AgCl, and the filtrate diluted with hexane. Careful removal of the dichloromethane on a rotary evaporator resulted in the precipitation of [Ru(dppe)$_2$Cl][OTf], which was collected, washed with hexane and dried to afford a dark red solid, which is stable in air and chlorinated solvents. Yield 3.22 g, 85%. Note: [Ru(dppe)$_2$Cl]PF$_6$ is obtained *via* the same procedure with AgPF$_6$ used in place of AgCl.

^{1}H NMR (CD$_2$Cl$_2$, 400 MHz, 295 K): δ 1.57 (m, 2H, CH$_2$), 2.35 (m, 4H, CH$_2$), 2.60 (m, 2H, CH$_2$), 6.65-6.70 (m, 4H, Ar-H), 6.98-7.04 (m, 12H, Ar-H), 7.17-7.29 (m, 16H, Ar-H), 7.36 (t, $^3J_{HH}$ = 7.1 Hz, 2H, Ar-H), 7.56 (t, $^3J_{HH}$ = 7.3 Hz, 2H, Ar-H), 7.72-7.76 (m, 4H, Ar-H).

^{31}P{^{1}H} NMR (CD$_2$Cl$_2$, 202 MHz, 295 K): δ 60.0 (t, $^3J_{PP}$ = 12 Hz, PPh$_2$), 83.2 (t, $^3J_{PP}$ = 12 Hz, PPh$_2$).

7.8 Synthesis of LiN(SiMe$_3$)$_2$

Prepared as described in the literature.[365]

To a diethyl ether solution of HN(SiMe$_3$)$_2$ (3.00 g, 3.88 mL, 18.6 mmol, in 50 mL) at 0°C was added ^{n}BuLi (1.6 M, 12 mL, 19 mmol) dropwise, affording a white precipitate. The mixture was stirred at room temperature for 3 hours. The solvent was removed *in vacuo* and the white solid product was washed twice with pentane (2 x 20 mL) at 0 °C. The solid was dried *in vacuo* and the product analysed by ^{1}H NMR. Yield = 2.78 g, 89 %.

^{1}H NMR (270 MHz, C_7D_8): 0.25 (s)

7.9 Synthesis of [Ru(η^5-C_5H_5)(PPh_3)$_2$Cl], [1-306]

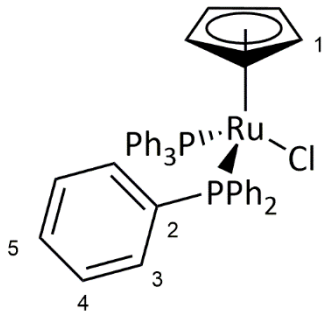

Prepared as described in the literature.[366]

An oven dried Schlenk was charged with [Ru(η^5-C_5H_5)(PPh_3)$_2$Cl] (2.00 g, 2.75 mmol) and 1,2-bis(triphenylphosphino)ethane (dppe, 1.15 g , 2.89 mmol) in toluene (40 mL). The reaction mixture was heated under reflux for 16 hours or until the phosphorus NMR spectrum indicated the reaction had reached completion. The solvent was removed *in vacuo* and the orange oil purified by alumina column chromatography. Dichloromethane was first used to elute free triphenylphosphine and acetone used to elute the orange band of the product. Removal of the solvent *in vacuo* afforded an orange oil; the unreacted dppe was removed by washing the oil with diethyl ether (2 x 5 mL) to afford [Ru(η^5-C_5H_5)(dppe)Cl] as an orange powder (yield: 974 mg, 59 %).

^{1}H NMR (400 MHz, CD_2Cl_2, 295 K): δ 2.37 - 2.49 (m, 2H, $H_{2a/b}$), 2.60 - 2.74 (m, 2H, $H_{2a/b}$), 4.57 (s, 5H, H_1), 7.14 - 7.20 (m, 4H, Ar-H), 7.28 - 7.36 (m, 6H, Ar-H), 7.42 - 7.46 (m, 6H, Ar-H), 7.88 - 7.92 (m, 4H, Ar-H)

^{31}P{^{1}H} NMR (162 MHz, CD_2Cl_2, 295 K): δ 81.8 (s, PPh_3).

7.10 Synthesis of [Ru(η^5-C_5H_5)(PPh_3)$_2$(-C≡CPh)], [14b]

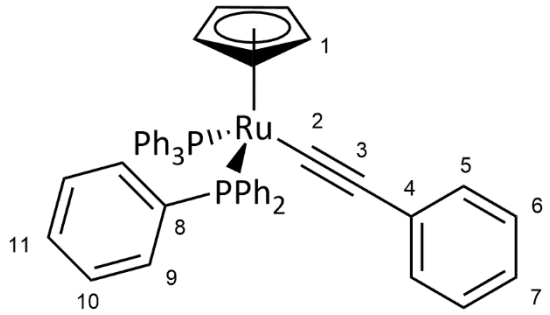

Prepared as described in the literature.[218]

An oven dried Schlenk was charged with RuCl(η^5-C_5H_5)(PPh_3)$_2$ (250 mg, 0.35 mmol) suspended in methanol (10mL). Phenylacetylene (75 µL, 51 mg, 0.5 mmol) was added and the reaction mixture was heated at reflux for 30 minutes and then allowed to cool to room temperature. Sodium methoxide (27 mg, 0.50 mmol) was added and the resulting solid yellow precipitate isolated by cannula filtration and washed with pentane (3 x 15 mL). The yellow precipitate was dried *in vacuo*. Yield = 145 mg, 53 %.

^{1}H NMR (400 MHz, CD_2Cl_2): δ 4.24 (s, 5H, H_1), 7.21 (m, 35H, $H_{5\text{-}7,9\text{-}11}$).

^{31}P{^{1}H} NMR (162 MHz, CD_2Cl_2): δ 50.8 (s).

7.11 Synthesis of [Ru(η^5-C_5H_5)(PPh_3)$_2$(-C≡CH)], [14e]

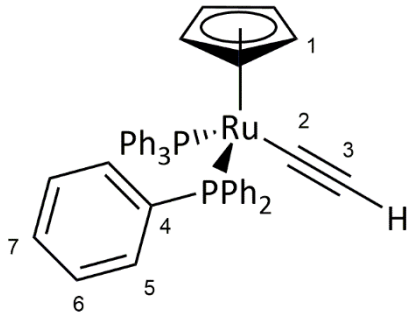

Prepared as described in the literature.[190]

To oven dried Schlenk tube containing a suspension of [Ru(η^5-C_5H_5)(PPh_3)$_2$(=C=CH_2)][PF_6] (257 mg, 0.30 mmol) in tetrahydrofuran (10mL) was added potassium *tert*-butoxide (56 mg, 0.5 mmol); the suspension was stirred at room temperature for 30 minutes. The solvent was removed *in vacuo* and the residue extracted with dichloromethane (5 mL) and filtered through a plug of alumina. The solvent was removed *in vacuo,* washed with pentane (2 x 5 mL), and dried *in vacuo* to yield a yellow solid. Yield = 162 mg, 76 %.

^{1}H NMR (400 MHz, CD_2Cl_2): δ 1.81 (t, $^4J_{FP}$= 2.2 Hz, 1H, ≡CH), 4.18 (s, 5H, C_5H_5), 7.22 (m, 30H, 6xPh).

^{31}P{^{1}H} NMR (162 MHz, CD_2Cl_2): δ 50.2 (s, PPh_3).

7.12 Synthesis of $[Ru(\eta^5\text{-}C_5H_5)(PPh_3)_2(=C=CFPh)]BF_4$, [15b]$BF_4$

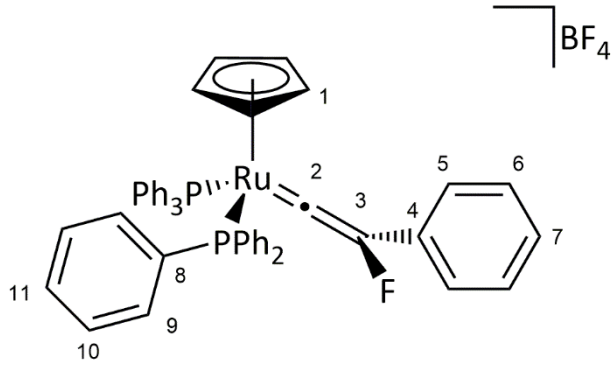

Prepared as described in the literature.[218]

An oven dried Schlenk tube in the glovebox was charged with a solution of [Ru(η^5-C_5H_5)(PPh_3)$_2$(C≡CPh)] (145 mg, 0.18 mmol) in dichloromethane (*ca.* 5 mL) to which was added 1-fluoro-2,4,6-trimethpyridinium tetrafluoroborate (37 mg, 0.16 mmol). The reaction mixture was stirred at room temperature for 20-30 min. The resultant green solution was reduced to the minimum volume and a green solid precipitated upon addition of pentane (*ca.* 10 mL). The solution was filtered and the precipitate washed with diethyl ether (3 x 5 mL). The green precipitate was isolated by filtration and dried *in vacuo* to afford a green solid. Yield = 101 mg, 64 %.

^{1}H NMR (400 MHz, CD_2Cl_2): δ 5.34 (s, 5H, H_1), 7.13 (m, 35H, $H_{5\text{-}7,9\text{-}11}$).

^{19}F NMR (376 MHz, CD_2Cl_2): δ 192.8 (s).

^{31}P{^{1}H} NMR (162 MHz, CD_2Cl_2): δ 41.3 (s, PPh_3).

7.13 Synthesis of [Ru(η^5-C_5H_5)(dppe)(=C=CFPh)]NSI, [19]NSI

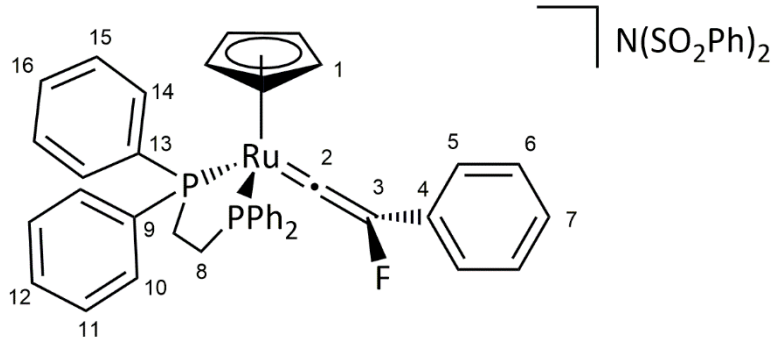

Prepared as described in the literature.[218]

An oven dried Schleck tube was charged with [Ru(η^5-C_5H_5)(dppe)(CCPh)] (100 mg, 0.15 mmol) in dichloromethane (*ca*. 3 mL); to the solution was added *N*-fluorobenzensulfonimde (47.4 mg, 0.15 mmol). After stirring the reaction for ten minutes at room temperature, a green precipitate was formed upon addition of pentane (10 mL). The solid was isolated by filtration, washed with toluene (5 mL) and pentane (2 x 5 mL), and dried *in vacuo* to yield [Ru(η^5-C_5H_5)(dppe)(CC(F)Ph)]N(SO_2Ph). Yield = 111 mg, 75 %.

^{1}H NMR (400 MHz, CD_2Cl_2, 295 K): 2.82 - 3.04 (m, 4H, H_8), 5.54 (s, 5H, H_1), 6.37 - 6.40 (m, 2H, H_5), 6.96 - 7.01 (m, 3H, H_{6+7}), 7.09 - 7.16 (m, 4H, Ar-H), 7.20 - 7.29 (m, 10 H, Ar-H), 7.32 - 7.40 (m, 10H, Ar-H), 7.49 - 7.50 (m, 2H, Ar-H), 7.74 - 7.75 (m, 4H, Ar-H).

^{19}F NMR (CD_2Cl_2, 376.2 MHz, 295 K): δ -209.5 (s, F_3)

^{31}P{^{1}H} NMR (162 MHz, CD_2Cl_2, 295 K): δ 76.9 (s, PPh_2).

ESI-MS (m/z): Expected for $C_{39}H_{34}FP_2Ru$ = 685.1168; Observed: 685.1147 [M^+] (Error = 2.1 mDa).

7.14 Synthesis of [Ru(η^5-C_5H_5)(dppe)(-CF=CFPh)], [23a]

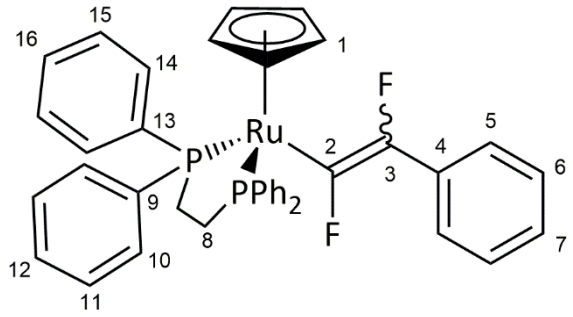

An oven dried Schlenk tube was charged with [Ru(η^5-C_5H_5)(dppe)(=C=CFPh)]NSI (100 mg, 0.10 mmol) and tetramethylammonium fluoride (37 mg, 0.40 mmol) suspended in tetrahydrofuran (15 mL). The suspension was sonicated for 20 minutes to afford a yellow solution which was evaporated to dryness *in vacuo*. The residue was extracted with dichloromethane (10 mL), filtered through a plug of alumina and the solvent removed *in vacuo*. The residue was washed with pentane (5 mL), agitated, and dried *in vacuo* to afford a yellow powder. Yield = 55 mg, 78 %.

Complex **[2-24]** is formed in a 1:1 ratio of *E*- : *Z*- isomers; after standing in dichloromethane for one week the complex isomerises to the *Z*- isomer.

***E*- Isomer**

Selected ^{1}H NMR (500 MHz, CD_2Cl_2, 295 K): δ 2.50 (m, 2H, H_{8a}), 2.82 (m, 2H, H_{8b}), 4.19 (s, 5H, H_1).

Selected ^{13}C{^{1}H} NMR (126 MHz, CD_2Cl_2, 295K): δ 28.8 (t, $^1J_{PC}$ = 23 Hz, C_8), 83.8 (s, C_1), 151.2 (C_3), 173.0 (C_2).

^{19}F NMR (471 MHz, CD_2Cl_2, 295 K): δ -67.8 (td, $^3J_{PF}$ = 37 Hz, $^3J_{FF}$ = 10 Hz, F_2), -107.3 (d, $^3J_{FF}$ = 10 Hz, F_3).

^{31}P{^{1}H} NMR (202 MHz, CD_2Cl_2, 295 K): δ 90.4 (d, $^3J_{PF}$ = 37 Hz, PPh_2).

***Z*- Isomer**

Selected ^{1}H NMR (500 MHz, CD_2Cl_2, 295 K): δ 2.65 (m, 2H, H_{8a}), 2.75 (m, 2H, H_{8b}), 4.73 (s, 5H, H_1), 6.83 (d, $^3J_{HH}$ = 8 Hz, 2H, H_5), 6.90 (t, $^3J_{HH}$ = 7Hz, 1H, H_7), 7.05 (app. t, $^3J_{HH}$ = 8 Hz, 2H, H_6).

Selected $^{13}C\{^{1}H\}$ NMR (126 MHz, CD_2Cl_2, 295K): δ 29.4 (t, $^{1}J_{PC}$ = 22 Hz, C_8), 83.6 (s, C_1), 123.6 (t, $^{4}J_{CF}$ = 8Hz, C_5), 124.0 (s, C_7), 127.3 (s, C_6), 158.8 (dd, $^{1}J_{CF}$ = 198 Hz, $^{2}J_{CF}$ = 51 Hz, C_3), 188.2 (ddt, $^{1}J_{CF}$ = 294 Hz, $^{2}J_{CF}$ = 89 Hz, $^{2}J_{PC}$ = 19 Hz, C_2).

^{19}F NMR (471 MHz, CD_2Cl_2, 295 K): δ -83.0 (dt, $^{3}J_{FF}$ = 113 Hz, $^{3}J_{PF}$ = 28 Hz, F_2), -107.3 (d, $^{3}J_{FF}$ = 113 Hz, F_3).

$^{31}P\{^{1}H\}$ NMR (202 MHz, CD_2Cl_2, 295 K): δ 92.8 (dd, $^{3}J_{PF}$ = 28 Hz, $^{4}J_{PF}$ = 3 Hz, PPh_2).

ESI-MS (m/z): Expected for $C_{39}H_{35}F_2P_2Ru$ = 705.1231 m/z; Observed: 705.1235 m/z [$M^{\cdot+}$] (Error = -0.4 mDa).

7.15 Synthesis of *Z*-[Ru(η^5-C_5H_5)(dppe)(-CH=CFPh)], [23b]

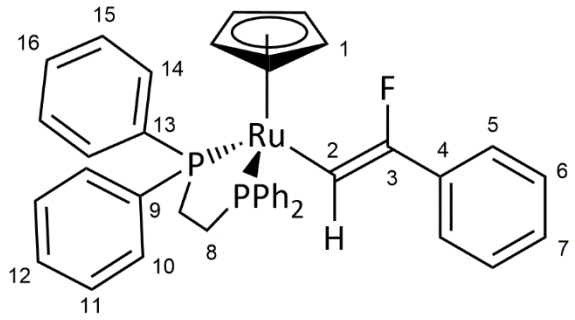

An oven dried Schlenk tube was charged with [Ru(η^5-C_5H_5)dppe(CC(F)Ph)]NSI (30 mg, 0.031 mmol) in THF (*ca.* 3 mL) and cooled to -78 °C. Separately an oven dried ampoule was charged with a solution of sodium borohydride (1.8 mg, 0.047 mmol) in ethanol (*ca.* 3 mL) and cooled to -78 °C. Once cooled, the sodium borohydride solution was added via cannula into the ruthenium solution and stirred for 10 minutes. After which the solution was allowed to warm up to room temperature and stirred for a further 10 minutes. The solvent was removed *in vacuo* and a yellow solution extracted with pentane (15 mL). The solvent was removed *in vacuo* to yield a yellow residue. Yield was not determined.

The residue was redissolved in deuterated dichloromethane without further purification. A mixture of the *Z*- isomer (26 % conversion) and [Ru(η^5-C_5H_5)(dppe)(-C≡CPh)] (58 % conversion) was obtained; the *E*- isomer was not observed.

Selected ^{1}H NMR (500 MHz, CD_2Cl_2, 295 K): δ 4.84 (s, 5H, H_1), 5.60 (dt, $^3J_{HF\text{-}trans}$ = 71 Hz, $^3J_{HP}$ = 7.9 Hz, H_2).

Selected ^{13}C{^{1}H} NMR (126 MHz, CD_2Cl_2, 295 K): δ 118.4 (dt, $^2J_{CF}$ = 45.5 Hz, $^2J_{CP}$ = 18 Hz, C_2), 136.6 (C_4), 161.1 (d, $^1J_{CF}$ = 227 Hz, C_3).

^{19}F NMR (471 MHz, CD_2Cl_2, 295 K): δ -99.9 (d, $^3J_{HF}$ = 71 Hz, F_3).

^{31}P{^{1}H} NMR (202 MHz, CD_2Cl_2, 295 K): δ 89.7 (s, PPh_2).

ESI-MS (m/z): Expected for $C_{39}H_{35}FP_2Ru$ = 686.1247 m/z; Observed: 686.1248 m/z [$M^{\cdot+}$] (Error = -0.2 mDa).

7.16 Synthesis of [Ru(η^5-C_5H_5)(PPh_3)$_2$Cl], [24]

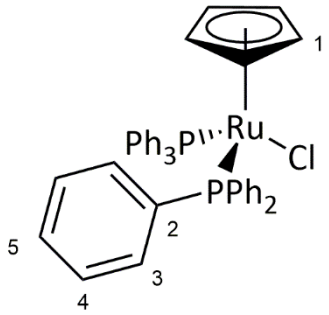

Prepared as described in the literature.[223]

Dicyclopentadiene (50 mL) was freshly cracked to afford cyclopentadiene using distillation apparatus, with the temperature at the top of the Vigreux column being maintained at 35 °C in order to prevent transfer of the dimer.

Ethanol (1 L) was degassed with nitrogen in a 2 litre, 3-necked round bottom flask for approximately 60 minutes. Anti-bumping granules and triphenylphosphine (21 g, 0.08 mol) were added and was heated to reflux.

$RuCl_3.3H_2O$ (4.98 g, 0.02 mol) was dissolved in deoxygenated ethanol (*ca.* 80 mL). Separately, freshly-distilled cyclopentadiene (10 mL) was added to degassed ethanol (approximately 10 mL).

The solution of $RuCl_3.3H_2O$ was added to the refluxing triphenylphosphine via syringe, followed by the cyclopentadiene solution. The reaction mixture was heated at reflux for 1 hour. The solution was allowed to cool to room temperature and stored at -20 °C overnight to produce bright red crystals. The air-stable crystals were collected by vacuum filtration in air and washed with ethanol (4 x 25 mL) and diethyl ether (4 x 25 mL). Further batches of crystals could be obtained by reduction of the solvent volume and storing the subsequent solutions in the freezer at -20 °C overnight. Yield = 11.2 g, 77 %.

^{1}H NMR (CD_2Cl_2, 400 MHz, 295 K): δ 4.10 (s, 5H, H_1), 7.15 (app.t, 12H, $^3J_{HH}$ = 7.2 Hz, H_3), 7.26 (t, 6H, $^3J_{HH}$ = 7.4 Hz, H_5), 7.33 – 7.37 (m, 12H, H_4).

^{31}P{^{1}H} NMR (CD_2Cl_2, 162 MHz, 295 K): δ 39.5 (s, PPh_3).

7.17 Synthesis of $[(Ru(\eta^5\text{-}C_5H_5)(PPh_3)_2)_2(\mu\text{-}C_4H_2F)]BF_4$, [27]$BF_4$

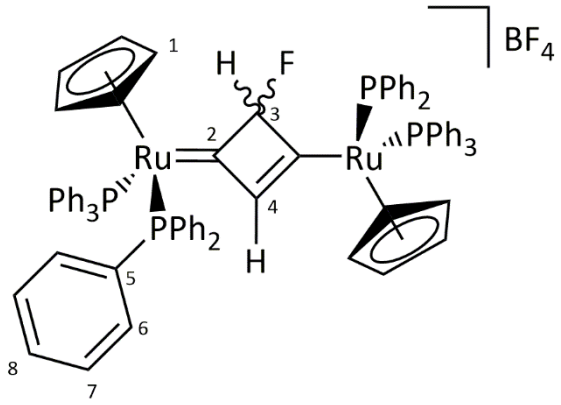

A mixture of $[Ru(\eta^5\text{-}C_5H_5)(PPh_3)_2(C{\equiv}CH)]$ (125 mg, 0.07 mmol) and 1-fluoro-2,4,6,-trimethylpyridinium tetrafluoroborate (10 mg, 0.04 mmol) dissolved in dichloromethane (10 mL) was added to an oven dried Schlenk tube and stirred at room temperature for 20 min. The resultant orange-brown solution was concentrated to *ca.* 3 mL and cannula filtered into rapidly stirring diethyl ether (25 mL). The orange-brown precipitate was isolated by cannula filtration and was washed further with diethyl ether (2 x 5 mL) and dried *in vacuo* to afford $[(Ru(\eta^5\text{-}C_5H_5)(PPh_3)_2)_2(\mu\text{-}C_4H_2F)]$ $[BF_4]$. Yield: 122 mg, 91 %.

^{1}H NMR (500 MHz, CD_2Cl_2, 295K): δ 4.37 (s, 10H, H_1), 4.84 (d, $^2J_{HF}$= 57.6 Hz, 1H, H_3), 7.02 (m, 24H, H_7), 7.17 (t, $^3J_{HH}$= 7.1 Hz, 24H, H_6), 7.37 (t, $^3J_{HH}$= 7.7 Hz, 12 H, H_8), 7.45 (d, $^4J_{HF}$= 12.5 Hz, 1H, H_4).

^{13}C{^{1}H} NMR (126 MHz, CD_2Cl_2, 295K): δ 89.4 (s, C_1), 108.7 (d, $^2J_{CF}$= 233.1 Hz, C_3), 128.4 (t, $^2J_{CP}$= 4.2 Hz, C_6), 130.2 (s, C_8), 133.8 (C_8), 138.5 (C_5), 183.2 (d, $^4J_{CF}$= 25.1 Hz, C_4), 250.6 (dt, $^3J_{CF}$= 20.1 Hz, $^3J_{CP}$= 13.5 Hz, C_2).

^{19}F NMR (471 MHz, CD_2Cl_2, 295K): δ -138.7 (dd, $^2J_{HF}$= 57.6 Hz, $^4J_{HF}$= 12.5 Hz).

^{31}P{^{1}H} NMR (202 MHz, CD_2Cl_2, 295K): δ 49.1 (s, PPh_3).

ESI-MS (m/z): Expected for $C_{86}H_{72}FP_4Ru_2$ $[M^+]$= 1451.2656; Observed= 1451.2690 $[M^+]$ (Error = 3.4 mDa).

UV-Vis: λ_{max} = 465 nm, ε = 41540 mol^{-1} dm^2 at a concentration of approximately 1 mmol dm^{-3} and a path length of 1 cm; calculated λ_{max} = 431 nm.

Suitable crystals for single crystal X-ray diffraction of the hexafluorophosphate salt were obtained by slow diffusion from a dichloromethane: pentane solvent system. The hexafluorophosphate salt was obtained by stirring **[x]**BF_4 with 20 equivalents of $NaPF_6$ in dichloromethane for one hours.

7.18 Synthesis of [Ru(η^5-C_5Me_5)(PPh_3)$_2$(C≡CH)], [28a]

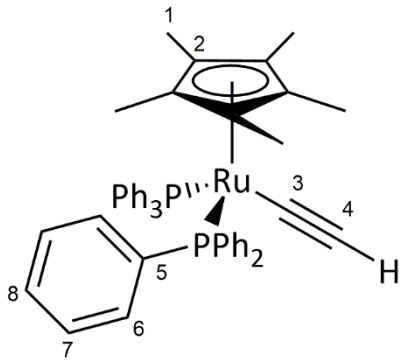

Prepared as described in the literature.[237]

[Ru(η^5-C_5Me_5)(PPh_3)$_2$(=C=CH_2)]PF_6 (159 mg, 0.17 mmol) was dissolved THF (10 mL) and stirred in the presence of *tert*-butoxide (22 mg, 0.19 mmol) for 25 minutes. The solvent was removed *in vacuo* and the complex was extracted with toluene (15 mL). The solution was reduced to a third of its original volume and a yellow solid precipitated by addition diethyl ether. The yellow solid was filtered and washed twice more with diethyl ether (2 x 20 mL), before being dried *in vacuo*. Yield = 72 mg, 54 %.

^{1}H NMR (400 MHz, CD_2Cl_2): δ 1.06 (s, 15H, H_1), 2.11 (t, $^4J_{FP}$= 2.1 Hz, 1H, H_4), 6.88-6.98 (m, 12 H, $H_{6/7}$), 7.00-7.05 (m, 6 H, H_8), 7.40-7.48 (m, 12 H, $H_{6/7}$).

^{31}P{^{1}H} NMR (162 MHz, CD_2Cl_2): δ 50.3 (s, PPh_3).

7.19 Synthesis of [Ru(η^5-C$_5$Me$_5$)(PPh$_3$)$_2$(-C≡CF)], [28b]

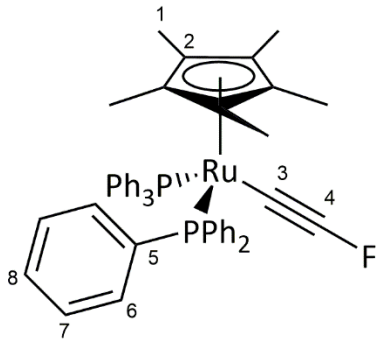

An oven dried Schlenk tube was charged with [Ru(η^5-C$_5$Me$_5$)(PPh$_3$)$_2$(=C=CFH)]PF$_6$ (100 mg, 0.11 mmol) and dissolved in THF (*ca*. 5 mL). An oven dried ampoule was charged with lithium bis(trimethylsilyl)amide (90 mg, 0.54 mmol) and dissolved in THF (ca. 5 mL). Both solutions were cooled to -78˚C and the lithium bis(trimethylsilyl)amide solution was transferred via cannula into the vinylidene solution. The reaction mixture was stirred for 20 minutes at -78˚C before being allowed to warm to room temperature over a further 20 minutes. The solvent was removed *in vacuo*, and the solid washed with pentane (*ca*. 5 mL). The solvent was removed *in vacuo* and this process was repeated once more to remove residual THF. A yellow solution was extracted using pentane (2 x 15 mL) and filtered via cannula. The solvent was removed *in vacuo* yielding a yellow solid which corresponded to an inseparable mixture of [Ru(η^5-C$_5$Me$_5$)(PPh$_3$)$_2$(-C≡CF)] and HN(SiMe$_3$)$_2$. Yield: 16 mg, 19 %.

^{1}H NMR (C$_6$D$_6$, 400 MHz, 295 K): δ 1.28 (t, $^3J_{HP}$= 1.41 Hz, 15 H, H$_1$).

(C$_6$D$_6$, 500 MHz, 295 K): δ 1.22 (bs, H$_1$), 6.86 (bs, H$_7$), 6.99 (bs, H$_{8/6}$), 7.70 (bs, H$_{6/8}$).

^{13}C{^{1}H} NMR (C$_6$D$_6$, 126 MHz, 295 K): δ 9.5 (s, C$_1$), 92.6 (t, $^2J_{CP}$= 2.0 Hz, C$_2$), 113.5 (d, $^2J_{CF}$= 336 Hz, C$_4$), 134.2 (d, $^2J_{CP}$= 11.8 Hz, C$_7$), 134.7 (bs, C$_8$), 137.7 (d, $^2J_{CP}$= 12.2 Hz, C$_6$), 138.0 (t, $^1J_{CP}$ + $^3J_{CP}$= 18.5 Hz, C$_5$).

C$_3$ could not be identified.

^{19}F NMR (C$_6$D$_6$, 376 MHz, 295 K): δ -186.9 (t, $^4J_{PF}$= 5.0 Hz).

^{31}P{^{1}H} NMR (C$_6$D$_6$, 162 MHz, 295 K): δ 50.9 (d, $^4J_{PF}$= 5.0 Hz).

Selected ATR IR: ν(C≡C) 1959 cm^{-1}.

ESI-MS (m/z): Expected for C$_{48}$H$_{46}$FP$_2$Ru [M+H$^+$]= 805.2096; Observed= 805.2083 [M + H$^+$] (Error = 1.3 mDa).

7.20 Synthesis of $[Ru(\eta^5\text{-}C_5Me_5)(PPh_3)_2(=C=CFH)]PF_6$, [30a]$PF_6$

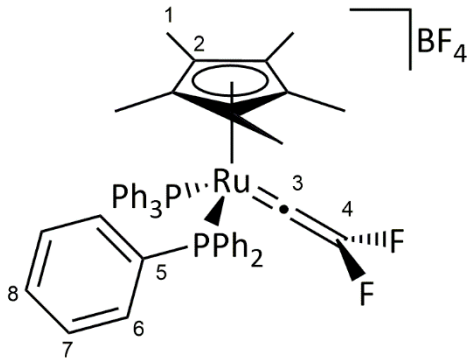

An oven-dried Schlenk tube charged with $[Ru(\eta^5\text{-}C_5Me_5)(PPh_3)_2(\text{-}C\equiv CH)]$ (100 mg, 0.11 mmol) suspended in acetonitrile (5 mL) was treated with a solution of Selectfluor (41.0 mg, 0.12 mmol) in acetonitrile (*ca.* 5 mL). The solution was stirred for 20 minutes, after which the solvent was removed *in vacuo*, and the green solid redissolved in dichloromethane (*ca*. 10 mL), to which sodium hexafluorophosphate (400 mg, 2.02 mmol) was added as a solid. The solution was stirred for 40 minutes before being reduced to a third of the initial volume and filtered. A green solid was precipitated upon addition of pentane (*ca.* 15 mL); the solution was filtered and the solid washed a further two times with pentane (2 x 5 mL) and dried *in vacuo*. Yield = 60 mg, 58 %.

^{1}H NMR (500 MHz, CD_2Cl_2, 295 K): δ 1.28 (t, $^4J_{HP}$ = 1.4 Hz, 15 H, H_1), 7.11 (app. t, ^3J = 8.3 Hz, 12 H, H_7), 7.22 (t, ^3J= 6.1 Hz, 12 H, H_6), 7.70 (t, $^3J_{HH}$=7.4, 6H, H_8), 8.60 (d, $^2J_{HF}$= 80.9 Hz, 1H, H_4).

^{13}C{^{1}H} NMR (126 MHz, CD_2Cl_2, 295 K): δ 9.6 (s, C_2), 107.0 (s, C_1), 128.3 (t, $^2J_{PC}$= 11.8 Hz, C_6), 131.0 (s, C_7), 132.1 (C_5), 133.7 (s, C_8), 178.7 (d, $^1J_{CF}$= 230.3 Hz, C_4), 367.9 (d, $^2J_{CF}$= 17.4 Hz, C_3).

^{19}F NMR (471 MHz, CD_2Cl_2, 295 K): δ -236.1 (d, $^2J_{HF}$= 81 Hz).

^{31}P{^{1}H} NMR (203 MHz, CD_2Cl_2, 295 K): δ 51.5 (s).

ESI-MS (m/z): Expected for $C_{48}H_{46}FP_2Ru$ [M^+]= 805.2096; Observed= 805.2092 [M^+] (Error = 0.4 mDa).

Selected ATR IR: ν(vinylidene C=C) 1644 cm^{-1}.

Elemental Analysis: $C_{57}H_{53}FP_4Ru$ + 1.1(CH_2Cl_2) Calc. /% C 56.53, H 4.66, Found /% C 56.56, H 4.58. Residual dichloromethane (two molecules) observed in the crystal structure.

Suitable crystals for X-ray crystallography were grown by slow diffusion from dichloromethane: pentane.

7.21 Synthesis of [Ru(η^5-C_5Me_5)(PPh_3)$_2$(=C=CF_2)]NSI, [30b]NSI

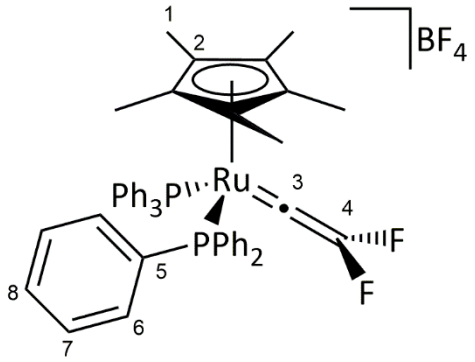

To an oven dried Schlenk tube was added a benzene-d^6 solution of [Ru(η^5-C_5Me_5)(PPh_3)$_2$(-C≡CF)] (approximately 25 mg in 2-3 mL) and cooled down to -78 ˚C. To the cooled solution was added NFSI (66 mg, 0.21 mmol) in toluene (*ca*. 5 mL). The solution was stirred for 20 minutes at -78 ˚C, and then allowed to warm up to room temperature over 20 minutes. The resultant dark green reaction mixture was filtered via cannula and the black/dark green solid washed with pentane. The solid was dried *in vacuo*; the yield was not determined. The product is obtained as a mixture of other unknown species according the ^{1}H NMR spectrum which displayed unidentified signals for aromatic and trimethylsilyl protons; nevertheless, [Ru(η^5-C_5Me_5)(PPh_3)$_2$(=C=CF_2)]NSI was observed as the only phosphorus- and fluorine-containing species.

^{1}H NMR (CD_2Cl_2, 400 MHz, 295 K): δ 1.27 (t, $^3J_{HP}$ = 1.4 Hz, 15H, H_1), 7.00-7.35 (m, H_6-H_8).

^{19}F NMR (CD_2Cl_2, 376 MHz, 295 K): δ -135.2 (s).

^{31}P{^{1}H} NMR (CD_2Cl_2, 162 MHz, 295 K): δ 49.5 (s).

MS-ESI (m/z/): Expected for $C_{48}H_{45}F_2P_2Ru$= 823.2009 $[M]^+$; Observed= 823.1996 $[M]^+$ (1.3 mDa error).

7.22 Synthesis of $[Ru(\eta^5\text{-}C_5H_5)(PPh_3)_2(=C=CFH)]BF_4$, [44a]$BF_4$

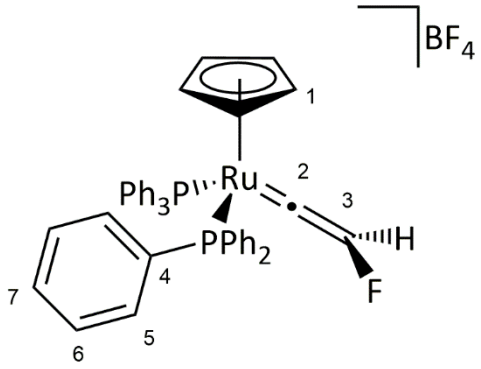

To an oven dried Schlenk charged with a suspension of $[Ru(\eta^5\text{-}C_5H_5)(PPh_3)_2(C\equiv CH)]$ (50 mg, 70 µmol) in acetonitrile (5 mL) was added an acetonitrile solution of Selectfluor (27 mg, 77 µmol). The suspension was stirred for 20 minutes, after which time the solvent was removed *in vacuo* and the residue extracted with dichloromethane (*ca.* 3 mL). The dichloromethane solution was transferred by cannula filtration into rapidly stirring pentane (15 mL). The resulting precipitate was isolated by cannula filtration and washed with diethyl ether (2 x 5 mL). The desired product was obtained as an inseparable mixture of multiple products, including **[2-x]**BF_4 (1:1 with respect to **[1]**BF_4).

Complex **[1]**BF_4 can obtained as the major species (57%) by addition of Selectfluor to a (d^3-)acetontrile solution of $[Ru(\eta^5\text{-}C_5H_5)(PPh_3)_2(C\equiv CH)]$ without further purification.

The complex **[1]**BF_4 was found to be unstable and rapidly decomposes over 16 hours; consequently, only partial characterisation has been achieved. Assignments were made based on the change in the NMR spectra after 16 hours.

Selected ^{1}H NMR (500 MHz, CD_2Cl_2, 295K): δ 5.31 (s, 5H, H_1), 8.27 (d, $^2J_{HF}$ = 80 Hz, 1H, H_2).

(500 MHz, CD_3CN, 298K): δ 5.37 (s, 5H, H_1), 8.56 (d, $^2J_{HF}$ = 80 Hz, 1H, H_3).

^{19}F NMR (471 MHz, CD_2Cl_2, 295K): δ -233.0 (d, $^2J_{HF}$= 80 Hz).

(471 MHz, CD_3CN, 298K): δ -235.5 (d, $^2J_{HF}$= 80 Hz).

^{31}P{^{1}H} NMR (202 MHz, CD_2Cl_2, 295K): δ 43.8 (s, PPh_3).

(202 MHz, CD_3CN, 298K): δ 44.1 (s, PPh_3).

ESI-MS (m/z): Expected for $C_{43}H_{36}FP_2Ru$ $[M^+]$= 735.1314; Observed= 735.1334 $[M^+]$ (Error = -0.2 mDa).

7.23 Synthesis of $[Ru(\eta^5\text{-}C_5H_5)(PPh_3)_2(=C=CH_2)]PF_6$, [44b]$PF_6$

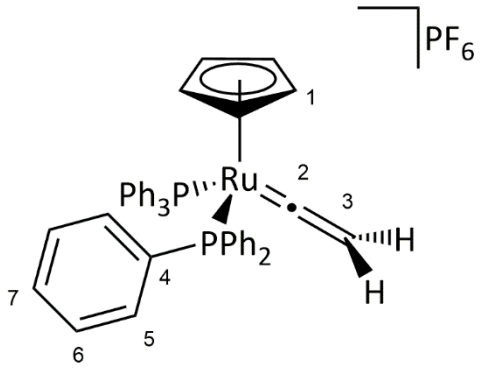

Prepared as described in the literature.[190]

Ethynyltrimethylsilane (195 µL, 1.36 mmol) was added under nitrogen to a suspension of $Ru(\eta^5\text{-}C_5H_5)(PPh_3)_2Cl$ (250 mg, 0.34 mmol) and ammonium hexafluorophosphate (112 mg, 0.68 mmol) in *tert*-butanol (10mL). The mixture was heated at 35 ˚C for 8 hours or until the $^{31}P\{^1H\}$ NMR of the reaction mixture indicated completion. The light orange solid was collected by vacuum filtration in air and washed with diethyl ether (*ca.* 20 mL) and dried. Yield = 257 mg, 87 %.

^{1}H NMR (400 MHz, CD_2Cl_2): δ 4.26 (t, $^4J_{FP}$= 2.2 Hz, 2H, H_3), 5.01 (s, 5H, H_1), 7.19 (m, 30H, $H_{5\text{-}7}$).

$^{31}P\{^1H\}$ NMR (162 MHz, CD_2Cl_2): δ 44.0 (s, PPh_3).

7.24 Formation of Fluorovinylphosphonium complex, [48]$^+$

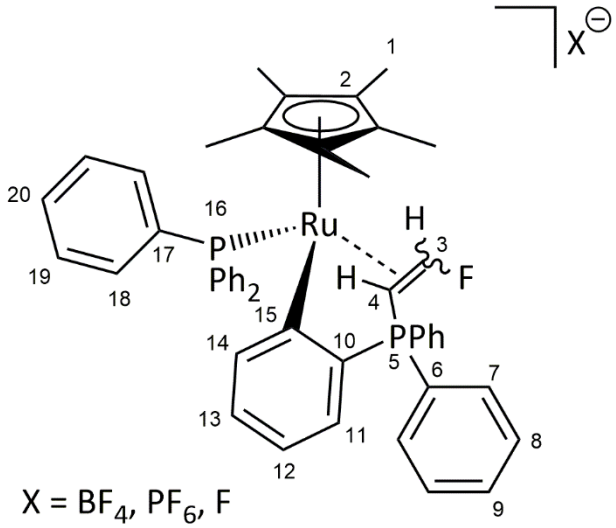

The fluorovinylphosphonium complex was obtained as the major by-product from the reaction of $[Ru(\eta^5\text{-}C_5Me_5)(PPh_3)_2(=C=CHF)]^+$ with either tetrabutylammonium fluoride, or lithium bis(trimethylsilyl)amide.

Addition of LiHMDS

In the procedure for obtaining $[Ru(\eta^5\text{-}C_5Me_5)(PPh_3)_2(\text{-}C\equiv CF)]$, **[x]**, (see above) the residue obtained after extraction of **[x]** was found to contain **[x]** as the major species.

Addition of TMAF

To Youngs tap NMR tube in the glovebox was added a suspension of $[Ru(\eta^5\text{-}C_5Me_5)(PPh_3)_2(=C=CHF)]BF_4$ (40 mg,) and tetrabutylammonium fluoride (4.1 mg,) in tetrahydrofuran (*ca.* 0.55 mL). The suspension was sonicated for 25 minutes and left for 36 hours to afford *E-/Z-* mixture of **[x]**. The solvent was removed *in vacuo*, and the residue redissolved in CD_2Cl_2, filtered, and used without further purification.

E- isomer

Selected ^{1}H NMR (CD_2Cl_2, 400 MHz, 295 K): δ 1.25 (d, $^3J_{HP}$= 1.1 Hz, 15H, H_1), 1.92 (dd, $^3J_{HF}$= 12.6 Hz, $^3J_{HH}$= 6.4 Hz, 1H, H_4), 6.37 ppm (dddd, $^2J_{HF}$= 69.2 Hz, $^3J_{HP}$= 11.3 Hz, $^3J_{HH}$= 6.3 Hz, $^3J_{HP}$= 1.9 Hz, 1H, H_3).

^{19}F NMR (CD_2Cl_2, 376 MHz, 295 K): δ -165.1 ppm (app. td, $^2J_{HF} + {}^3J_{PF}$= 69.3 Hz, $^3J_{HH}$ = 12.2 Hz).

$^{31}P\{^{1}H\}$ NMR (CD_2Cl_2, 162 MHz, 295 K): δ 41.3 (d, $^{3}J_{PP}$= 4.9 Hz, P_5), 48.7 ppm (dd, $^{3}J_{FP}$= 69.9 Hz, $^{3}J_{PP}$= 4.9 Hz, P_{16}).

Z- isomer

Selected ^{1}H NMR (CD_2Cl_2, 400 MHz, 295 K): δ 1.38 (d, $^{3}J_{HP}$= 1.3 Hz, 15H, H_1), 2.80 (app. dtd, $^{3}J_{HF}$= 21.5 Hz, $^{2}J_{HP}$/$^{3}J_{HH}$= 5.6 Hz, $^{3}J_{HP}$= 2.2 Hz, 1H, H_4), 5.99 ppm (dddd, $^{2}J_{HF}$= 69.0 Hz, $^{3}J_{HP}$= 23.1 Hz, $^{3}J_{HH}$= 8.1 Hz, $^{3}J_{HP}$= 5.6 Hz, 1H, H_3).

^{19}F NMR (CD_2Cl_2, 376 MHz, 295 K): δ -164.1 ppm (ddd, $^{2}J_{HF}$ = 69.1 Hz, $^{3}J_{HF}$ = 21.5 Hz, $^{3}J_{PF}$ = 13.0 Hz).

$^{31}P\{^{1}H\}$ NMR (CD_2Cl_2, 162 MHz, 295 K): δ 42.7 (dd, $^{3}J_{PF}$= 12.8 Hz, $^{3}J_{PP}$= 3.9 Hz, P_5), 56.5 ppm (d, $^{3}J_{PP}$= 3.9 Hz, P_{16}).

7.25 Synthesis of [Ru(η^5-C$_5$Me$_5$)(dppe)(=C=CFH)]NSI, [54a]NSI

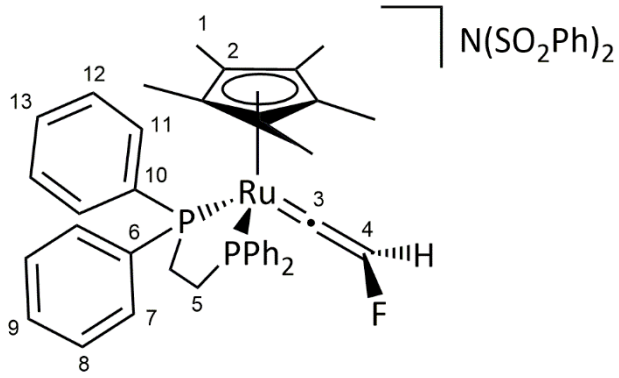

An oven dried Schlenk tube was charged with [RuCp*(dppe)(-C≡C-H)] (160 mg, 0.24 mmol) which was then dissolved in toluene (*ca*. 5 mL) and cooled to -78˚C. Separately a solution of NFSI (84.1 mg, 0.27 mmol) in toluene (*ca*. 5 mL) was prepared and added to the cold ruthenium solution. The solution was stirred for 15 minutes at -78˚C before being allowed to warm to room temperature over 1h. The green residue was isolated, and washed with toluene (1x 5 mL) and pentane (2 x 5 mL) before being dried *in vacuo* to yield **[x]**NSI as a pale green solid. Yield = 195 mg, 91 %.

^{1}H NMR (CD_2Cl_2, 500 MHz, 295 K): δ 1.59 (s, 15 H, H_1), 2.70 (m, 2 H, H_5), 2.94 (m, 2 H, H_5), 7.09 (dd, $^3J_{HH}$ = 10.8, 7.7 Hz, 4 H, H_9), 7.29 (m, 8 H, $H_{7/8}$), 7.32 (d, $^2J_{HF}$ = 80.2 Hz, 1 H, H_4), 7.49 (t, $^3J_{HH}$ = 7.3 Hz, 8 H, $H_{7/8}$).

^{13}C{^{1}H} NMR (CD_2Cl_2, 125 MHz, 295 K): δ 9.8 (s, C_1), 29.6 (m, C_5), 105.6 (s, C_2), 128.9 (t, *J* = 5.4 Hz, $C_{7/8/11/12}$), 129.0 (t, *J* = 4.6 Hz, $C_{7/8/11,12}$), 130.6 (d, *J* = 48.2 Hz, $C_{6/10}$), 131.8 (s, $C_{9/13}$), 132.0 (s, $C_{9/13}$), 132.1 (t, *J* = 5.3 Hz, $C_{7/8/11/12}$), 132.7 (t, *J* = 5.0 Hz, $C_{7/8/11/12}$), 134.5 (d, *J* = 58.0 Hz, C_6), 173.9 (d, $^1J_{CF}$ = 236.2 Hz, C_4), 362.8 (d, $^3J_{CF}$ = 43.5 Hz, C_3).

^{19}F NMR (CD_2Cl_2, 376 MHz, 295 K): δ -235.8 (d, $^2J_{HF}$ = 80.2 Hz, F_4).

^{31}P{^{1}H} NMR (CD_2Cl_2, 202 MHz, 295 K): δ 76.4 (s, PPh_2).

ESI-MS (m/z): Expected for $C_{38}H_{40}FP_2Ru$ = 679.1628 m/z; Observed: 679.1617 m/z [M^+] (Error = 1.1 mDa).

UV-Vis: λ_{max} = 601 nm, ε = 546 mol^{-1} dm^2 at a concentration of approximately 1 mmol dm^{-3} and a path length of 1 cm; calculated λ_{max} = 580 nm.

Selected ATR IR: ν(vinylidene C=C) 1652 cm^{-1}.

Elemental Analysis: $5(C_{38}H_{40}F_7P_3Ru).CH_2Cl_2$ Calc. /% C 54.58, H 4.84, Found /% C 54.56, H 4.84.

To obtain crystallographic data the dibenzenesulfonimide anion was exchanged for the hexafluorophosphate anion through ion metathesis. This was achieved by dissolving the dibenzenesulfonimide salt in dichloromethane with 20 equivalents of sodium hexafluorophosphate and stirred for 1 hour. Green crystals of the hexafluorophosphate salt were grown from a dichloromethane: pentane solvent system via slow diffusion.

7.26 Synthesis of [Ru(η^5-C$_5$Me$_5$)(dppe)(=C=CF$_2$)]NSI, [54b]NSI

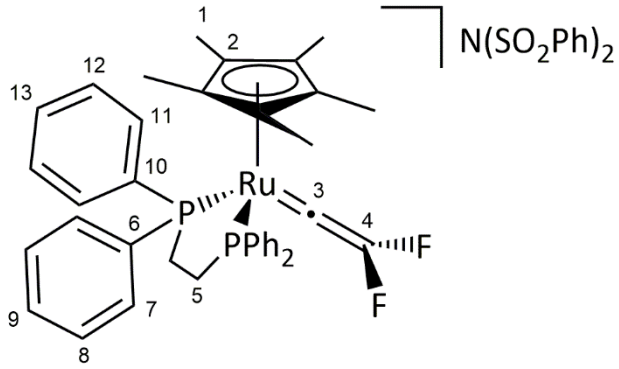

An oven dried Schlenk tube was charged with [RuCp*(dppe)(-C≡C-F)] (44 mg, 0.07 mmol) dissolved in THF (*ca*. 5 mL) and cooled to -78˚C. Separately a solution of NFSI (22.7 mg, 0.08 mmol) in THF (*ca*. 5 mL) was prepared and added to the cold ruthenium solution. The solution was stirred for 15 minutes at -78˚C before being allowed to warm up to room temperature over 1h. The solvent was removed *in vacuo* and the purple/red solid washed with toluene (2x 5 mL) and pentane (2 x 5 mL). The solid was dried *in vacuo* to yield the desired product. Yield = 32 mg, 55 %.

Selected ^{1}H NMR (CD_2Cl_2, 500 MHz, 295 K): δ 1.56 (t, $^4J_{HF}$ = 1.3 Hz, 15 H, H_1), 2.72 (m, 2 H, H_5), 2.82 (m, 2 H, H_5).

Selected ^{13}C{^{1}H} NMR (CD_2Cl_2, 125 MHz, 295 K): δ 9.8 (s, C_1), 29.7 (m, C_5), 106.9 (s, C_2), 231.3 (d, $^1J_{CF}$ = 277.6 Hz, C_4), 366.7 (d, $^3J_{CF}$ = 22.5 Hz, C_3).

^{19}F NMR (CD_2Cl_2, 376 MHz, 295 K): δ -134.0 (s, F_4).

^{31}P{^{1}H} NMR (CD_2Cl_2, 202 MHz, 295 K): δ 75.2 (s, PPh_2).

ESI-MS (m/z): Expected for $C_{47}H_{44}FP_2Ru$ = 697.1543 m/z; Observed: 697.1545 m/z [M^+] (Error = -0.2 mDa).

UV-Vis: λ_{max} = 693 nm, ε = 677 mol^{-1} dm^2 at a concentration of approximately 1 mmol dm^{-3} and a path length of 1 cm; calculated λ_{max} = 698 nm.

Selected ATR IR: ν(vinylidene C=C) 1725 cm^{-1}.

Elemental Analysis: $C_{38}H_{39}F_8P_3Ru$ Calc. /% C 54.23, H 4.67, Found /% C 54.29, H 4.70.

To obtain crystallographic data the dibenzenesulfonimide anion was exchanged for the hexafluorophosphate anion through ion metathesis. This was achieved by dissolving the dibenzenesulfonimide salt in dichloromethane with 20 equivalents of sodium hexafluorophosphate and stirring for 1 hour. Green crystals of the hexafluorophosphate salt were grown from a dichloromethane: pentane solvent system via slow diffusion.

7.27 Synthesis of [Ru(η^5-C$_5$Me$_5$)(dppe)(-C≡C-H)], [55a]

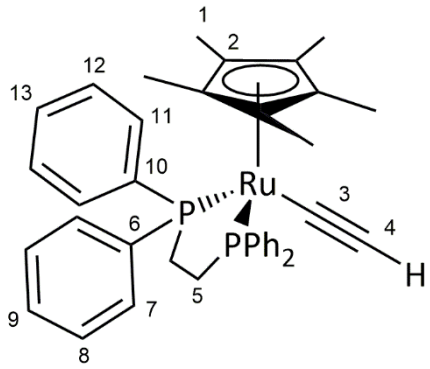

Prepared as described in the literature.[241]

To an oven dried Schlenk tube [Ru(η^5-C$_5$Me$_5$)(dppe)Cl] (215 mg, 0.32 mmol) was added. This was suspended in a methanol solution (*ca.* 10 mL) of ammonium hexafluorophosphate (104.6 mg, 0.64 mmol) and trimethylsilylacetylene (227 µL, 157.6 mg, 1.60 mmol) was added. The solution was heated under reflux for 2 hours. The solution was allowed to cool to room temperature and the solution filtered via cannula. A yellow precipitate formed upon addition of sodium methoxide (86.7 mg, 1.60 mmol) to the solution. The solid was isolated, washed with methanol (2 x 10 mL) and pentane (1 x 5 mL), and dried under vacuum. Yield = 160 mg, 76 %.

^{1}H NMR (CD_2Cl_2, 400 MHz, 295 K): δ 1.43 (t, $^4J_{HP}$ = 2.3 Hz, 1 H H_4) 1.39 (t, $^4J_{HP}$ = 1.4 Hz, 15 H, H_1), 2.00-2.14 (m, 2H, $H_{3a/b}$), 2.63-2.78 (m, 2H, $H_{3a/b}$), 7.11 (t, $^2J_{HH}$ = 7.9 Hz, 4H, $H_{5/6/9/10}$), 7.24-7.35 (m, 12H, $H_{5\text{-}7/9\text{-}11}$), 7.70-7.75 (m, 4H, $H_{5/6/9/10}$).

^{31}P{^{1}H} NMR (CD_2Cl_2, 162 MHz, 295 K): δ 81.6 (s, PPh_2).

7.28 Synthesis of [Ru(η^5-C$_5$Me$_5$)(dppe)(-C≡C-F)], [55b]

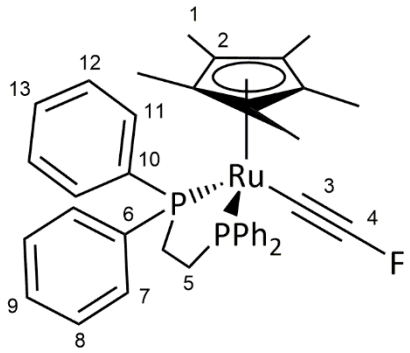

A tetrahydrofuran solution of [Ru(η^5-C$_5$Me$_5$)(dppe)(=C=CHF)][N(SO$_2$Ph)$_2$] (195 mg, 0.22 mmol in *ca*. 10 mL) was added to an oven dried Schlenk tube and cooled to -78˚C. Separately a THF solution of lithium *bis*(trimethylsilyl)amide (33 mg, 0.20 mmol in *ca*. 5 mL) was cooled to -78˚C and cannula transferred into the cold ruthenium solution. The solution rapidly turned yellow and left to stir for 15 min at -78˚C, then allowed to warm up to room temperature. A yellow solution was extracted with pentane and the solvent removed *in vacuo* to yield a yellow solid. Yield = 44 mg, 30 %.

^{1}H NMR (CD$_2$Cl$_2$, 500 MHz, 295 K): δ 1.63 (t, $^4J_{HP}$ = 1.4 Hz, 15 H, H$_1$), 1.86 (m, 2 H, H$_5$), 2.58 (m, 2 H, H$_5$), 7.06 (m, 8 H, H$_{7/8}$), 7.24 (m, 8 H, H$_{7/8}$), 7.83 (m, 4 H, H$_8$).

^{13}C{^{1}H} NMR (CD$_2$Cl$_2$, 125 MHz, 295 K): δ 10.0 (s, C$_1$), 29.3 (m, C$_5$), 36.8 (d, $^3J_{CF}$ = 42 Hz, C$_3$), 91.7 (s, C$_2$), 111.4 (d, $^1J_{CF}$= 332.2 Hz, C$_4$), 127.2 (t, $^nJ_{PC}$+ $^{n+2}J_{PC}$ = 4.2 Hz, C$_{7/8}$), 128.6 (s, C$_9$), 128.7 (s, C$_9$), 133.3 (t, $^nJ_{PC}$+ $^{n+2}J_{PC}$ = 5.2 Hz, C$_{7/8}$), 133.7 (t, $^nJ_{PC}$+ $^{n+2}J_{PC}$ = 4.7 Hz, C$_{7/8}$), 137.3 (d, $^1J_{PC}$+ $^3J_{PC}$ = 46.5 Hz, C$_6$), 139.6 (d, $^1J_{PC}$+ $^3J_{PC}$ = 32.9 Hz, C$_6$).

^{19}F NMR (CD$_2$Cl$_2$, 376 MHz, 295 K): δ -189.4 (t, $^4J_{FP}$ = 4.8 Hz, F$_4$).

^{31}P{^{1}H} NMR (CD$_2$Cl$_2$, 202 MHz, 295 K): δ 81.9 (d, $^4J_{FP}$ = 4.8 Hz, PPh$_2$).

LIFDI-MS (m/z): Expected for C$_{38}$H$_{39}$FP$_2$Ru = 678.16 m/z; Observed: 678.13 m/z [M$^+$].

UV-Vis: λ_{max} = 396 nm, ε = 10986 mol^{-1} dm^2 at a concentration of approximately 1 mmol dm^{-3} and a path length of 1 cm; calculated λ_{max} = 430 nm.

Selected ATR IR: ν(C≡C) 2148 cm^{-1}.

Elemental Analysis: C$_{38}$H$_9$FP$_2$Ru Calc. /% C 67.34, H 5.80, Found /% C 67.54, H 5.87.

Yellow crystals were grown by slow evaporation of pentane at *ca.* -23 °C.

7.29 Synthesis of $[Ru(\eta^5\text{-}C_5Me_5)(PPh_3)_2(=C=CH_2)]PF_6$, [56]$PF_6$

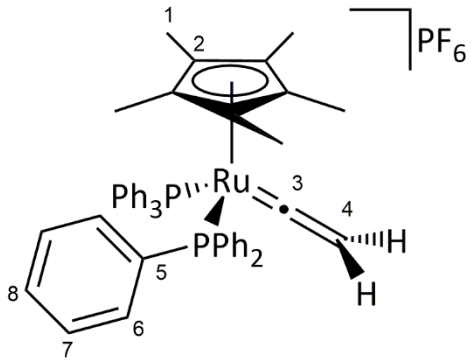

Method 1

To $[Ru(\eta^5\text{-}C_5Me_5)(PPh_3)_2Cl]$ (250 mg, 0.31 mmol) suspended in *tert*-butanol (10mL) was added ethynyltrimethylsilane (178 µL, 1.26 mmol) and ammonium hexafluorophosphate (102 mg, 0.63 mmol). The mixture was heated at 105 ˚C for 6 hours. The orange solid was filtered in air through a sinter, washed with diethyl ether (*ca.* 50 mL), and dried. Yield = 179 mg, 61 %.

Method 2

Prepared as described in the literature.[237]

To $[Ru(\eta^5\text{-}C_5Me_5)(PPh_3)_2Cl]$ (179 mg, 0.22 mmol) dissolved in dichloromethane (10 mL) was added ethynyltrimethylsilane (130 µL, 0.91 mmol) and ammonium hexafluorophosphate (73 mg, 0.45 mmol). The mixture stirred in the presence of 4 molecular sieves and was heated under reflux for 3 hours. The orange solid was precipitated by addition of pentane, filtered, and washed a further two time with pentane (2 x 15 mL). The orange solid was dried *in vacuo*. Yield = 159 mg, 76 %.

^{1}H NMR (400 MHz, CD_2Cl_2): δ 1.18 (s, 15H, H_1), 4.26 (t, $^4J_{FP}$ = 1.7 Hz, 2H, H_4), 7.16-7.25 (m, 30 H, Ar-H).

^{19}F NMR (376 MHz, CD_2Cl_2): δ -73.0 (d, PF_6).

^{31}P{^{1}H} NMR (162 MHz, CD_2Cl_2): δ -143.9 (m, PF_6), 47.5 (s, PPh_3).

ESI-MS (m/z): Expected for $C_{48}H_{47}P_2Ru$ = 787.2196 [M^+]; Observed= 787.2177 [M^+] (Error = 1.4 mDa).

7.30 Synthesis of [*trans*-Ru(dppe)$_2$Cl(-C≡C-H)], [57a]

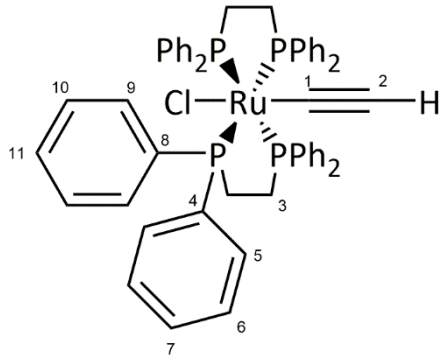

An oven dried Schlenk tube charged with *trans*-[Ru(dppe)$_2$Cl(=C=CH$_2$)][PF$_6$] (187 mg, 0.17 mmol) suspended in tetrahydrofuran (10 mL) was treated a tetrabutylammonium fluoride (169 µL, 1 M in THF). The solution was stirred for 10 minutes and the solvent removed *in vacuo*. The residue was washed with diethyl ether and the solvent removed *in vacuo*. The residue was washed with acetonitrile (3 mL) and the thick suspension filtered through a cotton wool plug. The yellow solid was washed further with acetonitrile (2 x 3 mL) and diethyl ether (3 mL). The solid was dissolved in dichloromethane, filtered, and precipitated out with excess diethyl ether to afford the product as a yellow powder. Yield = 112 mg, 69 %.

^{1}H NMR (CD_2Cl_2, 400 MHz, 295 K): δ 1.31 (quin, $^4J_{HP}$ = 1.6 Hz, 1H, H_2), 2.63-2.728 (m, 8H, H_{3a+b}), 7.98 (t, $^3J_{HH}$ = 7.6 Hz, 16H, H_{5+9}), 7.16-7.26 (m, 16H, $H_{6/10+7+11}$), 7.50 (m, 8H, $H_{6/10}$).

^{31}P{^{1}H} NMR (CD_2Cl_2, 202 MHz, 295 K): δ 49.3 (s, PPh_2).

UV-Vis: λ_{max} = 308/378 nm, ε = 30290/6598 mol^{-1} dm^2 at a concentration of 1 mmol dm^{-3} and a path length of 1 cm.

7.31 Synthesis of [*trans*-Ru(dppe)$_2$Cl(-C≡C-F)], [57b]

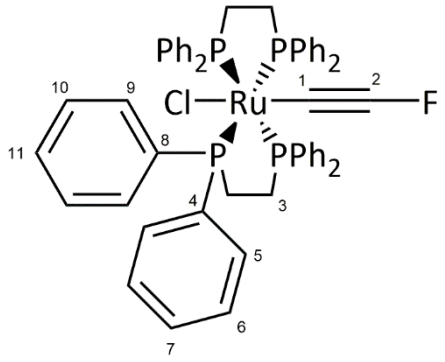

An oven dried Schlenk tube charged with a solution of *trans*-[Ru(dppe)$_2$Cl(=C=CFH)][BF$_4$]·[C$_7$H$_{14}$ClN][BF$_4$] (100 mg, 0.076 mmol) in tetrahydrofuran (10 mL) cooled to -78 °C was treated with lithium bis(trimethysilyl)amide (12.7 mg, 0.076 mmol) in tetrahydrofuran (3 mL). The solution was stirred for 15 mins at -78 °C, allowed to warm up to room temperature and the solvent removed *in vacuo*. A yellow solution was extracted with toluene (2 x 5 mL) and the solvent removed *in vacuo*. The residue was washed with n-pentane (2 x 3 mL) and diethyl ether (3 mL) and dried to afford the product as a yellow powder. Yield = 61 mg, 82 %.

^{1}H NMR (C$_6$D$_6$, 500 MHz, 298 K): δ 2.56 (m, 8H, H$_3$), 6.90 (t, $^3J_{HH}$ = 7.6 Hz, 8H, H$_{5/9}$), 6.96 (m, 8H, H$_{5/9}$), 7.01 (m, 8H, H$_{7+11}$), 7.18 (m, 8H, H$_{6/10}$), 7.91 (m, 8H, H$_{6/10}$).

^{13}C NMR (C$_6$D$_6$, 126 MHz, 298 K): δ 30.8 (quin, $^1J_{CP}$ + $^3J_{CP}$ = 12 Hz, C$_3$), 36.7 (d, $^2J_{CF}$ = 36 Hz, C$_1$), 111.5 (d, $^1J_{CF}$ = 327 Hz, C$_2$), 126.8 (quin, $^2J_{CP}$ + $^4J_{CP}$ = 2 Hz, C$_{5/9}$), 127.1 (quin, $^2J_{CP}$ + $^4J_{CP}$ = 2 Hz, C$_{5/9}$), 128.4 (s, C$_{7/11}$), 129.0 (s, C$_{7/11}$), 133.9 (quin, $^3J_{CP}$ + $^5J_{CP}$ = 2 Hz, C$_{6/10}$), 135.1 (quin, $^3J_{CP}$ + $^5J_{CP}$ = 3 Hz, C$_{6/10}$), 136.6 (quin, $^1J_{CP}$ + $^3J_{CP}$ = 10 Hz, C$_{4/8}$), 137.1 (quin, $^1J_{CP}$ + $^3J_{CP}$ = 10 Hz, C$_{4/8}$).

^{19}F NMR (C$_6$D$_6$, 471 MHz, 298 K): δ –182.1 (quin, $^4J_{FP}$ = 4 Hz).

^{31}P NMR (C$_6$D$_6$, 202 MHz, 298 K): δ 49.7 (d, $^4J_{FP}$ = 4 Hz, PPh$_2$).

LIFDI-MS (m/z): Expected for C$_{54}$H$_{48}$ClFP$_4$Ru = 976.1423 m/z [M]; Observed: 976.10 m/z [M].

UV-Vis: λ_{max} = 382 nm, ε = 6598 mol^{-1} dm^2 at a concentration of approximately 1 mmol dm^{-3} and a path length of 1 cm; calculated λ_{max} = 419 nm.

Selected Solution Phase IR (CH$_2$Cl$_2$): ν(C≡C) 1970 cm^{-1}

Elemental Analysis: C$_{54}$H$_{48}$FP$_4$Ru Calc. /% C 66.43, H 4.95, Found /% C 66.42, H 4.76.

7.32 Synthesis of [*trans*-Ru(dppe)$_2$Cl(-C≡C-C$_6$H$_4$-4-OMe)], [57c]

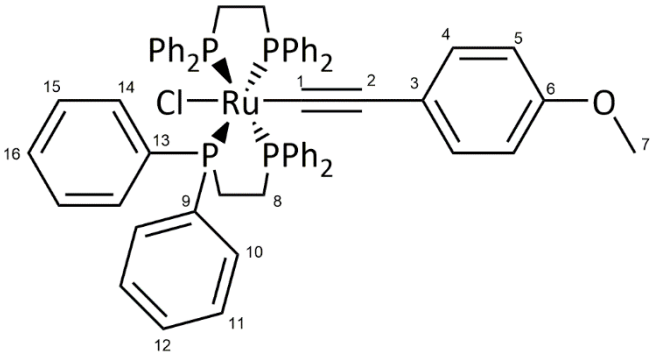

Prepared as described in the literature.[246]

An oven dried Schlenk tube was charged with a solution of [Ru(dppe)$_2$Cl][OTf] (100 mg, 0.092 mmol) and 4-ethynylanisole (12 mg, 0.09 mmol) in dichloromethane (5 mL). The solution was stirred for 2 hours, after which the solvent was removed *in vacuo*. The residue was washed with diethylether (2 x 5 mL) to remove excess alkyne. The residue was redissolved in dichloromethane (*ca.* 5 mL) and trimethylamine (51 µL, 37 mg, 0.37 mmol) added; after one hour of stirring at room temperature, the solvent was removed *in vacuo*. The product was purified by filtration through basic alumina using dichloromethane: diethyl ether (3:1) as the eluent. Removal of solvent *in vacuo* yielded the product as a yellow powder. Yield = 78 mg, 80 %.

^{1}H NMR (CD_2Cl_2, 400 MHz, 295 K): δ 2.66 (m, 8H, H_{8a+b}), 3.74 (s, 3H, H_7), 6.55-6.59 (m, 2H, $H_{4/5}$), 6.63-6.66 (m, 2H, $H_{4/5}$), 6.91 (t, $^3J_{HH}$ = 7.6 Hz, 8H, $H_{10/14}$), 7.01 (t, $^3J_{HH}$ = 7.4 Hz, 8H, $H_{10/14}$), 7.15 (t, $^3J_{HH}$ = 7.3 Hz, 4H, $H_{12/16}$), 7.20 (t, $^3J_{HH}$ = 7.3 Hz, 4H, $H_{12/16}$), 7.33-7.41 (m, 16H, H_{11+15}).

^{31}P{^{1}H} NMR (CD_2Cl_2, 202 MHz, 295 K): δ 49.5 (s, PPh_2).

7.33 Synthesis of [*trans*-Ru(dppe)$_2$Cl(-C≡C-C$_6$H$_5$)], [57d]

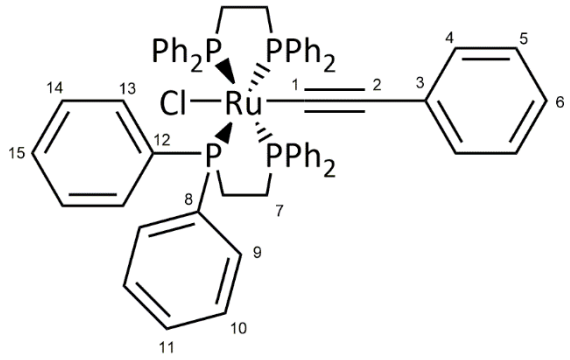

Prepared as described in the literature.[246]

An oven dried Schlenk tube was charged with a solution of [Ru(dppe)$_2$Cl][OTf] (100 mg, 0.092 mmol) and phenylacetylene (10 µL, 0.09 mmol) in dichloromethane (5 mL). The solution was stirred for 2 hours, after which the solvent was removed *in vacuo*. The residue was washed with diethylether (2 x 5 mL) to remove excess alkyne. The residue was redissolved in dichloromethane (*ca.* 2 mL) and treated with a solution of potassium *tert*-butoxide (35 mg) in methanol (5 mL). The yellow precipitate was isolated immediately by filtration and dried *in vacuo*. Yield = 75 mg, 79 %.

^{1}H NMR (CD_2Cl_2, 400 MHz, 295 K): δ 2.67 (m, 8H, H_{7a+b}), 6.64 (d, $^3J_{HH}$ = 7.7 Hz, 2H, H_4), 6.90-6.95 (m, 9H, $H_{6+9/13}$), 7.02 (t, $^3J_{HH}$ = 7.5 Hz, 8H, $H_{9/13}$), 7.07 (t, $^3J_{HH}$ = 7.7 Hz, 2H, H_5), 7.15 (t, $^3J_{HH}$ = 7.2 Hz, 4H, $H_{11/15}$), 7.21 (t, $^3J_{HH}$ = 7.2 Hz, 4H, $H_{11/15}$), 7.33-7.41 (m, 16H, H_{10+14}).

^{31}P{^{1}H} NMR (CD_2Cl_2, 202 MHz, 295 K): δ 49.5 (s, PPh_2).

7.34 Synthesis of [*trans*-Ru(dppe)$_2$Cl(-C≡C-C$_6$H$_4$-4-COOMe)], [57e]

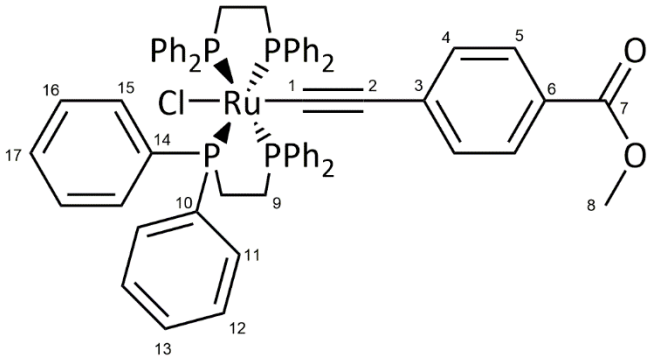

Prepared as described in the literature.[246]

An oven dried Schlenk tube was charged with a solution of [Ru(dppe)$_2$Cl][OTf] (100 mg, 0.092 mmol) and methyl 4-ethynylbenzoate (14 mg, 0.09 mmol) in dichloromethane (5 mL). The solution was stirred for 2 hours, after which the solvent was removed *in vacuo*. The residue was washed with diethylether (2 x 5 mL) to remove excess alkyne. The residue was redissolved in dichloromethane (*ca.* 2 mL) and treated with a solution of potassium *tert*-butoxide (35 mg) in methanol (5 mL). The yellow precipitate was isolated immediately by filtration and dried *in vacuo*. If required, the product was further purified by filtration through basic alumina using dichloromethane: diethyl ether (4:1, 10 % NEt_3) mix as the eluent. Yield = 74 mg, 74 %.

^{1}H NMR (CD_2Cl_2, 400 MHz, 295 K): δ 2.67 (m, 8H, H_{9a+b}), 3.83 (s, 3H, H_8), 6.53 (d, $^3J_{HH}$ = 8.4 Hz, 2H, H_5), 6.89 (t, $^3J_{HH}$ = 7.7 Hz, 8H, $H_{11/15}$), 7.03 (t, $^3J_{HH}$ = 7.6 Hz, 8H, $H_{11/15}$), 7.15 (t, $^3J_{HH}$ = 7.6 Hz, 4H, $H_{13/17}$), 7.22 (t, $^3J_{HH}$ = 7.4 Hz, 4H, $H_{13/17}$), 7.27 (m, 8H, $H_{12/16}$), 7.41 (m, 8H, $H_{12/16}$), 7.70 (d, $^3J_{HH}$ = 8.4 Hz, 2H, H_4).

^{31}P{^{1}H} NMR (CD_2Cl_2, 202 MHz, 295 K): δ 49.0 (s, PPh_2).

7.35 Synthesis of [*trans*-Ru(dppe)$_2$Cl(-C≡C-C$_6$H$_4$-4-COMe)], [57f]

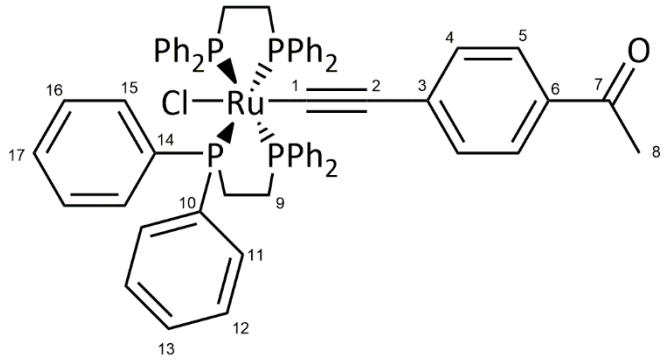

Prepared as described by the general procedure reported by Fox *et al*.[246]

An oven dried Schlenk tube was charged with a solution of [Ru(dppe)$_2$Cl][OTf] (100 mg, 0.092 mmol) and 4-ethynylacetophenone (13 mg , 0.09 mmol) in dichloromethane (5 mL). The solution was stirred for 3 hours, after which the solvent was removed *in vacuo*. The residue was washed with diethylether (2 x 5 mL) to remove excess alkyne. The residue was redissolved in dichloromethane (*ca.* 2 mL) and treated with a solution of potassium *tert*-butoxide (35 mg) in methanol (5 mL). The yellow precipitate was isolated immediately by filtration and dried *in vacuo*. If required, the product was further purified by filtration through basic alumina using dichloromethane: diethyl ether (4:1, 10 % NEt_3) mix as the eluent. Yield = 71 mg, 71 %.

^{1}H NMR (CD_2Cl_2, 400 MHz, 295 K): δ 2.94 (s, 3H, H_8), 2.67 (m, 8H, H_{9a+b}), 6.55 (d, $^3J_{HH}$ = 8.4 Hz, 2H, H_5), 6.90 (t, $^3J_{HH}$ = 7.6 Hz, 8H, $H_{11/15}$), 7.04 (t, $^3J_{HH}$ = 7.6 Hz, 8H, $H_{11/15}$), 7.15 (t, $^3J_{HH}$ = 7.2 Hz, 4H, $H_{13/17}$), 7.22 (t, $^3J_{HH}$ = 7.2 Hz, 4H, $H_{13/17}$), 7.28 (m, 8H, $H_{12/16}$), 7.40 (m, 8H, $H_{12/16}$), 7.66 (d, $^3J_{HH}$ = 8.4 Hz, 2H, H_4).

^{31}P{^{1}H} NMR (CD_2Cl_2, 202 MHz, 295 K): δ 49.0 (s, PPh_2).

7.36 Synthesis of [*trans*-Ru(dppe)$_2$Cl(-C≡C-C$_6$H$_4$-4-CF$_3$)], [57g]

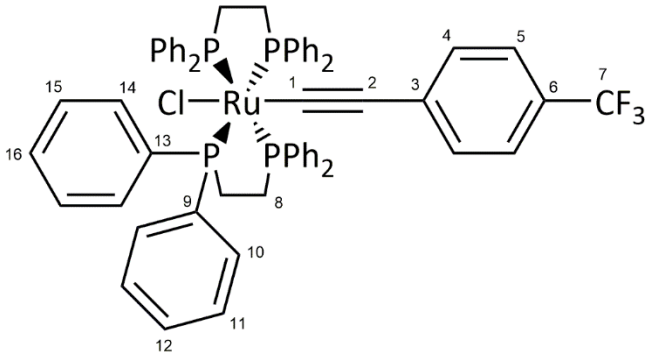

An oven dried Schlenk tube was charged with a solution of [Ru(dppe)$_2$Cl][OTf] (100 mg, 0.092 mmol) and 4-Ethynyl-α,α,α-trifluorotoluene (15 mg, 15 µL, 0.09 mmol) in dichloromethane (5 mL). The solution was stirred for 2 hours, after which the solvent was removed *in vacuo*. The residue was washed with diethylether (2 x 5 mL) to remove excess alkyne. The residue was redissolved in dichloromethane (*ca.* 2 mL) and treated with a solution of potassium *tert*-butoxide (35 mg) in methanol (5 mL). The yellow precipitate was isolated immediately by filtration and dried *in vacuo*. Yield = 68 mg, 67 %.

^{1}H NMR (C$_6$D$_6$, 500 MHz, 298 K): δ 2.74 (m, 8H, H$_{8a+b}$), 6.64 (d, $^{3}J_{HH}$ = 8.2 Hz, 2H, H$_4$), 6.97 (t, $^{3}J_{HH}$ = 7.7 Hz, 8H, H$_{10/14}$), 7.10 (t, $^{3}J_{HH}$ = 7.6 Hz, 8H, H$_{10/14}$), 7.23 (t, $^{3}J_{HH}$ = 7.3 Hz, 4H, H$_{12/16}$), 7.29 (t, $^{3}J_{HH}$ = 7.3 Hz, 4H, H$_{12/16}$), 7.33-7.37 (m, 10H, H$_{5+12/16}$), 7.48 (m, 8H, H$_{12/16}$).

^{13}C NMR (C$_6$D$_6$, 126 MHz, 298 K): δ 30.5 (quin, $^{1}J_{CP}$ + $^{3}J_{CP}$ = 11.7 Hz, C$_8$), 112.8 (s, C$_3$), 123.5 (q, $^{2}J_{CF}$ = 32 Hz, C$_6$), 124.2 (q, $^{3}J_{CF}$ = 4 Hz, C$_5$), 125.1 (q, $^{1}J_{CF}$ = 270 Hz, C$_7$), 127.0 (quin, $^{2}J_{CP}$ + $^{4}J_{CP}$ = 2 Hz, C$_{10/14}$), 127.2 (quin, $^{2}J_{CP}$ + $^{4}J_{CP}$ = 2 Hz, C$_{10/14}$), 128.6 (s, C$_2$), 128.8 (s, C$_{12/16}$), 129.1 (s, C$_{16/12}$), 130.0 (s, C$_4$), 133.9 (quin, $^{3}J_{CP}$ + $^{5}J_{CP}$ = 2 Hz, C$_{11/15}$), 134.6 (quin, $^{3}J_{CP}$ + $^{5}J_{CP}$ = 2 Hz, C$_{11/15}$), 135.9 (quin, $^{1}J_{CP}$ + $^{3}J_{CP}$ = 10 Hz, C$_{9/13}$), 136.3 (quin, $^{1}J_{CP}$ + $^{3}J_{CP}$ = 10 Hz, C$_{13/9}$).

^{19}F NMR (C$_6$D$_6$, 471 MHz, 298 K): δ -62.0 (s, F$_7$).

^{31}P NMR (C$_6$D$_6$, 202 MHz, 298 K): δ 48.5 (s, PPh$_2$).

LIFDI-MS (m/z): Expected for C$_{61}$H$_{52}$ClF$_3$P$_4$Ru = 1102.1704 m/z [M]; Observed: 1102.1680 m/z [M] (error = -2.4 mDa).

7.37 Synthesis of [*trans*-Ru(dppe)$_2$Cl(-C≡C-C$_6$H$_4$-4-NO$_2$)], [57h]

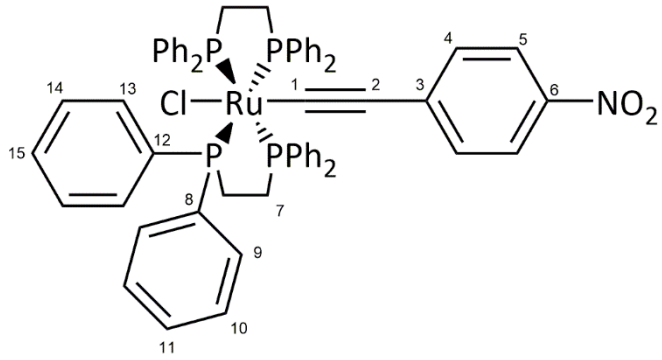

Prepared as described in the literature.[246]

An oven dried Schlenk tube was charged with a solution of [Ru(dppe)$_2$Cl][OTf] (100 mg, 0.092 mmol) and 4-ethynyl nitrobenzene (10 µL, 0.09 mmol) in dichloromethane (5 mL). The solution was stirred for 6 hours, after which the solvent was removed *in vacuo*. The residue was washed with diethylether (2 x 5 mL) to remove excess alkyne. The residue was redissolved in dichloromethane (*ca.* 2 mL) and treated with a solution of potassium *tert*-butoxide (35 mg) in methanol (5 mL). The red precipitate was isolated immediately by filtration and dried *in vacuo*. Yield 65 mg, 65 %.

^{1}H NMR (CD_2Cl_2, 400 MHz, 295 K): δ 2.68 (m, 8H, H_{7a+b}), 6.42 (d, $^3J_{HH}$ = 9.0 Hz, 2H, H_5), 6.90 (t, $^3J_{HH}$ = 7.6 Hz, 8H, $H_{9/13}$), 7.04 (t, $^3J_{HH}$ = 7.7 Hz, 8H, $H_{9/13}$), 7.14-7.25 (m, 16H, $H_{10/14+11+15}$), 7.45 (m, 8H, $H_{10/14}$), 7.89 (d, $^3J_{HH}$ = 9.0 Hz, 2H, H_4).

^{31}P{^{1}H} NMR (CD_2Cl_2, 202 MHz, 295 K): δ 49.5 (s, PPh_2).

7.38 Synthesis of [*trans*-Ru(dppe)$_2$Cl(-C≡C-C$_6$H$_4$-4-NMe$_2$)], [57i]

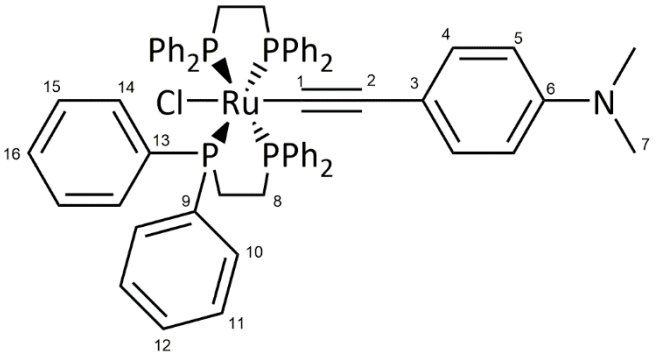

Prepared as described in the literature.[243]

An oven dried Schlenk tube was charged with [RuCl(dppe)2][OTf] (100 mg, 0.092 mmol) and 4-ethynylaniline (24 mg, 184 µmol) in dichloromethane (10 mL). The brown-orange solution was stirred 40 h at room temperature and the solvent was removed in vacuo. The remaining brownish solid was extracted with dichloromethane (2 × 5 mL), cannula filtered and the solvent was removed *in vacuo*. The green solid was washed with diethyl ether (5 mL) and n-pentane (5 mL), dissolved in tetrahydrofuran (10 mL) and excess potassium *tert*-butoxide was added (21 mg, 184 µmol). The green solution turned orange and was stirred a further 1 hour at room temperature. The solvent was removed *in vacuo* and the residue extracted with dichloromethane (5 mL). The orange solution was chromatographed on alumina (neutral grade) under nitrogen, using dichloromethane as eluent. The product was eluted first as a yellow band and after drying was isolated as a pale-yellow solid. Yield = 35 mg, 35 %.

^{1}H NMR (CD_2Cl_2, 400 MHz, 295 K): δ 2.66 (m, 8H, H_{8a+b}), 2.88 (s, 6H, H_7), 6.51-6.60 (m, 4H, H_{4+5}), 6.92 (t, $^3J_{HH}$ = 7.5 Hz, 8H, $H_{10/14}$), 7.01 (t, $^3J_{HH}$ = 7.5 Hz, 8H, $H_{10/14}$), 7.15 (t, $^3J_{HH}$ = 7.3 Hz, 4H, $H_{12/16}$), 7.20 (t, $^3J_{HH}$ = 7.3 Hz, 4H, $H_{12/16}$), 7.32 (m, 8H, $H_{11/15}$), 7.43 (m, 8H, $H_{11/15}$).

^{31}P{^{1}H} NMR (CD_2Cl_2, 202 MHz, 295 K): δ 49.6 (s, PPh_2).

7.39 Synthesis of [*trans*-Ru(dppe)$_2$Cl(-C≡C-C$_3$H$_5$)], [57j]

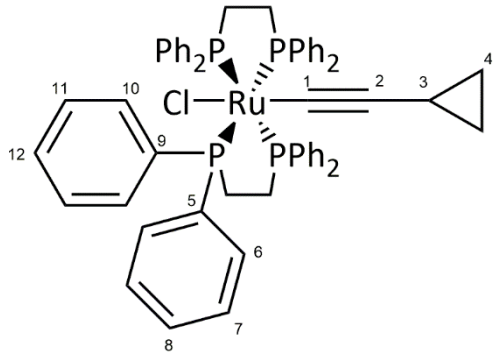

An oven dried Schlenk tube was charged with a solution of [Ru(dppe)$_2$Cl][OTf] (100 mg, 0.092 mmol) and ethynylcyclopropane (73 mg, 93 µL, 0.11 mmol) in dichloromethane (5 mL). The solution was stirred for 2 hours, after which the solvent was removed *in vacuo*. The residue was washed with diethylether (2 x 5 mL) to remove excess alkyne. The residue was redissolved in dichloromethane (*ca.* 5 mL) and trimethylamine (51 µL, 37 mg, 0.37 mmol) added; after one hour of stirring at room temperature, the solvent was removed *in vacuo*. The product was purified by filtration through basic alumina using dichloromethane: diethyl ether (3:1, 10 % NEt$_3$) as the eluent. Removal of solvent *in vacuo* yielded the product as a yellow powder. Yield 52 mg, 57 %.

^{1}H NMR (CD_2Cl_2, 500 MHz, 295 K): δ 0.17 (m, 2H, $H_{4a/b}$), 0.36 (m, 2H, $H_{4a/b}$), 1.05 (m, 1H, H_3), 2.69 (m, 8H, $H_{5a/b}$), 7.01 (t, $^3J_{HH}$ = 7 Hz, 8H $H_{7/11}$), 7.07 (t, $^3J_{HH}$ = 7 Hz, 8H, $H_{7/11}$), 7.22-7.2 (m, 8H, H_{9+13}), 7.36 (m, 8H, $H_{8/12}$), 7.44 (m, 8H, $H_{8/12}$).

^{13}C NMR (CD_2Cl_2, 126 MHz, 295 K): δ 3.9 (s, C_3), 5.4 (s, C_4), 30.8 (quin, $^1J_{CP}$ + $^3J_{CP}$ = 12 Hz, C_5), 95.8 (quin, $^2J_{CP}$ = 15 Hz, C_1), 111.1 (s, C_2), 126.7 (s, $C_{7/11}$), 126.9 (s, $C_{7/11}$), 128.5 (s, $C_{9/13}$), 128.8 (s, $C_{9/13}$), 134.2 (s, $C_{8/12}$), 134.6 (s, $C_{8/12}$), 136.5 (quin, $^1J_{CP}$ + $^3J_{CP}$ = 10 Hz, $C_{6/10}$), 137.0 (quin, $^1J_{CP}$ + $^3J_{CP}$ = 10 Hz, $C_{6/10}$).

^{31}P NMR (CD_2Cl_2, 202 MHz, 295 K): δ 48.6 (s, PPh_2).

LIFDI-MS (m/z): Expected for $C_{57}H_{53}ClP_4Ru$ = 998.18 m/z [M$^+$]; Observed: 998.16 m/z [M$^+$].

Elemental Analysis: $C_{57}H_{53}P_4Ru$ + 0.7(CH_2Cl_2) Calc. /% C 65.51, H 5.18, Found /% C 65.52, H 5.22.

Residual dichloromethane was observed in the proton NMR spectrum.

7.40 Synthesis of [*trans*-Ru(dppe)$_2$Cl(=C=CFH)]BF$_4$, [58a]BF$_4$

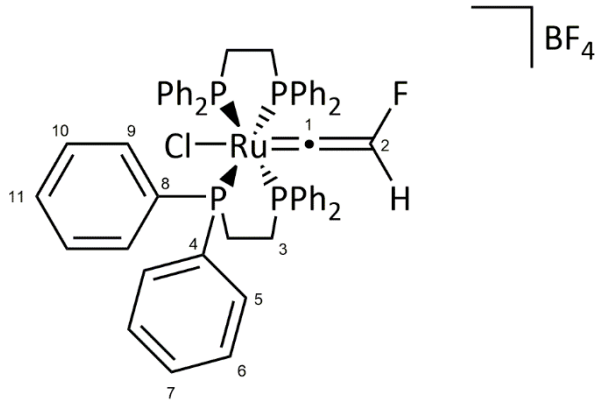

An oven dried Schlenk tube was charged with [Ru(dppe)$_2$Cl(-C≡C-H)] (112 mg, 0.12 mmol) in dichloromethane (*ca.* 3 mL). An acetonitrile solution of Selectfluor® (51 mg, 0.14 mmol, in 5 mL) was added slowly, stirred for 30 minutes, and the solvent was removed *in vacuo*. The residue was extracted with dichloromethane (*ca.* 3 mL) and filtered; a green solid precipitated upon addition of pentane (10 mL). The solid was isolated by filtration, washed with diethyl ether (2 x 5 mL), and dried *in vacuo*. The product was isolated as a 1:1 mixture of [*trans*-Ru(dppe)$_2$Cl(=C=CFH)][BF$_4$] and 1-chloromethyl-1,4-diazoniabicyclo[2.2.2]octane [BF$_4$]. Yield = 124 mg, 81 %.

Crystals of the hexafluorophosphate were grown by slow diffusion from dichloromethane: pentane solvent system. The hexafluorophosphate salt was obtained by salt metathesis; the tetrafluoroborate salt was stirred in dichloromethane with 20 equivalents of sodium hexafluorophosphate.

^{1}H NMR (CD_2Cl_2, 500 MHz, 295 K): δ 2.69 (m, 4H, $H_{3a/b}$), 3.00 (m, 4H, $H_{3b/a}$), 6.14 (d quin, $^2J_{HF}$ = 81 Hz, $^4J_{HP}$ = 2.7 Hz, 1H, H_2), 7.05 (m, 8H, $H_{5/9}$), 7.12 (t, $^3J_{HH}$ = 7.7 Hz, 8H, $H_{6/10}$), 7.20 (m, 8H, $H_{9/5}$), 7.24 (t, $^3J_{HH}$ = 7.7 Hz, 8H, $H_{6/10}$), 7.38 (t, $^3J_{HH}$ = 7.4 Hz, 4H, $H_{11/7}$) 7.46 (t, $^3J_{HH}$ = 7.4 Hz, 4H, $H_{7/11}$).

^{13}C NMR (CD_2Cl_2, 126 MHz, 295 K): δ 29.3 (quin, $^1J_{CP}$ + $^3J_{CP}$ = 11 Hz, C_3), 128.5 (quin, $^3J_{CP}$ + $^5J_{CP}$ = 3 Hz, $C_{6/10}$), 129.1 (quin, $^3J_{CP}$ + $^5J_{CP}$ = 2 Hz, $C_{10/6}$), 130.5 (quin, $^1J_{CP}$ + $^3J_{CP}$ = 12 Hz, $C_{4/8}$), 131.4 (quin, $^3J_{CP}$ + $^5J_{CP}$ = 12 Hz, $C_{8/4}$), 131.5 (s, $C_{7/11}$), 132.0 (s, $C_{11/7}$), 133.4 (quin, $^2J_{CP}$ + $^4J_{CP}$ = 3 Hz, $C_{5/9}$), 134.6 (quin, $^2J_{CP}$ + $^4J_{CP}$ = 2 Hz, $C_{9/5}$), 176.5 (d, $^1J_{CF}$ = 230 Hz, C_2), 382.4 (C_1).

^{19}F NMR (CD_2Cl_2, 471 MHz, 295 K): δ –242.6 (d, $^2J_{HF}$ = 81 Hz, F_2).

^{31}P NMR (CD_2Cl_2, 202 MHz, 295 K): δ 41.2 (s, PPh_2).

ESI-MS (m/z): Expected for $C_{54}H_{49}ClFOP_4Ru$ = 977.1507 m/z [M^+]; Observed: 977.1487 m/z [M^+] (Error = 2.0 mDa).

UV-Vis: No observable low energy transitions.

Selected ATR IR: ν(vinylidene C=C) 1614 cm^{-1}.

Elemental Analysis: $C_{54}H_{49}F_7P_5Ru$ + 0.25($C_7H_{14}N_2Cl$) Calc. /% C 55.85, H 4.41, N 0.58 Found /% C 55.88, H 4.36, N 0.59.

Contaminant 1-chloromethyl-1,4-diazoniabicyclo[2.2.2]octane was observed in the proton NMR spectrum.

7.41 Synthesis of [*trans*-Ru(dppe)$_2$Cl(=C=CF$_2$)]BF$_4$, [58b]BF$_4$

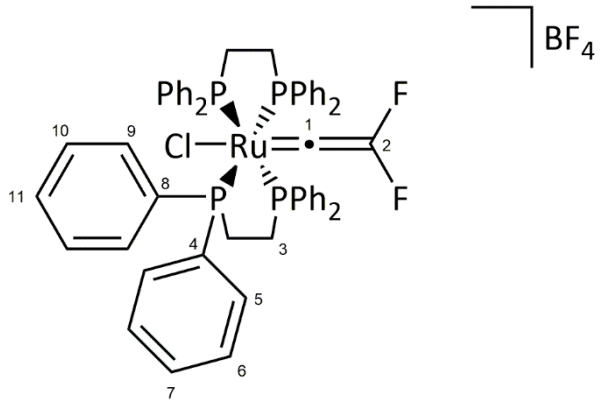

An oven dried Schlenk tube was charged with [Ru(dppe)$_2$Cl(-C≡C-F)] (30 mg, 0.031 mmol) in dichloromethane (*ca.* 3 mL). An acetonitrile solution of Selectfluor® (13 mg, 0.037 mmol, in 5 mL) was added slowly, stirred for 30 minutes, and the solvent was removed *in vacuo*. The residue was extracted with dichloromethane (*ca.* 3 mL) and filtered; a green solid precipitated upon addition of pentane (10 mL). The solid was isolated by filtration, washed with diethyl ether (2 x 5 mL), and dried *in vacuo*. The product was isolated as a 1:1 mixture of [*trans*-Ru(dppe)$_2$Cl(=C=CF$_2$)][BF$_4$] and 1-chloromethyl-1,4-diazoniabicyclo[2.2.2]octane [BF$_4$]. Yield = 24 mg, 59 %.

Crystals of the hexafluorophosphate were grown by slow diffusion from dichloromethane: pentane solvent system. The hexafluorophosphate salt was obtained by salt metathesis; the tetrafluoroborate salt was stirred in dichloromethane with 20 equivalents of sodium hexafluorophosphate.

^{1}H NMR (CD_2Cl_2, 500 MHz, 295 K): δ 2.49 (m, 4H, $H_{3a/b}$), 2.98 (m, 4H, $H_{3b/a}$), 6.97 (m, 8H, $H_{5/9}$), 7.13-7.21 (m, 16H, $H_{5/9+6/10}$), 7.27 (t, $^3J_{HH}$ = 7.6 Hz, $H_{6/10}$), 7.42 (t, $^3J_{HH}$ = 7.3 Hz, 4H, $H_{7/11}$), 7.51 (t, $^3J_{HH}$ = 7.3 Hz, 4H, $H_{7/11}$).

^{13}C NMR (CD_2Cl_2, 126 MHz, 295 K): δ 29.1 (quin, $^1J_{CP}$ + $^3J_{CP}$ = 11 Hz, C_3), 128.2 (quin, $^2J_{CP}$ + $^4J_{CP}$ = 3 Hz, $C_{5/9}$), 128.8 (quin, $^2J_{CP}$ + $^4J_{CP}$ = 3 Hz, $C_{5/9}$), 129.8 (quin, $^1J_{CP}$ + $^3J_{CP}$ = 12 Hz, $C_{4/8}$), 130.8 (quin, $^1J_{CP}$ + $^3J_{CP}$ = 11 Hz, $C_{4/8}$), 131.2 (s, $C_{7/11}$), 131.7 (s, $C_{7/11}$), 132.8 (quin, $^3J_{CP}$ + $^5J_{CP}$ = 3 Hz, $C_{6/10}$), 133.9 (quin, $^3J_{CP}$ + $^5J_{CP}$ = 3 Hz, $C_{6/10}$), 249.4 (d, $^1J_{CF}$ = 270 Hz, C_2), 408.2 (C_1).

^{19}F NMR (CD_2Cl_2, 471 MHz, 295 K): δ –145.2 (s).

^{31}P NMR (CD_2Cl_2, 202 MHz, 295 K): δ 39.7 (s, PPh_2).

ESI-MS (m/z): Expected for $C_{54}H_{48}ClF_2P_4Ru$ = 995.1401 m/z [M^+]; Observed: 995.1437 m/z [M^+] (Error = -3.6 mDa).

UV-Vis: λ_{max} = 823 nm, ε = 68 mol^{-1} dm^2 at a concentration of approximately 1 mmol dm^{-3} and a path length of 1 cm; calculated λ_{max} = 823 nm.

Selected ATR IR: ν(vinylidene C=C) 1723 cm^{-1}.

Elemental Analysis: $C_{54}H_{48}F_8P_4Ru$ Calc. /% C 56.88, H 4.24, Found /% C 56.42, H 4.13.

7.42 Synthesis of [*trans*-Ru(dppe)$_2$Cl(=C=C(F)C$_6$H$_4$-4-OMe)]BF$_4$, [58c]BF$_4$

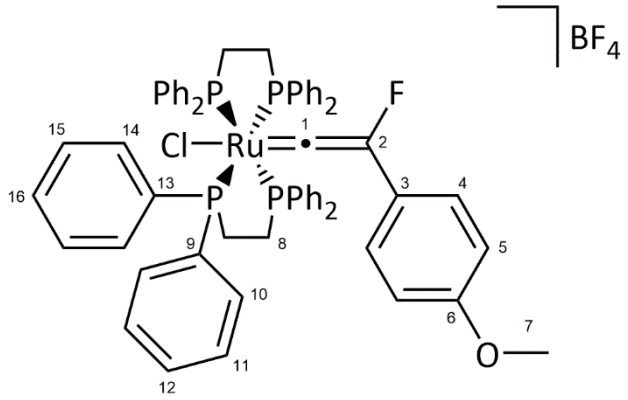

An oven dried Schlenk tube was charged with [Ru(dppe)$_2$Cl(-C≡C-C$_6$H$_4$-4-OMe)] (100 mg, 0.094 mmol) in dichloromethane (*ca.* 3 mL). An acetonitrile solution of Selectfluor® (40 mg, 0.113 mmol, in 5 mL) was added slowly, stirred for 30 minutes, and the solvent was removed *in vacuo*. The residue was extracted with dichloromethane (*ca.* 3 mL) and filtered; a brown solid precipitated upon addition of pentane (10 mL). The solid was isolated by filtration, washed with diethyl ether (2 x 5 mL), and dried *in vacuo*. The product was isolated as a 1:1 mixture of [*trans*-Ru(dppe)$_2$Cl(=C=C(F)C$_6$H$_4$-OMe)][BF$_4$] and 1-chloromethyl-1,4-diazoniabicyclo[2.2.2]octane [BF$_4$]. Yield = 109 mg, 82 %.

Crystals of the hexafluorophosphate were grown by slow diffusion from dichloromethane: pentane solvent system. The hexafluorophosphate salt was obtained by salt metathesis; the tetrafluoroborate salt was stirred in dichloromethane with 20 equivalents of sodium hexafluorophosphate.

^{1}H NMR (CD_2Cl_2, 500 MHz, 295 K): δ 2.62 (m, 4H, $H_{8a/b}$), 2.95 (m, 4H, $H_{8b/a}$), 3.67 (s, 3H, H_7), 5.72 (m, 2H, $H_{4/5}$), 6.82 (m, 2H, $H_{5/4}$), 7.06-7.15 (m, 32H, $H_{10+11+14+15}$), 7.31-7.39 (m, 8H, H_{12+16}).

^{13}C NMR (CD_2Cl_2, 126 MHz, 295 K): δ 29.2 (quin, $^1J_{CP}$ + $^3J_{CP}$ = 11.3 Hz, C_8), 55.6 (s, C_7), 113.9 (s, $C_{4/5}$), 115.7 (m, C_3), 125.6 (s, $C_{5/4}$), 128.5 (quin, $^nJ_{CP}$ + $^{n+2}J_{CP}$ = 2.4 Hz, $C_{10/11/14/15}$), 129.2 (quin, $^nJ_{CP}$ + $^{n+2}J_{CP}$ = 2.3 Hz, $C_{10/11/15/14}$), 131.0 (quin, $^1J_{CP}$ + $^3J_{CP}$ = 11.6 Hz, $C_{9/13}$), 131.3 (s, $C_{12/16}$), 131.8 (s, $C_{16/12}$), 132.1 (quin, $^1J_{CP}$ + $^3J_{CP}$ = 11.5 Hz, $C_{13/9}$), 133.2 (quin, $^nJ_{CP}$ + $^{n+2}J_{CP}$ = 2.6 Hz, $C_{10/11/15/14}$), 134.3 (quin, $^nJ_{CP}$ + $^{n+2}J_{CP}$ = 2.3 Hz, $C_{10/11/15/14}$), 160.0 (s, C_6), 201.0 (d, $^1J_{CF}$ = 209.7 Hz, C_2), 412.8 (C_1).

^{19}F NMR (CD_2Cl_2, 471 MHz, 295 K): δ –229.6 (s).

^{31}P NMR (CD_2Cl_2, 202 MHz, 295 K): δ 34.1 (s, PPh_2).

ESI-MS (m/z): Expected for $C_{61}H_{55}ClFOP_4Ru$ = 1083.1928 m/z [M^+]; Observed: 1083.1954 m/z [M^+] (Error = -2.6 mDa).

UV-Vis: 1 mmol dm^{-3} in DCM, λ_{max}= 820 nm, abs = 0.21730, ε = 217.3 dm^3 mol^{-1} cm^{-1} / 2173.0 dm^2 mol^{-1}, calculated λ_{max} = 856 nm

Selected ATR IR: ν(vinylidene C=C) 1603 cm^{-1}.

Elemental Analysis: $C_{61}H_{55}F_7OP_5Ru$ + CH_2Cl_2 Calc. /% C 56.70, H 4.37, Found /% C 56.52, H 4.33.

7.43 Synthesis of [*trans*-Ru(dppe)$_2$Cl(=C=C(F)Ph)]BF$_4$, [58d]BF$_4$

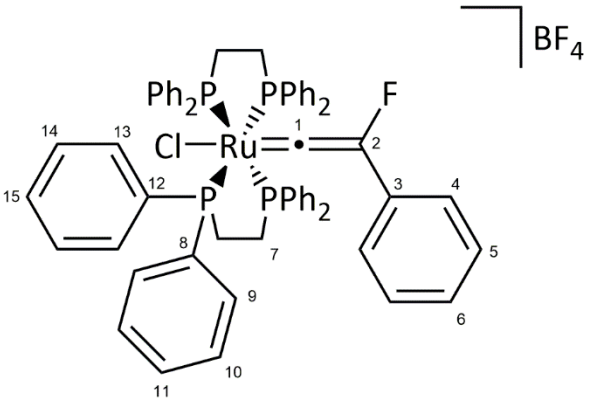

An oven dried Schlenk tube was charged with [Ru(dppe)$_2$Cl(-C≡C-C$_6$H$_5$)] (115 mg, 0.11 mmol) in dichloromethane (*ca.* 3 mL). An acetonitrile solution of Selectfluor® (47 mg, 0.13 mmol, in 5 mL) was added slowly, stirred for 30 minutes, and the solvent was removed *in vacuo*. The residue was extracted with dichloromethane (*ca.* 3 mL) and filtered; a green solid precipitated upon addition of pentane (10 mL). The solid was isolated by filtration, washed with diethyl ether (2 x 5 mL), and dried *in vacuo*. The product was isolated as a 1:1 mixture of [*trans*-Ru(dppe)$_2$Cl(=C=C(F)C$_6$H$_5$)][BF$_4$] and 1-chloromethyl-1,4-diazoniabicyclo[2.2.2]octane [BF$_4$]. Yield = 121 mg, 78 %.

Crystals of the hexafluorophosphate were grown by slow diffusion from dichloromethane: pentane solvent system. The hexafluorophosphate salt was obtained by salt metathesis; the tetrafluoroborate salt was stirred in dichloromethane with 20 equivalents of sodium hexafluorophosphate.

^{1}H NMR (CD_2Cl_2, 500 MHz, 295 K): δ 2.62 (m, 4H, $H_{7a/b}$), 2.94 (m, 4H, $H_{7b/a}$), 5.77 (d, $^3J_{HH}$ = 7.6 Hz, 2H, H_4), 6.82 (m, 3H, H_{5+6}), 7.05-7.18 (m, 32H, $H_{9/10/13/14}$), 7.32 (t, $^3J_{HH}$ = 7.4 Hz, 2H, $H_{11/15}$) 7.37 (t, $^3J_{HH}$ = 6.5 Hz, 2H, $H_{15/11}$).

^{13}C NMR (CD_2Cl_2, 126 MHz, 295 K): δ 29.0 (quin, $^1J_{CP}$ + $^3J_{CP}$ = 11.2 Hz, C_7), 123.2 (s, $C_{4/5}$), 128.0 (s, $C_{5/4}$), 128.5 (quin, $^nJ_{CP}$ + $^{n+2}J_{CP}$ = 2.3 Hz, $C_{9/10/15/14}$), 129.3 (quin, $^nJ_{CP}$ + $^{n+2}J_{CP}$ = 2.3 Hz, $C_{9/10/15/14}$), 130.9 (quin, $^1J_{CP}$ + $^3J_{CP}$ = 11.7 Hz, $C_{8/12}$), 131.4 (s, $C_{11/15}$), 131.9 (s, $C_{11/15}$), 132.1 (quin, $^1J_{CP}$ + $^3J_{CP}$ = 11.4 Hz, $C_{8/12}$), 133.1 (quin, $^nJ_{CP}$ + $^{n+2}J_{CP}$ = 2.5 Hz, $C_{9/10/15/14}$), 134.3 (quin, $^nJ_{CP}$ + $^{n+2}J_{CP}$ = 2.1 Hz, $C_{9/10/15/14}$), 201.3 (d, $^1J_{CF}$ = 209.0 Hz, C_2), 408.6 (C_1).

^{19}F NMR (CD_2Cl_2, 471 MHz, 295 K): δ -235.4 (s).

^{31}P NMR (CD_2Cl_2, 202 MHz, 295 K): δ 33.4 (s, PPh_2).

ESI-MS (m/z): Expected for $C_{60}H_{53}ClFP_4Ru$ = 1053.1822 m/z [M^+]; Observed: 1053.1831 m/z [M^+] (Error = -2.3 mDa).

UV-Vis: 1 mmol dm^{-3} in DCM, λ_{max}= 800 nm, abs = 0.11795, ε = 117.95 dm^3 mol^{-1} cm^{-1} / 1179.5 dm^2 mol^{-1}, calculated λ_{max} = 790 nm

Selected ATR IR: ν(vinylidene C=C) 1622 cm^{-1}.

Elemental Analysis: $C_{60}H_{53}F_7P_5Ru$ + 0.3(CH_2Cl_2) Calc. /% C 59.17, H 4.41, Found /% C 59.15, H 4.49.

Residual dichloromethane was observed in the proton NMR spectrum and the crystal structure.

7.44 Synthesis of [*trans*-Ru(dppe)$_2$Cl(=C=C(F)C$_6$H$_4$-4-COOMe)]BF$_4$, [58e]BF$_4$

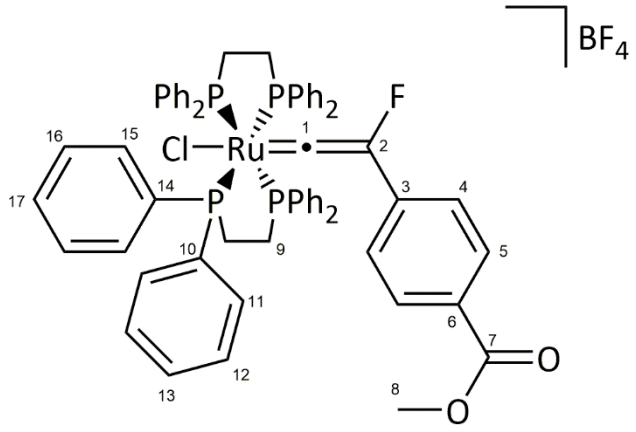

An oven dried Schlenk tube was charged with [Ru(dppe)$_2$Cl(-C≡C-C$_6$H$_4$-4-COOMe)] (100 mg, 0.092 mmol) in dichloromethane (*ca.* 3 mL). An acetonitrile solution of Selectfluor® (39 mg, 0.110 mmol, in 5 mL) was added slowly, stirred for 30 minutes, and the solvent was removed *in vacuo*. The residue was extracted with dichloromethane (*ca.* 3 mL) and filtered; a green solid precipitated upon addition of pentane (10 mL). The solid was isolated by filtration, washed with diethyl ether (2 x 5 mL), and dried *in vacuo*. The product was isolated as a 1:1 mixture of [*trans*-Ru(dppe)$_2$Cl(=C=C(F)C$_6$H$_4$-COOMe)][BF$_4$] and 1-chloromethyl-1,4-diazoniabicyclo[2.2.2]octane [BF$_4$]. Yield = 118 mg, 89 %.

Crystals of the hexafluorophosphate were grown by slow diffusion from dichloromethane: pentane solvent system. The hexafluorophosphate salt was obtained by salt metathesis; the tetrafluoroborate salt was stirred in dichloromethane with 20 equivalents of sodium hexafluorophosphate.

^{1}H NMR (CD_2Cl_2, 500 MHz, 295 K): δ 2.69 (m, 4H, $H_{9b/a}$), 2.99 (m, 4H, $H_{9b/a}$), 3.86 (s, 3H, H_8), 5.78 (vir. dt, $^3J_{HH}$ = 8.7 Hz, 2H, H_4), 7.10 (t, $^3J_{HH}$ = 7.8 Hz, 8H, $H_{11/12/15/16}$), 7.14-7.22 (m, 24H, $H_{11+12/16+15}$), 7.34 (t, $^3J_{HH}$ = 7.4 Hz, 4H, $H_{13/17}$), 7.38 (vir. dt, $^3J_{HH}$ = 8.8 Hz, 2H, H_5), 7.43 (t, $^3J_{HH}$ = 6.2 Hz, 4H, $H_{13/17}$).

^{13}C NMR (CD_2Cl_2, 126 MHz, 295 K): δ 28.5 (quin, $^1J_{CP}$ + $^3J_{CP}$ = 11 Hz, C_9), 68.3 (s, C_8), 121.4 (s, C_4), 128.2 (quin, $^nJ_{CP}$ + $^{n+2}J_{CP}$ = 2 Hz, $C_{11/12/15/16}$), 128.4 (s, C_5), 128.6 (d, $^2J_{CF}$ = 48 Hz, C_3), 129.0 (quin, $^nJ_{CP}$ + $^{n+2}J_{CP}$ = 2 Hz, $C_{11/12/15/16}$), 130.2 (quin, $^1J_{CP}$ + $^3J_{CP}$ = 12 Hz, $C_{10/14}$), 131.1 (s, $C_{13/17}$), 131.6 (s, $C_{13/17}$), 131.7 (quin, $^1J_{CP}$ + $^3J_{CP}$ = 11 Hz, $C_{10/14}$), 132.5 (quin, $^nJ_{CP}$ + $^{n+2}J_{CP}$ = 3 Hz, $C_{11/12/15/16}$), 133.9 (quin, $^nJ_{CP}$ + $^{n+2}J_{CP}$ = 2 Hz, $C_{11/12/15/16}$), 165.8 (s, C_6), 199.2 (d, $^1J_{CF}$ = 192 Hz, C_2), 400.3 (C_1).

^{19}F NMR (CD_2Cl_2, 471 MHz, 295 K): δ –236.4 (s).

^{31}P NMR (CD_2Cl_2, 202 MHz, 295 K): δ 32.3 (s, PPh_2).

ESI-MS (m/z): Expected for $C_{62}H_{55}ClFO_2P_4Ru$ = 1111.1863 m/z [M^+]; Observed: 1111.1857 m/z [M^+] (Error = 0.6 mDa).

UV-Vis: λ_{max} = 794 nm, ε = 2027 mol^{-1} dm^2 at a concentration of approximately 1 mmol dm^{-3} and a path length of 1 cm; calculated λ_{max} = 770 nm.

Selected ATR IR ν: 1598 cm^{-1} (vinylidene C=C), 1713 cm^{-1} (C=O).

7.45 Synthesis of [*trans*-Ru(dppe)$_2$Cl(=C=C(F)C$_6$H$_4$-4-COMe)]BF$_4$, [58f]BF$_4$

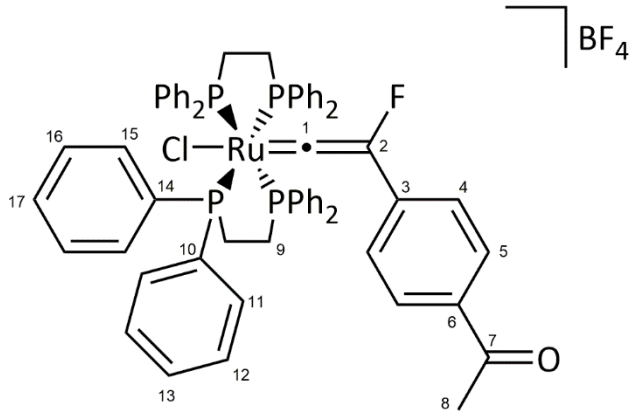

An oven dried Schlenk tube was charged with [Ru(dppe)$_2$Cl(-C≡C-C$_6$H$_4$-4-COMe)] (100 mg, 0.093 mmol) in dichloromethane (*ca.* 3 mL). An acetonitrile solution of Selectfluor® (40 mg, 0.112 mmol, in 5 mL) was added slowly, stirred for 30 minutes, and the solvent was removed *in vacuo*. The residue was extracted with dichloromethane (*ca.* 3 mL) and filtered; a yellow solid precipitated upon addition of pentane (10 mL). The solid was isolated by filtration, washed with diethyl ether (2 x 5 mL), and dried *in vacuo*. The product was isolated as a 1:1 mixture of [*trans*-Ru(dppe)$_2$Cl(=C=C(F)C$_6$H$_4$-COMe)][BF$_4$] and 1-chloromethyl-1,4-diazoniabicyclo[2.2.2]octane [BF$_4$]. Yield = 122 mg, 92 %.

Crystals of the hexafluorophosphate were grown by slow diffusion from dichloromethane: pentane solvent system. The hexafluorophosphate salt was obtained by salt metathesis; the tetrafluoroborate salt was stirred in dichloromethane with 20 equivalents of sodium hexafluorophosphate.

^{1}H NMR (CD_2Cl_2, 500 MHz, 295 K): δ 2.46 (s, 3H, H_8), 2.71 (m, 4H, $H_{9b/a}$), 3.00 (m, 4H, $H_{9b/a}$), 5.78 (vir. dt, $^3J_{HH}$ = 8.7 Hz, 2H, H_5), 7.11 (t, $^3J_{HH}$ = 7.6 Hz, 8H, $H_{12/16}$), 7.14-7.22 (m, 24H, $H_{11+12/16+15}$), 7.29 (vir. dt, $^3J_{HH}$ = 8.7 Hz, 2H, H_4), 7.33 (t, $^3J_{HH}$ = 7.4 Hz, 4H, $H_{13/17}$), 7.43 (t, $^3J_{HH}$ = 7.4 Hz, 4H, $H_{13/17}$).

^{13}C NMR (CD_2Cl_2, 126 MHz, 295 K): δ 26.2 (s, C_8), 28.7 (quin, $^1J_{CP}$ + $^3J_{CP}$ = 9 Hz, C_9), 121.4 (s, C_4), 127.2 (s, C_5), 128.2 (quin, $^nJ_{CP}$ + $^{n+2}J_{CP}$ = 2 Hz, $C_{11/12/15/16}$), 128.7 (d, $^2J_{CF}$ = 30 Hz, C_3), 129.0 (quin, $^nJ_{CP}$ + $^{n+2}J_{CP}$ = 2 Hz, $C_{11/12/15/16}$), 130.2 (quin, $^1J_{CP}$ + $^3J_{CP}$ = 12 Hz, $C_{10/14}$), 131.2 (s, $C_{13/17}$), 131.6 (s, $C_{13/17}$), 131.8 (quin, $^1J_{CP}$ + $^3J_{CP}$ = 11 Hz, $C_{10/14}$), 132.5 (quin, $^nJ_{CP}$ + $^{n+2}J_{CP}$ = 2 Hz, $C_{11/12/15/16}$), 133.9 (quin, $^nJ_{CP}$ + $^{n+2}J_{CP}$ = 2 Hz, $C_{11/12/15/16}$), 135.3 (s, C_6), 196.3 (s, C_7), 199.0 (d, $^1J_{CF}$ = 209 Hz, C_2), 399.8 (C_1).

^{19}F NMR (CD_2Cl_2, 471 MHz, 295 K): δ –236.1 (s).

^{31}P NMR (CD_2Cl_2, 202 MHz, 295 K): δ 32.1 (s, PPh_2).

ESI-MS (m/z): Expected for $C_{62}H_{55}ClFOP_4Ru$ = 1095.1914 m/z [M^+]; Observed: 1095.1918 m/z [M^+] (Error = -0.4 mDa).

UV-Vis: λ_{max} = 791 nm, ε = 1776 mol^{-1} dm^2 at a concentration of approximately 1 mmol dm^{-3} and a path length of 1 cm; calculated λ_{max} = 768 nm.

Selected ATR IR ν: 1626 cm^{-1} (vinylidene C=C), 1671 cm^{-1} (C=O)

Elemental Analysis: $C_{62}H_{55}F_7OP_5Ru$ + 0.7(CH_2Cl_2) Calc. /% C 57.93, H 4.37, Found /% C 57.84, H 4.43.

Residual dichloromethane was observed in the proton NMR spectrum and the crystal structure.

7.46 Synthesis of [*trans*-Ru(dppe)$_2$Cl(=C=C(F)C$_6$H$_4$-4-CF$_3$)]BF$_4$, [58g]BF$_4$

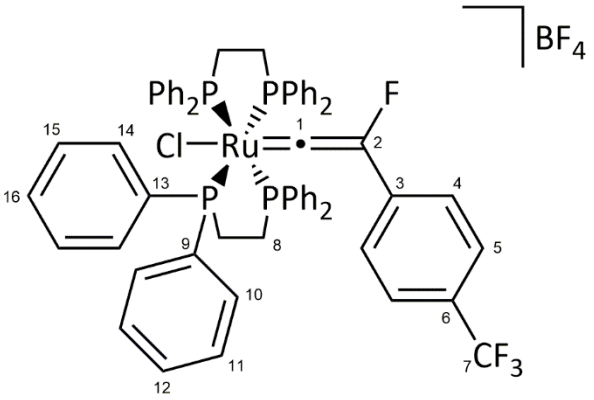

An oven dried Schlenk tube was charged with [Ru(dppe)$_2$Cl(-C≡C-C$_6$H$_4$-4-CF$_3$)] (100 mg, 0.091 mmol) in dichloromethane (*ca.* 3 mL). An acetonitrile solution of Selectfluor® (39 mg, 0.109 mmol, in 5 mL) was added slowly, stirred for 30 minutes, and the solvent was removed *in vacuo*. The residue was extracted with dichloromethane (*ca.* 3 mL) and filtered; a green solid precipitated upon addition of pentane (10 mL). The solid was isolated by filtration, washed with diethyl ether (2 x 5 mL), and dried *in vacuo*. The product was isolated as a 1:1 mixture of [*trans*-Ru(dppe)$_2$Cl(=C=C(F)C$_6$H$_4$-CF$_3$)][BF$_4$] and 1-chloromethyl-1,4-diazoniabicyclo[2.2.2]octane [BF$_4$]. Yield = 113 mg, 86 %.

Crystals of the hexafluorophosphate were grown by slow diffusion from dichloromethane: pentane solvent system. The hexafluorophosphate salt was obtained by salt metathesis; the tetrafluoroborate salt was stirred in dichloromethane with 20 equivalents of sodium hexafluorophosphate.

^{1}H NMR (CD_2Cl_2, 500 MHz, 295 K): δ 2.69 (m, 4H, $H_{8a/b}$), 2.98 (m, 4H, $H_{8b/a}$), 5.72 (d, $^3J_{HH}$ = 8.4, 2H, $H_{4/5}$), 6.89 (d, $^3J_{HH}$ = 8.4, 2H, $H_{5/4}$), 7.07 (t, J = 7.7 Hz, 8H, $H_{10+11+14+15}$), 7.12-7.20 (m, 24 H, $H_{10+11+14+15}$), 7.30 (t, $^3J_{HH}$ = 7.3 Hz, 4H, $H_{12/16}$), 7.40 (t, $^3J_{HH}$ = 7.3 Hz, 4H, $H_{16/12}$).

^{13}C NMR (CD_2Cl_2, 126 MHz, 295 K): δ 29.1 (quin, $^1J_{CP}$ + $^3J_{CP}$ = 11.1 Hz, C_8), 122.0 (s, C_4), 124.0 (q, $^1J_{CF}$ = 274 Hz, C_7), 124.4 (q, $^3J_{CF}$ = 4 Hz, C_5), 128.5 (C_3), 128.6 (s, C_4), 128.6 (quin, $^nJ_{CP}$ + $^{n+2}J_{CP}$ = 2.4 Hz, $C_{10/11/14/15}$), 128.7 (q, $^2J_{CF}$ = 32 Hz, C_6), 129.4 (quin, $^nJ_{CP}$ + $^{n+2}J_{CP}$ = 2.3 Hz, $C_{10/11/15/14}$), 130.7 (quin, $^1J_{CP}$ + $^3J_{CP}$ = 11.8 Hz, $C_{9/13}$), 131.6 (s, $C_{12/16}$), 132.0 (s, $C_{16/12}$), 132.2 (quin, $^1J_{CP}$ + $^3J_{CP}$ = 11.4 Hz, $C_{13/9}$), 132.8 (quin, $^nJ_{CP}$ + $^{n+2}J_{CP}$ = 2.3 Hz, $C_{10/11/15/14}$), 134.3 (quin, $^nJ_{CP}$ + $^{n+2}J_{CP}$ = 2.1 Hz, $C_{10/11/15/14}$), 199.3 (d, $^1J_{CF}$ = 213.6 Hz, C_2), 398.9 (C_1).

^{19}F NMR (CD_2Cl_2, 471 MHz, 295 K): δ –236.1 (s, 1F, F_2), -63.0 (s, 3F, F_7).

^{31}P NMR (CD_2Cl_2, 202 MHz, 295 K): δ 31.7 (s, PPh_2).

ESI-MS (m/z): Expected for $C_{61}H_{52}ClF_4P_4Ru$ = 1121.1696 m/z [M^+]; Observed: 1121.1697 m/z [M^+] (Error = -1.0 mDa).

UV-Vis: 1 mmol dm^{-3} in DCM, λ_{max}= 790 nm, abs = 0.15727, ε = 157.27 dm^3 mol^{-1} cm^{-1} / 1572.7 dm^2 mol^{-1}, calculated λ_{max} = 764 nm

Elemental Analysis: $C_{61}H_{52}ClF_{10}P_5Ru$ Calc. /% C 57.85, H 4.14, Found /% C 57.44, H 3.93.

7.47 Synthesis of [*trans*-Ru(dppe)$_2$Cl(=C=C(F)C$_6$H$_4$-4-NO$_2$)]BF$_4$, [58h]BF$_4$

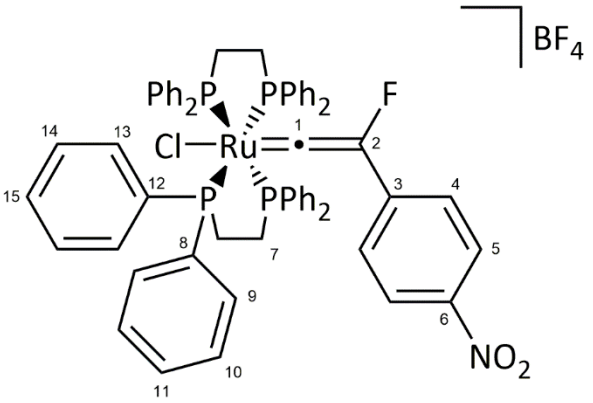

An oven dried Schlenk tube was charged with [Ru(dppe)$_2$Cl(-C≡C-C$_6$H$_4$-4-NO$_2$)] (65 mg, 0.06 mmol) in dichloromethane (*ca.* 3 mL). An acetonitrile solution of Selectfluor® (26 mg, 0.072 mmol, in 5 mL) was added slowly, stirred for 30 minutes, and the solvent was removed *in vacuo*. The residue was extracted with dichloromethane (*ca.* 3 mL) and filtered; a green solid precipitated upon addition of pentane (10 mL). The solid was isolated by filtration, washed with diethyl ether (2 x 5 mL), and dried *in vacuo*. The product was isolated as a 1:1 mixture of [*trans*-Ru(dppe)$_2$Cl(=C=C(F)C$_6$H$_4$-NO$_2$)][BF$_4$] and 1-chloromethyl-1,4-diazoniabicyclo[2.2.2]octane [BF$_4$]. Yield = 82 mg, 95 %.

Crystals of the hexafluorophosphate were grown by slow diffusion from dichloromethane: pentane solvent system. The hexafluorophosphate salt was obtained by salt metathesis; the tetrafluoroborate salt was stirred in dichloromethane with 20 equivalents of sodium hexafluorophosphate.

^{1}H NMR (CD_2Cl_2, 500 MHz, 295 K): δ 2.75 (m, 4H, $H_{7a/b}$), 3.03 (m, 4H, $H_{7b/a}$), 5.73 (vir. dt, $^3J_{HH}$ = 7.6 Hz, 2H, H_4), 7.12 (t, $^3J_{HH}$ = 7.4 Hz, 8H, $H_{10/14}$), 7.16-7.24 (m, 24H, $H_{9+10/14+13}$), 7.34 (t, $^3J_{HH}$ = 7.4 Hz, 2H, $H_{11/15}$) 7.44 (t, $^3J_{HH}$ = 6.5 Hz, 2H, $H_{15/11}$), 7.48 (vir. dt, $^3J_{HH}$ = 9.0 Hz, 2H, H_5)

^{13}C NMR (CD_2Cl_2, 126 MHz, 295 K): δ 29.0 (quin, $^1J_{CP}$ + $^3J_{CP}$ = 11 Hz, C_7), 121.4 (s, C_4), 122.8 (s, C_5), 128.7 (bs, $C_{10/14}$), 129.5 (bs, $C_{10/14}$), 130.4 (quin, $^1J_{CP}$ + $^3J_{CP}$ = 12 Hz, $C_{8/12}$), 131.2 (d, $^2J_{CF}$ = 51 Hz, C_3), 131.7 (s, $C_{11/15}$), 132.1 (s, $C_{11/15}$), 132.2 (quin, $^1J_{CP}$ + $^3J_{CP}$ = 11 Hz, $C_{8/12}$), 132.8 (bs, $C_{9/13}$), 134.3 (bs, $C_{9/13}$), 145.9 (s, C_6), 197.6 (d, $^1J_{CF}$ = 195 Hz, C_2), 391.5 (C_1).

^{19}F NMR (CD_2Cl_2, 471 MHz, 295 K): δ –234.8 (s).

^{31}P NMR (CD_2Cl_2, 202 MHz, 295 K): δ 31.4 (s, PPh_2).

ESI-MS (m/z): Expected for $C_{60}H_{52}ClFNO_2P_4Ru$ = 1098.1672 m/z [M^+]; Observed: 1098.1709 m/z [M^+] (Error = -3.7 mDa).

UV-Vis: λ_{max} = 781 nm, ε = 1920 mol^{-1} dm^2 at a concentration of approximately 1 mmol dm^{-3} and a path length of 1 cm; calculated λ_{max} = 744 nm.

Selected ATR IR: ν(vinylidene C=C) 1669 cm^{-1}.

Elemental Analysis: $C_{60}H_{53}F_7NO_2P_5Ru + 0.8(CH_2Cl_2)$ Calc. /% C 55.69, H 4.12, N 1.05, Found /% C 55.54, H 4.12, N 1.08.

Residual dichloromethane was observed in the proton NMR spectrum and the crystal structure.

7.48 Synthesis of [*trans*-Ru(dppe)$_2$Cl(=C=C(F)C$_3$H$_5$)]BF$_4$, [58j]BF$_4$

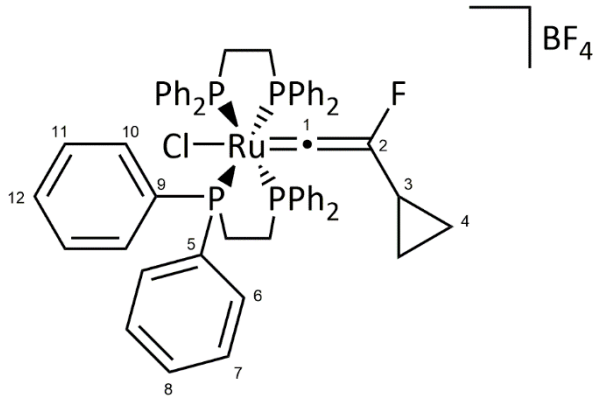

An oven dried Schlenk tube was charged with [Ru(dppe)$_2$Cl(-C≡C-C$_3$H$_5$)] (68 mg, 0.068 mmol) in dichloromethane (*ca.* 3 mL). An acetonitrile solution of Selectfluor® (29 mg, 0.082 mmol, in 5 mL) was added slowly, stirred for 15 minutes, and the solvent was removed *in vacuo*. The residue was extracted with dichloromethane (*ca.* 3 mL) and filtered; a green solid precipitated upon addition of pentane (10 mL). The solid was isolated by filtration, washed with diethyl ether (2 x 5 mL), and dried *in vacuo*. The product was isolated as a 1:1 mixture of [*trans*-Ru(dppe)$_2$Cl(=C=C(F)C$_3$H$_5$)] [BF$_4$] and 1-chloromethyl-1,4-diazoniabicyclo[2.2.2]octane [BF$_4$]. Yield = 70 mg, 76 %.

Crystals of the hexafluorophosphate were grown by slow diffusion from dichloromethane: pentane solvent system. The hexafluorophosphate salt was obtained by salt metathesis; the tetrafluoroborate salt was stirred in dichloromethane with 20 equivalents of sodium hexafluorophosphate.

^{1}H NMR (CD_2Cl_2, 500 MHz, 295 K): δ 0.54 (m, 2H, $H_{4a/b}$), 0.60 (m, 1H, H_3), 0.74 (m, 2H, $H_{4a/b}$), 2.41 (m, 4H, $H_{5a/b}$), 2.88 (m, 4H, $H_{5b/a}$), 7.11-7.19 (m, 16H, $H_{7/11+8/12}$), 7.24 (m, 8H, $H_{7/11}$), 7.29 (t, $^3J_{HH}$ = 7.6 Hz, $H_{8/12}$), 7.40 (tt, $^3J_{HH}$ = 7.0 Hz, $^4J_{HH}$ = 2.0 Hz, 4H, $H_{9/13}$), 7.50 (t, $^3J_{HH}$ = 7.2 Hz, 4H, $H_{9/13}$).

^{13}C NMR (CD_2Cl_2, 126 MHz, 295 K): δ 4.6 (d, $^2J_{HF}$ = 27 Hz, C_3), 4.9 (s, C_4), 28.9 (quin, $^1J_{CP}$ + $^3J_{CP}$ = 12 Hz, C_5), 128.0 (quin, $^2J_{CP}$ + $^4J_{CP}$ = 2 Hz, $C_{8/12}$), 128.7 (quin, $^2J_{CP}$ + $^4J_{CP}$ = 2 Hz, $C_{8/12}$), 130.4 (quin, $^1J_{CP}$ + $^3J_{CP}$ = 12 Hz, $C_{6/10}$), 130.5 (s, $C_{9/13}$), 131.5 (s, $C_{9/13}$), 131.8 (quin, $^1J_{CP}$ + $^3J_{CP}$ = 11.3 Hz, $C_{6/10}$), 133.3 (quin, $^3J_{CP}$ + $^5J_{CP}$ = 2 Hz, $C_{7/11}$), 134.0 (quin, $^3J_{CP}$ + $^5J_{CP}$ = 2 Hz, $C_{7/11}$), 198.5 (C_2), 412.3 (C_1).

^{19}F NMR (CD_2Cl_2, 471 MHz, 295 K): δ –249.0 (s).

^{31}P NMR (CD_2Cl_2, 202 MHz, 295 K): δ 38.7 (s, PPh_2).

ESI-MS (m/z): Expected for $C_{57}H_{53}ClFP_4Ru$ = 1017.1808 m/z [M^+]; Observed: 1017.1833 m/z [M^+] (Error = -2.5 mDa).

UV-Vis: λ = 757, 429 nm, ε = 352, 3464 mol^{-1} dm^2 at a concentration of approximately 1 mmol dm^{-3} and a path length of 1 cm; calculated λ = 757, 432 nm.

Selected ATR IR: ν(vinylidene C=C) 1677 cm^{-1}.

Elemental Analysis: $C_{57}H_{53}F_7P_4Ru$ + 0.7(CH_2Cl_2) Calc. /% C 56.72, H 4.49, Found /% C 56.81, H 4.48.

7.49 Synthesis of [*trans*-Ru(dppe)$_2$Cl(=C=CH$_2$)]PF$_6$, [59]PF$_6$

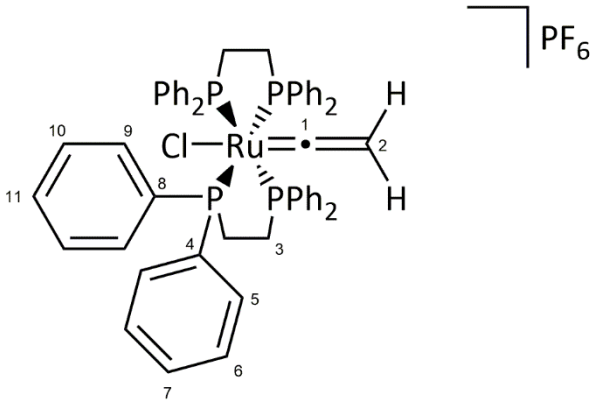

An oven dried Schlenk tube was charged with a solution of [Ru(dppe)$_2$Cl][PF$_6$] (200 mg, 0.19 mmol) and ethynyltrimethylsilane (36 mg, 51 µL, 0.37 mmol) in dichloromethane (5 mL). The solution was stirred for 4-6 hours, or until the phosphorus NMR spectrum indicated the reaction had reached completion, after which the solvent was removed *in vacuo*. The residue was washed with diethylether (2 x 5 mL) to remove excess alkyne and dried *in vacuo* to afford a red powder. Yield = 187 mg, 89 %.

^{1}H NMR (CD_2Cl_2, 400 MHz, 295 K): δ 2.43 (quin, $^4J_{HP}$ = 2.3 Hz, 2H, H_2), 2.73-2.98 (m, 8H, H_{3a+b}), 7.02 (m, 8H, $H_{6/10}$), 7.10 (t, $^3J_{HH}$ = 7.7 Hz, 8H, $H_{5/9}$), 7.19 (t, $^3J_{HH}$ = 7.6 Hz, 8H, $H_{5/9}$), 7.32-7.37 (m, 12H, $H_{6/10+7/11}$), 7.43 (t, $^3J_{HH}$ = 7.4 Hz, 4H, $H_{7/11}$).

^{31}P{^{1}H} NMR (CD_2Cl_2, 202 MHz, 295 K): δ 41.5 (s, PPh_2).

ESI-MS (m/z): Expected for $C_{54}H_{50}ClP_4Ru$ = 959.160110 m/z [M^+]; Observed: 959.159514 m/z [M^+] (Error = -0.6 mDa).

7.50 Synthesis of [Ru(η^5-C_5H_5)(dppe)(-C≡CPh)], [77]

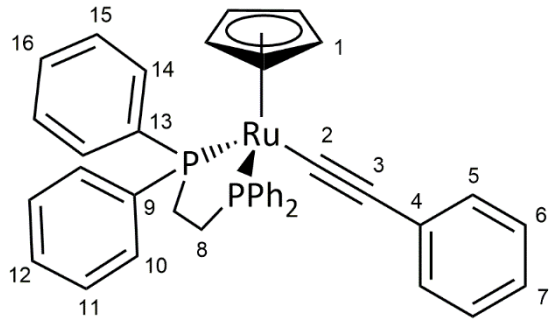

Prepared as described in the literature.[218]

An oven dried Schlenk charged with [Ru(η^5-C_5H_5)(dppe)Cl] (200 mg, 0.33 mmol), phenylacetylene (68 mg, 73 µL, 0.67 mmol), and ammonium hexafluorophosphate (109 mg, 0.67 mmol) was heated in refluxing methanol (15 mL) for 2 hours. The solvent was allowed to cool and the solution cannula filtered to remove unreacted starting material. The solvent was removed *in vacuo* and the residue extracted in dichloromethane (*ca.* 5 mL) and cannula filtered in stirring diethyl ether (25 mL). The pink precipitate was isolated by cannula filtration, washed further with diethyl ether (2 x 5 mL), and dried *in vacuo*. The powder was redissolved in dichloromethane (5 mL) and treated with a methanolic KOH (0.1 g in 2 mL). The solvent was removed *in vacuo* and the residue extracted with dichloromethane (3 mL). The extract was cannula filtered into stirring hexane (15 mL) to afford a yellow precipitate which was isolated by cannula filtration, washed with diethyl ether (3 mL), and dried *in vacuo*. Yield = 128 mg, 58 %.

^{1}H NMR (400 MHz, CD_2Cl_2, 295 K): δ 2.20 - 2.43 (m, 2H, $H_{2a/b}$), 2.58 - 2.73 (m, 2H, $H_{2a/b}$), 4.76 (s, 5H, H_1), 6.32 - 6.35 (m, 2H, H_5), 6.74 - 6.78 (m, 1H, H_7), 6.83 - 6.86 (m, 2H, H_6), 7.21 - 7.29 (m, 10H, Ar-H), 7.39 - 7.41 (m, 6H, Ar-H), 7.86 - 7.91 (m, 4H, Ar-H).

^{31}P{^{1}H} NMR (162 MHz, CD_2Cl_2, 295 K): δ 86.3 (s, PPh_2).

7.51 Synthesis of [Ru(η^5-C_5H_5)($P(OMe)_3$)$_2$(-C≡C-Ph)], [81]

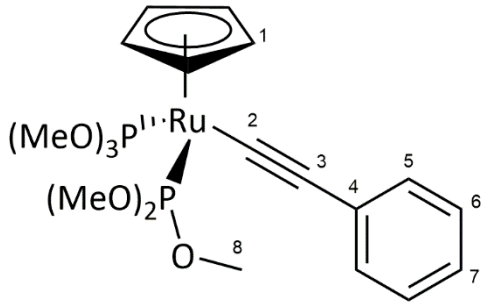

Prepared as described in the literature.[272]

To an oven dried Schlenk tube charged with a solution of [Ru(η^5-C_5H_5)($P(OMe)_3$)$_2$Cl] (100 mg, 0.22 mmol) in toluene (10 mL) was added Ag-C≡C-Ph (56 mg, 0.27 mmol) and the solution heated at reflux for 16 hours. The cooled solution was filtered by cannula and the solvent removed *in vacuo*. The yellow oil was chromatographed on preparative TLC plates (2:1 light petroleum: acetone). A colourless band (R_f 0.43) was collected and crystallised from ether:light petroleum solvent mixture to afford colourless-pale yellow crystals. Yield 76.2 mg, 66 %.

^{1}H NMR (CD_2Cl_2, 400 MHz, 295 K): δ 3.62 (m, $^3J_{HP}$ + $^5J_{HP}$ = 12.6 Hz, 18H, H_8), 4.95 (m, 5H, H_1), 6.91-6.96 (m, 1H, H_7), 7.07-7.08 (m, 4H, H_{5+6}), 7.47 (app t, $^3J_{HH}$ = 7.6 Hz, 2H, H_6).

^{31}P{^{1}H} NMR (CD_2Cl_2, 162 MHz, 295 K): δ 162.8 (s).

7.52 Synthesis of [Ru(η^5-C_5H_5)(P(OMe)$_3$)$_2$(CC(F)Ph)]NSI, [82]NSI

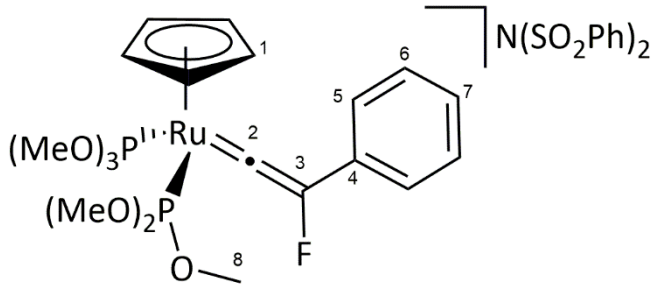

An oven dried Schlenk tube was charged with [Ru(η^5-C_5H_5)(P(OMe)$_3$)$_2$(-C≡CPh)] (15 mg, 0.014 mmol) in toluene (*ca.* 5 mL). A toluene solution of NFSI (5 mg, 0.014 mmol, in *ca.* 3 mL) was added slowly to the solution and stirred for 30 minutes. The solution stirred for 15 minutes after which the oil was isolated by filtration and washed with toluene (2 x 5 mL) and pentane (1 x 5 mL) before being dried *in vacuo*. Yield was not determined.

^{1}H NMR (CD_2Cl_2, 500 MHz, 295 K): δ 3.68 (m, $^3J_{HP}$ + $^5J_{HP}$ = 12.3 Hz, 18H, H_8), 5.87 (t, $^3J_{HP}$ = 0.8 Hz, 5H, H_1), 7.17 (m, 2H, H_5), 7.26 (tt, $^3J_{HH}$ = 7.4 Hz, $^4J_{HH}$ = 1.4 Hz, H_7), 7.47 (app t, $^3J_{HH}$ = 7.6 Hz, 2H, H_6).

^{13}C{^{1}H} NMR (CD_2Cl_2, 126 MHz, 295 K): δ 54.1 (t, $^3J_{CP}$ = 3.6 Hz, C_8), 93.3 (t, $^3J_{CP}$ = 2.0 Hz, C_1), 121.9 (s, C_5), 128.3 (s, C_7), 128.7 (s, C_6), 193.3 (d, $^1J_{CF}$ = 222.5 Hz, C_3), 398.6 (C_2).

^{19}F NMR (CD_2Cl_2, 471 MHz, 295 K): δ –213.9 (t, $^4J_{PF}$ = 6.5 Hz, F_3).

^{31}P{^{1}H} NMR (CD_2Cl_2, 202 MHz, 295 K): δ 168.7 (d, $^4J_{PF}$ = 6.5 Hz).

ESI-MS (m/z): Expected for $C_{19}H_{28}FO_6P_2Ru$ = 535.0388 m/z; Observed: 535.0398 m/z [M^{+}] (Error = -1.0 mDa).

UV-Vis: 1 mmol dm^{-3} in DCM, λ_{max}= 642 nm, abs = 0.12068, ε = 120.68 dm^3 mol^{-1} cm^{-1} / 1206.8 dm^2 mol^{-1}.

Due to the unstable nature of the complex, suitable crystals for single crystal X-ray diffraction of elemental analysis could not be obtained.

7.53 Synthesis of [Ru(η^5-C_5H_5)(dppe)(=CFCFHPh)]Cl, [104a]Cl

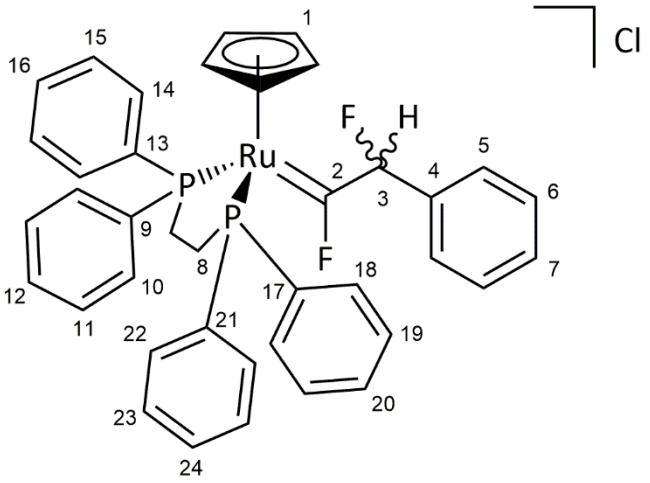

An NMR tube charged with [Ru(η^5-C_5H_5)(dppe)(-CF=CFPh)] (5 mg, 7.1 µmol) in CD_2Cl_2 was treated with anhydrous 2M HCl in diethyl ether (259 µg, 3.5 µL, 7.1 µmol). The sample was used without further purification. The sample was found to contain the desired complex as the major product (88 % conversion), as well as [Ru(η^5-C_5H_5)(dppe)(=CCFPh)]Cl, **[19]**Cl, and an additional unknown species (6% each).

^{1}H NMR (500 MHz, CD_2Cl_2, 295 K): δ 3.07- 3.41 (m, 4H, H_8), 4.61 (dd, $^2J_{HF}$= 46 Hz, $^3J_{HF}$= 8 Hz, H_3), 5.43 (s, 5H H_1), 7.04 (td, J_{HH}= 3, 8 Hz, 2H, Ar-H), 7.13 (d, J_{HH}= 8 Hz, 2H, H_5), 7.16-7.24 (m, 6H, Ar-H), 7.36 (d, J_{HH}= 8 Hz, 2H, H_6), 7.44-7.63 (m, 11H, Ar-H), 7.67 (d, J_{HH}= 8 Hz, 1H, Ar-H), 7.69 (d, J_{HH}= 8 Hz, 1H, Ar-H).

Selected ^{13}C{^{1}H} NMR (126 MHz, CD_2Cl_2, 295 K): δ 29.1 (C_8), 93.3 (s, C_1), 103.4 (dd, $^3J_{CF}$= 45 Hz, $^2J_{CF}$= 185 Hz, C_3), 299.0 ($^1J_{CF}$ = 388 Hz, C_2).

Assignment of the aromatic carbon environments was challenged by the broken symmetry of the complex and presence of [Ru(η^5-C_5H_5)(dppe)(=CCFPh)]Cl, **[19]**Cl, and an additional unknown species (6% each).

^{19}F NMR (471 MHz, CD_2Cl_2, 295 K): δ 115.8 (app. tdm, $^3J_{FF}$ + $^3J_{PF}$ = 43 Hz, $^3J_{PF}$ = 26 Hz, 1F, F_2), -90.3 (app. t, $^3J_{FF}$ + $^2J_{HF}$ = 44 Hz, 1F, F_3).

^{31}P{^{1}H} NMR (203 MHz, CD_2Cl_2, 295 K): δ 83.9 (dd, $^3J_{PP}$ = 19 Hz, $^4J_{FP}$ = 26 Hz), 88.8 (dd, $^3J_{PP}$ = 19 Hz, $^3J_{FP}$ = 42 Hz).

ESI-MS (m/z): Expected for $C_{39}H_{35}F_2P_2Ru$ = 705.1231 [M$^+$]; Observed= 705.1226 [M$^+$] (Error = -0.5 mDa).

To obtain crystallographic data the chloride anion was exchanged for the hexafluorophosphate anion through ion metathesis. This was achieved by dissolving the chloride salt in dichloromethane with 20 equivalents of sodium hexafluorophosphate and stirred for 1 hour. Crystals of the hexafluorophosphate salt were grown from a dichloromethane: pentane solvent system via slow diffusion. The crystal structure obtained consisted of a mixture of the desired carbene and the HF elimination product, $[Ru(\eta^5\text{-}C_5H_5)(dppe)(=C=CFPh)]PF_6$.

7.54 Synthesis of [Ru(η^5-C_5H_5)(dppe)(=CFCF$_2$Ph)]NSI, [104b]NSI

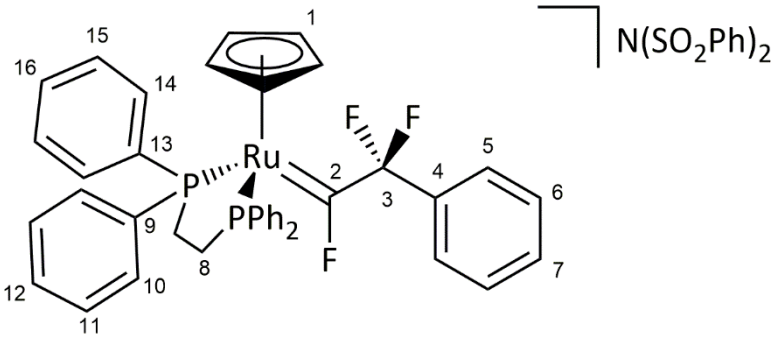

An oven dried Schlenk tube was charged with [Ru(η^5-C_5H_5)(dppe)(-CF=CFPh)] (55 mg, 78 µmol) and NFSI (28 mg, 78 µmol) in dichloromethane (5 mL). After the reaction was stirred for 10 minutes at room temperature, the solvent was removed *in vacuo*. The residue was washed with toluene (2 x 5 mL) and diethyl ether (2 x 5 mL), and the resultant green powder was dried *in vacuo*. Yield = 61 mg, 77 %.

^{1}H NMR (500 MHz, CD_2Cl_2, 295 K): δ 3.05- 3.19 (m, 2H, H_8), 3.23- 3.36 (m, 2H, H_8), 5.46 (s, 5H H_1), 7.12-7.18 (m, 6H, H_5 + $H_{10/11/14/15}$), 7.20-7.38 (m, 6H, H_6 + $H_{10/11/14/15}$), 7.39-7.44 (m, 4H, $H_{10/11/14/15}$), 7.48-7.56 (m, 9H, H_7 + $H_{10/11/14/15}$ + H_{12} + H_{16}).

^{13}C{^{1}H} NMR (126 MHz, CD_2Cl_2, 295 K): δ 28.6 (C_8), 94.1 (s, C_1), 119.2 (C_3), 125.8 (t, J_{CF}= 6 Hz, C_5), 128.9-129.0 ($C_{10/11/14/15}$ + C_6), 129.4 (t, $^nJ_{CP}$ + $^{n+2}J_{CP}$= 5 Hz, $C_{10/11/14/15}$), 130.3 (t, $^nJ_{CP}$ + $^{n+2}J_{CP}$= 5 Hz, $C_{10/11/14/15}$), 130.5 (t, $^2J_{CF}$= 28 Hz, C_4), 131.1 (s, C_7), 131.4 (s, $C_{12/16}$), 131.8 (s, $C_{12/16}$), 131.8 ($C_{9/13}$), 132.4 (t, $^nJ_{CP}$ + $^{n+2}J_{CP}$= 5 Hz, $C_{10/11/14/15}$), 136.7 ($C_{9/13}$), 284.5 (d, $^2J_{CF}$ = 398.8 Hz).

^{19}F NMR (471 MHz, CD_2Cl_2, 295 K): δ 113.6 (tt, $^3J_{FP}$ = 33 Hz, $^3J_{FF}$ = 12 Hz, 1F, F_2), -90.3 (d, $^3J_{FF}$= 11 Hz, 2F, F_3).

^{31}P{^{1}H} NMR (203 MHz, CD_2Cl_2, 295 K): δ 85.5 (d, $^3J_{FP}$ = 33 Hz, PPh_2).

ESI-MS (m/z): Expected for $C_{48}H_{46}FP_2Ru$ = 805.2096 [M$^+$]; Observed = 805.2092 [M$^+$] (Error = 0.4 mDa).

UV-Vis: λ_{max} = 395 nm, ε = 4214 mol^{-1} dm^2 at a concentration of approximately 1 mmol dm^{-3} and a path length of 1 cm.

Elemental Analysis: $C_{39}H_{34}F_9P_3Ru$ + 0.2($C_{12}H_{10}NO_4S$) + 0.3(CH_2Cl_2) Calc. /% C 52.59, H 3.87, N 0.29, Found /% C 52.42, H 3.91, N 0.27.

Elemental analysis sample was found to contain contaminant $N(SO_2Ph)_2$ from salt metathesis and residual dichloromethane in the NMR Spectrum..

To obtain crystallographic data the dibenzenesulfonimide anion was exchanged for the hexafluorophosphate anion through ion metathesis. This was achieved by dissolving the dibenzenesulfonimide salt in dichloromethane with 20 equivalents of sodium hexafluorophosphate and stirred for 1 hour. Crystals of the hexafluorophosphate salt were grown from a dichloromethane: pentane solvent system via slow diffusion.

7.55 Synthesis of [Ru(η^5-C_5H_5)(dppe)(=CClCFHPh)]Cl, [104c]Cl

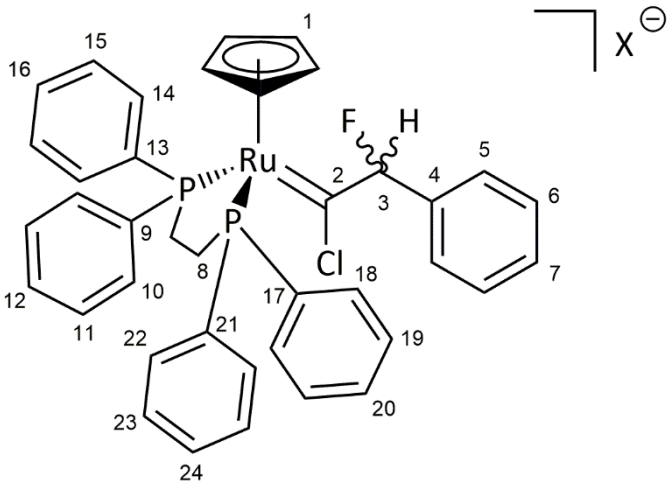

X = Cl or BF_4

An NMR tube charged with [Ru(η^5-C_5H_5)(dppe)(=C=CFPh)] (5 mg, 6.5 µmol) in CD_2Cl_2 was treated with anhydrous 2M HCl in diethyl ether (709 µg, 9.5 µL, 19.5 µmol). The sample was left to react over three hours and used without further purification. The compound could not be isolated due to loss of HCl in the solid state.

^{1}H NMR (500 MHz, CD_2Cl_2, 295 K): δ 3.26- 3.41 (m, 2H, H_8), 3.54-3.69 (m, 2H, H_8), 5.10 (d, $^2J_{HF}$= 48 Hz, H_3), 5.30 (s, 5H H_1), 7.10 (td, J_{HH}= 8, 3 Hz, 2H, Ar-H), 7.15 (m, 2H, Ar-H), 7.23 (m, 2H, Ar-H), 7.30 (dd, J_{HH}= 12, 8 Hz, 2H, Ar-H), 7.42-7.56 (m, 14H, Ar-H), 7.60-7.64 (m, 3H, Ar-H).

Selected ^{13}C{^{1}H} NMR (126 MHz, CD_2Cl_2, 295 K): δ 28.9 (t, $^1J_{CP}$ + $^3J_{CP}$ = 11 Hz, C_8), 29.2 (t, $^1J_{CP}$ + $^3J_{CP}$ = 11 Hz, C_8), 94.5 (s, C_1), 109.5 (d, $^1J_{CF}$ = 191 Hz, C_3), 128.6 (s, C_{Ar}), 128.7 (s, C_{Ar}), 128.8 (s, C_{Ar}), 128.9 (s, C_{Ar}), 129.0 (s, C_{Ar}), 129.3 (s, C_{Ar}), 129.4 (s, C_{Ar}), 129.5 (s, C_{Ar}), 129.6 (s, C_{Ar}), 129.8 (d, $^nJ_{CP}$ = 10 Hz, C_{Ar}), 130.1 (d, $^nJ_{CP}$ = 10 Hz, C_{Ar}), 130.9 (d, $^nJ_{CP}$ = 2 Hz, C_{Ar}), 131.1 (d, $^nJ_{CP}$ = 3 Hz, C_{Ar}), 131.4 (d, $^nJ_{CP}$ = 3 Hz, C_{Ar}), 131.7 (s, C_{Ar}), 131.9 (d, $^nJ_{CP}$ = 3 Hz, C_{Ar}), 133.0 (d, $^nJ_{CP}$ = 10 Hz, C_{Ar}), 133.2 (d, $^nJ_{CP}$ = 11 Hz, C_{Ar}), 138.5 (d, $^nJ_{CP}$ = 20 Hz, C_{Ar}), 138.9 (d, $^nJ_{CP}$ = 20 Hz, C_{Ar}), 292.2 (dt, $^2J_{CF}$ = 48 Hz, $^2J_{PF}$ = 10 Hz, C_2).

Assignment of the aromatic carbon environments was challenged by the broken symmetry of the complex.

^{19}F NMR (471 MHz, CD_2Cl_2, 295 K): δ -130.2 (d, $^2J_{HF}$ = 48 Hz, F_3).

^{31}P{^{1}H} NMR (203 MHz, CD_2Cl_2, 295 K): δ 89.6 (d, $^3J_{PP}$ = 16 Hz), 93.8 (d, $^3J_{PP}$ = 16 Hz).

7.56 Reactions of [Ru(η^5-C_5H_5)(PPh_3)$_2$(-C≡CH)], [28a], with FTMP, NFSI, and Selectfluor under dark and cold conditions.

Dark conditions

An oven dried Schlenk tube wrapped in foil was charged with [Ru(η^5-C_5H_5)(PPh_3)$_2$(C≡CH)] (5 mg, 7 μmol) dissolved in dichloromethane (*ca.* 3 mL). An acetonitrile solution of the desired fluorinating agent (10 μmol in *ca.* 3 mL) was cannula transferred into the ruthenium solution and stirred in the dark for 20 minutes. The solvent was removed *in vacuo* and redissolved in deuterated dichloromethane without further purification and submitted for NMR analysis in an amberised NMR tube. The reaction proceeded to form [(Ru(η^5-C_5H_5)(PPh_3)$_2$)$_2$(μ-C_4H_2F)]$^+$.

Dark and cold conditions

An oven dried Schlenk tube wrapped in foil was charged with [Ru(η^5-C_5H_5)(PPh_3)$_2$(C≡CH)] (5 mg, 7 μmol) dissolved in dichloromethane (*ca.* 3 mL) and cooled to -78 °C. An acetonitrile solution of the desired fluorinating agent (10 μmol in *ca.* 3 mL) was cannula transferred into the ruthenium solution and stirred in the dark at -78 °C for 5 minutes. The solution was then allowed to warm to room temperature over 15 minutes. The solvent was removed *in vacuo* and the residue redissolved in deuterated dichloromethane without further purification and submitted for NMR analysis in an amberised NMR tube. The reaction proceeded to form [(Ru(η^5-C_5H_5)(PPh_3)$_2$)$_2$(μ-C_4H_2F)]$^+$.

7.57 Heating Fluorovinylidene Complexes [54a]NSI, [58a]BF_4, and [82]NSI in d^3-Acetonitrile

In the glovebox, a Youngs tap NMR tube was charged with a d^3-acetonitrile solution of **[54a]**NSI, **[58a]**BF_4, **[82]**NSI (5 mg). The solutions were heated for one week at 50 °C and the reactions monitored by NMR spectroscopy and MS spectroscopy. The reaction mixture containing **[54a]**NSI was heated for a further week at 70 °C. Complex **[82]**NSI was heated for 24 hours at 70 °C.

The was no evidence for the liberation of fluoroethyne in any of the three reactions. In the case of **[58a]**BF_4 a new organometallic species was observed as the major product with following data:

Selected ^{1}H NMR (CD_2Cl_2, 400 MHz, 295 K): δ 6.68 (dd, *J*= 99, 14 Hz).

^{19}F NMR (CD_2Cl_2, 376 MHz, 295 K): δ -45.4 ppm (ddd, J_{PF} = 114, 23 Hz, J_{FH} = 99 Hz).

^{31}P{^{1}H} NMR (CD_2Cl_2, 162 MHz, 295 K): δ 23.4 (ddd, J_{PP} = 311, 25, 19 Hz), 27.5 (dd, J_{PF} = 114 Hz, J_{PP} = 19 Hz), 41.4 (ddd, J_{PP} = 311, 18 Hz, J_{PF} =23 Hz), 62.6 (dd, J_{PP} = 25, 18 Hz).

[54a]NSI: There was no evidence for any reactivity being observed.

[82]BF_4: Complete decomposition is observed to afford numerous fluorine- and phosphorus-containing species.

7.58 Heating Fluorovinylidene Complexes, [15b]BF_4, [19]BF_4, and [30a]BF_4 in the Presence of Triphenylphosphine

Reactions carried out based on the procedure reported in the literature.[264]

In the glovebox, an FEP lined Youngs tap NMR tube was charged with a toluene suspension of the fluorovinylidene complex (15 mg) and triphenylphosphine (1.2 equivalents). The suspension was heated at 100 °C for 16 hours (**[15b]**BF_4) and four days (**[19]**BF_4, and **[30a]**BF_4). The reactions were monitored by NMR spectroscopy and MS spectroscopy.

In all three reactions, there was no evidence to suggest the respective fluoroalkyne was displaced by triphenylphosphine.

[15b]BF_4: The NMR spectra of the suspension in toluene revealed formal loss of 'F^+' to afford **[14b]**.

[19]BF_4: **^{31}P{^{1}H} NMR** (CD_2Cl_2, 161.83 MHz, 295 K): δ 23.5 (s, PPh_3O), 41.3 (t, $^3J_{PP}$ = 34 Hz, **[76]**BF_4) 66.2 (d, $^3J_{PP}$ = 34 Hz, **[76]**BF_4), 78.9 (s, **[19]**BF_4), 84.6 (s, **[77]**), 91.6 (dd, J = 28, 3 Hz, *Z*-**[23a]**).

[30a]BF_4: No noticeable change in the NMR spectra.

7.59 Broadband UV Irradiation of [30a]BF_4, [54a]NSI, [19]BF_4, in d^3-Acetonitrile

In the glovebox, a Youngs tap NMR tube was charged with a d^3-acetonitrile solution of the fluorovinylidene complex (5 mg). The sample were irradiated with broadband UV light for two and five hours. The reactions were monitored by NMR spectroscopy and MS

spectroscopy. In all three reactions there was again no evidence to suggest the fluoroalkyne is liberated from the fluorovinylidene complex.

[19]BF_4: Minor decomposition to **[44c]**BF_4 (8%) and **[68]**BF_4 (4%) observed.

[30a]BF_4: Only decomposition to multiple unknown products was observed

[54a]NSI: Hydrolysis of **[54a]**NSI (64 % conversion) was observed to afford **[71]**NSI, acetic acid, and inorganic fluoride (from the reaction of HF with the glass).

7.60 Broadband UV Irradiation of [Ru(η^5-C_5H_5)(dppe)(-CF=CFPh)] in DCM

An NMR tube charged with [Ru(η^5-C_5H_5)(dppe)(-CF=CFPh)] (5 mg, 7.1 µmol) in CD_2Cl_2 was irradiated with broadband UV light (125 W) for 1 and 2 hours. The sample was analysed without purification.

Irradiation resulted in the formation of numerous phosphorus- and fluorine-containing species, of which trifluorostyrene and 1-chloro-1,2-difluorostyrene were identified in the ^{19}F NMR spectrum.

Due to the complexity of the ^1H NMR spectrum it was not possible to distinguish between the overlapping aromatic resonances.

1-chloro-1,2-difluorostyrene[292]

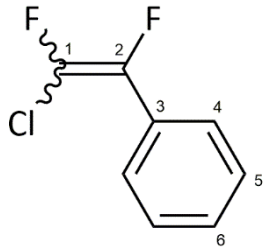

Z -Isomer

^{19}F NMR (CD_2Cl_2, 376.2 MHz, 295 K): δ -118.3 (d, $^3J_{FF}$ = 127 Hz), -148.1 (d, $^3J_{FF}$ = 127 Hz).

E-Isomer

^{19}F NMR (CD_2Cl_2, 376.2 MHz, 295 K): δ -102.1 (d, $^3J_{FF}$ = 11 Hz), -132.0 (d, $^3J_{FF}$ = 11 Hz).

Trifluorostyrene[293]

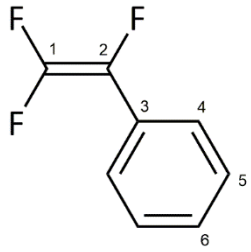

^{19}F NMR (CD_2Cl_2, 376.2 MHz, 295 K): δ -100.0 (dd, *J* = 32, 72 Hz), -114.8 (dd, *J* = 72, 110 Hz), and -177.1 (dd, *J* = 32, 110 Hz).

7.61 Broadband UV Irradiation of [Ru(η^5-C_5H_5)(dppe)(-CF=CFPh)] in THF

An NMR tube charged with [Ru(η^5-C_5H_5)(dppe)(-CF=CFPh)] (5 mg, 7.1 μmol) in d^8-THF was irradiated with broadband UV light (125 W) for 1 and 2 hours. The sample was analysed without purification. There was no evidence of any reaction having occurred by NMR spectroscopy.

7.62 Broadband UV Irradiation of [Ru(η^5-C_5H_5)(dppe)(-CF=CFPh)] with tetramethylammonium fluoride in THF

An NMR tube charged with [Ru(η^5-C_5H_5)(dppe)(-CF=CFPh)] (5 mg, 7.1 μmol) and tetramethylammonium fluoride (1.3 mg, 14.2 μmol) in d^8-THF was irradiated with broadband UV light (125 W) for 1 and 2 hours. The sample was analysed without purification. There was no evidence of any reaction having occurred by NMR spectroscopy.

7.63 Hydrolysis of [Ru(η^5-C_5Me_5)(dppe)(=C=CHF)]NSI, [54a]NSI

Adventitious Water

In the glovebox, a Youngs tap NMR tube was charged with a solution of [Ru(η^5-C_5Me_5)(dppe)(=C=CHF)]NSI (5 mg, 5.1 μmol) in d^3-acetontrile containing adventitious water. The solution was heated at 50 °C for five days resulting in partial hydrolysis of **[54a]**NSI to afford **[71]**NSI and **[85]**NSI, as well as **79** as a trace component.

Addition of Water to Rigorously Dried Acetontrile-d^3

In the glovebox, [Ru(η^5-C_5Me_5)(dppe)(=C=CHF)]NSI (10 mg, 10.2 µmol) was added to an FEP lined Youngs tap NMR tube. The NMR tube was charged with d^3-acetontrile, stored over CaH_2, by trap-to-trap transfer. One equivalent of deoxygenated water (0.2 µL, 10.2 µmol) was added to the solution and the reaction heated for 36 hours at 50 °C. No reaction was observed so an additional four equivalents of water were added and the reaction mixture was heated at 70 °C for 14 days and monitored by NMR spectroscopy.

NMR Spectroscopic data after 14 days at 70 °C:

Selected ^{1}H NMR (CD_3CN, 400 MHz, 295 K): δ 1.39 (a, **[71]**NSI), 1.55 (s, **[85]**NSI), 1.93 (s, acetic acid, approximately 54 %), 4.85 (d, $^2J_{NF}$ = 47 Hz, trace).

^{19}F NMR (CD_3CN, 376 MHz, 295 K): δ -181.5 (bs, HF, 95 %), -235.2 (d, $^2J_{HF}$ = 80 Hz, **[54a]**NSI, 5 %).

^{31}P{^{1}H} NMR (CD_3CN, 162 MHz, 295 K): δ 72.2 (s, **[85]**NSI, 20 %), 75.7 (s, **[71]**NSI, 73 %), 76.4 (s, **[54a]**NSI, 4 %).

7.64 Reactions of [15b]$^+$ with Allylic Alcohol, Styrene, and Ethynyltrimethylsilane

In the glovebox, a Youngs tap NMR tube was charged with a d^2-dichloromethane solution of [Ru(η^5-C_5H_5)(PPh_3)$_2$(=C=CFPh)]BF_4 (10 mg, 11.1 µmol). The respective reagent (CH_2=$CHCH_2OH$ (0.6 mg, 0.8 µL, 11.1 µmol), CH_2CHPh (1.2 mg, 1.3 µL, 11.1 µmol), or HCCTMS (1.1 mg, 1.5 µL, 11.1 µmol) was added to the Youngs NMR tube under nitrogen and heated at 50 °C for three days. In all reactions, **[15b]**BF_4 only undergoes phosphine activation to afford **[2-19]**BF_4.

7.65 General Procedure for Reacting Fluorovinylidenes with Gaseous Reactants

Oxygen and Carbon Monoxide

In the glovebox a Youngs tap NMR tube (with or without an FEP liner) was charged with a d^2-dichloromethane solution of the fluorovinylidene complex (10 mg). The sample was degassed by three freeze-pump-thaw cycles and the new atmosphere introduced. The reactions were monitored by NMR spectroscopy.

Reaction of [Ru(η^5-C_5Me_5)(dppe)(=C=CHF)]NSI with O_2

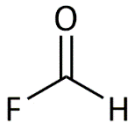

^{19}F NMR (CD_2Cl_2, 376.2 MHz, 295 K): δ 46.2 (d, $^2J_{HF}$ = 48 Hz).[279]

Aldehyde proton could not be observed in the ^{1}H NMR

Reaction of [Ru(η^5-C_5H_5)(PPh_3)$_2$(=C=CFPh)]BF_4 with O_2

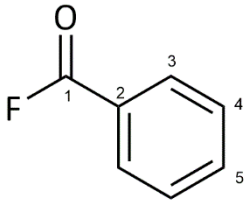

^{19}F NMR (CD_2Cl_2, 376.2 MHz, 295 K): δ 17.4 (s).[367]

Aromatic protons could not be distinguished from the other aromatic resonances in the ^{1}H NMR spectrum.

Hydrogen Atmosphere

In the glovebox, [Ru(η^5-C_5Me_5)(dppe)(=C=CHF)]NSI or [Ru(η^5-C_5H_5)(dppe)(=C=C(F)Ph)]NSI (10 mg) was added to a Youngs tap NMR tube. The NMR tube was placed under vacuum and the hydrogen atmosphere introduced. The reaction was heated for 11 days at 50 °C after which the hydrogen atmosphere was replaced with dinitrogen and the solid dissolved in d^2-dichloromethane and analysed without further purification.

Both reactions did not proceed to afford the expected hydrogenated complexes or organic products.

7.66 Liberation of *E*-1,2-difluorostyrene from [Ru(η^5-C$_5$H$_5$)(dppe)(-CF=CFPh)] or [Ru(η^5-C$_5$H$_5$)(dppe)(=CFCFHPh)]Cl/BF$_4$

From [Ru(η^5-C$_5$H$_5$)(dppe)(-CF=CFPh)]

In the glovebox, a Youngs tap NMR tube was charged with a THF solution of [Ru(η^5-C$_5$H$_5$)(dppe)(-CF=CFPh)] (5 mg, 7.1 µmol). Anhydrous 2M hydrochloric acid in diethyl ether (772 µg, 11 µL, 21.3 µmol) was added and the sample analysed by ^{19}F and ^{31}P{^{1}H} NMR spectroscopy and MS. Protonation affords *E*-1,2-difluorostyrene and [Ru(η^5-C$_5$H$_5$)(dppe)Cl].

Alternatively, *E*-1,2-difluorostyrene can be formed by the dissolution of [Ru(η^5-C$_5$H$_5$)(dppe)(-CFCFHPh)]Cl, or [Ru(η^5-C$_5$H$_5$)(dppe)(-CFCFHPh)]BF$_4$ with NBu$_4$Cl, in THF.

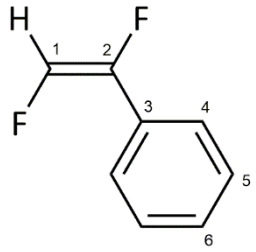

^{1}H NMR (THF-d^8, 500 MHz, 298 K): δ 7.61 (dd, $^2J_{HF}$ = 75 Hz, $^3J_{HF}$ = 6 Hz, H$_1$).

Aromatic resonances hidden under overlapping signals.

^{19}F NMR (THF-d^8, 471MHz, 295 K): δ -170.5 (dd, $^3J_{FF}$ = 125 Hz, $^3J_{HF}$ = 6 Hz, F$_2$), -177.6 (dd, $^3J_{FF}$ = 125 Hz, $^2J_{HF}$ = 75 Hz, F$_1$).

GC-ESI-MS (m/z): Expected for C$_8$H$_6$F$_2$ = 140.0438 m/z [M$^{+\cdot}$]; Observed: 140.0441 m/z [M$^+$] (Error = 0.3mDa).

7.67 Liberation of *E*-1-Chloro-2-fluorostyrene from [Ru(η^5-C$_5$H$_5$)(dppe)(=C=CFPh)]BF$_4$ or [Ru(η^5-C$_5$H$_5$)(PPh$_3$)$_2$(=C=CFPh)]BF$_4$

From [Ru(η^5-C$_5$H$_5$)(dppe)(=C=CFPh)]BF$_4$

In the glovebox, a Youngs tap NMR tube was charged with a THF solution of [Ru(η^5-C$_5$H$_5$)(dppe)(=C=CFPh)]BF$_4$ (5 mg, 6.5 µmol). The solution was treated with anhydrous 2M HCl in diethyl ether (709 µg, 9.8 µL, 19.5 µmol) and the reaction monitored by ^{19}F and

$^{31}P\{^{1}H\}$ NMR spectroscopy and MS. Protonation affords *E*-1-chloro-2-fluorostyrene and [Ru(η^5-C_5H_5)(dppe)Cl].

Alternatively, the reaction can be carried out in CD_2Cl_2 with the addition of 100 µL of THF.

From [Ru(η^5-C_5H_5)(PPh_3)$_2$(=C=CFPh)]BF_4

In the glovebox, a Youngs tap NMR tube was charged with a THF solution of [Ru(η^5-C_5H_5)(dppe)(=C=CFPh)]BF_4 (5 mg, 5.1 µmol). The solution was treated with anhydrous 2M HCl in diethyl ether (554 µg, 7.65 µL, 15.3 µmol) and the reaction monitored by ^{19}F and $^{31}P\{^{1}H\}$ NMR spectroscopy and MS. Protonation affords *E*-1-chloro-2-fluorostyrene and [Ru(η^5-C_5H_5)(PPh_3)$_2$Cl].

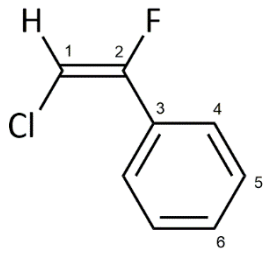

Selected ^{1}H NMR (THF-d^8, 400 MHz, 295 K): δ 6.45 (d, $^{3}J_{HF}$ = 14 Hz, H_1).[294]

Aromatic resonances hidden under overlapping signals.

^{19}F NMR (THF-d^8, 376 MHz, 295 K): δ -111.2 (d, $^{3}J_{HF}$ = 14 Hz, F_2)

GC-ESI-MS (m/z): Expected for C_8H_6FCl = 156.0142 m/z [$M^{+\cdot}$]; Observed: 156.0410 m/z [M^+] (Error = -0.4 mDa).

7.68 Reactions of [*trans*-Ru(dppe)$_2$Cl(-C≡C-R)] with NFSI and FTMP BF_4

In the glovebox, [*trans*-Ru(dppe)$_2$Cl(-C≡C-R)] (5 mg) in dichloromethane (0.3 mL) was added to an acetonitrile solution of the respective fluorinating agent (1.5 equivalents in 0.3 mL) in a Youngs tap NMR tube. The reactions were monitored by NMR spectroscopy and mass spectrometry.

There was no evidence for fluorination being observed with either fluorinating agents, with the exception of **[57a]** (R = H), and **[57b]** (R = F), which underwent fluorination with NFSI but not FTMP BF_4. In addition, the reactions were also carried out in just dichloromethane with the same reactivity being observed.

7.69 Monitoring the Reactions of [*trans*-Ru(dppe)$_2$Cl(-C≡C-R)] with NFSI, FTMP BF_4, and Selectfluor by UV-Vis spectroscopy

Solutions of [*trans*-Ru(dppe)$_2$Cl(-C≡C-R)] were made up in volumetric flasks with a 1:1 dichloromethane: acetonitrile solvent mix in the glovebox. Solutions of the fluorinating agents were also prepared in volumetric flasks with a 1:1 dichloromethane: acetonitrile solvent mix. The solutions (0.5 mM) were mixed immediately before UV-Vis spectroscopic data was recorded (*ca*. 15 seconds between start of mixing and recording data).

7.70 UV-Vis-NMR Combined Experiments Monitoring the Reactions of [57a], [57b], and [57e] with Selectfluor

In the glovebox, 0.5 mM solutions of **[57a]**, **[57b]**, **[57e]**, and Selectfluor in a 1:1 dichloromethane: acetonitrile solvent mix were prepared in volumetric flasks. Prior to the UV-Vis experiments, initial $^{31}P\{^1H\}$ and ^{19}F NMR spectra in the 1:1 dichloromethane: acetonitrile solvent mix were recorded of **[57]** at 0.25 mM (0.5 mL) in Youngs tap NMR tubes containing a capillary insert of triphenylphosphine in CD_2Cl_2. Separately, the 0.5 mM solutions of **[57]** were mixed with the 0.5 mM solutions of Selectfluor under nitrogen and the reactions monitored for one hour by UV-Vis spectroscopy in an air-tight quartz UV cuvette. After one hour the reaction mixtures were analysed by NMR spectroscopy in Youngs tap NMR tubes with the same volume (0.5 mL) as the initial NMR samples, and the same triphenylphosphine insert.

7.71 Crystallographic Data

Diffraction data was collected using an Oxford Diffraction SuperNova diffractometer equipped with a single Molybdenum source using Mo-Kα radiation (0.71073 Å), or single Copper source using Cu-Kα radiation (1.54184 Å), and an EOS CCD camera. The crystals were cooled with an Oxford Instruments CryoJet typically to 110K. Diffractometer control, data collection, initial unit cell determination, frame integration and unit-cell refinement was carried out with "CrysalisPro".[368] Face-indexed absorption corrections were applied either using spherical harmonics, implemented in SCALE3 ABSPACK scaling algorithm or analytical numeric absorption correction using a multifaceted crystal model based on expressions derived by Clark and Reid,[369] implemented within "CrysalisPro".[368]Olex2[370] was used for overall structure solution, refinement and preparation of computer graphics and publication data. Using Olex2, the structure was solved either with the Superflip[295] structure solution program using Charge Flipping or the ShelXS[371] structure solution program using Direct Methods. Refinement was carried out with the ShelXL refinement package using Least Squares minimisation.[371] All non-hydrogen atoms were refined anisotropically. Unless stated otherwise, hydrogen atoms were placed using a "riding model" and included in the refinement at calculated positions

7.72 Crystallographic Data for $[(Ru(\eta^5\text{-}C_5H_5)(PPh_3)_2)_2(\mu\text{-}C_4H_2F)]PF_6$, [27]$PF_6$

Identification code	jml1459
Empirical formula	$C_{89}H_{78}Cl_6F_7P_5Ru_2$
Formula weight	1850.20
Temperature/K	110.05(10)
Crystal system	triclinic
Space group	P-1
a/Å	10.5395(4)
b/Å	13.5656(4)
c/Å	14.0972(4)
α/°	88.796(2)
β/°	81.028(3)
γ/°	88.206(2)
Volume/Å^3	1989.63(11)
Z	1
ρ_{calc}g/cm^3	1.544
μ/mm^{-1}	6.402
F(000)	940.0
Crystal size/mm^3	0.176 × 0.144 × 0.055
Radiation	CuKα (λ = 1.54184)
2Θ range for data collection/°	8.496 to 134.154
Index ranges	-12 ≤ h ≤ 12, -11 ≤ k ≤ 16, -16 ≤ l ≤ 16
Reflections collected	21539
Independent reflections	7115 [R_{int} = 0.0319, R_{sigma} = 0.0367]
Data/restraints/parameters	7115/76/643
Goodness-of-fit on F^2	1.031
Final R indexes [I>=2σ (I)]	R_1 = 0.0359, wR_2 = 0.0929
Final R indexes [all data]	R_1 = 0.0418, wR_2 = 0.0964
Largest diff. peak/hole / e Å^{-3}	0.75/-1.05

7.73 Crystallographic Data for $[Ru(\eta^5\text{-}C_5Me_5)(PPh_3)_2(=C=CFH)]PF_6$, [30a]$PF_6$

Identification code	jml1437
Empirical formula	$C_{50}H_{48}Cl_6F_7P_3Ru$
Formula weight	1188.56
Temperature/K	110.05(10)
Crystal system	monoclinic
Space group	$P2_1/c$
a/Å	15.0997(2)
b/Å	14.5569(2)
c/Å	23.0412(4)
α/°	90
β/°	93.7823(14)
γ/°	90
Volume/Å^3	5053.56(14)
Z	4
ρ_{calc}mg/mm^3	1.562
m/mm^{-1}	0.784
F(000)	2408.0
Crystal size/mm^3	0.1516 × 0.119 × 0.0446
Radiation	MoKα (λ = 0.71073)
2Θ range for data collection	5.866 to 59.97°
Index ranges	-10 ≤ h ≤ 19, -10 ≤ k ≤ 20, -32 ≤ l ≤ 31
Reflections collected	25425
Independent reflections	13007 [R_{int} = 0.0389, R_{sigma} = 0.0521]
Data/restraints/parameters	13007/0/678
Goodness-of-fit on F^2	1.049
Final R indexes [I>=2σ (I)]	R_1 = 0.0379, wR_2 = 0.0880
Final R indexes [all data]	R_1 = 0.0538, wR_2 = 0.0974
Largest diff. peak/hole / e Å^{-3}	0.55/-0.75

7.74 Crystallographic Data for $[Ru(\eta^5\text{-}C_5Me_5)(dppe)(=C=CFH)]PF_6$, $[54a]PF_6$ - Green

Identification code	jml1518
Empirical formula	$C_{38}H_{40}F_7P_3Ru$
Formula weight	823.68
Temperature/K	110.05(10)
Crystal system	orthorhombic
Space group	$P2_12_12_1$
a/Å	12.40197(14)
b/Å	16.5318(2)
c/Å	17.6108(2)
α/°	90
β/°	90
γ/°	90
Volume/Å^3	3610.70(8)
Z	4
ρ_{calc}g/cm^3	1.515
μ/mm^{-1}	0.631
F(000)	1680.0
Crystal size/mm^3	0.2204 × 0.1987 × 0.0199
Radiation	MoKα (λ = 0.71073)
2Θ range for data collection/°	6.57 to 60.066
Index ranges	-17 ≤ h ≤ 17, -23 ≤ k ≤ 17, -24 ≤ l ≤ 24
Reflections collected	33109
Independent reflections	10414 [R_{int} = 0.0387, R_{sigma} = 0.0398]
Data/restraints/parameters	10414/0/458
Goodness-of-fit on F^2	1.060
Final R indexes [I>=2σ (I)]	R_1 = 0.0293, wR_2 = 0.0611
Final R indexes [all data]	R_1 = 0.0349, wR_2 = 0.0640
Largest diff. peak/hole / e Å^{-3}	0.43/-0.57
Flack parameter	0.44(2)

7.75 Crystallographic Data for $[Ru(\eta^5\text{-}C_5Me_5)(dppe)(=C=CFH)]PF_6$, [54a]$PF_6$ - Orange

Identification code	jml1517
Empirical formula	$C_{39}H_{42}Cl_2F_7P_3Ru$
Formula weight	908.60
Temperature/K	110.05(10)
Crystal system	monoclinic
Space group	C2
a/Å	19.5644(4)
b/Å	14.7377(3)
c/Å	14.0964(3)
α/°	90
β/°	99.1968(19)
γ/°	90
Volume/Å^3	4012.22(14)
Z	4
ρ_{calc}g/cm^3	1.504
μ/mm^{-1}	0.704
F(000)	1848.0
Crystal size/mm^3	0.498 × 0.368 × 0.273
Radiation	MoKα (λ = 0.71073)
2Θ range for data collection/°	6.906 to 58.256
Index ranges	-26 ≤ h ≤ 26, -20 ≤ k ≤ 20, -19 ≤ l ≤ 19
Reflections collected	28329
Independent reflections	10779 [R_{int} = 0.0336, R_{sigma} = 0.0402]
Data/restraints/parameters	10779/21/490
Goodness-of-fit on F^2	1.025
Final R indexes [I>=2σ (I)]	R_1 = 0.0292, wR_2 = 0.0671
Final R indexes [all data]	R_1 = 0.0322, wR_2 = 0.0692
Largest diff. peak/hole / e Å^{-3}	0.61/-0.52
Flack parameter	-0.041(11)

7.76 Crystallographic Data for $[Ru(\eta^5\text{-}C_5Me_5)(dppe)(=C=CF_2)]PF_6$, [54b]$PF_6$

Identification code	jml1516
Empirical formula	$C_{38}H_{39}F_8P_3Ru$
Formula weight	841.67
Temperature/K	110.05(10)
Crystal system	orthorhombic
Space group	$P2_12_12_1$
a/Å	12.42357(16)
b/Å	17.69642(19)
c/Å	16.5341(2)
α/°	90.00
β/°	90.00
γ/°	90.00
Volume/Å^3	3635.07(8)
Z	4
ρ_{calc}g/cm^3	1.538
μ/mm^{-1}	0.632
F(000)	1712.0
Crystal size/mm^3	0.2393 × 0.1985 × 0.0766
Radiation	MoKα (λ = 0.71070)
2Θ range for data collection/°	6.74 to 64.08
Index ranges	-17 ≤ h ≤ 18, -25 ≤ k ≤ 25, -23 ≤ l ≤ 24
Reflections collected	30563
Independent reflections	11241 [R_{int} = 0.0394, R_{sigma} = 0.0430]
Data/restraints/parameters	11241/0/456
Goodness-of-fit on F^2	1.066
Final R indexes [I>=2σ (I)]	R_1 = 0.0331, wR_2 = 0.0739
Final R indexes [all data]	R_1 = 0.0387, wR_2 = 0.0777
Largest diff. peak/hole / e Å^{-3}	0.41/-0.56
Flack parameter	-0.020(18)

7.77 Crystallographic Data for [Ru(η^5-C_5Me_5)(dppe)(-C≡CF)], [55b]

Identification code	jml1514
Empirical formula	$C_{38}H_{39}FP_2Ru$
Formula weight	677.70
Temperature/K	110.05(10)
Crystal system	monoclinic
Space group	$P2_1/n$
a/Å	12.40871(19)
b/Å	18.8181(2)
c/Å	13.9609(2)
α/°	90
β/°	102.7722(16)
γ/°	90
Volume/Å^3	3179.33(9)
Z	4
ρ_{calc}g/cm^3	1.416
μ/mm^{-1}	5.183
F(000)	1400.0
Crystal size/mm^3	0.2297 × 0.1025 × 0.0362
Radiation	CuKα (λ = 1.54184)
2Θ range for data collection/°	8.016 to 142.064
Index ranges	-15 ≤ h ≤ 15, -15 ≤ k ≤ 22, -17 ≤ l ≤ 16
Reflections collected	17492
Independent reflections	6002 [R_{int} = 0.0384, R_{sigma} = 0.0394]
Data/restraints/parameters	6002/0/384
Goodness-of-fit on F^2	1.038
Final R indexes [I>=2σ (I)]	R_1 = 0.0360, wR_2 = 0.0951
Final R indexes [all data]	R_1 = 0.0418, wR_2 = 0.1007
Largest diff. peak/hole / e Å^{-3}	1.29/-1.37

7.78 Crystallographic Data for [*trans*-Ru(dppe)$_2$Cl(-C≡C-F)], [57b]

Identification code	jml1807
Empirical formula	$C_{54}H_{48}FP_4ClRu$
Formula weight	976.32
Temperature/K	110.05(10)
Crystal system	monoclinic
Space group	$P2_1/n$
a/Å	10.98360(19)
b/Å	16.0671(2)
c/Å	13.1362(2)
α/°	90
β/°	104.7844(17)
γ/°	90
Volume/Å^3	2241.46(6)
Z	2
ρ_{calc}g/cm^3	1.447
μ/mm^{-1}	5.054
F(000)	1004.0
Crystal size/mm^3	0.309 × 0.203 × 0.093
Radiation	CuKα (λ = 1.54184)
2Θ range for data collection/°	8.874 to 134.158
Index ranges	-12 ≤ h ≤ 13, -19 ≤ k ≤ 19, -15 ≤ l ≤ 10
Reflections collected	8263
Independent reflections	4003 [R_{int} = 0.0214, R_{sigma} = 0.0300]
Data/restraints/parameters	4003/0/296
Goodness-of-fit on F^2	1.032
Final R indexes [I>=2σ (I)]	R_1 = 0.0264, wR_2 = 0.0633
Final R indexes [all data]	R_1 = 0.0317, wR_2 = 0.0668
Largest diff. peak/hole / e Å^{-3}	0.40/-0.38

7.79 Crystallographic Data for [*trans*-Ru(dppe)$_2$Cl(-C≡C-C$_6$H$_4$-CF$_3$)], [57g]

Identification code	jml1804
Empirical formula	$C_{62}H_{54}Cl_3F_3P_4Ru$
Formula weight	1187.35
Temperature/K	110.05(10)
Crystal system	triclinic
Space group	P-1
a/Å	9.23749(19)
b/Å	12.8979(3)
c/Å	24.0322(6)
α/°	91.337(2)
β/°	94.0064(19)
γ/°	99.2915(19)
Volume/Å^3	2817.08(12)
Z	2
ρ_{calc}g/cm^3	1.400
μ/mm^{-1}	0.583
F(000)	1216.0
Crystal size/mm^3	0.223 × 0.19 × 0.145
Radiation	MoKα (λ = 0.71073)
2Θ range for data collection/°	6.57 to 60.068
Index ranges	-13 ≤ h ≤ 13, -17 ≤ k ≤ 18, -33 ≤ l ≤ 33
Reflections collected	26490
Independent reflections	16372 [R_{int} = 0.0239, R_{sigma} = 0.0440]
Data/restraints/parameters	16372/80/696
Goodness-of-fit on F^2	1.032
Final R indexes [I>=2σ (I)]	R_1 = 0.0358, wR_2 = 0.0797
Final R indexes [all data]	R_1 = 0.0454, wR_2 = 0.0855
Largest diff. peak/hole / e Å^{-3}	1.05/-0.66

7.80 Crystallographic Data for [*trans*-Ru(dppe)$_2$Cl(=C=C(F)H)]PF$_6$, [58a]PF$_6$

Identification code	jml1706
Empirical formula	$C_{54}H_{49}ClF_7P_5Ru$
Formula weight	1122.30
Temperature/K	110.05(10)
Crystal system	orthorhombic
Space group	Fdd2
a/Å	49.0735(8)
b/Å	43.2585(9)
c/Å	9.0974(2)
α/°	90
β/°	90
γ/°	90
Volume/Å^3	19312.4(7)
Z	16
ρ_{calc}g/cm^3	1.544
μ/mm^{-1}	0.611
F(000)	9152.0
Crystal size/mm^3	0.349 × 0.15 × 0.128
Radiation	MoKα (λ = 0.71073)
2Θ range for data collection/°	6.642 to 52.744
Index ranges	-51 ≤ h ≤ 61, -26 ≤ k ≤ 54, -10 ≤ l ≤ 11
Reflections collected	13032
Independent reflections	7719 [R_{int} = 0.0330, R_{sigma} = 0.0494]
Data/restraints/parameters	7719/1/638
Goodness-of-fit on F^2	1.073
Final R indexes [I>=2σ (I)]	R_1 = 0.0312, wR_2 = 0.0708
Final R indexes [all data]	R_1 = 0.0338, wR_2 = 0.0718
Largest diff. peak/hole / e Å^{-3}	0.48/-0.46
Flack parameter	-0.04(3)

7.81 Crystallographic Data for [*trans*-Ru(dppe)$_2$Cl(=C=CF$_2$)]PF$_6$, [58b]PF$_6$

Identification code	jml1809
Empirical formula	$C_{54}H_{48}ClF_8P_5Ru$
Formula weight	1140.29
Temperature/K	110.05(10)
Crystal system	monoclinic
Space group	$P2_1/c$
a/Å	11.95735(8)
b/Å	25.53178(19)
c/Å	16.47743(12)
α/°	90
β/°	102.3722(7)
γ/°	90
Volume/Å^3	4913.61(6)
Z	4
ρ_{calc}g/cm^3	1.541
μ/mm^{-1}	5.211
F(000)	2320.0
Crystal size/mm^3	0.191 × 0.164 × 0.07
Radiation	CuKα (λ = 1.54184)
2Θ range for data collection/°	6.924 to 134.154
Index ranges	-14 ≤ h ≤ 11, -15 ≤ k ≤ 30, -18 ≤ l ≤ 19
Reflections collected	26385
Independent reflections	8778 [R_{int} = 0.0216, R_{sigma} = 0.0224]
Data/restraints/parameters	8778/0/622
Goodness-of-fit on F^2	1.019
Final R indexes [I>=2σ (I)]	R_1 = 0.0236, wR_2 = 0.0569
Final R indexes [all data]	R_1 = 0.0274, wR_2 = 0.0593
Largest diff. peak/hole / e Å^{-3}	0.49/-0.44

7.82 Crystallographic Data for [*trans*-Ru(dppe)$_2$Cl(=C=C(F)C$_6$H$_4$-4-OMe)]PF$_6$, [58c]PF$_6$

Identification code	jml1613
Empirical formula	$C_{62}H_{57}Cl_3F_7OP_5Ru$
Formula weight	1313.34
Temperature/K	102(1)
Crystal system	monoclinic
Space group	$P2_1$
a/Å	11.18875(11)
b/Å	21.8363(2)
c/Å	11.88734(12)
α/°	90
β/°	100.0816(10)
γ/°	90
Volume/Å^3	2859.48(5)
Z	2
ρ_{calc}g/cm^3	1.525
μ/mm^{-1}	0.620
F(000)	1340.0
Crystal size/mm^3	0.256 × 0.16 × 0.057
Radiation	MoKα (λ = 0.71073)
2Θ range for data collection/°	6.65 to 60.068
Index ranges	-15 ≤ h ≤ 15, -30 ≤ k ≤ 30, -16 ≤ l ≤ 16
Reflections collected	40239
Independent reflections	16672 [R_{int} = 0.0299, R_{sigma} = 0.0406]
Data/restraints/parameters	16672/1/713
Goodness-of-fit on F^2	1.029
Final R indexes [I>=2σ (I)]	R_1 = 0.0263, wR_2 = 0.0536
Final R indexes [all data]	R_1 = 0.0289, wR_2 = 0.0551
Largest diff. peak/hole / e Å^{-3}	0.32/-0.34
Flack parameter	-0.028(8)

7.83 Crystallographic Data for [*trans*-Ru(dppe)$_2$Cl(=C=C(F)C$_6$H$_5$)]PF$_6$, [58d]PF$_6$

Identification code	jml1802
Empirical formula	$C_{124}H_{114}Cl_{10}F_{14}P_{10}Ru_2$
Formula weight	2736.48
Temperature/K	110.00(14)
Crystal system	triclinic
Space group	P-1
a/Å	12.9300(3)
b/Å	21.7675(5)
c/Å	21.7719(5)
α/°	87.726(2)
β/°	74.961(2)
γ/°	86.030(2)
Volume/Å^3	5902.2(2)
Z	2
ρ_{calc}g/cm^3	1.540
μ/mm^{-1}	0.691
F(000)	2784.0
Crystal size/mm^3	0.29 × 0.159 × 0.059
Radiation	MoKα (λ = 0.71073)
2Θ range for data collection/°	6.468 to 64.306
Index ranges	-19 ≤ h ≤ 14, -32 ≤ k ≤ 32, -32 ≤ l ≤ 30
Reflections collected	73272
Independent reflections	37318 [R_{int} = 0.0352, R_{sigma} = 0.0544]
Data/restraints/parameters	37318/108/1563
Goodness-of-fit on F^2	1.047
Final R indexes [I>=2σ (I)]	R_1 = 0.0483, wR_2 = 0.1053
Final R indexes [all data]	R_1 = 0.0682, wR_2 = 0.1178
Largest diff. peak/hole / e Å^{-3}	1.77/-1.53

7.84 Crystallographic Data for [*trans*-Ru(dppe)$_2$Cl(=C=C(F)C$_6$H$_4$-4-COOMe)]PF$_6$, [58e]PF$_6$

Identification code	jml1813
Empirical formula	$C_{62}H_{55}ClF_7O_2P_5Ru$
Formula weight	1256.43
Temperature/K	110.05(10)
Crystal system	triclinic
Space group	P-1
a/Å	12.1653(3)
b/Å	13.1304(3)
c/Å	17.7315(5)
α/°	78.408(2)
β/°	82.214(2)
γ/°	78.034(2)
Volume/Å^3	2701.26(12)
Z	2
ρ_{calc}g/cm^3	1.545
μ/mm^{-1}	0.558
F(000)	1284.0
Crystal size/mm^3	0.304 × 0.21 × 0.166
Radiation	MoKα (λ = 0.71073)
2Θ range for data collection/°	6.448 to 60.068
Index ranges	-16 ≤ h ≤ 17, -16 ≤ k ≤ 18, -22 ≤ l ≤ 24
Reflections collected	29124
Independent reflections	15776 [R_{int} = 0.0246, R_{sigma} = 0.0406]
Data/restraints/parameters	15776/15/723
Goodness-of-fit on F^2	1.038
Final R indexes [I>=2σ (I)]	R_1 = 0.0311, wR_2 = 0.0739
Final R indexes [all data]	R_1 = 0.0381, wR_2 = 0.0782
Largest diff. peak/hole / e Å^{-3}	0.56/-0.45

7.85 Crystallographic Data for [*trans*-Ru(dppe)$_2$Cl(=C=C(F)C$_6$H$_4$-4-COMe)]PF$_6$, [58f]PF$_6$

Identification code	jml1722_twin1_hklf4
Empirical formula	$C_{64}H_{59}Cl_5F_7OP_5Ru$
Formula weight	1410.28
Temperature/K	110.05(10)
Crystal system	monoclinic
Space group	$P2_1$
a/Å	12.1456(5)
b/Å	21.3909(5)
c/Å	12.3604(6)
α/°	90
β/°	106.438(5)
γ/°	90
Volume/Å^3	3080.0(2)
Z	2
ρ_{calc}g/cm^3	1.521
μ/mm^{-1}	5.823
F(000)	1436.0
Crystal size/mm^3	0.224 × 0.105 × 0.066
Radiation	CuKα (λ = 1.54184)
2Θ range for data collection/°	7.456 to 134.248
Index ranges	-14 ≤ h ≤ 14, -25 ≤ k ≤ 25, -14 ≤ l ≤ 14
Reflections collected	13341
Independent reflections	13341 [R_{int} = ?, R_{sigma} = 0.0254]
Data/restraints/parameters	13341/1/750
Goodness-of-fit on F^2	1.039
Final R indexes [I>=2σ (I)]	R_1 = 0.0413, wR_2 = 0.1041
Final R indexes [all data]	R_1 = 0.0449, wR_2 = 0.1068
Largest diff. peak/hole / e Å^{-3}	0.69/-0.75
Flack parameter	0.134(9)

Refinement Special details

The crystal was non-merohedrally twinned with two components in a refined ratio of 0.5732:0.4268(12). There is evidence of racemic twinning from the Hooft and Flack parameters but it is not possible to model both non-merohedral and pseudomerohedral twinning with the current software.

7.86 Crystallographic Data for [*trans*-Ru(dppe)$_2$Cl(=C=C(F)C$_6$H$_4$-4-CF$_3$)]PF$_6$, [58g]PF$_6$

Identification code	jml1814
Empirical formula	$C_{61}H_{52}ClF_{10}P_5Ru$
Formula weight	1266.39
Temperature/K	110.05(10)
Crystal system	monoclinic
Space group	C2/c
a/Å	39.2856(6)
b/Å	13.22899(19)
c/Å	24.6558(4)
α/°	90
β/°	102.5279(15)
γ/°	90
Volume/Å^3	12508.7(3)
Z	8
ρ_{calc}g/cm^3	1.345
μ/mm^{-1}	0.487
F(000)	5152.0
Crystal size/mm^3	0.381 × 0.218 × 0.073
Radiation	MoKα (λ = 0.71073)
2Θ range for data collection/°	6.388 to 60.068
Index ranges	-35 ≤ h ≤ 55, -15 ≤ k ≤ 18, -34 ≤ l ≤ 34
Reflections collected	34097
Independent reflections	18274 [R_{int} = 0.0231, R_{sigma} = 0.0378]
Data/restraints/parameters	18274/0/703
Goodness-of-fit on F^2	1.108
Final R indexes [I>=2σ (I)]	R_1 = 0.0492, wR_2 = 0.1105
Final R indexes [all data]	R_1 = 0.0590, wR_2 = 0.1154
Largest diff. peak/hole / e Å^{-3}	0.66/-0.66

7.87 Crystallographic Data for [*trans*-Ru(dppe)$_2$Cl(=C=C(F)C$_6$H$_4$-4-NO$_2$)]PF$_6$, [57h]PF$_6$

Identification code	jml1718
Empirical formula	$C_{62}H_{56}Cl_5F_7NO_2P_5Ru$
Formula weight	1413.24
Temperature/K	110.00(10)
Crystal system	monoclinic
Space group	$P2_1$
a/Å	12.0345(2)
b/Å	21.1291(3)
c/Å	12.3878(2)
α/°	90
β/°	106.541(2)
γ/°	90
Volume/Å^3	3019.59(9)
Z	2
ρ_{calc}g/cm^3	1.554
μ/mm^{-1}	0.680
F(000)	1436.0
Crystal size/mm^3	0.225 × 0.138 × 0.108
Radiation	MoKα (λ = 0.71073)
2Θ range for data collection/°	6.726 to 52.744
Index ranges	-14 ≤ h ≤ 15, -26 ≤ k ≤ 26, -15 ≤ l ≤ 15
Reflections collected	23306
Independent reflections	11042 [R_{int} = 0.0314, R_{sigma} = 0.0469]
Data/restraints/parameters	11042/1/749
Goodness-of-fit on F^2	1.086
Final R indexes [I>=2σ (I)]	R_1 = 0.0384, wR_2 = 0.0908
Final R indexes [all data]	R_1 = 0.0411, wR_2 = 0.0927
Largest diff. peak/hole / e Å^{-3}	1.42/-0.51
Flack parameter	0.18(3)

7.88 Crystallographic Data for [*trans*-Ru(dppe)$_2$Cl(=C=C(F)C$_3$H$_5$)]PF$_6$, [58j]PF$_6$

Identification code	jml1806
Empirical formula	$C_{60}H_{59}Cl_7F_7P_5Ru$
Formula weight	1417.14
Temperature/K	110.05(10)
Crystal system	triclinic
Space group	P-1
a/Å	11.2673(5)
b/Å	11.7169(5)
c/Å	24.3794(11)
α/°	101.929(4)
β/°	96.410(4)
γ/°	100.497(4)
Volume/Å^3	3058.8(2)
Z	2
ρ_{calc}g/cm^3	1.539
μ/mm^{-1}	6.637
F(000)	1440.0
Crystal size/mm^3	0.128 × 0.114 × 0.085
Radiation	CuKα (λ = 1.54184)
2Θ range for data collection/°	7.504 to 134.148
Index ranges	-11 ≤ h ≤ 13, -13 ≤ k ≤ 13, -29 ≤ l ≤ 20
Reflections collected	18666
Independent reflections	10855 [R_{int} = 0.0312, R_{sigma} = 0.0455]
Data/restraints/parameters	10855/55/880
Goodness-of-fit on F^2	1.062
Final R indexes [I>=2σ (I)]	R_1 = 0.0641, wR_2 = 0.1657
Final R indexes [all data]	R_1 = 0.0756, wR_2 = 0.1753
Largest diff. peak/hole / e Å^{-3}	2.11/-1.22

Refinement Special Details

The crystal exhibited considerable disorder.

The complex itself was disordered by inversion of the vinylidene and chlorine about the ruthenium. The occupancy of the two forms refined to be 0.836:0.164(3). Corresponding C-C and C-F bond lengths in the vinylidenes were restrained to be equal, for example C2-C3 and C2A-C3A, F1-C2 & F1a-C2a. A dichloromethane of crystallisation adjacent to the chloride was also disordered and modelled in 3 sites with occupancies of 0.418:0.418:0.164. The ADP

of several atoms were constrained to be equal namely, C1A, C2A, Cl1 & Cl1A; C4A, C58, C5A & C58B.

Another dichloromethane was modelled in two positions with occupancies of 0.569:0.431(7). In this dichloromethane the C-Cl bond lengths were restrained to be equal. The ADP of Cl4A C59A & Cl5A were restrained to be approximately isotropic.

The third dichloromethane was modelled in three positions with refined occupancies of 0.414(5):0.412(6):0.173(7). The C-Cl bond lengths were restrained to be equal as were the Cl-C-Cl distances.

7.89 Crystallographic Data for [*trans*-Ru(dppe)$_2$Cl(=C=CH$_2$)]BF$_4$, [59b]BF$_4$

Identification code	jml1816
Empirical formula	$C_{54}H_{50}BClF_4P_4Ru$
Formula weight	1046.15
Temperature/K	110.05(10)
Crystal system	monoclinic
Space group	P2/n
a/Å	8.8966(2)
b/Å	12.0525(2)
c/Å	22.0351(4)
α/°	90
β/°	101.285(2)
γ/°	90
Volume/Å^3	2317.06(8)
Z	2
ρ_{calc}g/cm^3	1.499
μ/mm^{-1}	5.022
F(000)	1072.0
Crystal size/mm^3	0.241 × 0.122 × 0.095
Radiation	CuKα (λ = 1.54184)
2Θ range for data collection/°	7.334 to 134.16
Index ranges	-10 ≤ h ≤ 9, -14 ≤ k ≤ 13, -21 ≤ l ≤ 26
Reflections collected	14751
Independent reflections	4145 [R_{int} = 0.0301, R_{sigma} = 0.0275]
Data/restraints/parameters	4145/0/321
Goodness-of-fit on F^2	1.115
Final R indexes [I>=2σ (I)]	R_1 = 0.0360, wR_2 = 0.0822
Final R indexes [all data]	R_1 = 0.0385, wR_2 = 0.0837
Largest diff. peak/hole / e Å^{-3}	1.26/-0.72

7.90 Crystallographic Data for [*trans*-Ru(dppe)$_2$Cl(=C=CH(C$_6$H$_5$)]PF$_6$, [59d]PF$_6$

Identification code	jml1822
Empirical formula	$C_{60}H_{54}ClF_6P_5Ru$
Formula weight	1180.40
Temperature/K	110.05(10)
Crystal system	triclinic
Space group	P-1
a/Å	13.3930(2)
b/Å	19.9675(3)
c/Å	20.7612(3)
α/°	74.3090(10)
β/°	88.3460(10)
γ/°	89.0510(10)
Volume/Å^3	5342.71(14)
Z	4
ρ_{calc}g/cm^3	1.467
μ/mm^{-1}	4.758
F(000)	2416.0
Crystal size/mm^3	0.219 × 0.117 × 0.04
Radiation	CuKα (λ = 1.54184)
2Θ range for data collection/°	6.602 to 142.378
Index ranges	-16 ≤ h ≤ 16, -24 ≤ k ≤ 24, -25 ≤ l ≤ 25
Reflections collected	98299
Independent reflections	20512 [R_{int} = 0.0340, R_{sigma} = 0.0276]
Data/restraints/parameters	20512/48/1305
Goodness-of-fit on F^2	1.045
Final R indexes [I>=2σ (I)]	R_1 = 0.0267, wR_2 = 0.0620
Final R indexes [all data]	R_1 = 0.0317, wR_2 = 0.0649
Largest diff. peak/hole / e Å^{-3}	0.54/-0.51

7.91 Crystallographic Data for [*trans*-Ru(dppe)$_2$Cl(=C=CH(C$_6$H$_4$-4-COMe)]OTf, [59f]OTf[296]

Identification code	jml1728
Empirical formula	$C_{65}H_{60}Cl_5F_3O_4P_4RuS$
Formula weight	1395.75
Temperature/K	110.05(10)
Crystal system	triclinic
Space group	P-1
a/Å	12.32464(18)
b/Å	22.8008(3)
c/Å	23.3344(4)
α/°	77.5819(12)
β/°	75.2580(13)
γ/°	85.0411(11)
Volume/Å^3	6189.55(16)
Z	4
ρ_{calc}g/cm^3	1.498
μ/mm^{-1}	0.663
F(000)	2855.0
Crystal size/mm^3	0.24 × 0.22 × 0.125
Radiation	MoKα (λ = 0.71073)
2Θ range for data collection/°	6.568 to 60.066
Index ranges	-17 ≤ h ≤ 17, -31 ≤ k ≤ 32, -32 ≤ l ≤ 32
Reflections collected	145427
Independent reflections	36151 [R_{int} = 0.0323, R_{sigma} = 0.0273]
Data/restraints/parameters	36151/25/1549
Goodness-of-fit on F^2	1.109
Final R indexes [I>=2σ (I)]	R_1 = 0.0438, wR_2 = 0.1057
Final R indexes [all data]	R_1 = 0.0529, wR_2 = 0.1122
Largest diff. peak/hole / e Å^{-3}	1.38/-2.65

Refinement Special Details

The asymmetric unit contained two complexes, two anions and four dichloromethanes.

One of the complexes was disordered with the acetyl modelled in two positions with refined occupancies of 0.67:0.33(2). The acetyl C(O)-Me bond lengths (C71-C72 & C71A & C72A) were restrained to be equal as were the C-C(O)Me bond lengths (C68-C71 & C68-C71A). The

ADP of the major O and minor methyl carbon (O2 & C72A) were constrained to be equal as were the two acetyl, C(O)Me, carbons (C71 & C71A).

Three of the dichloromethanes were disordered.

For the first, one chlorine was modelled in two positions with refined occupancies of 0.780:0.220(4) with the ADP of these chlorines constrained to be equal.

For the second, the entire molecule was modelled in two positions with refined occupancies of 0.824:0.176(2). The C-Cl bond lengths were restrained to be 1.745 angstroms, the ADP of the each for the pairs C129 & C130, C7 & C7a, C8 & C8a were constrained to be equal and the ADP of the carbons restrained to be approximately isotropic.

For the third, the entire molecule was modelled in three positions with refined occupancies of 0.723(5):0.200(4):0.076(2). The C-Cl bond lengths were restrained to be 1.745 Å. ADP of proximal atoms were constrained to be equal, namely C131 & C132, Cl9 & Cl11, Cl10 & Cl12, Cl12 & Cl14, C132 & C133 Cl11 & Cl13

7.92 Crystallographic Data for [*trans*-Ru(dppe)$_2$Cl(=C=CH(C$_6$H$_4$-4-CF$_3$)]BF$_4$, [59g]BF$_4$

Identification code	jml1818_twin1_hklf4
Empirical formula	$C_{61}H_{53}ClF_9P_5Ru$
Formula weight	1248.40
Temperature/K	109.90(14)
Crystal system	monoclinic
Space group	$P2_1/n$
a/Å	20.0955(7)
b/Å	13.2932(4)
c/Å	21.6672(8)
α/°	90
β/°	107.340(4)
γ/°	90
Volume/Å^3	5525.0(3)
Z	4
ρ_{calc}g/cm^3	1.501
μ/mm^{-1}	4.716
F(000)	2544.0
Crystal size/mm^3	0.393 × 0.132 × 0.06
Radiation	CuKα (λ = 1.54184)
2Θ range for data collection/°	7.906 to 142.858
Index ranges	-24 ≤ h ≤ 18, -16 ≤ k ≤ 14, -26 ≤ l ≤ 26
Reflections collected	29019
Independent reflections	9946 [R_{int} = 0.1239, R_{sigma} = 0.1379]
Data/restraints/parameters	9946/216/679
Goodness-of-fit on F^2	1.007
Final R indexes [I>=2σ (I)]	R_1 = 0.0830, wR_2 = 0.1830
Final R indexes [all data]	R_1 = 0.1566, wR_2 = 0.2174
Largest diff. peak/hole / e Å^{-3}	2.42/-0.99

7.93 General Consideration for Computational Calculations

General considerations apply to all calculations unless otherwise outlined in the following sections. Calculations were performed with the TURBOMOLE V6.40 package using the resolution of identity (RI) approximation. Initial geometry optimisations were performed at the (RI-)BP86/SV(P) level followed by a frequency calculation at the same level. A 28 electron quasi-relativistic ECP replaced the core electrons of Ru. Transition states were located by initially performing a constrained minimisation (by freezing internal coordinates that change most during the reaction) of a structure close to the anticipated transition state. This was followed by a frequency calculation to identify the transition vector to follow during a subsequent transition state optimisation. A final frequency calculation was then performed on the optimised transition-state structure. All minima were confirmed as such by the absence of imaginary frequencies and all transition states were identified by the presence of only one imaginary frequency. All transition states were verified as connecting to the expected adjacent minima using the DRC module of TURBOMOLE (using an initial distortion length of 100, 50 cycles and a damping factor of 1). Dynamic reaction coordinate (DRC) calculations aim to follow a classical trajectory from a transition state to the minima on either side of it by moving along its imaginary vibrational mode.[372, 373] DRC calculations are similar to, but computationally less expensive than, intrinsic reaction coordinate (IRC) calculations, which attempt to find the minimum energy path (MEP) from the transition state to connecting minima.

Single-point calculations on the (RI-)BP86/SV(P) optimised geometries were performed using the hybrid PBE0 functional and the flexible def2-TZVPP basis set. The (RI-)PBE0/def2-TZVPP SCF energies were corrected for their zero-point energies, thermal energies and entropies (obtained from the (RI-)BP86/SV(P)-level frequency calculations). In all calculations, a 28 electron quasi-relativistic ECP replaced the core electrons of Ru. No symmetry constraints were applied during optimisations. All calculations were performed using the TURBOMOLE V6.40 package using the resolution of identity (RI) approximation.[363, 374-384] Solvation effects were modelled using the COSMO module of TURBOMOLE.[363] The pre-optimised gas-phase structures were computed in a single-point calculation at the (RI-)PBE0/def2-TZVPP level with solvent-corrected SCF energies. The dielectric constant used was dichloromethane (8.93 at 298 K).[385] Single-point DFT-D3 corrections (on the (RI-)BP86/SV(P) geometries) have been applied at the PBE0-D3 level using Grimme's DFT-D3 V3.0 Rev 2 program (with BJ-damping).[358-360]

All computational data can be found on the accompanying CD.

7.93.1 Chapter 2: Bond Dissociation Energies

In order to calculate accurate energies a number of calculations were performed using the G4 approach using Gaussian 09.[386] Bond dissociation energies were calculated using a modified procedure to that reported by Eisenstein and Perutz. The energies required for homolytic fission of C-H or C-F bonds were evaluated by calculating the difference between the zero-point energy-corrected electronic energies for all species involved. With the exception of the ruthenium complexes, geometry optimisations and frequency calculations were performed at the (RI-)PBE0/def2-TZVPP level. As noted previously,[387] hybrid functionals with greater than 22 % Hartree-Fock exchange are often required to obtain the correct geometries of alkynyl radicals. For the ruthenium complexes, geometry optimisations and frequency calculations were performed the (RI-)PBE0/SV(P) level and then single point calculations were then undertaken at the (RI-)PBE0/def2-TZVPP level. These energies were then corrected using the zero-point energies determined from the (RI-)PBE0/SV(P) calculations.

7.93.2 Chapter 2: Alkyne Dimerisation

Where required, broken-symmetry singlet diradical states were obtained from optimised triplet geometries using the “flip” function of the TURBOMOLE “define” script. This allows the user to select a localised alpha spin orbital involving a particular atom to become a beta spin orbital (or vice versa) to generate a broken symmetry (S = 0) state. Once suitable starting MOs had been obtained using this method, the geometries of the singlet diradical states were optimised from this point. Mulliken population analyses were performed on the converged wave functions to check that these did indeed correspond to the desired singlet diradical states.

7.93.3 Chapter 2: BCCD(T)-F12 calculations

Calculations at the CCSD(T)/cc-pVQZ level were performed using ORCA 3.03.[388-391] The computational details of the BCCD(T)-F12 calculations are as follows. The orbital basis set used was composed of the aug-cc-pVDZ sets for F, C and H, the aug-cc-pV(D+d)Z set for P and the aug-cc-pVDZ-PP set for Ru. The 28 electron effective core potential was used at the Ru atom to account for scalar relativistic effects. The accurate and efficient BCCD(F12*) approximation was used for the F12 treatment, with an exponent of 1 a_0 for the correlation factor. The 1s orbitals on the C and F atoms and the 1s2s2p orbitals on the P atoms were

excluded from the correlation treatment. For the complementary auxiliary basis set required for F12 calculations, double-zeta basis sets matching the orbital basis were taken from the Coulomb fitting basis sets. Triple-zeta quality basis sets were used for the density fitting approximation. The orbital plots presented in the manuscript result from semi-cannonicalisation of the Brueckner orbitals obtained from the coupled-cluster optimisation. The Slater determinant of these orbitals have maximal overlap with the correlated wavefunction and provide a qualitatively accurate molecular orbital picture of the electronic structure. Molecular geometries for HCCH, FCCH and FCCF were used from the calculations at the CCSD(T)/cc-pVQZ level (geometries and vibrational frequencies are given below), whereas for [CpRu(PH3)2(C≡C-H)] and [CpRu(PH3)2(C≡C-F)] the geometries were from the (RI-)PBE0/def2-TZVPP level.

7.93.4 Chapter 5: PES Scans

Direct fluorination of the alkynyl β-carbon of [*trans*-Ru(dppe)$_2$Cl(C≡C-C$_6$H$_5$)] by Selectfluor, FTMP BF_4, and NFSI, were investigated using relaxed PES scans (at the (RI-)PBE0/def2-TZVPP//(RI-)PBE0/SV(P) level with DCM solvent-correction. PES scans involved scanning along the reaction coordinate where a molecule of the fluorinating agent approaches the alkynyl β-carbon of [*trans*-Ru(dppe)$_2$Cl(C≡C-C$_6$H$_5$)]. A series of input structures were generated where the CF bond that is being formed was constrained to distances of between 3.0 and 1.4 Å in 0.1 Å steps, this was the only constraint applied. The geometries of these constrained structures were then optimised for the closed-shell singlet, triplet and singlet diradical states. Broken-symmetry singlet diradical states were obtained from the optimised triplet geometries using the “flip” function of the TURBOMOLE “define” script. This allows the user to select a localised alpha spin orbital involving a particular atom (Ru in this case) to become a beta spin orbital (or vice versa) to generate a broken symmetry (S = 0) state. Once suitable starting MOs had been obtained using this method, the geometries of the singlet diradical states were optimised from this point. Mulliken population analyses were performed on the converged wave functions to check that these did indeed correspond to the desired singlet diradical states. The geometries used in the relaxed PES scans for fluorination of [*trans*-Ru(dppe)$_2$Cl(C≡C-C$_6$H$_5$)] by Selectfluor were optimised with DCM solvent-correction.

Appendix I: Relaxed PES Scans

Table 33: [57b] + NFSI-Relative Solvated Electronic Energies

C-F Distance	Rel. E(elec)-DCM / kJ mol^{-1}		
	Closed-Shell Singlet	Triplet	Open-Shell Singlet
4.0 Angstrom	0	201	-
3.0 Angstrom	26	223	-
2.9 Angstrom	30	226	-
2.8 Angstrom	33	229	-
2.7 Angstrom	39	230	-
2.6 Angstrom	46	235	-
2.5 Angstrom	53	243	-
2.4 Angstrom	65	251	-
2.3 Angstrom	78	263	-
2.2 Angstrom	92	278	-
2.1 Angstrom	111	297	-
2.0 Angstrom	-34	-30	-
1.9 Angstrom	-57	-33	-
1.8 Angstrom	-85	-43	-
1.7 Angstrom	-118	-58	-
1.6 Angstrom	-151	-76	-
1.5 Angstrom	-192	-100	-
1.4 Angstrom	-214	-116	-
End point (fully relaxed)	-217	-119	-

Table 34: [57b] + [FTMP]BF_4- Relative Solvated Electronic Energies

	Rel. E(elec)-DCM / kJ mol^{-1}		
C-F Distance	Closed-Shell Singlet	Triplet	Open-Shell Singlet
4.0 Angstrom	0	4	-
3.0 Angstrom	14	21	-
2.9 Angstrom	19	24	-
2.8 Angstrom	24	27	-
2.7 Angstrom	29	31	-
2.6 Angstrom	32	35	-
2.5 Angstrom	40	41	39
2.4 Angstrom	50	47	44
2.3 Angstrom	62	54	48
2.2 Angstrom	15	-4	-
2.1 Angstrom	-1	-11	-
2.0 Angstrom	-21	-18	-
1.9 Angstrom	-44	-26	-
1.8 Angstrom	-73	-37	-
1.7 Angstrom	-106	-51	-
1.6 Angstrom	-140	-68	-
1.5 Angstrom	-170	-87	-
1.4 Angstrom	-189	-100	-
End point (fully relaxed)	-190	-101	-

Table 35: [57b] + Selectfluor- Relative Solvated Electronic Energies

	Rel. E(elec)-DCM / kJ mol^{-1}		
C-F Distance	Closed-Shell Singlet	Triplet	Open-Shell Singlet
4.0 Angstrom	0	-71	-81
3.0 Angstrom	6	-64	-57
2.9 Angstrom	8	-61	-54
2.8 Angstrom	10	-57	-51
2.7 Angstrom	13	-54	-47
2.6 Angstrom	17	-51	-43
2.5 Angstrom	22	-47	-39
2.4 Angstrom	29	-42	-34
2.3 Angstrom	-98	-36	-28
2.2 Angstrom	-106	-115	-
2.1 Angstrom	-117	-115	-
2.0 Angstrom	-131	-117	-
1.9 Angstrom	-148	-108	-
1.8 Angstrom	-170	-122	-
1.7 Angstrom	-194	-127	-
1.6 Angstrom	-221	-135	-
1.5 Angstrom	-244	-145	-
1.4 Angstrom	-257	-149	-
End point (fully relaxed)	-257	-164	-

Abbreviations

Å	Ångstrom
Ac	acetate
AIBN	2,2'-azo*bis*(2-methylpropionitrile)
App.	apparent
Ar	aromatic
b	broad
BCCD	Brueckner coupled-cluster
BDE	bond dissociation energy
BHT	2,6-di-*tert*-butyl-4-methylphenol
BO	Brueckner orbitals
Bpin	boron pinacolate
Bu	butyl
^{t}BuOH	*tert*-butanol
^{13}C	carbon-13
Cp / η^5-C_5H_5	cyclopentadienyl
Cp* / η^5-C_5Me_5	1,2,3,4,5-pentamethylcyclopentadienyl
cm	centimetres
cm^{-1}	wavenumbers
COSMO	conductor-like screening model
COSY	correlation spectroscopy
d	doublet
dd…	doublet of doublets….
dt…	doublet of triplets…
DCM	dichloromethane
DFT	density functional theory
DODS	different orbitals for different spins
dm	decimetre
DME	dimethoxyethane
dppe	1,2-*bis*(diphenylphosphino)ethane
EI	electron ionisation
EPR	electron paramagnetic resonance
eq. / equiv.	equivalents
ESI	electrospray ionisation
Et	ethyl
Et_2O	diethyl ether
^{19}F	fluorine-19
Fc	ferrocene
FDA	5'-fluoro-5'-deoxyadenosine
FEP	fluorinated ethylene propylene
[FTMP]	1-fluoro-2,4,6-trimethylpyridinium
g	grams
G	Gauss
GGA	generalised gradient approximation

h / hr	hours
^{1}H	proton
HF (Chapter 5)	Hartree Fock
HMBC	heteronuclear multiple bond correlation
HMDS	hexamethyldisilazane
HMQC	heteronuclear multiple quantum coherence
HOMO	highest occupied molecular orbital
HSQC	heteronuclear single quantum coherence
Hz	Hertz
ILCT	inter-ligand charge transfer
IR	infra-red
J	coupling constant
K	Kelvin
kJ	kilojoule
KS	Kohn Sham
L	ligand
LAPS	ligand-assisted proton shuttle
LDA	local-density approximation
LIFDI	liquid injection field desorption/ionisation
LiHMDS	lithium hexamethyldisilazide
LMCT	ligand-to-metal charge transfer
LUMO	lowest unoccupied molecular orbital
M	mol dm^{-3}
m	multiplet
m (prefix)	milli
mDA	milliDalton
Me	methyl
MeCN	acetonitrile
MeOH	methanol
mg	milligram
MHz	megahertz
min	minutes
mL	millilitre
MLCT	metal-to-ligand charge transfer
mmol	millimol
MO	molecular orbital
mol	mole
MS	mass spectrometry/ spectrum
m/z	mass/charge
^{n} (prefix)	*neo*
NFSI	*N*-fluorobenzenesulfonimde
NHC	*N*-heterocyclic carbene
nm	nanometre
NMR	nuclear magnetic resonance
OSEF	outer-sphere electrophilic fluorination
OTf	triflate

OTTLE cell	optically transparent thin layer electrochemical cell
^{31}P	phosphorus-31
PET	positron emission tomography
PFA	perfluoroalkoxy alkanes
Ph	phenyl
ppm	parts per million
PTFE	polytetrafluoroethylene
q	quartet
quin	quintet
RCY	radio chemical yield
RHF	restricted Hartree Fock
ROHF	restricted open Hartree Fock
rt	room temperature
s	singlet
SCF	self-consistent field
Selectfluor	1-chloromethyl-4-fluoro-1,,4-diazoniabicyclo[2.2.2]octane $2BF_4$
SET	single electron transfer
S_N2	bimolecular nucleophilic substitution
SV(P)	split valence plus polarisation
^{t} (prefix)	*tert*
t	triplet
td…	triplet of doublets…
tt…	triplet of triplets…
TD-DFT	time dependent density functional theory
TBAF	tetrabutylammonium fluoride
TEMPO	2,2,6,6-tetramethyl-1-piperidinyloxyl
THF	tetrahydrofuran
TMAF	tetrabutylammonium fluorine
TOF	time-of-flight
TREAT-HF	triethylamine trihydrogen fluoride
TS	transition state
TZVPP	triple-zeta valence plus polarisation
UHF	unrestricted Hartree Fock
UV-Vis	ultra-violet-visible
VT	variable temperature
ZPE	zero point energy
°	degrees
°C	degrees Celsius
δ	chemical shift
µL	microlitre
µmol	micromole

Glossary of Key Compounds

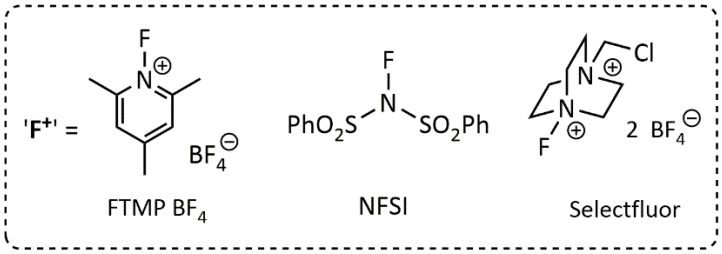

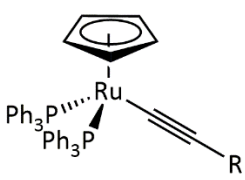

[14]

a R = ^{t}Bu
b R = C_6H_5
c R = C_6H_4-4-OMe
d R = C_6H_4-4-CF_3

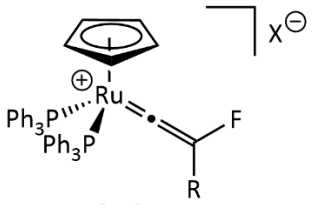

[15]

a R = ^{t}Bu
b R = C_6H_5
c R = C_6H_4-4-OMe
d R = C_6H_4-4-CF_3
X = BF_4 or NSI

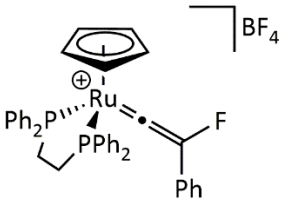

[19]BF_4

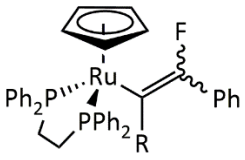

[23]

a R = F
b R = H

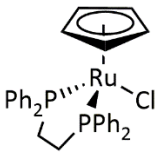

[24]

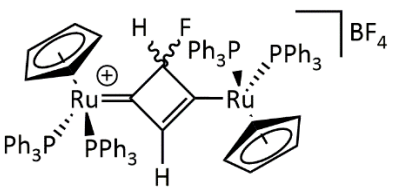

[27]BF_4

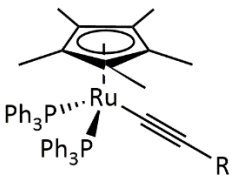

[28]

a R = H
b R = F

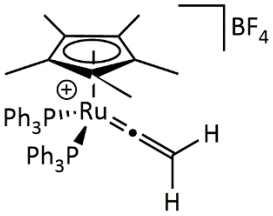

[29]BF_4

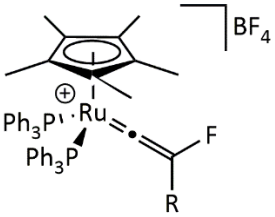

[30]BF_4

a R = H
b R = F

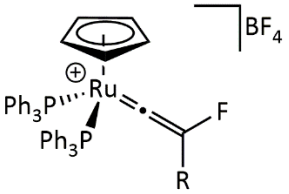

[44]BF_4

a R = H
b R = F

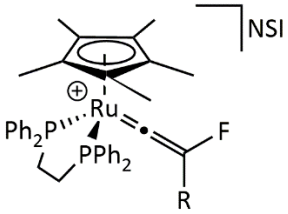

[54]NSI

a R = H
b R = F

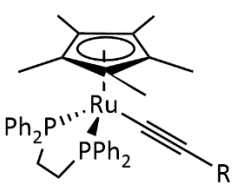

[55]

a R = H
b R = F

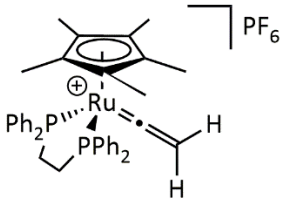

[56]PF_6

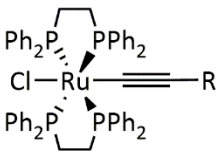

[57]

a R = H
b R = F
c R = C_6H_4-4-OMe
d R = C_6H_5
e R = C_6H_4-4-C(O)OMe

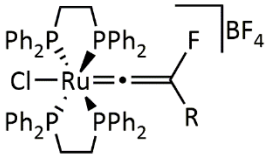

[58]BF_4

f R = C_6H_4-4-C(O)Me
g R = C_6H_4-4-CF_3
h R = C_6H_4-4-NO_2
i R = C_6H_4-4-NMe_2
j R = C_3H_5

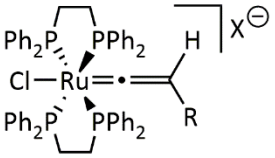

[59]BF_4

X = BF_4
NSI, PF_6

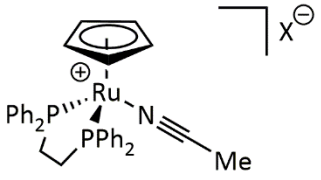

[68]$^+$
X = BF_4 or NSI

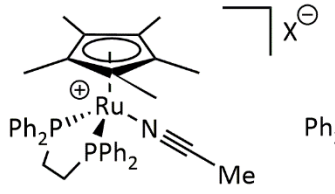

[71]$^+$
X = BF_4 or NSI

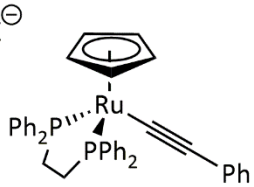

[77]

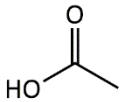

78

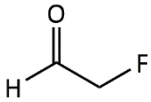

79

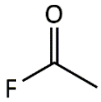

80

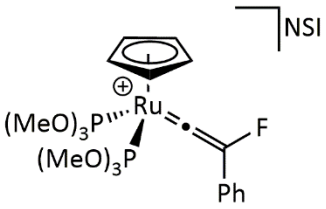

[82]NSI

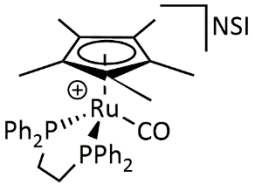

[85]NSI

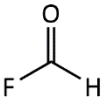

94

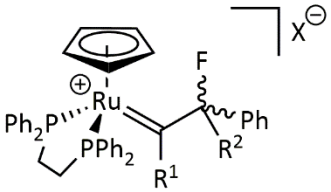

[104]$^+$
a R^1 = F, R^2 = H
b R^1 = F, R^2 = F
c R^1 = Cl, R^2 = H
X = BF_4 or Cl

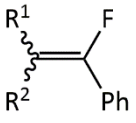

105

a R^1 = F, R^2 = H
b R^1 = F, R^2 = F
c R^1 = Cl, R^2 = F

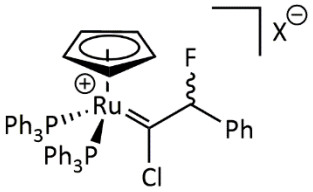

[112]$^+$
X = BF_4 or Cl

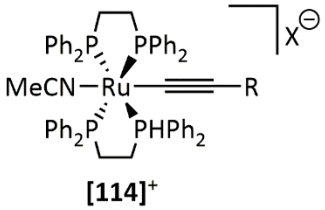

[114]$^+$
X = BF_4 or NSI

a R = H
b R = F
c R = C_6H_4-4-OMe
d R = C_6H_5
e R = C_6H_4-4-C(O)OMe

f R = C_6H_4-4-C(O)Me
g R = C_6H_4-4-CF_3
h R = C_6H_4-4-NO_2
i R = C_6H_4-4-NMe_2
j R = C_3H_5

References

1. M. Schlosser, *Angew. Chem. Int. Ed.*, 1998, **37**, 1497-1513.
2. C. D. Murphy, C. Schaffrath and D. O'Hagan, *Chemosphere*, 2003, **52**, 455-461.
3. R. Fuge and M. J. Andrews, *Environ. Geochem. Health*, 1988, **10**, 96-104.
4. G. W. Gribble, *Chemosphere*, 2003, **52**, 289-297.
5. C. Schaffrath, H. Deng and D. O'Hagan, *FEBS Lett.*, 2003, **547**, 111-114.
6. C. J. Dong, H. Deng, M. Dorward, C. Schaffrath, D. O'Hagan and J. H. Naismith, *Acta Crystallogr. D Biol. Crystallogr.*, 2003, **59**, 2292-2293.
7. C. J. Dong, F. L. Huang, H. Deng, C. Schaffrath, J. B. Spencer, D. O'Hagan and J. H. Naismith, *Nature*, 2004, **427**, 561-565.
8. C. D. Cadicamo, J. Courtieu, H. Deng, A. Meddour and D. O'Hagan, *Chembiochem*, 2004, **5**, 685-690.
9. P. Jeschke, *Chembiochem*, 2004, **5**, 570-589.
10. H. J. Bohm, D. Banner, S. Bendels, M. Kansy, B. Kuhn, K. Muller, U. Obst-Sander and M. Stahl, *Chembiochem*, 2004, **5**, 637-643.
11. K. Mueller, C. Faeh and F. Diederich, *Science*, 2007, **317**, 1881-1886.
12. C. Isanbor and D. O'Hagan, *J. Fluorine Chem.*, 2006, **127**, 303-319.
13. K. L. Kirk, *J. Fluorine Chem.*, 2006, **127**, 1013-1029.
14. S. Purser, P. R. Moore, S. Swallow and V. Gouverneur, *Chem. Soc. Rev.*, 2008, **37**, 320-330.
15. B. E. Smart, *J. Fluorine Chem.*, 2001, **109**, 3-11.
16. E. de Wolf, G. van Koten and B. J. Deelman, *Chem. Soc. Rev.*, 1999, **28**, 37-41.
17. I. T. Horvath and J. Rabai, *Science*, 1994, **266**, 72-75.
18. R. H. Fish, *Chem. Eur. J.*, 1999, **5**, 1677-1680.
19. E. G. Hope and A. M. Stuart, *J. Fluorine Chem.*, 1999, **100**, 75-83.
20. T. Imae, *Curr. Opin. Colloid Interface Sci.*, 2003, **8**, 307-314.
21. B. He, Y. Wang, N. Shao, H. Chang and Y. Cheng, *Acta Biomater.*, 2015, **22**, 111-119.
22. C. Dalvit, P. E. Fagerness, D. T. A. Hadden, R. W. Sarver and B. J. Stockman, *J. Am. Chem. Soc.*, 2003, **125**, 7696-7703.
23. R. E. London and S. A. Gabel, *J. Am. Chem. Soc.*, 1994, **116**, 2562-2569.
24. M. Kockerling and C. Mamat, *Int. J. Chem. Kinet.*, 2018, **50**, 31-40.
25. A. B. Shtarov, P. J. Krusic, B. E. Smart and W. R. Dolbier, *J. Am. Chem. Soc.*, 2001, **123**, 9956-9962.
26. R. E. London and S. A. Gabel, *J. Am. Chem. Soc.*, 1994, **116**, 2570-2575.
27. P. Espinet, A. C. Albeniz, J. A. Casares and J. M. Martinez-Ilarduya, *Coord. Chem. Rev.*, 2008, **252**, 2180-2208.
28. M. J. Avison, H. P. Hetherington and R. G. Shulman, *Annu. Rev. Biophys. Biophys. Chem.*, 1986, **15**, 377-402.
29. M. A. Danielson and J. J. Falke, *Annu. Rev. Biophys. Biomol. Struct.*, 1996, **25**, 163-195.
30. J. Ruiz-Cabello, B. P. Barnett, P. A. Bottomley and J. W. M. Bulte, *NMR Biomed.*, 2011, **24**, 114-129.
31. J. X. Yu, V. D. Kodibagkar, W. N. Cui and R. P. Mason, *Curr. Med. Chem.*, 2005, **12**, 819-848.
32. Y. G. Gakh, A. A. Gakh and A. M. Gronenborn, *Magn. Reson. Chem.*, 2000, **38**, 551-558.
33. J. C. Jackson, J. T. Hammill and R. A. Mehl, *J. Am. Chem. Soc.*, 2007, **129**, 1160-1166.
34. M. M. Alauddin, *Am. J. Nucl. Med. Mol. Imaging*, 2012, **2**, 55-76.

35. D. van der Born, A. Pees, A. J. Poot, R. V. A. Orru, A. D. Windhorst and D. J. Vugts, *Chem. Soc. Rev.*, 2017, **46**, 4709-4773.
36. D. O'Hagan and H. Deng, *Chem. Rev.*, 2015, **115**, 634-649.
37. G. S. Lal, G. P. Pez and R. G. Syvret, *Chem. Rev.*, 1996, **96**, 1737-1755.
38. J. L. Kiplinger, T. G. Richmond and C. E. Osterberg, *Chem. Rev.*, 1994, **94**, 373-431.
39. T. Ahrens, J. Kohlmann, M. Ahrens and T. Braun, *Chem. Rev.*, 2015, **115**, 931-972.
40. X. Yang, T. Wu, R. J. Phipps and F. D. Toste, *Chem. Rev.*, 2015, **115**, 826-870.
41. R. P. Singh and J. M. Shreeve, *Synthesis (Stuttg)*, 2002, 2561-2578.
42. R. P. Singh and J. M. Shreeve, *Acc. Chem. Res.*, 2004, **37**, 31-44.
43. M. G. Campbell and T. Ritter, *Chem. Rev.*, 2015, **115**, 612-633.
44. T. Liang, C. N. Neumann and T. Ritter, *Angew. Chem. Int. Ed.*, 2013, **52**, 8214-8264.
45. J. A. Ma and D. Cahard, *Chem. Rev.*, 2004, **104**, 6119-6146.
46. P. A. Champagne, J. Desroches, J. D. Hamel, M. Vandamme and J. F. Paquin, *Chem. Rev.*, 2015, **115**, 9073-9174.
47. J. Wu, *Tetrahedron Lett.*, 2014, **55**, 4289-4294.
48. D. P. Cox, J. Terpinski and W. Lawrynowicz, *J. Org. Chem.*, 1984, **49**, 3216-3219.
49. C. L. Liotta and H. P. Harris, *J. Am. Chem. Soc.*, 1974, **96**, 2250-2252.
50. G. Balz and G. Schiemann, *Ber. Dtsch. Chem. Ges.*, 1927, **60**, 1186-1190.
51. H. B. Gottlieb, *J. Am. Chem. Soc.*, 1936, **58**, 532-533.
52. H. Sun and S. G. DiMagno, *Angew. Chem. Int. Ed.*, 2006, **45**, 2720-2725.
53. A. J. Cresswell, S. G. Davies, P. M. Roberts and J. E. Thomson, *Chem. Rev.*, 2015, **115**, 566-611.
54. G. C. Finger and C. W. Kruse, *Journal of the American Chemical Society*, 1956, **78**, 6034-6037.
55. H. R. Sun and S. G. DiMagno, *J. Am. Chem. Soc.*, 2005, **127**, 2050-2051.
56. S. J. Ryan, S. D. Schimler, D. C. Bland and M. S. Sanford, *Org. Lett.*, 2015, **17**, 1866-1869.
57. G. Sandford, *J. Fluorine Chem.*, 2007, **128**, 90-104.
58. D. A. Watson, M. Su, G. Teverovskiy, Y. Zhang, J. Garcia-Fortanet, T. Kinzel and S. L. Buchwald, *Science*, 2009, **325**, 1661-1664.
59. P. S. Fier and J. F. Hartwig, *J. Am. Chem. Soc.*, 2012, **134**, 10795-10798.
60. E. Jimenez-Nunez and A. M. Echavarren, *Chem. Commun.*, 2007, 333-346.
61. V. A. Rassadin, V. P. Boyarskiy and V. Y. Kukushkin, *Org. Lett.*, 2015, **17**, 3502-3505.
62. L. Wang, L. Kong, Y. Li, R. Ganguly and R. Kinjo, *Chem. Commun.*, 2015, **51**, 12419-12422.
63. H. C. Shen, *Tetrahedron*, 2008, **64**, 7847-7870.
64. H. C. Shen, *Tetrahedron*, 2008, **64**, 3885-3903.
65. F. Alonso, I. P. Beletskaya and M. Yus, *Chem. Rev.*, 2004, **104**, 3079-3159.
66. J. A. Akana, K. X. Bhattacharyya, P. Mueller and J. P. Sadighi, *J. Am. Chem. Soc.*, 2007, **129**, 7736-7737.
67. B. C. Gorske, C. T. Mbofana and S. J. Miller, *Org. Lett.*, 2009, **11**, 4318-4321.
68. O. E. Okoromoba, J. Han, G. B. Hammond and B. Xu, *J. Am. Chem. Soc.*, 2014, **136**, 14381-14384.
69. M. C. Pacheco, S. Purser and V. Gouverneur, *Chem. Rev.*, 2008, **108**, 1943-1981.
70. A. Boukerb, D. Gree, M. Laabassi and R. Gree, *J. Fluorine Chem.*, 1998, **88**, 23-27.
71. M. H. Katcher, A. Sha and A. G. Doyle, *J. Am. Chem. Soc.*, 2011, **133**, 15902-15905.
72. C. Hollingworth, A. Hazari, M. N. Hopkinson, M. Tredwell, E. Benedetto, M. Huiban, A. D. Gee, J. M. Brown and V. Gouverneur, *Angew. Chem. Int. Ed.*, 2011, **50**, 2613-2617.
73. M. H. Katcher and A. G. Doyle, *J. Am. Chem. Soc.*, 2010, **132**, 17402-17404.
74. M. H. Katcher, P.-O. Norrby and A. G. Doyle, *Organometallics*, 2014, **33**, 2121-2133.

75. E. Benedetto, M. Tredwell, C. Hollingworth, T. Khotavivattana, J. M. Brown and V. Gouverneur, *Chem. Sci.*, 2013, **4**, 89-96.
76. K. L. Hull, W. Q. Anani and M. S. Sanford, *Journal of the American Chemical Society*, 2006, **128**, 7134-7135.
77. K. B. McMurtrey, J. M. Racowski and M. S. Sanford, *Org. Lett.*, 2012, **14**, 4094-4097.
78. T. Wu, G. Yin and G. Liu, *J. Am. Chem. Soc.*, 2009, **131**, 16354-+.
79. R. D. Chambers, T. Nakano, T. Okazoe and G. Sandford, *J. Fluorine Chem.*, 2009, **130**, 792-798.
80. C. B. McPake and G. Sandford, *Org. Process Res. Dev.*, 2012, **16**, 844-851.
81. C. B. McPake, C. B. Murray and G. Sandford, *Aust. J. Chem.*, 2013, **66**, 145-150.
82. A. Harsanyi and G. Sandford, *Green Chem.*, 2015, **17**, 3000-3009.
83. R. D. Chambers, M. P. Greenhall and J. Hutchinson, *Tetrahedron*, 1996, **52**, 1-8.
84. R. D. Chambers, J. Hutchinson, A. S. Batsanov, C. W. Lehmann and D. Y. Naumov, *J. Chem. Soc., Perk. Trans. 1*, 1996, 2271-2275.
85. J. Deyoung, H. Kawa and R. J. Lagow, *J. Chem. Soc., Chem. Commun.*, 1992, 811-812.
86. V. Snieckus, F. Beaulieu, K. Mohri, W. Han, C. K. Murphy and F. A. Davis, *Tetrahedron Lett.*, 1994, **35**, 3465-3468.
87. S. Yamada and P. Knochel, *Synthesis (Stuttg)*, 2010, 2490-2494.
88. P. Anbarasan, H. Neumann and M. Beller, *Angew. Chem. Int. Ed.*, 2010, **49**, 2219-2222.
89. V. V. Grushin, *Chem. Eur. J.*, 2002, **8**, 1006-1014.
90. T. Furuya and T. Ritter, *J. Am. Chem. Soc.*, 2008, **130**, 10060-10061.
91. N. D. Ball and M. S. Sanford, *Journal of the American Chemical Society*, 2009, **131**, 3796-3797.
92. T. Furuya, D. Benitez, E. Tkatchouk, A. E. Strom, P. Tang, W. A. Goddard, III and T. Ritter, *J. Am. Chem. Soc.*, 2010, **132**, 3793-3807.
93. J. R. Brandt, E. Lee, G. B. Boursalian and T. Ritter, *Chem. Sci.*, 2014, **5**, 169-179.
94. X. S. Wang, T. S. Mei and J. Q. Yu, *J. Am. Chem. Soc.*, 2009, **131**, 7520-7521.
95. K. S. L. Chan, M. Wasa, X. Wang and J.-Q. Yu, *Angew. Chem. Int. Ed.*, 2011, **50**, 9081-9084.
96. D. A. Gutierrez, W. C. C. Lee, Y. Shen and J. J. Li, *Tetrahedron Lett.*, 2016, **57**, 5372-5376.
97. C. Testa, E. Gigot, S. Genc, R. Decreau, J. Roger and J. C. Hierso, *Angew. Chem. Int. Ed.*, 2016, **55**, 5555-5559.
98. A. R. Mazzotti, M. G. Campbell, P. Tang, J. M. Murphy and T. Ritter, *J. Am. Chem. Soc.*, 2013, **135**, 14012-14015.
99. E. Lee, J. M. Hooker and T. Ritter, *J. Am. Chem. Soc.*, 2012, **134**, 17456-17458.
100. S. S. Stahl, J. A. Labinger and J. E. Bercaw, *Angew. Chem. Int. Ed.*, 1998, **37**, 2181-2192.
101. K. Yamamoto, J. K. Li, J. A. O. Garber, J. D. Rolfes, G. B. Boursalian, J. C. Borghs, C. Genicot, J. Jacq, M. van Gastel, F. Neese and T. Ritter, *Nature*, 2018, **554**, 511-514.
102. T. Furuya and T. Ritter, *Org. Lett.*, 2009, **11**, 2860-2863.
103. T. Furuya, A. E. Strom and T. Ritter, *J. Am. Chem. Soc.*, 2009, **131**, 1662-+.
104. P. Tang, T. Furuya and T. Ritter, *J. Am. Chem. Soc.*, 2010, **132**, 12150-12154.
105. I. A. I. Mkhalid, J. H. Barnard, T. B. Marder, J. M. Murphy and J. F. Hartwig, *Chem. Rev.*, 2010, **110**, 890-931.
106. S. R. Dubbaka, V. R. Narreddula, S. Gadde and T. Mathew, *Tetrahedron*, 2014, **70**, 9676-9681.
107. S. R. Dubbaka, S. Gadde and V. R. Narreddula, *Synthesis (Stuttg)*, 2015, **47**, 854-860.
108. C. Cazorla, E. Metay, B. Andrioletti and M. Lemaire, *Tetrahedron Lett.*, 2009, **50**, 3936-3938.

109. I. Vints, J. Gatenyo and S. Rozen, *J. Org. Chem.*, 2013, **78**, 11794-11797.
110. Y. Ye and M. S. Sanford, *J. Am. Chem. Soc.*, 2013, **135**, 4648-4651.
111. J. M. Racowski, J. B. Gary and M. S. Sanford, *Angew. Chem. Int. Ed.*, 2012, **51**, 3414-3417.
112. E. Emer, L. Pfeifer, J. M. Brown and V. Gouverneur, *Angew. Chem. Int. Ed.*, 2014, **53**, 4181-4185.
113. S. Qiu, T. Xu, J. Zhou, Y. Guo and G. Liu, *J. Am. Chem. Soc.*, 2010, **132**, 2856-2857.
114. S. B. Zhao, J. J. Becker and M. R. Gagne, *Organometallics*, 2011, **30**, 3926-3929.
115. A. Yahav, I. Goldberg and A. Vigalok, *J. Am. Chem. Soc.*, 2003, **125**, 13634-13635.
116. V. J. Scott, J. A. Labinger and J. E. Bercaw, *Abstr. Pap. Am. Chem. Soc.*, 2010, **239**.
117. M. S. Winston, W. J. Wolf and F. D. Toste, *J. Am. Chem. Soc.*, 2015, **137**, 7921-7928.
118. N. P. Mankad and F. D. Toste, *J. Am. Chem. Soc.*, 2010, **132**, 12859-12861.
119. N. P. Mankad and F. D. Toste, *Chem. Sci.*, 2012, **3**, 72-76.
120. S. Bloom, C. R. Pitts, D. C. Miller, N. Haselton, M. G. Holl, E. Urheim and T. Lectka, *Angew. Chem. Int. Ed.*, 2012, **51**, 10580-10583.
121. W. Liu, X. Huang, M.-J. Cheng, R. J. Nielsen, W. A. Goddard, III and J. T. Groves, *Science*, 2012, **337**, 1322-1325.
122. S. Bloom, C. R. Pitts, R. Woltornist, A. Griswold, M. G. Holl and T. Lectka, *Org. Lett.*, 2013, **15**, 1722-1724.
123. P. Xu, S. Guo, L. Wang and P. Tang, *Angew. Chem. Int. Ed.*, 2014, **53**, 5955-5958.
124. S. Thibaudeau and V. Gouverneur, *Org. Lett.*, 2003, **5**, 4891-4893.
125. W. M. Yuan, L. Eriksson and K. J. Szabo, *Angew. Chem. Int. Ed.*, 2016, **55**, 8410-8415.
126. A. Ford, H. Miel, A. Ring, C. N. Slattery, A. R. Maguire and M. A. McKervey, *Chem. Rev.*, 2015, **115**, 9981-10080.
127. C. Werle, R. Goddard, P. Philipps, C. Fares and A. Furstner, *J. Am. Chem. Soc.*, 2016, **138**, 3797-3805.
128. E. K. Leggans, T. J. Barker, K. K. Duncan and D. L. Boger, *Org. Lett.*, 2012, **14**, 1428-1431.
129. H. Shigehisa, E. Nishi, M. Fujisawa and K. Hiroya, *Org. Lett.*, 2013, **15**, 5158-5161.
130. Z. Li, Z. Wang, L. Zhu, X. Tan and C. Li, *J. Am. Chem. Soc.*, 2014, **136**, 16439-16443.
131. F. Yin, Z. Wang, Z. Li and C. Li, *J. Am. Chem. Soc.*, 2012, **134**, 10401-10404.
132. C. Zhang, Z. Li, L. Zhu, L. Yu, Z. Wang and C. Li, *J. Am. Chem. Soc.*, 2013, **135**, 14082-14085.
133. W. Yu, X.-H. Xu and F.-L. Qing, *Advanced Synthesis & Catalysis*, 2015, **357**, 2039-2044.
134. M. Rueda-Becerril, O. Mahe, M. Drouin, M. B. Majewski, J. G. West, M. O. Wolf, G. M. Sammis and J.-F. Paquin, *J. Am. Chem. Soc.*, 2014, **136**, 2637-2641.
135. S. Ventre, F. R. Petronijevic and D. W. C. MacMillan, *J. Am. Chem. Soc.*, 2015, **137**, 5654-5657.
136. C. R. Pitts, S. Bloom, R. Woltornist, D. J. Auvenshine, L. R. Ryzhkov, M. A. Siegler and T. Lectka, *J. Am. Chem. Soc.*, 2014, **136**, 9780-9791.
137. C. R. Pitts, B. Ling, R. Woltornist, R. Liu and T. Lectka, *J. Org. Chem.*, 2014, **79**, 8895-8899.
138. B. J. Groendyke, D. I. AbuSalim and S. P. Cook, *J. Am. Chem. Soc.*, 2016, **138**, 12771-12774.
139. H. Zhang, Y. Song, J. Zhao, J. Zhang and Q. Zhang, *Angew. Chem. Int. Ed.*, 2014, **53**, 11079-11083.
140. M. J. Frisch, R. Krishnan, J. A. Pople and P. V. Schleyer, *Chem. Phys. Lett.*, 1981, **81**, 421-423.
141. R. Krishnan, M. J. Frisch, J. A. Pople and P. V. Schleyer, *Chem. Phys. Lett.*, 1981, **79**, 408-411.

142. P. Dixneuf and C. Bruneau, *Metal Vinylidenes and Allenylidenes in Catalysis: From Reactivity to Applications in Synthesis*, WILEY-VCH Verlag GmbH & Co. KGaA, Weinheim, 2008.
143. R. F. C. Brown and F. W. Eastwood, *Synlett*, 1993, 9-19.
144. O. J. S. Pickup, I. Khazal, E. J. Smith, A. C. Whitwood, J. M. Lynam, K. Bolaky, T. C. King, B. W. Rawe and N. Fey, *Organometallics*, 2014, **33**, 1751-1761.
145. J. Breidung and W. Thiel, *J. Mol. Spectrosc.*, 2001, **205**, 28-37.
146. Z. H. Loh and R. W. Field, *J. Chem. Phys.*, 2003, **118**, 4037-4044.
147. B. Solaja, J. Huguet, M. Karpf and A. S. Dreiding, *Tetrahedron*, 1987, **43**, 4875-4886.
148. K. Schulz, J. Hofmann and G. Zimmermann, *Eur. J. Org. Chem.*, 1999, 3407-3412.
149. M. I. Bruce, *Chem. Rev.*, 1991, **91**, 197-257.
150. V. Cadierno, M. P. Gamasa and J. Gimeno, *Coord. Chem. Rev.*, 2004, **248**, 1627-1657.
151. M. C. Puerta and P. Valerga, *Coord. Chem. Rev.*, 1999, **193-5**, 977-1025.
152. F. De Angelis, A. Sgamellotti and N. Re, *Dalton Trans.*, 2004, 3225-3230.
153. J. M. Lynam, *Chem. Eur. J.*, 2010, **16**, 8238-8247.
154. H. Katayama and F. Ozawa, *Coord. Chem. Rev.*, 2004, **248**, 1703-1715.
155. P. J. Low and S. Bock, *Electrochimica Acta*, 2013, **110**, 681-692.
156. D. Touchard, P. Haquette, N. Pirio, L. Toupet and P. H. Dixneuf, *Organometallics*, 1993, **12**, 3132-3139.
157. Y. Wakatsuki, N. Koga, H. Yamazaki and K. Morokuma, *J. Am. Chem. Soc.*, 1994, **116**, 8105-8111.
158. M. A. J. Tenorio, M. J. Tenorio, M. C. Puerta and P. Valerga, *Organometallics*, 1997, **16**, 5528-5535.
159. Y. Wakatsuki, *J. Organomet. Chem.*, 2004, **689**, 4092-4109.
160. I. deLosRios, M. J. Tenorio, M. C. Puerta and P. Valerga, *Journal of the American Chemical Society*, 1997, **119**, 6529-6538.
161. D. B. Grotjahn, X. Zeng, A. L. Cooksy, W. S. Kassel, A. G. DiPasquale, L. N. Zakharov and A. L. Rheingold, *Organometallics*, 2007, **26**, 3385-3402.
162. M. J. Cowley, J. M. Lynam and J. M. Slattery, *Dalton Trans.*, 2008, 4552-4554.
163. B. Breit, U. Gellrich, T. Li, J. M. Lynam, L. M. Milner, N. E. Pridmore, J. M. Slattery and A. C. Whitwood, *Dalton Trans.*, 2014, **43**, 11277-11285.
164. D. G. Johnson, J. M. Lynam, J. M. Slattery and C. E. Welby, *Dalton Trans.*, 2010, **39**, 10432-10441.
165. J. Silvestre and R. Hoffmann, *Helv. Chim. Acta*, 1985, **68**, 1461-1506.
166. D. B. Grotjahn, X. Zeng and A. L. Cooksy, *J. Am. Chem. Soc.*, 2006, **128**, 2798-2799.
167. Y. Wakatsuki, N. Koga, H. Werner and K. Morokuma, *J. Am. Chem. Soc.*, 1997, **119**, 360-366.
168. J. R. Lomprey and J. P. Selegue, *J. Am. Chem. Soc.*, 1992, **114**, 5518-5523.
169. M. D. Fryzuk, L. Huang, N. T. McManus, P. Paglia, S. J. Rettig and G. S. White, *Organometallics*, 1992, **11**, 2979-2990.
170. M. Schafer, J. Wolf and H. Werner, *Organometallics*, 2004, **23**, 5713-5728.
171. T. B. Marder, D. Zargarian, J. C. Calabrese, T. H. Herskovitz and D. Milstein, *J. Chem. Soc., Chem. Commun.*, 1987, 1484-1485.
172. M. Olivan, E. Clot, O. Eisenstein and K. G. Caulton, *Organometallics*, 1998, **17**, 3091-3100.
173. M. Olivan, O. Eisenstein and K. G. Caulton, *Organometallics*, 1997, **16**, 2227-2229.
174. M. Tokunaga, T. Suzuki, N. Koga, T. Fukushima, A. Horiuchi and Y. Wakatsuki, *J. Am. Chem. Soc.*, 2001, **123**, 11917-11924.
175. A. J. Arita, J. Cantada, D. B. Grotjahn and A. L. Cooksy, *Organometallics*, 2013, **32**, 6867-6870.
176. D. Schneider and H. Werner, *Angew. Chem. Int. Ed.*, 1991, **30**, 700-702.

177. N. G. Connelly, A. G. Orpen, A. L. Rieger, P. H. Rieger, C. J. Scott and G. M. Rosair, *J. Chem. Soc., Chem. Commun.*, 1992, 1293-1295.
178. H. Werner, M. Baum, D. Schneider and B. Windmuller, *Organometallics*, 1994, **13**, 1089-1097.
179. H. Katayama, K. Onitsuka and F. Ozawa, *Organometallics*, 1996, **15**, 4642-4645.
180. J. Foerstner, A. Kakoschke, R. Goddard, J. Rust, R. Wartchow and H. Butenschon, *J. Organomet. Chem.*, 2001, **617**, 412-422.
181. M. Baum, N. Mahr and H. Werner, *Chemische Berichte*, 1994, **127**, 1877-1886.
182. D. C. Miller and R. J. Angelici, *Organometallics*, 1991, **10**, 79-89.
183. C. Lowe, H. U. Hund and H. Berke, *J. Organomet. Chem.*, 1989, **371**, 311-319.
184. M. Y. Lin, S. J. Maddirala and R. S. Liu, *Org. Lett.*, 2005, **7**, 1745-1748.
185. T. Miura, H. Murata, K. Kiyota, H. Kusama and N. Iwasawa, *J. Mol. Catal. A: Chem.*, 2004, **213**, 59-71.
186. Y. Ikeda, T. Yamaguchi, K. Kanao, K. Kimura, S. Kamimura, Y. Mutoh, Y. Tanabe and Y. Ishii, *J. Am. Chem. Soc.*, 2008, **130**, 16856-+.
187. Y. Mutoh, Y. Ikeda, Y. Kimura and Y. Ishii, *Chem. Lett.*, 2009, **38**, 534-535.
188. M. J. Shaw, S. W. Bryant and N. Rath, *Eur. J. Inorg. Chem.*, 2007, 3943-3946.
189. Y. Ikeda, S. Kodama, N. Tsuchida and Y. Ishii, *Dalton Trans.*, 2015, **44**, 17448-17452.
190. M. I. Bruce and G. A. Koutsantonis, *Aust. J. Chem.*, 1991, **44**, 207-217.
191. M. I. Bruce and A. G. Swincer, *Advances in Organometallic Chemistry*, 1983, **22**, 59-128.
192. M. I. Bruce and R. C. Wallis, *Aust. J. Chem.*, 1979, **32**, 1471-1485.
193. C. M. Widdifield and R. W. Schurko, *Concepts Magn. Reson. Part A*, 2009, **34A**, 91-123.
194. P. T. Czech, X. Q. Ye and R. F. Fenske, *Organometallics*, 1990, **9**, 2016-2022.
195. B. M. Trost and A. McClory, *Chem.-Asian J.*, 2008, **3**, 164-194.
196. C. Bruneau and P. H. Dixneuf, *Angew. Chem. Int. Ed.*, 2006, **45**, 2176-2203.
197. B. E. Bolandlussier, M. R. Churchill, R. P. Hughes and A. L. Rheingold, *Organometallics*, 1982, **1**, 628-634.
198. B. E. Bolandlussier and R. P. Hughes, *Organometallics*, 1982, **1**, 635-639.
199. P. C. Ting, Y. C. Lin, G. H. Lee, M. C. Cheng and Y. Wang, *J. Am. Chem. Soc.*, 1996, **118**, 6433-6444.
200. N. J. Beach, H. A. Jenkins and G. J. Spivak, *Organometallics*, 2003, **22**, 5179-5181.
201. R. G. Beevor, M. Green, A. G. Orpen and I. D. Williams, *J. Chem. Soc., Chem. Commun.*, 1983, 673-675.
202. R. G. Beevor, M. Green, A. G. Orpen and I. D. Williams, *Journal of the Chemical Society-Dalton Transactions*, 1987, 1319-1328.
203. A. J. L. Pombeiro, A. Hills, D. L. Hughes and R. L. Richards, *J. Organomet. Chem.*, 1988, **352**, C5-C7.
204. M. Fernanda, N. N. Carvalho, R. A. Henderson, A. J. L. Pombeiro and R. L. Richards, *J. Chem. Soc., Chem. Commun.*, 1989, 1796-1797.
205. A. Hohn and H. Werner, *Angew. Chem. Int. Ed.*, 1986, **25**, 737-738.
206. C. Kelley, N. Lugan, M. R. Terry, G. L. Geoffroy, B. S. Haggerty and A. L. Rheingold, *J. Am. Chem. Soc.*, 1992, **114**, 6735-6749.
207. T. Braun, P. Meuer and H. Werner, *Organometallics*, 1996, **15**, 4075-4077.
208. L. N. Novikova, M. G. Peterleitner, K. A. Sevumyan, O. V. Semeikin, D. A. Valyaev, N. A. Ustynyuk, V. N. Khrustalev, L. N. Kuleshova and M. Y. Antipin, *J. Organomet. Chem.*, 2001, **631**, 47-53.
209. K. Ouzzine, H. Lebozec and P. H. Dixneuf, *J. Organomet. Chem.*, 1986, **317**, C25-C27.
210. M. Murakami, M. Ubukata and Y. Ito, *Tetrahedron Lett.*, 1998, **39**, 7361-7364.

211. M. R. Terry, L. A. Mercando, C. Kelley, G. L. Geoffroy, P. Nombel, N. Lugan, R. Mathieu, R. L. Ostrander, B. E. Owenswaltermire and A. L. Rheingold, *Organometallics*, 1994, **13**, 843-865.
212. E. Elakkari, B. Floris, P. Galloni and P. Tagliatesta, *Eur. J. Org. Chem.*, 2005, 889-894.
213. Barry M. Trost and C.-J. Lin, *Modern Alkyne Chemistry: Catalytic and Atom-Economic Transformations*, Wiley-VCH Verlag GmbH & Co. KGaA, Weinheim, Germany, 2015.
214. T. Ohmura, S. Yorozuya, Y. Yamamoto and N. Miyaura, *Organometallics*, 2000, **19**, 365-367.
215. Y. Wakatsuki, H. Yamazaki, N. Kumegawa, T. Satoh and J. Y. Satoh, *J. Am. Chem. Soc.*, 1991, **113**, 9604-9610.
216. C. S. Yi and N. H. Liu, *Organometallics*, 1996, **15**, 3968-3971.
217. M. I. Bruce, G. A. Koutsantonis, M. J. Liddell and B. K. Nicholson, *J. Organomet. Chem.*, 1987, **320**, 217-227.
218. L. M. Milner, L. M. Hall, N. E. Pridmore, M. K. Skeats, A. C. Whitwood, J. M. Lynam and J. M. Slattery, *Dalton Trans.*, 2016, **45**, 1717-1726.
219. W. Schulze and K. Seppelt, *Inorganic Chemistry*, 1988, **27**, 3872-3873.
220. M. E. Slaney, D. J. Anderson, M. J. Ferguson, R. McDonald and M. Cowie, *J. Am. Chem. Soc.*, 2010, **132**, 16544-16558.
221. M. E. Slaney, M. J. Ferguson, R. McDonald and M. Cowie, *Organometallics*, 2012, **31**, 1384-1396.
222. D. J. Anderson, R. McDonald and M. Cowie, *Angew. Chem. Int. Ed.*, 2007, **46**, 3741-3744.
223. L. M. Milner, Mechanistic investigations of ruthenium-mediated reactions via vinylidene intermediates, PhD Thesis, University of York, 2016.
224. L. M. Hall, D. P. Tew, N. E. Pridmore, A. C. Whitwood, J. M. Lynam and J. M. Slattery, *Angew. Chem. Int. Ed.*, 2017, **56**, 7551-7556.
225. L. M. Milner, N. E. Pridmore, A. C. Whitwood, J. M. Lynam and J. M. Slattery, *J. Am. Chem. Soc.*, 2015, **137**, 10753-10759.
226. L. M. Hall, Electrophilic Fluorination of Organometallic Fragments, Masters Thesis, University of York, 2014.
227. W. J. Middleton and W. H. Sharkey, *J. Am. Chem. Soc.*, 1959, **81**, 803-804.
228. H. Burger and S. Sommer, *J. Chem. Soc., Chem. Commun.*, 1991, 456-458.
229. R. E. Banks, M. G. Barlow, W. D. Davies, R. N. Haszeldi, K. Mullen and D. R. Taylor, *Tetrahedron Lett.*, 1968, 3909-3910.
230. S. Y. Delavare and H. G. Viehe, *Chem. Ber.-Recl.*, 1970, **103**, 1209-&.
231. H. G. Viehe, R. Merenyi, J. F. M. Oth and P. Valange, *Angew. Chem. Int. Ed.*, 1964, **3**, 746.
232. Z. K. Yao and Z. X. Yu, *J. Am. Chem. Soc.*, 2011, **133**, 10864-10877.
233. H. G. Viehe, J. R. Senders, J. F. M. Oth, P. Valange and R. Merenyi, *Angew. Chem. Int. Ed.*, 1964, **3**, 755-&.
234. W. Q. Wu and H. F. Jiang, *Acc. Chem. Res.*, 2014, **47**, 2483-2504.
235. J. H. Bowie, M. I. Bruce, M. A. Buntine, A. S. Gentleman, D. C. Graham, P. J. Low, G. F. Metha, C. Mitchell, C. R. Parker, B. W. Skelton and A. H. White, *Organometallics*, 2012, **31**, 5262-5273.
236. M. I. Bruce, B. G. Ellis, M. Gaudio, C. Lapinte, G. Melino, F. Paul, B. W. Skelton, M. E. Smith, L. Toupet and A. H. White, *Dalton Trans.*, 2004, 1601-1609.
237. L. Dahlenburg, A. Weiss and M. Moll, *J. Organomet. Chem.*, 1997, **535**, 195-200.
238. I. Kaljurand, A. Kutt, L. Soovali, T. Rodima, V. Maemets, I. Leito and I. A. Koppel, *J. Org. Chem.*, 2005, **70**, 1019-1028.
239. K. Onitsuka, M. Nishii, Y. Matsushima and S. Takahashi, *Organometallics*, 2004, **23**, 5630-5632.

240. N. J. Brown, M. A. Fox, M. E. Smith, D. S. Yufit, J. A. K. Howard and P. J. Low, *J. Organomet. Chem.*, 2009, **694**, 4042-4048.
241. M. I. Bruce, B. G. Ellis, P. J. Low, B. W. Skelton and A. H. White, *Organometallics*, 2003, **22**, 3184-3198.
242. D. O'Hagan, *Chem. Soc. Rev.*, 2008, **37**, 308-319.
243. N. Gauthier, N. Tchouar, F. Justaud, G. Argouarch, M. P. Cifuentes, L. Toupet, D. Touchard, J.-F. Halet, S. Rigaut, M. G. Humphrey, K. Costuas and F. Paul, *Organometallics*, 2009, **28**, 2253-2266.
244. D. Touchard, P. Haquette, S. Guesmi, L. LePichon, A. Daridor, L. Toupet and P. H. Dixneuf, *Organometallics*, 1997, **16**, 3640-3648.
245. S. Rigaut, J. Perruchon, L. Le Pichon, D. Touchard and P. H. Dixneuf, *J. Organomet. Chem.*, 2003, **670**, 37-44.
246. M. A. Fox, J. E. Harris, S. Heider, V. Perez-Gregorio, M. E. Zakrzewska, J. D. Farmer, D. S. Yufit, J. A. K. Howard and P. J. Low, *J. Organomet. Chem.*, 2009, **694**, 2350-2358.
247. H. A. Bent, *Chem. Rev.*, 1961, **61**, 275-311.
248. W. A. Bernett, *J. Org. Chem.*, 1969, **34**, 1772-&.
249. H. Huang, R. P. Hughes, C. R. Landis and A. L. Rheingold, *J. Am. Chem. Soc.*, 2006, **128**, 7454-7455.
250. C. J. Pell, Y. J. Zhu, R. Huacuja, D. E. Herbert, R. P. Hughes and O. V. Ozerov, *Chem. Sci.*, 2017, **8**, 3178-3186.
251. T. Meiresonne, G. Verniest, N. De Kimpe and S. Mangelinckx, *J. Org. Chem.*, 2015, **80**, 5111-5124.
252. S. Y. Delavare and H. G. Viehe, *Chem. Ber.-Recl.*, 1970, **103**, 1198-1208.
253. G. Herzberg, *Molecular spectra and molecular structure II,Infrared and Raman spectra of polyatomic molecules*, Van Nostrand Reinhold, New York, 2nd edn., 1945.
254. L. Andrews, G. L. Johnson and B. J. Kelsall, *J. Phys. Chem.*, 1982, **86**, 3374-3380.
255. J. Breidung, T. Hansen and W. Thiel, *J. Mol. Spectrosc.*, 1996, **179**, 73-78.
256. M. Kaupp, B. Metz and H. Stoll, *Angew. Chem. Int. Ed.*, 2000, **39**, 4607-+.
257. P. Politzer and D. Habibollahzadeh, *J. Chem. Phys.*, 1993, **98**, 7659-7660.
258. A. Trujillo, M. Fuentealba, R. Arratia-Perez and J. A. K. Howard, *Acta Crystallogr. Sect. Sect. E: Struct. Rep. Online*, 2012, **68**, M1445.
259. E. Clot, O. Eisenstein, N. Jasim, S. A. Macgregor, J. E. McGrady and R. N. Perutz, *Acc. Chem. Res.*, 2011, **44**, 333-348.
260. M. E. Evans, C. L. Burke, S. Yaibuathes, E. Clot, O. Eisenstein and W. D. Jones, *J. Am. Chem. Soc.*, 2009, **131**, 13464-13473.
261. M. Bassetti, V. Cadierno, J. Gimeno and C. Pasquini, *Organometallics*, 2008, **27**, 5009-5016.
262. V. Cadierno, M. P. Gamasa, J. Gimeno, C. Gonzalez-Bernardo, E. Perez-Carreno and S. Garcia-Granda, *Organometallics*, 2001, **20**, 5177-5188.
263. V. Cadierno, M. P. Gamasa, J. Gimeno, E. Perez-Carreno and S. Garcia-Granda, *Organometallics*, 1999, **18**, 2821-2832.
264. Y. Mutoh, K. Imai, Y. Kimura, Y. Ikeda and Y. Ishii, *Organometallics*, 2011, **30**, 204-207.
265. M. Otsuka, N. Tsuchida, Y. Ikeda, Y. Kimura, Y. Mutoh, Y. Ishii and K. Takano, *J. Am. Chem. Soc.*, 2012, **134**, 17746-17756.
266. S. Solyntjes, B. Neumann, H. G. Stammler, N. Ignat'ev and B. Hoge, *Eur. J. Inorg. Chem.*, 2016, 3999-4010.
267. F. Klanberg and Muettert.El, *Inorganic Chemistry*, 1968, **7**, 155-&.
268. K. S. Singh, Y. A. Mozharivskyj and M. R. Kollipara, *Z. Anorg. Allg. Chem.*, 2006, **632**, 172-179.

269. N. R. Babij, E. O. McCusker, G. T. Whiteker, B. Canturk, N. Choy, L. C. Creemer, C. V. De Amicis, N. M. Hewlett, P. L. Johnson, J. A. Knobelsdorf, F. Z. Li, B. A. Lorsbach, B. M. Nugent, S. J. Ryan, M. R. Smith and Q. Yang, *Org. Process Res. Dev.*, 2016, **20**, 661-667.
270. M. I. Bruce and M. G. Humphrey, *Aust. J. Chem.*, 1989, **42**, 1067-1075.
271. L. Hintermann, L. Xiao, A. Labonne and U. Englert, *Organometallics*, 2009, **28**, 5739-5748.
272. M. I. Bruce, M. P. Cifuentes, M. R. Snow and E. R. T. Tiekink, *J. Organomet. Chem.*, 1989, **359**, 379-399.
273. F. Morandini, A. Dondana, I. Munari, G. Pilloni, G. Consiglio, A. Sironi and M. Moret, *Inorg. Chim. Acta*, 1998, **282**, 163-172.
274. M. I. Bruce, B. G. Benjamin, B. W. Skelton and A. H. White, *J. Organomet. Chem.*, 2005, **690**, 792-801.
275. J. Steinreiber, K. Fesko, C. Mayer, C. Reisinger, M. Schurmann and H. Griengl, *Tetrahedron*, 2007, **63**, 8088-8093.
276. D. D. Steiner, N. Mase and C. F. Barbas, *Angew. Chem. Int. Ed.*, 2005, **44**, 3706-3710.
277. B. M. Trost, G. Dyker and R. J. Kulawiec, *J. Am. Chem. Soc.*, 1990, **112**, 7809-7811.
278. G. M. Lee, R. Clement and R. T. Baker, *Catal. Sci. Technol.*, 2017, **7**, 4996-5003.
279. N. Muller and D. T. Carr, *J. Phys. Chem.*, 1963, **67**, 112-115.
280. R. P. Hughes, R. B. Laritchev, J. Yuan, J. A. Golen, A. N. Rucker and A. L. Rheingold, *J. Am. Chem. Soc.*, 2005, **127**, 15020-15021.
281. C. J. Bourgeois, R. P. Hughes, J. Yuan, A. G. DiPasquale and A. L. Rheingold, *Organometallics*, 2006, **25**, 2908-2910.
282. R. P. Hughes, *J. Fluorine Chem.*, 2010, **131**, 1059-1070.
283. D. J. Harrison, S. I. Gorelsky, G. M. Lee, I. Korobkov and R. T. Baker, *Organometallics*, 2013, **32**, 12-15.
284. D. J. Harrison, A. L. Daniels, I. Korobkov and R. T. Baker, *Organometallics*, 2015, **34**, 5683-5686.
285. G. R. Clark, S. V. Hoskins, T. C. Jones and W. R. Roper, *J. Chem. Soc., Chem. Commun.*, 1983, 719-721.
286. J. Yuan, R. P. Hughes, J. A. Golen and A. L. Rheingold, *Organometallics*, 2010, **29**, 1942-1947.
287. D. J. Harrison, G. M. Lee, M. C. Leclerc, I. Korobkov and R. T. Baker, *J. Am. Chem. Soc.*, 2013, **135**, 18296-18299.
288. G. M. Lee, D. J. Harrison, I. Korobkov and R. T. Baker, *Chem. Commun.*, 2014, **50**, 1128-1130.
289. J. T. Fuller, D. J. Harrison, M. C. Leclerc, R. T. Baker, D. H. Ess and R. P. Hughes, *Organometallics*, 2015, **34**, 5210-5213.
290. D. J. Harrison, A. L. Daniels, J. Guan, B. M. Gabidullin, M. B. Hall and R. T. Baker, *Angew. Chem. Int. Ed.*, 2018, **57**, 5772-5776.
291. Q. B. Liu and D. J. Burton, *J. Fluorine Chem.*, 2011, **132**, 78-87.
292. J. Kvicala, R. Hrabal, J. Czernek, I. Bartosova, O. Paleta and A. Pelter, *J. Fluorine Chem.*, 2002, **113**, 211-218.
293. P. L. Heinze and D. J. Burton, *J. Org. Chem.*, 1988, **53**, 2714-2720.
294. S. Martin, R. Sauvetre and J. F. Normant, *J. Organomet. Chem.*, 1986, **303**, 317-320.
295. F. Nahra, S. R. Patrick, D. Bello, M. Brill, A. Obled, D. B. Cordes, A. M. Z. Slawin, D. O'Hagan and S. P. Nolan, *ChemCatChem*, 2015, **7**, 240-244.
296. *Unpublished crystallograhic data obtained from PhD student Rachel Steen*.
297. J. D. Galloway, D. N. Mai and R. D. Baxter, *Org. Lett.*, 2017, **19**, 5772-5775.
298. B. He, Z. W. Xiao, H. Wu, Y. Guo, Q. Y. Chen and C. Liu, *RSC Adv.*, 2017, **7**, 880-883.
299. C. F. Ye and J. M. Shreeve, *J. Org. Chem.*, 2004, **69**, 8561-8563.

300. A. Alhalib, S. Kamouka and W. J. Moran, *Org. Lett.*, 2015, **17**, 1453-1456.
301. L. T. Ball, M. Green, G. C. Lloyd-Jones and C. A. Russell, *Org. Lett.*, 2010, **12**, 4724-4727.
302. Y. Q. Yang, Y. Lin and Y. Rao, *Org. Lett.*, 2012, **14**, 2874-2877.
303. H. Wang, S. B. Ren, J. Zhang, W. Zhang and Y. K. Liu, *J. Org. Chem.*, 2015, **80**, 6856-6863.
304. N. G. Connelly and W. E. Geiger, *Chem. Rev.*, 1996, **96**, 877-910.
305. F. Paul, B. G. Ellis, M. I. Bruce, L. Toupet, T. Roisnel, K. Costuas, J. F. Halet and C. Lapinte, *Organometallics*, 2006, **25**, 649-665.
306. S. P. Vincent, M. D. Burkart, C. Y. Tsai, Z. Y. Zhang and C. H. Wong, *J. Org. Chem.*, 1999, **64**, 5264-5279.
307. A. C. Albeniz, P. Espinet, R. Lopez-Fernandez and A. Sen, *J. Am. Chem. Soc.*, 2002, **124**, 11278-11279.
308. M. Newcomb and M. B. Manek, *J. Am. Chem. Soc.*, 1990, **112**, 9662-9663.
309. S. W. Wu, J. L. Liu and F. Liu, *Chem. Commun.*, 2017, **53**, 12321-12324.
310. M. A. Fox, R. L. Roberts, W. M. Khairul, F. Hartl and P. J. Low, *J. Organomet. Chem.*, 2007, **692**, 3277-3290.
311. V. I. Sorokin, A. F. Pozharskii and V. A. Ozeryanskii, *J. Fluorine Chem.*, 2013, **154**, 67-72.
312. B. I. Halperin, M. Krska, E. Levy and C. A. Vanderwerf, *J. Am. Chem. Soc.*, 1951, **73**, 1857-1858.
313. J. L. Fillaut, J. Andries, R. D. Marwaha, P. H. Lanoe, O. Lohio, L. Toupet and J. A. G. Williams, *J. Organomet. Chem.*, 2008, **693**, 228-234.
314. J. L. Fillaut, N. N. Dua, F. Geneste, L. Toupet and S. Sinbandhit, *J. Organomet. Chem.*, 2006, **691**, 5610-5618.
315. T. Umemoto, K. Harasawa, G. Tomizawa, K. Kawada and K. Tomita, *Bull. Chem. Soc. Jpn.*, 1991, **64**, 1081-1092.
316. S. Guckel, J. B. G. Gluyas, S. El-Tarhuni, A. N. Sobolev, M. W. Whiteley, J. F. Halet, C. Lapinte, M. Kaupp and P. J. Low, *Organometallics*, 2018, **37**, 1432-1445.
317. N. Lenarvor and C. Lapinte, *Organometallics*, 1995, **14**, 634-639.
318. N. Lenarvor and C. Lapinte, *J. Chem. Soc., Chem. Commun.*, 1993, 357-359.
319. E. C. Fitzgerald, N. J. Brown, R. Edge, M. Helliwell, H. N. Roberts, F. Tuna, A. Beeby, D. Collison, P. J. Low and M. W. Whiteley, *Organometallics*, 2012, **31**, 157-169.
320. M. I. Bruce, K. Costuas, T. Davin, J. F. Halet, K. A. Kramarczuk, P. J. Low, B. K. Nicholson, G. J. Perkins, R. L. Roberts, B. W. Skelton, M. E. Smith and A. H. White, *Dalton Trans.*, 2007, 5387-5399.
321. H. J. Jiao, K. Costuas, J. A. Gladysz, J. F. Halet, M. Guillemot, L. Toupet, F. Paul and C. Lapinte, *J. Am. Chem. Soc.*, 2003, **125**, 9511-9522.
322. M. Brady, W. Q. Weng, Y. L. Zhou, J. W. Seyler, A. J. Amoroso, A. M. Arif, M. Bohme, G. Frenking and J. A. Gladysz, *J. Am. Chem. Soc.*, 1997, **119**, 775-788.
323. M. I. Bruce, P. J. Low, K. Costuas, J. F. Halet, S. P. Best and G. A. Heath, *J. Am. Chem. Soc.*, 2000, **122**, 1949-1962.
324. M. Parthey, J. B. G. Gluyas, P. A. Schauer, D. S. Yufit, J. A. K. Howard, M. Kaupp and P. J. Low, *Chem. Eur. J.*, 2013, **19**, 9780-9784.
325. J. B. G. Gluyas, S. Guckel, M. Kaupp and P. J. Low, *Chem. Eur. J.*, 2016, **22**, 16138-16146.
326. A. L. G. Inzelt, F. Scholz, *Handbook of Reference of Electrodes*, Springer, Heidelberg New York Dordrecht London, 2013.
327. Y. B. Zhu, D. B. Millet, M. O. Wolf and S. J. Rettig, *Organometallics*, 1999, **18**, 1930-1938.

328. C. P. Andrieux, E. Differding, M. Robert and J. M. Saveant, *J. Am. Chem. Soc.*, 1993, **115**, 6592-6599.
329. A. G. Gilicinski, G. P. Pez, R. G. Syvret and G. S. Lal, *J. Fluorine Chem.*, 1992, **59**, 157-162.
330. E. Differding and P. M. Bersier, *Tetrahedron*, 1992, **48**, 1595-1604.
331. G. P. Girina, A. A. Fainzil'berg and L. G. Feoktistov, *Russ. J. Electrochem.*, 2000, **36**, 162-163.
332. T. Umemoto, S. Fukami, G. Tomizawa, K. Harasawa, K. Kawada and K. Tomita, *J. Am. Chem. Soc.*, 1990, **112**, 8563-8575.
333. H. Yamataka, Y. Kawafuji, K. Nagareda, N. Miyano and T. Hanafusa, *J. Org. Chem.*, 1989, **54**, 4706-4708.
334. T. Holm and Crosslan.I, *Acta Chem. Scand.*, 1971, **25**, 59-69.
335. T. M. Bockman, K. Y. Lee and J. K. Kochi, *J. Chem. Soc., Perk. Trans. 2*, 1992, 1581-1594.
336. K. Y. Lee and J. K. Kochi, *J. Chem. Soc., Perk. Trans. 2*, 1992, 1011-1017.
337. K. U. Ingold and D. A. Pratt, *Chem. Rev.*, 2014, **114**, 9022-9046.
338. D. Griller and K. U. Ingold, *Acc. Chem. Res.*, 1980, **13**, 317-323.
339. X. Zhang, *J. Mol. Struct.*, 2011, **1002**, 121-127.
340. E. Differding and G. M. Ruegg, *Tetrahedron Lett.*, 1991, **32**, 3815-3818.
341. G. Bucher and J. C. Scaiano, *J. Am. Chem. Soc.*, 1994, **116**, 10076-10079.
342. E. Differding and M. Wehrli, *Tetrahedron Lett.*, 1991, **32**, 3819-3822.
343. F. Jenson, *Introduction to Computational Chemistry*, John Wiley & Sons, Chichester, West Sussex, England, 2007.
344. P. Hohenberg and W. Kohn, *Phys. Rev. B: Condens. Matter*, 1964, **136**, B864-B871.
345. W. Kohn and L. J. Sham, *Phys. Rev.*, 1965, **140**, 1133-1137.
346. A. Jaoul, G. Nocton and C. Clavaguera, *Chemphyschem*, 2017, **18**, 2688-2696.
347. Y. Zhao and D. G. Truhlar, *Theor. Chem. Acc.*, 2008, **120**, 215-241.
348. M. Walker, A. J. A. Harvey, A. Sen and C. E. H. Dessent, *J. Phys. Chem. A*, 2013, **117**, 12590-12600.
349. A. S. Tiwary and A. K. Mukherjee, *Chem. Phys. Lett.*, 2014, **610**, 19-22.
350. S. Shil, D. Bhattacharya, S. Sarkar and A. Misra, *J. Phys. Chem. A*, 2013, **117**, 4945-4955.
351. N. Mardirossian and M. Head-Gordon, *J. Chem. Theory Comput.*, 2013, **9**, 4453-4461.
352. N. Mardirossian and M. Head-Gordon, *J. Chem. Theory Comput.*, 2016, **12**, 4303-4325.
353. M. G. Medvedev, I. S. Bushmarinov, J. W. Sun, J. P. Perdew and K. A. Lyssenko, *Science*, 2017, **355**, 49-52.
354. F. Neese, *J. Phys. Chem. Solids*, 2004, **65**, 781-785.
355. F. Neese, *Coord. Chem. Rev.*, 2009, **253**, 526-563.
356. O. V. Gritsenko, B. Ensing, P. R. T. Schipper and E. J. Baerends, *J. Phys. Chem. A*, 2000, **104**, 8558-8565.
357. T. D. Crawford and H. F. Schaefer, in *Reviews in Computational Chemistry, Vol 14*, eds. K. B. Lipkowitz and D. B. Boyd, 2000, vol. 14, pp. 33-136.
358. S. Grimme, *J. Comput. Chem.*, 2004, **25**, 1463-1473.
359. S. Grimme, *J. Comput. Chem.*, 2006, **27**, 1787-1799.
360. S. Grimme, J. Antony, S. Ehrlich and H. Krieg, *J. Chem. Phys.*, 2010, **132**, 19.
361. A. Klamt and G. Schuurmann, *J. Chem. Soc., Perk. Trans. 2*, 1993, 799-805.
362. A. Klamt, *Wiley Interdiscip. Rev.-Comput. Mol. Sci.*, 2011, **1**, 699-709.
363. A. Schafer, A. Klamt, D. Sattel, J. C. W. Lohrenz and F. Eckert, *PCCP*, 2000, **2**, 2187-2193.
364. U. Koelle and J. Kossakowski, *J. Organomet. Chem.*, 1989, **362**, 383-398.

365. C. E. Willans, A Combinatorial Approach to Non-Cyclopentadienyl Lanthanide Complexes and their Activity in polymerisation; Derivatisation of Cyclic Phosphorus-Rich Structures, PhD Thesis, University of York, 2006.
366. A. G. Alonso and L. B. Reventos, *J. Organomet. Chem.*, 1988, **338**, 249-254.
367. Y. Ogiwara, D. Sakino, Y. Sakurai and N. Sakai, *Eur. J. Org. Chem.*, 2017, 4324-4327.
368. CrysalisPro, 1.171.33.36d.
369. R. C. Clark and J. S. Reid, *Acta Crystallogr. Sect. A*, 1995, **51**, 887-897.
370. O. V. Dolomanov, L. J. Bourhis, R. J. Gildea, J. A. K. Howard and H. Puschmann, *J. Appl. Crystallogr.*, 2009, **42**, 339-341.
371. G. M. Sheldrick, *Acta Crystallogr. Sect. A*, 2008, **64**, 112-122.
372. J. J. P. Stewart, L. P. Davis and L. W. Burggraf, *J. Comput. Chem.*, 1987, **8**, 1117-1123.
373. S. A. Maluendes and M. Dupuis, *J. Chem. Phys.*, 1990, **93**, 5902-5911.
374. P. Csaszar and P. Pulay, *J. Mol. Struct.*, 1984, **114**, 31-34.
375. R. Ahlrichs, M. Bar, M. Haser, H. Horn and C. Kolmel, *Chem. Phys. Lett.*, 1989, **162**, 165-169.
376. K. Eichkorn, O. Treutler, H. Ohm, M. Haser and R. Ahlrichs, *Chem. Phys. Lett.*, 1995, **240**, 283-289.
377. K. Eichkorn, F. Weigend, O. Treutler and R. Ahlrichs, *Theor. Chem. Acc.*, 1997, **97**, 119-124.
378. O. Treutler and R. Ahlrichs, *J. Chem. Phys.*, 1995, **102**, 346-354.
379. M. von Arnim and R. Ahlrichs, *J. Chem. Phys.*, 1999, **111**, 9183-9190.
380. P. Deglmann, F. Furche and R. Ahlrichs, *Chem. Phys. Lett.*, 2002, **362**, 511-518.
381. P. Deglmann, K. May, F. Furche and R. Ahlrichs, *Chem. Phys. Lett.*, 2004, **384**, 103-107.
382. F. Furche, R. Ahlrichs, C. Hattig, W. Klopper, M. Sierka and F. Weigend, *Wiley Interdiscip. Rev.-Comput. Mol. Sci.*, 2014, **4**, 91-100.
383. P. Deglmann and F. Furche, *J. Chem. Phys.*, 2002, **117**, 9535-9538.
384. A. Baldes and F. Weigend, *Mol. Phys.*, 2013, **111**, 2617-2624.
385. W. H. Haynes, *CRC Handbook of Chemistry and Physics*, CRC Press, Taylor & Francis Group, Boca Raton, Fluorida, USA, 2011.
386. M. J. Frisch, G. W. Trucks, H. B. Schlegel, G. E. Scuseria, M. A. Robb, J. R. Cheeseman, G. Scalmani, V. Barone, B. Mennucci, G. A. Petersson, H. Nakatsuji, M. Caricato, X. Li, H. P. Hratchian, A. F. Izmaylov, J. Bloino, G. Zheng, J. L. Sonnenberg, M. Hada, M. Ehara, K. Toyota, R. Fukuda, J. Hasegawa, M. Ishida, T. Nakajima, Y. Honda, O. Kitao, H. Nakai, T. Vreven, J. A. M. Jr., J. E. Peralta, F. Ogliaro, M. J. Bearpark, J. Heyd, E. N. Brothers, K. N. Kudin, V. N. Staroverov, R. Kobayashi, J. Normand, K. Raghavachari, A. P. Rendell, J. C. Burant, S. S. Iyengar, J. Tomasi, M. Cossi, N. Rega, N. J. Millam, M. Klene, J. E. Knox, J. B. Cross, V. Bakken, C. Adamo, J. Jaramillo, R. Gomperts, R. E. Stratmann, O. Yazyev, A. J. Austin, R. Cammi, C. Pomelli, J. W. Ochterski, R. L. Martin, K. Morokuma, V. G. Zakrzewski, G. A. Voth, P. Salvador, J. J. Dannenberg, S. Dapprich, A. D. Daniels, Ö. Farkas, J. B. Foresman, J. V. Ortiz, J. Cioslowski and D. J. Fox, *Gaussian 09, Gaussian, Inc., Wallingford, CT, USA*.
387. V. B. Oyeyemi, J. A. Keith, M. Pavone and E. A. Carter, *J. Phys. Chem. Lett.*, 2012, **3**, 289-293.
388. F. Wennmohs and F. Neese, *Chem. Phys.*, 2008, **343**, 217-230.
389. F. Neese, A. Hansen, F. Wennmohs and S. Grimme, *Acc. Chem. Res.*, 2009, **42**, 641-648.
390. C. Kollmar and F. Neese, *Mol. Phys.*, 2010, **108**, 2449-2458.
391. F. Neese, *Wiley Interdiscip. Rev.-Comput. Mol. Sci.*, 2012, **2**, 73-78.